

# A COMPREHENSIVE KINETICS MODEL FOR CO OXIDATION DURING CHAR COMBUSTION

Greg Haussmann and Charles Kruger

Department of Mechanical Engineering  
Stanford University, Stanford, CA 94305

## INTRODUCTION:

The most important parameter in representing energy feedback to a particle during char combustion concerns the oxidation of CO to CO<sub>2</sub>. If substantial oxidation of CO occurs near a particle, then the greater heat of combustion for the complete oxidation of carbon to CO<sub>2</sub> (94.1 kcal/mole vs. 26.4 kcal/mole for oxidation to CO) is available for energy feedback mechanisms. "Energy feedback" is here defined as any situation in which an individual particle receives a significant fraction of its heat of combustion directly, through the localized oxidation of emitted combustible species, i.e. CO. Conversely, if the oxidation of CO does not occur near a particle, then energy feedback will only occur indirectly, through heating of the bulk gas. The primary reaction product at the particle surface during char combustion is generally considered to be CO, and the location of the subsequent CO oxidation zone plays a very important role in determining the particle temperature. Ayling and Smith (1) performed experimental and modeling work which indicates that CO oxidation is not of major importance under the conditions they investigated, although they noted a need for improved accuracy in measuring char reactivities, as well as for better modeling of the gas phase CO oxidation kinetics. The modeling work presented in this paper attempts to develop an improved understanding of the boundary layer oxidation of CO through the use of a comprehensive set of kinetics expressions. It is hoped that the use of a fundamental set of kinetics expressions will more accurately represent the transient conditions occurring around an oxidizing char particle, when compared to the use of global kinetics expressions. The transport and energy equations are solved, generating both species and temperature profiles surrounding a single particle.

## MODEL DEVELOPMENT:

The CO oxidation model developed at Stanford currently employs a number of assumptions, which are listed in Table 1. One critical assumption used is the restriction that the only mass fluxes at the particle surface are CO and O<sub>2</sub>. The species mass transport equation used assume convective and diffusive transport only, with source terms calculated from the kinetics expressions. The gas phase reactions are modeled through the use of a subset of a set of expressions developed by Westbrook, et al (2) to study the pyrolysis and oxidation of ethylene. This subset is listed in Table 2. The success of this model in predicting the properties of a laminar ethylene flame suggests that it is also valid for the more simple fuels contained as subsets (i.e. CO ).

The basic equation for mass transport in the particle boundary layer is below.

$$\underbrace{\frac{d}{dr} \left[ \frac{\rho_1}{\rho} \dot{m}_c 4\pi r^2 \right]}_{\text{Convection}} - \underbrace{\frac{d}{dr} \left[ 4\pi r^2 \rho D_1 \frac{d}{dr} (\rho_1/\rho) \right]}_{\text{Diffusion}} = \underbrace{4\pi r^2 \dot{p}_1}_{\text{Source}} \quad (1)$$

where

- $\rho_1$  = Mass fraction of species 1  
 $\rho$  = Density of local gas mixture, gm/cm<sup>3</sup>  
 $\dot{m}_c''$  = Carbon flux at particle surface, gm/cm<sup>2</sup>/sec  
 $a$  = Particle radius, cm  
 $D_1$  = Diffusion coefficient for species 1, cm<sup>2</sup>/sec  
 $\dot{p}_1$  = Source term for species 1 (from kinetics), gm/cm<sup>3</sup>/sec

Equation 1 is non-dimensionalized through the use of the parameters below.

- $y = a/r$  Non-dimensional coordinate  
 $x_1 = (\rho_1/\rho)_\infty$  Non-dimensional mass fraction  
 $\beta_1 = (\rho_1/\rho)_\infty \rho D_1 / (a \dot{m}_c'')$  Non-dimensional diffusion coefficient  
 $S_1 = a \dot{p}_1 / (y^4 \dot{m}_c'')$  Non-dimensional source term

The resulting form for the transport equation is:

$$F_1 = (\rho_1/\rho)_\infty x_1 + \beta_1 \frac{dx_1}{dy} \quad 2a)$$

$$\frac{dF_1}{dy} = -S_1 \quad 2b)$$

In equation 2a, the term  $F_1$  represents a non-dimensional flux, for species 1. The two equations above are solved, with the boundary conditions being:

$$x_1(y=1) = 1$$

$$F_1(y=1) = 0 \text{ except for:}$$

$$F_{CO}(y=1) = 28/12$$

$$F_{O_2}(y=1) = -16/12$$

$$\text{For } i = CO, CO_2, O_2, Ar, H_2O, O, H, OH, H_2$$

The mass transport equations in the boundary layer are solved along with a simple form of the energy equation, which is similar to the transport equation used.

$$K_g \frac{d}{dr} r^2 \frac{dT}{dr} - C_g \dot{m}_c'' a^2 \frac{dT}{dr} = r^2 \dot{q}''' \quad 3)$$

where      Conduction      Convection      Source

$K_g$  = The average bulk thermal conductivity, erg/cm sec K

$C_g$  = The average bulk heat capacity, erg/gm K

As with the species transport equation, this equation is transformed into non-dimensional coordinates.

$$\frac{d^2 T}{dy^2} + \left[ \frac{C_g \dot{m}'' a}{K_g} \right] \frac{dT}{dy} - \left[ \frac{a^2}{K_g y^4} \right] \dot{q}'''(y) = 0 \quad (4)$$

The solution procedure utilized to solve the mass and energy transport equations is outlined in Table 3. The solution is first broken down into two components. The first part,  $x_{1,1}(y)$  represents the solution to the homogenous portion of equations 2a and 2b, i.e. with no gas phase reactions occurring ( $S_1 = 0$ ). In this case the homogeneous solution takes a particularly simple analytical form.

$$x_{1,1}(y) = \frac{F_1}{(\rho_1/\rho)_\infty} + \left[ 1 - \frac{F_1}{(\rho_1/\rho)_\infty} \right] \exp\left[ \frac{-(\rho_1/\rho)_\infty y}{D_1} \right] \quad (5)$$

The complete solution is then represented as the sum of this homogeneous term and an inhomogeneous term,  $x_1'(y)$ . The boundary conditions on this inhomogeneous term now become particularly simple, being  $x_1'(y=1) = 0$ . One nice feature of this solution technique is that it allows the general character of the solution to be calculated immediately (the homogeneous solution), while the more difficult inhomogeneous portion can be dealt with separately. The inhomogeneous portion represents a very stiff equation, and a relaxation technique is applied to reach a solution. The species and energy equations are solved in series, as indicated in Table 3, and this procedure is repeated until a desired convergence criterion has been achieved.

#### MODEL RESULTS:

The input parameters required for this model, and the typical "base case" values used, are listed in Table 4. The values for the base case have been chosen to match conditions measured experimentally in the Stanford flow-tube reactor, in which the independent variation of many of the important reaction parameters is possible, in particular the bulk gas temperature, the oxygen concentration, and the particle size. For the current modeling results the input parameters have been independently varied around the single base case determined from the flow-tube reactor, without attempting to represent the interdependencies of the parameters. The base case value for the char reactivity at 1800K of 0.03 gm carbon/cm<sup>2</sup>/sec agrees very well with typical values measured for char reactivities (Smith (3)), although the free stream species concentrations in the Stanford flow-tube reactor can be significantly different than those found in typical pulverized coal combustion applications. The importance of this will be discussed later.

A typical temperature profile in the particle boundary layer is presented in Figure 1. The lower curve is the solution with no gas phase reactions, while the upper curve shows the effect of CO oxidation in the boundary layer. The case chosen is one in which the greatest effect of boundary layer CO oxidation was observed, although all cases show similar profiles. In both curves the particle temperature is substantially above the bulk gas temperature (by about 500K), with this temperature overshoot increased by about 60K when gas phase CO oxidation was included. Figure 1 indicates that one way to represent the effect of CO oxidation on the particle temperature would be to look at the increase in the particle surface temperature over that with no gas phase CO oxidation. This parameter has been calculated while parametrically varying the variables listed in Table 4, and the results are discussed below.

The dependence of the bulk gas oxygen concentration is seen in Figure 2. The dependence is a reasonably strong one, although for the conditions studied the temperature increase due to CO oxidation in the boundary layer is fairly low. Thus

the energy feedback due to CO oxidation, while not negligible, is not considered to be a dominant mechanism under these conditions. It is important to note that although the base case chosen indicates little CO oxidation in the boundary layer, the trends observed will give the relative importance of the various parameters studied.

The dependence on the bulk gas water concentration is seen in Figure 3. This parameter is important due to the limiting gas phase reaction  $\text{CO} + \text{OH} \rightarrow \text{CO}_2 + \text{H}$ . At low concentrations there is a strong dependence of the temperature increase due to CO oxidation in the boundary layer on the bulk gas water concentration, and this dependence tails off at higher concentrations. One reason that the temperature increase is relatively low for the base case considered in the current study is that the water concentrations present in the Stanford reactor are relatively low. The only source of water in the Stanford flow-tube reactor is the moisture and hydrogen present in the coal fed into the reactor, and the relatively low particle concentrations present ( $< 10$  particles/cm<sup>3</sup>) results in low water concentrations. Future work will consider conditions in which the water concentrations are at higher values, since this looks like a crucial parameter in studying gas phase CO oxidation, and many pulverized coal combustion environments involve water concentrations substantially above those seen in the Stanford flow-tube reactor.

The dependence of the temperature increase on the char reactivity is seen in Figure 4. The temperature increase is a relatively strong function of the char reactivity, but eventually becomes less important. This leveling off of the curve is the result of two competing processes. As the char reactivity is increased, the amount of CO present in the particle boundary layer increases, which increases the energy release due to CO oxidation near the particle. A competing effect with this is the resulting increase of the convective term in the heat transfer equation, which tends to reduce the feedback of energy released in the boundary layer back to the particle as the char reactivity increases. The net effect of these two processes is the leveling off of the curve seen in Figure 4.

The dependence on the particle radius is seen in Figure 5. It is important to note that the char reactivity has been held constant in this parametric run, while in reality the char reactivity is a strong function of the particle radius, and this must be taken into consideration in order to better represent the true effect of the particle radius. For a fixed reactivity, however, the temperature increase due to CO oxidation is a strong function of the particle radius, a quadratic type of dependence. This is due primarily to the increased heat transfer from a smaller particle to the surroundings, which tends to lessen the effect of boundary layer CO oxidation. The actual effect of particle size is some combination of this effect with the strong increase in the particle reactivity as the radius is decreased. These two effects result in opposing trends, so the net effect of the particle radius is not clear at this point.

The dependence on the bulk gas temperature is seen in Figure 6. Again there is an interdependence between this parameter and the char reactivity, a very strong influence which is not represented in the current modeling work. As expected, the effect of CO oxidation in the boundary layer is a very strong (exponential) function of the bulk gas temperature. A temperature increase of about 60K is seen at a bulk gas temperature of 2000K. When the accompanying effect of the char reactivity dependence on the temperature is included, an even stronger dependence of the temperature increase due to CO oxidation is expected.

## CONCLUSIONS:

For the conditions studied, the effect of CO oxidation in the boundary layer during char combustion does not appear to be of major importance. It is important to note that the model input parameters studied were designed to simulate conditions present in the Stanford flow-tube reactor, and that the importance of boundary layer CO oxidations in typical pulverized coal combustion environments has not yet been studied with this model.

The interdependencies between the model input parameters need to be modeled in order to better represent the actual processes occurring during CO oxidation. In particular, the parameters which indicate the possibility of a strong synergistic interaction are the water concentration, oxygen concentration, and/or the bulk gas temperature with the char reactivity.

The model results indicate the relative importance of the various parameters. The water concentration is considered to be a crucial parameter for two reasons. First, it has a strong influence on OH concentration in the particle boundary layer, which in turn plays a dominant role in the oxidation kinetics of CO. Secondly, many pulverized coal combustion environments are expected to have substantially higher water concentrations than that chosen for the base case condition used with this model. Other parameters which appear to be very important are the bulk gas temperature and the oxygen concentration, especially when their influence on the char reactivity is taken into account.

## REFERENCES:

1. Ayling, A.B. and I.W. Smith, "Measured Temperatures of Burning Pulverized-Fuel Particles, and the Nature of the Primary Reaction Product", *Combustion and Flame*, V 18, 1972, pp. 173-184.
2. Westbrook, C.K., Dryer, F.L., and Schug, K.P., "A Comprehensive Mechanism for the Pyrolysis and Oxidation of Ethylene", 19<sup>th</sup> Symposium (Int'l) on Combustion, The Combustion Institute, 1982, pp. 153-166.
3. I.W. Smith, "The Combustion Rates of Coal Chars: a Review", 19<sup>th</sup> Symposium (Int'l) on Combustion, The Combustion Institute, 1982, pp. 1045-1065.

TABLE 1. ASSUMPTIONS

- Steady State.
- Diffusive and convective transport only.
- Constant particle radius.
- Spherical symmetry.
- Surface mass flux is given.
- CO and O<sub>2</sub> are the only surface fluxes.
- Quiescent atmosphere.
- HO<sub>2</sub> and H<sub>2</sub>O<sub>2</sub> are unimportant at the temperatures studied.
- Convective and Conductive gas phase heat transfer only.

TABLE 2. REACTIONS CONSIDERED

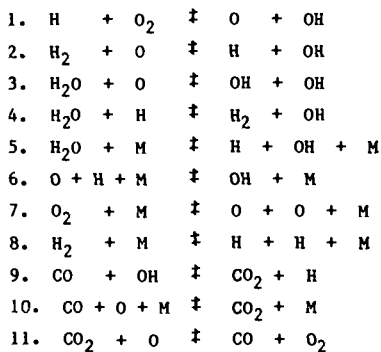


TABLE 3. SOLUTION PROCEDURE

SOLVE FOR A "FIRST CUT" VERSION,  $x_{1,1}(y)$

$$B_1 \frac{dx_1}{dy} + (\rho_1/\rho)_\infty = F_1 \quad 1)$$

with  $F_1 = 0$  except  $F_{CO} = 28/12$ ,  $F_{O2} = -16/12$

NOW WRITE THE SOLUTION AS  $x_1 = x_{1,1} + x'_1$

where  $x'_1$  satisfies the equation .....

$$D_1 \frac{dx'_1}{dy} + (\rho_1/\rho)_\infty = F_1(y) \quad 2)$$

with all  $x'_1(y=0) = 0$

Use  $x_1(y)$  and the current temperature profile to calculate the terms  $S_1(y)$  and  $\dot{q}'''(y)$  from the kinetics expressions.

Integrate  $S_1(y)$  to get a new  $F_1(y)$

SOLVE EQUATION 2) USING THIS  $F_1(y)$ , 4<sup>th</sup> Order Runge-Kutta Routine Used

THE SOLUTION IS THE NEW VALUE FOR  $x'_1(y)$

SOLVE THE ENERGY EQUATION, GIVEN  $\dot{q}'''(y)$  (See next page)

REPEAT UNTIL THE SYSTEM CONVERGES

TABLE 3. SOLUTION PROCEDURE (cont.)

The Energy Equation:

$$\frac{d^2 T}{dy^2} + \left[ \frac{C_g \dot{m}''_c a}{K_g} \right] \frac{dT}{dy} - \left[ \frac{a^2}{K_g y^4} \right] \dot{q}'''(y) = 0 \quad 3)$$

Given a particle temperature, the temperature gradient at the particle surface  $\left[ \frac{dT}{dy} (y=1) \right]$  is calculated from an energy balance.

$$\frac{dT}{dy} (y=1) = \frac{a \dot{m}''_c}{K_g} (\text{factor}) - \frac{a \epsilon \sigma T_p}{K_g} + \frac{a \sigma}{K_g} T_w^4$$

where  
 factor = ergs released per gram carbon oxidized to CO  
 $\epsilon$  = emissivity of the char particle (taken as 0.9)  
 $\sigma$  = the Stefan-Boltzman radiation constant

Given these initial conditions, Equation 3 is solved with a 4<sup>th</sup> order Runge-Kutta routine, marching from  $y = 1$  to  $y = 0$ .

The calculated value  $T(y=0)$  is compared with the bulk gas temperature, and the procedure is repeated until convergence is obtained. (Shooting method).

TABLE 4. INPUT PARAMETERS

$\dot{m}''_c = .01, .02, \underline{.03}, .04, .05 \text{ gm/cm}^2/\text{sec}$

$T_g = 1600, 1700, \underline{1800}, 1900, 2000 \text{ K}$

$a = 10, 20, 30, \underline{40}, 50, 60 \text{ microns}$

Species Mass Fractions at infinity:

$O_2 = .0040, \underline{.0820}, .0.124, .0.167, .0.211$

$H_2O = 0.00046, \underline{0.0023}, .0.0046, .0.0116, .0.0236$

$CO_2 = 0.0056$

$CO, O, H, OH, H_2 =$  Calculated from chemical equilibrium.

Ar = The balance.

NOTE: The underlined quantities represent the "base case", measured from experimental results with the Stanford reactor.



## TEMPERATURE PROFILES

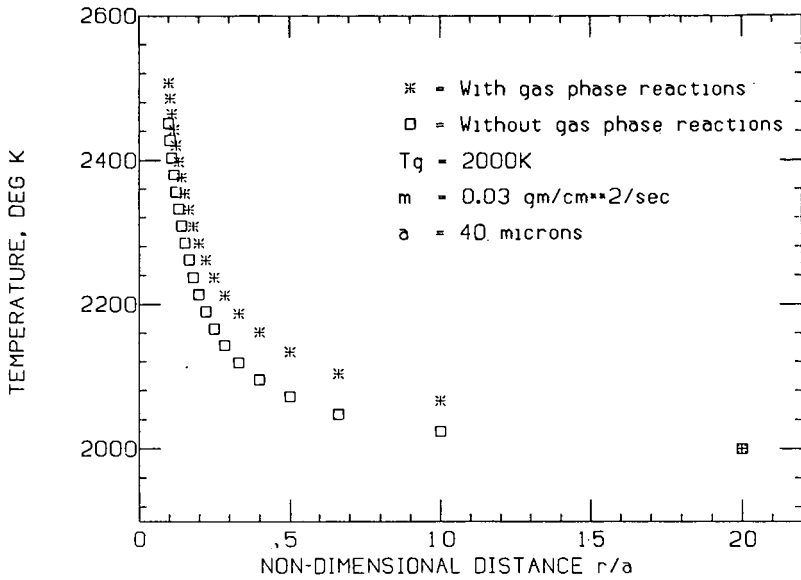


Figure 1. Temperature Profiles.

## OXYGEN CONCENTRATION DEPENDENCE

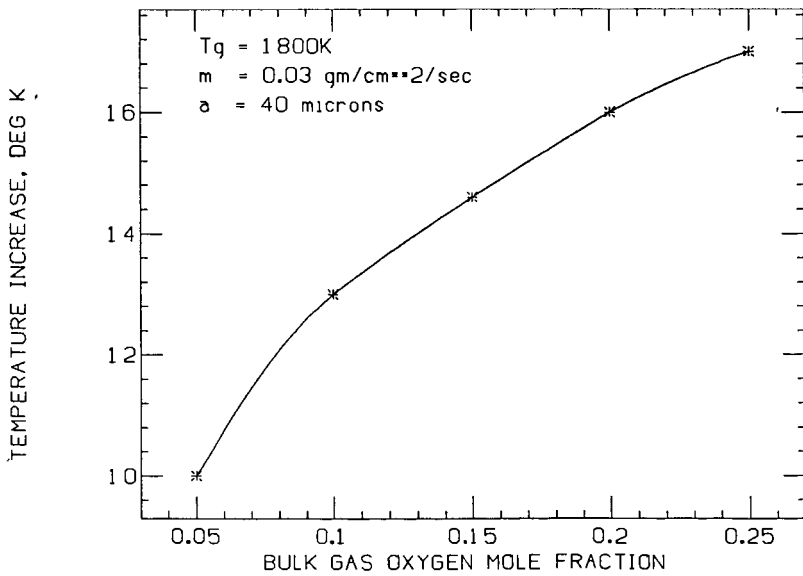


Figure 2. Oxygen Concentration Dependence.

### WATER CONCENTRATION DEPENDENCE

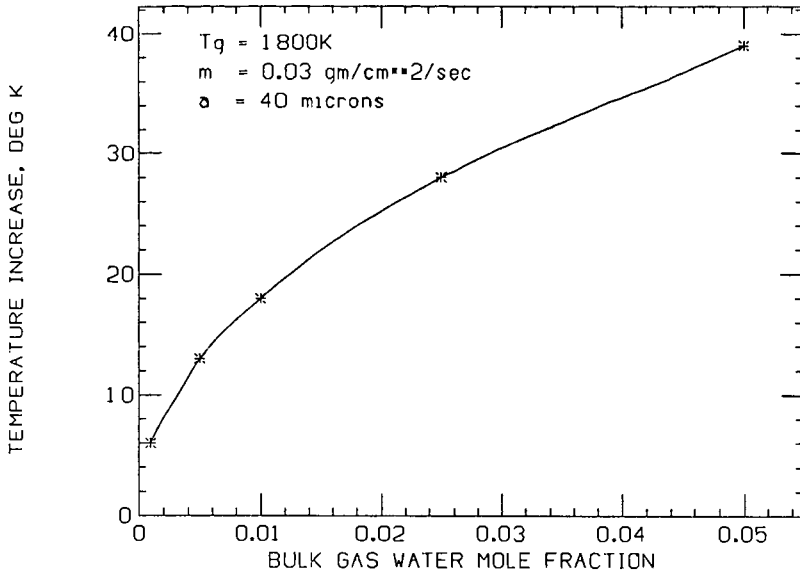


Figure 3. Water Concentration Dependence.

### CHAR REACTIVITY DEPENDENCE

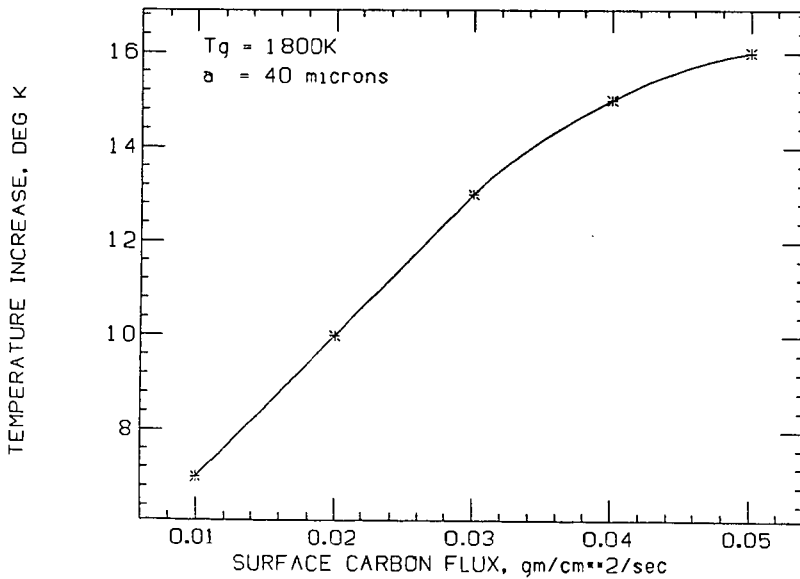


Figure 4. Char Reactivity Dependence.

## PARTICLE RADIUS DEPENDENCE

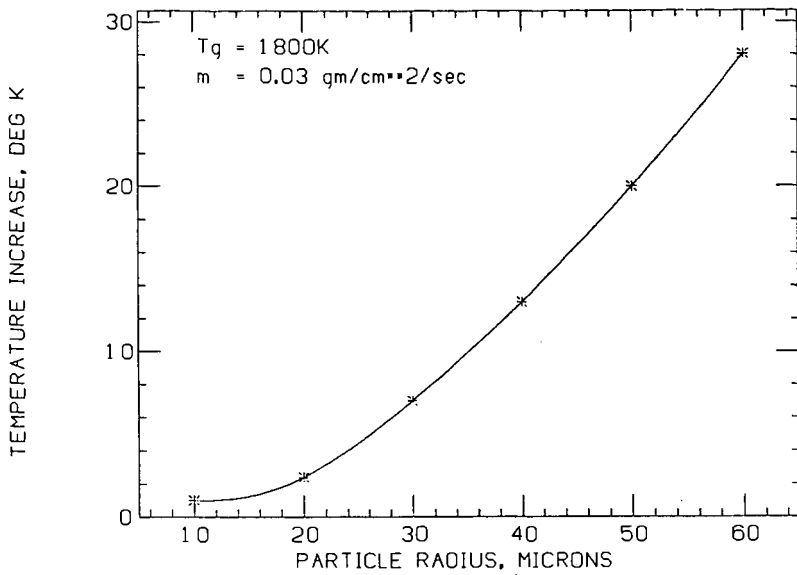


Figure 5. Particle Radius Dependence.

## BULK GAS TEMPERATURE DEPENDENCE

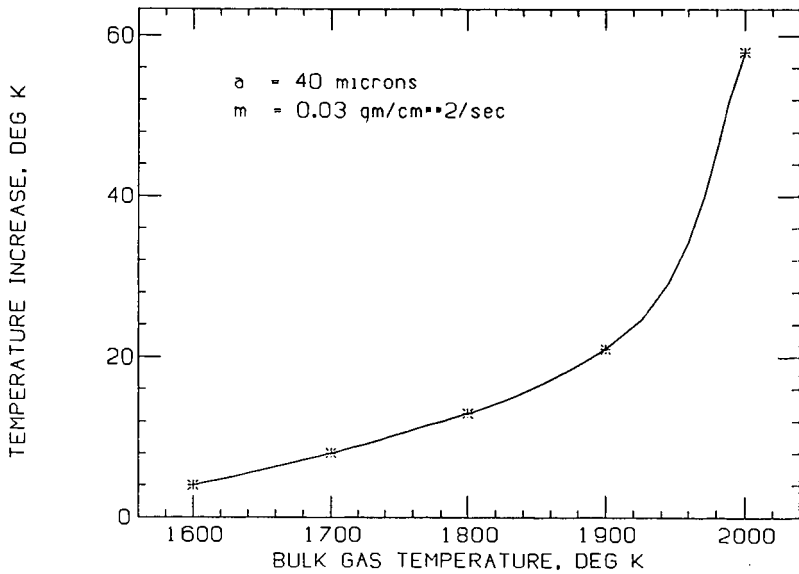


Figure 6. Bulk Gas Temperature Dependence.

DETERMINATION OF OVERALL KINETIC RATES AND  
OXYGEN REACTION ORDER FOR SARAN CHAR COMBUSTION

B.J. Waters, R.E. Mitchell<sup>\*</sup>, R.G. Squires and N.M. Laurendeau

Purdue University, West Lafayette, IN 47907

<sup>\*</sup> - Sandia National Laboratories, Livermore, CA 94550

Introduction

Recent work by Mitchell and co-workers [1,2,3] on a novel entrained flow reactor has demonstrated the feasibility of extracting kinetic rate parameters from the simultaneous measurement of the temperature, diameter and velocity of individual coal particles. These rate parameters are obtained by solving the conservation equations for a coal particle as it burns in a laminar, coflowing gas stream. In this analysis, assumptions must be made about the devolatilization processes which occur during particle heatup. Specifically, the char density, ash composition and heat gain of the particle due to homogeneous combustion of volatiles become parameters in the reactor model that depend on the parent coal.

In this work, the entrained flow reactor is used to investigate the combustion of Saran char, a very low ash, high surface area, amorphous carbon. The highly irregular Saran char particles offer a coal analog without the complicating effects associated with devolatilization and catalytic impurities. We report overall particle burning rates, apparent rate coefficients, and the apparent reaction order with respect to oxygen.

Experimental Procedure

The combustion of Saran char particles is followed in a transparent, rectangular, entrained flow reactor which is described in detail elsewhere [4]. Briefly, the particles are entrained in a cold  $N_2$  stream and are then injected along the centerline at the base of the 40 cm high reactor. Particle loadings are kept low to insure that their presence has no influence on the free-stream gas properties. A two-color pyrometer is used to measure the temperature of the burning particles at discrete heights in the reactor. As the particle traverses the focal volume of the collection optics, the radiant emission passes through two different sized slits. The first slit is wider (1000  $\mu m$ ) than the diameter of the largest particle and the second is narrower (45  $\mu m$ ) than the diameter of the smallest particle. The ratio of the intensity of the radiant emission measured in the first slit to that measured in the second slit is directly proportional to the diameter of the particle. The temperature measurements are calibrated with a tungsten strip lamp; the size measurements are calibrated by comparison with the size distribution of well-characterized Spherochar particles. The particle temperatures measured in this work ranged from  $1440 \pm 20$  K in 12 kPa  $O_2$  to  $2100 \pm 150$  K in 36 kPa  $O_2$ . The measured particle diameters ranged from 80 to 170

$\mu\text{m}$  which corresponds well with the -100/+170 mesh (90-150  $\mu\text{m}$ ) particles used to feed the reactor. The velocity of each particle is determined by measuring the time it takes the particle to traverse the large slit. The particle velocities measured in this work ranged from 2.40 to 3.10 ( $\pm 0.05$ ) m/s depending on the gas temperature.

To reduce the influence of spurious signals, 200 to 300 particles were monitored at each height and the particles were grouped in bins approximately 10  $\mu\text{m}$  apart, based on their measured diameter. In this paper, a measured particle diameter refers to the diameter at the center of a bin containing at least 10 particles. A measured particle temperature or velocity refers to the average temperature or velocity for all of the particles in a given bin.

A hot, one-dimensional, laminar oxidizing gas environment is generated by a 5 cm x 5 cm array of 0.2 cm diameter  $\text{CH}_4/\text{H}_2/\text{O}_2/\text{N}_2$  diffusion flamelets. The total pressure in the reactor is constant and equal to 101 kPa. Post flame  $\text{O}_2$  partial pressures from 3 to 36 kPa and gas temperatures from 1400 to 1900 K are attained by careful control of the inlet gas mixture. During analysis of the experimental data, we found that Saran char had a negligible burning rate in 3 and 6 kPa  $\text{O}_2$  environments. Therefore, in the remainder of this paper, we only present data obtained at 12, 24, and 36 kPa  $\text{O}_2$ . Typical post flame partial pressures of  $\text{H}_2\text{O}$  and  $\text{CO}_2$  are 16 and 2 kPa, respectively.

Gas temperatures,  $T$ , are determined from radiation-corrected measurements using a Pt-Pt/13%Rh thermocouple. The gas velocity in the reactor can be modeled as,

$$\sqrt{\frac{v}{T_g}} = C_1 + 0.5 \sqrt{C_2 z T_g^{0.68}} + \frac{C_2 z T_g^{0.68}}{8 \sqrt{C_1}} \quad (1)$$

where  $z$  is the height in the reactor,  $C_1$  and  $C_2$  are constants that are fit to the data for each gas condition, and the two  $T_g^{0.68}$  terms account for the influence of  $T_g$  on the gas viscosity.<sup>8</sup> Eqn. (1) represents the solution of the<sup>8</sup> conservation equation governing one-dimensional flow in a square conduit, assuming that the boundary layer along each wall develops independently and that the fraction of the total mass flowing in the boundary layer is proportional to the boundary layer thickness.  $C_1$  and  $C_2$  are chosen to give the best fit between the measured particle velocities and the particle velocities calculated by solving the particle momentum balance (see Eqn. (3) below). An important implicit assumption in this analysis is that the density of the particles are approximately independent of burning time. This assumption is consistent with the results of the kinetic analysis discussed below.

The Saran char is made by heating Saran co-polymer (supplied by the Dow Chemical Company) to 1300 K in flowing  $\text{N}_2$  for three hours. The exact procedure used to manufacture the Saran char is described elsewhere [5]. Saran char contains no volatiles and approximately 0.5 wt% ash. Its apparent bulk density is 0.35 g/ml and its total surface

area is  $1260 \text{ m}^2/\text{g}$ , as determined by  $\text{CO}_2$  adsorption at 298 K analyzed using the Dubinin-Radushkevich isotherm. The only impurities detected by Proton Induced X-ray Emission Spectroscopy (PIXE) are 2300 ppm Cl, 22-30 ppm Ti, 10 ppm Fe, 7.2 ppm Cu, 1 ppm Zr, and 1 ppm Re.

### Theory

The equations used to follow the mass, velocity and temperature of a particle as it burns in the laminar flow reactor are given below:

$$v_p \frac{dm}{dz} = -\pi d_p^2 \quad (2)$$

$$m v_p \frac{dv}{dz} = -mg - 3\pi\mu d_p (v_p - v_g) \quad (3)$$

$$\frac{-m v_p C_p}{\pi d_p^2} \frac{dT}{dz} + \rho H = \frac{2k(T_p - T_g)}{d_p} + \sigma \epsilon_p (T_p^4 - T_w^4) \quad (4)$$

The momentum equation (Eqn. (3)) accounts for gravitational and Stokes forces and the energy balance (Eqn. (4)) accounts for the thermal inertia of the particle, the heat of reaction, gas phase conduction, and radiation. The mass,  $m$ , of the char particle is determined from its apparent density and diameter,  $d_p$ . The particle velocity is  $v_p$  and  $\rho$  is the particle burning rate per unit external surface area. The velocity of the gas is given by  $v_g$  and  $g$  is the gravitational constant. The heat capacity of the particle,  $C_p$ , is taken to be that of graphite and the physical properties of  $\text{N}_2$ , the major component in the gas stream, are used for the free-stream gas properties. The viscosity,  $\mu$ , and thermal conductivity,  $k$ , of the gas are evaluated at the mean temperature ( $T$ ) between the gas and particle temperatures. The temperatures of the particle, the gas, and the medium to which the particle radiates are given by  $T_p$ ,  $T_g$  and  $T_w$  (500 K), respectively. The Stefan-Boltzmann constant is denoted by  $\sigma$ , and  $\epsilon_p$  denotes the particle emissivity (taken as 0.85). The heat released per gram of carbon consumed,  $H$ , is calculated assuming that CO is the primary combustion product.

The overall burning rate of the particle is described by:

$$\rho = k_d (P_g - P_s) = k_s P_s^n, \quad (5)$$

where  $P_g$  and  $P_s$  are the oxygen partial pressures in the bulk stream and at the surface of the particle, respectively,  $k_s$  and  $k_d$  are the chemical rate and diffusion coefficients, respectively, and  $n$  is the apparent oxygen reaction order. The chemical reaction rate coefficient includes contributions from intraparticle diffusion limitations and the intrinsic reactivity of the Saran particle. In the Arrhenius form,  $k_s$  is given as,

$$k_s = A \exp\left(\frac{-E}{RT_p}\right), \quad (6)$$

where A is the preexponential factor, E is the activation energy, and R is the universal gas constant. The external diffusion rate coefficient is given by:

$$k_d = \frac{2M D_{ox}}{RT_m d_p}, \quad (7)$$

where M is the molecular weight of carbon and  $D_{ox}$  is the diffusion coefficient of oxygen evaluated at  $T_m$ .

The computational scheme employed to obtain the overall particle burning rate parameters, A, E, and n, is initiated by setting  $dT/dz$  equal to zero in Eqn. (4) and then using the measured  $d_p$  and  $T_p$  to calculate  $\rho$ . Using Eqns. (5) and (7),  $P_s$  can be calculated from  $\rho$ . The rate parameters are then obtained from Eqns. (5) and (6) by fitting  $T$  and  $P_s$  to the calculated rate using a linear least-squares routine. These parameter values are used as the first guess in the numerical integration of Eqns. (2), (3) and (4), where  $\rho$  is obtained from an implicit expression which is independent of  $P_s$  by rearrangement of Eqn. (5). The integration employs the measured  $T_p$  profile. The initial conditions used for the integration are  $T = 300$  K and  $v = 0.3$  m/s. A range of initial particle diameters (from 90  $\mu m$  to 190  $\mu m$ ) in 5  $\mu m$  intervals is used. When the integration reaches a height (z) where experimental measurements have been taken, the calculated relationship between  $dT/dz$  and  $d_p$  is used to find  $dT_p/dz$  for each measured particle size. This measured  $dT_p/dz$  is then used in Eqn. (4) to obtain a new  $\rho$ , from which updated values of the kinetic parameters are obtained for the next numerical integration. Successive iterations of this strategy are used to converge on the rate parameter values that best describe the behavior of the Saran particles. The quality of fit can be judged from the agreement between the calculated and measured  $T$  as a function of  $d_p$ . Both constant density and constant diameter burning are considered as limiting cases for effectiveness factors of approximately zero and one respectively. The particle ignition temperature is taken as 1000 K below which the particle burning rate is set equal to zero. Changing the ignition temperature from 300 K to 1100 K does not affect the results of this analysis.

### Results and Discussion

Equations (2), (3) and (4) can be solved to calculate the predicted relationship between particle temperature and size for a given gas environment. For the 12 kPa  $O_2$  environments at a peak gas temperature less than 1700 K and in all  $O_2$  environments less than 12 kPa, the measured particle temperatures can be fit by setting  $\rho$  equal to zero. This is in direct contrast to the burning characteristics of an hvb-bituminous coal observed by Mitchell and co-workers [2], which exhibited appreciable reaction rates in  $O_2$  environments as low as 3 kPa. This may be attributed to two factors: (1) the homogeneous combustion of the volatile matter (33% by weight) in the coal

increases the temperature of the resulting char and (2) the catalytic properties of the ash (21% by weight) increase the burning rate of the char.

If the measured particle temperature does not exceed the calculated zero-burning temperature by the approximate error in our temperature measurement ( $\pm 20$ -150 K), we can not calculate a statistically significant burning rate. Defining  $\chi$  as the ratio of the calculated burning rate to the diffusion-limited burning rate ( $\chi = \rho/k_d P_s$ ), we observed that the difference in particle temperature between  $\chi$ 's of 0.0 and 0.1 approximately corresponds to the error in the measured particle temperature. Therefore, no measurements which give a  $\chi$  below 0.1 are considered in the determination of the rate coefficients and oxygen reaction order. For the conditions of these experiments, values of  $\chi$  ranged from 0.1 to 0.6 which indicates that the overall burning rate has a high sensitivity to the kinetic rate.

For an  $O_2$  partial pressure of 36 kPa, 100  $\mu m$  particles are predicted to burn out at approximately 10 cm in the reactor, if constant diameter burning is assumed. This contradicts the experimental observation of particles as small as 90  $\mu m$  at 19 cm in the reactor. While a constant diameter model may be more applicable at lower  $O_2$  pressures, this model was not used in our analysis of the combustion kinetics. An analysis incorporating an effectiveness factor into the particle burning rate expression will be considered in future work.

Constant density burning gives good fits to the experimental data at bulk oxygen pressures of 12 and 24 kPa and poor fits to the 36 kPa data (see Figures 1, 2 and 3). A least squares fit of the kinetic rate parameters and oxygen reaction order to the calculated reaction rates at 12, 24 and 36 kPa gives

$$\rho = 6.3 \times 10^{-3} \exp\left(\frac{-27000}{RT_p}\right) P_s^{0.8} \quad (8)$$

where R is given in cal/mol K and  $P_s$  is given in Pa. An Arrhenius plot of the rate coefficient,  $k_s$ , versus  $1/T_p$  is presented in Figure 4. The relationship between  $(\rho/k_s)$  and  $P_s$  is depicted in Figure 5.

A possible reason for the discrepancy between the calculated and experimental rates for the 36 kPa data set is that the simple diffusion model considered here does not account for the large amount of CO which must diffuse out of the particle boundary layer at higher burning rates (Stefan flow). We do note, however, that when the 36 kPa data is analyzed alone, the calculated rates fit the data better, but the activation energy is lower ( $\sim 17000$  cal/mol) which is indicative of intraparticle diffusion limitations.

#### Acknowledgements

The experimental work was performed at the Combustion Research Facility, Sandia National Laboratories and was sponsored by the U.S. Dept. of Energy through PETC. The computational work was performed at



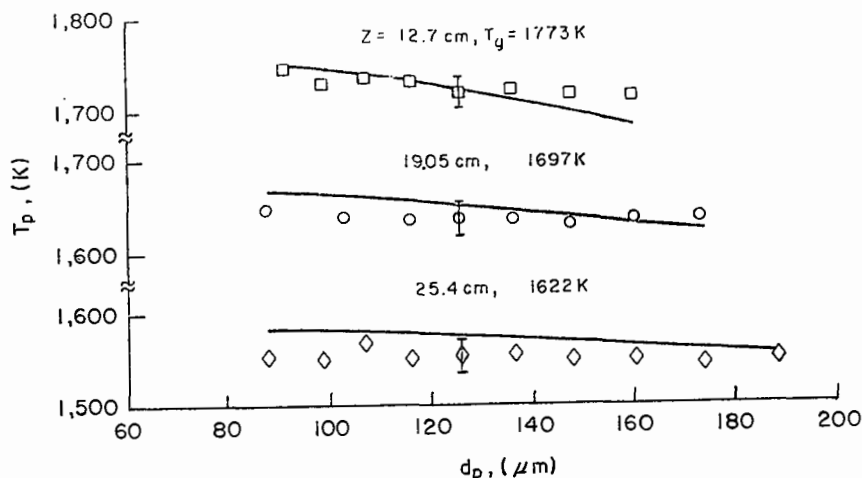


Figure 1. Particle temperature versus diameter as a function of height in the reactor. Free stream oxygen pressure is 12 kPa. ( $\chi = 0.1-0.3$ )

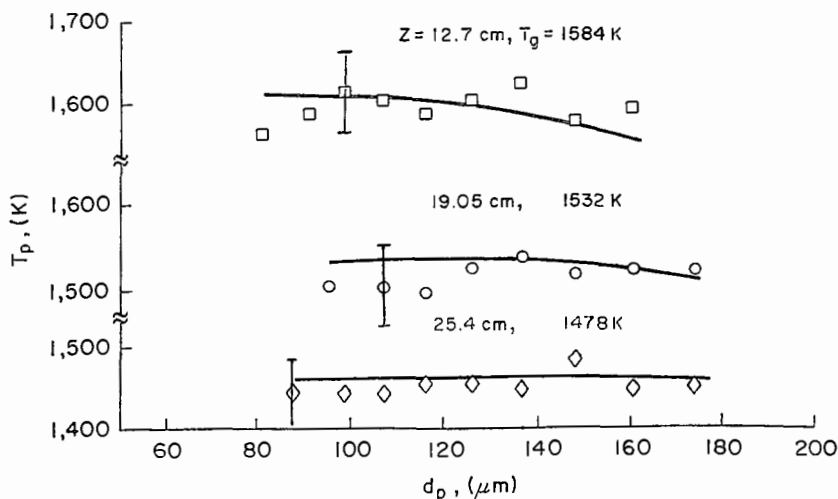


Figure 2. Particle temperature versus diameter as a function of height in the reactor. Free stream oxygen pressure is 24 kPa. ( $\chi = 0.1-0.3$ )

the Purdue University Computing Center and was sponsored by the Coal Research Center at Purdue University. B.J.W. acknowledges the support provided by the D.O.E. through Associated Western Universities.

#### References

1. Mitchell, R.E., Tichenor, D.A. and Hencken, K.R., Proceedings of the 1985 International Conference on Coal Science, International Energy Agency, 1985, p.375.
2. Mitchell, R.E., Tichenor, D.A. and Hencken, K.R., Second Annual Pittsburgh Coal Conference Proceedings, Pittsburgh, Sept. 16-20, 1985, p.648.
3. Tichenor, D.A., Mitchell, R.E., Hencken, K.R., and Niksa, S., Twentieth Symposium (Int.) on Combustion, Ann Arbor, Aug. 12-17, 1984.
4. Hardesty, D.R., Pohl, J.A. and Stark, A.H., Sandia Report SAND78-8234, Sandia National Laboratories, Livermore, CA, 1978.
5. Waters, B.J., M.S. Thesis, Purdue University, 1985.

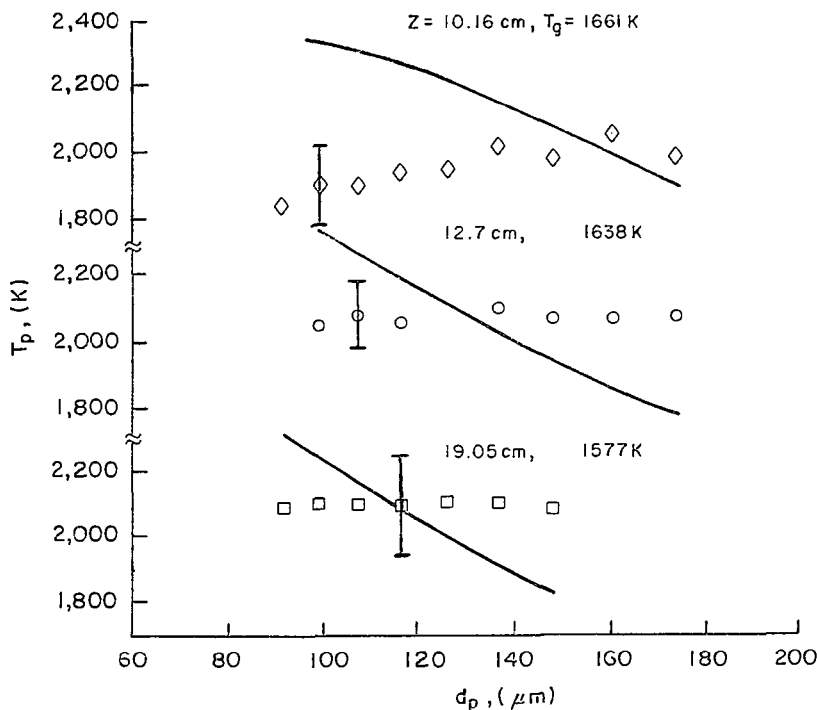


Figure 3. Particle temperature versus diameter as a function of height in the reactor. Free stream oxygen pressure is 36 kPa. ( $\chi = 0.3-0.6$ )

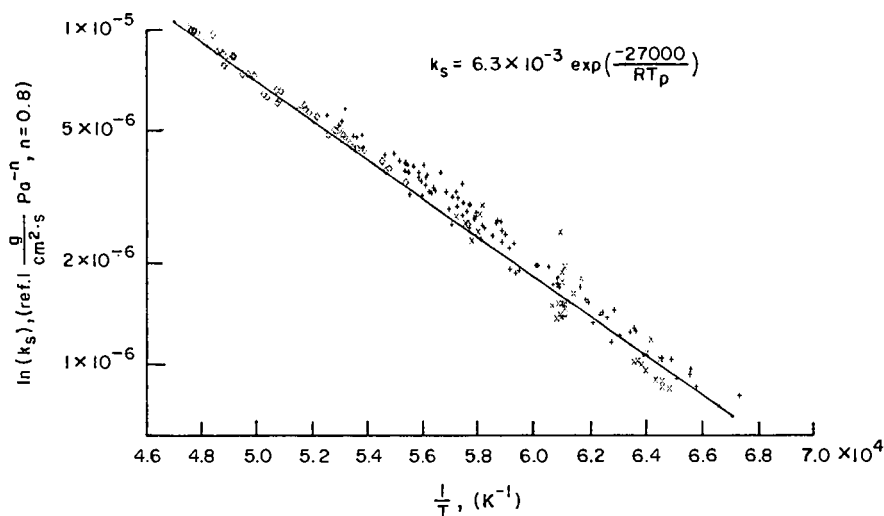


Figure 4. Temperature dependence of  $k$ .  
Free stream oxygen:  $\diamond$  - 36 kPa;  $+$  - 24 kPa;  $\times$  - 12 kPa.

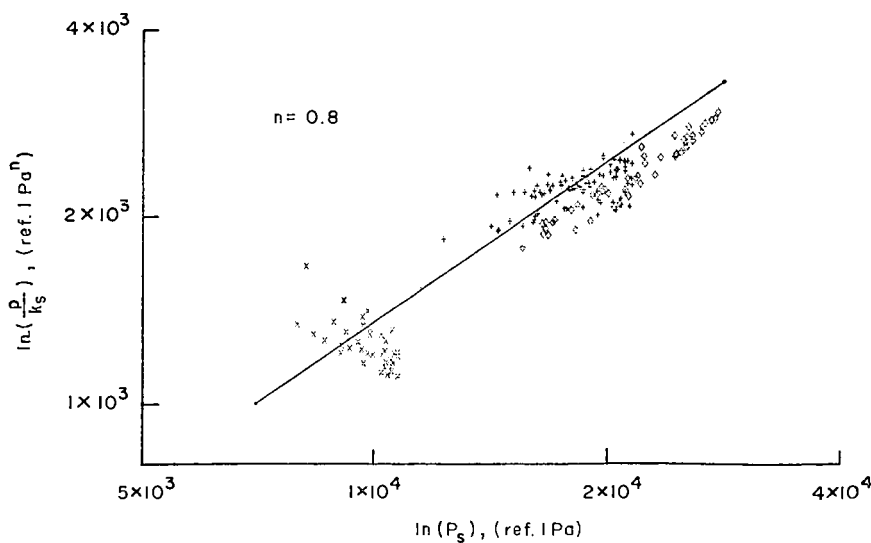


Figure 5. Surface oxygen pressure dependence of  $\frac{P}{k}$ .  
Free stream oxygen:  $\diamond$  - 36 kPa;  $+$  - 24 kPa;  $\times$  - 12 kPa.

## Effect of $\text{CaCl}_2$ on Char Reaction Kinetics

M. A. Serageldin and W. P. Pan

Department of Chemistry and Chemical Engineering  
Michigan Technological University  
Houghton, MI 49931

### INTRODUCTION

This work describes the effect of  $\text{CaCl}_2$  on coal char reactivity; it is the third part in a series of studies related to boiler application (1,2) involving this metal-based salt. The information obtained in this work should be useful in understanding the effect of similar materials on the oxidative behavior of coal-char. The char was combusted in a thermogravimetric analyzer, TGA, under different partial pressures of oxygen (0.16 - 70% by vol.) in nitrogen and at constant temperature. The furnace temperatures (isothermal) varied between 673 and 1223 K. The sample mass and volumetric flow rate were close to 2 mg and 5 ml/s, respectively. This temperature range should cover the regions where oxidation occurs mainly by diffusion and mainly by chemical control (3,4).

### EXPERIMENTAL

#### Materials

Lignite coal from Velva Mine, North Dakota, was used in this work; its proximate and ultimate analysis is given in Table I.

#### Char preparation

The coal was placed in a boat made of ceramic material and pyrolyzed in a Hoskin electric furnace (Hoskin Co.), which was regulated by an Omega 6000 temperature controller. The boat was made by splitting a length,  $l$ , of high purity alumina tube ( $l = 75$  mm and I.D. = 10 mm); it was positioned in the center of the furnace. A shielded Chromel Alumel thermocouple ( $d = 3$  mm) was placed approximately 5 mm above the boat to measure the sample temperature. The sample thermocouple reading (in the absence of a sample) was a few degrees lower than that of the furnace set temperature; for example, at the set temperature of 1248 K, the sample thermocouple (inside the furnace) recorded 1223 K.

Coal pyrolysis in a constant stream of nitrogen (0.425 ml/s at S.T.P.) was achieved over a number of steps (5). The sample was first purged at room temperature for 900 s (0.9 ks). The furnace was then switched on, setting the maximum temperature to 1248 K (which was reached in about 2.58 ks). It was left for one hour at the maximum temperature. The furnace was then turned off and left to cool in nitrogen for one hour, after which the remaining part of the coal sample, i.e. char, was emptied in a clean, dry container which was subsequently stored in a dessicator for later use.

#### Apparatus

The char was burned in a DuPont 951 thermogravimetric analyzer (TGA) coupled with a DuPont 990 recorder unit. Each sample (2 mg) was spread evenly on the platinum pan to avoid establishing a thermal gradient in the sample.  $\text{O}_2$  and  $\text{N}_2$  were mixed by different proportions. The total gas flow made by  $\text{O}_2$  and  $\text{N}_2$  was maintained at 5 ml/s. This provided a linear velocity of 18 mm/s. The percentage of  $\text{O}_2$  in the  $\text{O}_2/\text{N}_2$  mixture depended on the isothermal temperature: at the higher isothermal temperature (1223 K), the lower concentration (or partial pressure) of oxygen was used, i.e. 0.16% by volume, whereas a concentration of 70%  $\text{O}_2$  was used when the isothermal temperature was set to the lowest value investigated, i.e. 683 K. Such combinations were necessary to maintain the value of the time to 50% decomposition,  $t_{0.5}$ , above 1200 s, thus ensuring that the effect of temperature gradient is negligible (4). Lastly, before pushing the sample into the furnace, the latter was heated to the desired isothermal temperature

and left to equilibrate for 300 s. This procedure helped to reduce the time-lag before the sample reached the desired temperature.

## RESULTS

Information regarding the influence of  $\text{CaCl}_2$  on char reactivity, reaction mode, and kinetic parameters is presented in this section.

### Reactivity

The influence of oxygen concentrations and temperature on char reactivity is shown in Figure 1. A greater effect (on conversion) was produced as a result of increasing the temperature by a small percentage than by an equivalent increase in oxygen percentage in the gas. Treating the char with  $\text{CaCl}_2$  also increased its level of conversion, Figure 2. Considering that conversion vs. time plots for chars under different atmospheres are similar in appearance, a more satisfactory representation, in terms of reactivity, can be achieved by replotting conversion against a dimensionless time,  $t/t_{0.5}$  (6). Such a plot is given in Figure 3 and indicates that  $\text{CaCl}_2$  produces an insignificant effect below a conversion of  $\sim 0.58$  which would suggest that the mechanism of reaction is not altered within this zone. Between 0.58 conversion and up to  $\sim 0.68$  the "master curve" separated into two curves, one for char and the other for char plus  $\text{CaCl}_2$ . Above a conversion of 0.68 each of the above curves split into three curves, producing a total of six curves. Such a spread was not observed when char from demineralized coal was carbonized at around 1273 (6). However, evidence showing the effect of naturally occurring mineral matter in coal-char may be found (beyond a char conversion of 0.7) in Figure 1 of Tseng and Edgar's paper (4). It is, therefore, understandable that in the presence of additional mineral matter (i.e.  $\text{CaCl}_2$ ), as in this study, a more pronounced effect occurs. This is clearly indicated (Figure 3) by a greater shift of the catalyzed reaction to the left, i.e. towards a pore diffusion mode of reaction (Figure 4). The spread in the curves may be attributed to the effect of particle temperature rise (7).

### Reaction Mode of Control

To determine the mechanism controlling the reaction the data used to plot Figures 3 and 4 was replotted in terms of specific rate,  $dC/dt$ , and  $t_{0.5}$ , the time to 50 percent conversion. Values of  $dC/dt$  were obtained using the cubic spline interpolation technique (8) and the cubic spline smoothed technique. Figure 5 illustrates the extent of scatter when the cubic spline smoothed technique was not applied (white circles) to the data from Figure 3. This method was previously used by Tseng and Edgar (4) to compare the reactivities of different chars in the absence of catalysts. Figure 6 shows a number of curves obtained using this procedure for char combusted at several of the low temperatures investigated and different oxygen levels. A maximum occurred in all cases at around 0.25 conversion, which indicates that the control mechanism is chemical (3,4). Beyond 0.58 the curves delineating the different experimental conditions separated and were therefore clearly identifiable. From this presentation one can see that the maximum specific rate at a given temperature was somewhat increased by treatment with  $\text{CaCl}_2$ . It should be stated that when the conversion was less than 0.5, Figure 6 provided more detail than Figure 3.

Figure 4 was obtained by treating the data corresponding to the runs at high temperature ( $>1123$  K). The data for the six experiments followed very closely the film diffusion theoretical curve (dotted line). The theoretical lines in Figure 4 were calculated using the equations provided in reference 4.

### Kinetic Parameters

The order of reaction in the kinetic control regime was determined by plotting  $t_{0.5}$  against oxygen partial pressure (0.16 - 70 KPa) on log-log paper (4) and measuring the slope. Figure 8 shows such plots obtained at different temperatures for untreated char. The slope of the different lines was practically the same, suggesting that the average value of  $n$  for the char was 0.84. This figure is somewhat higher than 0.70 reported by a number of workers for lignite coal (see ref. 4). The value of  $n$  for char treated with  $\text{CaCl}_2$  was 0.73. Both values of  $n$  are valid for a limited temperature range, i.e. 683 - 723 K. In the diffusion control regime  $n$  equals

one (9). The activation energy was obtained by plotting  $t_{0.5}^*$  against  $1/T$  on semi-log paper as is illustrated in Figure 9. The former value is defined as follows (4):

$$t_{0.5}^* = (P_{O_2}/P^*_{O_2})^n \cdot t_{0.5} \quad 1)$$

where  $t_{0.5}$  corresponds to the value at a base of reference partial pressure of oxygen,  $P_{O_2}$ . This was chosen to be 0.005 MPa in the present study. On the other hand, the values marked with an asterisk correspond to char reacted at the same temperature under other partial pressures of oxygen.  $n$  is the reaction order. Figure 9 illustrates results for both the high temperature runs (lower left of figure) and the low temperature runs (upper right of figure). Each circle shown in Figure 9 represents the average of four runs at different  $P_{O_2}$ , i.e. the points at a given temperature fall within the bounds of such circles. However, for calculating the activation energy, all the points were used. For example, all the runs shown in Figure 8 were used to calculate the activation energy,  $E$ , in the kinetic regime. This was equal to 154 KJ/mol for char and was reduced to 141 KJ/mol when the char was treated with  $CaCl_2$ . However, for the higher temperature runs where the mode of control was diffusional, the value of  $E$  for the untreated char was  $29.5 \pm 0.5$  and for the treated char was  $28.0 \pm 0.5$  KJ/mol. The fact that the difference is insignificant suggests that char combustion under such a regime is independent of the nature of the catalyst, a point made before by others (3,10). The activation energy in the chemical control regime may also be obtained using the following equation:

$$\log_e (P_{O_2}^n \cdot t_{0.5}^*) = \log_e A' + E/RT \quad 2)$$

where  $A'$  is a measure of the char reactivity (4) and can be expressed as :

$$A' = (1/AS_0) \int_0^{0.5} (S_0/S) dC \quad 3)$$

$A$  in Equation 3 is the Arrhenius pre-exponential factor;  $S_0$  is the specific surface area at time zero and  $dC$  is the fraction converted. Values of  $A'$  and  $E$  obtained using Equation 2 are shown in Table 2 and indicate that the reactivity of the treated char was significantly increased as a result of adding  $CaCl_2$ . The higher reactivity can also be deduced from Figure 10.

To evaluate the mass transfer resistance the Sherwood number of the char samples were calculated (Appendix 1) (4) for the data in the film diffusion controlled regime and summarized in Table 3. These values are significantly increased in the presence of  $CaCl_2$  and by temperature; however, they have a value less than 2 which refers to a spherical particle suspended in stagnant air. The occurrence of a lower Sherwood number was attributed by Tseng and Edgar (4) to a reduction in mass transfer efficiency by the sample pan (4). They also concluded that the mass transfer resistance around a single large particle would be lower than that around smaller particles on a pan. In the latter case the particle packing is also important.

## DISCUSSION

This work shows that  $CaCl_2$  promotes the overall decomposition of coal-char, i.e. it occurs during a shorter time, at constant temperature. This is in agreement with previous results but under temperature programming (non-isothermal) conditions (11). In this case the same level of conversion occurred at a lower temperature which indicates agreement between isothermal and non-isothermal studies.

Since changes in porosity and density prior to oxidation can influence reactivity, these were measured for char prepared from coal and that for coal mixed with  $CaCl_2$  (12). From Table 4 we can deduce that there is no significant change in density, total pore volume and porosity prior to combustion. Therefore the effectiveness of the additive in promoting char-oxygen reaction may be explained in terms of the following carbon-oxygen reactions (13,14):



In the above model the catalyst promotes the dissociation of the oxygen molecule adsorbed making it thus more reactive. In other words, dissociative adsorption is promoted (14). Such a

mechanism could account for the observed decrease in activation energy in the chemical control regime.

In the diffusion control regime E did not vary significantly, which would suggest that the above explanation is not applicable in this case. However, the fact that E was  $\sim 28$  KJ/mol, i.e. higher than the usually accepted range of 8 - 12 KJ/mol (9), would suggest that it is possible that the regime is not totally film diffusion controlled, but that pore diffusion may also be important during the initial decomposition stage, Figures 7 and 9. (E for pore diffusion is around half of the intrinsic activation energy.) This reasoning could account for the observed shorter char decomposition time, which is indicated by lower values of  $t_{0.5}$ . The significance of the Sherwood numbers in Table 3 is now questionable. The results indicate that  $\text{CaCl}_2$  increases this number significantly and, therefore, under these conditions, mass transfer resistance was reduced. However, we can see that the values of the constant b for the film diffusion controlled regime was not significantly altered by  $\text{CaCl}_2$ . The theoretical value of b is 0.55 (4). The use of this form of the Sherwood number may be misleading considering that we do not have single spherical particles as assumed in the derivation by the authors (4) and considering that we have reason to believe that pore diffusion may also be involved.

### CONCLUSIONS

1.  $\text{CaCl}_2$  decreased the activation energy and increased the reactivity of coal char in the chemical control regime. It did not, however, have an important effect the diffusion control regime.
2. In the kinetic control regime the mechanism was not altered below a conversion of 0.58. However, at higher conversion the reaction was moved towards the pore diffusion regime.
3. At the higher temperatures pore diffusion may also play a role during decomposition, which explains why the activation energies obtained were higher than that for a totally film diffusion controlled regime.

### REFERENCES

1. Serageldin, M.A. and Pan, W.-P., "Effect of  $\text{CaCl}_2$  on Coal Decomposition: Pollution", presented at the 39th ACS Fall Scientific Meeting, Midland, Michigan, 1983.
2. Serageldin, M.A. and Pan, W.-P., "Corrosion-Effects of Increasing the Chloride Level in Coal", Proceedings of the 9th International Congress on Metallic Corrosion, Toronto, Canada, Vol. 1, 1984, pp. 504-11.
3. Dutta, S. and Wen, C.Y., *Ind. Eng. Chem., Process Des. Dev.*, 16(1), 1977, pp 31-7.
4. Tseng, H.P. and Edgar, T.F., *Fuel*, 63, 1984, pp. 385-93.
5. Hippo, E.J., Jenkins, R.G. and Walker, P.L., Jr., *Fuel*, 58, 1979, pp. 338-44.
6. Mahajan, O.P., Yaizab, R. and Walker, P.L., Jr., *Fuel*, 57, 1978, pp. 643-6.
7. Essenhigh, R.H., in "Coal Conversion Technology" (Eds, Wen, C.Y. and Stanley Lee, E.), Ch. 3, 1979, pp. 171-312.
8. IMSL Library Reference, IMSL Inc., 9th Edition, Vol. 2, 1982, pp I-1, ICSCCU-1.
9. Satterfield, C.N., "Mass Transfer in Heterogeneous Catalysis", MIT Press, Massachusetts, 1970.
10. Weisz, P.B. and Goodwin, R.D., *J. Of Catalysis*, 2, 1963, pp. 397-404.
11. Pan, W.-P. and Serageldin, M.A., "Effects of  $\text{CaCl}_2$  on reactivity of coal under non-isothermal condition", in preparation, 1985.
12. Pan, W.-P. and Serageldin, M.A., "Structure Characterization in Coal and Char with  $\text{CaCl}_2$ ", in preparation, 1985.
13. McKee, D.W. in "Chemistry and Physics of Coal Utilization - 1980" (Eds, Cooper, B.P. and Petvabis, L.) AIP, 1981, pp. 236-55.
14. Morgan, B.A. and Scaroni, A.W. in "The Chemistry of Low-Rank Coals", ACS Symposium Ser. 264, Ch. 16, 1984, pp. 255-66.

### Appendix 1: Sherwood Number

$$\text{Sh} = \frac{(1-X_a)\rho p_o^{2RT}}{D_b \omega P_o t_{0.5}} (1 - \sqrt[3]{1/4}) \quad 1)$$

where  $X_a$  is the ash yield;  $\rho_p$ , particle density;  $r_0$ , initial particle radius;  $D_b$ , bulk diffusivity;  $R$ , the gas constant;  $T$ , the absolute temperature;  $P_{O_2}$ , partial pressure of oxygen;  $t_{0.5}$ , time to 50% decomposition and  $\omega = 12$ , assuming all  $C \rightarrow CO_2$ .

Table 1: Analysis of lignite coal (-100, +270) mesh

|               | <u>Proximate analysis</u> |          | <u>Ultimate Analysis</u> |  |
|---------------|---------------------------|----------|--------------------------|--|
|               | <u>As received</u>        |          | <u>Moisture-Ash free</u> |  |
| Moisture(wt%) | 34.00                     | Carbon   | 64.55                    |  |
| Fixed Carbon  | 27.46                     | Hydrogen | 4.72                     |  |
| Volatiles     | 32.86                     | Nitrogen | 1.02                     |  |
| Ash           | 5.68                      | Sulfur   | 0.33                     |  |
|               |                           | Oxygen*  | 29.38                    |  |

\*by difference

Table 2: Values of A' and activation energy

| Sample                         | A'                     | Activation energy (KJ/mol) |
|--------------------------------|------------------------|----------------------------|
| untreated char                 | $9.3 \times 10^{-10}$  | $154 \pm 1$                |
| CaCl <sub>2</sub> treated char | $68.4 \times 10^{-10}$ | $141 \pm 4$                |

Table 3: Sherwood number and film diffusion constant (b) of char samples

| Temperature (K) | <u>Sherwood number</u> |                                | $\frac{dC}{dT} = b(1-C)^{1/3}$ |                                |
|-----------------|------------------------|--------------------------------|--------------------------------|--------------------------------|
|                 | Untreated char         | CaCl <sub>2</sub> treated Char | untreated char                 | CaCl <sub>2</sub> treated char |
| 1123            | 0.76                   | 1.11                           | $0.59 \pm 0.03$                | $0.56 \pm 0.02$                |
| 1173            | 0.91                   | 1.23                           | $0.59 \pm 0.02$                | $0.57 \pm 0.02$                |
| 1223            | 1.26                   | 1.52                           | $0.57 \pm 0.03$                | $0.57 \pm 0.02$                |

Table 4: Density, total pore volume and porosity (12)

| Sample                         | <u>Density (g/cm<sup>3</sup>)</u> |         | Total pore volume (cm <sup>3</sup> /g) | Porosity (%) |
|--------------------------------|-----------------------------------|---------|--|--------------|
|                                | Helium                            | Mercury |  |              |
| untreated char                 | 2.12                              | 1.30    | 0.298                                  | 38.7         |
| CaCl <sub>2</sub> treated char | 2.14                              | 1.32    | 0.29                                   | 38.5         |



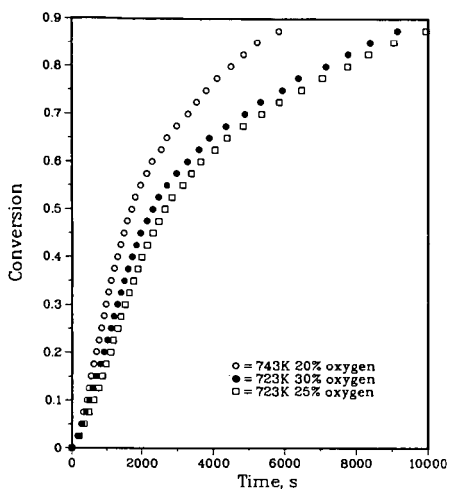


Figure 1: Influence of oxygen concentration and temperature on reactivity of char.

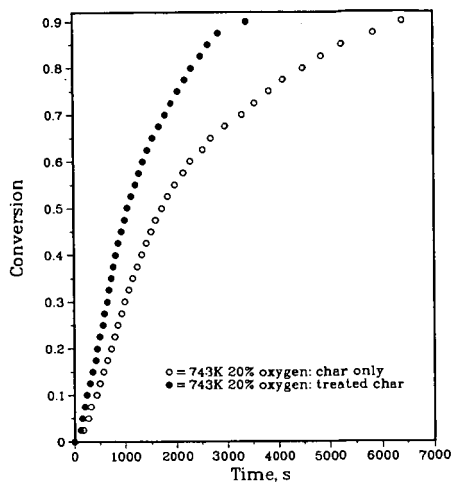


Figure 2: Effect of  $\text{CaCl}_2$  on the reactivity of char.

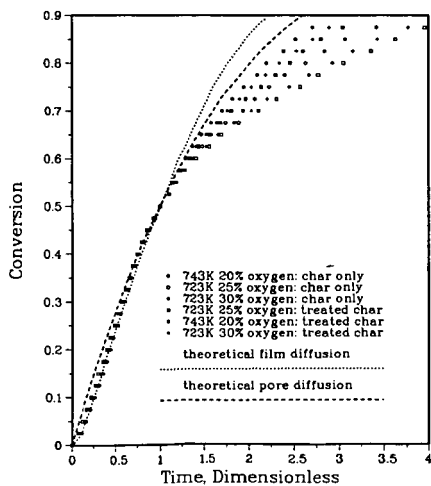


Figure 3: Effect of  $\text{CaCl}_2$  on the normalized plot of char at different temperatures and oxygen concentrations.

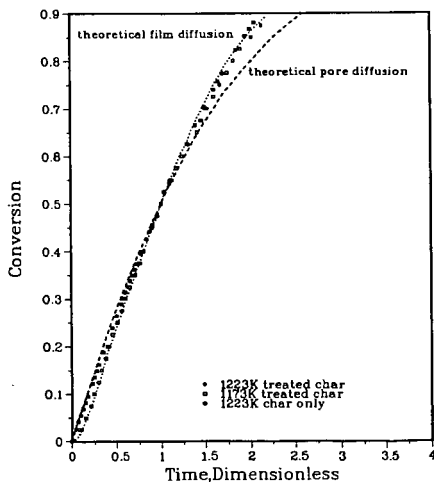


Figure 4: Effect of  $\text{CaCl}_2$  on the normalized plot of char under diffusional control.

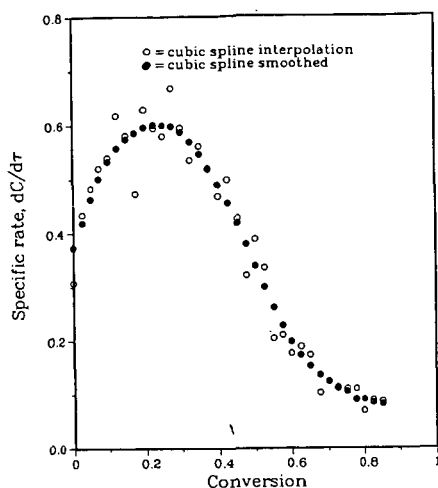


Figure 5: Application of cubic spline interpolation technique and cubic spline smoothed technique.

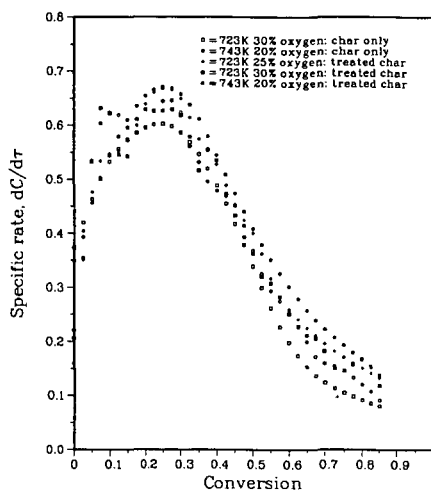


Figure 6: Effect of  $\text{CaCl}_2$  on the combustion characteristic curve of char under chemical control.

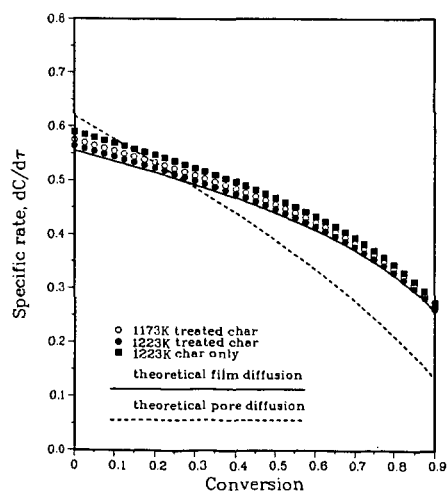


Figure 7: Effect of  $\text{CaCl}_2$  on the combustion characteristic curve of char under diffusional control.

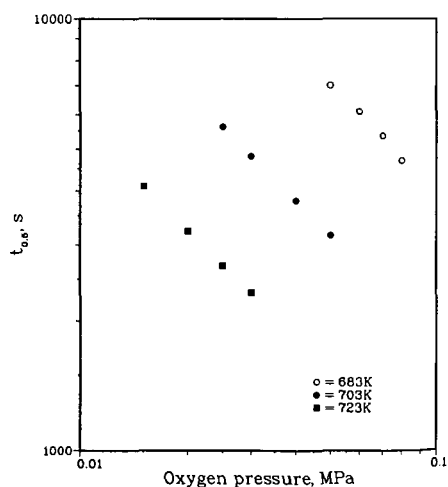


Figure 8: The reaction order of char.

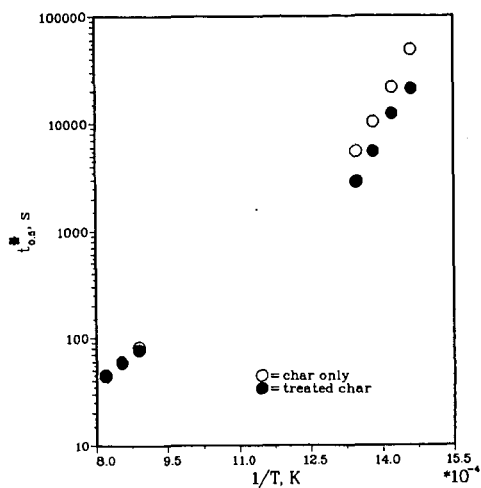


Figure 9: The effect of  $\text{CaCl}_2$  on the char activation energy.

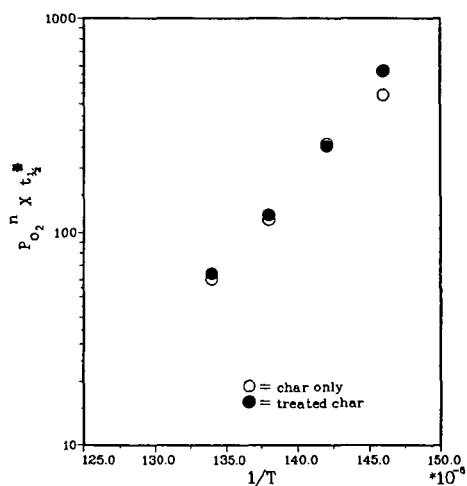


Figure 10: Comparison of the reactivity of char in the presence and absence of  $\text{CaCl}_2$ .

## INFLUENCE OF METAL IONS AND PYROLYSIS CONDITIONS ON CARBON DIOXIDE GASIFICATION OF WOOD CHAR

William F. DeGroot and G.N. Richards

Wood Chemistry Laboratory, University of Montana, Missoula, MT 59812

### INTRODUCTION

The rate of biomass gasification is limited by the reaction rate of the thermally stable char which forms as a result of the initial pyrolytic degradation. This char also represents a large proportion of the energy content of the original biomass (1), and efficient conversion of the biomass should recover the energy value of this fraction. This can be achieved by reaction with oxygen, steam, or carbon dioxide, and the intent of this research was to investigate the effects of reaction conditions and inorganic catalysts on the gasification of wood chars. These chars also provide an excellent model for studying the gasification reactions of coal, since sample pretreatment and pyrolysis conditions can be varied to provide a wide range of chemical functionality in the resulting chars. Studying the chemical structure and reactivity of these chars can provide important insight into parallel reactions in coal and other carbonaceous materials.

Previous work in our laboratory on the gasification of biomass chars indicated that the inorganic species naturally present in wood were effective gasification catalysts (2), and that some of the natural inorganic species were exchangeable with cations of salts added to the wood in solution. We have studied this ion exchange process further and have found that the wood sample used in these studies contains approximately 8 meq/100 g of carboxylic acid groups, primarily as 4-O-methylglucuronic acid groups associated with the hemicellulose fraction of the wood (3). In this study we have added catalysts to previously acid-washed wood through ion exchange in order to incorporate a single catalytic species in a highly dispersed form and at a reproducible level. Selected samples were also treated beyond the ion exchange capacity in order to distinguish the effects of exchanged cations as opposed to adsorbed salts.

### EXPERIMENTAL

The wood sample used in this study was black cottonwood (*Populus trichocarpa*), a low-grade western hardwood. The heartwood and sapwood were separated and the sapwood was the primary sample studied. The wood was ground in a Wiley mill, and the 20/30 mesh fraction was retained for analysis.

Acid-washing ( $H^+$ -exchange) and ion exchange treatments were carried out by column percolation. The wood was degassed in a small quantity of the solution used for ion-exchange and transferred to a glass chromatography column. A 0.01 M solution of the acetate salt of the cation to be exchanged (at least a ten-fold excess) was then washed slowly through the column. The column was washed thoroughly with distilled, deionized water to remove any of the salt which was not bound by ion exchange. In order to add catalytic species beyond the exchange capacity of the wood, the wood was soaked in a 0.01 M solution of the acetate salt and then air-dried. All of the catalyst treatments were carried out using acid-washed wood in order that the treated samples contain only a single catalytic species.

The inorganic constituents of the wood samples were analyzed by inductively coupled argon plasma (ICP) emission spectroscopy, except for nickel which was analyzed by atomic absorption (AA) spectroscopy. Ash contents were determined by thermogravimetry (TG) at 550°C in air.

Chars were prepared in a tube furnace purged with flowing nitrogen. The wood sample was held in a porcelain boat which was pulled into the preheated furnace. After heating for a prescribed time the sample was pulled into a water condenser at the downstream end of the furnace tube, where it was cooled to approximately 10°C before being exposed to the air. Samples were stored in nitrogen- or argon-purged containers.

Cross polarization/magic angle spinning  $^{13}\text{C}$  nuclear magnetic resonance spectrometry (CP/MAS  $^{13}\text{C}$  n.m.r.) of the chars was carried out at the Colorado State University Regional N.M.R. Center.

Gasification was carried out in the gasification reactor/detector system depicted in Figure 1. The reactor consisted of a 1/8" I.D. alumina tube (99.8% alumina) heated by an external nichrome wire coil. The sample (3-10 mg) was confined within a 1.0 cm section of the tube by 1/8" O.D. 4-hole ceramic insulators, which also carried gas flows into and out of the reactor. The lower insulator contained a chromel-alumel thermocouple that extended 3-4 mm into the reactor and provided a reliable measure of the sample temperature throughout the reaction. The reactor was purged with a 30 cc/min flow of  $\text{N}_2$  for inert conditions and an equivalent flow rate of  $\text{CO}_2$  for gasification. Switching of gas flows and reactor temperature were under control of a data acquisition/control system.

Effluent gases from the reactor were mixed with a 10 cc/min air flow, causing the oxygen level of the air flow to be reduced by the stoichiometric quantity of oxygen required for combustion of any combustible gases formed by pyrolysis or gasification of the sample. The oxygen concentration of the combined gas streams was monitored by a 1/4" O.D. zirconium oxide oxygen sensor tube maintained at 900-950°K. This sensor was enclosed in a 1/2" O.D. quartz tube and produced an output proportional to the differential pressure of oxygen across its inner surface (flowing air reference gas) and outer surface (combined reactor and combustion air flows). The output of the oxygen sensor was converted to oxygen concentration during data acquisition according to the Nernst equation:

$$E = \frac{RT}{4F} \ln(P/P_{\text{ref}})$$

where  $R$  and  $F$  have their usual meanings,  $T$  is the detector temperature (°K) and  $P$  and  $P_{\text{ref}}$  are the partial pressures of oxygen in the sample and reference gases, respectively.

For the purposes of this study it was assumed that all of the combustible gases produced were  $\text{CO}$ , and the removal of one molar equivalent of  $\text{O}_2$  from the gas stream was therefore due to the gasification of one molar equivalent of carbon. The extent of gasification determined in this manner was consistently within 10% of the measured change in char weight.

The rate of gasification of a char (HTT 800°C) prepared from cottonwood is shown in Figure 2. The detector output can be integrated over the entire run to give the total extent of gasification, or it can be integrated above the baseline defined by the rate of pyrolytic gasification to give the extent of gasification due to reaction with  $\text{CO}_2$ .

## RESULTS AND DISCUSSION

The ash contents and composition of the inorganic fraction of the samples used in this study are shown in Table 1. The heartwood of the cottonwood has a very high ash content, approximately four times higher than the sapwood taken from the same tree. The main components of the natural inorganic fraction are calcium, potassium, and magnesium; in addition to these elements the lignite sample has a high concentration of iron. All of these elements are potentially active gasification catalysts.

Table 1. Composition of cottonwood, treated cottonwood and lignite samples.

| Sample                          | % Ash | Composition of Ash (% dry weight) |      |      |      |      |                   |      |
|---------------------------------|-------|-----------------------------------|------|------|------|------|-------------------|------|
|                                 |       | K                                 | Mg   | Ca   | Fe   | Co   | Ni                | Cu   |
| COTTONWOOD                      |       |                                   |      |      |      |      |                   |      |
| Untreated                       |       |                                   |      |      |      |      |                   |      |
| Heartwood                       | 2.01  | 0.32                              | 0.08 | 0.50 | --   | --   | --                | --   |
| Sapwood                         | 0.51  | 0.10                              | 0.02 | 0.12 | --   | --   | --                | --   |
| Ion-exchanged                   |       |                                   |      |      |      |      |                   |      |
| Sapwood                         |       |                                   |      |      |      |      |                   |      |
| Acid-washed                     | 0.02  | --                                | --   | 0.01 | --   | --   | n.d. <sup>b</sup> | --   |
| K <sup>+</sup> -exchanged       | 0.41  | 0.28                              | --   | 0.02 | --   | --   | n.d.              | --   |
| Mg <sup>2+</sup> -exchanged     | 0.17  | --                                | 0.09 | 0.01 | --   | --   | n.d.              | --   |
| Ca <sup>2+</sup> -exchanged     | 0.34  | --                                | --   | 0.14 | --   | --   | n.d.              | --   |
| Co <sup>2+</sup> -exchanged     | 0.34  | --                                | --   | 0.01 | --   | 0.23 | n.d.              | --   |
| Ni <sup>2+</sup> -exchanged     | 0.33  | --                                | --   | --   | --   | --   | 0.21              | --   |
| Cu <sup>2+</sup> -exchanged     | 0.42  | --                                | --   | --   | --   | --   | n.d.              | 0.32 |
| Acetate Salt-treated            |       |                                   |      |      |      |      |                   |      |
| Sapwood (0.01 M)                |       |                                   |      |      |      |      |                   |      |
| KAc                             | 0.91  | 0.38                              | --   | 0.02 | --   | --   | n.d.              | --   |
| Ca(Ac) <sub>2</sub>             | 0.83  | --                                | --   | 0.36 | --   | --   | n.d.              | --   |
| Co(Ac) <sub>2</sub>             | 0.89  | --                                | --   | 0.01 | --   | 0.40 | n.d.              | --   |
| LIGNITE <sup>c</sup> (PSOC-837) | 11.88 | 0.04                              | 0.64 | 1.81 | 0.39 | --   | --                | --   |

<sup>a</sup>Ion-exchanged samples were acid washed (H<sup>+</sup>-exchanged) prior to treatment.

<sup>b</sup>n.d. = "not determined"; no value (--) = <50 ppm.

<sup>c</sup>Lignite sample and analysis provided by the Penn State Coal Data Base.

Table 2. Conversion due to pyrolysis (P) and gasification (G) of chars prepared from cottonwood and lignite at various heat treatment temperatures (HTT) and pyrolysis times. Chars were gasified for 30 minutes at 800°C in 90.9 kPa CO<sub>2</sub>.

| Sample               | HTT (°C) | Time (min) | Char Yield (%) | % Conversion at 800°C |      |       |
|----------------------|----------|------------|----------------|-----------------------|------|-------|
|                      |          |            |                | P                     | G    | Total |
| COTTONWOOD (Sapwood) | 800      | 10         | 13.1           | 1.6                   | 32.5 | 34.1  |
|                      | 900      | 10         | 11.5           | 1.7                   | 30.9 | 32.6  |
|                      | 1000     | 10         | 10.4           | 1.2                   | 15.9 | 17.1  |
|                      | 800      | 5          | 13.2           | 3.2                   | 32.9 | 36.1  |
|                      | 800      | 30         | 12.6           | 1.7                   | 31.9 | 33.6  |
|                      | 800      | 60         | 12.3           | 1.2                   | 34.0 | 35.2  |
| LIGNITE              | 800      | 10         | 61.5           | 3.6                   | 66.5 | 70.1  |
|                      | 900      | 10         | 59.0           | 1.9                   | 51.8 | 53.7  |
|                      | 1000     | 10         | 58.0           | 1.6                   | 34.7 | 36.3  |

Acid-washing of the cottonwood sapwood removed most of the inorganic fraction, with the exception of a small quantity of residual calcium. When the acid-washed wood was treated by ion exchange with dilute salt solutions, the resulting samples contained 7-8 milliequivalents/100g with the exception of the  $\text{Cu}^{+2}$ -exchanged sample, which was treated at the 10 meq/100 g level. This is in agreement with the carboxyl content of 8 meq/100 g found previously for this sample, and indicates that ion exchange provides a high level of control for addition of inorganic cations to wood. The overall ash contents of the treated samples were all lower than that of the untreated sapwood. When the salt solution was dried onto the acid-washed wood without removing the free salts, the level of cation addition was 1.5-2.5 times higher than in the ion-exchanged samples.

Table 2 shows the effects of heat treatment temperature (HTT) and pyrolysis time on the char yields and reactivities of the resulting chars toward  $\text{CO}_2$  gasification at  $800^\circ\text{C}$ . The char yields of the wood and lignite do not vary significantly within the temperature range and pyrolysis times studied. However, it is important to notice the differences in char yields between the wood and lignite samples, especially with respect to the concentration of inorganic species in the chars. The char yields from wood suggest that the ash is concentrated by a factor of 7-10, resulting in an ash content of 4-5% in the char. Similarly, the ash content of lignite char would be concentrated to nearly 20% of the weight of the char.

Reactivities of both the wood and lignite chars decreased by a factor of approximately two as the HTT was increased from  $800^\circ\text{C}$  to  $1000^\circ\text{C}$ . The contribution of pyrolysis to the gas yields in both samples was relatively small and it did not vary significantly under the conditions shown. Lignite char reactivity decreased approximately linearly between  $800^\circ$  and  $1000^\circ\text{C}$ . The reactivity declined more sharply above  $900^\circ\text{C}$  in the wood sample. This may indicate that one of the natural catalytic species in wood undergoes a specific transformation above  $900^\circ\text{C}$ , rendering it inactive, and that the reactivity of wood char is otherwise less dependent on HTT than is that of coal char. The extent of wood char gasification is independent of time of pyrolysis between 5 and 60 minutes. The dependence of reaction rate on HTT found in this study is somewhat less than that reported by Hippo *et al.* for a raw lignite gasified in steam (4). These workers report nearly a three-fold increase in reactivity in steam at  $750^\circ\text{C}$  as the HTT is reduced from  $900^\circ$  to  $800^\circ\text{C}$ .

The rates shown in Table 2 for the lignite char gasification are similar to data reported previously by other workers for  $\text{CO}_2$  gasification of lignite chars prepared under similar conditions (5,6). Rates of wood char gasification indicate a substantially higher reactivity than reported previously for another lignocellulose-derived char gasified in  $\text{CO}_2$  at  $900^\circ\text{C}$  (7). The lignite char was nearly twice as reactive as the wood char over the temperature range studied, which is no doubt due in part to its higher ash content. The lower reactivity of the wood char is also explained in part by the CP/MAS  $^{13}\text{C}$  n.m.r. spectrum of the char prepared by 10 minutes pyrolysis at  $600^\circ\text{C}$ , shown in Figure 3. This spectrum contains a single peak centered at 130 ppm, corresponding to aromatic carbon. The spectrum is nearly identical to that of an anthracite coal (8), and anthracite coals have been shown to be more than ten times less reactive than lignite under gasification by  $\text{CO}_2$  (5). Wood chars prepared at higher temperatures contained insufficient hydrogen to provide for transfer of spin polarization to carbon, as required in the cross-polarization n.m.r. technique, and they did not give well-resolved spectra. However, it is clear that chars prepared above  $600^\circ\text{C}$  are highly aromatic and their gasification will require effective catalysis if it is to be carried out at lower temperatures. These n.m.r. data are somewhat surprising in view of earlier work on the n.m.r. spectroscopy of wood chars which showed a significant aliphatic component in chars prepared at temperatures up to  $400^\circ\text{C}$  (9).

The char yields and reactivities of chars (HTT 800°C) prepared from untreated cottonwood and catalyst-treated samples are shown in Table 3. The catalysts were added by ion exchange to the acid-washed sapwood as described earlier. Acid washing had a dramatic effect on the char yield, reducing it by a factor of more than two. Addition of transition metal and alkaline earth metal catalysts had little effect on the char yield, but the alkali metal catalysts restored the char yield to near the level found for the untreated wood. Acid-washing also resulted in complete loss of the cellular structure of the wood during pyrolysis. All of these effects parallel those reported previously for the effects of inorganic species on the carbonization of the cottonwood (10).

Table 3. Ash content and char yields (HTT 800°C) of untreated and ion-exchanged cottonwood samples and extents of conversion due to pyrolysis (P) and gasification (G) of cottonwood chars gasified for 30 minutes at 800°C in 90.9 kPa CO<sub>2</sub>.

| Sample                      | Ash Content<br>(%, d.a.f.) | Char Yield<br>(%, d.a.f.) | Percent Conversion |     |                  |
|-----------------------------|----------------------------|---------------------------|--------------------|-----|------------------|
|                             |                            |                           | P                  | G   | Total            |
| Cottonwood Heartwood        |                            |                           |                    |     |                  |
| Untreated                   | 2.01                       | 16.8                      | (100% in <20 min)  |     |                  |
| Cottonwood Sapwood          |                            |                           |                    |     |                  |
| Untreated                   | 0.51                       | 14.8                      | 2                  | 40  | 42               |
| Acid-washed                 | <0.02                      | 7.1                       | 2                  | <1  | 2                |
| Na <sup>+</sup> -exchanged  | 0.31                       | 14.0                      | 4                  | 16  | 20               |
| K <sup>+</sup> -exchanged   | 0.40                       | 13.9                      | 2                  | 13  | 15               |
| Mg <sup>2+</sup> -exchanged | 0.17                       | 9.4                       | 3                  | 15  | 18               |
| Ca <sup>2+</sup> -exchanged | 0.34                       | 9.7                       | 5                  | 102 | 107 <sup>a</sup> |
| Co <sup>2+</sup> -exchanged | 0.33                       | 9.5                       | 9                  | 73  | 82               |
| Ni <sup>2+</sup> -exchanged | 0.32                       | 8.0                       | 3                  | 34  | 37               |
| Cu <sup>2+</sup> -exchanged | 0.40                       | 7.3                       | 1                  | 3   | 4                |

<sup>a</sup>Percent of conversion determined by integration of combustible gas detector signal was consistently 100-110% of weight of samples which gasified completely.

The most reactive sample was found to be the untreated cottonwood heartwood. The reactivity of this char reflects its higher ash content, and further illustrates the catalytic properties found previously for the natural inorganic fraction (2). The most effective ion-exchanged catalysts were found to be calcium and cobalt, which gave reactivities intermediate between the untreated sapwood and heartwood samples. Chars containing alkali metal catalysts were surprisingly unreactive in view of the excellent catalytic properties of these catalysts for lignite chars gasified in steam (4) and in air (11). Alkali metals are known to be lost during pyrolysis and gasification at these temperatures (12), but the char from potassium-treated wood contained 2.3% of ash by TG, suggesting that a large proportion of the catalyst was retained, at least during char formation.

The catalytic activities of the alkaline earth metals in wood gasification more closely parallel effects reported in the CO<sub>2</sub> gasification of coal char (5). The high catalytic activity of calcium suggests that it is the dominant factor controlling the reactivity of the untreated cottonwood sapwood and heartwood samples (see metals analysis in Table 1).

The transition metals are known to be active catalysts of CO<sub>2</sub> gasification, although they are often deactivated by oxidation during reaction (13). We have previously found this to be the case in the CO<sub>2</sub> gasification of wood chars (HTT 1000°) as well (2). The wide range of reactivities shown in Table 3 for the gasification of wood chars catalyzed by transition metals could, therefore,



represent the inherent activity of the catalyst or the activity of the catalyst under these specific conditions of pyrolysis and gasification. However, the high catalytic activity of the cobalt indicates the potential utility of these catalysts, and we are continuing to investigate the effects of pyrolysis and gasification conditions on catalysis of wood char gasification by cobalt.

The effects of different catalyst treatments are further illustrated by the reaction rate profiles shown in Figures 4-6. Figure 4 shows the rate of  $\text{CO}_2$  gasification of char prepared from  $\text{K}^+$ -exchanged wood. The rate is nearly constant throughout the reaction, suggesting that the reaction is zero order with respect to the mass of the char. The reaction does not appear to undergo the initial induction period which is often observed in gasification reactions. By contrast, Figure 5 shows that the gasification of the char containing calcium does exhibit an induction period, and the rate decays in a more nearly first order manner following the induction period. The char was completely gasified in this case. A third type of behavior is exhibited in catalysis by cobalt, as shown in Figure 6. In this case the reaction is very rapid at the outset and decays more rapidly than would be expected for a reaction which is first order with respect to the char. The rate approaches zero well before the char is depleted, indicating that the catalyst is being deactivated during reaction, and that a very high level of catalysis could be attained if this deactivation could be avoided.

We have also determined the rates of gasification of chars prepared from wood treated beyond the exchange capacity with the acetate salts of potassium, cobalt and calcium. Gasification rates of these chars are compared to those of the chars from ion-exchanged wood in Figure 7. In all three treatments the reactivity increased at least linearly with the quantity of added catalyst. This implies that the catalyst dispersion afforded by ion exchange is lost during carbonization, or that the catalyst added as the aqueous salt solution was equally well dispersed, presumably on the hydrophilic carbohydrate portions of the wood cell wall.

Loss of dispersion of ion-exchanged catalysts has been conclusively demonstrated in calcium-exchanged coals heated at  $1000^\circ\text{C}$  (14). Although the temperatures employed in the current study were somewhat lower, it is possible the same processes occur, and the potential advantage of the ion-exchanged catalyst is lost due to catalyst agglomeration. If this is the case, the relative effectiveness of the ion-exchanged catalyst should be enhanced by reducing the carbonization temperatures, and studies now underway should provide additional information on the nature of these processes.

The most surprising feature of Figure 7 is the dramatic increase in reactivity of chars prepared from wood treated beyond the ion exchange capacity with cobalt acetate. This sample was so reactive that the reaction rate at  $800^\circ\text{C}$  could not be accurately measured in our system. The two cobalt-treated chars (HTT  $800^\circ\text{C}$ ) were therefore gasified at  $600^\circ\text{C}$  with similar results, as indicated by the dotted line in Figure 7. It is difficult to envision a mechanism whereby the acetate salt would be a more effective catalyst than ion-exchanged carboxylate salts. It is possible that the two forms of the catalyst decompose to different products, which could have different catalytic activities, although it is not clear at this time what these forms might be. In any case, the catalytic efficiency of the higher level of cobalt treatment is very promising. The reactivity at  $600^\circ\text{C}$  is much higher than that found previously for  $\text{CO}_2$  gasification at  $650^\circ\text{C}$  of wood chars treated with even higher levels of iron and nickel salts (2), and it appears to be less subject to deactivation during gasification. Cobalt has previously been studied with respect to its effects on  $\text{CO}_2$  gasification of graphite (13) and a highly carbonized cellulose char (HTT  $1000^\circ\text{C}$ ) (15). In each case it was found to be similar in effectiveness to nickel and iron catalysts. The results reported here indicate a unique catalytic capacity for cobalt, which may also indicate unique properties of wood chars formed in the temperature range employed in this study.

#### ACKNOWLEDGEMENT

This work was supported by the Gas Research Institute under Grant No. 5082-260-0683. The CP/MAS  $^{13}\text{C}$  n.m.r. spectrum was provided by the Colorado State University Regional NMR Center, funded by National Science Foundation Grant No. CHE-8208821. The lignite sample and analysis was provided by the Penn State Coal Data Base.

#### REFERENCES

1. R.A. Susott, W.F. DeGroot and F. Shafizadeh, J. Fire Flamm., 6 (1975) 311.
2. W.F. DeGroot and F. Shafizadeh, Fuel, 63 (1984) 210.
3. W.F. DeGroot, Carbohydr. Res., 142 (1985) 172.
4. E.J. Hippo, R.G. Jenkins and P.L. Walker, Jr., Fuel, 58 (1979) 338.
5. E.J. Hippo and P.L. Walker, Jr., Fuel, 54 (1975) 245.
6. L.R. Radovic, K. Steczko, P.L. Walker, Jr. and R.G. Jenkins, Fuel Processing Technology, 10 (1985) 311.
7. D.M. Mackay and P.V. Roberts, Carbon, 58 (1982) 105.
8. G.E. Maciel, V.J. Bartuska and F. Miknis, Fuel, 58 (1979) 391.
9. Y. Sekiguchi, J.S. Frye and F. Shafizadeh, J. Appl. Polym. Sci., 28 (1983) 3513.
10. W.F. DeGroot and F. Shafizadeh, J. Anal. and Appl. Pyr., 6 (1984) 217.
11. L.R. Radovic, P.L. Walker, Jr. and R.G. Jenkins, Fuel, 63 (1984) 1028.
12. D.A. Sams, T. Talverdian and F. Shadman, Fuel, 64 (1985) 1208.
13. P.L. Walker, Jr., M. Shelef and R.A. Anderson in Chemistry and Physics of Carbon, Vol 4 (P.L. Walker, Jr. ed.), Marcel Dekker, New York, 1968, pp. 287-383.
14. L.R. Radovic, P.L. Walker, Jr. and R.G. Jenkins, Fuel, 62 (1983) 209.

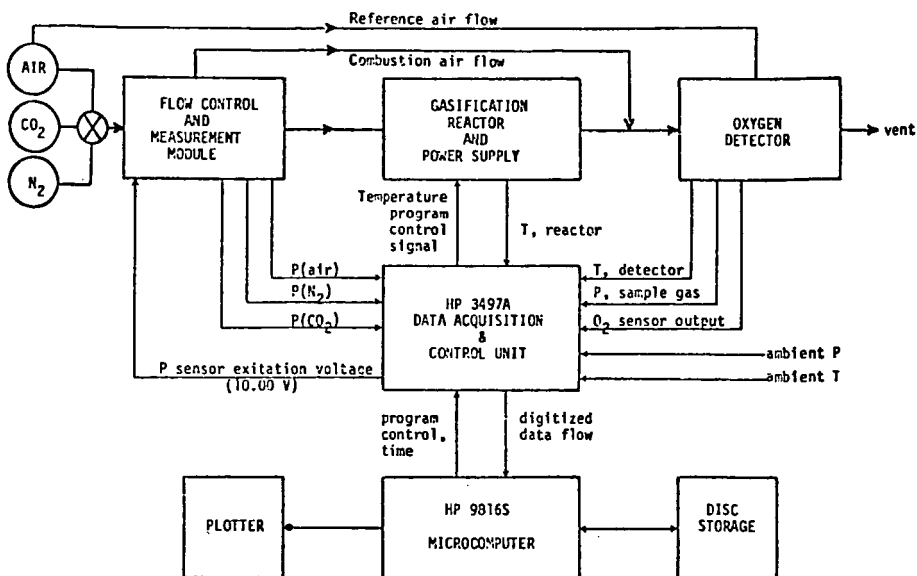


Figure 1. Schematic diagram of gasification reactor and combustible gas detector system.

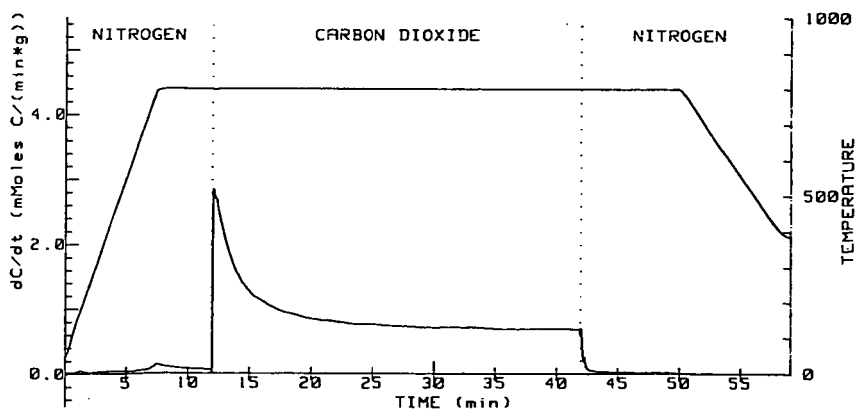


Figure 2. Reaction rate profile for the gasification of untreated cottonwood char in 90.9 kPa CO<sub>2</sub> at 800°C.

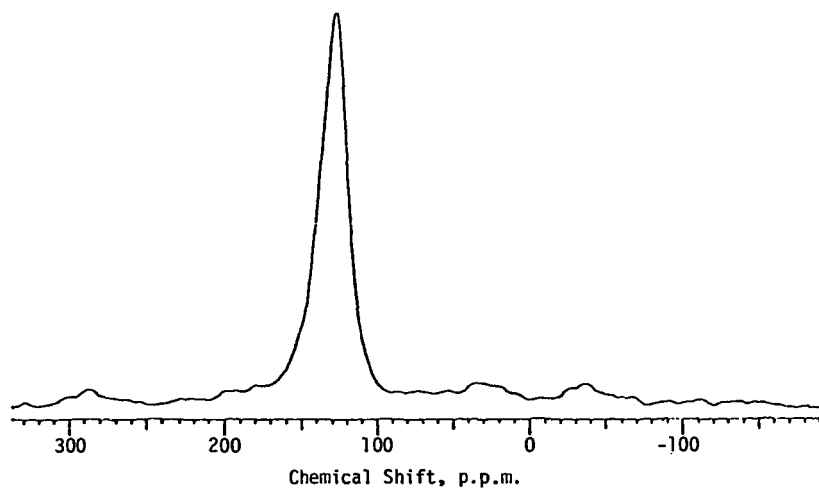


Figure 3. CP/MAS  $^{13}\text{C}$  n.m.r. spectrum of char prepared from untreated cellulose (HTT 600°C).

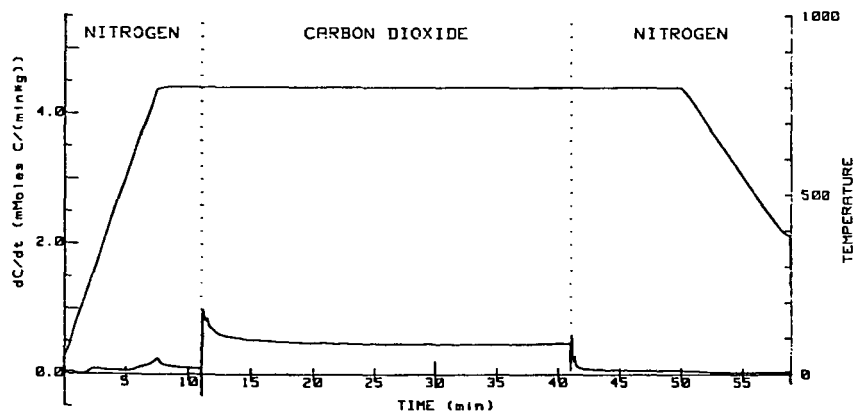


Figure 4. Reaction rate profile for the  $\text{CO}_2$  gasification of char (HTT 800°C) prepared from  $\text{K}^+$ -exchanged cottonwood.

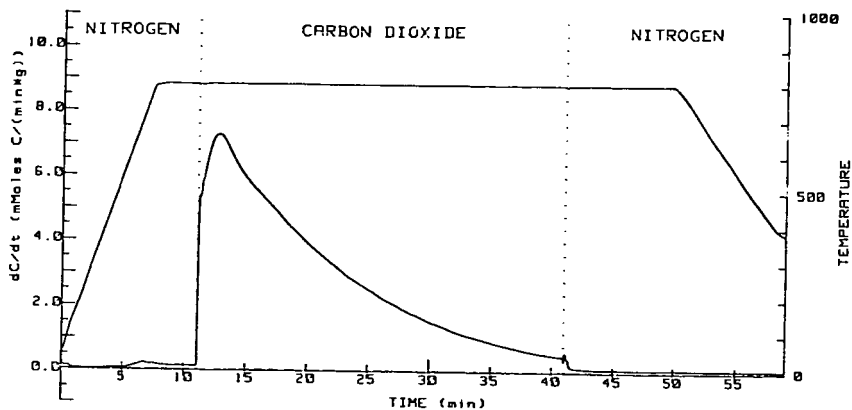


Figure 5. Reaction rate profile for the  $\text{CO}_2$  gasification of char (HTT  $800^\circ\text{C}$ ) prepared from  $\text{Ca}^{+2}$ -exchanged cottonwood.

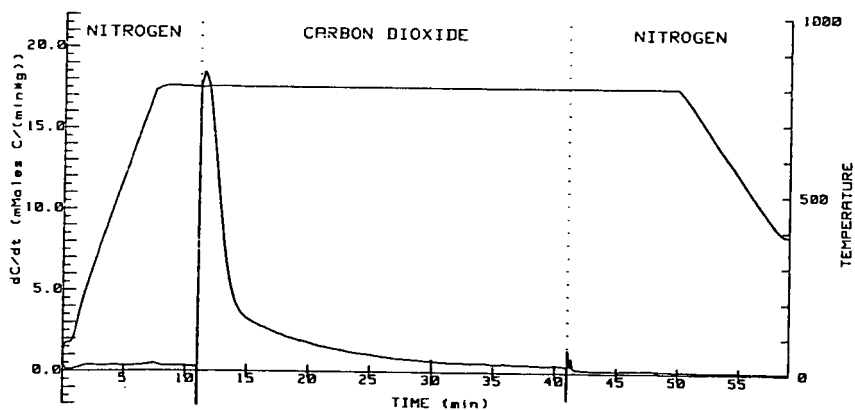


Figure 6. Reaction rate profile for the  $\text{CO}_2$  gasification of char (HTT  $800^\circ\text{C}$ ) prepared from  $\text{Co}^{+2}$ -exchanged cottonwood.

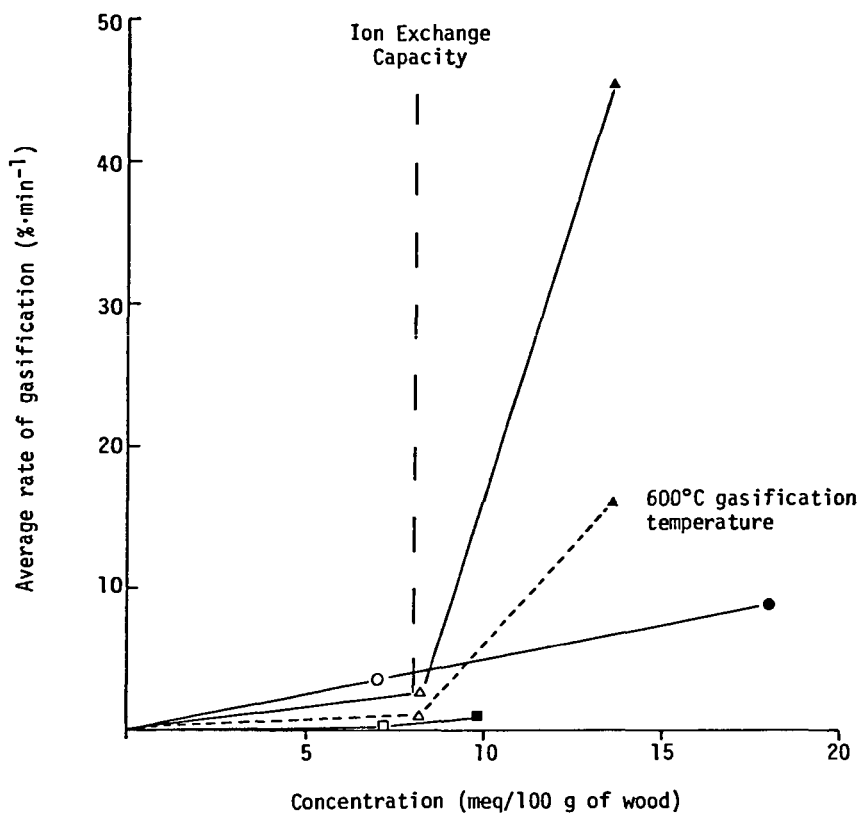


Figure 7. Average rate of  $\text{CO}_2$  gasification at  $800^\circ\text{C}$  of chars prepared from cottonwood treated with inorganic catalysts at the ion exchange capacity (open symbols) and beyond the ion exchange capacity (solid symbols): potassium ( $\square, \blacksquare$ ); cobalt ( $\triangle, \blacktriangle$ ); calcium ( $\circ, \bullet$ ).

## OXYGEN-ENRICHED COMBUSTION OF A COAL-WATER FUEL

by

Timothy S. McIlvried, Alan W. Scaroni, and Robert G. Jenkins

Fuel Science Program  
Department of Material Science and Engineering  
The Pennsylvania State University  
University Park, PA 16802

### INTRODUCTION

Several successful test firings have been performed with coal-water fuels (CWF's) in industrial boilers. However, even with advances in atomization and burner design, there are still inherent limitations associated with CWF's which cause decreased combustor performance. These include:

- 1) Temperatures and heat liberation from CWF flames are lower than those of oil flames. This is due, mainly, to the high water concentrations, which must be vaporized.
- 2) Successful ignition and flame stabilization of CWF's usually require high primary air preheat temperatures and/or a pilot flame.
- 3) Ignition delay and burnout times of CWF droplets are longer than those of oil droplets. The residence time of CWF droplets in oil fired boilers is usually not sufficient for complete carbon burnout. Thus, the CWF firing rate must be reduced, resulting in a derating of the boiler.

One means of overcoming, or at least reducing, the combustion problems associated with CWF's is oxygen enrichment of the combustion air. Moderate amounts of oxygen enrichment, usually between 1-4 volume percent, have been used in industry to either boost production levels or improve combustion efficiency in pulverized coal and oil fired boilers (1). Oxygen enrichment increases the partial pressure of oxygen leading to acceleration of the combustion rate and, thus, the rate of char burnout of the CWF droplets. Correspondingly, there is a decrease in the total

amount of nitrogen in the combustion air, which reduces the volume of the air and flue gases. This in turn, causes an increased residence time of the CWF droplets because of lower gas velocities. Both increased combustion rate and longer residence time will help offset some of the derating associated with converting to CWF's. This study is aimed at determining the effect that a 2% increase in the oxygen content of the primary combustion air will have on the combustion characteristics of a CWF.

#### EXPERIMENTAL

A horizontally fired laboratory scale combustor, designed and built at Penn State to fire fuel oil, was modified to fire CWF's (2,3). Using this combustor, the effect of enriching the oxygen content of the primary air on the heat distribution in the furnace, the quantity of unburned carbon in the flyash and pollutant formation ( $\text{NO}_x$  and  $\text{SO}_2$ ) were investigated.

The CWF used was supplied by The Atlantic Research Corporation, Fredericksburg, Virginia. Analyses of the CWF and parent coal are given in Table 1. The origin of

TABLE 1  
ANALYSES OF THE CWF

|                   | AS RECEIVED (wt%) | DRY BASIS (wt%) |
|-------------------|-------------------|-----------------|
| C                 | 57.4              | 80.8            |
| H                 | 3.4               | 4.8             |
| N                 | 1.1               | 1.6             |
| S                 | 0.5               | 0.7             |
| O (by difference) | 4.3               | 6.0             |
| ASH               | 4.3               | 6.1             |
| H <sub>2</sub> O  | 28.9              | -               |

Higher Heating Value  $2.44 \times 10^7$  J/kg (10,500 BTU/lb)

#### PROXIMATE ANALYSIS (DRY BASIS)

| VM    | ASH  | FIXED CARBON |
|-------|------|--------------|
| 30.9% | 6.1% | 63.0%        |



the parent coal is unknown but the analyses are typical of a high volatile eastern bituminous coal. The CWF has a solids loading of 70 wt% and a higher heating value of  $2.44 \times 10^7$  J/kg (10,500 BTU/lb). Thus, the CWF is typical of many of those that are currently under consideration by industry. The furnace was operated at a firing rate of 48 kW (164,000 BTU/lb). Oxygen enrichment was achieved by combining a stream of pure oxygen with the combustion air in order to increase the oxygen content to the desired 23% concentration. The oxygen/fuel ratio was varied from 95% to 115% theoretical oxygen. Centerline furnace temperatures were measured at various axial distances along the combustor using shielded thermocouples. Stack gases were continuously monitored for  $O_2$ ,  $CO_2$ , CO,  $NO_x$ , and  $SO_2$ . Flyash samples were analyzed for carbon content.

Furnace preheat and CWF ignition were achieved by a methane pilot flame. It should be noted that stable CWF flames were not able to be maintained without pilot flame support. Thus, the methane pilot flame was maintained during all trials and provided approximately 25% of the total heat input to the combustor.

## RESULTS

Combustion trials were performed on the CWF with normal air and air enriched to 23% oxygen (2% oxygen enrichment). A 2% increase in oxygen content of the primary combustion air provided an 8.7% decrease in the volume of combustion air required and a 7.9% decrease in the volume of flue gases produced. Figure 1 shows higher furnace temperatures for the oxygen enriched case. There was approximately a 60 K increase at 5% excess oxygen. This increase in temperature appears to be quite constant over the length of the combustor. The amount of carbon in the flyash was reduced by about 5% at this excess oxygen level. The oxygen enriched flames also appeared visually brighter and closer to the burner (i.e. a shorter ignition delay).

Sulfur oxides are formed when sulfur in the fuel is oxidized during the combustion process. Figure 2 shows  $SO_2$  emissions as a function of excess air (normalized to a 0% excess air basis and taking into account the reduced volume of flue gas in the oxygen enriched cases). It was found that  $SO_2$  concentrations were

virtually independent of amount of excess air or oxygen enrichment for the fuel lean flames. However, the  $\text{SO}_2$  concentrations appear to be increased for the oxygen enriched fuel rich flame.

As is well known,  $\text{NO}_x$  is formed in two ways during combustion; that is by oxidation of atmospheric nitrogen (thermal  $\text{NO}_x$ ) and oxidation of nitrogen in the fuel (fuel  $\text{NO}_x$ ). The formation of thermal  $\text{NO}_x$  is very temperature dependent and is not considered to be a significant source of  $\text{NO}_x$  formation at temperatures below about 1770 K (4). The maximum temperature reached in the experimental combustor was about 1450 K therefore, most of the  $\text{NO}_x$  was assumed to be fuel  $\text{NO}_x$ . Figure 3 shows the variation of  $\text{NO}_x$  with percent excess air for both the normal and oxygen enriched combustion.  $\text{NO}_x$  concentrations were approximately 70 PPM higher in the fuel lean oxygen enriched flames. As the flames become more fuel rich the  $\text{NO}_x$  concentrations in the oxygen enriched flames somewhat approach the concentrations found in the ambient air flames.

#### CONCLUSIONS

Oxygen enriched combustion of a CWF was studied in a small scale (48 kW) combustor. It was found that a 2% increase in oxygen content of the combustion air produced:

- 1) Increase of about 60 K in furnace temperature.
- 2) More luminous flame with shorter ignition delay.
- 3) Approximately a 5% reduction of carbon in the flyash
- 4) No effect on  $\text{SO}_2$  formation in fuel lean flames.
- 5) Somewhat higher  $\text{NO}_x$  emissions for fuel lean flames but only slightly higher  $\text{NO}_x$  concentrations for fuel rich flames.

# ACKNOWLEDGEMENTS

Financial support for this research was provided by the Penn State coal-water fuel project funded by the Commonwealth of Pennsylvania. The coal-water fuel was provided by the Atlantic Research Corporation.

# REFERENCES

1. Taschler, D.R., Nolte, F.S., Stringfello, T.E., The Impact of Oxygen Enriched Combustion of Coal Water Slurries on the Economics and Performance of Large Scale Boilers, Sixth International Symposium on Coal Slurry Combustion and Technology, Orlando, Florida, June 1984
2. Lima, J.G.H., Effect of Oxygen Enrichment on NO<sub>x</sub> from Distillate Petroleum Flames in a 25 Kilowatt Combustor, M.S. Thesis, The Pennsylvania State University, 1983
3. Rodriguez-Pereira, R., Effect of an Atomizing Medium on Coal-Water Mixture Combustion, M.S. Thesis, The Pennsylvania State University, 1985
4. Morrison, G.F., Nitrogen Oxides from Coal Combustion - Abatement and Control, IEA Coal Research Report Number ICTIS/TR 11, November 1980
5. Wagner, J., Sommer, T.M., Taylor, B.E., Johnson, S.A., Coal-Water Mixture Firing in an Industrial Package Boiler - A Users Perspective, Seventh International Symposium on Coal Slurry Fuels Preparation and Utiliization, New Orleans, Louisiana, May 1985

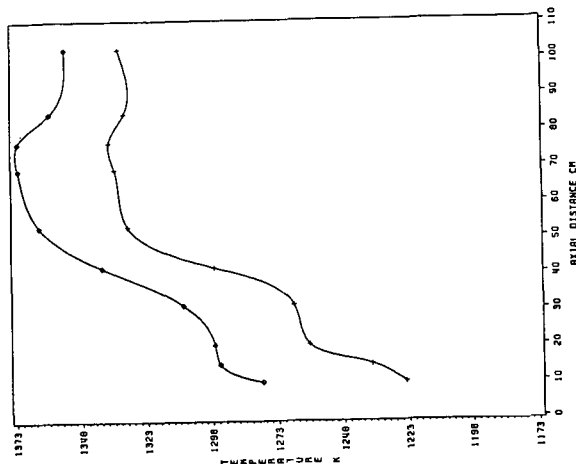


Figure 1. Centerline Furnace Temperature. + 21 % Oxygen; o 23% Oxygen.

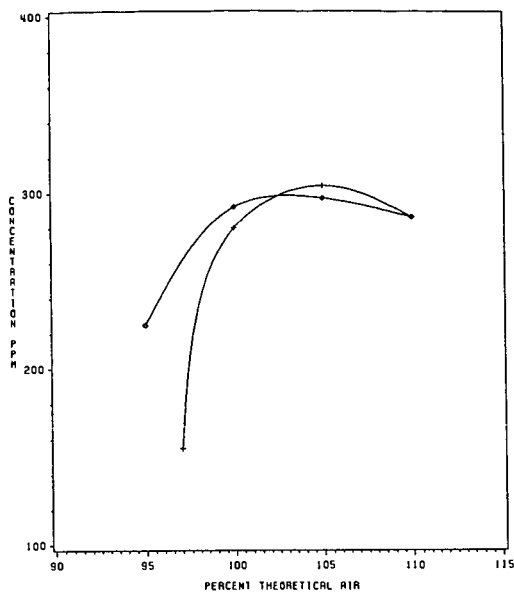


Figure 2. Sulfur Dioxide Concentration Versus Percent Theoretical Air on an Oxygen Free Basis. + 21% Oxygen;  $\diamond$  23% Oxygen.

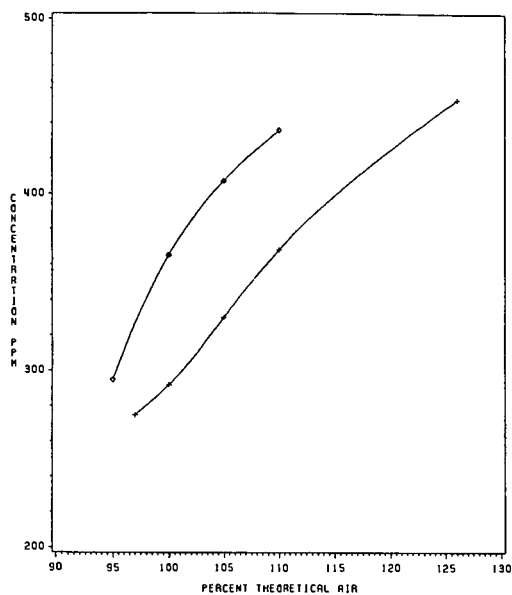


Figure 3. NO<sub>x</sub> Concentration Versus Percent Theoretical Air on an Oxygen Free Basis. + 21% Oxygen;  $\diamond$  23% Oxygen.

## Secondary Atomization of Coal-Water Fuel Droplets Resulting from Exposure to Intense Radiant Heating Environments

Daniel J. Maloney and James F. Spann (ORAU)

U.S. DOE, Morgantown Energy Technology Center  
P.O. Box 880, Morgantown, WV 26505

### Introduction

The use of coal-water fuels (CWF) for direct firing in heat engines presents some challenges because conventional turbine combustors and diesel engines require short duration, intense combustion processes. It is generally understood that burning times required for efficient carbon utilization in these systems is a function of the fuel droplet size. For CWF droplets, the early stages of heating are critical. Under certain heating conditions, water is evaporated from a droplet leaving a relatively slow burning agglomerate of coal particles. Under other heating conditions, however, fuel droplets may boil explosively producing many small fragments having characteristically shorter combustion times. The behavior of CWF in a combustor depends on a number of factors including droplet size, the amount and size distribution of coal particle inclusions, and the primary mode and rate of droplet heating. A detailed knowledge of slurry droplet evaporation mechanisms is required, therefore, for accurate prediction of slurry droplet combustion times and for the design of CWF-fired heat engines.

The objective of this work is to determine the radiant energy flux conditions required to achieve explosive boiling of CWF droplets. Radiant heating is important because, when considering coal particle sizes typical of highly beneficiated micronized CWF (2 to 3 microns mean radius) proposed for use in heat engine applications, the black body radiation prevalent in combustion environments can penetrate into the droplet. The resulting internal heating of coal particles can result in superheating of the water within the droplet and thereby establish conditions necessary for explosive boiling.

Experimentally, conditions required to achieve explosive boiling were determined by electrostatically suspending and irradiating single CWF droplets with well characterized radiation pulses. Droplet behavior in these experiments was monitored using high-speed cinematography. The energy flux required for explosive boiling was determined at ambient temperature and pressure as a function of incident radiation intensity and CWF droplet size and composition. The results were then compared with theoretical predictions of the explosive boiling threshold for CWF droplets in high-temperature black body radiation fields. The primary question we wish to address is: do sufficient conditions exist, or can they be made to exist, to cause explosive boiling of CWF droplets ranging from 20 to 200 microns in diameter in realistic combustor configurations?

### Experimental

Single CWF droplets were isolated and held in an electrodynamic balance apparatus which was designed and fabricated based on the work of Davis and Ray (1). The balance, as illustrated in Figure 1, is a quadrupole trap consisting of two hyperboloidal endcap electrodes and a central ring electrode. When an AC voltage is applied between the ring and the two endcap electrodes the resulting field has a well defined null point at the geometric center of the balance. A charged droplet in the electric field is subject to a time averaged force directed toward the null point. The droplet is held at the null point by

applying a DC field across the endcap electrodes to counterbalance gravitational forces.

CWF droplets are delivered to the balance chamber from a CWF droplet generator developed specifically for use in these experiments. The basic device consists of a cylindrical piezoelectric transducer element with a capillary tube attached to one end and a fuel supply line attached to the other. The operating principle is the same as that used in ink-jet printers. Voltage pulses applied to the transducer cause sudden volume contractions which force fuel through the capillary orifice. The extruded fuel forms a monodisperse stream of droplets of uniform composition with the droplet size being determined by the capillary diameter and by the amplitude and duration of the voltage pulses. Details of the design and operating characteristics of the CWF droplet generator are provided elsewhere (2). Droplets are inductively charged by passing the droplet stream through an orifice in a charged plate prior to delivery into the electrodynamic balance chamber.

The droplet mass to charge ratio ( $m/q$ ) is directly proportional to the DC voltage required to bring the droplet to the null point. For CWF droplets the mass (and so  $m/q$ ) is continuously changing due to water evaporation and the balance voltage must be adjusted to hold the droplet at the null point during an experiment. To facilitate droplet position control and to provide accurate and precise measurements of changes in droplet size and mass, a microprocessor controlled, droplet imaging system (DIS) was developed. The DIS utilizes a Vidicon (video camera) detector to monitor droplet position and size. A microprocessor scans the vidicon every 17 ms and image processing techniques are employed to determine the droplet location and size. A control signal is then generated to maintain droplet position at the balance null point. Digital values corresponding to droplet cross-sectional area and balancing voltage (proportional to droplet mass) are generated at a rate of 60 Hz. The droplet size information is used to trigger the high-speed camera and to activate the pulsed radiation (laser) source. In addition, droplet diameter, mass and composition (percent coal by mass) are determined from the droplet size and balance control data. Figure 2 illustrates the capabilities of the DIS for droplet size and mass determination. The data shows the strong dependence of the droplet mass with changing droplet radius. Since droplet density increases as water evaporates from the CWF, the droplet mass dependence deviates slightly from the  $r^3$  relationship expected for a constant density droplet. The confidence interval (95 percent) for droplet size resolution with the DIS is  $\pm 3$  microns for droplets ranging in diameter from 50 to 200 microns. The confidence interval for mass resolution is  $\pm 50$  nanograms.

The CWF used in these experiments was a physically beneficiated (3 percent ash) micronized (3 micron mean particle radius) slurry having a composition of 62 percent coal by mass. During a typical experiment a water or dilute CWF (1 to 20 percent coal by mass) droplet was delivered to the balance chamber. The droplet size and weight were monitored by the DIS until a preselected size was attained. The high-speed movie camera was then activated and the laser was pulsed. A schematic of the experimental configuration is provided in Figure 3.

CWF droplets delivered to the balance chamber were on the order of 250 microns in diameter. Droplet size and composition were controlled by changing the initial coal composition in the droplet and by carefully monitoring the water evaporation. In this manner droplet sizes (50 to 200 microns in diameter) and compositions (50 to 70 percent coal by mass) of interest for combustion applications could be easily accessed.

## Results

Experiments were conducted using an eximer laser (wavelength 0.248 microns) to determine explosive boiling thresholds for water and CWF droplets at radiation pulse times of 10 nanoseconds. The test variables included droplet size and composition and radiation intensity. Single droplets of water and CWF (25 and 50 percent coal by mass) with radii of 25, 50, and 75 microns were irradiated from two sides (see Figure 3). The geometric cross section of the droplets then was twice  $\pi r^2$  and the incident radiation intensity was varied from  $2.5 \times 10^7$  W/cm<sup>2</sup> to  $5 \times 10^8$  W/cm<sup>2</sup> by defocussing the laser beam. At the most intense radiant heating conditions the beam cross section was larger than 300 microns so that in all cases the droplets were completely blanketed by the incident radiation.

The results of experiments performed on CWF droplets containing 50 percent coal by mass are presented in Figure 4. The results can best be described in the context of Figure 5. Over the range of conditions employed CWF droplet behavior varied from oscillatory distortions to violent fragmentation as the radiant intensity was increased. The onset of fragmentation occurred over a narrow range of intensities from about  $5 \times 10^7$  to  $1.5 \times 10^8$  W/cm<sup>2</sup>. Figure 5 shows high speed film records for 75 micron radius droplets containing 50 percent coal by mass. The framing rate was 5,000 frames per second. Figure 5A illustrates the oscillatory behavior observed for these droplets when irradiated at an intensity of  $2.5 \times 10^7$  W/cm<sup>2</sup>. At this radiant intensity no droplet fragmentation was observed. Lower radiation intensities resulted in no observable fragmentation or oscillation. When the radiant intensity was increased to  $5 \times 10^7$  W/cm<sup>2</sup> (Figure 5B) droplet fragmentation was observed. The first frame in sequence 5B shows the CWF droplet prior to initiation of the radiation pulse. The second frame of the sequence shows the droplet 0.2 ms later, after the laser pulse. The droplet appears to be a large prolated sphere suggesting the possible growth of vapor bubbles within the droplet. However, the time resolution available was not sufficient to conclusively show the existence of vapor bubbles. The third frame in the sequence shows the collapse of the prolated sphere and the formation of fuel "ligaments" attached to a central droplet core. This is followed by the breakup of the droplet to form three fragments. At this radiant heating intensity we consistently observed the formation of one or two small satellite fragments and a larger core droplet. After breakup, the fragments moved with a minimum velocity of 1 m/s. Figure 5C illustrates that as the radiant intensity was increased to  $1.2 \times 10^8$  W/cm<sup>2</sup> the fragmentation of the droplets was more violent resulting in the formation of many small fuel droplets having minimum velocities ranging from 0.5 to 2 m/s. At higher radiant intensities (Figure 5D), fragmentation was evident, however, droplet fragments had velocities in excess of 3 m/s and resolution of droplet fragments was poor.

Based on the different behavior evident in the high-speed film records modes of droplet behavior have been arbitrarily defined as: NF, no fragmentation of the droplets, F, fragmentation of the droplets to form a few relatively large droplet fragments, and EF, explosive fragmentation of the droplet to produce many small droplet fragments. Figure 4 summarizes the results of experiments using CWF droplets containing 50 percent coal by mass. The dashed line in the figure represents the theoretical predictions of Sitarski (3-5) for explosive boiling thresholds for CWF droplets exposed to high-temperature black body radiation. The theoretical predictions illustrated in Figure 4 have been modified to reflect the fact that the droplets were irradiated from two sides with a geometric cross section of  $2\pi r^2$ . Figure 4 illustrates that explosive boiling thresholds decreased as droplet size was reduced. Experiments performed on droplets with 25 percent coal by mass showed a similar trend with decreasing

droplet size. Within the error of the experiment there was no observable difference between the behavior of CWF droplets as the coal loading was increased from 25 to 50 percent coal by mass. The presence of coal in the droplet did play an important role, however. Pure water droplets showed no evidence of oscillation or fragmentation at radiation fluxes of  $5 \times 10^8 \text{ W/cm}^2$  and below. This observation is consistent with the fact that pure water is essentially transparent to radiation at 0.248 micron wavelength.

### Discussion

The theory developed by Sitarski (4) assumes that electromagnetic radiation is absorbed uniformly within the droplet causing strong superheating of the liquid at the center of the droplet where thermodynamic conditions approach those on the spinodal line. The sudden burst of vapor bubbles produced at the spinodal temperature then leads to disruption of the droplet. The experimental observations are consistent with this physical description of the explosive boiling phenomena and the agreement between the experimentally determined thresholds for explosive fragmentation are in excellent agreement with the explosive boiling thresholds predicted by Sitarski.

Two alternative mechanisms for droplet breakup were also considered. They were the effect of radiation pressure and the potential for significant ionization and plasma formation. Calculations were performed to evaluate the radiation pressure associated with the laser pulse. The momentum imparted to the droplet due to the light pressure was found to be two orders of magnitude lower than the observed momentum (determined from the velocity of the fragments). Therefore, the contribution due to radiation pressure was insignificant. At radiation intensities similar to those employed in the present study, plasma formation has been observed for aerosol particles in air (6, 7). The accompanying laser breakdown depends on a number of factors including, the radiation wavelength, intensity and pulse time and the optical properties and size of the aerosol particles. Plasma formation and growth is usually accompanied by a characteristic flash of light followed by an acoustic pressure pulse (shock wave) as the plasma cloud expands at a rate of 2 to 3 km/s. Over the range of radiant heating conditions reported in Figure 4 there were no observations supporting the formation of a plasma cloud. At radiation intensities above  $10^9 \text{ W/cm}^2$ , however, the characteristic signs of plasma formation were evident.

### Conclusion

Capabilities have been developed to determine radiant intensities required to achieve explosive boiling (secondary atomization) of CWF droplets of well defined size and composition. The system has been used to determine explosive boiling thresholds for CWF droplets at short duration high intensity radiant heating conditions. The experimental results are both qualitatively and quantitatively in good agreement with theoretical predictions for explosive boiling thresholds. Attention has now been directed toward applying these techniques to make measurements of explosive boiling thresholds at radiation wavelengths in the infrared region of the energy spectrum with millisecond heating times to address conditions which are representative of combustion applications.

### Acknowledgements

The efforts of G. E. Fasching and L. O. Lawson in the development of the DIS are gratefully acknowledged. Discussions with Dr. M. Sitarski have been stimulating and insightful and are gratefully appreciated. This work was funded out of the United States Department of Energy Advanced Research and Technology Development Program.



## References

1. Davis, E. J., and A. K. Ray, J. Colloid and Interface Science, 75, 566-576, 1980.
2. Maloney, D. J., L. A. McCarthy, W. F. Lawson, G. E. Fasching, and K. H. Casleton, "Laboratory Coal-Water Fuel Droplet Generator," Sixth International Symposium on Coal Slurry Combustion and Technology, Orlando, Florida, June 25 to 27, 1984.
3. Sitarski M., "Thresholds for Explosive Evaporation of Water and Coal-Water Mixture Fine Droplets Exposed to High-Temperature Black Body Radiation," Proceedings of Condensed Papers, International Symposium-Workshop on "Particulate and Multi-Phase Processes," 16th Annual Meeting of the Fine Particle Society, Miami Beach, Florida, April 22 to 26, 1985.
4. Sitarski, M., "Modification of an Analytical Model Which Predicts the Effect of Radiative Heating on Two-Phase Aerosols," presented at the AR&TD Direct Utilization Contractors Meeting, Morgantown, West Virginia, August 13 to 15, 1985.
5. Sitarski, M., Private Communication, October, 1985.
6. Danilychev, V. A., and V. D. Zvorykin, JSRLDU 5(6), 647-758, 1984.
7. Akhtyrchenko Y. V., L. A. Vasil'ev, Y. P. Vysotskii, and V. N. Soshnikov, JSRLDU, 5(2), 233-236, 1984.

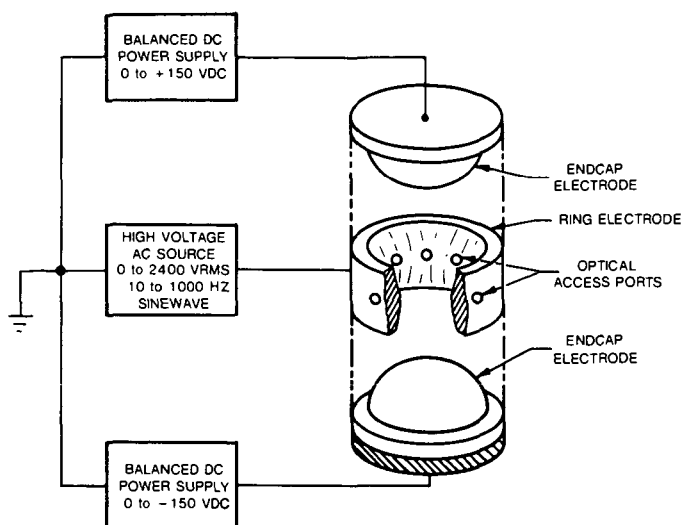


Figure 1. Electrodynamic Balance Apparatus

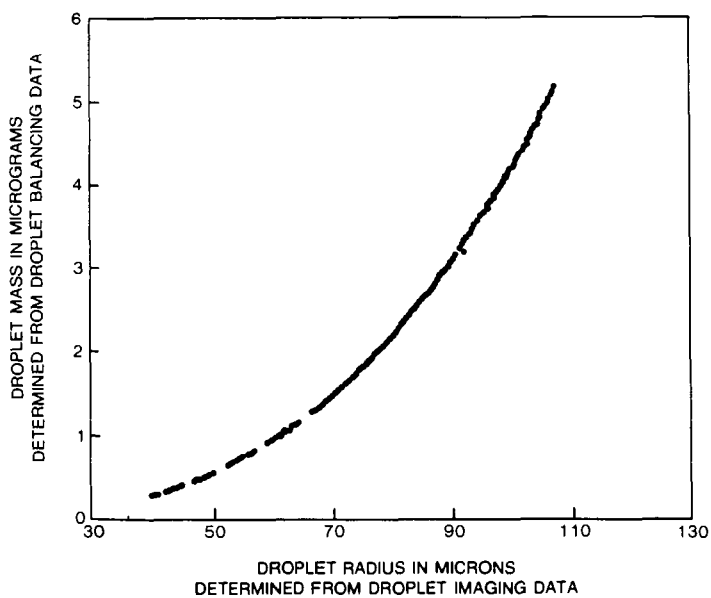


Figure 2. Droplet Mass and Size Resolution Capabilities for an Evaporating CWF Droplet

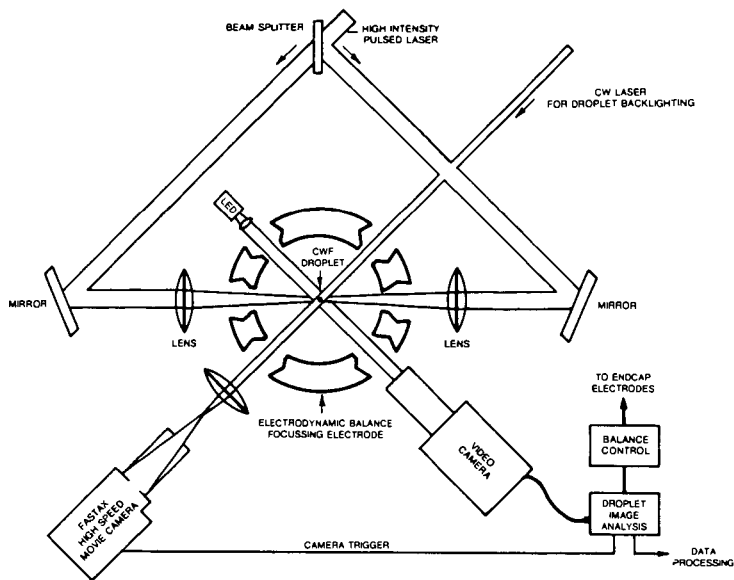


Figure 3. Experimental Configuration for Explosive Evaporation Studies

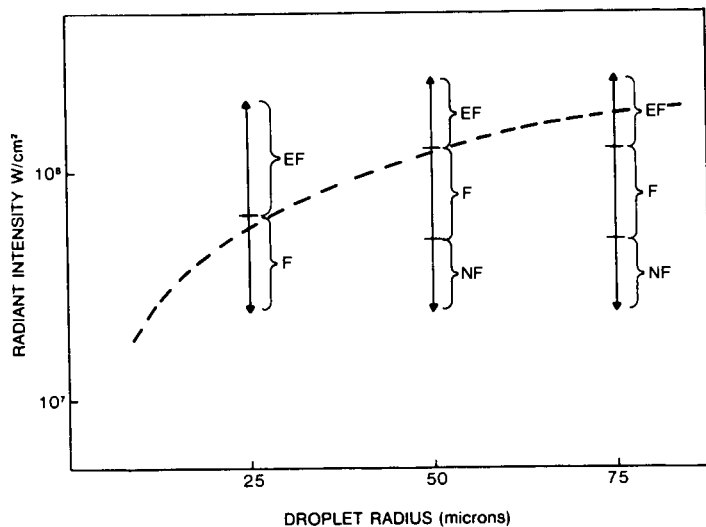


Figure 4. CWF Droplet Response as a Function of Radiant Heating Intensity at 10 ns Heating Time

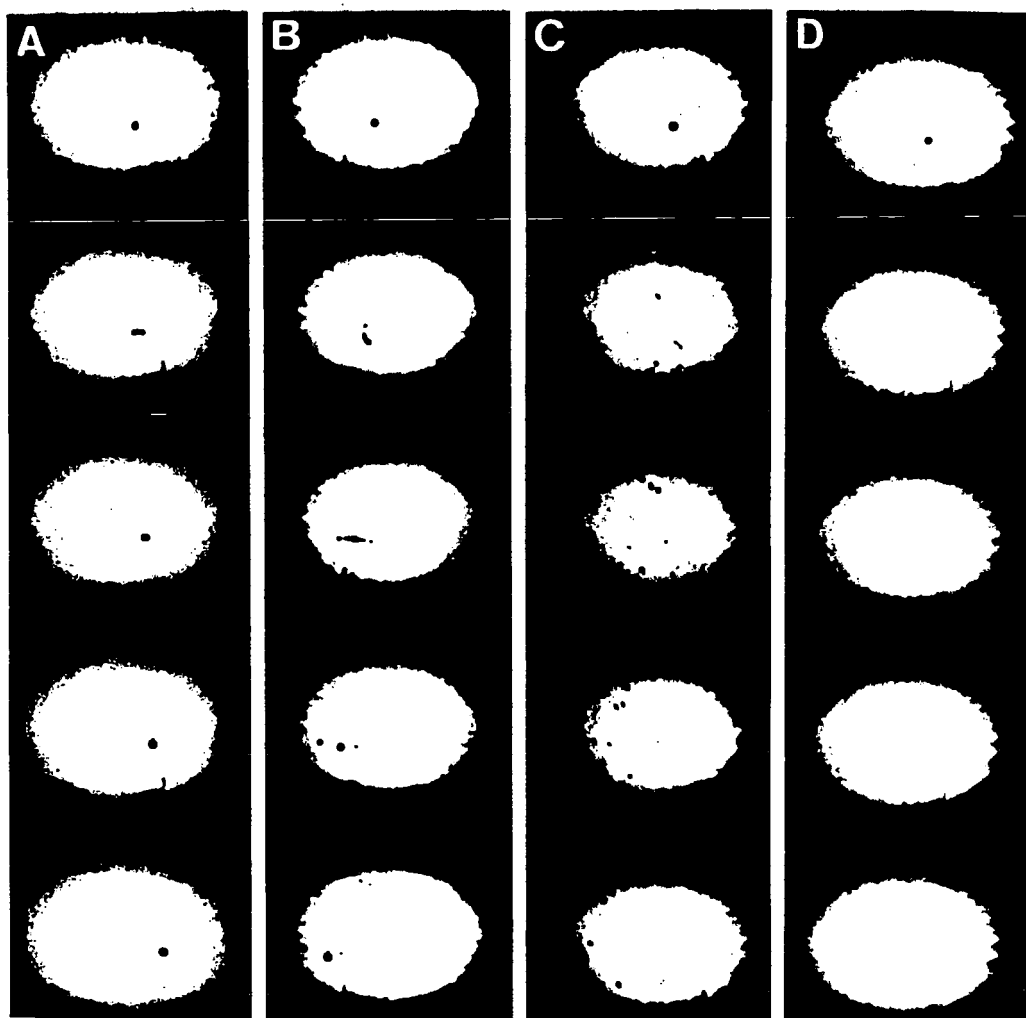


Figure 5. High-Speed Motion Picture Records of CWF Droplet Response to High-Intensity Radiant Heating. Radiant Intensity: A -  $2.5 \times 10^7$  W/cm<sup>2</sup>, B -  $5 \times 10^7$  W/cm<sup>2</sup>, C -  $1.2 \times 10^8$  W/cm<sup>2</sup>, D -  $2.5 \times 10^8$  W/cm<sup>2</sup>. Framing Rate of 5000 fps.

## A BI-DIMENSIONAL OPTICALLY ACCESSIBLE F.B.C. FOR COAL COMBUSTION STUDIES

P.G. Lignola\*, G. Raso\*\*, N. Di Muro\*\*, R. Parri\*, M. Bader\*

(\*) - Dipartimento di Ingegneria Chimica - Università - 80125 Napoli

(\*\*) - Istituto di Ricerche sulla Combustione - CNR - 80125 Napoli

### INTRODUCTION

Bi-dimensional fluidized beds have been since long adopted for studying fundamentals of fluidization. Optical accessibility has been a valid tool for analysis of bubbles and their interaction, in spite of the existing behavioural difference between three and two dimension experiments. A bi-dimensional bed has been recently used for application of mass spectrometric analysis of gas concentration profiles in single bubbles rising through a bed kept at minimum fluidization velocity (1).

Coal combustion and gasification in fluidized bed is now actively and intensively studied. Models of coal combustion process, including volatilization have been proposed. However lack of optical access into traditional fluidized bed combustors, renders difficult the comparison between model prediction and experimental result.

The idea of developing a bi-dimensional combustor, fitted with mass spectrometric probe seemed very appealing, though of not easy design and construction.

In this paper design and construction of a bi-dimensional fluidized bed combustor (F.B.C.) and result of first experiments performed are reported.

### F.B.C. DESIGN

Very crude and preliminary calculations show that it is not possible to operate steadily a bi-dimensional fluidized bed coal combustor normally exposed to ambient. Assuming for a quartz sand bed (70-600  $\mu\text{m}$  size) a temperature of 1150-1200 K, radiant heat transfer reaches values of 80 kW/sqm, which cannot be carried by enthalpy of fluidizing gas. Generation of this substantial power is not possible by means of combustion itself, owing to the small amount of coal in the bed. Consequently it is necessary to feed the F.B.C. with extra power in order to obtain a steady operation. Hypothesis of adopting Vycor<sup>TM</sup> silica glass covered with thin tin oxide layer has been discarded, since its application at these temperatures are not known, neither it was possible to assess the semiconductivity properties at high temperature of tin oxide layer.

The obvious solution to the problem was to design a furnace, fitted with windows, in which the bed had to be enclosed. The furnace essentially consists of a parallelepipedic enclosure, the dimension of which are 1070 mm height, and 890 mmx1440 mm base. Starting from the inside, furnace walls are made of Triton Kaowall<sup>TM</sup>, which is particularly suitable for high temperature, of Calsil<sup>TM</sup>, which has good insulating properties and is asbestos free and, for the outer layer, of Monolux 500<sup>TM</sup>, which has good mechanical properties, but can stand lower temperatures. The bottom has been made of CER 21/M<sup>TM</sup> which presents good mechanical properties even at high temperature. Thickness of insulation has been calculated on the basis of following assumption: outer wall temperature <333 K, inner wall temperature equal to maximum operation temperature, linear temperature gradient through walls. Constant thermal conductivity for each material, averaged on temperature has been used in calculations. Front, rear and top walls are removable. Furnace top possesses a slot, which coincides with highest level of bed free-board and can be connected to an exhaust line. A square window, 250 mmx250 mm, made of polished Vycor<sup>TM</sup> glass as been made on front and rear panel. Windows are parallel to the bed and permit its optical observation. Four electrical resistances, each providing 3.6 kW, are immersed into a ceramic support, which is 50 mm thick, 300 mm wide and 600 mm high. These resistances give the necessary power to furnace, for every possible regime of operation, since several series and series-parallel insertions are possible. Calculations show that at steady state about 4 kW are necessary for keeping furnace at 1223 K. However resistances are

capable of producing 14.4 kW, which are useful for shortening apparatus start up.

A proportional, integral temperature controller has been designed which features a thyristor power unit, and safety set points which can be triggered by maximum and minimum temperature and which can be overridden during start up procedure. For safety reasons, thermocouple failure triggers the power off. Owing to large heat capacity of furnace and prevalent radiant heat transfer within enclosure, uniform temperature is achieved throughout the bed.

The bed is confined by means of two polished Vycor ( $^{TM}$ ) glass walls, 18 mm apart, inserted into slots created on furnace sides. The transparent walls are made of a double layer of sheets, 6 mm thick, 300 mm wide and 300 mm high. Owing to the limited size of Vycor ( $^{TM}$ ) sheets the two layers are skintiled in order to prevent air and solid materials leakage during operation. Vycor ( $^{TM}$ ) glass walls continue up to the top of furnace, consequently free board is kept at the same temperature of the bed. Figure 1 shows the apparatus.

Even gas distribution at bottom of bed is achieved by means of a distributor made of aluminum silicate, which practically consists of a porous plate (140-200  $\mu$ m pore size) 20 mm thick. Great care has been taken to seal the junction between distributor and bed. To this end a special Triton Kaowall ( $^{TM}$ ) cement has been used.

Flow of fluidizing gas is measured by means of conventional rotameter. Inlet gas pressure is measured by conventional open tube manometers. Temperature of bed is measured by means of thermocouple. On each side of the bed at different heights three channels have been drilled and fitted with 12 mm alumina tubes for coal feeding and gas sampling.

Arriflex cine camera, 16 mm, at 50 frames per second has been used for optical observation and recording of F.B.C. behaviour. Analysis of single frames has been carried out by means of a graphic tablet hooked to an Apple IIe personal computer. Bubble areas were evaluated by means of specific software. Time variation of dimension of coal and char particles was also analyzed by means of the same technique.

A continuous sampling CO<sub>2</sub> analyzer was also used for monitoring coal combustion.

The whole apparatus performed as expected. The bed could be kept steady at temperature of 1223 K as long as necessary.

## RESULTS

To the best of authors' knowledge, the bi-dimensional F.B.C. is the first that has been ever constructed. Consequently it seems that up to now no direct optical test has been made yet on general fluidodynamics behaviour of fluid beds at high temperatures. Results reported in the following refer to a bed 260 mm wide and 140 mm high of sand (density 2.6 g/cm<sup>3</sup>). Mass of solids was kept constant at 1 kg. The first set of experiments that has been run was aimed at assessing the possibility of testing these fundamental aspects of fluidization.

Minimum fluidization velocity  $U_{mf}$  has been experimentally evaluated for sand of two different sizes: 300+400  $\mu$ m and 850+1000  $\mu$ m. In fig. 2  $U_{mf}$  values measured at experimental conditions are reported against temperature. For both sizes  $U_{mf}$  decreases with increasing temperature. Results are in accord with those obtained by Botterill and Teoman (2) and can be easily explained on the basis of viscosity increase with increasing temperature. Comparison with available theoretical models has not been fully accomplished yet, owing to the limited number of data. However first trials seem to indicate that for smaller size, available theory extrapolated at operation temperatures underestimate  $U_{mf}$ , whereas for larger size  $U_{mf}$  is nearly correctly estimated at temperatures lower than 673 K and is overestimated at higher temperatures.

Several films have been shot by means of cine camera with the aim of measuring bed expansion and bubble volume fraction at different temperatures. Results refer to bed of sand 300+400  $\mu$ m size. In fig. 3 bed voidage is reported against relative fluidization velocity  $U/U_{mf}$  for different bed temperatures. Bed voidage was evaluated by measuring on film frame bed height at different  $U/U_{mf}$ . Data show that bed voidage depends on temperature.

Experimental technique features the possibility of measuring bubble size on film frame by means of graphic tablet digitization. In fig. 4 an example of digitized frame is reported. Bubble fraction at different  $U/U_{mf}$  and temperatures have been measured by means of the above technique. Results are reported in fig. 5.

Combustion at 1123 K of batch of five particles of South African char, approximately spherical, of 130 mg mass and 6 mm diameter each, has been followed by cine camera recording and by monitoring  $CO_2$  concentration in exhaust gases. Burn-out time has been determined by observation of particle disappearance and by  $CO_2$  monitoring. Same experiment has also been performed with batch of three particles of South African coal, each of 400 mg mass and of 9 mm diameter. Data are reported in fig. 6. Cine camera was run at immission of particles into the bed and after 228 s and 552 s. In fig. 7 char particle diameter against time is reported as evaluated by the two methods. Data obtained by film frame analyses and data obtained by calculation of particle diameter reduction from  $CO_2$  concentration measurement, to compare fairly well. On the same diagram theoretical variation of char particle diameter with time has been reported. Curve is drawn assuming shrinking particle model and diffusion control.

Combustion of a batch of three South Africal coal particles tested also apparatus capabilities of following devolatilization. Coal particles were spherical with 9 mm diameter and with a weight of 400 mg each. Devolatilization phase could be followed at ease and flamelets generated by gas combustion were observed.

#### CONCLUSIONS

The first results confirm that the apparatus that has been developed can be a powerful tool for studying high temperature processes in fluidized beds. Specifically fundamental fluidodynamics of beds can be investigated and combustion process of coal can be followed, even during devolatilization phase. Hypotheses of current models can also be checked, though with the limitation deriving from bi-dimensionality.

#### ACKNOWLEDGMENT

The work has been performed with partial financial support from Ministero della Pubblica Istruzione of Italy.

#### REFERENCES

- 1) Lignola P.G., Donsì G. and Massimilla L.: A.I.Ch.E. Symposium Series 79, 19 (1983)
- 2) Botterill J.S.M., Teoman Y.: in "Fluidization" ed. Grace J.R. and Matsen J.M., Plenum Press, N.Y. (1980), p. 93

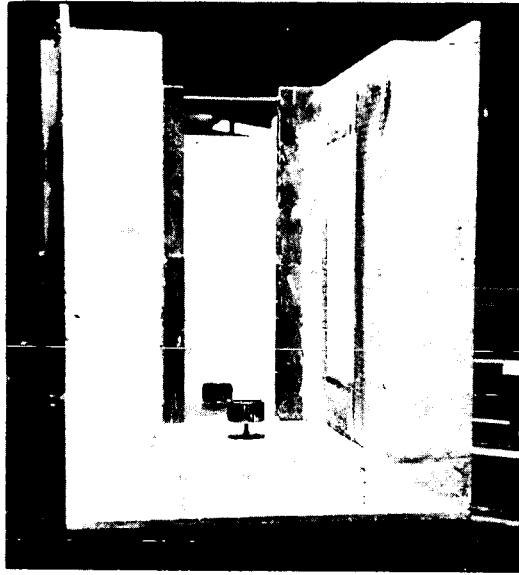


Fig. 1 - Furnace encloses F.B.C.

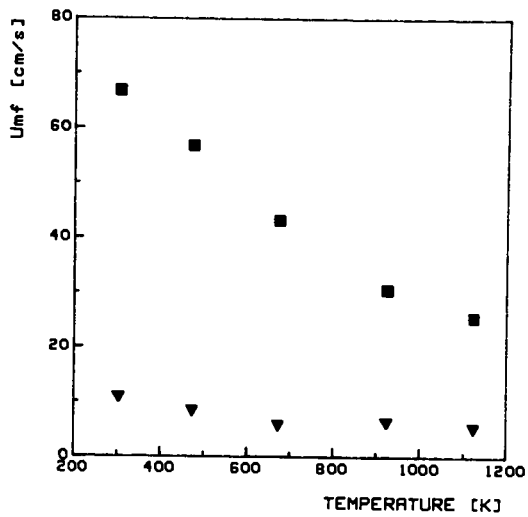


Fig. 2 - Minimum fluidization velocity vs temperature.  
Bed solids: sand; ▼ 300 ± 400 μm; ■ 850 ± 1000 μm.



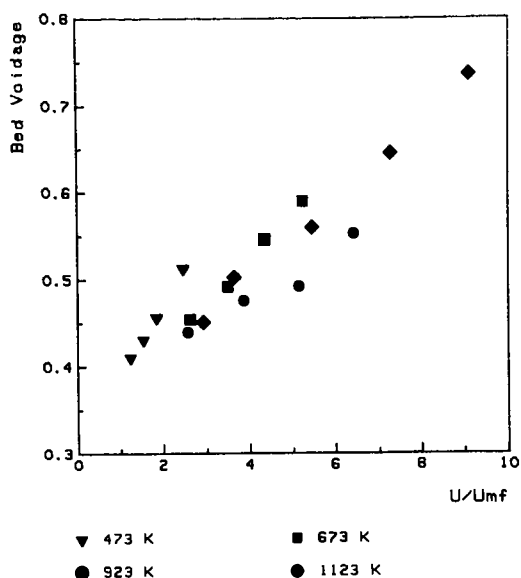


Fig. 3 - Bed voidage vs relative fluidization velocity for different temperatures.  
Bed solids: sand;  $300 \div 400 \mu\text{m}$ .

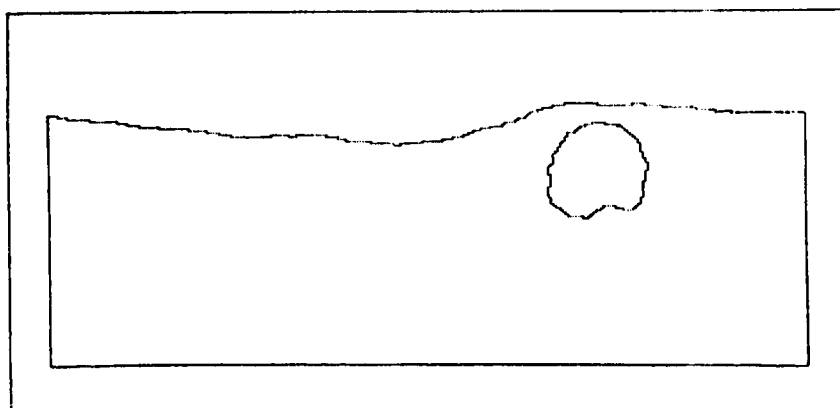


Fig. 4 - Example of digitized film frame showing a bubble rising through the bed.  
Solid displacement caused by bubble ascent is evident.  
Bed solids: sand;  $300 \div 400 \mu\text{m}$ ; 1123 K.

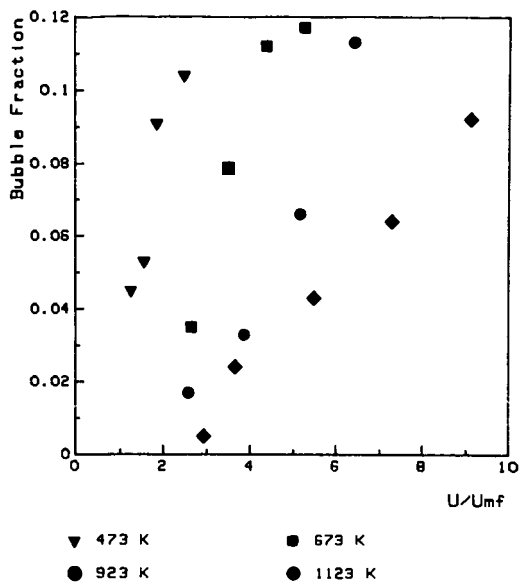


Fig. 5 - Bubble fraction vs relative fluidization velocity for different temperatures.  
Bed solids: sand;  $300 \div 400 \mu\text{m}$ .

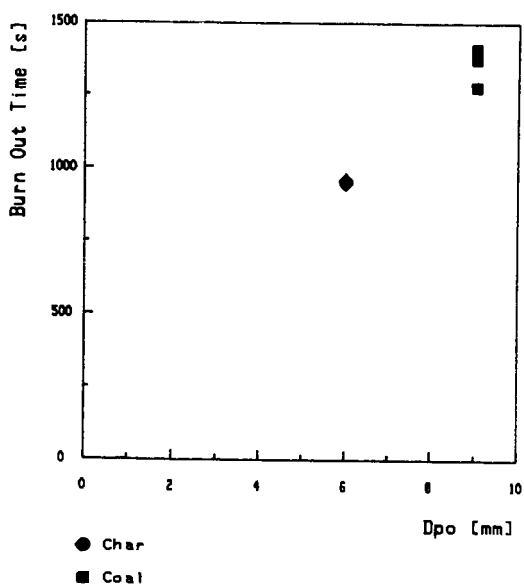


Fig. 6 - Burn out time vs particle diameter.  
Bed solids: sand;  $300 \div 400 \mu\text{m}$ .

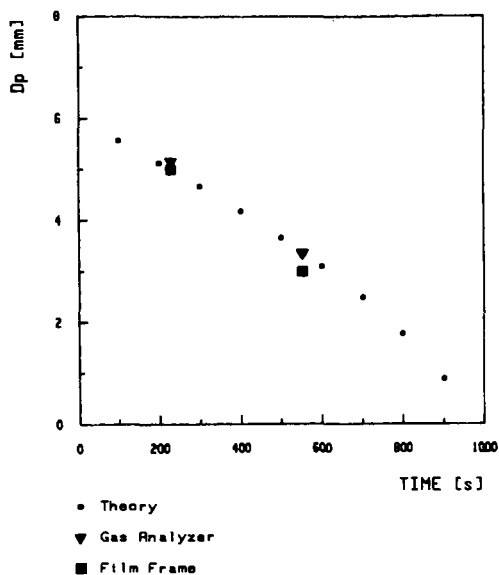


Fig. 7 - Reduction of char particle diameter vs time during combustion, as determined by film frame analysis and by treatment of the  $\text{CO}_2$  analysis data. Bed solids: sand;  $300 \div 400 \mu\text{m}$ ; 1123 K.

## Intra-Particle Sulfur Capture During Battelle Treated Coal Combustion Under Simulated Turbine Conditions

J. J. Reuther, H. N. Conkle, and H. F. Feldmann

BATTELLE  
Columbus Division  
505 King Avenue  
Columbus, Ohio 43201

### Introduction

For the last several years, Battelle Columbus Laboratories has been actively conducting research on the development of a practical, cost-effective process for improving both the fixed-bed gasification(1) and the boiler combustion(2) characteristics of high-sulfur, agglomerating, low-reactivity bituminous coal. The product of this research is a calcium-impregnated coal called Battelle Treated Coal (BTC), given the acronym BTC. The properties of BTC are much different from those of the raw coal from which it is processed(1,2). Specifically, these differences are:

- Increased ASTM volatile matter content.
- Higher char reactivity.
- Reduced tar formation tendency.
- Hotter ash fusion temperatures.
- Diminished coal particle agglomeration tendency.
- Enhanced sulfur retention by the ash.

As near-term markets for gasifier and boiler coal diminish or stabilize, respectively, Battelle has expanded the search for other old or new applications for bituminous coal that would also benefit from the alterations that could be given it by the Battelle calcium impregnation process. Recent planning studies by the United States Department of Energy (U.S. DOE) have forecast a need for coal-fired combustion turbines for the repowering of electric utilities when they become capacity-limited or deficient in the early-to-mid 1990s(3). The purpose of the program reported here is to demonstrate the promise of utilizing BTC as a fuel in advanced, coal-capable combustion turbines.

This paper is the second(4) in a series to present the results of a U.S. DOE-sponsored program designed to determine the intra-particle sulfur capture efficiency of BTC under simulated combustion turbine conditions. The BTC consisted of either of two high-sulfur (>4 percent by weight) Illinois No. 6 coals that had been impregnated with calcium-containing catalysts using a proprietary Battelle process. The simulated turbine combustion conditions consisted of super-atmospheric pressure, ultra-high excess air levels, average firing temperatures, and near-quantitative carbon conversion. Combustion test results reported here will focus on the parametric and comparative effects of raw coal organic sulfur content, calcium source, and calcium impregnation technique on sulfur capture efficiency. The effects of pressure and temperature on sulfur capture efficiency, as well as on ignition, burnout, and ash deposition, were the subjects of the earlier report(4).

## Experimental

A coal-fired combustion turbine simulator was constructed at Battelle by converting a continuous high-pressure reactor from a gasifier to a combustor(4). A schematic of the combustion turbine simulator is shown in Figure 1. This device is capable of simulating(3,4) the following combustion turbine conditions:

- Super-atmospheric pressure: 4 atmospheres.
- Maximum coal flame temperature: 2600 F.
- Maximum firing temperature: 1900-2100 F.
- Maximum liner temperature: 1000-1500 F.
- Primary fuel/air ratio: 20 percent excess air.
- Overall residence time: 150-300 milliseconds.
- Carbon conversion efficiency: 99+ percent.

A premixed methane/air pilot flame was first used to ignite the down-flowing pulverized coal feed at atmospheric pressure. The coal firing rate was then adjusted to about 40,000 Btu/hour. Primary air amounted to 20-30 percent of the total air required for combustion at 20 percent excess air. Secondary air made up the remainder. Temperatures were continuously monitored down the vertical axis of the combustor at locations in the pre-to-post flame zones using Inconel-sheathed Chromel-Alumel thermocouples. Firing temperature was adjustable over a 200 F range by either varying the amount of tertiary dilution air introduced or by oxygen enriching the secondary air to various levels. After combustion was completed within the 12-foot long, 6-inch diameter combustion chamber, samples of gaseous and solid products were collected using an uncooled stainless steel probe or a cyclone mounted in the exhaust, respectively. Flue gases were analyzed for CO<sub>2</sub>, CO, O<sub>2</sub>, and SO<sub>2</sub> using conventional analytical instrumentation(4). Once the diagnosis of atmospheric-pressure combustion conditions was completed, the system was pressurized to 65 pounds per square inch absolute (psia) and the gas/solid sampling procedure repeated.

The combustion test plan consisted of experiments designed to determine the comparative in situ sulfur capture efficiency, under simulated combustion turbine conditions of: (a) raw pulverized bituminous coal, (b) pulverized BTC prepared from this raw coal, and (c) a physical mixture of the raw pulverized coal and pulverized lime with the same amount of calcium added as for the BTC.

The two raw bituminous coals used were both from the Illinois No. 6 seam. As Table 1 shows, both had total sulfur contents of greater than 4.50 weight percent. The difference between them was that one's total sulfur was predominately organic, whereas the other's consisted of a near-equal split between organic and inorganic sulfur.

The raw coals were first dried to about 2 percent moisture, pulverized to 85-90 percent minus 200 mesh (75 microns), and then fired.

To produce BTC, coarse raw coal, 100 percent minus 20 mesh (850 microns), was first treated via the proprietary Battelle calcium impregnation process (1) to increase its molar Ca/S ratio to the levels listed in Table 1. Either commercial grade or technical grade lime was used as the source of the calcium. The difference between these calcium sources is purity and cost with the commercial grade being less pure and less expensive. The BTC was then dried to 2-3 percent moisture, pulverized to 85-90 minus 200 mesh, and then fired.

For the third fuel, finely-pulverized (85-90 percent minus 200 mesh) raw coal was physically mixed with either the commercial or the technical grade lime, each having a particle size of 100 percent minus 325 mesh (45 microns), and then fired. The physical mixtures' molar Ca/S ratios were adjusted to be as equivalent as possible to that of the BTCs (see Table 1).

### Results

The following are the significant new results regarding sulfur capture of these latest combustion tests, the results of which are documented in Table 1:

- Inherent sulfur capture by raw Illinois No. 6 seam coal appears to be independent of sulfur form, i.e., organic vs inorganic.
- Sulfur capture by Illinois No. 6 seam coal treated via the Battelle calcium impregnation process (BTC) appears to be independent of sulfur form and grade of lime at both low and high Ca/S ratios.
- Sulfur capture by BTC made from Illinois No. 6 seam coal is at least 50 percent more efficient than that achievable upon physically mixing raw coal and either grade of lime.
- Sulfur capture by BTC at low levels of calcium impregnation exhibits a positive pressure dependence over the entire range of pressures studied.
- All other positive effects of Battelle calcium impregnation on raw coal combustion performance(4) -- higher ash fusion temperatures, lower free-swelling indices, smaller fly ash, negative pressure dependence for NO<sub>x</sub> -- are observed for the organic sulfur enriched Illinois No. 6 seam coal.

### Acknowledgements

The authors gratefully acknowledge the financial support of this research by the U.S. Department of Energy under Contract No. DE-AC21-84MC21289, which is monitored by Mr. Nelson F. Rekos, Jr. of the Morgantown Energy Technology Center.

### References

1. Feldmann, H. F. and Conkle, H. N., "Coal Catalysis Expands Gasifier Application Options", Energy Progress, 3:2, 105-109 (1983).
2. Merryman, E. L. and Levy, A., "In-Situ Capture of Sulfur in Combustion", Central States Section Combustion Institute, CSS/CI-82-10, 23 pp (1982).
3. Crouse, F. W., Chairman, Proceedings of the First Annual Heat Engines Contractors Review Meeting, Morgantown Energy Technology Center, United States Department of Energy, DOE/METC/84/31, 369 pp., November 1984.
4. Reuther, J. J., Conkle, H. N., Webb, P. R., and Feldmann, H. F., "In-Situ Sulfur Capture by Battelle Treated Coal Under Simulated Combustion Turbine Conditions", Processing and Utilization of High Sulfur Coals, pp. 485-498, Elsevier Science Publishers (1985).

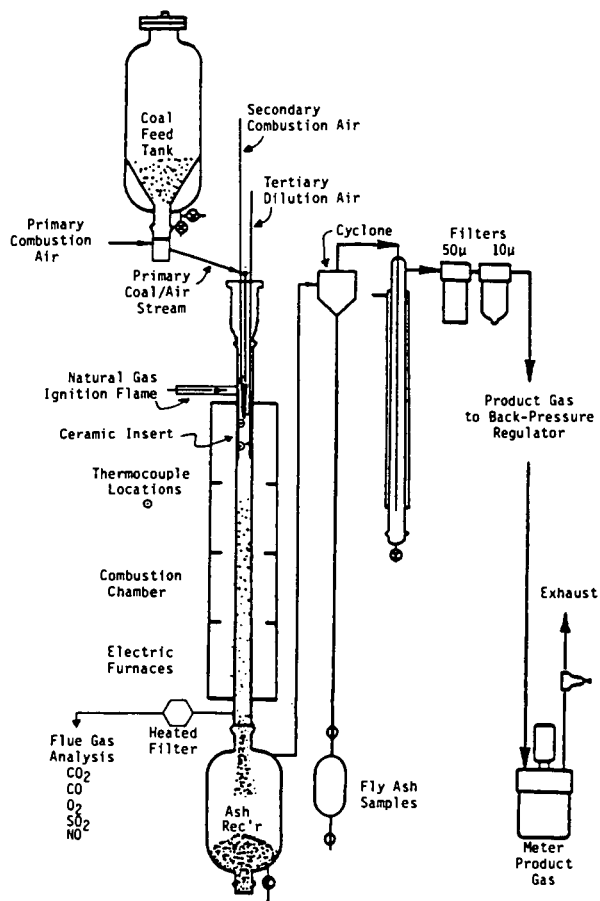


FIGURE 1. BATTELLE COMBUSTION TURBINE SIMULATOR

TABLE 1. SIGNIFICANT RESULTS OF TESTS TO STUDY THE EFFECT OF ORGANIC SULFUR CONTENT AND CALCIUM SOURCE ON SULFUR CAPTURE AS A FUNCTION OF PRESSURE, CALCIUM IMPREGNATION TECHNIQUE, AND Ca/S RATIO

| Illinois No. 6 Seam Coal<br>Total Sulfur<br>(Weight %, DAF) | Organic Sulfur<br>(%) | Calcium<br>Impregnation<br>Technique | Calcium<br>Source | Ca/S<br>Ratio | Sulfur Capture  |                 |
|---|-----------------------|--------------------------------------|-------------------|---------------|-----------------|-----------------|
|   |                       |                                      |                   |               | @15 PSIA<br>(%) | @70 PSIA<br>(%) |
| 5.24  | 72                    | None                                 | Nature            | 0.08          | 12±5            | 18±9            |
| 4.55  | 47                    | None                                 | Nature            | 0.17          | 17±9            | 13±6            |
| 5.24  | 72                    | BTC                                  | CGL               | 1.12          | 61±2            | 80±3            |
| 4.55  | 47                    | BTC                                  | CGL               | 1.31          | 60±5            | 81±6            |
| 5.24  | 72                    | BTC                                  | CGL               | 3.50          | 75±4            | 92±3            |
| 4.55  | 47                    | BTC                                  | CGL               | 4.11          | 83±7            | 95±8            |
| 5.24  | 72                    | PM                                   | CGL               | 0.98          | 35±10           | 57±18           |
| 5.24  | 72                    | PM                                   | CGL               | 3.10          | 59±7            | 74±3            |
| 5.24  | 72                    | BTC                                  | TGL               | 1.15          | 68±2            | 82±2            |
| 5.24  | 72                    | BTC                                  | TGL               | 3.25          | 86±1            | 96±2            |

BTC = Battelle Treated Coal  
PM = Physical Mix of Raw Coal and Lime  
CGL = Commercial Grade Lime  
TGL = Technical Grade Lime





Huzinaga[7] (9s,5p) sets of oxygen and carbon centered primitive Gaussians. For the hydrogens the (4s/2s) contraction was used with a scale factor of 1.2. In addition sets of d polarization functions were centered on the carbon and oxygen ( $\alpha_C=0.75$ ,  $\alpha_O=0.85$ ) and one set of p polarization functions on each of the hydrogens ( $\alpha=1.0$ ).

With this basis set, four electron, four orbital complete active space, self-consistent field (CASSCF) calculations were carried out. In this wavefunction the four electrons involved in the two CH bonds of formaldehyde are correlated with all possible orbital occupations of four orbitals, a total of 20 configurations. The remaining electrons are not correlated. With the exception of minor differences in the basis set, this is the same wavefunction used by Dupuis et al[1].

The calculations were carried out with the Argonne QUEST-164[8] programs, SOINTS and UEXP. An average calculation on a planar point took approximately 11 minutes on the FPS-164 while a typical nonplanar point required 16 minutes. The energy was evaluated at a total of approximately 300 points.

Initially it was assumed that the addition and abstraction reaction coordinates could be approximated by the distance between the carbon and the incoming hydrogen. The grids of points were calculated at 0.5 au increments in this CH distance along the two paths. A total range of CH distances from 5 to 10 au was covered. Variations in the inactive geometrical parameters of 0.05 au for bond lengths,  $5^\circ$ - $10^\circ$  for bond angles and  $10^\circ$ - $20^\circ$  for the dihedral angle were used. These grids of points were then fit separately to Simons-Parr-Finlan type expansions, using the program SURVIB[9], in order to obtain local representations of the potential surface in the region of the abstraction and addition reaction paths. The dependence of the energy on the angle of approach is depicted in Figure 1. From this figure it can be seen that there are two distinct reactive channels, one corresponding to abstraction and one to addition. The calculations predict no significant barrier in either channel.

The two reaction paths were then obtained by following steepest descent paths in mass-weighted, atomic cartesian coordinates. The starting points for the two paths were obtained by freezing the CH distance at 8 au and optimizing the remaining geometrical parameters. Two minima were found in this procedure (see Figure 1), one in which the incoming hydrogen is trans to the HCO hydrogen and a second in which the two hydrogens are cis, these were used as starting points for the addition and abstraction paths respectively. A plot of the energy along the two reaction paths is given in Figure 2. Vibrational frequencies were obtained along the reaction paths by numerically calculating the second derivative matrix in mass-weighted atomic cartesian coordinates, projecting out the translations, rotations, and gradient vector, and then diagonalizing the resulting 5 dimensional matrix. Plots of the vibrational frequencies along the two reaction paths are given in Figures 3 and 4.

### III. Rate Constant Calculations

The calculated frequencies, structures and energetics as a function of distance along the reaction path can be used directly in a variational transition state theory (VTST) calculation to produce the abstraction rate constant, i.e., for Reaction (1a). In this calculation, the rate constant at each temperature is that one which is a minimum with respect to position along the reaction path. Two of

the vibrational frequencies go to free rotations of the HCO in the reactant asymptote. The partition function used in the VTST expression for these two degrees of freedom is approximated as the minimum of the vibration or free rotation partition function. Subsequent calculations will include the hindered rotor effects. The resulting abstraction rate constant is shown in Fig. 5 along with the three rate constants measurements referred to in the introduction.

The measurements include both abstraction and addition processes. The VTST rate constant for addition is also in Fig. 5. This rate constant was determined in the same way as for abstraction, only with the calculated addition frequencies, structures and energetics. However, unlike abstraction, this rate constant can not be directly compared to experiment because it is only an adduct formation rate constant to form metastable, highly vibrationally excited  $\text{H}_2\text{CO}^*$ .  $\text{H}_2\text{CO}^*$  may decay back to reactants, may go on to products by eliminating  $\text{H}_2$ , i.e., Reaction (1b), or may be stabilized by buffer gas to thermalized  $\text{H}_2\text{CO}$ , i.e., Reaction (1c). That fraction of the adduct formation rate constant that corresponds to elimination or stabilization is what is needed for comparison to experiment. To determine that fraction, characterizations of the potential energy surface in the region of the  $\text{H}_2\text{CO}$  equilibrium and the elimination transition state  $\text{H}\cdots\text{H}\cdots\text{CO}$  are required. Then the stabilization rate constant and variational RRKM theory can be used to calculate the rate constant for Reactions (1b) and (1c).

In electronic structure calculations of comparable quality, Dupuis et al.[1] characterized the structure and frequencies of both  $\text{H}_2\text{CO}$  at equilibrium and the  $\text{H}\cdots\text{H}\cdots\text{CO}$  elimination transition state. The calculated properties at the equilibrium are very close to the experimental values and for consistency are used in the rate constant calculations. In a careful study of the energetics, the best estimate of the calculated barrier height to elimination is  $81\pm 3$  kcal/mole with the zero point energy correction. Experimental values[2] for the energetics give a number of about  $84\pm 1$  kcal/mole. The experimental value for the energetics of  $\text{H}_2\text{CO}$  dissociation to  $\text{H}+\text{HCO}$  is about  $86\pm 2$  kcal/mole and is due to thermochemical measurements with the uncertainty from the heat of formation of HCO[10]. These experimental values for the energetic placement of asymptotes and barrier heights will be used in the rate constant calculations.

With the transition states selected at each temperature by the VTST calculation for formation of the adduct, chemically activated RRKM calculations were performed to determine the subsequent fate of the adduct. These calculations are of a standard form[11] with total angular momentum approximately included only as a thermally averaged value. A direct count Beyer-Swinehart algorithm[12] is used. Tunneling through the elimination barrier is included in an Eckhart manner[13]. The final pressure dependent rate constant produced is in the high pressure limit the adduct formation rate constant in Fig. 5.

The calculations require as input the rate constant for stabilization of the  $\text{H}_2\text{CO}^*$  by buffer gas. In the three experiments, the buffer gas differs. CO,  $\text{H}_2\text{CO}$ , and Ar were used at pressures ranging from a few torr to atmospheric. Under these conditions, stabilization of the adduct turns out to be an unlikely event and the calculations are not particularly sensitive to detailed specifications of the stabilization rate constant. The rate constant used is the Lennard-Jones gas kinetic rate constant

times an efficiency factor for stabilization. The Lennard-Jones parameters are taken from the tabulation of Ref. 14 with the values for ethylene used for  $\text{H}_2\text{CO}^*$ . The efficiency factor is determined in a way to empirically mimic a master equation solution[15] and requires as input the average energy  $\langle \Delta E \rangle$  transferred between buffer gas and metastable adduct per up and down collision. This value used ( $\sim 20 \text{ cm}^{-1}$ ) were those measured[16] for  $\text{CS}_2$ , the only triatomic where direct measurement of  $\langle \Delta E \rangle$  have been published.  $\langle \Delta E \rangle$  was presumed to be independent of temperature[17].

To complete the input for the chemically activated RRKM calculations, the external rotations of the equilibrium and saddle points must be classified as either active or adiabatic. The external rotations are presumed similar to those of a symmetric top. The conserved total angular momentum and its projection on a space fixed axis are associated with the two larger moments of inertia and are treated adiabatically. The projection of the total angular momentum on the molecular axis is associated with the smallest moment of inertia and is not necessarily a conserved quantity. If there is substantial vibration-rotation interaction through centrifugal stretching or Coriolis coupling, the energy associated with this projection becomes active[18]. The amount of vibration-rotation interaction in  $\text{H}+\text{HCO}$  is unknown and so in the calculations this degree of freedom was treated both ways, either actively or adiabatically. Fortunately the results are not particularly sensitive to the choice and only those for the active treatment will be discussed.

In Fig. 5 the final calculated rate constant for reactions (1b) and (1c) as a function of pressure in Ar buffer gas is displayed for two different choices of the energetics of dissociation of formaldehyde. As mentioned above the experimental uncertainties in both the height of the elimination barrier and the  $\text{H}+\text{HCO}$  asymptote relative to the bottom of the  $\text{H}_2\text{CO}$  well are a few kcal/mole. The two cases in Fig. 5 are for the difference between the asymptote and barrier (i.e.,  $\Delta E$ ) being as large or as small as these uncertainties allow. The pressure dependence of the calculated rate constants show that stabilization (1c) is a minor process relative to elimination (1b) although, as expected, it is more important if the elimination barrier and the  $\text{H}+\text{HCO}$  asymptote are very close to one another. The importance of elimination should increase with changing the buffer gas to CO or  $\text{H}_2\text{CO}$  but not so as to qualitatively change the results. The figure also shows by comparison to the adduct formation rate that the most likely fate of the adduct is to decompose back to reactants. This is due to the fact that the elimination transition state is a tight, constricted configuration and the lifetime of the adduct (which controls stabilization) is short because it is only a 4 atom system. As a result, direct abstraction is the dominant process. The sum of abstraction, addition-elimination, and stabilization rate constants gives a total rate constant at or slightly below (depending on the choice of energetics) the lowest and most recent experimental value[5].

## References

1. M. Dupuis, W. A. Lester, Jr., B. H. Lengsfeld III and B. Liu, *J. Chem. Phys.* **79**, 6167 (1983) and references therein.
2. C. B. Moore, *Ann. Rev. Phys. Chem.* **34**, 525 (1983).
3. J. P. Reilly, J. H. Clark, C. B. Moore and G. C. Pimentel, *J. Chem. Phys.* **69**, 4381 (1978).
4. V. A. Nadtochenko, O. M. Sarkisov and V. I. Vedeneev, *Dokl. Akad. Nauk SSSR* **244**, 152 (1979).
5. C. J. Hochenadel, T. J. Sworski and P. J. Ogren, *J. Phys. Chem.* **84**, 231 (1980).
6. T. H. Dunning Jr., and P. J. Hay, "Methods of Electronic Structure Theory", H. F. Schaefer III, Ed., Plenum Press, New York, 1971, Chapter 1.
7. S. Huzinaga, "Approximate Atomic Wavefunctions. I", Chemistry Report, University of Alberta, Edmonton, Alberta, Canada, 1971.
8. R. Shepard, R. A. Bair, R. A. Eades, A. F. Wagner, M. J. Davis, L. B. Harding, T. H. Dunning Jr., *Int. J. Quantum Chem. Symp.* **1983**, 17, 613.
9. L. B. Harding and W. C. Ermler, *J. Comp. Chem.* **1985**, 6, 13.
10. P. Warneck, *Z. Naturforsch. Teil A* **29**, 350 (1974).
11. P. J. Robinson and K. A. Holbrook, *Unimolecular Reactions* (Wiley-Interscience, New York, 1972) Chaps. 4 and 8.
12. D. C. Asholtz, J. Troe and W. Wieters *J. Chem. Phys.* **70**, 5107 (1979).
13. W. H. Miller, *J. Amer. Chem. Soc.* **101**, 6810 (1979).
14. H. Hippler, J. Troe and H. J. Wendelken *J. Chem. Phys.* **78**, 6709 (1983).
15. J. Troe, *J. Phys. Chem.* **1983**, 87, 1800.
16. J. E. Dove, H. Hippler and J. Troe *J. Chem. Phys.* **82**, 1907 (1985).
17. M. Heymann, H. Hippler and J. Troe *J. Chem. Phys.* **80**, 1853 (1984).
18. W. Forst, *Theory of Unimolecular Reactions* (Academic Press, New York, 1973) Chap. 5.

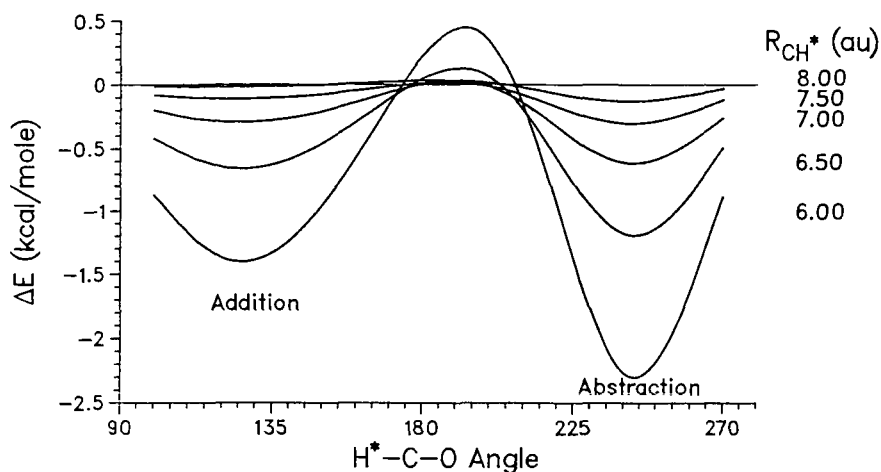


Figure 1. Angular dependence of the energy in the approach of atomic hydrogen to the formyl radical.

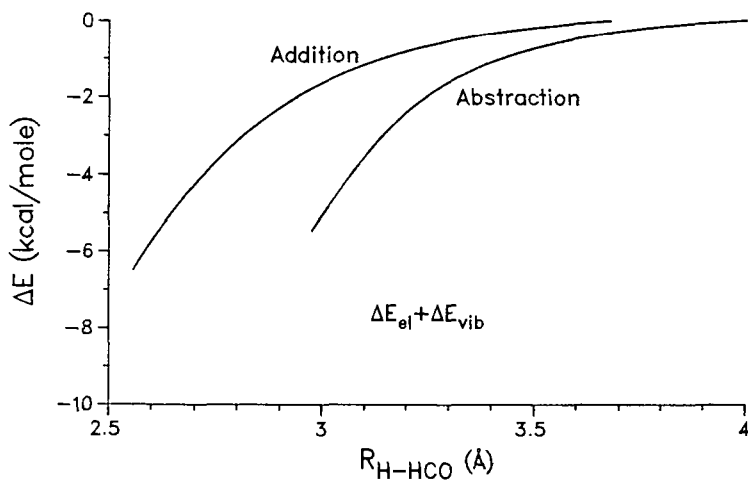


Figure 2. Energy profiles along the addition and abstraction reaction paths.

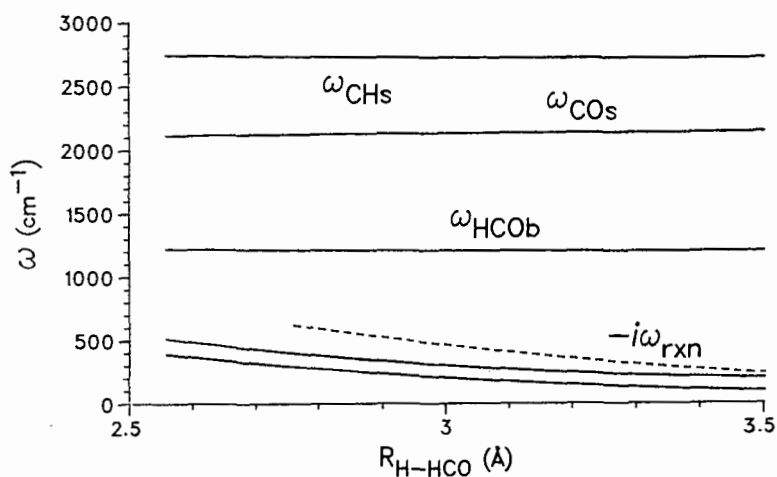


Figure 3. Vibrational frequencies along the addition reaction path.

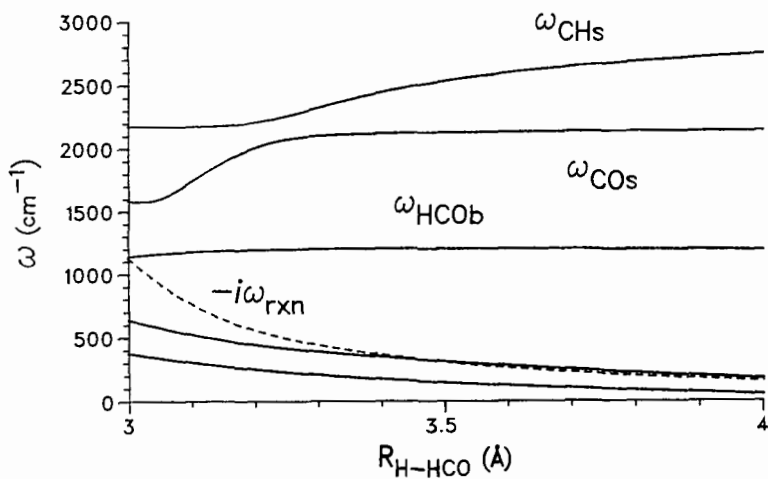


Figure 4. Vibrational frequencies along the abstraction reaction path.

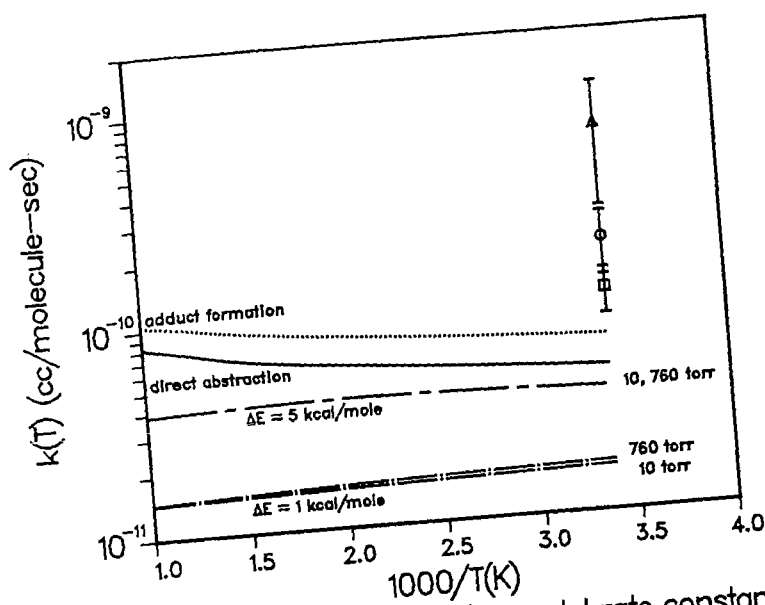


Figure 5. Calculated and experimental rate constants versus inverse temperature



Thermal and State-Selected Rate Constant Calculations  
for  $O(3P) + H_2 \rightarrow OH + H$  and Isotopic Analogs

Donald G. Truhlar

Department of Chemistry  
University of Minnesota  
Minneapolis, Minnesota 55455

Bruce C. Garrett  
Chemical Dynamics Corporation  
1550 West Henderson Road  
Columbus, Ohio 43220

Abstract

We use *ab initio* potential energy surfaces, including new parametrizations of the bending potentials for the two lowest electronic states, to calculate the rate constants for the reaction  $O(3P) + H_2$ . The dynamics calculations are based on variational transition state theory with multidimensional semiclassical tunneling corrections. We present results for the temperature range 250-2400K. In general the calculated rate constants for the thermal reaction are in excellent agreement with available experiments. We also calculate the enhancement effect for exciting  $H_2$  to the first excited vibrational state. For the reaction of vibrationally excited  $H_2$  the rate constant is based on a dynamical bottleneck of 7.2 kcal/mol, as compared to a saddle point value of 12.6 kcal/mol, and it is in good agreement with experiment. The good agreement of theory and experiment for the excited state rate provides a dramatic demonstration of the reality of dynamical bottlenecks at locations far from the saddle point.

1. Introduction

Theoretical advances in chemical kinetics often require integration of several kinds of information. The combination of electronic structure and chemical dynamics calculations provides one particularly fruitful way to gain a detailed understanding of the forces responsible for observed kinetic phenomena. In our own work we have made several calculations of chemical reaction rates based on potential energy surfaces derived in whole or in part on *ab initio* electronic structure theory. Systems studied have included the reactions  $H + H_2$ ,  $OH + H_2$ ,  $O + OH$ ,  $F + H_2$ , and  $O + H_2$ .

The  $O + H_2$  reaction, unlike all the others on the above list, has more than one low-lying potential energy surface. In addition to the  $1A'$  water surface, that does not correlate adiabatically to the  $3P$  state of  $O$ , there are two  $3A'$  surfaces and a  $3A''$  one that do. One  $3A'$  surface and the  $3A''$  surface form a degenerate  $\Pi$  state for all collinear geometries but have different bend potentials: The  $3A''$  state has a significantly broader bending valley, and hence it dominates the thermal rate at most temperatures of interest, although the  $3A'$  state may make a non-negligible contribution at high temperature (1,2). The second  $3A'$  state is unimportant for the thermal reaction rate. In our previous calculations (3,4) we included only the contributions from reaction on the lowest-energy  $3A''$  surface. The collinear part of this surface was treated by the modified rotated Morse oscillator spline fit of Lee et al. (5) to the *ab initio* calculations of Walch et al. (1,2,6) and the bend potential was treated by an anti-Morse bend model (7-9) with one parameter adjusted to reproduce the harmonic bend potential at the saddle point for the same *ab initio* calculations. In the present paper we include both electronic states, and the potential energy surfaces are treated by an improved parametrization. The improved parametrization consists, for each of the two surfaces, of a three-parameter fit to the bend potential so that it agrees with the newest *ab initio* calculations (10)

for large-amplitude ( $45^\circ$ ) bends at three points along the reaction path, including both the saddle point and a point close to the vibrationally adiabatic ground-state barrier maximum. We use the PolCI calculations of Walch et al. (1,6,10) because (i) they are available at enough geometries to determine both potential energy surfaces in the regions important for the reaction rate and (ii) they appear reasonably accurate. We note that in our previous study (4) of the  $O+H_2$  reaction, we calculated rate constants for five potential energy surfaces. Two of these, called surfaces P and M, were based on the PolCI calculations, and the results appeared to show that these were the most accurate of the five.

The procedure used to fit the bend potential in the present study is a specific example of a strategy that may be very useful in many cases (11), namely the fitting of a globally defined potential in the wide vicinity of a reaction path with special emphasis on dynamical bottleneck locations (12) as determined by variational transition state theory (13,14) or the adiabatic theory of reactions (15).

Having obtained a representation of the potential energy surface, we calculated both thermal rate constants and state-selected rate constants for vibrationally excited  $H_2$  by variational transition state theory with semiclassical ground-state transmission coefficients (3,16-18). These methods have been shown to provide reasonably accurate estimates of the quantum mechanical local-equilibrium and state-selected reaction rates for most chemical reactions (3,13,14,19,20). In general we believe we can use these methods to calculate rate constants that are reliable for a given potential energy surface to within a factor of two or better at room temperature and above. This is sufficient to compare computed rate constants to experiment, to test *ab initio* potential energy surfaces, and to draw useful conclusions about which features of the potential energy surface are significant for determining the magnitudes of observed rate constants and kinetic isotope effects.

## 2. Potential Energy Surfaces

The  $3\pi$  potential energy surface is represented by the rotated Morse oscillator spline function of Lee et al. (5) for collinear geometries augmented by an anti-Morse bend (AB) potential (7-9). The parameters of the bend potential are adjusted to *ab initio* calculations (1,6,10) in the region near the saddle point and the vibrationally adiabatic ground-state barrier maximum (the maximum of  $V_B^G(s)$  in the notation used previously (12,17)). Further details are given elsewhere (21).

## 3. Dynamical Calculations

We calculated a separate rate constant for each potential energy surface. Denoting these results by  $k_A''$  and  $k_A'$  respectively, the thermal (i.e., canonical ensemble) rate constant is

$$k = k_A' + k_A'' \quad (1)$$

Each of the single-surface rate constants includes a multiple-surface coefficient (22) equal to  $3/Q_B^{\dagger}$  where 3 is the electronic degeneracy of the generalized transition state and  $Q_B^{\dagger}$  is the electronic partition function of atomic O.

The single-surface rate constants were calculated by improved canonical variational transition-state-theory (ICVT) with semiclassical ground-state transmission coefficients. The methods are described in detail elsewhere (3,16-18). First we calculate the minimum energy path (MEP) by following the negative gradient of the potential in mass-scaled coordinates. Then for each distance  $s$  along the MEP we calculate the improved generalized standard-state free energy of activation  $\Delta G_{GT,0}^{\dagger}(T,s)$  for a generalized transition state at this  $s$ , where  $T$  is the temperature. The hybrid ICVT rate constant for temperature  $T$  is then given by

$$k^{ICVT}(T) = \min_s \frac{kT}{h} k^{\ddagger,0} \exp[-\Delta G^{IGT,0}(T,s)/kT] \quad (2)$$

where  $k$  is Boltzmann's constant,  $h$  is Planck's constant, and  $k^0$  is the reciprocal of the standard-state concentration. This rate constant is a hybrid because the reaction coordinate is treated classically but other degrees of freedom are all treated quantally. In the final step we add quantal effects on the reaction coordinate by a ground-state (G) transmission coefficient  $\kappa^G(T)$ :

$$k^{ICVT/G}(T) = \kappa^G(T) k^{ICVT}(T) \quad (3)$$

We consider two methods to approximate  $\kappa^G(T)$ : the minimum-energy-path semiclassical adiabatic method (MEPSAG) (17) and the least-action method (LAG) (18). The latter accounts for the shortening of the tunneling path due to the system "cutting the corner" of the curved MEP through mass-scaled coordinates by finding the dynamically optimal tunneling path by evaluating an imaginary-action functional along a one-parameter sequence of trial paths. These vary linearly between the MEP at one extreme and a straight line through mass-scaled coordinates from the translational turning point on the MEP in the entrance channel to the translational turning point on the MEP in the exit channel at the other extreme.

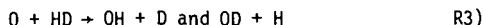
Anharmonicity is included as discussed elsewhere (3,17).

The evaluation of state-selected rate constants for  $H_2$  in the  $n=1$  excited vibrational state requires further assumptions. Figure 1 shows the vibrationally adiabatic potential curves for  $n=0$  and 1 for the  $3A'$  surface. The potential curves in Fig. 1 are defined by

$$V_a^G(n,s) = V_{MEP}(s) + \epsilon_{str}(n,s) + 2\epsilon_{bend}^G(s) \quad (4)$$

where  $V_{MEP}(s)$  is the Born-Oppenheimer potential on the MEP,  $\epsilon_{str}(n,s)$  is the local vibrational energy of the stretching mode orthogonal to the MEP and in quantum state  $n$ , and  $2\epsilon_{bend}^G(s)$  is the local zero point energy of the twofold-degenerate bending mode. Figure 2 shows the same quantities for the  $3A'$  state. In both cases we also show the curvature  $\kappa(s)$  of the MEP through mass-scaled coordinates (17). We will consider two limits for the excited-state rate constants. The first is the adiabatic limit (4,16,18,23), in which case we perform calculations identical to those for the thermal reaction rate except that in both  $\Delta G^{IGT,0}(T,s)$  and the tunneling calculation we neglect all stretching vibrational states except the  $n=1$  state. The second treatment is a sudden nonadiabatic model explained elsewhere (21).

We will consider three reactions:



#### 4. Results

Table I shows results for two methods of calculating transmission coefficients. The MEPSAG results are based on a semiclassical adiabatic treatment of tunneling along the minimum energy path (17). As compared to the LAG method this underestimates the rate constant by a factor of 24 at 200K and a factor of 3.3 at 300K. This

confirms, as first discovered for the  $H+H_2$  reaction (24) and then found in many cases (4,13,16-19,25-31), that multidimensional effects on the tunneling probabilities are very important and reduction to a one-dimensional problem by simply straightening out the minimum-energy reaction path seriously underestimates the extent of tunneling.

Table I also compares the final thermal rate constants of this study for reaction R1) to a selection of experimental (32-34) results. For 297-472K, the table shows only the most recent experimental data (32). The ICVT/LAG rate constants are usually larger than these results but agree within 25%. Rate constants in this temperature range are very sensitive to the barrier height, and the uncertainty in the ab initio potential energy surface is certainly great enough to yield larger errors. Thus the agreement of the present calculations with experiment is better than could have been expected. Furthermore the other recent experimental measurements in this range do not all agree with those of Presser and Gordon within a factor of two. The most recent evaluation (33) of experimental data for the  $O+H_2$  reaction concludes that for  $T \geq 400K$  the expression of Baulch *et al.* (34) fits most of the data within experimental error. We use this expression for the experimental values at 600-1500K. In this temperature range the present calculated rate constants are all larger than these experimental results, but the ICVT/LAG results are high only by factors of 1.2-1.5. At 2400K the agreement with experiment (35) is excellent.

We also calculated thermal rate coefficients for the isotopic analog reactions and the kinetic isotope effects and compared them to experimental (32,34-37) results. Because of space limitations we simply point out here that the calculated results agree with the experimental ones within the reliability of the latter. We also calculated kinetic isotope effects by conventional transition state theory (TST). These are qualitatively similar to the ICVT/LAG results, and hence also to the experimental results, but that is at least partly fortuitous since TST greatly underestimates the individual isotopic rate constants. For example for reaction R1) the TST rate constant is a factor of 9.3 lower than the ICVT/LAG one at 300K and a factor of 2.5 smaller at 400K. The LAG transmission coefficients are even larger, 12.6 at 300K and 3.1 at 400K, but the lack of quantal effects on reaction-coordinate motion in conventional TST is partly compensated by the lack of variational minimization of the hybrid rate constant with respect to the location of the generalized transition state. Then a further cancellation of errors occurs in the kinetic isotope effect ratio.

The adiabatic and sudden nonadiabatic rate constants for reaction R1) with vibrationally excited  $H_2$  are very similar for the present potential energy surface; thus we tabulate only the adiabatic values. The rate constants calculated by the adiabatic theory for reaction R1) when  $H_2$  is excited to the  $n=1$  vibrational state are given in Table II. We see that the transmission coefficients (ratios of ICVT/LAG tunneling-corrected rate constants to ICVT hybrid ones) are 2.6-2.7 at 302K, which are very significant factors but are smaller than for the thermal reaction rate. At 302K the calculated vibrational enhancement factor in the ICVT/LAG approximation is  $1.4 \times 10^3$  by Light (38), but it is only  $8.2 \times 10^2$  times larger than the interpolated value of Presser and Gordon (32). The agreement of theory with experiment is satisfactory.

Table III shows some of the properties of the dynamical bottlenecks for the vibrationally excited reaction. The variational transition states are farther from the saddle point ( $s=0$ ) for the vibrationally excited reaction than for the thermal reaction. Similar results have been found previously for  $H+H_2$  (23) and  $OH+H_2$  (39) for vibrationally excited reactants. This means that the improved parametrization of the bend potential for geometries far from the saddle point becomes more important for  $n=1$ . It also means that conventional TST becomes worse. Conventional TST predicts a vibrational enhancement factor of  $2.5 \times 10^5$  at 302K, which is two orders larger than the accurate values. The good agreement of the ICVT/LAG values with experiment provides a dramatic demonstration of the reality of dynamical bottlenecks at locations far from the saddle point.

### 5. Acknowledgments

The authors are grateful to A. F. Wagner for helpful correspondence. The work at the University of Minnesota was supported in part by the U.S. Department of Energy, Office of Basic Energy Sciences, under contract no. DE-AC02-79ER10425 and that at Chemical Dynamics Corporation was supported in part by the Army Research Office through contract no. DAAG-29-84-C-0011.

TABLE I. Thermal rate constants ( $\text{cm}^3 \text{molecule}^{-1} \text{s}^{-1}$ ) for  $\text{O} + \text{H}_2 \rightarrow \text{OH} + \text{H}$ .

| T(K) | ICVT      | ICVT/MEPSAG | ICVT/LAG  | Exp.                  |
|------|-----------|-------------|-----------|-----------------------|
| 250  | 2.94(-20) | 2.35(-19)   | 1.77(-18) | ...                   |
| 297  | 8.45(-19) | 3.32(-18)   | 1.15(-17) | 1.0(-17) <sup>a</sup> |
| 318  | 2.76(-18) | 8.85(-18)   | 2.38(-17) | 1.9(-17) <sup>a</sup> |
| 370  | 2.93(-17) | 6.66(-17)   | 1.20(-16) | 1.1(-16) <sup>a</sup> |
| 422  | 1.75(-16) | 3.24(-16)   | 4.70(-16) | 3.8(-16) <sup>a</sup> |
| 472  | 6.84(-16) | 1.10(-15)   | 1.43(-15) | 1.2(-15) <sup>a</sup> |
| 600  | 8.21(-15) | 1.09(-14)   | 1.24(-14) | 1.0(-14) <sup>b</sup> |
| 1000 | 3.89(-13) | 4.28(-13)   | 4.45(-13) | 3.4(-13) <sup>b</sup> |
| 1500 | 3.31(-12) | 3.43(-12)   | 3.52(-12) | 2.3(-12) <sup>b</sup> |
| 2400 | 2.10(-11) | 2.07(-11)   | 2.15(-11) | 2.1(-11) <sup>c</sup> |

<sup>a</sup> Presser and Gordon (32).

<sup>b</sup> Baulch *et al.* (34).

<sup>c</sup> Pamidimukkala and Skinner (35).

TABLE II. Rate constants ( $\text{cm}^3 \text{molecule}^{-1} \text{s}^{-1}$ ) for the state-selected reaction  $\text{O} + \text{H}_2(n=1) \rightarrow \text{OH} + \text{H}$ .

| T(K) | ICVT      | ICVT/LAG  | Exp. <sup>a</sup> |
|------|-----------|-----------|-------------------|
| 250  | 1.03(-15) | 4.25(-15) | ...               |
| 302  | 7.31(-15) | 1.89(-14) | 1.0(-14)          |
| 400  | 7.68(-14) | 1.31(-13) | ...               |
| 1000 | 8.58(-12) | 9.33(-12) | ...               |
| 2400 | 7.73(-11) | 7.84(-11) | ...               |

<sup>a</sup> from Light (38).

TABLE III. Bottleneck properties at conventional and canonical variational transition states for  $O + H_2(n=1) \rightarrow OH + H$ .<sup>a</sup>

| Surface | T<br>(K) | s<br>(a <sub>0</sub> ) | r <sub>12</sub><br>(a <sub>0</sub> ) | r <sub>23</sub><br>(a <sub>0</sub> ) | V <sub>MEP</sub><br>(kcal/mol) | V <sub>a</sub> <sup>g</sup> (n=1)<br>(kcal/mol) | ε <sub>str</sub> <sup>(n=1)</sup><br>(kcal/mol) | 2ε <sub>bend</sub> <sup>g</sup><br>(kcal/mol) |
|---------|----------|------------------------|--------------------------------------|--------------------------------------|--------------------------------|---|---|---|
| 3A"     | ...      | 0.00                   | 2.29                                 | 1.74                                 | 12.58                          | 19.07   | 4.89  | 1.61  |
|         | 300      | -0.55                  | 2.95                                 | 1.45                                 | 7.22                           | 23.02   | 14.74   | 1.07  |
|         | 1000     | -0.51                  | 2.91                                 | 1.45                                 | 7.64                           | 22.96   | 14.22   | 1.10  |
| 3A'     | ...      | 0.00                   | 2.29                                 | 1.74                                 | 12.58                          | 20.00   | 4.89  | 2.53  |
|         | 300      | -0.54                  | 2.93                                 | 1.45                                 | 7.36                           | 23.92   | 14.57   | 1.98  |
|         | 1000     | -0.51                  | 2.90                                 | 1.45                                 | 7.69                           | 23.87   | 14.14   | 2.04  |

<sup>a</sup> r<sub>12</sub> and r<sub>23</sub> are the nearest-neighbor OH and HH distances at the saddle point (s=0) or the variational transition state for the temperature indicated.  
1 a<sub>0</sub> = 1 bohr = 0.5292 Å.

#### References

- (1) S. P. Walch, A. F. Wagner, T. H. Dunning, Jr., and G. C. Schatz, *J. Chem. Phys.* **72**, 2894 (1980).
- (2) T. H. Dunning, Jr., S. P. Walch, and A. F. Wagner, in *Potential Energy Surfaces and Dynamics Calculations*, edited by D. G. Truhlar (Plenum Press, New York, 1981), p. 329.
- (3) B. C. Garrett and D. G. Truhlar, *J. Chem. Phys.* **81**, 309 (1984).
- (4) D. G. Truhlar, K. Runge, and B. C. Garrett, in *Proc. Twentieth Int. Symp. Combustion* (Combustion Institute, Pittsburgh), p. 585.
- (5) K. T. Lee, J. M. Bowman, A. F. Wagner, and G. C. Schatz, *J. Chem. Phys.* **76**, 3563 (1982).
- (6) S. P. Walch, T. H. Dunning Jr., F. W. Bobrowicz, and R. Raffanetti, *J. Chem. Phys.* **72**, 406 (1980).
- (7) H. S. Johnston, *Gas Phase Reaction Rate Theory* (Ronald Press, New York, 1966).
- (8) B. C. Garrett and D. G. Truhlar, *J. Am. Chem. Soc.* **101**, 4534 (1979).
- (9) B. C. Garrett, D. G. Truhlar, and A. W. Magnuson, *J. Chem. Phys.* **76**, 2321 (1982).
- (10) J. M. Bowman, A. F. Wagner, S. P. Walch, and T. H. Dunning, Jr., *J. Chem. Phys.* **81**, 1739 (1984).
- (11) D. G. Truhlar, F. B. Brown, R. Steckler, and A. D. Isaacson, in *Proceedings of the NATO/CECAM Workshop on Theory of Chemical Reaction Dynamics*, Orsay, France, June 1985.
- (12) B. C. Garrett, D. G. Truhlar, and R. S. Grev, in *Potential Energy Surfaces and Dynamics Calculations*, edited by D. G. Truhlar (Plenum Press, New York, 1981), p. 587.

- (13) D. G. Truhlar and B. C. Garrett, *Acc. Chem. Res.* 13, 440 (1980).
- (14) D. G. Truhlar and B. C. Garrett, *Annu. Rev. Phys. Chem.* 35, 159 (1984).
- (15) D. G. Truhlar, *J. Chem. Phys.* 53, 2041 (1970).
- (16) B. C. Garrett and D. G. Truhlar, *J. Phys. Chem.* 83, 1079 (1979), errata: 84, 682 (1980), 87, 4553 (1983).
- (17) B. C. Garrett, D. G. Truhlar, R. S. Grev, and A. W. Magnuson, *J. Phys. Chem.* 84, 1730 (1980); errata: 87, 4554 (1983).
- (18) B. C. Garrett and D. G. Truhlar, *J. Chem. Phys.* 79, 4931 (1983).
- (19) D. G. Truhlar, A. D. Isaacson, R. T. Skodje, and B. C. Garrett, *J. Phys. Chem.* 86, 2252 (1982); errata: 87, 4554 (1983).
- (20) D. G. Truhlar, W. L. Hase, and J. T. Hynes, *J. Phys. Chem.* 87, 2664 (1983); errata: 87, 5523 (1983).
- (21) B. C. Garrett and D. G. Truhlar, *Int. J. Quantum Chem.*, to be published.
- (22) D. G. Truhlar, *J. Chem. Phys.* 56, 3189 (1972), 61, 440(E) (1974).
- (23) B. C. Garrett and D. G. Truhlar, *J. Phys. Chem.* 89, 2204 (1985).
- (24) D. G. Truhlar and A. Kuppermann, *Chem. Phys. Lett.* 9, 269 (1971).
- (25) R. A. Marcus and M. E. Coltrin, *J. Chem. Phys.* 67, 2609 (1977).
- (26) B. C. Garrett and D. G. Truhlar, *J. Chem. Phys.* 72, 3460 (1980).
- (27) B. C. Garrett, D. G. Truhlar, R. S. Grev, and R. B. Walker, *J. Chem. Phys.* 73, 235 (1980).
- (28) D. K. Bondi, D. C. Clary, J. N. L. Connor, B. C. Garrett, and D. G. Truhlar, *J. Chem. Phys.* 76, 4986 (1982).
- (29) R. T. Skodje, D. G. Truhlar, and B. C. Garrett, *J. Chem. Phys.* 77, 5955 (1982).
- (30) D. K. Bondi, J. N. L. Connor, B. C. Garrett, and D. G. Truhlar, *J. Chem. Phys.* 78, 5981 (1983).
- (31) A. D. Isaacson, M. T. Sund, S. N. Rai, and D. G. Truhlar, *J. Chem. Phys.* 82, 1338 (1985).
- (32) N. Presser and R. J. Gordon, *J. Chem. Phys.* 82, 1291 (1985).
- (33) N. Cohen and K. Westberg, *J. Phys. Chem. Ref. Data* 12, 531 (1983).
- (34) D. L. Baulch, D. D. Drysdale, D. G. Horne, and A. C. Lloyd, *Evaluated Kinetic Data for High-Temperature Reaction*, Vol. 1 (Butterworths, London, 1972), p. 49.
- (35) K. M. Pamidimukkala and G. B. Skinner, *J. Chem. Phys.* 76, 311 (1982).
- (36) A. Westenberg and N. deHaas, *J. Chem. Phys.* 47, 4241 (1967).
- (37) A. Westenberg and N. deHaas, *J. Chem. Phys.* 50, 2512 (1969).

- (38) G. C. Light, J. Chem. Phys. 68, 2831 (1978).  
 (39) D. G. Truhlar and A. D. Isaacson, J. Chem. Phys. 77, 3516 (1982).

# Figure captions

Fig. 1. Vibrationally adiabatic potential curves (solid curves with scale at left) defined by eq. 4) for  $n=0$  and 1 and curvature of the reaction path (dashed curve with scale at right) as functions of the distance  $s$  along the minimum energy path through mass-scaled coordinates for the  $3A''$  potential energy surface. The saddle point is at  $s=0$ . The long tick marks on the ordinate scales denote the energies of  $O+H_2(n=1)$ , left side, and  $OH(n=1)+H$ , right side.

Fig. 2. Same as Fig. 1 except for  $3A'$  surface.

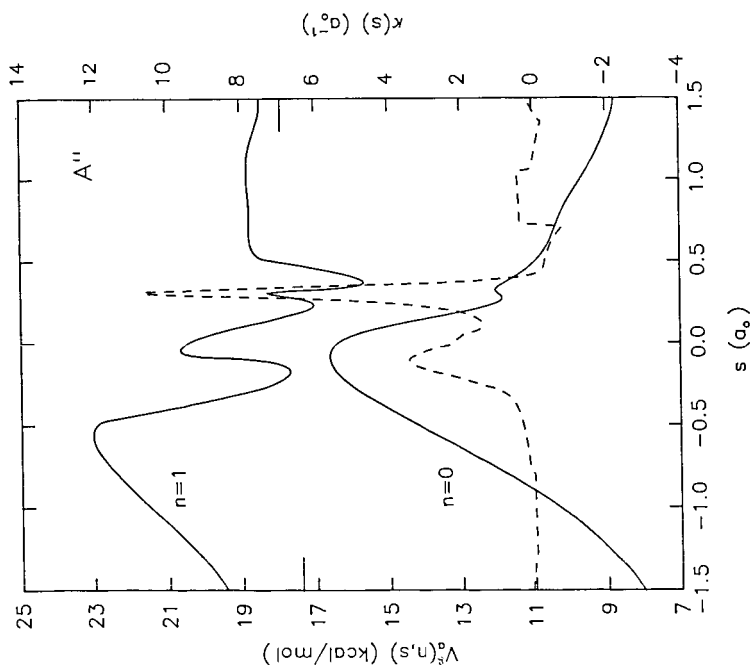


Fig. 1. Vibrational adiabatic potential curves (solid curves with scale at left) defined by eq. 4) for  $n=0$  and 1 and curvature of the reaction path (dashed curve with scale at right) as functions of the distance  $s$  along the minimum energy path through mass-scaled coordinates for the  $3A''$  potential energy surface. The saddle point is at  $s=0$ . The long tick marks on the ordinate scales denote the energies of  $O+H_2(n=1)$ , left side, and  $OH(n=1)+H$ , right side.



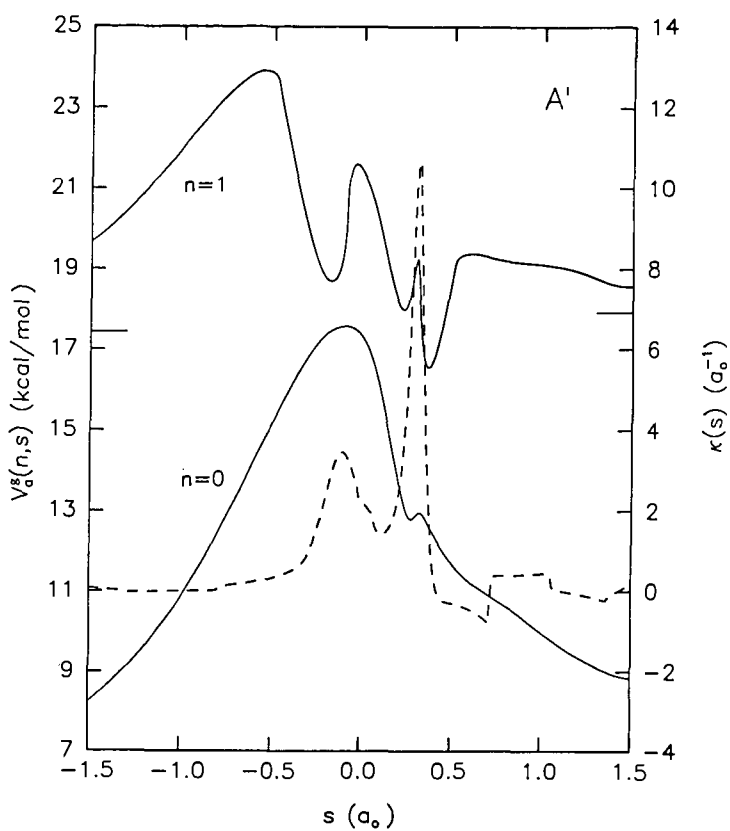


Fig. 2. Same as Fig. 1 except for  $3A'$  surface.

## FUNDAMENTALS OF NITRIC OXIDE FORMATION IN FOSSIL FUEL COMBUSTION

Thomas J. Houser, Michael E. McCarville and Gu Zhuo-Ying

Chemistry Department, Western Michigan University  
Kalamazoo, MI 49008

### INTRODUCTION

Combustion of fossil fuels in large stationary furnaces causes the emission of nitrogen oxides, a large fraction of which arise from the nitrogen-containing components in the fuel, producing a major pollution problem which is expected to increase in severity in the future. The results being reported in this paper are part of those obtained from a continuing study to determine the mechanism by which these oxides may form. Because studies have shown that most of the nitrogen in heavy oils is in the form of heterocycles (1-3) and it is believed that the nitrogen components of coal are similar, pyridine was selected as representative of these components. It was assumed that the radical fragments formed during pyridine pyrolysis and rich, low temperature oxidation would be similar to those obtained from the same reactions of fossil fuels that occur during the pre-flame stages of combustion. Later experiments emphasized HCN oxidation since several studies indicated that it was the key volatile, nitrogen-containing intermediate formed during fuel nitrogen combustion (4-8). In addition, HCN used with several fuel additives allowed a greater control of the chemical nature of the reaction environment. We have previously reported on the inert pyrolysis kinetics of pyridine (9), the rate of formation of HCN during pyridine pyrolysis (10), the oxidation kinetics of cyanogen (11), and of pyridine (12) and HCN (13) at low temperatures.

### EXPERIMENTAL

A flow system designed to operate at atmospheric pressure was constructed for the study of the oxidation of the pertinent nitrogen-containing reactants. The system is suitable for the introduction of volatile liquids (reactants and solutions with additives) into a heated helium stream through the use of a syringe pump to drive a calibrated, tuberculin syringe. The system can also utilize gaseous species; these reactants and additives, mixed with helium at the desired concentrations, are maintained in steel storage tanks. The flow stream is examined by a quadrupole mass analyzer equipped with capillary probe atmospheric sampler which functioned as an on stream monitor for the consumption of reactants. Helium is used as the carrier gas because it is chemically inert and has a very high thermal conductivity, thus providing rapid heating and quenching. The system has a group of removable Vycor reactors heated by an electric furnace. One reactor was a stirred-flow design (40 cc) which had been previously tested for stirring efficiency (14), the others were plug-flow type (10 to 40 cc). A flow line which bypasses the reactor was used so that entrance and exit concentrations of reactants could be measured. A Thermo Electron Chemiluminescent NO/NO<sub>x</sub> analyzer with on stream sampling was used for the oxidation studies of pyridine, HCN and N<sub>2</sub>O. A modification of the flow stream was required to obtain direct samples from the reactor effluent to measure the light gases with a gas chromatograph. A linear switching valve was used to provide a series-bypass capability with

constant back pressure for the two columns. A molecular sieve 5A column was used for  $O_2$ ,  $N_2$  and CO while a porous polymer Chromosorb 101 column was used for  $CO_2$  and  $N_2O$ . In order to determine the amounts of HCN and  $NH_3$  produced from the oxidation of pyridine and HCN, dilute solutions of NaOH or HCl in the bubble towers were used in separate experiments to trap the HCN or  $NH_3$  respectively, for ion-specific electrode analysis. A second bubbler in series with the first was found to be unnecessary.

## RESULTS AND DISCUSSION

The current study has shown that in order to produce significant yields of NO from the oxidation of pyridine or HCN-fuel mixtures, conditions which promote a flame must exist in the flow reactor. The existence of a flame was confirmed by visual observation in several, but not all, experiments. The capability of producing a flame depends on the nature of the fuel (Tables 1, 2 and 3, all data are stirred-flow), temperature (Tables 1, 2, 3 and 5), concentrations (Tables 1-5), reactor design (stirred - or plug-flow, Table 5), and flow rate (Tables 1 and 5). The conditions which promoted NO formation were characterized by complete consumption of fuel-nitrogen at all flow rates in the stirred-flow reactor, however, the plug-flow reactor exhibited an inverse consumption at intermediate temperatures, at first decreasing from complete consumption at high flows, passing through a minimum then increasing again (Table 5,  $C_5H_5N$  and  $HCN/C_6H_6$  mixtures at 800 C and  $HCN/CO$  at 700 C) while the NO yield continually decreased. After a threshold temperature was reached in the plug-flow reactor, the NO yield did not appear to depend on temperature significantly (Table 5). The non-flame conditions, at relatively low temperatures and/or concentrations of fuels, were characterized by a flow rate dependent consumption of fuel-nitrogen which was converted essentially completely to  $N_2$  and  $N_2O$  (maximum yield of about 50% of the latter) (12, 13). This was observed in both types of reactors, however, the flame condition persisted to a much lower temperature in the entrance of the plug-flow reactor as evidenced by visual observation and NO production. The observed dependence of NO yields on flow rate, first increasing to a maximum then decreasing (Tables 1, 2 and 5) in the stirred-flow reactor was not observed with plug-flow, thus is thought to be an anomaly due to reactor-induced flame instability. However, other yield dependencies are qualitatively the same in both types of reactors. The transition between flame and non-flame reaction was abrupt as evidenced by a rapid increase in fuel nitrogen consumption and shift in products, thus is attributed to a change in mechanism rather than a sequential process.

Specifically it was found that pyridine and benzene/HCN mixtures give similar results (Tables 1, 2 and 5) while CO (Tables 2 and 5) and acetylene (13) added to HCN promoted NO formation at lower temperatures and concentrations (on an atom or heat equivalent basis), than the other fuel combinations. Mixtures of  $H_2/HCN$  were very different from other fuel combinations, producing lower extents of HCN consumption and very low to negligible yields of NO at conditions which normally gave high yields of NO with other fuels (Table 1). Finally, it has been clearly established that  $N_2O$  was the prevalent oxide of nitrogen at low temperatures (Table 5 and Reference 15) and/or equivalence ratios (Table 4), whereas NO became prevalent at higher temperatures and fuel concentrations (up to stoichiometric mixtures) and that their concentrations were inversely related. In order to further check the possibility of NO/ $N_2O$  interconversion experiments were performed by adding  $NO_2$  (NO did not exist in our reactant storage tank) to the

reaction mixture at low temperatures and by oxidizing  $N_2O$  in the presence of various fuels (Table 7). The results with NO were somewhat inconclusive since some experiments showed some increase in  $N_2O$  and others did not (16). The relatively small increases observed indicate that  $NO/NO_2$  could not be a major source of  $N_2O$  at those conditions. The results with  $N_2O$  clearly show that NO is not formed from  $N_2O$  in large yields.

In addition to the volatile products observed, it was noted that a white solid was formed (about a 3% yield) at non-flame conditions with lean mixtures of  $HCN/CO/O_2$  and  $HCN/H_2/O_2$ . Samples of these solids were examined by infrared and elemental analyses which indicated that those from  $HCN/CO$  were  $NH_4NCO$ , whereas most, but not all, of those from  $HCN/H_2$  were urea (Table 8). It was also found that a room temperature sublimate from  $NH_4NCO$  was urea, indicating an easy conversion was possible. These solids show the presence of  $NH_3$  and  $HNCO$  in the reactor at non-flame conditions. In an attempt to determine the nature of the intermediate that leads to  $N_2O$  formation, oxidation studies of methylisocyanate and dimethylhydrazine, with and without additive fuels, were made. No increase in  $N_2O$  formation was noted from these over that obtained from HCN.

#### CONCLUSIONS

The conclusions reached from the above observations are: (1) That  $N_2O$  and NO are probably formed from a common precursor in the mechanistic chain, although possibly not the same immediate intermediate, and neither are formed from each other. The data strongly shows that NO does not form at those lower temperatures which promote  $N_2O$  formation and  $N_2O$  does not oxidize to NO. In addition, the equivalence ratio dependence shows that  $N_2O$  forms at leaner conditions than does NO, which is most likely due to maintenance of flame conditions at the more rich conditions. Thus, the reported mechanism steps for the formation of  $N_2O$  from NO, at least at our conditions, are not applicable (17). (2) That NO formation cannot occur primarily by an interaction between NH or N and OH, as usually assumed in mechanisms (17), because of the observed influence of different fuels on the conditions necessary to produce NO.

#### ACKNOWLEDGEMENT

We are grateful to the U.S. Department of Energy for the financial support of this study under Contract No. DE-FG22-81PC408).

# REFERENCES

1. L.R. Snyder, Anal. Chem., 41, 314 (1969).
2. C.F. Brandenburg and D.R. Latham, J. Chem. Eng. Data, 13, 391 (1968).
3. D.K. Albert, Anal. Chem., 39, 1113 (1967).
4. R.A. Altenkirch, R.E. Peck and S.L. Chen, Combustion Science and Tech., 20, 49 (1979).
5. C.P. Fenimore, Combustion and Flame, 26, 249 (1976).
6. B.S. Haynes, Combustion and Flame, 28, 81 (1977).
7. C. Morley, Combustion and Flame, 27, 189 (1976).
8. C. Morley, Eighteenth Symposium (International) on Combustion, 23 (1981).
9. T.J. Houser, M.E. McCarville and T. Biftu, Int. J. Chem. Kinet., 12, 555 (1980).
10. T.J. Houser, M. Hull, R.M. Alway and T. Biftu, Int. J. Chem. Kinet., 12, 569 (1980).
11. T.J. Houser and P.K. Lee, Combustion Science and Tech., 23, 177 (1980).
12. T.J. Houser, M.E. McCarville and B.D. Houser, Combustion Science & Tech., 27, 183 (1982).
13. T.J. Houser, M.E. McCarville and B.D. Houser, Combustion Science and Tech., 29, 101 (1982).
14. J.M. Sullivan and T.J. Houser, Chem. Ind. (London), 1057 (1965).
15. T.J. Houser and M.E. McCarville, "Fundamentals of Nitric Oxide Formation in Fossil Fuel Combustion", DOE/PC/40805-4, May 1983.
16. T.J. Houser and M.E. McCarville, "Fundamentals of Nitric Oxide Formation in Fossil Fuel Combustion", DOE/PC/40805-7, July 1984.
17. G.T. Chen, J.V. Shang and C.Y. Wen, "NO<sub>x</sub> Emission from Combustors - A State of the Art Review", DOE/MC/11284-166, May 1981 (Table 6).

TABLE 1 Fuel Type Effects on NO Yields (% of Reacted N) at 950 C  
Reactants - Initial Concentrations (mole %)

|                       | <u>.9C<sub>5</sub>H<sub>5</sub>N/70<sub>2</sub></u> | <u>1HCN/.5C<sub>6</sub>H<sub>6</sub>/70<sub>2</sub></u> | <u>1HCN/3CO/70<sub>2</sub></u> | <u>1HCN/3H<sub>2</sub>/70<sub>2</sub></u> | <u>1HCN/3H<sub>2</sub>/60<sub>2</sub><sup>b</sup></u> |
|-----------------------|---|---|--------------------------------|---|---|
| Time(sec)\ <u>ERA</u> | <u>.87</u>  | <u>.79</u>  | <u>.46</u>                     | <u>.46</u>                                | <u>.54</u>  |
| 0.375                 | 13  | 18  | 42                             | --  | 0.4   |
| 0.5                   | 12  | 26  | 35                             | 0.5                                       | 0.3   |
| 0.75                  | 27  | 67  | 34                             | --  | --  |
| 1.0                   | 69  | 66  | 32                             | 0.3                                       | 0.2   |
| 2.0                   | 44  | 42  | 19                             | --  | --  |
| 4.0                   | 6   | 14  | 5                              | --  | --  |

|                       | <u>.5C<sub>5</sub>H<sub>5</sub>N/70<sub>2</sub></u> | <u>.2HCN/.25C<sub>6</sub>H<sub>6</sub>/3.50<sub>2</sub></u> | <u>2HCN/5CO/70<sub>2</sub></u> | <u>2HCN/140<sub>2</sub></u> | <u>2HCN/70<sub>2</sub></u> |
|-----------------------|---|---|--------------------------------|-----------------------------|----------------------------|
| Time(sec)\ <u>ERA</u> | <u>.48</u>  | <u>.64</u>  | <u>.86</u>                     | <u>.25</u>                  | <u>.50</u>                 |
| 0.375                 | 17  | --  | --                             | --                          | --                         |
| 0.5                   | 24  | 24  | 70                             | 2.0                         | 2.1                        |
| 1.0                   | 32  | 26  | 60                             | 2.2                         | 5.0                        |
| 2.0                   | 44  | 52  | 35                             | 1.1                         | 5.5                        |
| 4.0                   | 24  | 29  | 14                             | 0.5                         | 2.8                        |

(a) Equivalence ratios were calculated on the basis of CO<sub>2</sub>, H<sub>2</sub>O and NO as products  
(b) These were run at 900 C

TABLE 2 Temperature Effects on NO<sub>x</sub> Yield (% of Reacted N) for Various Fuels

| Time(sec) | .9C <sub>5</sub> H <sub>5</sub> N/70 <sub>2</sub> (.87) <sup>a</sup> |       | .5C <sub>5</sub> H <sub>5</sub> N/70 <sub>2</sub> (.48) |       | 1HCN/.25C <sub>6</sub> H <sub>6</sub> /70 <sub>2</sub> (.52) |  |
|-----------|--|-------|---|-------|--|--|
|           | 900 C  | 950 C | 900 C   | 950 C | 900 C  |  |
| 0.5       | 6  | 12    | 13  | 24    | 5  |  |
| 0.75      | 14   | 27    | --  | --    | --   |  |
| 1.0       | 20   | 69    | 13  | 32    | 6  |  |
| 1.5       | 10   | 54    | --  | 56    | --   |  |
| 2.0       | 7  | 44    | 9   | 44    | 5  |  |
| 4.0       | --   | 6     | 12  | 24    | 3  |  |

| Time(sec) | .25HCN/.2C <sub>6</sub> H <sub>6</sub> /3.50 <sub>2</sub> (.53) |       |        | 2HCN/4CO/70 <sub>2</sub> (.79) |       |        |
|-----------|---|-------|--------|--------------------------------|-------|--------|
|           | 925 C   | 950 C | 1000 C | 800 C                          | 900 C | 1000 C |
| 0.5       | 15  | 24    | --     | 8                              | 40    | 56     |
| 1.0       | 15  | 26    | 96     | 8                              | 41    | 52     |
| 2.0       | 12  | 52    | 80     | 2                              | 30    | 48     |
| 4.0       | --  | 29    | 44     | --                             | --    | 26     |

| Time(sec) | 1HCN/6CO/120 <sub>2</sub> (.40) |       |       | 1HCN/8CO/120 <sub>2</sub> (.48) |       |
|-----------|---------------------------------|-------|-------|---------------------------------|-------|
|           | 700 C                           | 800 C | 900 C | 700 C                           | 800 C |
| 0.5       | 2                               | 29    | 70    | 7                               | 46    |
| 1.0       | 4                               | 62    | 66    | 27                              | 80    |
| 2.0       | 2                               | 56    | 56    | 70                              | 69    |
| 4.0       | --                              | 20    | 20    | 1                               | 27    |

(a) Reactant concentrations and (equivalence ratios) are the same basis as in Table 1

TABLE 3 Fuel Rich  $\text{NO}_x$  Yields (% Reacted N)

| Time(sec) | $.65\text{C}_5\text{H}_5\text{N}/3.50_2(1.25)^a$ | $1\text{HCN}/8\text{CO}/30_2(1.92)$ |       |
|-----------|--|-------------------------------------|-------|
|           | 1000 C <sup>b</sup>                              | 800 C                               | 900 C |
| 0.5       | 12   | 6                                   | 55    |
| 1.0       | 22   | 7                                   | 51    |
| 2.0       | 22   | 1                                   | 30    |
| 4.0       | 12   | 0.2                                 | 8     |
|           | $1\text{HCN}/4\text{CO}/20_2(1.88)$              | $1\text{HCN}/5\text{CO}/40_2(1.06)$ |       |
|           | 1000 C   | 800 C                               | 900 C |
| 0.5       | 3  | 10                                  | 48    |
| 1.0       | 4  | 33                                  | 44    |
| 2.0       | 2  | 24                                  | 32    |
| 4.0       | --   | 3                                   | 10    |

(a) See Table 1 footnote (a) for ER calculation

(b) Yields were negligible for this mixture at 900 C

TABLE 4 Equivalence Ratio Effects on  $\text{NO}_x/\text{N}_2\text{O}$  Yields

| % $\text{C}_6\text{H}_6^a$ | ER   | Yield $\text{NO}_x/\text{N}_2\text{O}^b$ |              |
|----------------------------|------|--|--------------|
|                            |      | Stirred (775 C)                          | Plug (800 C) |
| 0                          | 0.25 | 0.7/29                                   | 0.2/30       |
| 0.12                       | 0.38 | 0.5/39                                   | --           |
| 0.25                       | 0.52 | 0.4/40                                   | 0.2/28       |
| 0.5                        | 0.79 | 0.5/34                                   | 12/14        |
| 0.75                       | 1.05 | 1.1/23                                   | 26/2         |
| 1.00                       | 1.32 | 2.5/1.2                                  | 24/--        |

(a) Reactants are  $1\text{HCN}/70_2$  plus benzene in mole % - ER as in Table 1, footnote (a)

(b) Both stirred and plug flow reactors were used with one second contact time for all experiments

TABLE 5 Comparison of Plug and Stirred-Flow Data:  
NO/N<sub>2</sub>O Yields in % Reacted Nitrogen

| Time(sec) | <u>1HCN/.25C<sub>6</sub>H<sub>6</sub>/70<sub>2</sub><sup>a</sup></u> |         |              |         |              |         |
|-----------|--|---------|--------------|---------|--------------|---------|
|           | <u>800 C</u>   |         | <u>900 C</u> |         | <u>950 C</u> |         |
|           | Plug   | Stirred | Plug         | Stirred | Plug         | Stirred |
| 0.25      | 40/13  | --      | 39/22        | --      | 39/10        | 10/--   |
| 0.5       | 16/25  | n/45    | 16/22        | 5/41    | 29/13        | 15/--   |
| 1.0       | n/30   | n/40    | 3/45         | 6/39    | 10/15        | 46/--   |
| 2.0       | n/34   | n/43    | n/8          | 5/33    | 1/11         | 28/--   |
| 4.0       | n/28   | n/40    | n/8          | 3/31    | n/5          | 11/--   |

|      | <u>.5C<sub>5</sub>H<sub>5</sub>N/70<sub>2</sub></u> |              |         |              |         |              |
|------|---|--------------|---------|--------------|---------|--------------|
|      | <u>725 C</u>  | <u>800 C</u> |         | <u>900 C</u> |         | <u>950 C</u> |
|      | Plug  | Plug         | Stirred | Plug         | Stirred | Plug Stirred |
| 0.25 | --  | 56/6         | --      | --           | --      | 56/6 --      |
| 0.5  | n/n   | 34/18        | n/--    | 42/12        | 13/28   | 40/8 24/--   |
| 1.0  | 4/3   | 9/33         | --      | 18/24        | 13/30   | 19/13 32/--  |
| 2.0  | 3/32  | n/37         | --      | 4/26         | 9/30    | 5/10 44/--   |
| 4.0  | 5/43  | n/40         | --      | --           | 12/26   | 1/5 24/--    |

|      | <u>1HCN/4CO/60<sub>2</sub><sup>b</sup></u> |         |              |         |              |         |
|------|--|---------|--------------|---------|--------------|---------|
|      | <u>700 C</u>                               |         | <u>750 C</u> |         | <u>800 C</u> |         |
|      | Plug                                       | Stirred | Plug         | Stirred | Plug         | Stirred |
| 0.25 | 40/5                                       | --      | --           | --      | 35/1         | --      |
| 0.5  | 17/11                                      | n/--    | 21/7         | 1/37    | 32/3         | 9/13    |
| 1.0  | 3/26                                       | n/28    | 21/11        | 2/37    | 16/22        | 33/18   |
| 2.0  | n/32                                       | n/27    | n/14         | 1/40    | n/36         | 23/22   |
| 4.0  | n/22                                       | n/25    | n/--         | --      | n/23         | 2/22    |

- (a) Compositions in mole %, n is for negligible amounts  
 (b) For CO added fuels below 700 C the HCN consumption dropped drastically and was time dependent, whereas, above 700 C the HCN was more than 90% consumed at all flow rates



TABLE 6 Low Temperature - Pyridine Oxidation (Plug Flow Reactor)  
% Yields of HCN/N<sub>2</sub>O

| <u>.5C<sub>5</sub>H<sub>5</sub>N/70<sub>2</sub><sup>a</sup></u>     |              |              |      |
|---|--------------|--------------|------|
| Time(sec)   | <u>750 C</u> | <u>725 C</u> |      |
| 0.25  | 68/n         | --           | --   |
| 0.5   | 11/48        | 30/n         | --   |
| 1.0   | 2/55         | 58/3         | 47/n |
| 2.0   | --           | 16/32        | 9/50 |
| 4.0   | --           | 2/43         | 7/48 |
| <u>800 C</u>  |              |              |      |
| NO <sub>x</sub> high at .25 and .5 sec. HCN negligible at all flows |              |              |      |
| (a) Concentrations in mole %  |              |              |      |

TABLE 7 N<sub>2</sub>O Oxidation Data  
% N<sub>2</sub>O Reacted/NO<sub>x</sub> Yield (% of Reacted N<sub>2</sub>O)<sup>a</sup>

|   |       | <u>2.2N<sub>2</sub>O/70<sub>2</sub><sup>b</sup></u> |        | <u>2.2N<sub>2</sub>O/8C0/70<sub>2</sub></u> |        | <u>2.2N<sub>2</sub>O/.5C<sub>6</sub>H<sub>6</sub>/70<sub>2</sub></u> |
|---|-------|---|--------|---|--------|--|
| Time(sec)   |       | 900 C   | 1000 C | 900 C                                       | 1000 C | 1000 C   |
| 0.5   | 10/13 | 53/12   | 84/14  | 94/18                                       | --     | --   |
| 1.0   | 20/9  | 80/9  | 79/11  | 91/14                                       | 91/9   | --   |
| 2.0   | 33/9  | 91/7  | 76/9   | 98/8  | --     | --   |
| 4.0   | 54/3  | 92/5  | 83/5   | 99/6  | 99/3   | --   |
| (a) Similar low yields of NO <sub>x</sub> were found at 800 and 750 |       |   |        |   |        |  |
| (b) Concentrations in mole %  |       |   |        |   |        |  |

TABLE 8 Solids Formation

| <u>%N-Fuel Reacted</u>                             | <u>Temperature (C)</u> | <u>Principal Solid Product</u> |
|--|------------------------|--------------------------------|
| <u>2HCN/8C0/70<sub>2</sub></u>                     |                        |                                |
| 15   | 650                    | NH <sub>4</sub> NCO            |
| 18   | 650                    | NH <sub>4</sub> NCO            |
| 17   | 650                    | NH <sub>4</sub> NCO            |
| 40   | 675                    | NH <sub>4</sub> NCO            |
| <u>2HCN/4H<sub>2</sub>/70<sub>2</sub></u>          |                        |                                |
| 50   | 650                    | Urea                           |
| 29   | 700                    | Urea                           |
| 20   | 600                    | NH <sub>4</sub> NCO            |
| <u>2C<sub>5</sub>H<sub>5</sub>N/70<sub>2</sub></u> |                        |                                |
| 97   | 750                    | NH <sub>4</sub> NCO            |

Kinetics of the Reaction of NCO with Ethene and Oxygen  
Over the Temperature Range 295-662K\*

Robert A. Perry

Sandia National Laboratories  
Combustion Research Facility  
Livermore, California 94550

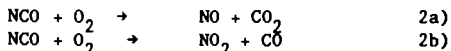
Introduction

The NCO radical is intimately connected with nitric oxide formation from fuel-bound nitrogen in combustion systems.<sup>1,2</sup> In order to model nitrogen chemistry in combustion systems, it is essential to explore the possible chemical reactions that might enter into any extensive model of nitrogen chemistry in these systems. While little has been done toward understanding the detailed chemistry of the NCO radical with combustion species,<sup>1-5</sup> certain reactions can be anticipated to occur based upon analogous electrophilic radical/molecule reactions. One of these reactions is the reaction of NCO with ethene.



Unsaturated hydrocarbons are found extensively in combustion, with ethene being a major component after pyrolysis of larger fuels. This reaction was chosen to facilitate predictions of NCO radical reactions with unsaturated hydrocarbons and hence to understand more fully nitrogen chemistry in rich combustion systems. To the extent that this reaction occurs at combustion temperatures, it is a pathway to recycle reactive nitrogen radicals back into fuel-bound nitrogen i.e., HCN.

Other possible important reactions, if they occurred, are the exothermic reactions of NCO with oxygen.



Besides being of potential importance in combustion systems, these reactions could be important in atmospheric oxidation of HCN. An upper limit has been placed on the exothermic, although sterically restricted, reactions between NCO and oxygen.

In this paper current research that employs a laser photolysis/laser-induced fluorescence technique to measure absolute rate constants for the reaction of NCO radicals with ethene and oxygen over the

temperature range 295-662K is discussed. In addition, the pressure dependence of the reaction between NCO and ethene is explored at room temperature. The implications for combustion modeling will be addressed.

#### EXPERIMENTAL

The technique is essentially identical to that which was developed to study the products of the reaction of  $O(^1P)$  with HCN.<sup>6</sup> NCO radicals are produced from the excimer laser photolysis of HNCO that was introduced along with the reactant of interest in a flowing gas mixture of HNCO:Ar:reactant at total pressures (primarily argon) of 10-372 Torr. The NCO radicals result either directly from the photolysis of HNCO or, as suggested by Drozdowski et al.,<sup>7</sup> from the rapid reaction of  $NH(^1\Delta)$  with HNCO. (Recent experiments at 157 nm and 193 nm suggest that the latter is the dominant mechanism.<sup>8</sup>) Both 193 nm and 157 nm radiation are used to photolyze HNCO in order to check for interference due to photolysis products.

An argon ion pumped ring dye laser, operating with stilbene-3 dye at 416.8 nm (100mW), is used to pump the  $A^2\Sigma(1,0,0) \leftarrow X^2\Pi(0,0,0)$  transition of NCO. The resulting fluorescence is monitored using an EMI 9789QA photomultiplier tube fitted with an interference filter at 438.5nm (FWHM=8.0nm) mounted at right angles to the crossed laser beams. The intersection of the detection system aperture and the laser-induced fluorescence radiation defined a fluorescence viewing zone at the center of the reaction vessel whose cross section was ~2cm in diameter. This region was well separated from the reaction vessel walls, minimizing wall losses of the NCO radicals. The reactor consisted of a quartz reaction vessel enclosed in a ceramic furnace that could be heated to temperatures as high as 1200K. The temperature of the furnace was monitored by Chromel/Alumel thermocouples mounted inside the reaction vessel, with the temperature of the vessel maintained to  $\pm 5K$  over the entire temperature range.

The HNCO was synthesized according to the procedure of Okabe.<sup>9</sup> Cyanuric acid was heated in an evacuable pyrex vessel to 400K. The HNCO generated was passed through a  $P_2O_5$  and  $Ag_2O$  trap to remove the water, and HCN and was then condensed in a liquid nitrogen trap. The liquid was vacuum distilled using a dry-ice/acetone trap until constant vapor pressure (0.88 Torr) resulted. Argon was bubbled through the liquid and the resulting Ar/HNCO mixture was flowed to the reaction vessel. The flow rate was monitored by use of a rotameter. All other flows were monitored by the use of Tylan flow controllers that were calibrated prior to use.

The excimer laser intensity was varied by a factor of 2 using a purge tube situated between the excimer laser and the reaction vessel. Mixtures of nitrogen and oxygen were used to attenuate the 157 nm radiation, while nitrous oxide and air were used to attenuate radiation at 193 nm. All experiments were performed at a repetition rate of 0.3Hz. Signals were obtained by photon counting in conjunction with multichannel scaling. Decay curves of NCO radicals were accumulated from 25-500 pulses

depending on the signal strengths. NCO half-lives ranged from 2.43-200 msec, and the NCO radical concentrations were followed for at least three half-lives.

All experiments were carried out under slow-flow conditions so that the premixed reactant gas mixture could be replenished between laser pulses, thereby avoiding the accumulation of photolysis or reaction products. The partial pressure of HNCO was approximately 1.8-19 mTorr. The gases used had the following purity levels according to the manufacturer: Ar  $\geq 99.995\%$ ;  $C_2H_4 \geq 99.0\%$ ;  $O_2 \geq 99.9995\%$ .

## RESULTS AND DISCUSSION

Over the entire temperature range 295-652K, and in the presence of excess reactant gas, pseudo-first order kinetics is observed, and the bimolecular rate constant is obtained using the expression:

$$\ln [NCO]_0 / [NCO]_t = \ln S_0 / S_t = (k_0 + k_1 [\text{Reactant}])(t - t_0)$$

Here  $[NCO]_0$  and  $[NCO]_t$  are the concentrations of NCO radicals at times  $t_0$  and  $t$ , respectively,  $S_0$  and  $S_t$  are the corresponding fluorescence intensities,  $k_0$  is the first order rate coefficient for removal of the NCO in the absence of added reactant, and  $k_1$  is the rate constant for reaction with the added reactant, i.e., ethene or oxygen.

The decay was analyzed following a  $\sim 1$  ms delay after the excimer laser pulse to minimize interference from laser-induced emission from the silica vessel and to ensure that secondary reactions of other radical species formed during the photolysis event, such as  $NH(1\Delta)$  would not interfere with the reaction of interest.<sup>7</sup> In all experiments exponential decays were observed after the first millisecond supporting the contention that secondary reactions were not important. Also, at low pulse energies ( $\leq 1$  mJ/pulse) no effect, within experimental uncertainty, due to laser intensity was observed with a factor of two change. (Without attenuating the excimer laser radiation the apparent rate was measured to be faster and decays were nonexponential.)

The data were analyzed by numerical least squares fitting of the decays. The measured decay rates were found to depend linearly on the concentration of added reactant for fixed total pressure and temperature. The absolute rate constants were determined by plotting the measured decay rate against reactant concentration and performing a least squares fit to obtain the slope,  $k_1$ .

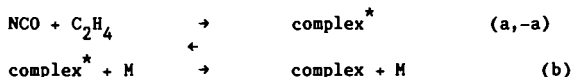
Rate constants,  $k_1$ , for the reaction of NCO with ethene were determined over the temperature range of 295-652K with the total pressure being varied from 10-372 Torr at 295K. Figures 1 and 2 show the plots of the data at 295K and higher temperatures, respectively, while Figure 3 shows a plot of the pressure dependence. Table I gives the rate constants determined for this reaction by least squares analysis over the entire temperature range.

Figure 4 shows an Arrhenius plot of the rate constants  $k_1$  with the region from 295-447K being described by the following Arrhenius expression:

$$k_1 = 3.0 \times 10^{-12} e^{(230 \pm 300)/RT} \text{ cm}^3 \text{ molecule}^{-1} \text{ s}^{-1},$$

where the error limit in the activation energy is the estimated overall error limit.

The pressure dependence observed at 295K (figure 3) is best explained by a Lindemann mechanism.



where  $\text{complex}^*$  is the complex formed by the terminal addition of NCO to ethene. The pressure dependent rate is given by the expression:

$$k_{bi} = k_a k_b [M] / (k_{-a} + k_b [M])$$

In the high pressure region where  $k_b [M]$  is much greater than  $k_{-a}$ ,  $k_{bi} = k_a$ , while in the low pressure region  $k_{bi} = k_a (k_b [M] / k_{-a})$ .

At temperatures greater than 447K a dramatic reduction in the bimolecular rate constant was observed. As seen in Figure 4 the reaction rate drops by greater than two orders of magnitude from 447K to 652K. This reduction in bimolecular rate constant apparently occurs due to the very rapid decomposition of the complex formed between NCO and ethene. Although such a dramatic reduction in reaction rate has been observed in the past for OH radical reactions,<sup>10-14</sup> nonexponential decays (after 1ms) were not apparent in these experiments. The absence of nonexponential decays suggest that the life time of the complex formed must be short in comparison to the experimental observation time. A proposed reaction mechanism whereby the thermalized adduct, [complex], begins to dissociate on a time scale that is comparable to the time frame of the experiments, analogous to the explanation of the effect observed for OH radical reaction with unsaturated hydrocarbons,<sup>10-14</sup> could explain the sharp drop in rate with increasing temperatures ( $\geq 447\text{K}$ ), but in order to explain fully the essentially exponential decays observed in all of the experiments, competitive reactions that turn off at higher temperatures (or a different reaction mechanism that regenerates NCO radicals at higher temperatures) is required. Calculations are presently under way to address the possible alternate channels, such as ring closure to form the ethylene imine analog.

Using 193nm photolysis of HNO, with a mixture of nitrous oxide and oxygen as a UV attenuator/filter, the reaction of NCO with oxygen was not observed to occur at room temperature and 372 Torr argon with

$2.27 \times 10^{16}$  molecule/cm<sup>3</sup> of oxygen added. In addition no reaction was observed at 662K and 389 Torr when  $2.4 \times 10^{16}$  molecule/cm<sup>3</sup> of oxygen was added. From these data the rate of reaction with oxygen was estimated to be less than  $1 \times 10^{-16}$  cm<sup>3</sup>molecule<sup>-1</sup>s<sup>-1</sup> at 295 and less than  $5 \times 10^{-17}$  cm<sup>3</sup>molecule<sup>-1</sup>s<sup>-1</sup> at 662K. These data suggest that under the conditions that exist in combustion environments or in the stratosphere, it is unlikely that the reaction of NCO with oxygen will be important. As suggested by Cicerone and Zellner<sup>15</sup>, the primary fate of NCO in the atmosphere is most likely photolysis at wavelengths less than 300 nm.

## CONCLUSIONS

At low temperatures the NCO radical will react with ethene to form a complex. At temperatures greater than 450K a marked decrease in the rate of reaction occurs until finally at 650K the reaction has decreased by two orders of magnitude. This effect suggests that the reaction with ethene, or, by inference, other unsaturated hydrocarbons, will not serve to recycle the NCO radical in combustion environments.

At the temperatures of this study NCO radicals do not react with molecular oxygen. The reaction of NCO with oxygen should be unimportant in combustion or atmospheric systems.

## ACKNOWLEDGEMENT

This work was supported by the U. S. Department of Energy, Office of Basic Energy Sciences. I would like to thank Mark Jaska for his assistance in carrying out the experiments.

Table I. Rate constants,  $k_1$ , for the reaction of NCO radicals with ethene. The indicated error limits are the estimated overall error limits; they include the least squares standard deviations (2.0-15%), as well as the estimated accuracy limits of other parameters such as pressure and reactant concentrations.

| Temperature (K) | Total Pressure (Torr) | $k_1 \times 10^{12}$<br>(cm <sup>3</sup> molecule <sup>-1</sup> s <sup>-1</sup> ) |
|-----------------|-----------------------|---|
| 295             | 10.5                  | 3.37 ± 0.57   |
| 295             | 25.0                  | 3.78 ± 0.38   |
| 295             | 53.3                  | 4.37 ± 0.44   |
| 296             | 102.0                 | 4.39 ± 0.44   |
| 296             | 204.0                 | 4.58 ± 0.46   |
| 295             | 372.0                 | 4.69 ± 0.47   |
| 330             | 198.0                 | 4.00 ± 0.40   |
| 381             | 203.0                 | 3.99 ± 0.40   |
| 447             | 200.0                 | 3.88 ± 0.39   |
| 487             | 202.0                 | 2.56 ± 0.64   |
| 535             | 201.0                 | 1.30 ± 0.26   |
| 585             | 372.0                 | 0.112 ± 0.02  |
| 652             | 372.0                 | 0.027 ± 0.005   |

## REFERENCES

1. J. A. Miller, M. C. Branch, W. J. McLean, D. W. Chandler, M. D. Smooke, and R. J. Kee, 20th Symposium (International) on Combustion, The Combustion Institute, 673 (1985).
2. R. A. Perry, J. Chem. Phys., 84 5485 (1985).
3. M. Y. Louge and R. K. Hanson, 20th Symposium (International) on Combustion, The Combustion Institute, 665 (1985).
4. M. Y. Louge and R. K. Hanson, Combustion Flame 58, 291 (1984).
5. J. L. Cookson, G. Hancock, and K. G. McKendrick, Ber. Bunsenges. Phys. Chem. 89, 335 (1985).
6. R. A. Perry and C. F. Melius, 20th Symposium (International) on Combustion, The Combustion Institute, 639 (1985).
7. W. S. Drozdowski, A. P. Baronavski, and J. R. McDonald, Chem. Phys. Letts., 64 421 (1979).
8. T. Spiglanin, R. A. Perry, D. W. Chandler, private communication.
9. H. Okabe, J. Chem. Phys., 53 3507 (1970).
10. R. A. Perry, R. Atkinson, J. N. Pitts, Jr., J. Phys. Chem. 81 296 (1977).
11. R. A. Perry, R. Atkinson, J. N. Pitts, Jr., J. Phys. Chem. 81 1607 (1977).
12. F. P. Tully, A. R. Ravishankara, R. L. Thompson, J. M. Nicovich, R. C. Shah, N. M. Kreutter and P. H. Wine, J. Phys. Chem. 85, 2262 (1981).
13. F. P. Tully, Chem. Phys. Letts., 96 148 (1983).
14. K. Lorenz, and R. Zellner, Ber. Bunsenges Phys. Chem. 87, 629 (1983).
15. R. J. Cicerone, and R. Zellner, J. Geophys. Research, 88 10,689 (1983).

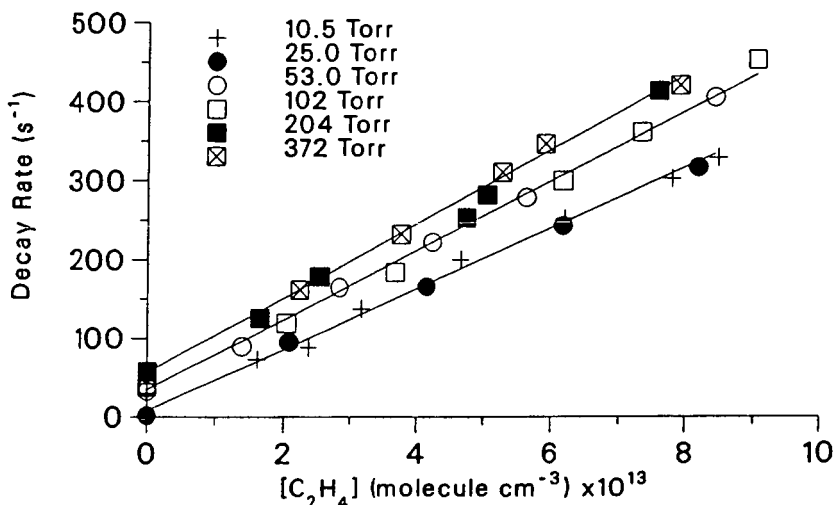


Figure 1. Plots of the decay rate against ethene concentration for the reaction on NCO with ethene at 295K. The solid lines represent best fit to data at 25 Torr, 53 Torr and 372 Torr.

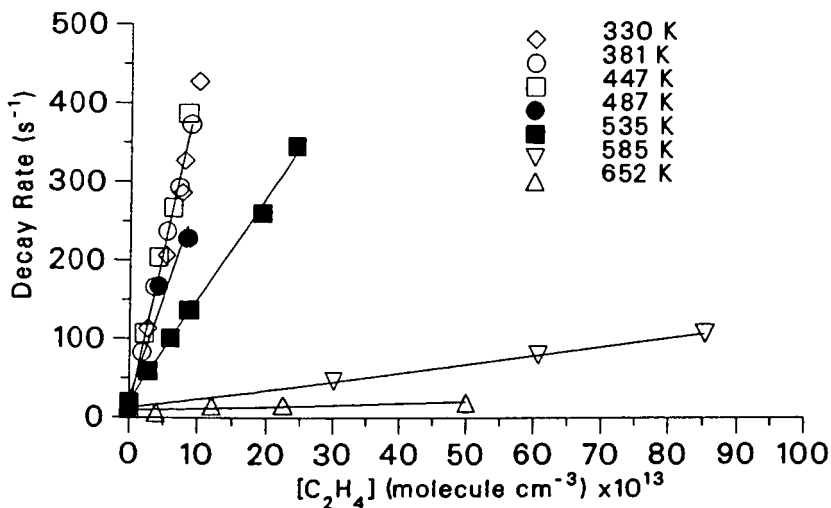


Figure 2. Plots of the decay rate against ethene concentration.



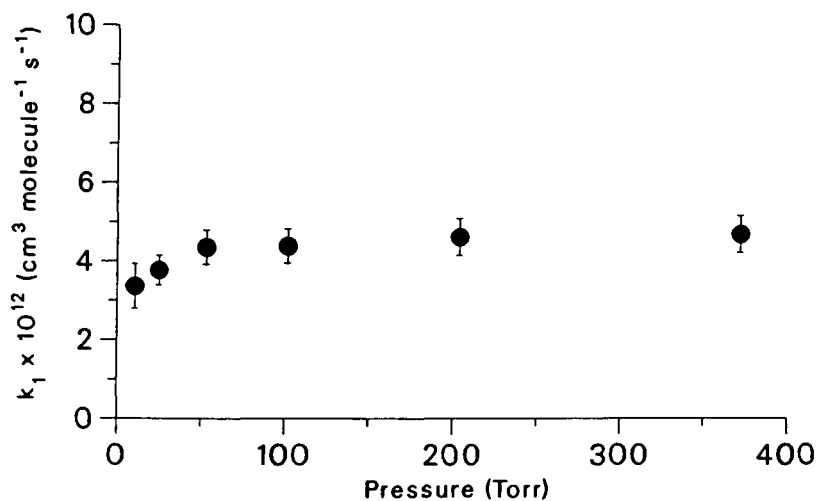


Figure 3. Plot of the rate constant versus pressure at room temperature.

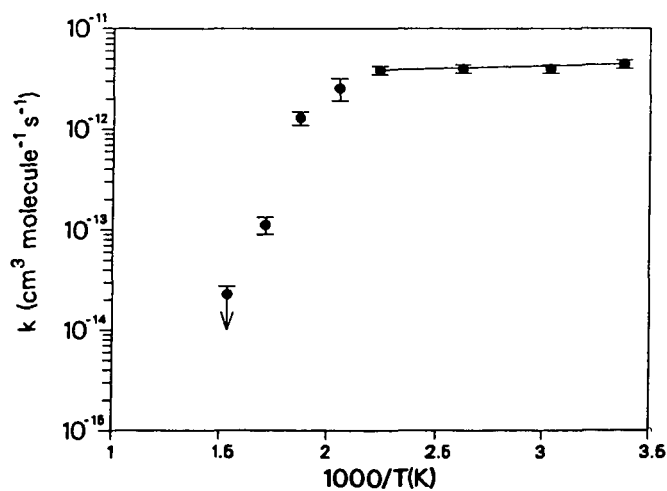


Figure 4. Arrhenius plot of  $\log k_1$  for the reaction of NCO with ethene against  $1000/T(K)$ . The solid line is the least squares fit to the data for the temperature range 295-447.

# Pyrolysis of $C_6H_6$

by

M. B. Colket, III

United Technologies Research Center  
Silver Lane, East Hartford, CT 06108

## Introduction

Several mechanisms for the pyrolysis of benzene at elevated temperatures have been previously proposed. Unfortunately, none of these mechanisms is entirely satisfactory when both experiments and thermodynamics are considered. Yet, knowledge of benzene decomposition will increase the understanding of the breakup and formation of other aromatic compounds. Consequently, a single-pulse shock tube (SPST) investigation of the pyrolysis of benzene has been performed over the temperature range of 1200 to 2400K. In addition, thermochemical estimates and detailed chemical kinetic modeling have been performed to evaluate the previously proposed mechanisms for benzene pyrolysis.

## Description of Facilities and Model

The 3.8 cm (i.d.) single-pulse shock tube (SPST) used in this experiment utilizes the "magic hole" technique for quenching pyrolyzed samples at rates above  $10^5$  K/sec. SPSTs were developed by Glick, Squire, and Hertzberg (1) and the UTRC facility has been described by Colket (2). Gas samples, after dwell times of approximately 700 microseconds, were automatically collected and analyzed for reactant and products using heated gas sampling valves and a Hewlett Packard 5880A gas chromatograph. With a CP Sil 5 CB (from Chrompack, Inc.) capillary column and a silica gel packed column,  $H_2$  and hydrocarbons up to  $C_{10}$  were identified and quantitatively analyzed.

Argon (99.999% pure) was obtained from Matheson and LC-grade benzene was obtained from the Burdick and Jackson Laboratory. The initial mixture concentration was 130 ppm benzene in argon and was prepared gravimetrically. Gas chromatographic analysis indicated that impurities included unidentified  $C_5$ ,  $C_6$  and  $C_7$  hydrocarbons as well as toluene, although the total concentration of impurity was less than 0.2% of the initial benzene.

Detailed chemical kinetics calculations are performed using CHEMKIN(3), LSODE (4), and a version of a shock tube code (5) which has been modified to include the quenching effects in a SPST. Quenching rates varied with shock strength and were calculated using measured pressure traces and assuming isentropic expansion. The modified code also allows monitoring of time-dependent contributions from each reaction to the formation and/or destruction of each species.

### Proposed Mechanisms

Mechanisms for the decomposition of benzene are listed in Table I. It is important to note that most are not single-step mechanisms. Radical intermediates equilibrate rapidly and their concentrations are sufficiently low to render them (nearly) undetectable in many systems. Experimental results from the present and previous high temperature works (6,7) suggest that primary stable products are acetylene, diacetylene, and hydrogen and the initial production rate of acetylene is two to three times higher than that of diacetylene. Unfortunately, this information is of minimal use in sorting out the mechanisms since benzene pyrolyzes at high temperatures (relative to pyrolysis temperatures of other hydrocarbons) and all intermediates shown in Table II rapidly pyrolyze to the approximate mixture of acetylene and diacetylene that has been observed.

Mechanism A is the generally accepted reaction sequence; however, only Reaction 1 is understood. The breaking of the C-H bond is believed to be the initiation step in both pyrolytic and some oxidation studies. Its rate has been determined from D-atom production (in pyrolysis of  $C_6D_6$ ) (8) and from detailed modeling studies of both pyrolysis (9) and oxidation (10). An RRKM fit has been performed by Kiefer, et al (9) using available experimental data and is consistent with thermodynamics. Their  $k_1^0$  is given by  $10^{17.3} \exp(-118 \text{ kcal/RT}) \text{ sec}^{-1}$ . Knowledge of the mechanism for phenyl decomposition is substantially less than that for Reaction 1. Some information is available on the overall rate,  $k_3$ ; yet the details of the ring fracturing process have not been defined. The thermochemical estimate by Fujii and Asaba (11) has been until recently the most often quoted rate for this process. More recent modeling (8,9) of benzene pyrolysis has produced similar rates as Ref. 11; however, since Reaction 1 is rate limiting over most of the temperatures regimes examined, the modeling results for  $k_3$  are expected to be lower limit estimates with large uncertainties in the temperature dependence. The Fujii and Asaba (11) estimate,  $k_3 = 3.16 \times 10^{14} \exp(-86 \text{ kcal/RT}) \text{ sec}^{-1}$ , was based on an "old" value for the heat of formation for  $i\text{-C}_4\text{H}_9$  of 102 kcal/mole (12); however, more recent estimates using group additivity (13) and BAC-MP4 (14) techniques fix this value closer to 115 kcal/mole. In addition,  $n\text{-C}_4\text{H}_9$ , which has a  $\Delta H_f^\circ$  of 126 kcal/mole, is the preferred isomer for phenyl decomposition. Consequently, Reaction 3 is over 100 kcal/mole endothermic. If this process involves direct  $C_6H_5$  elimination, then the previous modeling efforts that produced lower limit rates strongly suggest that the high pressure A-factor is at least  $10^{17.8}$ . This value is orders of magnitude higher than what would be expected for this multibond process. Consequently, it must be assumed that Reaction 3 represents an overall process or that processes involving radicals other than, or in addition to, phenyl are important to benzene decomposition.

One alternative route for benzene decomposition is direct  $C_6H_5$  elimination (Mechanism B) and has received recent support (6,8); however, Kiefer, et al (9) have shown it is not necessary to invoke this step to describe experimental profiles. In addition, it should be noted that the direct elimination is a multibond process which should be unlikely, and presumably involves the intermediate formation of the  $C_6H_4$  diradical. For this intermediate, the effective activation barrier to Reaction 4 may be as high as 180 kcal/mole.

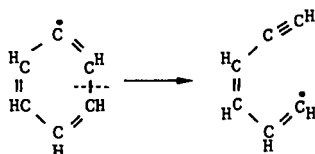
Another possible pyrolysis route involves the production of benzyne, which subsequently decomposes. Unimolecular decomposition of phenyl (Reaction 5) to benzyne is endothermic by 93 kcal/mole, which is nearly as much as Reaction 3. Similar thermochemical arguments can eliminate this decomposition route. The other route, Reaction 6, is a radical termination step and would produce an overall slowing of benzene pyrolysis. Knudsen cell pyrolysis experiments (7) have shown the formation of a  $C_6H_4$  compound. Assuming this compound is benzyne or another product of phenyl decomposition, Smith and Johnson (7) argued that  $C_6H_4$  is an important intermediate during benzene decomposition, especially at elevated temperatures. At least some of the product, however, may be composed of the chained isomers of  $C_6H_4$ . These isomers may be produced via hydrogenation of triacetylene, which was also observed in significant concentrations. Consequently, no clear evidence of the importance of Mechanism C is apparent.

Mechanism D appears to be very attractive, since an extrapolation of the rate coefficient (15) for H-atom addition to benzene (Reaction 8) is approximately an order of magnitude higher (Ref. 9) than H-atom abstraction (Reaction 2) at 1600 K. The addition reaction, however, competes with its reverse reaction. Using thermodynamics for  $c-C_6H_7$ , derived from measurement of the forward and reverse rates of Reaction 8 (15), Mechanism D can be shown to have a negligible impact on benzene pyrolysis. However, a different set of thermodynamics for  $c-C_6H_7$ , reported in Ref. 15 suggests that Mechanism D may play an important role at low temperatures. Detailed modeling calculations using Mechanism D were limited, due to what appears to be rather large uncertainties in both the heat of formation and entropy. Nevertheless, there are attractive features of this decomposition mechanism, especially at low temperatures, and it should be explored further. It is worth noting that Reaction 8 is not sufficiently energetic (only 16 to 26 kcal), that it can be followed immediately by Reaction 9 (71-81 kcal required). Instead,  $c-C_6H_7$  will collisionally thermalize prior to its decomposition to products. Only a minimal acceleration in rate due to the formation of an excited complex can be expected. Further exploration of this route (Mechanism C) should be performed.

With no fully satisfactory alternatives, and the expectation that phenyl must decompose to aliphatics at sufficiently elevated temperatures (when production of phenyl via Reaction 1 is fast), it is prudent to re-examine Mechanism A. One can separate Reaction 3 into the following sequence:



This sequence is the reverse of the processes suggested for the formation of phenyl during acetylene pyrolysis (17) and has been shown to compare favorably with recent experimental data (2). If one assumes that the ring breaks at the single bond as shown



then this is a relatively straightforward process analogous to the decomposition of  $n\text{-C}_6\text{H}_5$ ; i.e.  $\text{CH}:\text{CH}:\text{CH}:\text{CH}_2 + \text{C}_2\text{H}_2 + \text{C}_2\text{H}_3$ . Breakage of either of the other two single-bonds would require a more complex process involving H-atom shifting or the formation of energetic intermediates. The resultant linear compound would be expected to decompose to acetylene and  $n\text{-C}_4\text{H}_3$  or re-cyclize to phenyl. Detailed chemical modeling was performed using the reaction sequence in Table II coupled with an acetylenic mechanism similar to that reported (17, 18). A comparison of the model and single-pulse shock tube data is presented in Figure 1 for a series of shocks at an initial concentration of 130 ppm benzene in argon. In this figure, final concentrations produced after a dwell time of 700 microseconds followed by quenching are plotted as a function of initial post-shock temperature. Total pressure for these experiments is approximately seven atmospheres.

The comparison is quite reasonable. The higher fractional decomposition at low temperatures observed in the experiment may be due to impurities from the wall initiating the reaction at low temperature. The residual benzene observed experimentally at elevated temperatures may be caused by sampling a portion of the boundary-layer near the walls of the shock tube. The mechanism proposed in Table II is essentially consistent with Kiefer et al's except that Reaction 3 has been separated to 3a and b. An effective rate constant for Reaction 3 can be estimated by assuming a steady-state concentration for  $1\text{-C}_6\text{H}_5$ , i.e.

$$[1\text{-C}_6\text{H}_5]_{\text{s.s.}} = \frac{k_{3a}[\text{C}_6\text{H}_5]}{(k_{-3a} + k_{3b})}$$

$$\text{therefore } k_3^{\text{effective}} = \frac{k_{3a} k_{3b}}{k_{-3a} + k_{3b}}$$

This curved evaluation is depicted as a solid line in Fig. 2 over the temperature regime where sensitivity to this rate was observed. The curve is extrapolated to both low and high temperatures to facilitate comparisons to other evaluations. The relatively high values obtained in this work for  $k_3$  and  $k_3^{\text{effective}}$  are not surprising since the rate constant determined in these experiments are expected to be close to the high pressure limiting value.

#### Conclusions

Previously proposed mechanisms for the pyrolysis of benzene at high temperatures have been reviewed using detailed chemical modeling and a brief thermochemical examination. The most widely accepted sequence,  $\text{C}_6\text{H}_6 \rightarrow \text{C}_6\text{H}_5(+\text{H}) \rightarrow \text{C}_6\text{H}_4 + \text{C}_2\text{H}_2$ , is slightly modified to  $\text{C}_6\text{H}_6 \rightarrow \text{C}_6\text{H}_5(+\text{H}) \rightarrow 1\text{-C}_6\text{H}_5 \rightarrow n\text{-C}_4\text{H}_3 + \text{C}_2\text{H}_2$  and the structure of the linear  $\text{C}_6\text{H}_5$  intermediate is proposed. Forward and reverse rates are consistent with thermochemistry and experimental data. A benzene decomposition route involving  $\text{c-C}_6\text{H}_7$  and  $1\text{-C}_6\text{H}_7$  was examined, yet sufficiently accurate thermochemistry was not available to reach final conclusions.

### Acknowledgements

This work has been supported by the Air Force Office of Scientific Research (AFSC) under Contract No. F49620-85-C-0012. The United States Government is authorized to reproduce and distribute reprints for governmental purposes notwithstanding any copyright notation hereon.

### References

1. Glick, H. S., Squire, W., and Hertzberg, A., Fifth Symposium (International) on Combustion, p. 393, Reinhold Publishing Corp., New York, 1955.
2. Colket, M. B., To be published in Proceedings of the Fifteenth International Symposium on Shock Waves and Shock Tubes, 1986.
3. Kee, R. J., Miller, J. A., Jefferson, T. H., "CHEMKIN: A General Purpose, Problem-Independent, Transportable, Fortran Chemical Kinetics Code Package," Sandia Laboratories, SAND80-8003, March, 1980.
4. Hindmarsh, A. C., "LSODE and LSODI, Two New Initial Value Differential Equation Solvers," ACM SIGNUM Newsletter, 15, No. 4, December 1980.
5. Mitchell, R. E. and Kee, R. J., "A General-Purpose Computer Code for Predicting Chemical Kinetic Behavior Behind Incident and Reflected Shocks", Sandia National Laboratories, SAND82-8205, March 1982.
6. Kern, R. D., Wu, C. H., Skinner, G. B., Rao, V. S., Kiefer, J. H., Towers, J. A., and Mizerka, L. J., Twentieth Symposium (International) on Combustion, The Combustion Institute, p. 789, Pittsburgh, 1984.
7. Smith, R. D. and Johnson, A. L., Combustion and Flame 51, 1 (1983).
8. Rao, V. S. and Skinner, G. B., J. Phys. Chem. 88, 5990 (1984).
9. Kiefer, J. H., Mizerka, L. J., Patel, M. R., and Wei, H. C., J. Phys. Chem. 89, 2013 (1985).
10. Hsu, D. S. Y., Lin, C. Y. and Lin, M. C., Twentieth Symposium (International) on Combustion, The Combustion Institute, p. 623, Pittsburgh, 1985.
11. Fujii, N. and Asaba, T., Fourteenth Symposium (International on Combustion), p. 433, The Combustion Institute, Pittsburgh, 1973.
12. Duff, R. E., and Bauer, S. H., J. Chem. Phys. 36, 1754 (1962).
13. Benson, S. W., Thermochemical Kinetics, 2nd Ed., John Wiley and Sons, New York, 1976.
14. Melius, C., personal communication.
15. Nicovich, J. M. and Ravishankara, A. R., J. Phys. Chem. 88, 2534 (1984).
16. Weissman, M. and Benson, S. W., Int'l. J. Chem. Kin. 16, 307 (1984).
17. Frenklach, M., Clary, D. W., Gardiner, W. C., Jr., and Stein, S., Twentieth Symposium (International) on Combustion, p. 887, The Combustion Institute, Pittsburgh, 1985.
18. Kiefer, J. H., Kapsalis, S. A. Al-Alami, M. Z., and Budach, K. A., Combust. Flame 51, 79 (1983).

TABLE I  
Previous Mechanisms for  
Benzene Pyrolysis

|   |  |      |
|---|--|------|
| A | $C_6H_6 \rightarrow C_6H_5 + H$          | (1)  |
|   | $H + C_6H_6 \rightarrow C_6H_5 + H_2$    | (2)  |
|   | $C_6H_5 \rightarrow C_4H_3 + C_2H_2$     | (3)  |
| B | $C_6H_6 \rightarrow C_4H_4 + C_2H_2$     | (4)  |
| C | $C_6H_5 \rightarrow C_6H_4 + H$          | (5)  |
|   | $H + C_6H_5 \rightarrow C_6H_4 + H_2$    | (6)  |
|   | $C_6H_4 \rightarrow C_4H_2 + C_2H_2$     | (7)  |
| D | $H + C_6H_6 \rightarrow c-C_6H_7$        | (8)  |
|   | $c-C_6H_7 \rightarrow 1-C_6H_7$          | (9)  |
|   | $1-C_6H_7 \rightarrow n-C_4H_5 + C_2H_2$ | (10) |

TABLE II  
Proposed Reaction Sequence  
for Benzene Pyrolysis

|  | Forward rate  |                 | Reverse Rate  |       |                 |
|--|---------------|-----------------|---------------|-------|-----------------|
|  | $\log_{10} A$ | $E$<br>cal/mole | $\log_{10} A$ | n     | $E$<br>cal/mole |
| 1. $C_6H_6 \rightleftharpoons C_6H_5 + H$              | 16.18         | 107,900.        | 10.05         | 0.98  | -5690.          |
| 2. $H + C_6H_6 \rightleftharpoons C_6H_5 + H_2$        | 14.40         | 16,000.         | 8.35          | 1.12  | 6420.           |
| 3a. $C_6H_5 \rightleftharpoons l-C_6H_5$               | 14.00         | 65,000.         | 13.11         | -0.68 | 3300.           |
| 3b. $l-C_6H_5 \rightleftharpoons n-C_4H_3 + C_2H_2$    | 15.34         | 38,000.         | 5.97          | 1.97  | -3610.          |
| 11. $n-C_4H_3 \rightleftharpoons H + C_4H_2$           | 12.43         | 37,000.         | 11.29         | 0.44  | -2790.          |
| 12. $n-C_4H_3 \rightleftharpoons C_2H + C_2H_2$        | 14.60         | 54,000.         | 7.89          | 1.66  | -3120.          |
| 13. $C_2H + C_6H_6 \rightleftharpoons C_2H_2 + C_6H_5$ | 13.30         | 0               | 12.00         | 0     | 12520.          |

FIGURE 1. 130PPM BENZENE PYROLYSIS  
COMPARISON OF MODEL AND EXPERIMENT

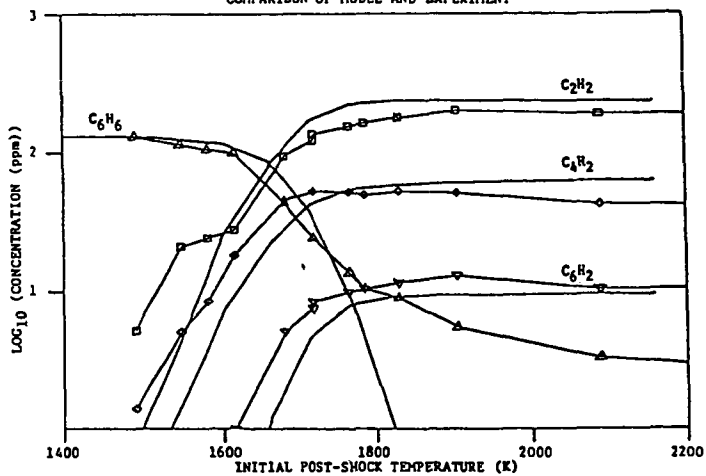
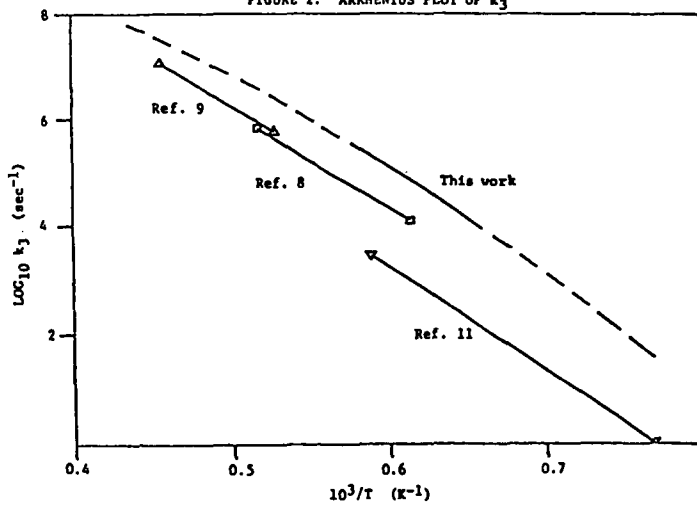


FIGURE 2. ARRHENIUS PLOT OF  $k_3$





The Chemical Structure of Methane/Air Diffusion Flames:  
Concentrations and Production Rates of Intermediate Hydrocarbons.

J. Houston Miller

Department of Chemistry  
George Washington University  
Washington, DC 20052

and Kermit C. Smyth

Center for Fire Research  
National Bureau of Standards  
Gaithersburg, MD 20899

INTRODUCTION:

The production of intermediate and large hydrocarbon species is common to most combustion systems. These products range in size from acetylene, benzene and polynuclear aromatic hydrocarbons (PAH) to very large soot particles. Radiation from particles is the dominant mode of heat transfer in large fires. In addition, sampled particles often have PAH adsorbed onto them. Many of these molecules are known carcinogens and their presence on inhalable soot particles poses an obvious long-term health hazard. Despite the important role that such species play in flames and the danger they present as combustion byproducts, the mechanism for their formation is as yet unknown.

Extensive profile studies have led to a detailed understanding of the chemical structure of premixed flames [1]. This information has been combined with the time-temperature history in these one-dimensional systems to produce simple models for the condensation chemistry of premixed flames. Modelling efforts have also been undertaken in shock tubes, although the data set available as input has generally been less extensive [2,3]. Despite the significant progress towards an understanding of soot formation which has resulted from these studies, most practical combustion devices are diffusion flames, and chemical structure data for these environments has only recently been available. Workers in this [4] and other [5] laboratories have recently reported concentration measurements for molecular species, including intermediate hydrocarbons, in laminar diffusion flames. Our work has shown that a knowledge of the local chemical composition alone is not sufficient to predict the concentrations of PAH and soot. We have therefore also collected profile data for temperature and convective velocity in our flame system. In this paper, results for the chemical structure of a methane/air diffusion flame are reviewed. Species concentrations are combined with profiles of velocity and temperature to calculate production rates for intermediate hydrocarbons. The relevance of these calculations to an understanding of soot formation chemistry is discussed.

#### EXPERIMENTAL APPROACH:

The experimental system has been described in detail elsewhere [4], and will be discussed only briefly below. Laminar methane/air diffusion flames were burned at atmospheric pressure on a Wolfhard-Parker slot burner. Fuel exits a central 8mm wide slot and air flows through two 16mm wide adjacent slots. Thus, two flame sheets are formed near the fuel/air interfaces, which are symmetric about the burner centerline. The flame is stabilized by wire screen "gulls" located 45mm above the burner surface. Concentration profiles of numerous stable flame species were collected via a direct-sampling mass spectrometer equipped with a quartz microprobe [6]. Calibrations were performed by measuring the signal for a particular molecule sampled from a mixture of known composition of the species with argon at room temperature. Calibration factors were then corrected for the variation of the mass flow through the sampling orifice as a function of temperature. For species which could not be calibrated directly, factors for similar species were adjusted by multiplying by the ratio of their respective ionization cross-sections.

Temperature profiles were measured with an uncoated fine wire Pt/Pt-10%Rh thermocouple. Corrections due to radiation effects are less than 7% at the highest temperatures in this flame [4], while catalytic effects are expected to be small [7] and in the opposite direction. Horizontal and vertical components of the convective velocity were determined using laser Doppler velocimetry. These measurements were made by seeding the flow with nominal 1  $\mu$ m diameter aluminum oxide particles. The temperature and velocity profiles were obtained at heights ranging from near the burner surface to 20 mm above the burner. Mass spectrometric measurements were limited to a minimum height of 3 mm above the burner (due to the 6mm diameter of the microprobe) and a maximum height of 15 mm above the burner. Above 15 mm, clogging of the probe orifice by soot particles was observed and quantitative sampling was no longer possible. The gradients in concentration and temperature in this flame are steepest in the horizontal direction. Therefore, profile data points were collected every 0.2 mm in the lateral direction and every 2 mm in the vertical direction.

#### RESULTS:

Figure 1 illustrates the temperature and velocity fields for this flame. Shown in solid lines are isothermal contours determined from the thermocouple profiles. Note the bowing out of the flame along the 1900 K contour away from the slot separators located at  $\pm 4$  mm with respect to the burner centerline. Also shown are streamlines of convective velocity calculated from the two measured velocity components. The streamlines exhibit trajectories which begin in the lean region of the flame, cross the high temperature reaction zones, and continue into the fuel-rich regions.

Figure 2 shows mass-spectrometric profiles of the concentrations of a variety of stable flame species at a height of 9 mm above the burner. A number of points are noteworthy in comparing

Figures 1 and 2. First, the concentrations of oxygen and methane disappear near the high temperature reaction zone at  $\pm 6$  mm from the burner centerline, where the concentration of water is at a maximum. Second, the high concentration of nitrogen near the burner centerline reveals that significant entrainment of air (as shown by the velocity measurements in Fig. 1) and diffusion of nitrogen toward the burner centerline occur. Also shown in Fig. 2 is a summation of mole fractions for all species present in the flame at a concentration of 1% or greater. The close agreement to an ideal mass balance of 1 throughout the flame is a measure of the success of our calibration scheme.

Figure 3 illustrates profiles collected at 9mm above the burner surface for a variety of intermediate hydrocarbons: acetylene, benzene, diacetylene, and butadiene. Peak concentrations at this height for these species are 6200, 800, 570, and 110 parts per million, respectively. Profiles for a large number of additional intermediate hydrocarbons were obtained, and all have concentration maxima in the same region of the flame.

#### DATA ANALYSIS

One of the primary goals of our work is the application of kinetic modelling to a methane/ air diffusion flame. The approach we have adopted is to compare the predictions of models which have been used successfully in premixed flames and shock tubes with our experimental results. A successful model must not only account for the steady state concentrations of species involved in the soot formation process, but also for the net rate of reactions for these species in the flame. Therefore, as a first step in the application of detailed kinetic modelling to our flame we have sought to derive the net chemical flux for profiled species from our concentration, temperature and velocity measurements. The procedure for this calculation is described below.

A laminar flame is a steady-state system: the value of any macroscopic variable (such as a species concentration) does not change with time at a particular spatial location [6]. Because there is a flux into and out of a given volume element due to mass transport, there must be a corresponding change in the species concentration due to chemical reactions:

$$R_i = \nabla [N_i (v + V_i)] \quad 1)$$

Here,  $R_i$  is the net chemical rate,  $N_i$  is the species concentration,  $v$  is the mass average (convective) velocity, and  $V_i$  is the diffusion velocity of the species into the local mixture. This diffusion velocity can be calculated by first computing the effective diffusion coefficient,  $D_{i,mix}$ , where contributions from all species present in the flame with a concentration greater than 1% are included:

$$V_i = - \frac{D_{i,mix}}{x_i} \cdot \nabla x_i \quad 2)$$

Figure 4 illustrates this calculation for acetylene production rates at a height of 9mm above the burner. Contributions from the convective and diffusive velocities to the net chemical rates are shown. Note the strong diffusive velocity away from the burner centerline into the high temperature reaction zone, where acetylene is oxidized. Figure 5 indicates that the chemical role of acetylene changes with height above the burner. Low in the flame the destruction rate exhibits a maximum value ( $R_i = -1.0 \times 10^{19}$  molecules/(cc·sec)) near the high temperature, primary reaction zone, and the production rate feature ( $R_i = 1.5 \times 10^{19}$  molecules/(cc·sec)) occurs slightly toward the fuel side. This peak in the production rate is located on the high temperature side of the observed maximum in the concentration profile (see Fig. 3). Higher in this flame it appears that the production rate peak is diminished by a new destruction feature (see arrow in Figure 5). An additional loss mechanism for acetylene higher in the flame is consistent with the proposed importance of this intermediate hydrocarbon in particle growth chemistry. The location of this new feature coincides with the peak concentrations of very small soot particles detected in our earlier work [4].

#### CONCLUSIONS AND FUTURE DIRECTIONS:

We have made quantitative species concentration measurements and analyzed these profile data to obtain chemical rates for production and destruction of intermediate hydrocarbons in a methane/air flame. In the near future detailed kinetic models will be evaluated at specific flame locations in an attempt to verify their application to diffusion flame systems. Specifically, can the models (given as inputs measured concentrations, temperature, and mass transport) predict net chemical fluxes which agree with our measured production rates? An analysis such as this will indicate possible shortcomings in both our knowledge of the chemical structure of these systems (i.e., radical concentrations are not well known) as well as deficiencies in proposed models for chemical growth.

#### REFERENCES:

- 1) J.D. Bittner, Ph. D. Dissertation, Massachusetts Institute of Technology, 1982.
- 2) M. Frenklach, D.W. Clary, W.C. Gardiner, Jr., and S.E. Stein, Twentieth Symp (Intnl) on Combustion. (The Combustion Institute, Pittsburgh, 1984). p. 887.
- 3) M. Frenklach, D.W. Clary, and M.K. Ramachandra, NASA Contractor Report 174880, May 1985.
- 4) K.C. Smyth, J.H. Miller, R.C. Dorfman, W.G. Mallard, and R.J. Santoro, Combust. Flame 62, 157 (1985).
- 5) K. Saito, A.S. Gordon, and F.A. Williams, ASME/AICHE National Heat Transfer Conference, 1985.
- 6) R.M. Fristrom and A.A. Westenberg, Flame Structure, (McGraw-Hill, New York, 1965).
- 7) S.M. Schoenung and R.K. Hanson, Comb. Sci. Tech. 24, 227 (1981).

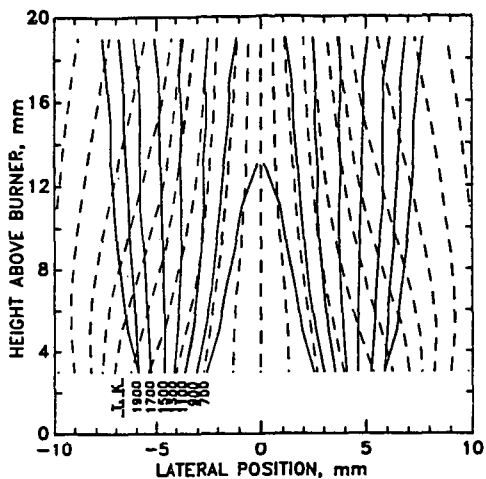


Figure 1: Isothermal contours (solid lines) calculated from uncorrected thermocouple measurements and streamlines (dashed lines) calculated from the velocity measurements for the methane/air flame.

Figure 2: Mass spectrometric measurements of some of the major species. The  $N_2$  profile has not been corrected for the small amount of CO detected at the same mass. At the top of the figure the sum of the mole fractions of all of the species present in the flame at a concentration of 1% or greater is shown. The dashed line represents the average value of  $1.01 \pm 0.04$ .

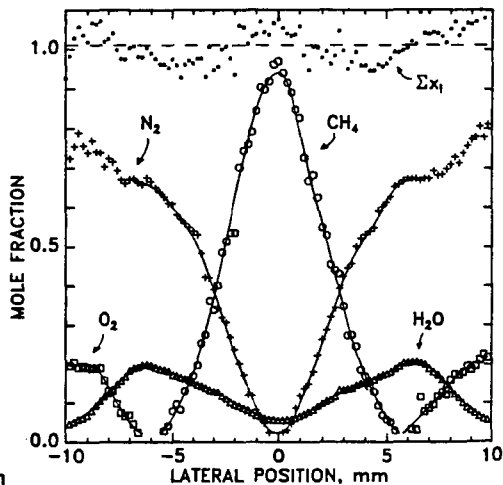
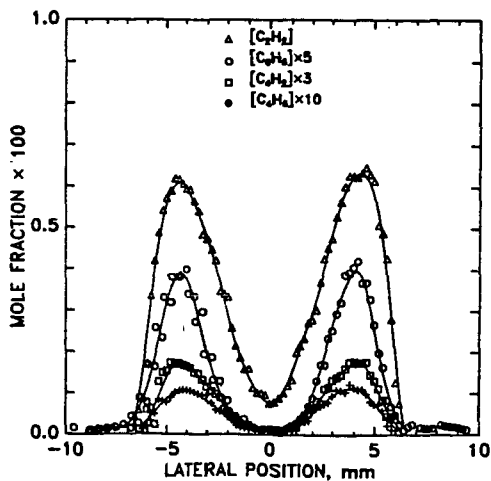


Figure 3: Mass spectrometric profile measurements of several minor species: acetylene, benzene, diacetylene, and butadiene at a height of 9mm above the burner.



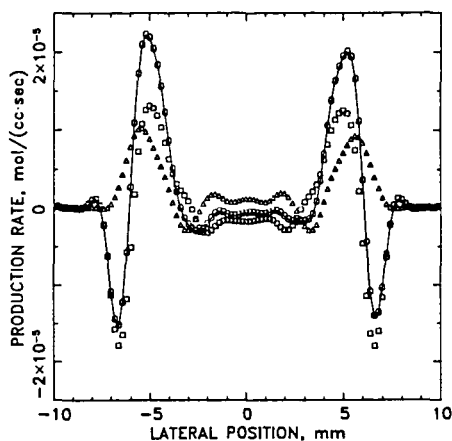


Figure 4: Contributions to the net chemical production rate (the connected circles) from diffusive (squares) and convective (triangles) terms in Eq. 1 at 9mm above the burner.

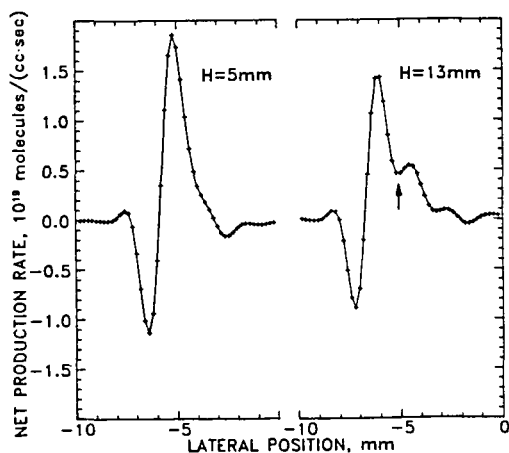


Figure 5: Profiles of the net chemical production rate for acetylene at two heights in the flame; only the left hand side of the flame is shown.

## SULFUR TRIOXIDE FORMATION IN HIGH SULFUR RESIDUAL OIL FLAMES

Peter M. Walsh, Walter F. Farmayan,\* Thomas Kolb,† János M. Beér

Energy Laboratory and Department of Chemical Engineering  
Massachusetts Institute of Technology  
Cambridge, MA 02139

### INTRODUCTION

Heavy residual fuel oils usually contain between 1 and 4 wt% sulfur. Although  $\text{SO}_2$  is the principal product of fuel sulfur oxidation, as much as 8 to 10 mol% of the sulfur oxides are present as  $\text{SO}_3$  in the flue gas arriving at the cold end of the convective section in an electric utility boiler. Sulfur trioxide is quantitatively converted to sulfuric acid vapor in the presence of typical flue gas water vapor concentrations at temperatures below about 500 K (Halstead and Talbot, 1980). Condensation of sulfuric acid on surfaces at temperatures below the acid dewpoint is responsible for corrosion of cold end components, especially the air preheater. The accumulation of unburned carbon particles on the wet surfaces and reentrainment of their agglomerates is the source of acid smuts (Blum, Lees and Rendle, 1959; Conolly and Kelsell, 1982). The adsorption of sulfuric acid on ash and unburned carbon may make a significant contribution to the mass of stack gas particulates.

The most severe acid deposition and sulfate emissions problems are associated with catalytic oxidation of  $\text{SO}_2$  to  $\text{SO}_3$  over vanadium-containing deposits on tubes in the convective section. However, 1 to 2 mol% of the sulfur oxides are thought to be present as  $\text{SO}_3$  in the furnace exit gas. Reidich and Reifenhäuser (1980) reported 2 mol% of the sulfur oxides as  $\text{SO}_3$  (25 mol ppm of total gas) at the furnace exit in a 300 MW, tangentially fired boiler operated at 0.6 mol% excess  $\text{O}_2$  with 2 wt% sulfur fuel. This is an amount sufficient to cause troublesome acid deposition and make a significant contribution to particulate loading, even in the absence of additional  $\text{SO}_3$  formation in the convective section. Experience has shown that  $\text{SO}_3$  formation can be controlled by reducing excess air, but this is accompanied by an increase in unburned carbon (coke cenospheres). Sulfur trioxide formation in the furnace is one component of a set of coupled processes making contributions to acid deposition and stack particulates (Cunningham and Jackson, 1978; Harada, Naito, Tsuchiya, and Nakajima, 1981).

Substantial progress has recently been made in the quantitative description of sulfur chemistry in flames (Muller, Schofield, Steinberg, and Broida, 1979; Kramlich, Malte, and Grosshandler, 1981; Smith, Wang, Tseregounis, and Westbrook, 1983; Wendt, Wootan, and Corley, 1983). Squires (1982) combined a detailed chemical kinetic description of reactions in the furnace with a global model for heterogeneous oxidation of  $\text{SO}_2$  over tube deposits in the convective section. The predictions of this model were in good agreement with observed levels of  $\text{SO}_3$  in the flue gases of 500 MW and 60 MW boilers. The present paper describes the initial steps of an investigation in which the results of fundamental kinetic studies are applied to the interpretation of direct measurements of  $\text{SO}_3$  in boiler-type turbulent diffusion flames.

\*Present address: Chemical Engineering Department, Shell Development Co.,  
Westhollow Research Center, Houston, TX 77001

†Present address: Engler-Bunte-Institut, University of Karlsruhe, West Germany



Table 1. Experimental Conditions.

| Run No. | Fuel Treatment      | Atomizer Location w.r.t. Air Nozzle (mm) | Comb. Swirl | Air No. | Mole Fraction $O_2$ in Flue Gas (%) | Excess Air (%) | Air Velocity at Nozzle (m/s) | Fuel Temperature (K) | Fuel Pressure (MPa) | Atomizing Air Pressure (MPa) |
|---------|---------------------|--|-------------|---------|-------------------------------------|----------------|------------------------------|----------------------|---------------------|------------------------------|
| 212     | None                | -25                                      | 0.9         | 0.9     | 1.5                                 | 7.3            | 49                           | 389                  | 1.48                | 1.48                         |
| 213     | Additive B          | +25                                      | 0.9         | 0.9     | 1.5                                 | 7.3            | 49                           | 389                  | 1.51                | 1.51                         |
| 214     | None                | +46                                      | 0.5         | 0.5     | 1.0                                 | 4.7            | 48                           | 389                  | 1.25                | 1.14                         |
| 215     | Additive D          | +46                                      | 0.5         | 0.5     | 1.0                                 | 4.7            | 48                           | 389                  | 1.25                | 1.14                         |
| 216     | Additive E          | +46                                      | 0.5         | 0.5     | 1.0                                 | 4.7            | 48                           | 389                  | 1.25                | 1.14                         |
| 217     | 7.0% Water Emulsion | +46                                      | 0.5         | 0.5     | 1.0                                 | 4.7            | 48                           | 391                  | 1.25                | 1.14                         |
| 218     | Additive B          | +46                                      | 0.5         | 0.5     | 1.0                                 | 4.7            | 48                           | 389                  | 1.25                | 1.14                         |
| 219     | Additive F          | +46                                      | 0.5         | 0.5     | 1.0                                 | 4.7            | 48                           | 389                  | 1.25                | 1.14                         |
| 220     | Additive C          | +46                                      | 0.5         | 0.5     | 1.0                                 | 4.7            | 48                           | 389                  | 1.25                | 1.14                         |
|         |                     | $\pm 0.5$                                |             |         | $\pm 0.1$                           |                |                              | $\pm 3$              | $\pm 0.04$          | $\pm 0.04$                   |

## EXPERIMENTAL

The measurements were made in the 1.2 x 1.2 m combustion tunnel in the MIT Combustion Research Facility (Beér, Jacques, Farmayan, and Taylor, 1981). The fuel was a mixture of residual oils produced by the Exxon refinery at Aruba. Its analysis was (wt%): carbon 85.80, hydrogen 10.86, nitrogen 0.47, sulfur 2.15, oxygen 0.57, and ash 0.10. Asphaltenes (IP 143/57) were 10.5 wt%, and the metal contents (wt ppm) were: vanadium 421, nickel 51, iron 15, sodium 9.8, calcium 20, and magnesium 4.8. The heating value was 42.5 MJ/kg and viscosity was 213 Saybolt Furol seconds at 50°C. The fuel was heated to 389 K, fired at 0.05 kg/s (2 MW thermal), and atomized by a 70° (full angle) six-hole "Y" jet nozzle with air as the atomizing medium. Combusting air was preheated to 560 K and supplied through a 0.176 m diameter duct to a 50° (full angle) divergent quarl mounted flush with one end wall of the combustion chamber. Several parameters were varied in order to examine their effects on carbon burnout and SO<sub>3</sub> formation: atomizer position, atomizing air/fuel ratio, combustion air swirl, and excess air. Five different commercial preparations designed to promote carbon burnout were added to the fuel; these contained compounds of the metals iron, zirconium, and cerium. One run was made with fuel emulsified with 7 wt% water. The experimental conditions are given in Table 1.

Gas temperature and composition (O<sub>2</sub>, CO<sub>2</sub>, CO, SO<sub>2</sub>, NO) were determined using standard techniques. The axial component of the gas velocity was measured using a two-hole impact probe. A representative set of gas temperature, velocity, and composition profiles is shown in Fig. 1. Axial positions are measured from the exit of the 0.176 m diameter combustion air nozzle. For calculation purposes, the temperature, velocity, and carbon monoxide profiles in the region following the peak flame temperature at  $z = z_0 = 0.95$  m were fit by the following relations, shown as solid lines in Fig. 1:

$$T = T_0 - \alpha(z - z_0) \quad 1)$$

$$u = \beta/z \quad 2)$$

$$x_{CO} = x_{CO,0} \exp[-\gamma(z - z_0)] \quad 3)$$

Table 2. Data used in the calculations. The mole fractions of CO<sub>2</sub>, O<sub>2</sub>, and SO<sub>2</sub> are calculated flue gas values (wet) based on the fuel analysis and air/fuel ratio.

| Run No. | T <sub>0</sub> (K) | α (K/m) | β (m <sup>2</sup> /s) | x <sub>CO,0</sub> | γ (m <sup>-1</sup> ) | x <sub>CO2</sub> | x <sub>O2</sub> | x <sub>SO2</sub> (ppm) |
|---------|--------------------|---------|-----------------------|-------------------|----------------------|------------------|-----------------|------------------------|
| 212     | 2005               | 175     | 16                    | .0133             | 1.517                | .131             | .0133           | 1220                   |
| 213     | 2045               | 172     | 16                    | .0319             | 1.499                | .131             | .0133           | 1220                   |
| 214     | 2000               | 138     | 15                    | .0435             | 1.992                | .134             | .00885          | 1250                   |
| 215     | 2000               | 131     | 15                    | .0319             | 1.859                | .134             | .00885          | 1250                   |
| 216     | 1975               | 130     | 15                    | .0291             | 1.829                | .134             | .00885          | 1250                   |
| 217     | 1985               | 143     | 15                    | .0319             | 1.925                | .133             | .00878          | 1240                   |
| 218     | 2005               | 133     | 15                    | .0368             | 1.906                | .134             | .00885          | 1250                   |
| 219     | 2000               | 130     | 15                    | .0338             | 1.776                | .134             | .00885          | 1250                   |
| 220     | 1990               | 133     | 15                    | .0338             | 1.776                | .134             | .00885          | 1250                   |

Values of the parameters are given in Table 2. A mean gas residence time of 1 s, typical of a tightly designed oil-fired utility boiler, is reached at a distance of about 2.9 m from the combustion air nozzle.

$\text{SO}_3$  in the flame gases was determined using the Severn Science Ltd./Marchwood Engineering Laboratories (Central Electricity Generating Board, UK) continuously recording  $\text{SO}_3/\text{H}_2\text{SO}_4$  monitor (Jackson, Hilton, and Buddery, 1981). This instrument is intended primarily as a flue or stack gas monitor. The 2 m long heated sampling probe supplied with the instrument was adapted for sampling in the flame by enclosing it in a water-cooled sheath. The glass sampling tube was replaced with one made of quartz. The indicated mole fractions of  $\text{SO}_3$  along the flame axis are shown in Fig. 2.

After making a measurement, brown, orange, black, and yellow deposits were observed over 60 mm of the inside wall at the tip of the quartz sampling tube. Most of the deposit was soluble in 0.05 M  $\text{H}_2\text{SO}_4(\text{aq})$ . If this deposit contains vanadium it may catalyze the oxidation of  $\text{SO}_2$  to  $\text{SO}_3$ . Even though the composition and physical properties of the probe deposit have not been determined, the available information can be used to place some approximate limits on the change in  $\text{SO}_3$  content of the gas during sampling. Kinetic studies of related systems have been reviewed by Urbanek and Trela (1980), although most of this work has been conducted at relatively high  $\text{SO}_2$  and  $\text{O}_2$  (order of 10 mol%) and in the temperature range (650 to 850 K) over which conversion of  $\text{SO}_2$  to  $\text{SO}_3$  is greatest in flow reactors. The portion of the sampling tube coated with deposit was treated as a one-dimensional tubular reactor with catalytic wall. The wall temperature was assumed to decrease linearly from a value equal to the gas temperature at the probe tip to the melting point of  $\text{V}_2\text{O}_5$  (943 K) at the end of the deposit. The sample enters the quartz tube at high temperature and with  $\text{SO}_3$  at greater than equilibrium concentration. Conversion near the tube entrance was assumed to be controlled by boundary layer diffusion of  $\text{SO}_3$  to and from the deposit surface, where  $\text{SO}_3$  is in equilibrium with excess amounts of  $\text{SO}_2$  and  $\text{O}_2$ . The composition of the bulk gas then shifts until it is equal to the equilibrium composition at the deposit. When the entering gas is at 1625 K and contains 10 mol ppm  $\text{SO}_3$ , 1250 mol ppm  $\text{SO}_2$ , and 1 mol%  $\text{O}_2$ , this occurs at a distance of 20 mm into the probe, at which point the mole fraction of  $\text{SO}_3$  has decreased to 7 mol ppm. Production of  $\text{SO}_3$  from this point onward is assumed to be kinetically controlled, with a rate proportional to the deposit geometric surface area. The mechanism of Mars and Maessen (1968) was used with activity per unit area estimated from the total areas and effectiveness factors reported by Livbjerg and Villadsen (1972). This calculation resulted in  $\text{SO}_3$  equal to 27 mol ppm at a distance of 60 mm from the tube entrance. Therefore, in the event that the deposit has an activity comparable with that of an industrial alkali-promoted vanadium catalyst whose kinetic parameters are the same at 1400 K as at 800 K,  $\text{SO}_3$  could be altered by the sampling procedure. Inspection of the  $\text{SO}_3$  profiles shows that amounts of about 10 mol ppm were observed in 6 of the 9 runs under the conditions of the above calculation ( $z = 3$  to 4 m). This indicates that the greatest errors would have occurred if  $\text{SO}_3$  in the entering gas had actually been near equilibrium, with most of the observed  $\text{SO}_3$  produced in the probe. Based on these observations the limits of error in the measurements are tentatively estimated to be plus 100% and minus 50% of the indicated values. Further study of this problem is warranted, not only by its importance to the sampling technique, but because the situation is analogous to that encountered in the convective section of a boiler, where vanadium and alkali metal tube deposits catalyze the oxidation of  $\text{SO}_2$  as the flue gas is cooled.

#### CALCULATIONS

Notwithstanding the uncertainty in the accuracy of the  $\text{SO}_3$  measurements, it is worthwhile to compare the observations with calculations based on a simple set of assumptions. The objective is to determine if  $\text{SO}_3$  in the furnace exit gas of a

utility boiler might be correlated with flame characteristics which are known or can be estimated, such as fuel sulfur content, peak flame temperature, furnace exit gas temperature, excess air, and carbon monoxide.

A set of reactions which might account for the behavior of  $\text{SO}_3$  in the present system is (Kramlich, Malte, and Grosshandler, 1981):



The rate coefficient for Reaction 1 is given by Troe (1978); that for Reaction 2 by Smith, Wang, Tseregounis, and Westbrook (1982). The reverse of Reaction 2 has a negligible rate under the conditions of interest here. Reaction 3 is neglected in the present calculation, although Kramlich et al. provide evidence that it is important in lean hydrocarbon combustion. The concentration of third bodies, M, is taken equal to the total gas concentration, C (but see Kramlich et al., 1981). The net rate of  $\text{SO}_3$  production, apparently quite small over much of the region of the measurements, is then:

$$r_{\text{SO}_3} = k_1 C_{\text{SO}_2} C_{\text{O}} C - k_{-1} C_{\text{SO}_3} C - k_2 C_{\text{SO}_3} C_{\text{O}} \approx 0 \quad 4)$$

$$\frac{C_{\text{SO}_3}}{C_{\text{SO}_2}} = \frac{x_{\text{SO}_3}}{x_{\text{SO}_2}} \approx \frac{k_1 C_{\text{O}} C}{k_{-1} C + k_2 C_{\text{O}}} \quad 5)$$

Under the above assumptions the ratio of  $\text{SO}_3$  to  $\text{SO}_2$  is limited to the range

$$K_1 C_{\text{O},\text{eq}} \leq \frac{x_{\text{SO}_3}}{x_{\text{SO}_2}} \leq \frac{k_1}{k_2} C \quad 6)$$

as long as the system is not frozen. The total equilibrium mole fractions of  $\text{SO}_3$ , shown as dashed lines in Fig. 2, are everywhere less than the measured values, which are, in turn, much less than the right hand side of Equation 6, especially near the furnace exit. In order to apply Equation 5 we require an estimate of the oxygen atom concentration. In discussing this same problem Merryman and Levy (1979) suggested that an estimate of the oxygen atom concentration might be obtained by assuming equilibration of the principal reactions by which they are formed during CO oxidation:



$$C_0 = \frac{K_4 C_{CO} C_{O_2}}{C_{CO_2}} \quad 7)$$

The mole fractions of  $O_2$ ,  $CO_2$ , and  $SO_2$  were taken constant and equal to the outlet values, given in Table 2. Sulfur trioxide mole fractions calculated using Equations 1, 3, 5, and 7 are shown as solid lines in Fig. 2.

The calculated profiles satisfactorily reproduce the magnitude of the  $SO_3$  measurements near a mean residence time of 1 s ( $z = 2.9$  m) in most of the lower excess  $O_2$  (1 mol%) cases. Large discrepancies are observed in two instances (Runs 212 and 213); these are distinguished by low temperature (212), high levels of CO (213), and high excess  $O_2$  (both). The calculated values are especially sensitive to temperature. Most important is the fact that the calculation predicts  $SO_3$  increasing with distance near the furnace outlet, while most of the measurements show a tendency of  $SO_3$  to approach equilibrium. The assumption of equilibration of Reaction 4 was not originally intended by Merryman and Levy (1979) to be applied at points so far into the postflame region, but at shorter times. As the rate of CO oxidation slows, due to CO consumption and decreasing temperature, Equation 7 becomes a progressively poorer approximation. The CO mole fractions at  $z = 3.1$  m are in the range 320 to 950 ppm, no longer sufficient to maintain significant super-equilibrium concentration of oxygen atoms against competition with recombination, for example, by Reactions 1 and 2 themselves. Because the calculation is least reliable near the furnace exit, it would be unwise to use this approximation to estimate  $SO_3$  in furnace exit gas. The steady state approach (Equation 5) might still be useful however, if the decay of oxygen atoms at long times can be related to CO and stable species concentrations.

#### SUMMARY

Mole fractions of sulfur trioxide were measured along the axis of a confined turbulent diffusion flame, under conditions simulating those in electric utility boilers. The fuel was a No. 6 residual oil containing 2.2 wt% sulfur, fired at the rate of 0.05 kg/s or 2 MW(thermal). The sulfur trioxide mole fractions were in the range from 3 to 25 mol ppm; representing 0.2 to 2% of the total sulfur. An estimate was made of the contribution of catalytic  $SO_3$  formation by ash constituents deposited in the probe. The uncertainty introduced from this source was estimated to be plus 100% and minus 50% of the indicated value. The observed mole fractions were approximately steady and everywhere greater than the local total equilibrium values. Sulfur trioxide mole fractions were calculated by assuming that the steady state is determined by atomic oxygen reactions, with atomic oxygen in partial equilibrium with carbon monoxide, carbon dioxide, and molecular oxygen. The results of this calculation approximately reproduced the experimental measurements under most, but not all, sets of conditions investigated. Because of its sensitivity to temperature, carbon monoxide, and oxygen this approximation is not recommended for the estimation of  $SO_3$  in furnace exit gases.

#### ACKNOWLEDGEMENTS

We thank Bonnie Caputo of the MIT Energy Laboratory for the layout and typing of the drafts and final manuscript. This work is supported by Babcock and Wilcox Canada, Canadian Electrical Association, Electric Power Research Institute, Empire State Electric Energy Research Corp., Florida Power and Light Co., Northeast Utilities Service Co., and Shell Development Co.

## NOMENCLATURE

|          |   |
|----------|---|
| C        | total gas concentration, $\text{kmol/m}^3$  |
| $C_i$    | concentration of gaseous species i, $\text{kmol/m}^3$                               |
| $k_j$    | rate coefficient of Reaction j in forward direction, various units                  |
| $k_{-j}$ | rate coefficient of Reaction j in reverse direction, various units                  |
| $K_j$    | equilibrium constant for reaction j, $= k_j/k_{-j}$                                 |
| $r_i$    | net rate of production of species i by chemical reaction, $\text{kmol/m}^3\text{s}$ |
| Sw       | combustion air Swirl Number   |
| T        | temperature, K  |
| u        | axial component of gas velocity, m/s  |
| $X_i$    | mole fraction of species i  |
| z        | axial distance from the combustion air nozzle, m                                    |
| $\alpha$ | mean temperature gradient along the flame axis, Equation 1, K/m                     |
| B        | gas velocity decay constant, Equation 2, $\text{m}^2/\text{s}$                      |
| $\gamma$ | carbon monoxide decay constant, Equation 3, $\text{m}^{-1}$                         |

## Subscripts

|    |  |
|----|--|
| o  | evaluated at $z = z_o = 0.95 \text{ m}$ from the combustion air nozzle |
| eq | total equilibrium concentration  |

## REFERENCES

- J.M. Beér, M.T. Jacques, W. Farmayan, and B.R. Taylor, Eighteenth Symposium (International) on Combustion, The Combustion Institute, Pittsburgh, PA, 1981, p. 101.
- H.A. Blum, B. Lees, and L.K. Rendle, J. Inst. Fuel 32(1959)165.
- R. Conolly and P.H. Kelsell, J. Inst. Energy 55(1982)47.
- A.T.S. Cunningham and P.J. Jackson, J. Inst. Fuel 51(1978)20.
- W.D. Halstead and J.R.W. Talbot, J. Inst. Energy 53(1980)142.
- Y. Harada, S. Naito, T. Tsuchiya, and Y. Nakajima, Problems of Low Grade Oil Firing Boilers and their Solutions, Mitsubishi Technical Review 18(1981)85.
- P.J. Jackson, O.A. Hilton, and J.H. Buddery, J. Inst. Energy 54(1981)124.
- J.C. Kramlich, P.C. Malte, and W.L. Grosshandler, Eighteenth Symposium (International) on Combustion, The Combustion Institute, Pittsburgh, PA, 1981, p. 151.
- H. Livbjerg and J. Villadsen, Chem. Eng. Sci. 27(1972)21.
- E.L. Merryman and A. Levy, Seventeenth Symposium (International) on Combustion, The Combustion Institute, Pittsburgh PA, 1979, p. 727.
- P. Mars and J.G.H. Maessen, J. Catal. 10(1968)1.

C.H. Muller III, K. Schofield, M. Steinberg, and H.P. Broida, Seventeenth Symposium (International) on Combustion, The Combustion Institute, Pittsburgh, PA, 1979, p. 867.

H. Reidick and R. Reifenhäuser, Combustion, Feb. 1980, p. 17.

O.I. Smith, S.-N. Wang, S. Tseregounis, and C.K. Westbrook, Combustion Science and Technology 30(1983)241.

R.T. Squires, J. Inst. Energy 55(1982)41.

J. Troe, Ann. Rev. Phys. Chem. 29(1978)223.

A. Urbanek and M. Trela, Catal. Rev. Sci. Eng. 21(1980)73.

J.O.L. Wendt, E.C. Wootan, and T.L. Corley, Combustion and Flame 49(1983)261.

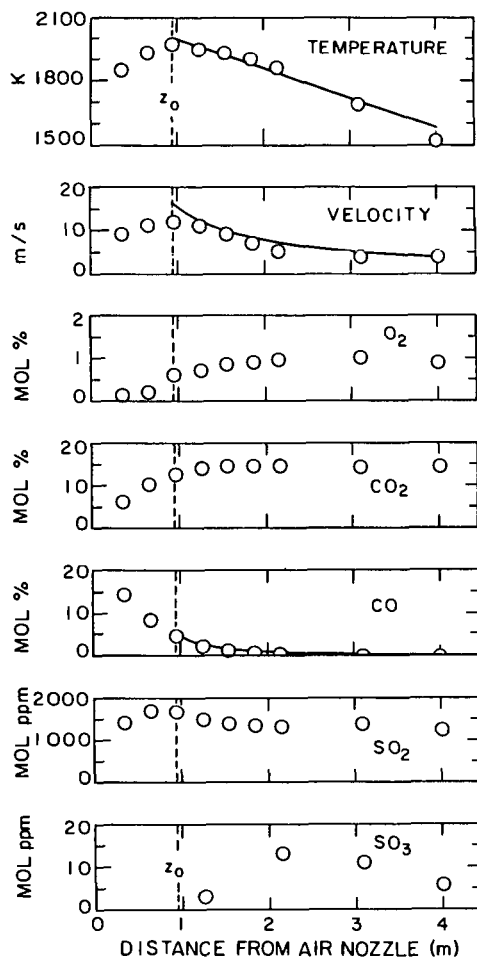


Figure 1. Measurements of gas temperature, axial component of gas velocity, and mole fractions (dry basis) of  $O_2$ ,  $CO_2$ ,  $CO$ ,  $SO_2$ , and  $SO_3$  along the axis of a 2 MW residual oil spray flame. Run No. 214, combustion air Swirl No. = 0.5. The location of the peak flame temperature,  $z = 0.95$  m, is taken as the starting point for calculations. Solid lines are fits of Equations 1, 2, and 3 to the data points.



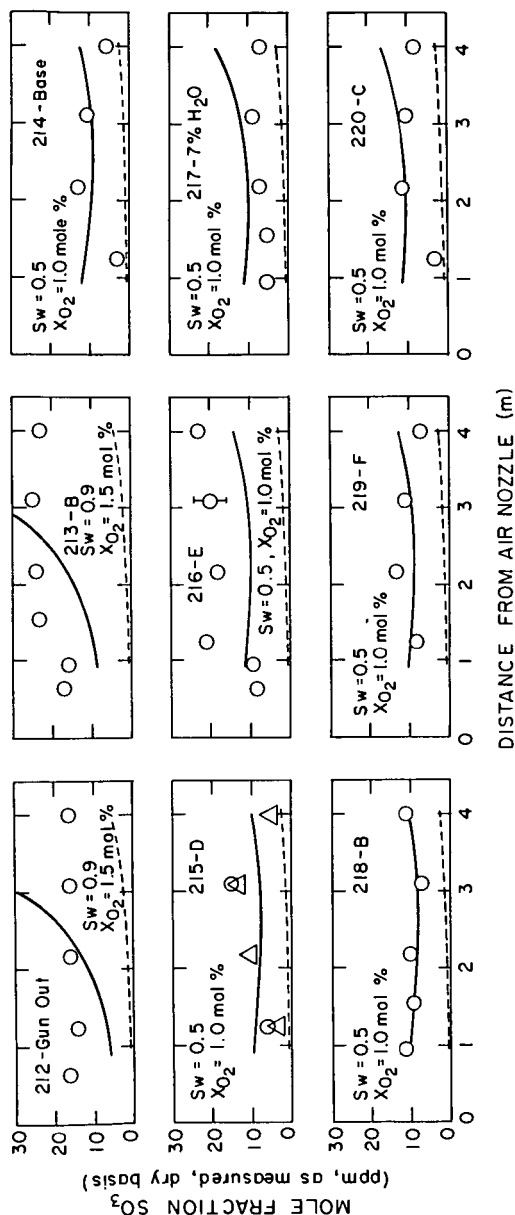


Figure 2. Mole fractions (dry basis) of  $SO_3$  measured along the flame axis and comparison with calculations. The combustion air Swirl No. and flue gas  $O_2$  mole fraction (dry) are indicated in each figure. A distinguishing feature of each run is indicated after the run number. The letters B to F correspond to various fuel additives designed to promote carbon burnout.

Circles: measured value

Triangles: duplicate measurements in separate trial

Dashed line: calculated, total equilibrium

Solid line: calculated, steady state, with oxygen atoms in partial equilibrium with  $CO$ ,  $CO_2$ , and  $O_2$ .

## RAMAN STUDIES OF HALON FIRE RETARDANTS.

J. H. May, F. S. Allen, M. R. Ondrias, R. E. Tapscott,  
H. D. Beeson, and D. M. Zallen.

Chemistry Department, and New Mexico Engineering Research Institute,  
University of New Mexico, Albuquerque, New Mexico 87131.

Raman spectroscopy can be used as a passive probe for the study of active systems. Various types of analytical determinations can be made without perturbing the system under study. Of interest is the elucidation of the extinction processes employed by Halon type extinguishing agents. Raman has in the past been used to study molecules such as  $H_2O$ ,  $N_2$ , and  $CO_2$  in flames (1). Halons and pyrolyzed products, having vibrations that are more polarization sensitive than the above molecules, should then be readily analyzed in flames. As an initial approach to this problem we are studying the pyrolysis of Halon 2402 (1,2 dibromotetrafluoroethane). The pyrolysis products are isolated using vacuum line techniques, and identified using GC/MS and Raman. A library of the Raman spectra from each component is being formed for subsequent use in flame analysis.

Experimentally, we use a tube furnace with a specially designed tube, having detachable nitrogen traps on each end, and also capable of holding a vacuum. To simulate the combustion process, Halon 2402 is frozen in one of the nitrogen traps, and the whole system is brought to high vacuum. The Halon is then allowed to vacuum transfer through the pyrolysis tube, which is at approximately  $790^\circ C$ , to the other nitrogen trap. This process is repeated several times. The products are then vacuum distilled, capturing fractions as they come over, in different, sealable cuvettes. Presently all fractions are studied in the gas phase at room temperature.

The Raman data are collected on an instrument made up of:

1) An EG&G Princeton Applied Research model 1420 intensified silicon photodiode array tube coupled with its model 1218 solid state detector controller, and the model 1215 computer console.

2) A SPEX model 1877 triplemate monochromator.

3) A Coherent model CR-4 Argon ion laser, capable of producing over 3 watts of continuous wave power at the 488.0 nm. line.

Spectra, in the range of  $100\text{ cm}^{-1}$  to  $1000\text{ cm}^{-1}$  can be obtained at a single setting of the monochromator. Since Raman spectra of many of the thermal degradation products are not available, we have used a Finnigan, series 4900, GC/MS to identify the products that are obtained from the pyrolysis experiment. Raman spectra collected on these components will subsequently form a spectral library of the pyrolysis products.

Figures 1. and 2. are the Raman spectra of the first fraction collected from the vacuum distillation process on the pyrolyzed 2402. The complexity of the spectra suggests that more than one component is present. The GC/MS revealed that the gas contained only tetrafluoroethylene, and bromotrifluoromethane (Halon 1301) in significant concentrations. Figures 3. and 4. are the Raman spectra of pure 1301, and it is evident that its spectral bands match many of the bands in the distilled fraction.

Pure tetrafluoroethylene will be examined to identify its spectral contribution to pyrolysis products spectra. The vacuum distillation was done at 500 millitorr, later distillations using higher pressures should provide better separation of the fractions.

Each of these spectra took thirty minutes to collect, fifteen minutes for the signal spectra, and another fifteen for the background ( Raman spectra normally require the subtraction of the background spectra, taken with the excitation source off, from the signal spectra. This is especially true for photodiode array detectors.). Accurate spectra, to within 2 cm(-1), of all but the weaker bands can be taken in a minute or less if desired ( This includes background spectra.). Using pulsed, or higher intensity C.W. lasers, spectra could be taken in less time with even better signal to noise ratios.

As a result of these preliminary studies, we will build a library of Raman spectra for the stable products produced by the simulated combustion of the Halon 2402 in a vacuum, as well as in oxidizing and reducing environments. This library will then be used in subsequent studies to identify which of the products are present in flames near extinction due to the presence of Halon 2402.

#### REFERENCE.

1. Lapp, M. and Penny, C. M. . Laser Raman Gas Diagnostics. Plenum Press, New York and London. 1974.

ACKNOWLEDGMENTS: Partial support for this project provided by the Air Force Engineering Services Center, Tyndall A.F.B., Fl. We would like also to acknowledge Mr. Joseph L. Walker for fruitful discussions.

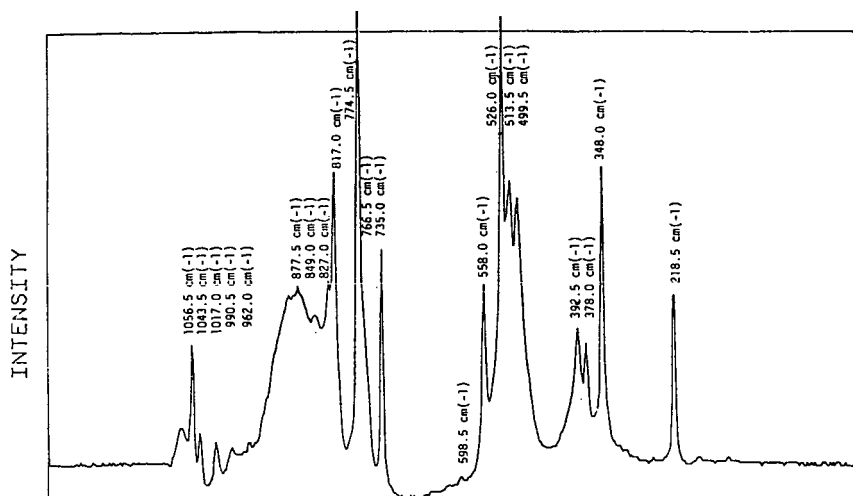


Figure 1. Raman spectrum of the first fraction collected from the vacuum distillation process, for the products of the pyrolyzed Halon 2402.

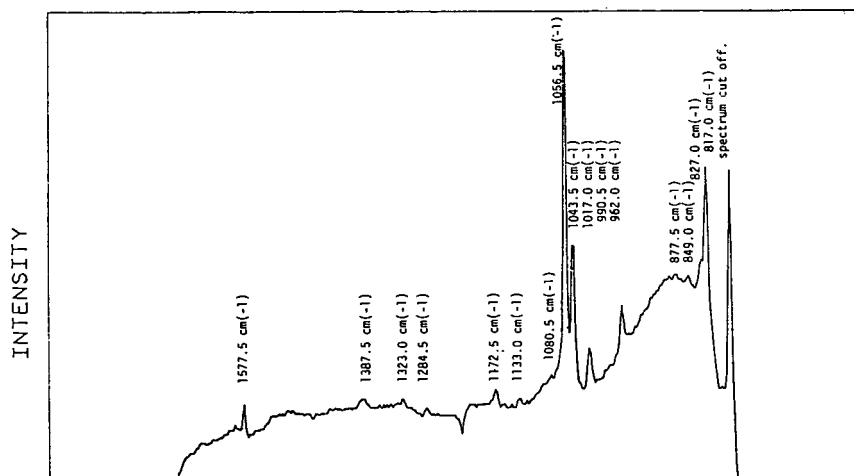


Figure 2. Raman spectrum of the first fraction collected from the vacuum distillation process, for the products of the pyrolyzed Halon 2402. Y axis has been expanded.

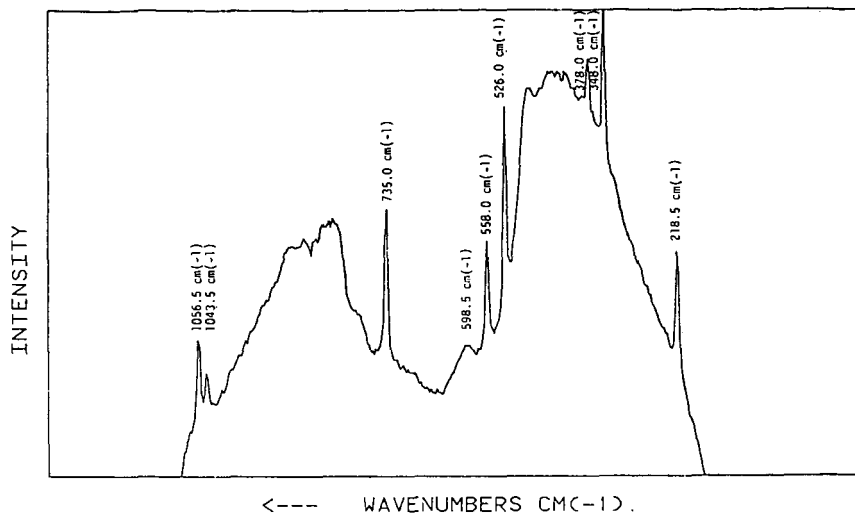


Figure 3. Raman spectrum of pure Halon 1301 ( Bromotetrafluoromethane ).

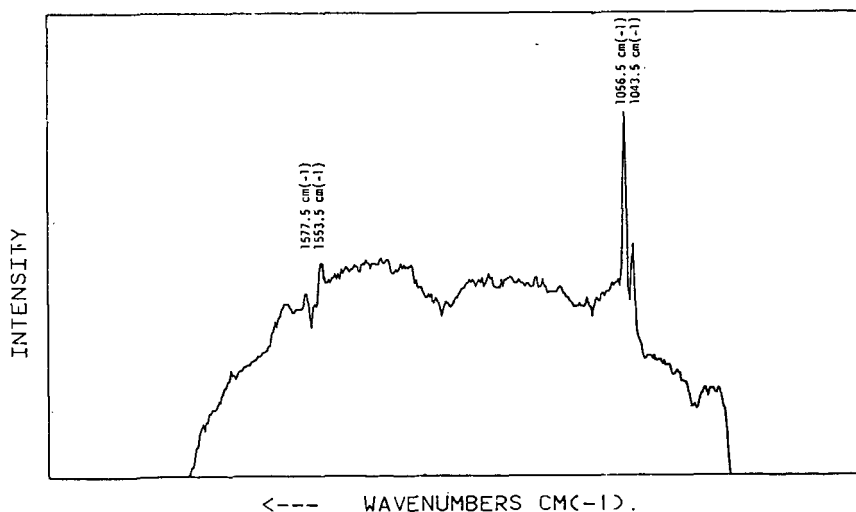


Figure 4. Raman spectrum of pure Halon 1301 ( Bromotetrafluoromethane ). Y axis has been expanded.

SEPARATION AND ANALYSIS OF HYDROXYAROMATIC SPECIES IN LIQUID  
FUELS II. COMPARISON OF ArOH IN SRC-II COAL LIQUID,  
WILMINGTON, CA, PETROLEUM AND OSCR SHALE OIL

J. B. Green, C. A. Treese, S. K-T Yu, J. S. Thomson,  
C. P. Renaudo, and B. K. Stierwalt

Department of Fuels Research  
National Institute for Petroleum and Energy Research  
Division of IIT Research Institute  
P.O. Box 2128  
Bartlesville, OK 74005

INTRODUCTION

Part I of this series, presented in the symposium, "New Applications of Analytical Techniques to Fossil Fuels," describes a general analytical approach for detailed analysis of hydroxyaromatics (ArOH) in fuels (1). An inherent step in development of analytical methods is evaluation of their performance on actual samples. Thus, ArOH concentrates were isolated from a wide spectrum of fuels, chemically derivatized, and analyzed in detail by GC/MS. Results from three of the fuels studied during development of the analytical method are presented here to 1) demonstrate the viability of the analytical methodology and more importantly to 2) contrast the levels and types of ArOH in three distinctly different fuel types: petroleum, shale oil, and liquified coal.

Although numerous compositional studies on one or more fuels of a given type have been published, papers comparing composition of different types of fuels are quite rare. Tomkins and Ho (2) compared levels of selected polycyclic aromatic amines in coal liquids, shale oil and petroleum, and Allen, *et al.* (3), compared overall structural profiles of heavy fractions from a coal liquid, shale oil, petroleum and tar sand. A comparison of the levels of phenol, and C<sub>1</sub>- and C<sub>2</sub>-phenols in a shale oil and a coal liquid has also been published (4). These three papers are a fairly complete listing of published reports comparing different fuel types.

Prior work on ArOH in individual fuel types has shown coal liquids to contain phenols, indanols/tetralinols, hydroxybiphenyls/hydroxyacenaphthalenes, hydroxyfluorenes, and naphthylphenols (5,6). A study on coal tar cited similar compounds plus dibenzofuranols and pyrenols/fluoranthenols (7). White and Li (8) identified over 20 specific ArOH compounds ranging from 6 to 15 carbons in an SRC-II coal liquid. McClennen, *et al.* (9), studied changes in phenol and indanol distributions induced by hydrotreating, and Scheppele, *et al.* (10), studied ArOH and multihydroxylated aromatics in raw and hydrogenated anthracene oil. Recently, hydroxylated thiophenic compounds and nitrogen heterocycles have also been identified in coal liquids (11,12). Finally, ArOH in coal liquid oils, asphaltenes, and preasphaltenes have been compared (13); the hexane-insoluble fractions contain higher levels of ArOH and generally more polycyclic ArOH.

Shale oil contains mostly phenols, with lesser amounts of naphthols and trace levels of higher-ring ArOH (14-17). Dihydroxyaromatics are also present (16,17).

Petroleum ArOH cover a wide range of structural types and molecular weights from phenol up to highly substituted polycyclic ArOH (18-21). ArOH usually make up less than 10% of the total acidic compound types in petroleum, whereas they are the dominant acidic class in coal liquids and shale oil.

#### EXPERIMENTAL

Fuels selected for this work were an SRC-II coal liquid from the Fort Lewis pilot plant run 77SR-12 (22,23), an *in situ* produced shale oil, OSCR 76-552, kindly supplied by the Western Research Institute, Laramie, WY, and a Wilmington, CA, petroleum which underwent extensive study during the API-60 project (18,19,24).

The analytical methodology for isolation and analysis of ArOH is described in a separate preprint (1). The results presented here are a composite of the GC/MS analysis of underivatized, silylated and acylated ArOH concentrates; although, as previously explained (1), analysis of acylated ArOH usually gave the most comprehensive data set.

#### RESULTS AND DISCUSSION

Only qualitative or semiquantitative results are presented, since the relative GC/MS responses of various derivatized ArOH are unknown. The general format for presentation of data is based on the commonly used Z-number convention, where the Z-number of a given ArOH series is defined by its empirical formula:  $C_nH_{2n+2}O$ . Although the ArOH were analyzed as either acylated or silylated derivatives, all the tables report ArOH composition on an underivatized basis.

Table 1 shows results from the distillation and liquid chromatographic separations to obtain whole acid and ArOH concentrates. The relative abundance of ArOH is coal liquid > shale oil >> petroleum, as expected. Also, the percentage of total acids attributed to ArOH is greatest in the coal liquid and least in the petroleum.

Tables 2(A-I) show the number of isomers separated and detected by GC/MS at each carbon number of the major ArOH Z-series for the three fuels. If a given distillate contained no members of a given series, it is omitted from that section of Table 2.

Results for the Wilmington 370-535° C ArOH are not included in Table 2. Current GC/MS profiles of this fraction do not show sufficient chromatographic resolution to obtain more than a superficial analysis of ArOH present. Acylation did decrease the retention of ArOH present, as expected, but did not improve chromatographic resolution enough for detailed analysis. The few peaks which were resolved corresponded to Z-series ranging from -16 0 to -24 0. Fragment ions from these series do not correspond with those present in synfuel ArOH--probably because the Wilmington ArOH are primarily less condensed structures with naphthene rings attached to 1- and 2-ring aromatic nuclei.

Table 3 compares the overall composition of ArOH in the three fuels. All three fuels contain phenols, indanols/tetralinols and members of the -14 O and -16 O series of ArOH. The major differences between the fuels lie in the relative abundances of these series and in the individual structures of ArOH in these and the other series present. These differences are discussed below for each ArOH series.

#### -6 O

The coal liquid contains the largest overall abundance of phenols as seen by the large proportion (10.3% of the whole oil) of ArOH in the 200-325° C distillate (Table 1) and by the fact that they are the major ArOH type in that distillate (Table 3). The coal liquid GC/MS profile showed large peaks corresponding to individual C<sub>2</sub>-C<sub>4</sub> phenol isomers, which in total probably accounted for nearly half of the ArOH present. C<sub>5</sub>- and C<sub>6</sub>-phenols were relatively minor components in the coal liquid and no C<sub>7</sub>- or higher homologs were detected.

The distribution of phenolic homologs in the Wilmington petroleum was similar to that of the coal liquid (Table 2A). However, their overall abundance was lower by about three orders of magnitude, as estimated by the total ArOH present (225-370° C ArOH were 0.03% of the whole crude, Table 1) and the intensity of phenolic GC/MS peaks observed.

On the other hand, the distribution of phenols in the shale oil was markedly different than the other fuels. Species with a total alkyl carbon number up to C<sub>17</sub> were observed, and mass spectral fragmentation patterns indicated predominantly straight-chain alkyl substituents or substituents with one or two methyl-branches. In total, phenolic species probably accounted for two-thirds of the shale oil ArOH.

#### -8 O

Indanols/tetralinols were present in all fuels, but were not a dominant series in any fuel. Their abundance was highest in the coal liquid, since they were the second most prevalent type in the 200-325° C ArOH concentrate which comprised 10.3% of the whole SRC-II oil. Based on mass spectral fragmentation patterns (1), indanols dominated tetralinols in all fuels. The pre-dominance of indanols over tetralinols has been reported previously (5,9). Due to the relatively low amounts of naphthols observed in all fuels, especially the coal liquid, it seems likely that this series may be largely derived from hydrogenation of naphthols during coal liquifaction, shale retorting and petroleum maturation processes.

#### -10 O

This series was not conclusively identified in any fuel. McClennen, *et al.* (9), alluded to the presence of hydroxytetrahydroacenaphthalenes in their study of coal liquid ArOH, and the authors have tentatively identified a -10 O ArOH series of compounds in a marine diesel fuel. Overall, -10 O ArOH compounds appear to be present at low levels or nonexistent in most fuels.



#### -12 O

Naphthols were positively identified in the petroleum and shale oil ArOH concentrates, but they were not major components in either fuel. Based on the intensity of the GC/MS peaks and overall amount of ArOH present, naphthols comprised a much more significant percentage of the shale oil than any other fuel. Minor amounts of a higher molecular weight -12 O series, corresponding to tricycloalkylphenols, have tentatively been identified in the SRC-II >325° C ArOH concentrate.

#### -14 O

Compounds in this series were quite prevalent in the coal liquid and petroleum, but relatively minor in the shale oil. As discussed earlier (1), distinguishing between the various isomers of this series on the basis of mass spectral fragmentation patterns is quite difficult. Possible structures include hydroxybiphenyls, hydroxyacenaphthalenes, benzindanols and benztetralinols. Taking into account the uncertainties in mass spectral interpretation, the petroleum and coal liquid are nevertheless believed to contain all of the possible -14 O isomers, with hydroxybiphenyls being the dominant species. Figure 1A shows evidence for presence of benztetralinols in the Wilmington petroleum ArOH concentrate. Thus, one or both of the acylated parent (M+) -14 O species, represented by ions at m/e 364 and 350, give rise via loss of 42 or 28 mass units respectively to the fragment ion at m/e 322. Although it is possible that the m/e 322 ion is a parent (M+) ion resulting from some abnormally high-boiling -14 O isomer, its production via retro-Diels-Alder loss of propylene or ethylene is much more likely. This fragmentation behavior is characteristic of cyclohexylaromatic systems (25), and thus indicates a benztetralinol structure. The intense ion at m/e 225 in Figure 1A occurs from loss of  $\text{CF}_3\text{C}(\text{O})^+$  from the m/e 322 ion; the ion at m/e 344 is a molecular ion from a coeluting -20 O species. Also, this and other spectra in Figure 1 indicate the complexity of spectra from later eluting GC/MS peaks.

#### -16 O

In the coal liquid and shale oil, this series consists largely of hydroxyfluorenes. In the petroleum, the major structural types are probably phenylindanols/phenyltetralinols. Next to -14 O compounds, -16 O compounds were the second most prevalent type in the SRC-II >325° C ArOH. On the other hand, the -16 O series was a very minor one in the shale oil, and intermediate in the petroleum. The -16 O series was the most condensed ArOH species found in shale oil.

Besides hydroxyfluorenes, the coal liquid contains -16 O compounds which produce retro-Diels-Alder fragmentation patterns similar to those discussed for -14 O compounds. Figure 1B shows an example where the parent (M+) ion at m/e 334 gives rise to a 306 fragment. This pattern is consistent with either a phenyltetralinol or dicycloalkynaphthol (e.g., hexahydropyrenol) structure.

#### -18 0

Only the >325° C coal liquid ArOH concentrate showed easily detectable amounts of this series. Based on its mass range (Table 2F) and the prevalence of phenanthrenes/anthracenes in coal liquids, this series is believed to be hydroxylated phenanthrenes/anthracenes.

#### -20 0

This series was found in both the coal liquid and petroleum, but was more prevalent in the coal liquid. Possible structures include phenylnaphthols, cycloalkylphenanthrols and dihydropyrenols. Figures 1 (D-F) show example acylated -20 0 series spectra representing the different types present in the coal liquid >325° C residue. Figure 1D shows a fragmentation pattern most likely produced from a C<sub>1</sub>-phenylnaphthol. The relatively large M-69 ion (m/e 261) from loss of CF<sub>3</sub> is also exhibited by hydroxybiphenyls--which would be expected to give spectra analogous to phenylnaphthols. Biphenyls also show a pronounced tendency to form another carbon-carbon bridging bond yielding a m/e 152 ion (26); analogous behavior by phenylnaphthols would yield fluoranthene. Thus, the m/e 218 ion in figure 1D should have a structure analogous to an oxyfluoranthene, and the m/e 202 ion a structure similar to fluoranthene itself.

Figure 1E shows a fragment corresponding to loss of 28 (C<sub>2</sub>H<sub>4</sub>) from the parent ion at m/e 358. This pattern is typical of a C<sub>1</sub>-cyclohexylphenanthrol compound type. No M-69 ion is apparent, but the M-97 (m/e 233) fragment is fairly intense.

Figure 1F shows a large parent ion (m/e 330) relative to fragment ions as well as a long GC retention time relative to its molecular weight. For example, the retention of the compound of equal mass in Figure 1D was only 22.5 min, and the retention of the compound 28 mass units heavier in Figure 1E was only 0.3 min longer than that in Figure 1F. These facts all point to a highly condensed species such as C<sub>1</sub>-dihydropyrenol. A dihydropyrene species would be expected to form pyrene (m/e 202) during fragmentation (25), as observed in Figure 1F. Also, Figure 1F correlates closely with Figure 1C, which is believed to be a pyrenol. Both figures show a fragment at m/e 189 corresponding to loss of CO from the m/e 217 fragment. Phenol shows this same fragmentation pattern (27); thus a 1- or 2-pyrenol structure is the most logical for Figure 1C, and a 1- or 2-hydroxy-4,5-dihydromethylpyrene structure is the best choice for Figure 1F. For example, 4-hydroxypyrene or 9-hydroxy-4,5-dihydropyrene would not be expected to give rise to a fragmentation pattern promoting loss of CO to form a cyclopentadienyl-type cation.

Structures for -20 0 ArOH in the petroleum could not be defined as well as those from the coal liquid because of coelution of -14 0 and -16 0 compounds which complicated the resulting spectra.

#### -22 0, -24 0

As discussed previously, the coal liquid contained -22 0 compounds believed to be pyrenols. The possibility of other types of ArOH in this series could not be definitely confirmed or ruled out. -24 0 Species in the coal liquid appear to be cycloalkylpyrenols rather than chrysenols or some

other condensed species based on the mass range observed. Again, because of the complexity of the petroleum ArOH spectra, no definite structures for -22 O species were assigned. Based on the mass range of -22 O ArOH in the petroleum, loosely condensed structures such as naphthylindanol, naphthyltritalinols or hydroxytriphenyls seem the most probable.

#### Non-ArOH species

In contrast to earlier reports citing no or only trace amounts of carboxylic acids in shale oil (14-17), a major series of aliphatic acids ranging from 5 to 27 carbons was observed here. From C<sub>14</sub> to C<sub>20</sub>, 2-3 isomers were observed at every carbon number; only one isomer was found at most of the other carbon numbers. Silylated fatty acids yielded characteristic fragment ions at m/e 117, 129, 132, 145, and M-15. During liquid chromatographic separation of the shale oil strong acid fraction, the retention region corresponding to carboxylic acids was not cut as a separate fraction but simply lumped into the ArOH fraction (1). Since previous work had not shown presence of significant amounts of carboxylic acids in shale oil and since their presence in the authors' sample could not be detected by the UV (280nm) detector employed for the HPLC separation, there was no apparent reason for cutting a separate carboxylic acid fraction. Based on total ion intensities of silylated carboxylic acids vs. silylated ArOH, carboxylic acids accounted for nearly 50% of the total "ArOH" concentrate. Thus, the result given in Table 1 for concentration of ArOH in shale oil may be high by a factor of two. Figure 2 shows GC/MS total ion chromatograms for underivatized, acylated and silylated shale oil ArOH concentrate. The later eluting, evenly spaced, peaks in the silylated (2C) sample are all aliphatic acids. Since underivatized carboxylic acids chromatograph poorly, they are not evident in the underivatized or acylated samples. The shale oil investigated in this work was retorted *in situ*; carboxylic acids present in oil shale (28) apparently survived temperatures reached during that type of oil recovery process.

Small amounts of nitrogen compounds (1) and carboxylic acids were present in petroleum ArOH concentrates, largely from chromatographic overlap usually encountered in liquid chromatographic separations. Coal liquid ArOH concentrates were virtually free of non-ArOH compounds.

#### CONCLUSIONS

The two most distinguishing features of coal liquid ArOH are their high concentration in the whole oil and presence of condensed ring species such as pyrenols and partially hydrogenated pyrenols. Shale oil ArOH are predominantly phenols, some which possess alkyl side chains up to nearly 20 carbons. Petroleum contains relatively low amounts of ArOH but has the greatest diversity of types and isomers present.

The methodology used for analysis of ArOH generally performed well on the wide range of samples examined, except in the case of the 370-535° C petroleum ArOH concentrate. Further improvements including more liquid chromatographic separations, higher resolution GC columns, etc., will be needed for analysis of that sample or one of similar complexity.

#### ACKNOWLEDGEMENT

The financial support of the U.S. Department of Energy and industrial co-sponsors under Cooperative Agreement DE-FC01-83FE60149 is greatly appreciated.

#### REFERENCES

1. Green, J. B., J. S. Thomson, S. K-T Yu, C. A. Treese, B. K. Stierwalt, and C. P. Renaudo, Amer. Chem. Soc., Div. Fuel Chem. Prepr., 31, Spring 1986.
2. Tomkins, B. A., and C-h. Ho, Anal. Chem., 54, (1982) 91.
3. Allen, D. T., D. W. Grandy, K.-M. Jeong, and L. Petrakis, Ind. Eng. Chem. Process Des. Dev., 24 (1985) 737.
4. Guenther, F. R., R. M. Parris, S. N. Chesler, and L. R. Hilpert, J. Chromatogr., 207 (1981) 256.
5. Later, D. W., M. L. Lee, K. D. Bartle, R. C. Kong and D. L. Vassellaros, Anal. Chem., 53 (1981) 1612.
6. Schweighardt, F. K., C. M. White, S. Friedman, and J. S. Shultz in "Organic Chemistry of Coal", J. W. Larsen (Ed.), American Chemical Society, Wash. D.C., 1978, pp. 240-257.
7. Novotny, M., J. W. Strand, S. L. Smith, D. Wiesler, and F. J. Schwende, Fuel, 60 (1981) 213.
8. White, C. M., and N. C. Li, Anal. Chem., 54 (1982) 1570.
9. McClennen, W. H., H. L. C. Meuzelarr, G. S. Metcalf, and G. R. Hill, Fuel, 62 (1983) 1422.
10. Scheppele, S. E., G. J. Greenwood, R. J. Pancirov, and T. R. Ashe in "Upgrading Coal Liquids", R. F. Sullivan (Ed.), American Chemical Society, Wash. D.C., 1981, pp. 39-74.
11. Nishioka, M., M. L. Lee, H. Kudo, D. R. Muchiri, L. J. Baldwin, S. Pakray, J. G. Stuart, and R. N. Castle, Anal. Chem., 57 (1985) 1327.
12. Nishioka, M., R. M. Campbell, M. L. Lee, D. R. Muchiri, J. G. Stuart, and R. N. Castle, Anal. Chem., 57 (1985) 2211.
13. Boduszynski, M. M., R. J. Hurtubise, and H. F. Silver, Fuel, 63 (1984) 93.
14. Regtop, R. A., P. T. Crisp, and J. Ellis, Fuel, 61 (1982) 185.
15. Bett, G., T. G. Harvey, T. W. Matheson, and K. C. Pratt, Fuel, 62 (1983) 1445.
16. Aczel, T., S. G. Colgrove, L. W. Dennis, and S. D. Reynolds, Amer. Chem. Soc., Div. Fuel Chem. Prepr., 30 (4) (1985) 122.

17. McKay, J. F., M. M. Boduszynski, and D. R. Latham, Liquid Fuels Technol., 1 (1983) 35.
18. McKay, J. F., T. E. Cogswell, J. W. Weber and D. R. Latham, Fuel, 54 (1975) 51.
19. McKay, J. F., D. R. Latham, and W. E. Haines, Fuel, 60 (1981) 27.
20. Snyder, L. R., B. E. Buell, and H. E. Howard, Anal. Chem., 40 (1968) 1303.
21. Snyder, L. R., Anal. Chem. 41 (1969) 1084.
22. Harrison, R. H., S. E. Scheppele, G. P. Sturm, Jr., and P. L. Grizzle, J. Chem. Eng. Data, 30 (1985) 183.
23. Green, J. B., P. L. Grizzle, J. S. Thomson, R. J. Hoff, and J. A. Green, Fuel, 64 (1985) 1581.
24. Hirsch, D. E., J. E. Dooley, H. J. Coleman, and C. J. Thomson, "Compound-Type Separation and Characterization Studies for a 370-535° C Distillate of Wilmington, Calif., Crude Oil," U.S. BuMines Rept. of Investigation, RI 7893, 1974.
25. Wozniak, T. J., and R. A. Hites, Anal. Chem., 57 (1985) 1314.
26. Elder, V. A., B. L. Proctor, and R. A. Hites, Environ. Sci. Technol., 15 (1981) 1237.
27. Budzikiewicz, H., C. Djerassi, and D. H. Williams, "Interpretation of Mass Spectra of Organic Compounds", Holden-Day, San Francisco, 1964, pp. 167-169.
28. Chong, S.-L., and J. F. McKay, Fuel, 63 (1984) 303.

TABLE 1. - Results from distillation and liquid chromatographic separations

| Fuel        | Distillate Boiling Range (°C) <sup>1</sup> | Distillate Yield (Wt%) | Total Acids (Wt%) |                  | A-OH (Wt%)                  |                  |                  |
|-------------|--|------------------------|-------------------|------------------|-----------------------------|------------------|------------------|
|             |  |                        | Distillates Basis | Whole Fuel Basis | Distillate Total Acid Basis | Distillate Basis | Whole Fuel Basis |
| Coal liquid | 200-325                                    | 66.3                   | 25.1              | 16.6             | 62                          | 15.5             | 10.3             |
|             | 325  | 16.0                   | 30.9              | 4.94             | 40.0                        | 12.4             | 1.98             |
| Shale oil   | >200                                       | 89.8                   | 16.3              | 14.6             | 34.3                        | 5.57             | 5.00             |
| Petroleum   | 225-370                                    | 25.2                   | 2.24              | 0.56             | 5.7                         | 0.13             | 0.03             |
|             | 370-535                                    | 24.7                   | 10.1              | 2.49             | 4                           | 0.4              | 0.1              |

<sup>1</sup> Phenol b.p. = 182° C, p-cresol b.p. = 202° C.

TABLE 2A. - Results for -6 0 series of ArOH ( $C_nH_{2n-6}O$ )<sup>1</sup>

| Fuel (Distillate Boiling Range, °C) |                  |                                |                     |                        |
|-------------------------------------|------------------|--------------------------------|---------------------|------------------------|
|                                     |                  | Coal Liquid<br>(200-325)       | Shale Oil<br>(>200) | Petroleum<br>(225-370) |
| $C_x$ <sup>2</sup>                  | Molecular Weight | Number of Isomers <sup>3</sup> |                     |                        |
| C <sub>0</sub>                      | 94               | 0                              | 1                   | 1                      |
| C <sub>1</sub>                      | 108              | 2                              | 3                   | 3                      |
| C <sub>2</sub>                      | 122              | 6                              | 6                   | 5                      |
| C <sub>3</sub>                      | 136              | 9                              | 11                  | 4                      |
| C <sub>4</sub>                      | 150              | 4                              | 12                  | 5                      |
| C <sub>5</sub>                      | 164              | 4                              | 12                  | 5                      |
| C <sub>6</sub>                      | 178              | 2                              | 9                   | 2                      |
| C <sub>7</sub>                      | 192              |                                | 9                   | 1                      |
| C <sub>8</sub>                      | 206              |                                | 11                  | 1                      |
| C <sub>9</sub>                      | 220              |                                | 7                   |                        |
| C <sub>10</sub>                     | 234              |                                | 7                   |                        |
| C <sub>11</sub>                     | 248              |                                | 7                   |                        |
| C <sub>12</sub>                     | 362              |                                | 4                   |                        |
| C <sub>13</sub>                     | 376              |                                | 3                   |                        |
| C <sub>14</sub>                     | 290              |                                | 1                   |                        |
| C <sub>15</sub>                     | 304              |                                | 2                   |                        |
| C <sub>16</sub>                     | 318              |                                | 2                   |                        |
| C <sub>17</sub>                     | 332              |                                | 2                   |                        |

<sup>1</sup> All -6 0 compounds were phenols.<sup>2</sup>  $C_x$  = total number of carbons in alkyl substituents.<sup>3</sup> Number of isomers detected at each alkyl homolog.

TABLE 2B. - Results for -8 O series of ArOH ( $C_nH_{2n-8}O$ )<sup>1</sup>

|       |                  | Fuel (Distillate Boiling Range, °C) |                     |                        |
|-------|------------------|-------------------------------------|---------------------|------------------------|
|       |                  | Coal Liquid<br>(200-325)            | Shale Oil<br>(>200) | Petroleum<br>(225-370) |
| $C_x$ | Molecular Weight | Number of Isomers                   |                     |                        |
| $C_0$ | 134              | 2                                   | 2                   | 1                      |
| $C_1$ | 148              | 7                                   | 6                   | 4                      |
| $C_2$ | 162              | 8                                   | 10                  | 7                      |
| $C_3$ | 176              | 4                                   | 11                  | 6                      |
| $C_4$ | 190              | 4                                   | 12                  | 4                      |
| $C_5$ | 204              |                                     | 7                   | 1                      |

<sup>1</sup> The dominant structure based on GC/MS fragmentation patterns was indanol for all fuels. Some tetralinols ( $C_0$ -tetralinol corresponds to  $C_1$ -indanol in mass) were detected in all fuels, however.

TABLE 2C. - Results for -12 O series of ArOH ( $C_nH_{2n-10}O$ )<sup>1,2</sup>

|       |                  | Fuel <sup>3</sup> (Distillate Boiling Range, °C) |                        |
|-------|------------------|--|------------------------|
|       |                  | Shale Oil<br>(>200)                              | Petroleum<br>(225-370) |
| $C_x$ | Molecular Weight | Number of Isomers                                |                        |
| $C_0$ | 144              | 2  | 1                      |
| $C_1$ | 158              | 4  | 1                      |
| $C_2$ | 172              | 6  | 2                      |
| $C_3$ | 186              | 6  | 2                      |
| $C_4$ | 200              | 2  | 2                      |
| $C_5$ | 214              | 1  |                        |

<sup>1</sup> No appreciable amounts of -10 O ArOH were detected in any fuel.

<sup>2</sup> All -12 O compounds were naphthols.

<sup>3</sup> Ions corresponding to naphthols were detected in SRC-II, but they were small in intensity and not definitive enough for a positive identification. A -12 O series corresponding to octahydropyrenols or some similar structure has tentatively been identified in SRC-II >325° C ArOH.



TABLE 2D - Results for -14 0 series of ArOH ( $C_nH_{2n-14}O$ )

| $C_x$ <sup>1</sup> | Molecular Weight | Fuel (Distillate Boiling Range, °C) |                     |                     |
|--------------------|------------------|-------------------------------------|---------------------|---------------------|
|                    |                  | Coal Liquid<br>(200-325)            | Shale Oil<br>(>325) | Petroleum<br>(>200) |
| C <sub>0</sub>     | 170              | 2                                   | 0                   | 2                   |
| C <sub>1</sub>     | 184              | 5                                   | 10                  | 3                   |
| C <sub>2</sub>     | 198              | 2                                   | 19                  | 5                   |
| C <sub>3</sub>     | 212              |                                     | 20                  | 10                  |
| C <sub>4</sub>     | 226              |                                     | 15                  | 12                  |
| C <sub>5</sub>     | 240              |                                     | 11                  | 11                  |
| C <sub>6</sub>     | 254              |                                     | 5                   | 8                   |
| C <sub>7</sub>     | 268              |                                     | 1                   | 4                   |
| C <sub>8</sub>     | 282              |                                     |                     | 4                   |
| C <sub>9</sub>     | 296              |                                     |                     | 2                   |

<sup>1</sup> Unsubstituted hydroxybiphenyls and hydroxyacenaphthalenes have molecular weights of 170. C<sub>0</sub>-benzindanol has molecular weights of 184, and C<sub>0</sub>-benztetralinols have molecular weights of 198. Hydroxybiphenyls are believed to be the dominant -14 0 structure, but all other isomers are also believed to be present.

TABLE 2E. - Results for -16 O series of ArOH ( $C_nH_{2n-16}O$ )

| Fuel (Distillate Boiling Range, °C) |                  |                                      |                                  |                                     |
|-------------------------------------|------------------|--------------------------------------|----------------------------------|-------------------------------------|
|                                     |                  | Coal Liquid <sup>1,2</sup><br>(>325) | Shale Oil <sup>1</sup><br>(>200) | Petroleum <sup>3</sup><br>(225-370) |
| C <sub>x</sub> <sup>1</sup>         | Molecular Weight | Number of Isomers                    |                                  |                                     |
| C <sub>0</sub>                      | 182              | 4                                    | 1                                | 0                                   |
| C <sub>1</sub>                      | 196              | 12                                   | 3                                | 0                                   |
| C <sub>2</sub>                      | 210              | 19                                   | 5                                | 0                                   |
| C <sub>3</sub>                      | 224              | 19                                   | 3                                | 1                                   |
| C <sub>4</sub>                      | 238              | 15                                   | 2                                | 5                                   |
| C <sub>5</sub>                      | 252              | 6                                    |                                  | 6                                   |
| C <sub>6</sub>                      | 266              | 1                                    |                                  | 4                                   |
| C <sub>7</sub>                      | 280              |                                      |                                  | 2                                   |
| C <sub>8</sub>                      | 294              |                                      |                                  | 1                                   |

<sup>1</sup> Predominantly fluorenols. MW C<sub>0</sub>-fluorenol = 182.

<sup>2</sup> Compounds analogous to hexahydropyrenols and phenyltetralinols are also present. MW C<sub>0</sub>-hexahydropyrenol = 224.

<sup>3</sup> Based on mass, predominantly phenyltetralinols.  
MW C<sub>0</sub>-phenyltetralinol = 224.

TABLE 2F. - Results for -18 O series of ArOH ( $C_nH_{2n-18}O$ )<sup>1</sup>

| <u>Fuel (Distillate Boiling Range, °C)</u> |                         |                          |
|--|-------------------------|--------------------------|
| Coal liquid<br>(>325)                      |                         |                          |
| <u>C<sub>x</sub></u>                       | <u>Molecular Weight</u> | <u>Number of Isomers</u> |
| C <sub>0</sub>                             | 194                     | 4                        |
| C <sub>1</sub>                             | 208                     | 5                        |
| C <sub>2</sub>                             | 222                     | 9                        |
| C <sub>3</sub>                             | 236                     | 5                        |
| C <sub>4</sub>                             | 250                     | 3                        |

<sup>1</sup> Presumably hydroxyphenanthrenes/anthracenes. (MW C<sub>0</sub> = 194)  
A spectrum of a -18 O compound free of other types was not obtained, so positive identification was not possible.

TABLE 2G. - Results for -20 O series of ArOH ( $C_nH_{2n-20}O$ )

|                |                  | Fuel (Distillation Boiling Range, °C) |                                     |
|----------------|------------------|---------------------------------------|-------------------------------------|
|                |                  | Coal Liquid <sup>1</sup><br>(>325)    | Petroleum <sup>2</sup><br>(225-370) |
| $C_x$          | Molecular Weight | Number of Isomers                     |                                     |
| C <sub>0</sub> | 220              | 8                                     | 1                                   |
| C <sub>1</sub> | 234              | 20                                    | 1                                   |
| C <sub>2</sub> | 248              | 16                                    | 4                                   |
| C <sub>3</sub> | 262              | 10                                    | 4                                   |
| C <sub>4</sub> | 276              | 3                                     | 4                                   |
| C <sub>5</sub> | 290              | 1                                     | 1                                   |

<sup>1</sup> Dihydroxyrenols, phenylnaphthols, and cycloalkylphenanthrols/anthracenols.  
MW C<sub>0</sub>-dihydroxyrenol, C<sub>0</sub>-phenylnaphthol and C<sub>0</sub>-benzacenaphthalenol = 220.

<sup>2</sup> Unknown structure.

TABLE 2H. - Results for -22 O series of ArOH ( $C_nH_{2n-22}O$ )

|                |                  | Fuel (Distillation Boiling Range, °C) |                                     |
|----------------|------------------|---------------------------------------|-------------------------------------|
|                |                  | Coal Liquid <sup>1</sup><br>(>325)    | Petroleum <sup>2</sup><br>(225-370) |
| $C_x$          | Molecular Weight | Number of Isomers                     |                                     |
| C <sub>0</sub> | 218              | 2                                     | 0                                   |
| C <sub>1</sub> | 232              | 3                                     | 0                                   |
| C <sub>2</sub> | 246              | 2                                     | 0                                   |
| C <sub>3</sub> | 260              | 3                                     | 2                                   |
| C <sub>4</sub> | 274              | 3                                     | 2                                   |
| C <sub>5</sub> | 288              | 1                                     | 1                                   |

<sup>1</sup> Pyrenols/fluoranthenols. MW C<sub>0</sub> = 218.

<sup>2</sup> Unknown. Possibly naphthylindanols, naphthyltetralinols and/or hydroxytriphenyls. (MW of C<sub>0</sub> homologs = 260, 274, and 246, respectively.)

TABLE 2I. - Results for -24 0 series of ArOH ( $C_nH_{2n-24}O$ )

| Fuel (Distillation Boiling Range, °C) |                         |                          |
|---------------------------------------|-------------------------|--------------------------|
| Coal Liquid <sup>1</sup><br>(>325)    |                         |                          |
| <u>C<sub>x</sub></u>                  | <u>Molecular Weight</u> | <u>Number of Isomers</u> |
| C <sub>0</sub>                        | 258                     | 4                        |
| C <sub>1</sub>                        | 272                     | 3                        |

<sup>1</sup> Probably cycloalkylpyrenols/cycloalkylfluoranthenols. MW C<sub>0</sub>-cyclopentylpyrenol = 258. MW C<sub>0</sub>-chrysenol = 244 (not observed).

TABLE 3. - Summary of ArOH in the three fuel types

|                                   | Fuel (Distillation Boiling Range, °C) |  |  |                          |
|-----------------------------------|---------------------------------------|--|--|--------------------------|
|                                   | Coal Liquid<br>(200-325)              | Shale Oil<br>(>200)                                  | (225-370)  | Petroleum<br>(370-535)   |
| Major ArOH compound type Present  | phenols                               | -14 0  | phenols  | -14 0                    |
| Other important ArOH types        | Indanols/<br>tetralinols              | -16 0, -20 0,<br>-22 0                               | Indanols/<br>tetralinols,<br>naphthols                       | phenols,<br>-16 0, -20 0 |
| Unique structural features        | lack of<br>naphthols                  | pyrenols and<br>partially hydro-<br>genated pyrenols | long chain<br>C <sub>10</sub> -C <sub>17</sub> phenols       | cycloalkyl<br>ArOH       |
| Non-ArOH compounds present        | none                                  | none   | C <sub>5</sub> -C <sub>27</sub> carboxylic<br>acids, indoles | cycloalkyl<br>ArOH       |
| Overall complexity of concentrate | simple                                | intermediate   | intermediate   | complex                  |

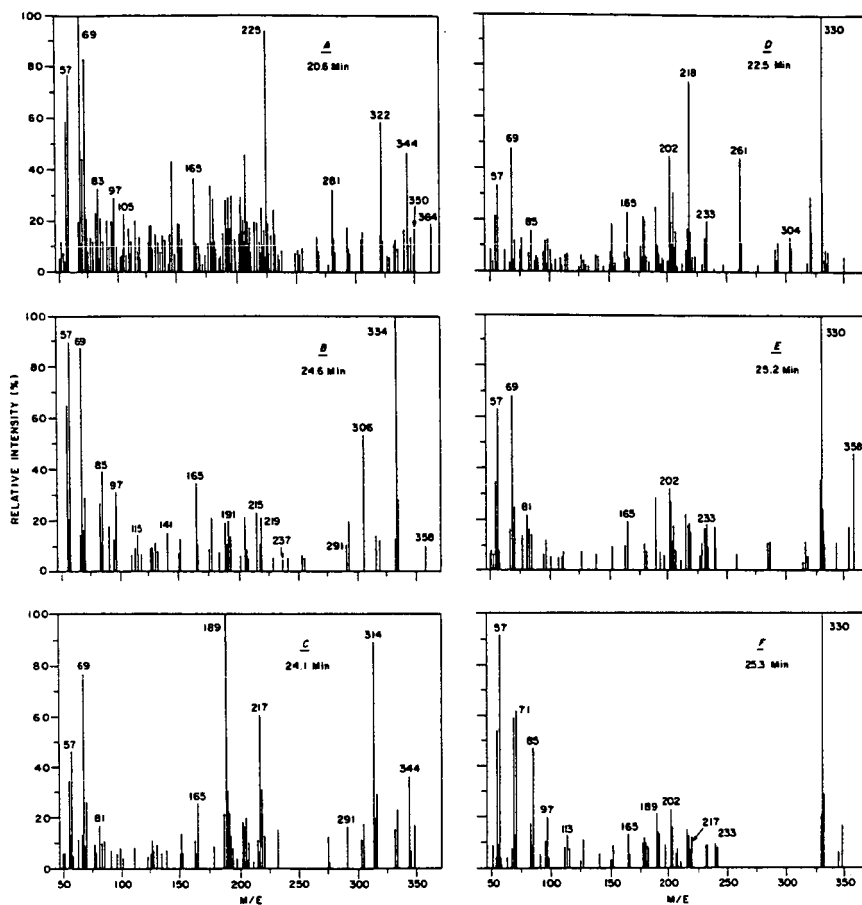


Figure 1 - Mass spectra from GC/MS analysis of acylated Wilmington 225-370° C (A) and SRC-II >325° C (B-F) ArOH concentrates. The GC retention times are noted on each. (A) shows primarily -14 O compounds (m/e 344 is -20 O) (B) shows primarily -16 O (m/e 358 is -20 O) (C) shows -22 O (m/e 314) with minor amounts of other series and (D-F) shows different types of -20 O compounds. For details, see text.

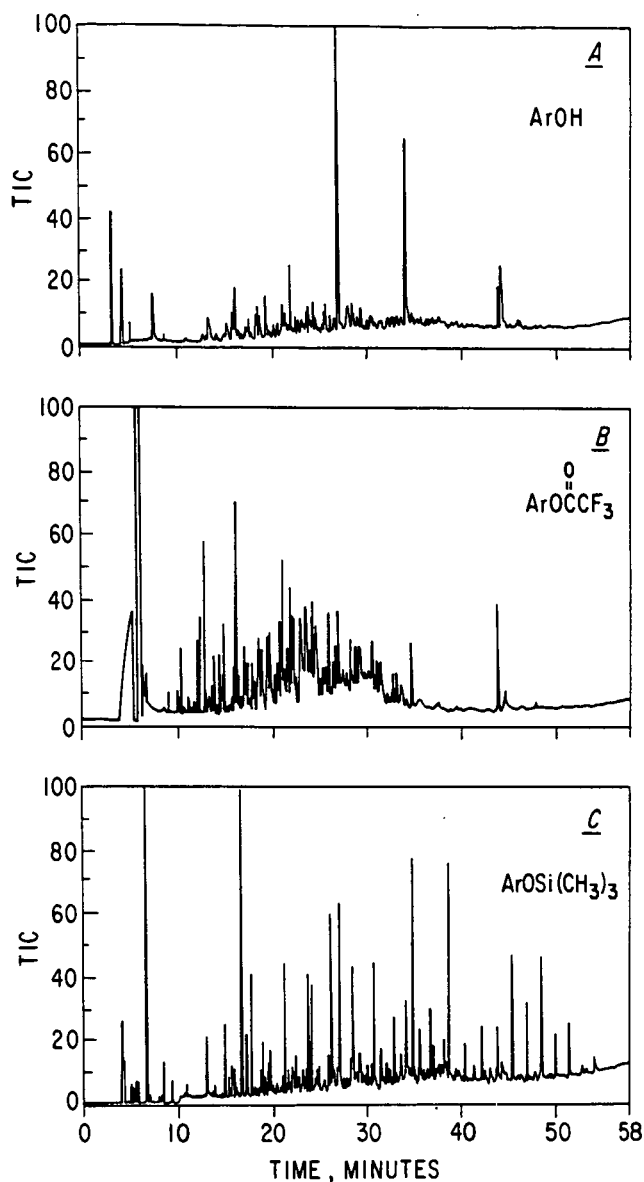


Figure 2 - Total ion GC/MS traces of plain and derivatized >200° C OSCR shale oil ArOH concentrate. Later eluting peaks in (C) are silylated aliphatic acids. Note the high degree of resolution obtained via acylation (B).

Comparative toxicity of crude and refined coal liquids and analogous petroleum products. I. Chronic dermal toxicity in mice.

H. P. Witschi, L. H. Smith, M. E. Goad, M. R. Guerin, W. H. Griest,  
and C-h. Ho

Biology Division and Analytical Chemistry Division, Oak Ridge National  
Laboratory, Oak Ridge, TN 37831

### Introduction

Human exposure to crude and refined coal liquids is most likely to occur via skin contact. In order to estimate eventual risks to human health as a consequence of incidental and prolonged skin contact it is necessary to obtain some information on the potential of coal-derived liquids to elicit skin cancer. This can be done with animals in experimental studies which mimic anticipated human exposure. In addition it also must be established whether prolonged dermal exposure will produce signs of toxicity not only on the skin, but internal organs. This paper reports data obtained in a life-long skin painting study with mice designed to explore these questions.

### Materials and Methods

The following materials were tested: Raw H-coal blend, containing 5700 ppm N; H-coal blend after low hydrotreatment (2650 ppm N); H-coal blend after high hydrotreatment (0.2 ppm N); H-coal "home heating oil", a devolatilized version of the high-hydrotreatment H-coal blend; and an H-coal reformed naphtha. Two petroleum-derived reference samples were obtained from the American Petroleum Institute: Petroleum No. 2 fuel oil and high catalytically cracked naphtha (gasoline). Benzo(a)pyrene (99% pure; Sigma Chemical Company) was used as reference substance.

Experimental animals were male and female C3H mice, bred and maintained in the barrier facility of the Biology Division, Oak Ridge National Laboratory. The test agents were applied three times a week onto the shaved skin of the back. The following concentrations were used: 50 ul of undiluted material, 50 ul of a 1:1 or 50 ul of a 1:3 dilution with acetone. Positive controls received 50 ug, 25 ug, or 12.5 ug of benzo(a)pyrene in 50 ul of acetone per application (three times a week) and negative controls were painted with acetone alone or not painted at all. Twenty-five animals of each sex were used per dose level.

All animals had free access to food and water and were kept 5 to a cage on hardwood shavings for the duration of the study. They were weighed periodically. The animals were treated on Mondays, Wednesdays and Fridays. Whenever a skin abnormality became visible at the site of test agent application, painting continued for another two weeks. When the skin mass was found to persist, the animal was killed, and the skin lesion excised and fixed in neutral buffered formalin. A complete necropsy was performed, all observations were noted and selected tissues were fixed in neutral buffered formalin. All skin lesions were examined on paraffin sections under the light microscope. Animals not showing any skin lesions were continuously painted until found moribund or dead. A complete necropsy was performed on all animals killed or found dead.

### Results and Discussion

Data on overall tumor incidence are shown in Table 1 and can be summarized as follows: In animals treated with 50 ug of benzo(a)pyrene per application, the first skin lesions began to appear 14 weeks later. In animals given the lowest dose of benzo(a)pyrene (12.5 ug per application) the first tumors appeared after 19 weeks. Tumor incidence then rose dramatically in all animals exposed to benzo(a)pyrene within 5-10 weeks after appearance of the first skin lesion. All animals exposed



eventually developed skin tumors. Histologically, the majority of tumors, 70%, were squamous cell carcinomas. On the other hand, in animals painted with acetone alone or not painted at all, very few skin tumors were observed which were benign papillomas.

Among the coal liquids only the raw H-coal blend produced an almost 100% incidence of skin tumors at all 3 concentrations tested. The first tumors were seen 10 weeks after the first application of 50 ul of the undiluted material (highest dose group). With the lower concentrations, the first tumors were seen after 20 and 33 weeks, respectively. Once the first tumor was discovered in any group, it took approximately one year until most animals in a given group had developed skin tumors. Of these tumors 46% were malignant squamous cell carcinomas.

Hydrotreatment dramatically reduced the carcinogenic potential. The low hydrotreatment preparation, painted undiluted onto the skin, produced the first tumors after 58 weeks, and 92 weeks after beginning of the experiment, tumor incidence was only 14%. In animals exposed to the high hydrotreated preparation, tumors began to appear usually after 70 to 80 weeks and the final tumor incidence in all 3 dose groups was between 16% and 44%. Only 2 tumors were found in the 150 animals exposed to H-coal reformed naphtha. However, in animals exposed to H-coal "home heating oil", the devolatilized version of the highly hydrotreated H-coal blend, tumors began to appear around 40 to 50 weeks of exposure and final tumor incidence in animals exposed to the undiluted material was 30%.

The two petroleum-derived samples had practically no carcinogenic potential; only 3 animals with tumors overall were found in animals painted with gasoline and only a total of 13 animals had tumors 95 weeks after beginning of the experiment. An evaluation of the gross necropsy findings showed that many animals suffered from lesions usually expected to develop in a certain percentage of aging animals, such as myocardial calcification, renal failure, liver tumors, ovarian tumors, and lymphomas, among others. However, the gross lesions were not associated with any particular treatment regimen and were also seen in the control and untreated animals.

It is concluded that the carcinogenic potential of a raw H-coal blend can be mostly abolished by hydrotreatment; however some carcinogenic potential remains associated with a devolatilized version of a severely hydrotreated sample. Petroleum derived products have considerably less carcinogenic activity, an observation compatible with earlier findings. Finally we did not find gross signs of toxicity in organs other than the skin, and the compounds treated seemed not to act as systemic carcinogens.

#### Acknowledgement

We wish to thank the American Petroleum Institute (API) for having made the two samples available to us.

Research sponsored by the Office of Health and Environmental Research, U. S. Department of Energy under contract DE-AC05-84OR21400 with the Martin Marietta Energy Systems, Inc.

By acceptance of this article, the publisher or recipient acknowledges the U.S. Government's right to retain a nonexclusive, royalty-free license in and to any copyright covering the article.

Table 1: Skin Tumor Incidence

| Compound                             | Dose per <sup>1</sup><br>application | No. of animals with skin<br>tumors/ No. of animals exposed | Median<br>time to<br>tumor<br>(days) <sup>2</sup> |
|--------------------------------------|--------------------------------------|--|---|
| 931 Raw H-coal blend                 | 50                                   | 41/50  | 45  |
|                                      | 25                                   | 45/50  | 52  |
|                                      | 12.5                                 | 44/50  | 62  |
| 934 Low hydrotreated<br>(2650 ppm N) | 50                                   | 7/50   | 112   |
|                                      | 25                                   | 6/50   | 117   |
|                                      | 12.5                                 | 1/50   | 149   |
| 935 High hydrotreated<br>(0.2 ppm N) | 50                                   | 10/50  | 100   |
|                                      | 25                                   | 17/50  | 111   |
|                                      | 12.5                                 | 8/50   | 119   |
| 978 H-coal "home<br>heating oil"     | 50                                   | 14/50  | 97  |
|                                      | 25                                   | 12/50  | 108   |
|                                      | 12.5                                 | 8/50   | 112   |
| 936 H-coal reformed<br>naphtha       | 50                                   | 0/50   | -   |
|                                      | 25                                   | 0/50   | -   |
|                                      | 12.5                                 | 2/50   | 155   |
| 975 API No. 2 fuel oil               | 50                                   | 5/50   | 120   |
|                                      | 25                                   | 6/50   | 131   |
|                                      | 12.5                                 | 2/50   | 144   |
| 976 API gasoline                     | 50                                   | 3/50   | 125   |
|                                      | 25                                   | 4/50   | 130   |
|                                      | 12.5                                 | 6/50   | 143   |
| Benzo(a)pyrene <sup>3</sup>          | 0.1                                  | 25/25  | 21  |
|                                      | 0.05                                 | 25/25  | 24  |
|                                      | 0.025                                | 25/25  | 31  |

<sup>1</sup>High dose was 50 ul of undiluted material; 50 ul lower doses obtained by dilution with acetone; all doses applied 3 times weekly.

<sup>2</sup>Animals killed 2 weeks after appearance of skin tumors; all tumors confirmed by histological diagnosis.

<sup>3</sup>Doses are in percent (w/v) benzo(a)pyrene, 50 uL per mouse.

## NON-ADDITIVE MUTAGENIC RESPONSES BY COMPONENTS OF COAL-DERIVED MATERIALS

R. Schoeny,<sup>1</sup> D. Warshawsky,<sup>2</sup> and G. Moore<sup>3</sup>

<sup>1</sup> U.S. EPA, Cincinnati, Ohio 45268

<sup>2</sup> Department of Environmental Health, University of Cincinnati Medical Center, Cincinnati, Ohio 45267

<sup>3</sup> U.S. DOE, Pittsburgh Energy Technical Center, Pittsburgh, PA 15236

In the last decade major efforts have been made to ensure the energy self-sufficiency of this country. Included in that effort has been the development and refinement of coal conversion technologies as a means of permitting increased usage of coal resources without attendant increases in pollution. Processes of coal liquefaction and gasification are not, however, free from hazard risk. Solvent refined coal materials SRCI and SRCII, fractions from Bergius and Fisher-Tropsch operations, and H-coal process products have been shown to produce adverse biological effects, such as tumors in experimental animals or mutations in various test system (e.g. 1-3, 7-10). Analytical data indicate that polycyclic aromatic hydrocarbons (PAH), heterocyclic compounds, aromatic amines and other materials with carcinogenic potential are likely to be produced by liquefaction processes (1, 3-6, 16). Coal conversion materials are highly complex and ill-defined mixtures. Coal liquids, for example, have a more complex composition than do crude petroleum of a similar boiling range. Mutagenic or carcinogenic components may, in fact, constitute a very minor percentage of the mass of these materials.

For these, as for other mixtures of biologically active materials, the question has been raised whether the individual activities of constituents are additive or if there are interactive effects contributing to the overall biological activity observed for the mixture. There are a few examples of non-additive biological responses in the literature. It is known, for instance, that mixtures of PAH and aromatic amines showed greater than additive effects when assayed for mutagenicity of *Salmonella typhimurium* (11). Likewise, a mixture of benzo[a]pyrene (BaP) dihydrodiols was more directly mutagenic than would be expected based on the mutagenic activities of the individual diols. When rat liver homogenates (S9) were added to assay system, the reverse was true (12). Our laboratory has also observed that fractions of coal-derived materials exhibited non-additive mutagenic responses in *Salmonella typhimurium* (14). Current research has been directed toward an examination of synergistic or antagonistic biological activities of coal conversion mixture components.

### MATERIALS AND METHODS

#### Samples and Preparation

Samples were supplied through U.S. DOE PETC by R.A. Winschel of the Coal Research Division of Conoco. All materials were collected on a daily basis, combined and distilled by Conoco. Sample PDU-9 is a hydroclone overflow material from an H-coal process design unit. Lummus Feed and Lummus Product are the second stage feed and product, respectively from run 3LCF9 of a Lummus Integrated Two Stage Liquefaction process. Samples were stored in the dark at 5°C. They were prepared for assay by weighing 100-500 mg and adding dimethylsulfoxide (DMSO) so as to obtain a presumptive concentration of 10 or 20 mg/ml. Sample solutions were filter sterilized and applied as 0.1 ml aliquots for reverse mutation assays and as 1 ul aliquots for forward mutation assays. Tared vessels containing undissolved materials were dried and weighed, and this figure used in calculation of the true concentration of the test solutions.

#### Preparation of Solvent Extracts of Samples

Approximately 5g of each sample was weighed and a volume of solvent equal to 5x of the weight was added in capped tubes. This mixture was agitated vigorously in the dark at room temperature for 2 hrs. After centrifugation to settle particulates, the solvent was removed and an equal amount of fresh solvent was added. The mixture was agitated for another 2 hours followed again by centrifugation. The two solvents with extracted material were pooled and evaporated under N<sub>2</sub>. This procedure was carried out sequentially with hexane, toluene, methylene chloride, and acetonitrile. There was generally a quantity of unextracted material remaining, which is referred to in the text and tables as the residue fraction. The DMSO soluble portion of this material and all the dried extracts were prepared for assay in the same manner as the whole sample.

#### Preparation of "Reconstructed Whole" Samples

"Reconstructed whole" mixtures were prepared by adding individual fractions in the same proportions in which they were extracted. For example, PDU-9 fraction III reconstruction consisted of 1.71% hexane fraction, 42.76% toluene fraction, etc. Materials were dissolved in the original extracting solvents or weighed out, combined, and the solvents evaporated under N<sub>2</sub>. The reconstructions were assayed as DMSO solutions on the same occasion as were aliquots of the unfractionated sample and the individual fractions.

#### Mutagenicity Assays in Salmonella Typhimurium

Liver homogenates (S9) for mammalian metabolism were prepared from male Sprague-Dawley rats which had been injected i.p. with 500 mg/kg Aroclor 1254 and killed five days thereafter. Livers were homogenized in 3 volumes cold buffer (0.15 M KCl, 0.05M Tris HCl). The supernatant fraction from 20 min. centrifugation at 9000g was dispensed into 0.5 ml aliquots and stored at -70°C until use.

Reverse mutation plate incorporation assays using Salmonella typhimurium strains TA97 and TA98 were done according to published procedures (9). All assays included use of 50 ul S9/plate plus appropriate buffers and cofactors.

Strain TM677 was used in forward mutation assays wherein resistance to 8-azaguanine toxicity was measured as the endpoint (15). Fresh cultures (from frozen aliquots) of approximately  $3 \times 10^7$  organisms were used in microvolume suspension assays, total volume 100 ul. The test material was added as 1 ul aliquots and S9 comprised 1% of the total assay volume. Duplicate assay tubes per experimental point were incubated for 2 hr at 37°C in a gyrotory bath. At the end of the incubation period cells were diluted 1/5 with phosphate buffered saline and 145 ul plated in triplicate for selection of mutant organisms. An aliquot was further diluted and plated in the absence of selection for determination of bacterial survival. Numbers of revertants/ $10^5$  surviving cells were calculated from the 6 mutagenicity and 6 toxicity plate counts per experimental point. A positive response in this assay is one in which the number of mutants/ $10^5$  survivors is greater than the upper 99% confidence limit on both day of assay and mean historical spontaneous controls.

#### Results and Discussion

Sample PDU-9 is a vacuum still bottom material from an H-coal process design unit using Kentucky 11 coal and run in the Syncrude mode. The Lummus process which provided the Feed and Product samples consisted of a short contact time liquefaction, followed by antisolvent deashing and subsequent upgrading of

the deashed coal liquids in a Lummus-Cities Service LC fining unit. The Lummus Feed is the LC-Finer feed stock, and Lummus Product the recycle oil produced by this unit.

All materials were assayed for mutagenicity as DMSO solutions. All were mutagenic in both reverse mutation assays to histidine prototrophy (Ames test) and in a forward mutation assay using selection of 8-azaguanine resistant clones. Note that the latter test incorporates a 2-hour period wherein the Salmonella and test items are incubated in liquid suspension. For all assays mutagenicity was detectable only when rat liver homogenates (S9) were included to provide mammalian enzymes for metabolism of the materials to reactive forms.

Of the three samples, PDU-9 was most mutagenic, and is, in fact the most mutagenic fuel material assayed in our laboratory. This sample, and all others, was diluted and assayed at 5 concentrations. The assay was repeated on this set of solutions and then a fresh set of sample solutions was prepared and tested on two occasions. As these coal materials are heterogenous in composition, there are variations both in the amount of material soluble in DMSO and in the mutagenicity observed. Data from assay of PDU-9 graphed in Figure 1, illustrate the variation in mutagenic response. It is also clear from this figure that, at low sample concentrations, there is a linear sample-dose/mutagenic response relationship. It is possible, therefore, to obtain an estimate of the mutagenic response per unit sample by applying regression analysis to those points and obtaining the slope of the regression line. For the PDU-9 data graphed in Figure 1, one obtains an estimate of 50.6 TA98 colonies/ug sample and 48.1 TA97 colonies/ug. Mutagenicity observed for Lummus Feed was 13.4 TA97 and 4.2 TA98 Colonies/ug and for Lummus Product 17.9 TA97 and 11.7 TA98 colonies/ug. Strain TA98 is known to respond to a variety of compounds which cause frameshift mutations, including PAH and aromatic amines. Strain TA97 also is reverted by frameshift mutagens but is particularly sensitive to acridine compounds and probably to other heterocyclics as well (8). The difference in response by the two strains of the Lummus vs the H-coal (PDU-9) samples is suggestive of variations in their composition. It is expected that the Lummus materials will be shown to be composed of a greater percentage acridines and related compounds than the H-coal sample.

The forward mutation assay presumably detects all types of mutagenic events, including deletions and translocations, that are compatible with bacterial viability. The use of a suspension incubation gives the added advantage of providing a relevant quantitation of test item toxicity. None of the test materials when assayed with S9 were toxic to the Salmonella; that is, caused a reduction of more than 40% viability. All three proved to give positive results, as measured by increases in numbers of mutants/ $10^5$  survivor greater than the upper 99% confidence limit on both day-of-assay and mean historical spontaneous controls. Furthermore, the magnitude of the mutagenicity response was seen to increase in a linear fashion with sample concentration, allowing the same sort of estimation as for the reverse assay data. Sample PDU-9 was also the most mutagenic sample as measured in the forward mutation assay, with 2.94 mutants/ $10^5$  survivors/ug compared to Lummus Feed (0.11 mutants/ $10^5$  survivors/ug) and Lummus Product (0.45 mutants/ $10^5$  survivors/ug).

As a first step in the analysis of these fuel materials, a simple fractionation process was undertaken. Sequential organic solvent extracts were prepared using solvents of increasing polarity; namely, hexane, toluene, methylene chloride, and acetonitrile. The DMSO-soluble portion of the non-extractable material (residue) left at the end of the process, and all fractions were assayed for mutagenicity in forward and reverse assays as described for the uncut samples. Two sets of fractions were prepared and assayed.

Generally these materials were similar in their extraction properties to other H-coal vacuum bottoms we have assayed (13, 14, 17). Little material is extracted by hexane and less than 1% of the total mass was acetonitrile extractable. From 20-36% of the material was left at the end of the procedure as the residue fraction. In the course of the fractionation, the sample gains weight, presumably due to retained solvent or water. Use of solvents which had been dried by the addition of a water sieve agent did not reduce this weight gain.

The fractions differ markedly from one another in their mutagenic activity (Tables 1-5). As one would expect, the residue fraction of the extraction process is the least mutagenic material. The components extracted by acetonitrile are generally highly mutagenic (e.g. PDU-9 100,940 TA98 colonies/mg; 73,272 TA97 colonies/mg). This latter fraction, presumably the most polar components of the coal-conversion materials, is present in small amounts. The proportionate activity of the whole mixture is, therefore, very small, assuming additivity. If one multiplies the calculated mutagenicity of a fraction in colonies/mg by the percent of the whole mixture that fraction represents, a determination of fraction specific activity can be made. For example, in Table 1, the TA98 mutagenicity of the residue fraction was low, 2544 colonies/mg, but these components constitute 23.84% of the sample. The specific activity of the residue, or its contribution to the mutagenicity of the whole sample, was 606 colonies/mg whole sample. The highly mutagenic acetonitrile fraction contributed to the same extent to whole sample mutagenicity (596 colonies/mg whole sample) as it constituted only 0.59% of the PDU-9 sample mass.

If there are no interactive effects among fractions of these coal-conversion materials, the sum of the specific activities should equal the mutagenicity observed for the unfractionated material. When these summations have been calculated for a variety of coal-conversion samples the percentages have been found to be comparable to the whole sample mutagenicity. There have also been observed sums of fractional activities less than the whole as well as greater than the whole (14). PDU-9, Lummus Product and Lummus Feed fall into the former category. This non additivity of fraction mutagenic activities is unlikely to be due to dilution as a result of weight increase of the material during the extraction process. In no instance was the weight gain more than 20% of the original sample weight (PDU-9). Table 1 indicates that the "loss" of PDU-9 mutagenicity with fractionation was about 50% for the reverse mutation assay (Table 2). The data for Lummus Feed are similar (Tables 4,5), whereas dilution cannot be discounted as accounting for the majority of the non-additivity observed with the Lummus Product sample (Table 3).

Another explanation for non-additivity is the loss or alteration of mutagenic compounds as a consequence of the extraction process. It was believed that this mild extraction, which entails no changes in pH or temperature of the material, would be unlikely to generate oxygenated or otherwise modified compounds. The protocol was undertaken under yellow lights to minimize photoreactions of PAHs and other aromatic compounds. A third possibility is that the fractional components act as co-mutagens.

To elucidate the mechanism of the observed non-additivity, "reconstructed whole" mixtures were prepared. This was done by recombining the sample fractions in the same proportions which they were extracted. The reconstructions were assayed in reverse and forward mutation assays on the same occasions as the unfractionated whole and the individual fractions. If there are, in fact, co-mutagenic interactions among fractions, the mutagenicity of the reconstructed mixture should be increased relative to the fraction sums. For PDU-9 this proved not to be the case (Table 1). For both strains TA97 and TA98, the reconstruction

mutagenicity was not increased, but was roughly equivalent to the fraction sum. This was also the case for forward mutation assay of the reconstructed sample (Table 2). Data derived from assay of the set B fractions corroborate these results (not shown). The Lummus Product reconstruction assay showed only a very little increase in TA97 mutagenicity. For both of these samples it would appear that non-additivity of organic fraction mutagenicity is due to artifacts of extract preparation.

This does not appear to be the case for the Lummus Feed material. Data from reverse mutation assay of both sets of fractions (Tables 4,5) indicate an increase in mutagenesis on the order of 28% to 65% relative to the fraction sums. That there were alterations in the fractions as artifacts of preparation cannot be discounted, but it is also clear that there is evidence of co-mutagenicity among fractions of the Lummus Feed sample. It should be noted parenthetically that the data in these tables also illustrate the potential for loss or change of biological activity that occurs in these complex mixtures as a function of time. Fraction sets A & B were prepared in assayed over a period of several months.

The premise that single mixtures compounds behave independently or additively when mixed is a subject of continuing discussion. The work described here indicates that complex mixtures of compounds may not have biological activity which can be estimated on the basis of summation of activities of known components. It also points out, however, the difficulty of separating mixture components in a way which leaves them unchanged.

#### ACKNOWLEDGEMENTS

This work was supported by U.S. DOE Contract #DE-AC22-83PC62999. We thank Ms. Lois Hollingsworth for her expert technical assistance and Ms. Carol Haynes for typing of the manuscript.

#### REFERENCES

1. Battelle Pacific Northwest Laboratories (1979). Biomedical studies on solvent refined coal (SRC II) liquefaction materials: A status report. PNL-3189.
2. Cowser, K.E. (Ed.) (1984). Synthetic Fossil Fuel Technologies. Results of Health and Environmental Studies. Proceedings of the Fifth Life Sciences Symposium, Gatlinburg, TN, Butterworth Publishers, Boston, MA.
3. Freudenthal, R.I., Lutz, G.A., Mitchell, R.I. (1975). Carcinogenic potential of coal and coal conversion products. Battelle-Columbus Laboratories, Columbus, OH.
4. Guerin, M.R., Ho, C-h, Rao, T.K., Clark, B.R. and Epler, J.L. (1980). Polycyclic aromatic primary amines as determinant chemical mutagens in petroleum substitutes. Environ. Res. 23: 42-53.
5. Guerin, M.R., Rubin, I.B., Rao, T.K., Clark, B.R., and Epler, J.L. (1981). Distribution of mutagenic activity in petroleum and petroleum substitutes, Fuel 60: 282-288.
6. Ho, C-h., Ma, C.Y, Clark, B.R., Guerin, M.R., Rao, T.K. and Epler, J.L. (1980). Separation of neutral nitrogen compounds from synthetic crude oils for biological testing. Environ. Res. 22: 412-422.

7. Heuper, W.C. (1953). Experimental studies on carcinogenesis of synthetic liquid fuels and petroleum substitutes. AMA Arch. Indust. Hygiene Occup. Med. 8: 307-327.
8. Levin, D.E., Yamasaki, E. and Ames, B.M. (1982). A new Salmonella tester strain, TA97, for the detection of frameshift mutagens. Mutat. Res. 94: 315-330.
9. Maron, D., Ames, B.M. (1983). Revised method for the Salmonella mutagenicity test. Mutat. Res. 113: 173-215.
10. Munro, N.B., Fry, R.J.M., Gammage, R.B., Haschek, W.M., Calle, E.F., Klein, J.A., Schultz, T.W. (1983). Indirect Coal Liquefaction: A Review of Potential Health Hazards and Worker Exposure During Gasification and Synthesis. ORNL-5938, Oak Ridge National Lab., Oak Ridge, TN.
11. Salamone, M.F., Heddle, J.A., Katz, M. (1979). The use of Salmonella/microsomal assay to determine mutagenicity in paired chemical mixtures. Can. J. Genet. Cytol. 21: 101-107.
12. Schoeny, R., Cody, T., Radike, M. and Warshawsky, D. (1985). Mutagenicity of algal metabolites of benzo(a)pyrene for Salmonella typhimurium. Environ. Mutagen., in press.
13. Schoeny, R. and Warshawsky, D. (1983). In Vitro mutagenicity testing of Ohio coal-derived materials. In: M. Waters, S. Sandhu, J. Lewtas, L. Claxton, N. Chernoff and S. Nesnow (Eds.). Short-term Bioassays in the Analysis of Complex Environmental Mixtures, III, pp. 285-295.
14. Schoeny, R., Warshawsky, D., Hollingsworth, L., Hund, M. and Moore, G. (1981). Mutagenicity of products from coal gasification and liquefaction in the Salmonella microsome assay. Environ. Mutagen 3: 181-195.
15. Skopek, T.R., Liber, H.L., Krolewski, J.J., Thilly, W.G. (1978). Quantitative forward mutation assay in Salmonella typhimurium using 8-azaguanine resistance as a genetic marker. Proc. Natl. Acad. Sci. USA, 75: 410-414.
16. Tanita, R., Telesca, D., Walker, J., Beradinelli, S. (1980). Organic contaminants in direct coal liquefaction - a preliminary assessment. Amer. Indust. Hygiene Assoc. J. 41: 851-853.
17. Warshawsky, D., Schoeny, R. and Moore, G. Evaluation of coal liquefaction technologies by Salmonella mutagenesis. Toxicol. Lett. 10: 121-127, 1982.



Table 1

COMPARISON OF PDU-9 FRACTION (SET A) AND RECONSTRUCTED MIXTURE  
MUTAGENICITIES: REVERSE MUTATION PLATE INCORPORATION ASSAYS

| SAMPLE             | PERCENT<br>EXTRACTION | COLONIES/mg <sup>a</sup> |         | SPECIFIC ACTIVITY<br>COLONIES/mg <sup>b</sup> |                   |
|--------------------|-----------------------|--------------------------|---------|---|-------------------|
|                    |                       | TA97                     | TA98    | TA97  | TA98              |
| Hexane             | 1.71                  | 16,850                   | 18,881  | 288   | 323               |
| Toluene            | 42.76                 | 9,516                    | 15,903  | 4,069   | 6,800             |
| Methylene Chloride | 31.11                 | 29,319                   | 49,017  | 9,121   | 15,249            |
| Acetonitrile       | 0.59                  | 73,272                   | 100,940 | 432   | 596               |
| Residue            | 23.84                 | 1,404                    | 2,544   | 335   | 606               |
| Whole              |                       |                          |         | 28,056  | 49,092            |
| Sum of Fractions   |                       |                          |         | 14,245<br>(50.8%)                             | 23,574<br>(48.0%) |
| Reconstruction     |                       |                          |         | 15,829<br>(56.4%)                             | 16,389<br>(33.4%) |

<sup>a</sup> Calculated from linear portions of dose response curves

<sup>b</sup> Colonies/mg x per cent extraction

Table 2

COMPARISON OF PDU-9 FRACTION (SET A) AND RECONSTRUCTED  
MIXTURE MUTAGENICITIES: FORWARD MUTATION ASSAY

| SAMPLE             | PERCENT<br>EXTRACTION | TM677 COLONIES/<br>10 SURVIVORS/mg | SPECIFIC ACTIVITY<br>COLONIES/10 <sup>5</sup> SURVIVORS/mg |
|--------------------|-----------------------|------------------------------------|--|
|                    |                       |                                    |  |
| Hexane             | 1.71                  | 187                                | 3  |
| Toluene            | 42.76                 | 405                                | 173  |
| Methylene Chloride | 31.11                 | 1,084                              | 337  |
| Acetonitrile       | 0.59                  | 2,514                              | 15   |
| Residue            | 23.84                 | 57                                 | 14   |
| Whole              |                       |                                    | 2,911  |
| Sum of Fractions   |                       |                                    | 542<br>(18.6%)   |
| Reconstruction     |                       |                                    | 313<br>(10.8%)   |

<sup>a</sup> Calculated from linear portion of dose response curves

<sup>b</sup> Colonies/10<sup>5</sup> survivors/mg x per cent extracted

Table 3

COMPARISON OF LUMMUS PRODUCT FRACTION (SET A) AND RECONSTRUCTED MIXTURE  
MUTAGENICITIES: REVERSE MUTATION PLATE INCORPORATION ASSAYS

| SAMPLE             | PERCENT<br>EXTRACTED | COLONIES/mg <sup>a</sup> |        | SPECIFIC ACTIVITY<br>COLONIES/mg <sup>b</sup> |                   |
|--------------------|----------------------|--------------------------|--------|---|-------------------|
|                    |                      | TA97                     | TA98   | TA97  | TA98              |
| Hexane             | 4.76                 | 31,373                   | 6,309  | 1,493   | 300               |
| Toluene            | 26.39                | 13,128                   | 11,880 | 3,463   | 3,135             |
| Methylene Chloride | 16.50                | 28,341                   | 38,141 | 4,676   | 6,293             |
| Acetonitrile       | 1.26                 | 18,862                   | 23,775 | 238   | 300               |
| Residue            | 51.08                | 2,545                    | 4,686  | 1,300   | 2,394             |
| Whole              |                      |                          |        | 15,730  | 21,844            |
| Sum of Fractions   |                      |                          |        | 11,170<br>(71.0%)                             | 12,422<br>(56.9%) |
| Reconstruction     |                      |                          |        | 12,718<br>(80.9%)                             | 13,482<br>(61.7%) |

<sup>a</sup> Calculated from linear portion of dose response curves

<sup>b</sup> Colonies/mg x per cent extracted

Table 4

COMPARISON OF LUMMUS FEED FRACTION AND RECONSTRUCTED MIXTURE MUTAGENICITIES:  
REVERSE MUTATION PLATE INCORPORATION ASSAYS, STRAIN TA97

| SAMPLE                | PER CENT<br>EXTRACTED |       | TA97<br>COLONIES/mg <sup>b</sup> |        | SPECIFIC ACTIVITY<br>TA97 COLONIES/mg <sup>c</sup> |                   |
|-----------------------|-----------------------|-------|----------------------------------|--------|--|-------------------|
|                       | A                     | B     | A                                | B      | A  | B                 |
| Hexane                | 2.48                  | 2.13  | 8,862                            | 376    | 220  | 8                 |
| Toluene               | 25.94                 | 17.88 | 9,603                            | 8,721  | 2,491  | 1,559             |
| Methylene<br>Chloride | 34.28                 | 37.76 | 15,106                           | 10,200 | 5,178  | 3,852             |
| Acetonitrile          | 1.06                  | 0.75  | 22,265                           | 28,732 | 236  | 215               |
| Residue               | 36.24                 | 41.48 | 2,540                            | 726    | 920  | 301               |
| Whole                 |                       |       |                                  |        | 17,952   | 13,411            |
| Sum of Fractions      |                       |       |                                  |        | 9,045<br>(50.4%)                                   | 5,935<br>(44.2%)  |
| Reconstruction        |                       |       |                                  |        | 15,385<br>(85.7%)                                  | 12,162<br>(90.7%) |

<sup>a</sup> Refers to fraction set A or B

<sup>b</sup> Calculated from linear portions of dose response curves

<sup>c</sup> Colonies/mg x per cent extractor

Table 5

COMPARISON OF LUMMUS FEED FRACTION AND RECONSTRUCTED MIXTURE MUTAGENICITIES:  
REVERSE MUTATION PLATE INCORPORATION ASSAYS, STRAIN TA98

| SAMPLE             | PER CENT EXTRACTED |       | TA98 COLONIES/mg <sup>b</sup> |        | SPECIFIC ACTIVITY TA98 COLONIES/mg <sup>c</sup> |                   |
|--------------------|--------------------|-------|-------------------------------|--------|---|-------------------|
|                    | A <sup>a</sup>     | B     | A                             | B      | A   | B                 |
| Hexane             | 2.48               | 2.13  | 4,376                         | 458    | 108   | 10                |
| Toluene            | 25.94              | 17.88 | 4,876                         | 3,454  | 1,265   | 618               |
| Methylene Chloride | 34.28              | 37.76 | 4,436                         | 3,973  | 1,521   | 1,500             |
| Acetonitrile       | 1.06               | 0.75  | 20,630                        | 10,192 | 902   | 151               |
| Residue            | 36.24              | 41.48 | 2,490                         | 364    |   |                   |
| Whole              |                    |       |                               |        | 11,127  | 5,002             |
| Sum of Fractions   |                    |       |                               |        | 4,015<br>(36.1%)                                | 2,355<br>(47.1%)  |
| Reconstruction     |                    |       |                               |        | 7,183<br>(64.6%)                                | 5,643<br>(112.8%) |

<sup>a</sup> Refers to fraction set A and B

<sup>b</sup> Calculated from linear portion of dose response curves

<sup>c</sup> Colonies/mg x per cent extracted

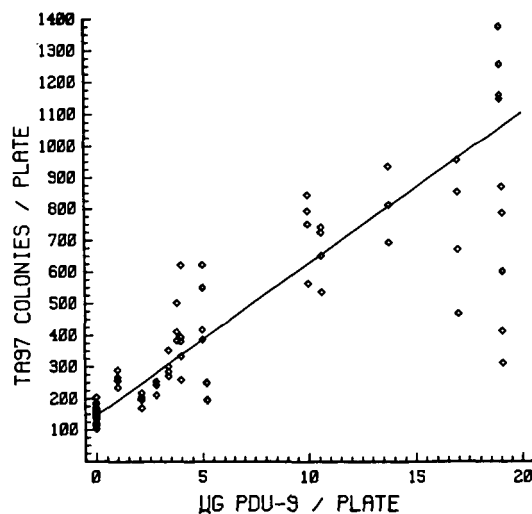


Figure 1. Mutagenicity of coal hydrogenation sample PDU-9 for *Salmonella typhimurium* strain TA98. The solid lines the least squares line for these data,  $n = 97$ ,  $r = 0.9259$ .

IDENTIFICATION AND MUTAGENICITY OF AMINO- AND HYDROXY-SUBSTITUTED  
NITROGEN AND SULFUR HETEROCYCLES IN A SOLVENT-REFINED COAL LIQUID

Masaharu Nishioka, Gary M. Booth, and Milton L. Lee

Departments of Chemistry and Zoology  
Brigham Young University  
Provo, UT 84602

Raymond, N. Castle

Department of Chemistry  
University of South Florida  
Tampa, FL 33620

INTRODUCTION

Development of coal upgrading processes such as gasification and liquefaction must be continued because of the long-term uncertainty in the availability of petroleum resources. Identification of components and investigation of the environmental effects of coal-derived products produced in these upgrading processes are required. Although numerous studies describing the identification and characterization of polycyclic aromatic hydrocarbons (PAH) and polycyclic aromatic compounds (PAC) containing a single heteroatom have been reported, PAC containing more than one heteroatom have been only tentatively identified until recently. In the last year, many new PAC containing two heteroatoms in a solvent-refined coal liquid were positively identified using capillary column gas chromatography. These compounds include hydroxylated thiophenic compounds (1), aminodibenzothiophenes (2), hydroxylated nitrogen heterocycles (3), azathiophenic compounds (4), and amino-substituted nitrogen heterocycles (5). In this paper, the analytical methods for the identification of trace amounts of PAC containing two heteroatoms in complex coal-derived materials are reviewed. The structural characteristics of the PAC formed in a solvent-refined coal liquid and a coal tar were compared, and standard compounds were synthesized for verification of identifications and for mutagenicity testing.

EXPERIMENTAL

A solvent-refined coal heavy distillate (SRC II HD: 260-450°C boiling point range) was obtained from the Fort Lewis, Washington, pilot plant (operated by the Pittsburg & Midway Coal Mining Co.). A coal tar was obtained from the National Bureau of Standards, Washington, DC. This was a medium crude coke oven tar. Standard compounds were obtained commercially or synthesized by us (6).

The SRC II HD material and coal tar were fractionated into chemical classes by adsorption chromatography on neutral alumina and silicic acid (3, 7). The third (A-3) and fourth (A-4) alumina column fractions which were composed of the nitrogen- and hydroxy-containing PAC, respectively; the second (S-2) and third (S-3) silicic acid column fractions from the A-3 fraction which were composed of the amino- and tertiary nitrogen-containing PAC, respectively; and the second (S-2') silicic acid column fraction from the A-4 fraction which was composed of hydroxy nitrogen-containing PAC were analyzed in this study.

Hewlett-Packard Model 5880 gas chromatographs equipped with flame ionization (FID), sulfur-selective flame photometric (FPD), nitrogen-selective thermionic (NPD), and  $^{63}\text{Ni}$  electron capture (ECD) detectors were used in this study. The capillary columns were prepared by coating 10-20 m x 0.2 or 0.3 mm i.d. fused silica tubing (Hewlett-Packard, Avondale, PA) with SE-54, a 25% biphenyl polymethylsiloxane (8,9), or a smectic liquid-crystalline polymethylsiloxane stationary phase (10-13) (0.25  $\mu\text{m}$  film thicknesses). A Hewlett Packard Model 5982A GC-MS system was used to obtain mass spectral confirmation of identified compounds. The Ames mutagenicity assays were performed as described by Ames *et al.* (14) with minor modifications.

## RESULTS AND DISCUSSION

The chemical complexities typically associated with coal-derived products require stationary phase selectivity in addition to high efficiency for their analysis by capillary column gas chromatography. We have recently synthesized a new polarizable stationary phase, a biphenyl polysiloxane (8,9), and several liquid-crystalline polysiloxanes (10-13) for the analysis of PAC. The biphenyl polysiloxane provided unique selectivity for the polar amino- and hydroxy-substituted nitrogen and sulfur heterocycles. The polar substituent groups on the PAC interact with the  $\pi$ -electron cloud of the biphenyl group. Blocking of polar groups is sometimes recommended for strongly polar compounds. Blocking of the polar group leads to a decrease in the dipole-induced dipole interactions between solutes and the stationary phase. This "softer" interaction often results in improved resolution. All isomers of the hydroxydibenzothiophenes in the coal tar were resolved and identified using a 25% substituted biphenyl phase (Figure 1) after blocking of the hydroxyl group. In comparison, only the 1- and 2-hydroxydibenzothiophenes were detected in the SRC II HD. Similarly, improved resolution was observed for the pentafluoropropyl (PFP) derivatives of the alkylated aminodibenzothiophenes (2). The large retention differences between the original polar compounds and their derivatives gave complementary evidence for their identification (1,2).

The separations achieved on liquid-crystalline stationary phases is based on the molecular geometries of solutes, such as size, shape, and planarity, in addition to other factors associated with conventional stationary phases. Positive identifications of the hydroxylated thiophenic compounds were achieved using both a smectic liquid-crystalline stationary phase and the 25% biphenyl stationary phase (1). This liquid-crystalline phase was also used for the separation of isomeric PAH (15), sulfur heterocycles (16), and amino-PAH (5).

Approximate concentrations of the amino- and hydroxy-substituted nitrogen and sulfur heterocycles were estimated to be 1-10 ppm in the SRC II HD. In comparison, corresponding PAC containing only one heteroatom were present at approximately 100-1000 ppm, and PAH were found to be present at 0.1-5% in the same sample (17). The amino- and hydroxy-substituted heterocycles were identified at low levels by utilizing selective detectors during the analysis of fractions in which one of the two functional groups was enriched: FPD for the nitrogen heterocycles and amino-PAC fraction, FPD for the hydroxyl-PAC fractions, ECD for the tertiary nitrogen PAC fraction, and NPD for the hydroxyl and nitrogen-PAC fractions. Compounds were positively identified by comparison of retention data with those of standard compounds and by selected ion mass spectrometry. Figure 2 shows one example: the ECD chromatogram of the PFP-derivatized SRC II HD S-3 fraction. This chromatogram shows only the

PFPP-amide and tertiary nitrogen-containing compounds; the aminophenylpyridines, aminophenylquinolines, and their alkylated derivatives were identified by GC-MS.

All isomers of the aminodibenzothiophenes and the azadibenzothiophenes were assayed for mutagenicity using the Ames test (2,4). The 2- and 3-aminodibenzothiophenes were strongly mutagenic, and their average response was ten to one hundred times greater than the average response of benzo[a]pyrene, while all isomers of the azadibenzothiophenes were inactive. Recently, the microbial mutagenicities of numerous isomeric 3- to 5-ring sulfur heterocycles have been extensively studied (18-20). The presence of a sulfur heteroatom was found to have little effect on mutagenicity. Likewise, compounds containing both nitrogen and sulfur heteroatoms in the rings also demonstrated little mutagenic activity.

Representative PAC structures found in the SRC II HD and the coal tar containing one heteroatom and two heteroatoms are given in Tables 1 and 2, respectively. It is thought that the major reason for the difference between the two samples was auto-catalytic mild hydrogenation in the SRC II process. This would explain the difference in abundance of the amino compounds, hydroxyl PAC, sulfur heterocycles with fusion on only one side of the thiophene ring, 4H-benzo[def]carbazole, etc. The amino and hydroxyl groups in the SRC II HD are thought to be derived from nitrogen and oxygen heterocycles by hydrogenation. The 2- and 3-ring amino-PAH in the SRC II HD were the major components of the amino-PAH fraction, while only the aminonaphthalenes were detected in the coal tar, and then only at a low level (5). Likewise, the aminodibenzothiophenes in the SRC II HD were present as major components, but only the azathiophenic compounds were present in the coal tar (4). Also, the hydroxyphenylthiophenes and the hydroxyphenylbenzothiophenes were more abundant than the hydroxybenzothiophenes and hydroxydibenzothiophenes in the SRC II HD (1). On the other hand, only the hydroxybenzothiophenes and hydroxydibenzothiophenes were present in the coal tar. Figures 3 and 4 show chromatograms of the hydroxyl nitrogen-PAC fractions of both samples. Marked abundances of the hydrogenated compounds, i.e. hydroxyphenylpyridines, was noticeable in the SRC II HD.

Structural similarities between the heteroatom-containing PAC and the PAH were found. Structures of the PAC containing two heteroatoms were similar to those of the PAC containing one heteroatom, and the structures of the PAC containing one heteroatom reflect the parent PAH structures. The relationships between structure and abundance for these compounds are discussed in detail elsewhere (17).

#### ACKNOWLEDGMENT

This work was supported by the Department of Energy, Office of Health and Environmental Research, Contract No. DE-AC02-79EV10237.

#### REFERENCES

1. Nishioka, M., Lee, M. L., Kudo, H., Muchiri, D. R., Baldwin, L. J., Pakray, S., Stuart, J. G. and Castle, R. N. Anal. Chem. 1985, 57, 1327.
2. Nishioka, M., Campbell, R. M., West, W. R., Smith, P. A., Booth, G. M., Lee, M. L., Kudo, H. and Castle, R. N. Anal. Chem. 1985, 57, 1868.
3. Nishioka, M., Campbell, R. N., Lee, M. L., Muchiri, D. R., Stuart, J. G. and Castle, R. N. Anal. Chem. 1985, 57, 2211.

4. Nishioka, M., Smith, P. A., Booth, G. M., Lee, M. L., Kudo, H., Muchiri, D. R., Castle, R. N. and Klemm, L. H. Fuel in press.
5. Nishioka, M., Lee, M. L., and Castle, R. N. Fuel submitted.
6. Refer to references cited in (1)-(5).
7. Later, D. W., Lee, M. L., Bartle, K. D., Kong, R. C. and Vassilaros, D. L. Anal. Chem. 1981, 53, 1612.
8. Kuei, J. C., Shelton, J. I., Castle, L. W., Kong, R. C., Richter, B. E., Bradshaw, J. S. and Lee, M. L. J. High Resolut. Chromatogr. Chromatogr. Commun. 1984, 7, 13.
9. Lee, M. L., Kuei, J. C., Adams, N. W., Tarbet, B. J., Nishioka, M., Jones, B. A. and Bradshaw, J. S. J. Chromatogr. 1984, 302, 303.
10. Jones, B. A., Bradshaw, J. S., Nishioka, M. and Lee, M. L. J. Org. Chem. 1984, 49, 4947.
11. Markides, K. E., Nishioka, M., Tarbet, B. J., Bradshaw, J. S. and Lee, M. L. Anal. Chem. 1985, 57, 1296.
12. Markides, K. E., Chang, H.-C., Schregenberger, C. M., Tarbet, B. J., Bradshaw, J. S. and Lee, M. L. J. High Resolut. Chromatogr. Chromatogr. Commun. in press.
13. Nishioka, M. Jones, B. A., Tarbet, B. J., Bradshaw, J. S. and Lee, M. L. J. Chromatogr. submitted.
14. McCann, J. and Ames, B. N. Proc. Natl. Acad. Sci. 1976, 73, 950.
15. Nishioka, M., Chang, H.-C. and Lee, M. L. Env. Sci. Tech. submitted.
16. Nishioka, M., Lee, M. L. and Castle, R. N. Fuel in press.
17. Nishioka, M. and Lee, M. L. Fuel submitted.
18. Pelroy, R. A., Stewart, D. L., Tominaga, Y., Iwao, M., Castle, R. N. and Lee, M. L. Mutat. Res. 1983, 117, 31.
19. Eastmond, D. A., Booth, G. M. and Lee, M. L. Arch. Environ. Contam. Toxicol. 1984, 13, 105.
20. Pelroy, R. A., Stewart, D. L., Lee, M. L., Pratap, R., Tominaga, Y., Iwao, M., Thompson, R. D. and Castle, R. N. Mutation Res. in press.

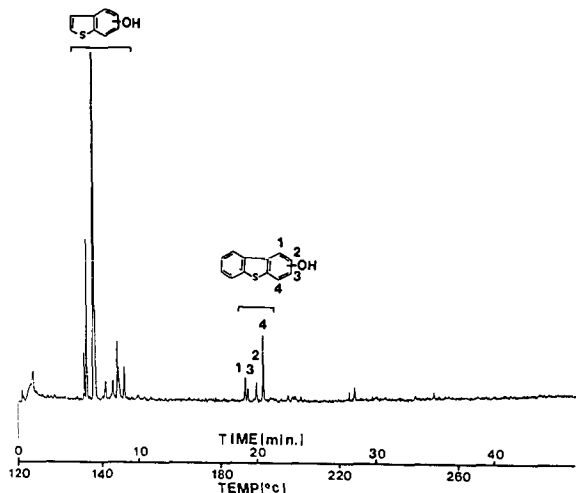


Figure 1. FPD chromatogram of the coal tar A-4 trimethylsilyl derivatized fraction on a 25% biphenyl polysiloxane stationary phase. Conditions: temperature program from 120°C to 265°C at 4°C min<sup>-1</sup>, after an initial 2-min isothermal period; hydrogen carrier gas at 100 cm s<sup>-1</sup>.

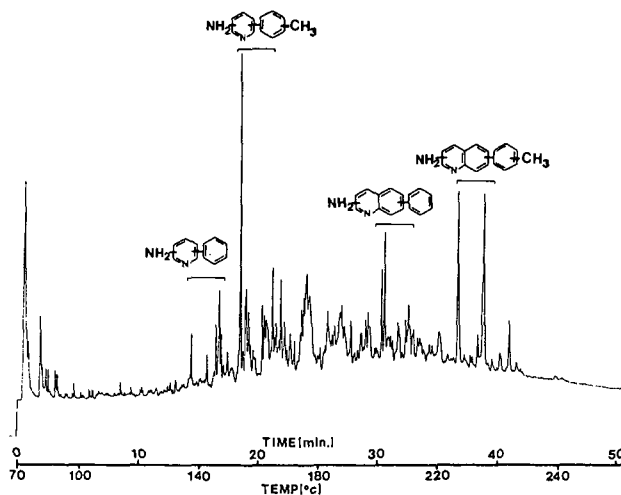


Figure 2. ECD chromatogram of the SRC II HD S-3 PFP derivatized fraction on SE-54. Conditions: temperature program from 70°C to 100°C at 10°C min<sup>-1</sup>, then from 100°C to 265°C at 4°C min<sup>-1</sup> after an initial 2-min isothermal period; helium carrier gas at 50 cm s<sup>-1</sup>.



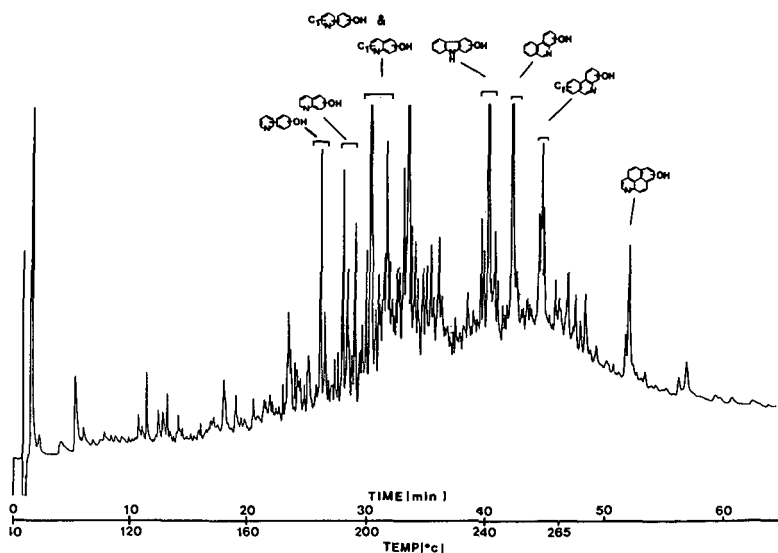


Figure 3. NPD chromatogram of the SRC II HD S-2' fraction on a 25% biphenyl polysiloxane stationary phase. Conditions: temperature program from 40°C to 120°C at 10°C min<sup>-1</sup>, then from 120°C to 265°C at 4°C min<sup>-1</sup>, after an initial 2-min isothermal period; helium carrier gas at 50 cm s<sup>-1</sup>.

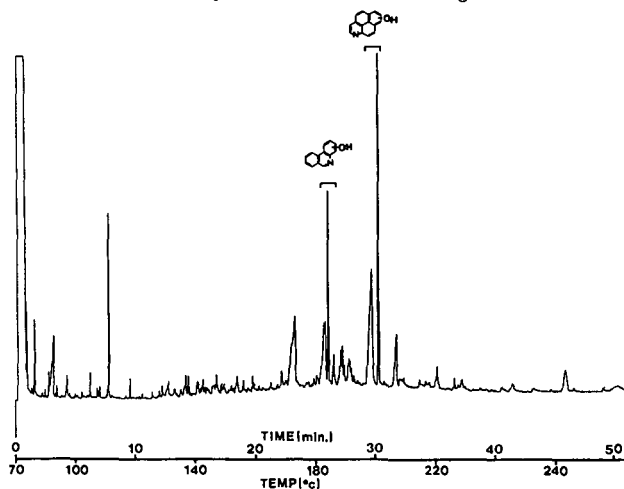


Figure 4. FID chromatogram of the coal tar S-2' fraction on SE-54. Conditions: temperature program from 70°C to 100°C at 10°C min<sup>-1</sup>, then from 100°C to 265°C at 4°C min<sup>-1</sup>, after an initial 2-min isothermal period; hydrogen carrier gas at 100 cm s<sup>-1</sup>.

Table 1. Comparison of the PAC containing one heteroatom identified in the SRC II coal liquid and the coal tar.

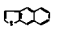
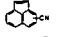
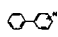
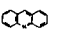
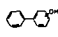
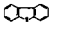
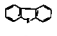
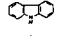
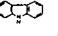
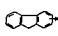
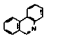

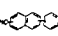
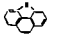
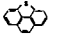
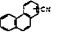
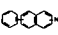
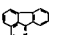
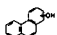
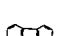
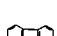
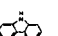
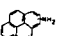
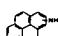
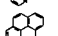
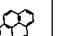
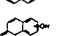
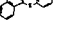


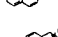
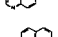
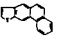

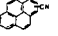



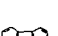
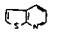
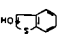
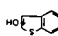
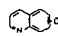
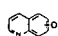
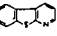
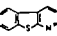
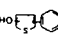
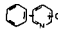
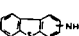

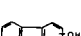
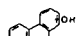
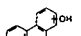
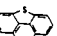
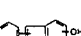
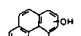
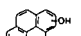
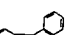
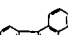
| PASH  |   | N-PAC   |   |   |   |   |   | HPAH  |   |
|---|---|---|---|---|---|---|---|---|---|
|   |   | 2'-PANH   |   | APAH  |   | 3'-PANH   |   |   |   |
| Coal tar  | SRC II  | Coal tar  | SRC II  | Coal tar  | SRC II  | Coal tar  | SRC II  | Coal tar  | SRC II  |
|  | -   |  | -   | -   |  |  | -   | -   |  |
|  |  |  |  | -   |  |  |  | -   |  |
|  |  |  | -   | -   |  |  | -   |  | -   |
|  |  |  | -   |  |  |  |  |  | -   |
|  | -   |  | -   |  |  |  | -   |   |   |
|  |  |  |  |   |   |   |   |   |   |
|  |  |  | -   |   |   |   |   |   |   |

Table 2. Comparison of the PAC containing two heteroatoms identified in the SRC II coal liquid and the coal tar.

| PANSH / APASH   |   | HPASH   |   | HPANH   |   |
|---|---|---|---|---|---|
| Coal tar  | SRC II  | Coal tar  | SRC II  | Coal tar  | SRC II  |
|  | -   |  |  |  |  |
|  |  | -   |  | -   |  |
| -   |  |  |  |  |  |
|  | -   | -   |  |  |  |
|  |  |   |   |   |   |

Classes of Compounds Responsible for Mutagenic and Cytotoxic Activity in  
Tars and Oils Formed During Low BTU Gasification of Coal

R.F. Henderson, W.E. Bechtold, J.M. Benson, G.J. Newton, R.L. Hanson,  
A.L. Brooks, J.S. Dutcher, R.E. Royer, and C.H. Hobbs

Lovelace Inhalation Toxicology Research Institute  
P.O. Box 5890, Albuquerque, NM 87185

Summary

The Lovelace Inhalation Toxicology Research Institute (ITRI), in cooperation with the Morgantown Energy Technology Center (METC), has completed toxicity screening of vapors, liquids and solids formed during operation of an experimental pressurized, stirred-bed, coal gasifier at METC. Vapors collected from the cooled process stream on Tenax resins had no mutagenic activity in the Ames *Salmonella* assay. Dichloromethane extracts of liquids and solids collected from the effluent or process streams were fractionated by gel chromatography into fractions containing mostly aliphatic compounds; neutral polycyclic aromatic hydrocarbons (PAH); polar PAH and heterocyclic compounds; and salts. The polar fraction was partitioned into acids, bases, water soluble compounds and phenols. Bacterial mutagenic activity was highest in the basic fraction with additional activity in the neutral PAHs. Highest cytotoxicity toward both the bacteria and canine alveolar macrophages was in the phenolic fraction. Treatment of the gasifier tars by nitrosation or by acetylation to remove primary aromatic amines (PAA) reduced the bacterial mutagenicity by 50-60%, indicating that some, but not all, of the mutagenicity was due to PAA.

Introduction

The Lovelace Inhalation Toxicology Research Institute (ITRI), working in cooperation with the Morgantown Energy Technology Center (METC), has completed studies to obtain information on the possible inhalation toxicity of airborne effluents associated with low BTU coal gasification (1-4). Such information is needed to enable an improved assessment of potential health risks to man arising from this technology.

The METC coal gasifier is an experimental pressurized, stirred-bed coal gasifier (Figure 1) and differs from commercial fixed-bed producers in its smaller size (1.1 m ID) and its provisions for stirring the bed. The gasifier uses a Lurgi process for low BTU coal gasification using heat, air, steam and coal. The gas cleanup devices are experimental and evolving and are designed to produce a low BTU gas suitable for use in combined cycles with turbines.

The main process stream cleanup devices in use at the time of this research program included a cyclone to remove dust; a humidifier, tar trap and Venturi scrubber to remove tar; a muffler and a flare. Other cleanup devices indicated in Figure 1 were bypassed during sampling periods for this project.

## Experimental

### Sampling

Vapors, liquids, and solids were sampled from both the process and effluent streams. The process stream was sampled at points A, B, C, D, and E (Figure 1) using two sampling systems. An analytical system extracted cooled, diluted process stream material and measured the concentration (by filters), the size of aerosols (by cascade impactors) and the concentration of vapors (by adsorption on Tenax traps). Condensor traps were used to collect larger samples of tars and oils. In addition to the process stream material, bulk quantities of bottom ash from the gasifier, dust from the cyclone, and tar from the humidifier, tar trap and Venturi scrubber were collected.

### Fractionation of Tars and Oils

Tars from the tar scrubbing devices and condensed oils from the process stream were fractionated on Sephadex LH-20 gel columns using tetrahydrofuran (THF) to elute separate fractions containing, 1) mainly aliphatic and polymeric material (F1, F2); 2) neutral polyaromatic hydrocarbons (PAH) (F3, F4); and 3) polar compounds including nitrogen heterocyclic compounds and PAH with polar fractional groups (F5) (See Figure 2). The polar fraction was subfractionated into acidic, basic and neutral components.

### Mutagenicity Testing

The potential mutagenicity of each subfraction was assessed using the Ames Salmonella bacterial mutagenicity assay, using strain TA-98 (detects frame-shift mutations) both with and without addition of liver metabolizing enzymes (S-9). Cytotoxicity toward the bacterial cells and toward canine alveolar macrophages was also measured.

### Effect of Removal of Primary Aromatic Amines (PAA) on Mutagenicity

To determine the contribution of PAA to the mutagenic activity of gasifier tar, the PAA were removed by nitrosation at pH 2.5 or by acetylation. Several PAA, one aza-arene and a coal oil sample from the Fossil Fuels Research Matrix Program, Oak Ridge National Laboratory, were included as control samples. The treated samples were then re-tested for mutagenic activity.

## Results

The vapor phase material collected on Tenax traps did not have mutagenic activity in the bacterial mutagenicity assay used. All tar and oil samples collected from the process or potential effluent streams had mutagenic activity when S-9 metabolizing enzymes were included. The subfractions showing the most activity were the neutral PAH (F3, F4) and the polar fraction (F5) in both process stream samples and the potential effluent material (Tables 1, 2, 3). The basic and neutral portions of the polar fraction had

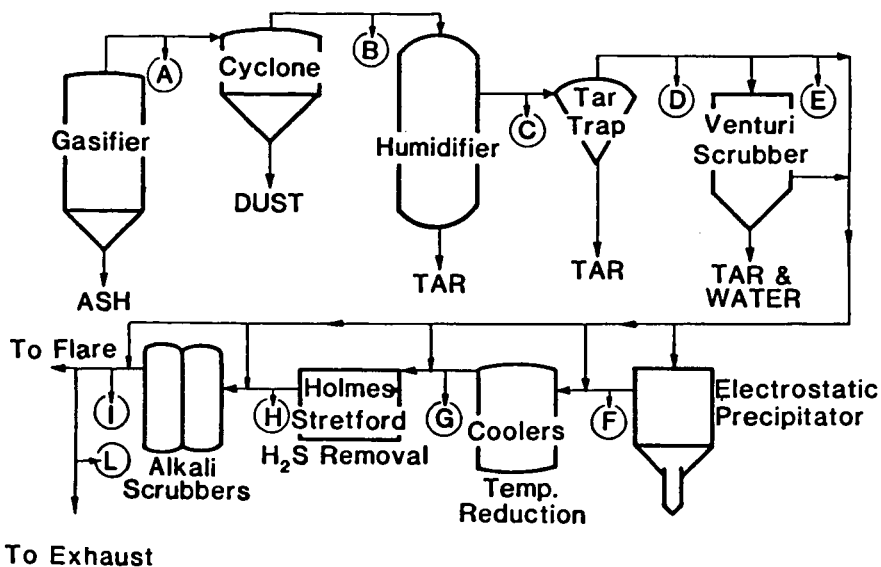


Figure 1. Schematic diagram of the METC low Btu coal gasifier and cleanup system.

#### LH-20 - THF ELUTION PROFILE

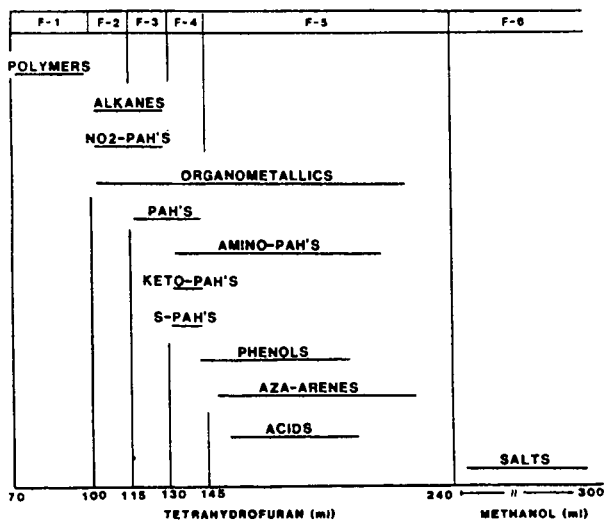


Figure 2. Elution profiles of compounds from Sephadex LH-20 column using tetrahydrofuran (THF) as eluant. The lines for each compound indicate the volume of THF in which the compounds eluted. The dot indicates the center of the elution peak.

TABLE 1

Mutagenic Activity of Process Stream Samples  
and their Sephadex LH-20 Fractions

| <u>Fraction</u>                             | <u>Mass<sup>a</sup><br/>Percent</u> | <u>Revertants<sup>b</sup><br/>per <math>\mu</math>g<br/>(with S-9)</u> | <u>Mutagenicity<sup>c</sup><br/>Percent</u> | <u>Revertants<br/>per L<br/>Process Stream</u> |
|---|-------------------------------------|--|---|--|
| <u>Position B -- Raw Gas</u>                |                                     |  |   |  |
| Crude                                       | 100.0                               | $6.7 \pm 0.6$  | 100   | 50,000   |
| LH-20 Fraction                              |                                     |  |   |  |
| 1   | 27.8                                | $0.7 \pm 0.2$  | 3   | 1,600  |
| 2   | 6.5                                 | $2.8 \pm 0.3$  | 3   | 1,900  |
| 3   | 21.8                                | $10.4 \pm 1.1$   | 39  | 17,000   |
| 4   | 16.7                                | $5.0 \pm 0.6$  | 14  | 6,200  |
| 5   | 21.7                                | $10.4 \pm 1.0$   | 38  | 17,000   |
| 6   | 5.5                                 | $2.8 \pm 0.2$  | 3   | 1,100  |
| <u>Position D -- After Tar Trap</u>         |                                     |  |   |  |
| Crude                                       | 100.0                               | $3.7 \pm 0.2$  | 100   | 9,700  |
| LH-20 Fraction                              |                                     |  |   |  |
| 1   | 35.4                                | 0.0  | 0   | 0  |
| 2   | 8.4                                 | $3.2 \pm 0.4$  | 14  | 700  |
| 3   | 18.6                                | $1.9 \pm 0.6$  | 18  | 900  |
| 4   | 15.6                                | $4.5 \pm 0.4$  | 35  | 1,900  |
| 5   | 15.3                                | $4.1 \pm 0.2$  | 31  | 1,600  |
| 6   | 6.7                                 | $0.5 \pm 0.3$  | 2   | 80   |
| <u>Position E -- After Venturi Scrubber</u> |                                     |  |   |  |
| Crude                                       | 100.0                               | $4.1 \pm 0.3$  | 100   | 2,200  |
| LH-20 Fraction                              |                                     |  |   |  |
| 1   | 7.0                                 | $0.2 \pm 0.2$  | 0   | 10   |
| 2   | 5.0                                 | $2.8 \pm 0.4$  | 6   | 70   |
| 3   | 23.0                                | $1.8 \pm 0.3$  | 24  | 200  |
| 4   | 14.0                                | $2.3 \pm 0.4$  | 18  | 200  |
| 5   | 29.0                                | $2.9 \pm 0.2$  | 49  | 400  |
| 6   | 21.0                                | $0.2 \pm 0.2$  | 3   | 25   |

<sup>a</sup> Mass percent of material fractionated.

<sup>b</sup> TA-98 revertants/ $\mu$ g determined from slope of dose-response curve by linear regression analysis.

<sup>c</sup> Mutagenicity percent is the percent of the mutagenicity each fraction contributes to the crude material.

TABLE 2  
Mutagenic Activity of Process Stream LH-20  
Fractions 5 and their Subfractions

| <u>Fraction</u>                             | <u>Mass<sup>a</sup><br/>Percent</u> | <u>Revertants<sup>b</sup><br/>per <math>\mu</math>g<br/>with S-9</u> | <u>Mutagenicity<sup>c</sup><br/>Percent</u> |
|---|-------------------------------------|--|---|
| <u>Position B -- Raw Gas</u>                |                                     |  |   |
| LH-20 Fraction 5                            | 21.7                                | $9.7 \pm 0.5$  | 100   |
| Acids                                       | 0.9                                 | $1.0 \pm 0.5$  | 1   |
| Bases                                       | 4.1                                 | $5.5 \pm 1.0$  | 20  |
| Neutrals                                    | 1.6                                 | $46.7 \pm 2.6$   | 79  |
| Amphoterics -<br>Water solubles             | 15.2                                | Not tested   | -   |
| <u>Position D -- After Tar Trap</u>         |                                     |  |   |
| LH-20 Fraction 5                            | 15.3                                | $2.1 \pm 0.2$  | 100   |
| Acids                                       | 0.03                                | $0.4 \pm 0.1$  | 0   |
| Bases                                       | 3.8                                 | $4.2 \pm 0.4$  | 50  |
| Neutrals                                    | 4.6                                 | $5.2 \pm 0.3$  | 50  |
| Amphoterics -<br>Water solubles             | 6.6                                 | Not tested   | -   |
| <u>Position E -- After Venturi Scrubber</u> |                                     |  |   |
| LH-20 Fraction 5                            | 29.0                                | $2.3 \pm 0.3$  | 100   |
| Acids                                       | 0.7                                 | 0.0  | 0   |
| Bases                                       | 1.6                                 | $12.4 \pm 0.7$   | 83  |
| Neutrals                                    | 2.1                                 | $2.2 \pm 0.2$  | 17  |
| Amphoterics -<br>Water solubles             | 24.6                                | Not tested   | -   |

<sup>a</sup> Mass percent of material fractionated.

<sup>b</sup> TA-98 revertants/ $\mu$ g determined from slope of dose-response curve by linear regression analysis.

<sup>c</sup> Mutagenicity percent is the percent of the mutagenicity each fraction contributes to the crude material.

TABLE 3  
Mutagenic Activity of Tar Trap Tar and Venturi Scrubber Water  
and their LH-20 Fractions

| <u>Fraction</u>                      | <u>Mass<sup>a</sup></u><br><u>Percent</u> | <u>TA-98 Revertants<sup>b</sup></u><br><u>per <math>\mu</math>g (with S-9)</u> | <u>Mutagenicity<sup>c</sup></u><br><u>Percent</u> |
|--------------------------------------|---|--|---|
| <u>Position B -- Raw Gas</u>         |   |  |   |
| Tar Trap Tar                         | 100                                       | 21.6 $\pm$ 1.8   | 100   |
| LH-20 Fraction                       |   |  |   |
| 1                                    | 16  | 2.9 $\pm$ 0.2  | 2   |
| 2                                    | 18  | 2.9 $\pm$ 0.5  | 2   |
| 3                                    | 34  | 2.5 $\pm$ 0.8  | 3   |
| 4                                    | 14  | 107.0 $\pm$ 49.1   | 60  |
| 5                                    | 14  | 56.6 $\pm$ 8.0   | 32  |
| 6                                    | 3   | 10.2 $\pm$ 0.5   | 1   |
| Venturi Scrubber                     |   |  |   |
| Inlet Water                          |   |  |   |
| Lyophilized (50ml)                   | 100                                       | 0.0  | 0   |
| Venturi Scrubber                     |   |  |   |
| Outlet Water                         |   |  |   |
| Lyophilized (50ml)                   | 100                                       | 1.14 $\pm$ 0.06  | 100   |
| Outlet Water                         |   |  |   |
| Dichloromethane-<br>Solubles (0.07%) | 100                                       | 0.72 $\pm$ (0.18)  | 100   |
| LH-20 Fraction                       |   |  |   |
| 1                                    | 6   | 0.8 $\pm$ 0.2  | 7   |
| 2                                    | 2   | 1.1 $\pm$ 0.3  | 3   |
| 3                                    | 3   | 1.7 $\pm$ 0.3  | 7   |
| 4                                    | 5   | 1.8 $\pm$ 0.4  | 13  |
| 5                                    | 75  | 0.6 $\pm$ 0.2  | 64  |
| 6                                    | 10  | 0.4 $\pm$ 0.2  | 6   |

<sup>a</sup> Mass percent of material fractionated.

<sup>b</sup> TA-98 revertants/ $\mu$ g determined from slope of dose-response curve by linear regression analysis.

<sup>c</sup> Mutagenicity percent is the percent of the mutagenicity each subfraction contributes to the total.



the greatest mutagenicity (Table 2). Nitrosation or acetylation of the tar-trap tar removed some ( 50-60%) of the mutagenic activity (Table 4) but not as much as was removed by similar treatment of a coal oil.

The most cytotoxic fractions of the coals and tars were the polar fractions containing phenols.

#### Discussion

Tars and oils produced during a low BTU coal gasification process were mutagenic toward Salmonella bacteria. The mutagenic activity could be attributed to PAH and to neutral and basic compounds in the polar fraction. In contrast to coal liquids, in which most of the mutagenic activity has been attributed to PAA (5), the mutagenic activity of the tars was reduced by only approximately one-half after treatment to remove PAA.

#### Acknowledgements

The authors acknowledge the extensive technical assistance of members of the ITRI staff and are especially appreciative of the cooperation of Dr. John D. Koroch and other members of the staff at the Morgantown Energy Technology Center. This research was supported by DOE Contract No. DE-AC04-76EV01013.

#### References

1. Benson, J.M., Hill, J.O., Mitchell, C.E., and Carpenter, R.L., Arch. Environm. Contam. Toxicol. 1982, 11, 363-371.
2. Benson, J.M., Mitchell, C.E., Royer, R.E., Clark, C.R., Carpenter, R.L., and Newton, G.J., Arch. Environm. Contam. Toxicol. 1982, 11, 547-551.
3. Benson, J.M., Hanson, R.L., Royer, R.E., Clark, C.R., and Henderson, R.F., Environm. Res. 1984, 33, 396-412.
4. Bechtold, W.E., Dutcher, J.S., Brooks, A.L., and Henderson, R.F., Mutation Res. 1985, 155, 7-16.
5. Pelroy, R.A., and Stewart, D.L., Mutation Res. 1982, 90, 297-308.

TABLE 4  
Mutagenic Activity Remaining After Treatment  
(%)

| <u>Chemical</u>         | <u>Nitrosation</u> | <u>Acetylation</u> |
|-------------------------|--------------------|--------------------|
| 2-Aminoanthracene       | 4                  | 7                  |
| 3-Aminofluoranthene     | 0                  | 20                 |
| 2-Aminofluorene         | 0                  | 21                 |
| 6-Aminochrysene         | 13                 | 6                  |
| 9-Aminophenanthrene     | 0                  | 0                  |
| Phenathridine           | 100                | 86                 |
| Coal oil A <sup>a</sup> | 9                  | 30                 |
| Tar trap tar            | 39                 | 52                 |

<sup>a</sup> Obtained as a comparative research material from the Fossil Fuels Research Matrix Program, Oak Ridge National Laboratory.

## CHEMICAL BASIS FOR PHOTOMUTAGENICITY IN SYNTHETIC FUELS

Christopher P. Selby<sup>1,2</sup>, John Calkins<sup>1,2</sup>, Harry G. Enoch<sup>2,3</sup>,  
Cherylyn W. Wright<sup>4</sup> and Bary W. Wilson<sup>4</sup>

<sup>1</sup>Department of Radiation Medicine  
and

<sup>2</sup>Graduate Center for Toxicology,  
University of Kentucky, Lexington, KY 40536;

<sup>3</sup>Kentucky Center for Energy Research,  
P. O. Box 11888, Lexington, KY 40578;

<sup>4</sup>Biology and Chemistry Department,  
Pacific Northwest Laboratory,  
Richland, WA 99352.

### ABSTRACT

Photomutagens (chemicals that enhance the mutagenicity of near UV-visible radiation) have been detected in a variety of experimental coal- and oil shale-derived synthetic fuels using S.typhimurium strain TA98 and fluorescent light. In this study, photomutagenic activity was measured among synfuel samples that included crude and hydrotreated shale oil, coal oil distillation fractions, and chemical class fractions of coal and shale oils. Photomutagenic activity was found to increase with increasing boiling point and was concentrated in fractions enriched in neutral polycyclic aromatic hydrocarbons (PAH). These results point to high molecular weight neutral PAH constituents as important photomutagenic components among the samples tested. The photomutagenic activities of the materials tested correlate well with the previously reported tumorigenic activities of the same samples on mouse skin but correlate poorly with the previously reported mutagenic activities in the conventional Salmonella/mammalian-microsome mutagenicity test in which neutral PAH fractions were inactive.

### INTRODUCTION

A need currently exists for developing alternative energy technologies such as producing petroleum substitutes from coal and oil shale. However, the elevated risk for skin cancers seen among past coal and shale oil production and maintenance workers (1,2) points to a potential problem that must be addressed by the developing synthetic fuels technologies. The hazards associated with synfuel processes and materials should be identified and minimized prior to commercial production. Accurate toxicological data is, therefore, needed for risk assessment purposes. In addition, inexpensive and rapid tests that can predict tumor initiating, tumor promoting, co-carcinogenic and anticarcinogenic activities among synfuel samples are needed due to the potentially large number of feedstocks, conversion processes and process streams.

The S. typhimurium histidine reversion bioassay (the Ames assay) (3,4) utilizing strain TA98 and a rat liver enzyme preparation has been only partially successful as a short-term bioassay for detecting tumor initiators and/or complete carcinogens in synfuels as mutagens. Although positive correlations between the microbial mutagenicity and the relative tumor initiating capacity of synfuels and related materials have been observed (5,6), "false negatives" have been reported. For example, a hydrotreated Paraho shale oil has been reported to be carcinogenic (7-10) but not mutagenic

(9-12). Microbial mutagens and carcinogens have both been reported to be concentrated in the highest boiling distillation fractions from synthetic fuels (5, 12-19). However, the microbial mutagenicity of synfuel chemical class fractions has been found to reside primarily in fractions enriched in amino-substituted polycyclic aromatic compounds (20,21). Neutral polycyclic aromatic hydrocarbon-enriched synfuel fractions, which have shown relatively high carcinogenic activity, have demonstrated little or no microbial mutagenicity (17,22). Based upon these latter results, Holland *et al.* (22) have suggested that with synfuels, the "apparent correlation between Ames mutagenicity and mammalian skin tumorigenicity may be due to the coincidental occurrence of two dissimilar classes of molecules."

Coal- and shale-derived liquids have been known to possess potent phototoxic properties for many years (i.e., they enhance the lethality of non-ionizing radiation) (23). In addition, a positive correlation has been reported to exist between the phototoxic and carcinogenic activities of polycyclic aromatic compounds (24-27). More recently, a number of synfuel materials have been shown to possess photomutagenic activity, i.e., the ability to enhance the mutagenicity of non-ionizing radiation (11,28-34). However, the significance of this photomutagenic activity towards potential occupational hazards and the role of photomutagens in effects seen in mammals are not yet clear. In an effort to determine the chemical nature of photomutagens in synthetic fuels and to determine the relationship between photomutagenic and carcinogenic activities, we have begun testing synfuel fractions (isolated based upon boiling point and chemical class) that have been chemically characterized and tested for skin tumor initiating capacity. We report here our progress to date and preliminary conclusions.

## MATERIALS AND METHODS

### Samples

Samples included coal-derived materials from the Solvent Refined Coal-I (SRC-I) and SRC-II processes. An SRC-II blend of recycle process solvent and atmospheric flash column bottoms was collected at the Harmarville, PA process development unit and was distilled by Gulf Science and Technology Co. into the following boiling point cuts (°F): 300-700, 700-750, 750-800, 800-850, and 850+. An SRC-I process solvent was collected from the Wilsonville, AL pilot plant operated by Catalytic, Inc. and Southern Company Services and was distilled by Air Products, Inc. (Linwood, PA) into boiling point cuts which included an 800°F+ cut, the only SRC-I cut used in this study. (Sample descriptions are summarized in ref. 17).

A crude Paraho shale oil and a hydrotreated Paraho shale oil were obtained from the Oak Ridge National Laboratory Synfuels Research Materials Repository (Repository ref. # 4601 and 4602, respectively). The crude shale oil was produced by the Paraho Development Corp. at Anvil Points, CO and hydrotreated at Sohio's Toledo (OH) refinery. The densities of these samples are reported to be 0.917 g/ml (crude) and 0.842 g/ml (hydrotreated) (44). A more complete description of the shale oil samples is available in ref. 35.

The coal oil and shale oil samples were acquired from pilot plant or process development unit test facilities and should not

necessarily be considered to be representative of synthetic fuel materials that may eventually be produced at commercial-scale facilities.

#### Chemical Class Separation

The hydrotreated Paraho shale oil sample was chemically fractionated prior to bioassay using the procedure of Later *et al.* (36). The separation procedure involved adsorption of approximately 0.1-0.2 g of sample onto 3 g of neutral alumina, packing the alumina onto 6 g of fresh alumina, and successive elution with hexane (fraction A1), benzene (A2), chloroform:ethanol (99:1)(A3) and 10% ethanol in tetrahydrofuran (A4) to give fractions enriched in aliphatic hydrocarbons, polycyclic aromatic hydrocarbons (PAH), nitrogen-containing polycyclic aromatic compounds (NPAC) and hydroxy-substituted polycyclic aromatic compounds (HPAC), respectively. The coal-derived samples were fractionated using a slightly modified procedure which has been routinely used at Pacific Northwest Laboratory to generate fractions for chemical and biological analysis. The alumina was activated by storing at 150°C, the water content of the alumina was maintained at approximately 1.5% and methanol replaced ethanol:tetrahydrofuran as the final eluent. Also, the sample-adsorbed (3g) and fresh alumina (11g) were solvent-packed with hexane (37,38). It should be noted that oxygen and sulfur heterocyclic compounds elute primarily with the neutral PAH-enriched fraction (A2) using these procedures (36).

#### Preparation of Samples for Photomutagenicity Testing

Synfuel samples were diluted and mixed in DMSO (Sigma, Grade 1) prior to bioassay. Most of the materials tested, including the A2-A4 chemical class fractions, were completely soluble in DMSO; however, when some of the coal oil distillate cuts were diluted in DMSO, a small amount of insoluble material was observed. A considerable portion of the crude and hydrotreated shale oils appeared to be DMSO-insoluble. In all cases the DMSO-insoluble components had the same appearance (waxy, aggregating particles) as the aliphatic hydrocarbon fractions (A1) diluted in DMSO. The insoluble materials present in the DMSO preparations of the SRC crude distillate cut materials and the shale oils were assumed to be the aliphatic hydrocarbon components. The aliphatic hydrocarbon fraction weight percent compositions of the SRC-II 300-700°F, 700-750°F, 750-800°F, 800-850°F and 850°F+ distillates have been reported to be 32, 15, 15, 4 and 2%, respectively (39). The crude and hydrotreated Paraho shale oils have been reported to contain 45 and 16% DMSO-extractable material, respectively (29). An aqueous solution of an aliphatic hydrocarbon-enriched (A1) fraction was prepared using the detergent Tween 80 (Sigma) and methods previously described (40-42). In brief, an aqueous preparation was made with the A1 fraction at 2 mg/ml and 20% (v/v) Tween 80 in distilled water. Bacterial suspensions were exposed to the test substances by adding 0.1 ml of the aqueous or DMSO preparation to 3.9 ml of bacterial suspension, giving final treatment concentrations of either 2.5% DMSO (v/v) or 0.5% Tween 80 (v/v). In treatments with DMSO preparations having an insoluble aliphatic hydrocarbon component, the actual oil concentration in solution would be reduced in proportion to the amount of DMSO-insoluble (aliphatic) material present.

## Bioassay

Photomutation assay procedures were performed essentially as described previously (11) and were slight modifications of the method of Ames et al. (3) and Maron and Ames (4). Suspensions of Salmonella containing  $1-2 \times 10^9$  cells/ml in phosphate buffer (0.1 M, pH 7.4) were untreated or treated with 1) fluorescent radiation, 2) test substance (in the dark), or 3) fluorescent radiation and test substance, concurrently. Fluorescent radiation was from General Electric and Philips (Westinghouse) 15 Watt cool white fluorescent tubes with an irradiance to the suspensions of  $18 \text{ W/m}^2$ . (The irradiance was  $17 \text{ W/m}^2$  in tests of the unfractionated shale oils.) Following predetermined durations of exposure to test substance and/or radiation, 0.1 ml volumes of treated suspensions were removed for measurements of mutation (as reversion to histidine prototrophy) or survival. Histidine reversion was measured using the plate incorporation method (3) with top agar supplemented with 0.1 ml of nutrient broth and insufficient histidine for growth of non-revertants to macroscopic colonies. Survival was measured following dilution in nutrient broth by plating 0.1 ml volumes using the plate incorporation method (3) with top agar supplemented with 0.15 ml of 0.1 M histidine HCl (Sigma). Strain TA98 was used in all experiments.

The Salmonella/mammalian-microsome test procedure of Ames et al. (3) and Maron and Ames (4) was used with minor modifications as described in ref. 33. Strain TA98 was used in all experiments.

Revertant and surviving colonies were counted following 2-3 days incubation at  $37.5^\circ\text{C}$ . The spontaneous number of revertants/plate observed in the absence of treatment was subtracted from revertant/plate values observed on mutation assay plates to give corrected revertant/plate values for each treatment. Based upon the number of corrected revertants/plate and the corresponding number of survivors for each treatment, the mutation frequency response (in revertants/ $10^9$  survivors) was calculated by the method of Green and Muriel (43). The mutation frequency response to fluorescent light (in the absence of test substance) was subtracted from the mutation frequency responses to light and test substances to give the corrected revertants/ $10^9$  survivors (plotted in the text figures). Text Figures 2 and 3 and Tables 1 and 2 give means and standard deviations for values obtained from multiple, independent experiments (where they can be plotted).

## RESULTS

### Effect of Hydrotreatment on the Mutagenicity of Shale Oil

Crude and hydrotreated Paraho shale oil samples were tested for mutagenicity 1) in the Salmonella/mammalian-microsome test and 2) in the photomutation assay. When the parent crude and hydrotreated oils were tested in the Salmonella/mammalian-microsome test in the absence of microsomal enzymes and in the photomutation assay in the absence of light, mutagenic responses to the oils were not detected; direct-acting mutagens were not detected in either oil. When the oils were tested using a microsomal enzyme preparation (S9), the results shown in Figure 1 were obtained. These results (Fig. 1) are in agreement with other studies (9-10,12) in showing that the crude Paraho shale oil is mutagenic and the hydrotreated shale oil is not detectably mutagenic towards Salmonella when tested in the presence

of rat liver microsomal enzymes (i.e., the Ames assay). Slope values (revertants/ug) for the responses shown in Figure 1 were calculated using data from initial linear regions of dose-response curves and are given in Table 1 (in the "Ames assay" column).

The photomutagenic responses of *Salmonella* suspensions to fluorescent light plus either the crude shale oil or the hydrotreated product oil are shown in Figure 2. The shale oils were tested at several concentrations and the mutation frequency responses are plotted in Figure 2 as a function of the product of shale oil concentration times duration of irradiation. The apparent dependency of the photomutagenic responses on the product of oil concentration times light exposure demonstrates a form of "reciprocity" of oil and light doses on the photomutagenic response, a phenomenon observed previously with an Eastern U.S. shale oil sample (34). The responses shown in Figure 2 were normalized to reflect the response to 100 ug/ml and slope values for linear fits of the mutation frequency responses as a function of minutes irradiated are given in Table 1. Based upon these slope values, hydrotreatment reduced photomutagenicity by approximately 78%.

#### Photomutagenicity of Hydrotreated Paraho Shale Oil Chemical Class Fractions

Column chromatography of the hydrotreated Paraho shale oil on neutral alumina (as described in refs. 36-38) yielded fractions termed A1, A2, A3 and A4 which were enriched in aliphatic hydrocarbons, neutral polycyclic aromatic hydrocarbons (PAH), nitrogen-containing polycyclic aromatic compounds (NPAC), and hydroxy-substituted PAC (HPAC) respectively. Fractions from several chemical class fractionations were bioassayed; the total recovery of material eluted by alumina column chromatography was >84%. The percentage of the original material recovered in each fraction was: A1, 70-71%; A2, 10-11%; A3, 1%; and A4, 2-10%. (Values represent the range of recoveries from multiple determinations.) These results are in reasonably good agreement with values reported for a different separation procedure; i.e., 66.5% saturates, 9.8% PAH, 5.4% NPAC, 0.9% polars and 82.6% total recovery (45). The differences in recoveries of polar compounds may reflect an effect of alkyl substitutions (alkylation resulting in part from hydrotreatment) on chemical class separation schemes based upon the polarity of the sample. The A2-A4 fractions were each tested for photomutagenicity using 100 ug/ml; the mutation frequency responses are shown in Figure 3. Figure 3 shows that the A2 fraction was the most photomutagenic fraction, although all three fractions were active. The recovery of fraction A4 from the shale oil was highly variable (2-10%). The photomutagenicity of the A4 fraction was generally lower when the recovery of fraction A4 was low and the data for fraction A4 plotted in Figure 3 are from an A4 fraction in which high recovery was obtained. Slope values for mutation frequency responses as a function of minutes irradiated are given in Table 1.

#### Photomutagenicity of Coal Oils as a Function of Boiling Point Range

SRC-II distillation cuts having different boiling point ranges were tested for photomutagenic activity using 50 ug/ml of each oil (less the DMSO-insoluble component, see Materials and Methods). Slope values for mutation frequency responses as a function of minutes irradiated are given in Table 2. The data show a trend towards higher photomutagenic activity with increasing boiling point of the

material tested. In the absence of fluorescent light irradiation, the same SRC-II cuts were not detectably mutagenic, except the 800-850°F cut, which gave responses that were suggestive of a very low level of direct-acting (non-photosensitized) mutagenic activity. Treatment with 100 ug/ml of the 800-850° cut for two hours in the dark resulted in 34 revertants per plate above background.

#### Photomutagenicity of Coal Oil Chemical Class Fractions

The SRC-II 800-850° distillation cut was also separated into chemical class fractions by column chromatography on neutral alumina. Fractions from several separations were bioassayed; in these separations total recovery was  $\geq 98\%$ . The percentage of the original material recovered in each fraction was: A1, 3-4%; A2, 54-55%; A3, 23-25%; and A4, 17%; values that are in reasonable agreement with previously reported values (17,39,46). Fractions were prepared for bioassay as solutions in DMSO except fraction A1, which was insoluble in DMSO and was prepared as a DMSO "slurry" and as an aqueous solution with Tween 80. The slope values representing the mutation frequency response to fractions A1-A4 as a function of minutes irradiated are given in Table 2. The A2 fraction was clearly the most photomutagenic fraction; the A3 fraction was also photomutagenic, but the A1 fraction was inactive when tested either as a DMSO slurry or as an aqueous preparation with Tween 80. The A4 fraction was only slightly active or inactive. The SRC-II A1-A4 fractions were not detectably mutagenic when tested in the dark, except fraction A3, which induced 34 revertants per plate above background following two hours of exposure.

An SRC-I 800°+ distillate was also separated into fractions A1-A4; however, only the A2 fraction was soluble in the bioassay system. The A2 fraction was tested in a preliminary experiment (data not shown) and found to have no detectable mutagenicity in the dark; however, in the presence of light the A2 fraction was highly photomutagenic, showing a level of activity similar to that induced by the A2 fraction of the SRC-II 800-850° cut (Table 2).

#### DISCUSSION

Although a relatively limited number of samples have been tested, our data suggest that high boiling point components in the PAH-enriched fraction are the determinant chemical photomutagen(s) in synthetic fuels. Substantial photomutagenicity was also measured in coal oil and shale oil NPAC fractions and the HPAC shale oil fraction. The HPAC and aliphatic hydrocarbon fractions isolated from the SRC materials were relatively inactive. Strniste et. al. (31) has reported similar results in which essentially all the photomutagens (measured using cultured mammalian cells) present in a shale oil retort by-product water partitioned into a base- and neutral-enriched fraction.

Chemical analyses of PAH present in the materials tested are available in the literature (e.g., 17,18,45). Numerous PAH have been identified among the samples tested, including a variety of four- and five-ring compounds and alkyl derivatives thereof, and carcinogens such as benzo(a)anthracene, methylchrysenes, benzo(a)fluoranthene and benzo(a)pyrene. It is not yet known which compounds present in the PAH fractions were responsible for photomutagenic activity. Benzo(a)pyrene has been reported to be photomutagenic in cultured mammalian cells (32) and UV radiation can enhance (and



inhibit) the carcinogenic response of mammalian cells to benzo(a)pyrene (47). The occurrence of carcinogens and mutagens such as benzo(a)pyrene in samples that were not mutagenic with enzyme activation (SRC-II 800-850° A2 fraction, SRC-I 800°+ A2 fraction, hydrotreated Paraho shale oil, see Tables 1 and 2) suggests the presence of antimutagens in these samples. Haugen and Peak (48) have shown that undefined components can inhibit the microsomal enzyme activation of mutagens in coal liquids. Some heteroatomic compounds can also be expected to be present in the A2 fractions. For example, an SRC-II heavy distillate (from which the 800-850°F cut was in part derived) has been shown to contain three and four ring thiophene analogs, as well as dibenzofuran and methyl dibenzofuran (30). Nitrogen heterocyclics identified in the hydrotreated Paraho shale oil include alkylated and unsubstituted carbazoles, benzocarbazole(s), and azapyrene(s) (36). The NPAC fraction of the SRC-II 800-850°F cut has been reported to contain a high concentration of benzo(a)carbazole (20.5 mg/g) and lower amounts of azapyrenes, 2-azafluoranthene, and numerous amino-substituted PAH (17).

This study was conducted in part to determine the relationship between mutagenic and carcinogenic activities in complex mixtures such as synthetic fuels. Tables 1 and 2 give data indicative of carcinogenicity, photomutagenicity, and mutagenicity in the presence of microsomal enzymes (Ames assay) for shale oil (Table 1) and coal oil (Table 2) materials. Both the crude and hydrotreated Paraho shale oil samples have been reported to be carcinogenic following chronic dermal applications to mouse skin. Hydrotreatment was reported to reduce but not eliminate carcinogenicity (7-10), and the carcinogenic potencies of the crude and hydrotreated Paraho shale oils given in Table 1 are relative to the response to benzo(a)pyrene (8). The carcinogenic potencies of the coal oil materials given in Table 2 were derived from chronic and/or initiation-promotion (IP) mouse skin painting tests. The carcinogenicity results and the mutagenicity with enzyme activation (i.e., Ames assay results using strain TA98) for the coal oils (Table 2) have been normalized to give responses relative to the response to an SRC-II heavy distillate, arbitrarily given a value of 100 (39).

A comparison of the carcinogenic and mutagenic activities given in Tables 1 and 2 should be approached with caution. The data in Tables 1 and 2 were to some degree derived by procedures that provide estimates and different analyses were apparently used to arrive at the carcinogenicity values given for the shale oils, the SRC-II distillates and the SRC-II 800-850° chemical class fractions. A cautious approach for comparing the bioassay results would be to consider only whether a test substance produced positive or negative results. The most obvious discrepancy between assays was observed with the SRC-II 800-850° A2 fraction (Table 2), which was highly carcinogenic and highly photomutagenic but was not mutagenic with enzyme activation. Similarly, an SRC-I 800°+ A2 fraction (not shown in Table 2) was observed to be highly carcinogenic in the initiation-promotion test (49), highly photomutagenic in a preliminary test (see Results), but not mutagenic with enzyme activation (19). The hydrotreated Paraho shale oil (Table 1) was also found to be positive for carcinogenicity and photomutagenicity but not mutagenic with enzyme activation (9,10,12, Table 1), although one study (50) reported a low level of enzyme-mediated mutagenicity (0.24 revertants/ug) for this sample. The SRC-II 300-700° cut (Table 2) elicited an apparently "false positive" response, being apparently

negative for carcinogenicity and photomutagenicity but positive for enzyme-mediated mutagenicity. Another report (51) also found this sample to be mutagenic with enzyme activation, although two others (18,46) did not. Of the remaining samples, the crude Faraho shale oil, the SRC-II 700-750<sup>0</sup>, 750-800<sup>0</sup>, and 800-850<sup>0</sup> cuts and the 800-850<sup>0</sup> A3 fraction were all positive for carcinogenicity, photomutagenicity, and mutagenicity with enzyme activation; the SRC-II 800-850<sup>0</sup> A1 and A4 fractions were all negative in the three bioassays or gave responses that were suggestive of a low level of activity.

In summary, of 11 samples that have been tested for carcinogenicity, photomutagenicity and enzyme-mediated mutagenicity, in 7 cases there was agreement between all three assays and in 4 cases the photomutagenicity data was in better qualitative agreement with carcinogenicity than were the mutagenicity data obtained using enzyme activation. The strong agreement between photomutagenicity and carcinogenicity among the synfuel materials could be coincidental. However, the agreement is sufficiently extensive to consider possible fundamental underlying relationships. It is possible that animals exposed to the synfuels were also exposed to significant amounts of environmental radiation (such as fluorescent room light), and the positive correlation shown in Table 2 may reflect a mediation of coal oil-induced tumorigenesis by photochemical processes. Alternatively, photosensitized effects caused by chemicals such as those present in synthetic fuels may have served as a selective pressure for the evolution of the enzymes that degrade photosensitizers and apparently have a role in FAC-induced carcinogenesis. It is also possible that photomutagenesis and carcinogenesis by FAC synfuel components proceed by the same mechanism(s). One possible common mechanism could involve the participation of reactive oxygen species such as superoxide anion, which is generated 1) by endogenous cellular chromophores when irradiated with near UV light (52), 2) in human lungs in response to chronic tobacco smoke exposure (53), and 3) possibly also in mouse skin following treatment with synfuel materials.

#### ACKNOWLEDGEMENTS

We wish to thank Ms. Rebecca A. Meacham for her excellent secretarial assistance. This work was supported by grants from the Kentucky Energy Cabinet.

#### REFERENCES

1. Sexton, R. J. (1960) Arch. Environ. Health **1**, 208.
2. Furde, M. and M. Rahu (1979) Environ. Health Perspect. **30**, 209.
3. Ames, B. N., J. McCann and E. Yamasaki (1975) Mutat. Res. **31**, 347.
4. Maron, D. M. and B. N. Ames (1983) Mutat. Res. **113**, 173.
5. Calkins, W. H., J. F. Deye, R. W. Hartgrove, C. F. King and D. F. Krahn (1983) Fuel **62**, 857.
6. Holland, J. M., R. O. Rahn, L. H. Smith, B. R. Clark, S. S. Chang and T. J. Stephens (1979) J. Occup. Med. **21**, 614.
7. Lewis, S. C. (1981) in ref. 35, p. 123.
8. Holland, J. M., G. C. Gipson, M. J. Whitaker, T. J. Stephens, G. M. Clemmer and D. A. Wolf (1981) in ref. 35, p. 97.
9. Holland, L. M., C. G. Stafford and S. K. Bolen (1981) The Los Alamos Life Sciences Division's Biomedical and Environmental

- Research Programs: Status Report, LA-8948-PR, Los Alamos Scientific Laboratory, Los Alamos, NM, p. 48.
10. Schultz, T. W., H. Witschi, L. H. Smith, W. M. Haschek, J. M. Holland, J. L. Epler, R. J. M. Fry, T. K. Rao, F. W. Larimer and J. N. Dumont (1981) Health Effects Research in Oil Shale Development, ORNL/TM-8034, Oak Ridge National Laboratory, Oak Ridge, TN.
  11. Selby, C. P., J. Calkins and H. G. Enoch (1986) Environ. Res. 39 (in press).
  12. Guerin, M. R., I. R. Rubin, T. K. Rao, B. R. Clark and J. L. Epler (1981) Fuel 60, 282.
  13. Holland, J. M. (1981) in Life Sciences Synthetic Fuels Semi-annual Progress Report for the Period Ending June 30, 1981 (K. E. Cowser, ed.) ORNL/TM-7926, Oak Ridge National Laboratory, Oak Ridge, TN, p. 79.
  14. Heuper, W. C. (1956) Ind. Med. Surg. 25, 51.
  15. Mahlum, D. D. (1983) J. Appl. Tox. 3, 31.
  16. Mahlum, D. D. (1983) J. Appl. Tox. 3, 254.
  17. Wright, C. W., D. W. Later, D. D. Dauble and B. W. Wilson (1985) Fractionally Distilled SRC-I, SRC-II, EDS, H-Coal and ITS Direct Coal Liquefaction Process Materials: A Comparative Summary of Chemical Analysis and Biological Testing, PNL-5528, Pacific Northwest Laboratory, Richland, WA.
  18. Pelroy, R. A., M. E. Frazier, D. W. Later, C. W. Wright and B. W. Wilson (1985) Fuel 64, 639.
  19. Wilson, B. W., R. A. Pelroy and D. D. Mahlum (1982) Chemical Characterization and Genotoxic Potential Related to Boiling Point for Fractionally Distilled SRC-I Coal Liquids, PNL-4277, Pacific Northwest Laboratory, Richland, WA.
  20. Guerin, M. R., C. -H. Ho, T. K. Rao, B. R. Clark and J. L. Epler (1980) Environ. Res. 23, 42-53.
  21. Wilson, B. W., R. Pelroy and J. T. Cresto (1980) Mutat. Res. 79, 193-202.
  22. Holland, J. M., F. W. Larimer, T. K. Rao, J. L. Epler, C. -H. Ho, M. V. Buchanan and M. R. Guerin (1984) J. Appl. Tox. 4, 117.
  23. Mottram, J. C. and I. Doniach (1938) Lancet 234, 1156.
  24. Doniach, I. (1939) Brit. J. Exp. Path. 20, 227.
  25. Epstein, S. S., M. Small, H. L. Falk and N. Mantel (1964) Cancer Res. 24, 855.
  26. Malling, H. V. and E. H. Y. Chu (1970) Cancer Res. 30, 1236.
  27. Morgan, D. D. and D. Warshawsky (1977) Photochem. Photobiol. 25, 39.
  28. Strniste, G. F. and D. J. Chen (1981) Environ. Mutagenesis 3, 221.
  29. Strniste, G. F., J. M. Bingham, R. T. Okinaka and D. J. Chen (1982) Tox. Let. 13, 163.
  30. Strniste, G. F., D. J. -C. Chen and R. T. Okinaka (1982) JNCI 69, 199.
  31. Strniste, G. F., J. M. Bingham, W. D. Spall, J. W. Nichols, R. T. Okinaka and D. J. -C. Chen (1983) in Short-Term Bioassays in the Analysis of Complex Mixtures III, (M. D. Waters, S. S. Sandhu, J. Lewtas, L. Claxton, N. Chernoff and S. Nesnow, eds.) Plenum Press, New York, NY p. 139.
  32. Barnhart, B. J. and S. H. Cox (1980) Mutat. Res. 72, 135.
  33. Selby, C., J. Calkins and H. Enoch (1983) Mutat. Res. 124, 53.
  34. Selby, C., J. Calkins and H. G. Enoch (1984) Photochem. Photobiol. 40, 329.
  35. Griest, W. H., M. R. Guerin and D. L. Coffin (eds.) Health Effects Investigation of Oil Shale Development, 1981, Ann Arbor Science, Ann Arbor, MI.

36. Later, D. W., M. L. Lee, K. D. Bartle, R. C. Kong and D. L. Vassilaros (1981) Anal. Chem. **53**, 1612.
37. Later, D. W. and M. L. Lee (1983) in Advanced Techniques in Synthetic Fuels Analysis (C. W. Wright, W. C. Weimer and W. Dale Felix, eds.) Technical Information Center, Springfield, VA, p. 44.
38. Later, D. W., B. W. Wilson and M. L. Lee (submitted) Anal. Chem.
39. Mahlum, D. D., M. E. Frazier, R. A. Pelroy and R. A. Renne (1983) Comparison of In Vitro and In Vivo Studies with Coal Liquids from the SRC-II Process, PNL-4836, Pacific Northwest Laboratory, Richland, WA.
40. Hermann, M., O. Chaude, N. Weill, H. Bedouelle and M. Hofnung (1980) Mutat. Res. **77**, 327.
41. Lockard, J. M., J. W. Prater, C. J. Viau, H. G. Enoch and P. S. Sabharwal (1982) Mutat. Res. **102**, 221.
42. Ma, C. Y., C. -H. Ho, R. B. Quincy, M. R. Guerin, T. K. Rao, B. E. Allen and J. L. Epler (1983) Mutat. Res. **118**, 15.
43. Green, M. H. L. and W. J. Muriel (1976) Mutat. Res. **38**, 3.
44. Griest, W. H., M. R. Guerin, L. B. Yeatts and B. R. Clark (1981) in ref. 35, p. 27.
45. Robbins, W. K. and S. C. Blum (1981) in ref. 35, p. 45.
46. Pelroy, R. A. and B. W. Wilson (1981) Fractional Distillation as a Strategy for Reducing the Genotoxic Potential of SRC-II Coal Liquids: A Status Report, PNL-3787, Pacific Northwest Laboratory, Richland, WA.
47. Santamaria, L., G. G. Giordano, M. Alfisi and F. Cascione (1966) Nature **210**, 824.
48. Haugen, D. A. and M. J. Peak (1983) Mutat. Res. **116**, 257.
49. Mahlum, D. D., C. W. Wright, E. K. Chess and B. W. Wilson (1984) Cancer Res. **44**, 5176.
50. Timourlian, H., A. Carrano, J. Carver, J. S. Felton, F. T. Hatch, D. S. Stuermer and L. H. Thompson (1981) in ref. 29, p. 173.
51. Later, D. W., R. A. Pelroy, D. D. Mahlum, C. W. Wright, M. L. Lee, W. C. Weimer and B. W. Wilson (1982) in Polynuclear Aromatic Hydrocarbons: Seventh International Symposium on Formation, Metabolism and Measurement (M. W. Cook and A. J. Dennis, eds.), Battelle Press, Columbus, OH, p. 771.
52. Cunningham, M. L., J. S. Johnson, S. M. Giovanazzi and M. J. Peak (1985) Photochem. Photobiol. **42**, 125.
53. Hoidal, J. R., R. B. Fox, P. M. LeMarbe, R. Perri and J. E. Repine (1981) Am. Rev. Resp. Dis. **123**, 85.

Table 1. Carcinogenicity and Mutagenicity of Shale Oils

| Material  | Carcinogenicity <sup>a</sup><br>(chronic test) |                 | Mutagenicity      |                            |
|---|--|-----------------|-------------------|----------------------------|
|   |  |                 | Ames <sup>b</sup> | Photomutation <sup>c</sup> |
| Crude Paraho Shale Oil                                  |  | 1/998           | 3.7±0.1           | 45±20                      |
| Hydrotreated<br>Paraho Shale Oil                        |  | 1/2780          | -0.0004±0.0009    | 10±1.7                     |
| Hydrotreated<br>Paraho Shale<br>Oil Chemical<br>Classes | A2   | ND <sup>d</sup> | ND                | 48±9.0                     |
|   | A3   | ND              | ND                | 39±8.2                     |
|   | A4   | ND              | ND                | 32±7.8                     |

<sup>a</sup>From ref. 8, carcinogenic potencies relative to benzo(a)pyrene.

<sup>b</sup>This study, revertants/ug oil.

<sup>c</sup>This study, revertants/10<sup>9</sup> survivors/minute irradiated, 100 ug/ml tested or normalized to give responses to 100 ug/ml.

<sup>d</sup>ND-not determined.

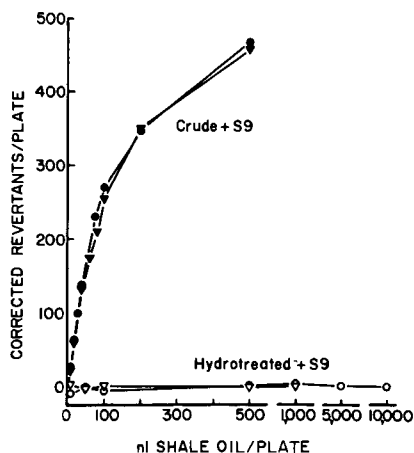


Figure 1. Mutagenicity of crude (closed symbols) and hydrotreated (open symbols) Paraho shale oils tested in two separate experiments (circles and triangles) with a microsomal enzyme preparation (S9).

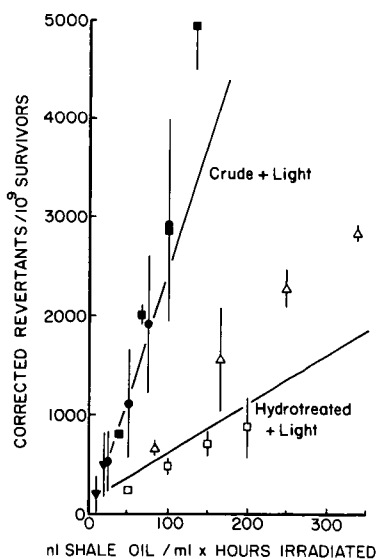


Figure 2. Photomutagenicity of crude (closed symbols) and hydrotreated (open symbols) Paraho shale oils tested using 10 (▽), 50 (○), 100 (□), or 250 (△) nl oil/ml.

Table 2. Carcinogenicity and Mutagenicity of SRC-II Distillates and Chemical Classes

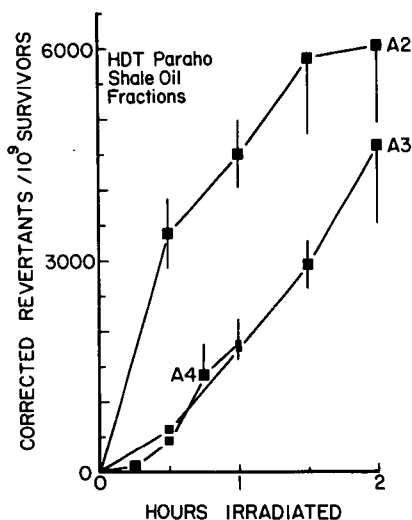
| Material              | Relative Carcinogenicity |                       | Relative Mutagenicity |                            |
|-----------------------|--------------------------|-----------------------|-----------------------|----------------------------|
|                       | IP <sup>a</sup>          | Chronica <sup>a</sup> | Ames <sup>a</sup>     | Photomutation <sup>b</sup> |
| Distillates:          |                          |                       |                       |                            |
| Heavy distillate      | 100                      | 100                   | 100                   | ND                         |
| 300-700°F             | 0                        | 0                     | 70                    | 2.0 $\pm$ 2.3              |
| 700-750°F             | 18                       | 87                    | 95                    | 12 $\pm$ 9.3               |
| 750-800°F             | 14                       | 120                   | 138                   | 15 $\pm$ 3.7               |
| 800-850°F             | 49                       | 157                   | 148                   | 27 $\pm$ 2.2               |
| Chemical classes:     |                          |                       |                       |                            |
| 800-850°F fraction A1 | 10 <sup>c</sup>          |                       | 0                     | 1.3 $\pm$ 3.8              |
| A2                    | 158                      |                       | 0                     | 200 $\pm$ 101              |
| A3                    | 79                       |                       | 700                   | 32 $\pm$ 9.2               |
| A4                    | --- <sup>c</sup>         |                       | 0                     | 6.6 $\pm$ 7.7              |

<sup>a</sup>From ref. 39. Values are relative to heavy distillate, given a value of 100. IP - initiation-promotion test.

<sup>b</sup>This study, revertants/10<sup>9</sup> survivors/minute irradiated, 50 ug/ml tested. ND - not determined.

<sup>c</sup>Not a significant response.

Figure 3. Photomutagenicity of hydrotreated Paraho shale oil chemical class fractions tested at 100 ug/ml.



**A Ranking Tool for Potentially Carcinogenic  
Polynuclear Aromatic Compounds in Synfuel Products\***

**Tuan Vo-Dinh**

**Advanced Monitoring Development Group  
Health and Safety Research Division  
Oak Ridge National Laboratory  
Oak Ridge, Tennessee 37831**

**ABSTRACT**

This paper describes the use of a screening procedure to rank the content of polynuclear aromatic (PNA) species in synfuel samples. The ranking procedure is based on a cost-effective and rapid screening technique based on synchronous luminescence spectroscopy. The use of the screening procedure as a basis for screening of complex mixtures will be discussed.

**INTRODUCTION**

An important class of organic pollutants are PNA compounds because some of them are known to be converted by metabolic activation to ultimate carcinogens (1,2). Consequently, it is important to monitor PNA compounds in synfuel samples on a routine basis. A variety of analytical procedures have been developed to determine the concentrations of specific PNAs. High-performance liquid chromatography (HPLC) and gas chromatography/mass spectrometry (GC/MS) have been used to provide detailed analyses for a variety of PNAs in environmental samples (3,4). In many monitoring situations, the precise determination of various specific PNAs may be unnecessary and a prescreening phase is required to reduce the cost of environmental analysis.

This presentation describes the use of a ranking methodology that can be used to screen synfuel samples for their PNA content. The technique of synchronous luminescence (SL) is applied to fluorescence and phosphorescence measurements for establishing a ranking index (RI) for PNA species.

---

\*Research sponsored by the Office of Health and Environmental Research, U.S. Department of Energy, under contract DE-AC05-84OR21400 with Martin Marietta Energy Systems, Inc.

By acceptance of this article, the publisher or recipient acknowledges the U.S. Government's right to retain a nonexclusive, royalty-free license in and to any copyright covering the article.

## EXPERIMENTAL

### The Luminescence Screening Technique

The screening procedure evaluated in this study is based on the synchronous luminescence technique (5,6). In conventional luminescence spectroscopy, only one of the two spectral wavelengths,  $\lambda_{em}$  (emission) or  $\lambda_{ex}$  (excitation), is scanned while the other remains fixed. For complex samples, the resulting spectra obtained with this conventional procedure are often poorly resolved and featureless because of the spectral overlays of the emissions from individual components. However, by scanning both  $\lambda_{em}$  and  $\lambda_{ex}$  synchronously with a constant interval between the two wavelengths ( $\lambda_{em} - \lambda_{ex} = \Delta\lambda$ ), the luminescence spectrum becomes more resolved with sharp peaks that are more readily identified.

The synchronous excitation technique can be applied both to fluorescence, i.e., synchronous fluorimetry (SF), and to phosphorescence, i.e., synchronous phosphorimetry (SP). For SF, the optimum value of  $\Delta\lambda$ , usually set at 3 nm, is determined by the Stokes Shift, i.e., the wavelength difference between the 0 to 0 bands in emission and absorption. For SP, the optimal value of  $\Delta\lambda$  is determined by the singlet-triplet energy difference of PNA species to be monitored by room temperature phosphorimetry (RTP) (7-9).

The RTP technique is characterized by the simplicity and versatility of its methodology and consists generally of four steps: (1) substrate preparation (optional pretreatment with heavy-atom salts); (2) sample delivery; (3) drying; and (4) spectroscopic measurement. Three microliters of sample solution were then spotted on the paper circles using microsyringes with a volume of 3 microliters. Since moisture can quench the RTP emission, predrying was achieved with infrared heating lamps. Continued drying during the measurement was accomplished by blowing warm, dry air through the sample compartment. Phosphorimetric measurements were conducted with a commercial Perkin-Elmer spectrofluorimeter (Model 43A) equipped with a rotating phosphoroscope. Details on the measurement procedures have been described elsewhere (7,9).

The presence of heavy atoms in the immediate environment of the molecule can significantly enhance the population of the triplet state (external heavy-atom effect) and, therefore, the phosphorescence intensity. For PNA compounds, a large variety of heavy atom salts such as thallium and lead acetate have been found to be very efficient in enhancing the phosphorescence quantum yields. The detection limits for most PNA compounds investigated can be lowered, in some cases, by several orders of magnitude and are in the subnanogram range. It is also possible to selectively enhance the phosphorescence emission of a given compound (or group of compounds) in a complex mixture. Selective triplet emission enhancement considerably extends the specificity of the RTP technique in multicomponent analysis.

The rationale for ranking the samples for luminescence spectroscopy is based upon the fact that the majority of PNA species, especially the polyaromatic hydrocarbons, fluoresce and/or phosphoresce. Luminescence is known as two of the most sensitive techniques to detect these compounds. Provided that all the spectral interferences are accounted for, the screening procedure can be based on the principle that the higher the total intensity of the SL bands, the more concentrated the samples are in PNA content.



## APPLICATIONS

Screening Profiles of Coal Liquid Samples

Figure 1 shows the synchronous fluorescence spectra of five synfuel products collected at different locations of a synfuel production facility. In order to test the capability of the rapid screening procedures, no prior attempt had been made to analyze these samples and obtain compound-specific information about the individual components. All of the five samples were diluted in ethanol by serial dilution ( $10^3$ ,  $10^4$ ,  $10^5$ , and  $10^6$  dilution factor). A wavelength interval of  $\Delta\lambda = 3$  nm was used in the synchronous fluorescence measurements. With the use of the  $\Delta\lambda$  value, the resulting synchronous fluorescence peaks correspond approximately to the 0,0 band emissions of most PNA compounds. The synchronous profile, therefore, is not just a spectral fingerprint, but contains useful information about the nature and PNA composition of the samples.

The main relationship between the size of the benzenoid structure of a polyaromatic hydrocarbon and its fluorescence emission is the dependence of its 0,0 band upon the number of benzene rings (5). The wavelength position of the 0,0 band of a high-number, linear fused-ring size cyclic compound generally occurs at longer wavelengths than that of a lower number ring-size compound.

Synchronous fluorescence measurements were conducted with the five products at various concentrations. The results indicated that the SF profile remained unchanged when the samples were diluted to  $10^4$  fold or less. This indicated that spectral interferences did not occur at these concentration levels for the products investigated. Without any identification and quantification procedure, a rapid examination of the synchronous fluorescence profiles of the five synfuel products A, B, C, D, and E at  $10^5$  fold dilution levels can readily provide the following conclusions (Figure 1). A rapid comparison of the SL profiles first indicates that product C should contain the least amount of PNA compound. The compound that contributes to the peak at 285-290 nm in sample C is a monocyclic aromatic species and it is also present in similar amounts in other samples (A, B, D, and E). The intensity of the peak at about 305 nm is approximately 10-fold less intense in sample C than in the other samples. Besides a weak shoulder at about 325 nm, no other band was detected in sample C at wavelengths longer than 320 nm.

In order of increasing PNA content, product D is the next sample to consider. The peak at 305 nm is about 10-fold more intense than that of sample C. A rapid examination of the SL profile of sample A also shows that this product is similar to product B. Product B, however, contains slightly more PNA compounds that have 0,0 bands at 346 nm, 382 nm, 402 nm, and 442 nm. Although the general structure of the spectra for products A and D are similar, these spectral differences are still noticeable. Finally, the synchronous profiles show that the PNA content of products B and E are similar. These two samples contain more PNA compound with 3-5 rings than samples A, C, and D as indicated in Figures 1b and 1c.

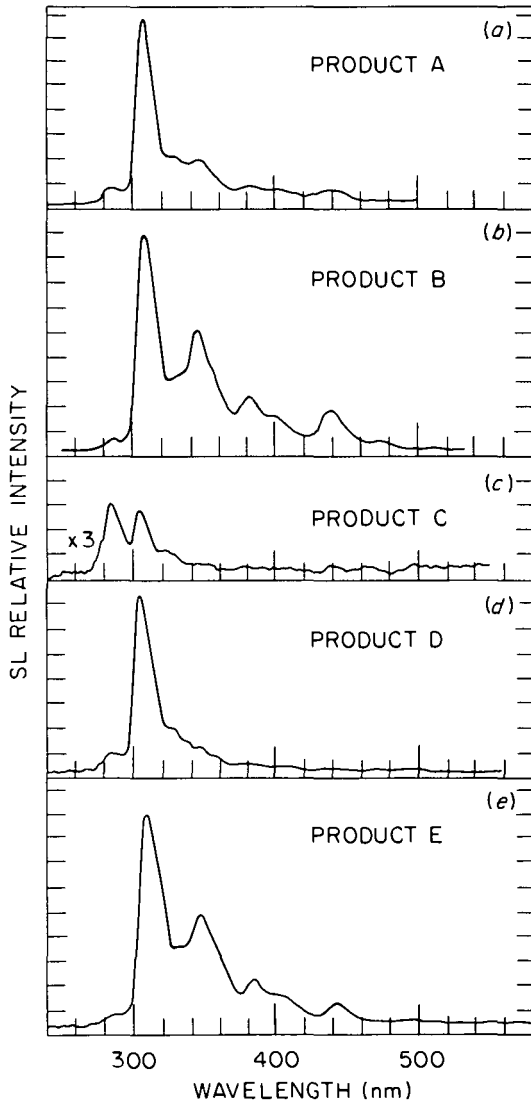
Another example of the screening procedure by RTP is the characterization of another series of coal liquids produced by a synfuel production process. The results of this screening procedure are shown in Figure 2. All the samples were diluted in ethanol by serial dilution ( $10^{-2}$ ,  $10^{-3}$ ,  $10^{-4}$ ,  $10^{-5}$ , and  $10^{-6}$ ) and spotted on filter paper (Schleicher and Schuell, No. 2043A) treated with a mixture of thallium acetate and lead acetate. The excitation used to obtain the RTP spectra was 315 nm. This wavelength was used to excite most of the PNA compounds having 3 to 5 fused rings. The samples shown in this figure were  $10^{-6}$  fold diluted. Without any identification and quantification procedure, it is possible to rank these

samples as follows: B > A > D > C. Note that sample C exhibited stronger intensity at approximately 600 to 650 nm where pyrene and other 4- to 5- ring PNA compounds mainly emit.

The above examples show that it is possible to obtain a preliminary ranking of coal products after a rapid synchronous scanning procedure. All the samples were screened without any prior prefractionation or precleaning process. Each SL and RTP measurement was conducted in less than five minutes, after the appropriate concentration range had been selected. Recently the SL technique has been developed for measuring important biomarkers including PNA metabolites and PNA-DNA adducts produced by human exposure to PNA pollutants (10,11).

#### REFERENCES

1. Searle, C. E., ed. (1976), Chemical Carcinogens, ACS Monograph No. 173, Library of Congress, Washington, D.C.
2. Grimmer, G., ed. (1983), Environmental Carcinogens: Polycyclic Aromatic Hydrocarbons, CRC Press, Boca Raton, Florida
3. Greenberg, A., Yokoyama, R., Barcia, P., and Cannova, F., (1980): in Polyaromatic Hydrocarbons: Chemistry and Biological Effects, ed. by Bjorseth, A., and Dennis, A. J., Battelle Press, OH, p. 193.
4. Funke, W., Romanowski, T., Konig, J., Balfanz, E., (1982): Detection of High Molecular Polycyclic Aromatic Hydrocarbons in Airborne Particulate Matter Using MS, GC, and GC/MS, in Polyaromatic Hydrocarbons: Physical and Biological Chemistry, ed. by Cooke, M., Dennis, A. J., and Fisher, G. L., Battelle Press, Ohio, p. 305.
5. Vo-Dinh, T., (1981): Synchronous Excitation Spectroscopy, in Modern Fluorescence Spectroscopy Volume 4, Wehry, E. L., Editor, Plenum Press, New York, p. 167.
6. Vo-Dinh, T., (1982): Synchronous Luminescence Spectroscopy: Methodology and Applicability, Appl. Spectrosc., 36: 576.
7. Vo-Dinh, T., and Hooyman, J. R., (1979): Selective Heavy-Atom Perturbation for Analysis of Complex Mixtures by Room Temperature Phosphorimetry, Anal. Chem., 51: 1915.
8. Vo-Dinh, T., and Gammage R. B., (1978): Singlet-Triplet Energy Difference as a Parameter of Selectivity in Synchronous Phosphorimetry, Anal. Chem., 50: 2054.
9. Vo-Dinh, T., (1984): Room Temperature Phosphorimetry for Chemical Analysis, John Wiley and Sons, New York.
10. Vahakangas, K., Hangen, A., and Harris, C. (1985): An Applied Synchronous Fluorescence Spectrometric Assay to Study Benzo[a]pyrene-diolepoxide-DNA Adducts, Carcinogenesis, 6: 1109.
11. Uziel, M., Miller, G. H., Moody, R. L., and Vo-Dinh, T. (1985): Analysis of an Important Biomarker, Pseudouridine, by Fluorescence Spectrometry, Anal. Lett. (in press).



**Figure 1: Ranking Procedure of several Coal Liquid Products by Synchronous Fluorescence.**

RTP SCREENING OF SYNFUEL PRODUCTS

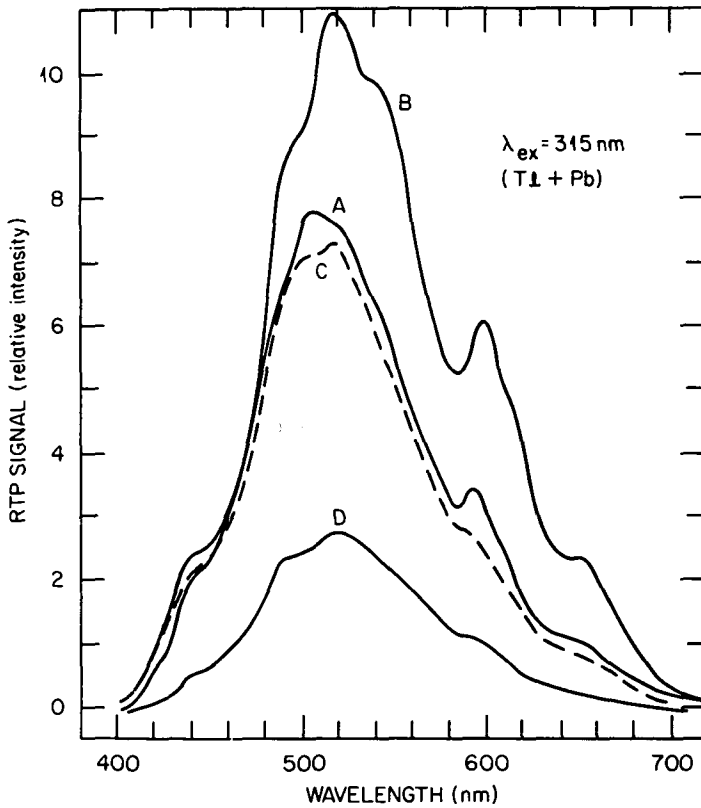


Figure 2: Ranking Procedure of Synfuels Products by Room Temperature Phosphorimetry.

Comparative Toxicity of Crude and Refined Coal Liquids and  
Analogous Petroleum Products: II. Chemical Characterization\*

W. H. Griest<sup>a</sup>, C.-h. Ho<sup>a</sup>, M. R. Guerin<sup>a</sup>, H. P. Witschj<sup>b</sup>, and L. H. Smith<sup>b</sup>

Analytical Chemistry Division<sup>a</sup> and Biology Division<sup>b</sup>,  
Oak Ridge National Laboratory, Oak Ridge, Tennessee 37831

### Introduction

In Part I of this paper, the dermal tumorigenicity of crude and hydrogenated H-Coal Blends, a home heating oil and a reformed naphtha refined from the hydrotreated H-Coal Blend, and two analogous petroleum products is reported. This paper compares the tumorigenicity assay results with the chemistry of the samples.

### Experimental

**Samples:** The crude and upgraded coal liquids consisted of a water-washed 60/40 (wt./wt.) blend of Light and Heavy Oils from the H-Coal Pilot Plant at Catlettsburg, KY) (H-Coal Blend-AWW, sample identification no. 931), the blend hydrotreated under "low severity" conditions resulting in 900 SCF/Bbl of hydrogen incorporation (H-Coal Blend-HDT/L, no. 934), the blend hydrotreated under "medium severity" conditions for 1400 SCF/Bbl of hydrogen consumption (H-Coal Blend-HDT/M, no. 933), and the blend hydrotreated under "high severity" conditions for 3000 SCF/Bbl hydrogen consumption (H-Coal Blend-HDT/H, no. 935). In addition, two products were prepared as petroleum product substitutes. No. 935 H-Coal Blend-HDT/H was devolatilized to meet most of the ASTM specifications for no. 2 fuel oil and was designated as H-Coal Home Heating Oil (no. 978). A 96 octane "gasoline" product (H-Coal Reformed Naphtha) was prepared by a high severity hydrogenation of the no. 931 H-Coal Blend, followed by hydrocracking and catalytic reforming. Blending, catalytic hydrogenation, and hydrocracking were conducted by the Chevron Research Corporation (Richmond, CA), and catalytic reforming was performed by Universal Oil Products, Inc. (Des Plaines, IL). Two petroleum products, API no. 2 Fuel Oil (no. 975) and API Light Catalytically Cracked Naphtha (no. 976) were supplied by the American Petroleum Institute (Washington, DC). Sample origin and processing are described in detail elsewhere (1,2).

**Mouse Skin Dermal Tumorigenicity:** (See Part I.)

**Bacterial Mutagenicity:** Bacterial mutagenicity was determined using the plate incorporation assay of Ames with strain TA-98 and Aroclor-induced S-9 metabolic activation.

**Organic Chemical Characterization:** Benzo(a)pyrene was measured using a sequential high performance liquid chromatography/high performance liquid chromatography (HPLC/HPLC) procedure and quinoline was estimated by direct injection of a diluted sample into a gas chromatograph (GC) equipped with a packed column and a nitrogen-compound-selective thermionic detector. The 5-ring polycyclic aromatic hydrocarbons (PAH) were estimated by capillary column GC following preparation of a PAH-enriched fraction using semi-preparative HPLC. Major organic compounds in the fuels were identified by capillary column GC-mass spectroscopy. The chemical class distribution was determined gravimetrically after acid/alkaline partitioning of the sample and gel chromatography of the neutral fraction. More detailed descriptions of these procedures are given in reference (1).

---

\*Research sponsored by the Office of Fossil Energy, U. S. Department of Energy under contract DE-AC05-84OR21400 with Martin Marietta Energy Systems, Inc.

## Results and Discussion

The changes in bulk composition and properties of the H-Coal Blend as the severity of hydrogenation is increased are consistent with those found in other studies, and are not reported in detail here (see reference 1). Briefly, the heteroatomic content decreases while the hydrogen concentration increases, with S being reduced most readily and O least easily. The density and viscosity decrease, the boiling range is lowered, and both the flash point and pour point decrease with increasing severity of hydrotreatment.

The more toxicologically important compositional changes are compared in Table 1 with summaries of the mutagenicity and dermal tumorigenicity assays. It is evident that tumorigenicity and mutagenicity are dramatically reduced by hydrogenation. Mutagenicity is undetectable in the hydrogenated blends when the sample is assayed as a slurry in dimethylsulfoxide. Tumorigenicity is reduced by low severity hydrotreatment, but no further reduction is evident for the high severity hydrotreated sample. The concentrations of toxic components or chemical classes in the samples also decrease with increasing severity of hydrotreatment, but not in direct proportion to the reductions in toxicity. BaP, a classic PAH dermal tumorigen drops to less than 0.4% of its original level upon low severity hydrotreating of the blend. A more gradual decrease in concentration is noted for the polycyclic aromatics chemical class fraction, which includes the PAH dermal tumorigens. The PAH are associated with the tumorigenicity (3-5) of crude coal liquids.

Quinoline, one of the major N-heterocyclics, decreases in concentration with increasing hydrotreatment severity. The ether-soluble base chemical class fraction also decreases in concentration. This fraction includes the polycyclic aromatic primary amines, which are the determinant mutagens in crude coal liquids (6,7).

In contrast, phenol appears to resist reduction until high severity hydrogenation conditions are employed. This behavior parallels the relative difficulty in reducing the total O content as gauged by ASTM Ultimate Analyses of the crude and hydrotreated blends (1). This trend is not reflected in the ether-soluble acid fraction, which contains most of the oxygenates such as phenols and carboxylic acids.

The PAH content and dermal tumorigenicity of the refined products derived from coal liquids and petroleum are compared in Table 2. It is evident that the further refining (hydrocracking and catalytic reforming) to produce the H-Coal Reformulated Naphtha has eliminated the tumorigenicity of the original crude H-Coal Blend. The API Light Catalytically Cracked Naphtha is only slightly tumorigenic. The home heating oils are somewhat more tumorigenic than the naphthas, with the H-Coal Home Heating Oil being more tumorigenic than the API No. 2 Fuel Oil. It also is apparent that the least tumorigenic product (the H-Coal Reformulated Naphtha) has the highest BaP and 5-ring PAH concentrations. The fuel oils have lower BaP and PAH content than does the H-Coal Reformulated Naphtha, but much higher tumorigenic activities.

One hypothesis for this apparent disparity between PAH content and tumorigenicity is that there are differences in tumor promoting activity among the samples. This hypothesis is being tested. An alternate hypothesis is that the expression of tumorigenicity by the PAH is mediated by differences in the sample matrix composition. The capillary column GC separations shown in Figure 1 illustrate that major compositional differences do exist between the H-Coal Home Heating Oil and the API No. 2 Fuel Oil. Mass spectral analysis of the samples confirmed these differences. The API No. 2 Fuel Oil is composed mainly of C<sub>7</sub>-C<sub>24</sub> n-alkanes and alkylated 1-3 ring aromatic hydrocarbons (in order of decreasing concentration: C<sub>9</sub>-C<sub>5</sub>-naphthalenes, C<sub>9</sub>-C<sub>4</sub>-benzenes, C<sub>1</sub>-C<sub>4</sub>-indanes, and C<sub>9</sub>-C<sub>1</sub>-phenanthrenes). In contrast, the H-Coal Home Heating Oil is comprised mainly of cycloparaffins (in order of decreasing concentration): decahydronaphthalene, C<sub>1</sub>-C<sub>4</sub>-decahydronaphthalenes, C<sub>9</sub>-C<sub>4</sub>-cyclohexanes, and C<sub>9</sub>-C<sub>4</sub>-tetralins. Aromatic and partially saturated aromatic hydrocarbons

and alkanes also are present, but at much lower levels (in order of decreasing concentration): C<sub>1</sub>-C<sub>4</sub>-indanes, C<sub>7</sub>-C<sub>25</sub> n-alkanes, and C<sub>0</sub>-C<sub>4</sub>-benzenes.

The chromatograms of the naphthas (Figure 2) show that they are quite different as a group from the home heating oils. The two naphthas share many components, such as C<sub>4</sub>-C<sub>7</sub>-alkanes and C<sub>0</sub>-C<sub>3</sub>-benzenes. However, the H-Coal Reformed Naphtha is more aromatic than the API Light Catalytically Cracked Naphtha, having 7-fold more benzene, 4.5-times more toluene, and 2-fold greater levels of C<sub>2</sub>-benzenes. In contrast, the API Light Catalytically Cracked Naphtha is more olefinic, being more enriched in partially unsaturated C<sub>5</sub>-C<sub>8</sub> hydrocarbons. The fluorescent indicator assay results reported by the Universal Oil Products, Inc., and the American Petroleum Institute reflect these compositional differences: H-Coal Reformed Naphtha (58.4% [vol./vol.] aromatic, 0.9% olefin, 40.7% saturate) and API Light Catalytically Cracked Naphtha (20.3% aromatic, 29.6% olefin, 50.0% saturate). It is possible that these compositional differences among the samples affects the absorption, metabolism, and uptake of PAH tumorigens, and modifies or potentiates their tumorigenic activities.

### Conclusions

The decrease in tumorigenicity of the crude H-Coal Blend by catalytic hydrogenation is associated with the reduction of tumorigens. Comparison of the composition and residual tumorigenicity in refined products derived from the H-Coal Blend and from petroleum suggests that the tumorigenicity associated with PAH is modified by the presence of tumor promoting agents, by matrix composition differences, or both.

### Acknowledgement

The American Petroleum Institute (API) is gratefully acknowledged for supplying the two petroleum-derived samples.

### References

1. M. R. Guerin, W. H. Griest, C.-h. Ho, L. H. Smith, and H. P. Witschi, "Integrated Report on the Toxicological Beneficiation of Coal Liquids by Hydrotreatment and Other Processes," ORNL/TM, Oak Ridge National Laboratory, Oak Ridge, TN (in press).
2. R. F. Sullivan, "Refining and Upgrading of Synfuels from Coal and Oil Shale by Advanced Catalytic Processes," FE-2315-74, -80, and -84, Chevron Research Company, Richmond, CA (March, 1981, August, 1982, January, 1983).
3. J. M. Holland, R. O. Rahn, L. H. Smith, B. R. Clark, S. S. Chang, and T. J. Stephens, "Skin Carcinogenicity of Synthetic and Natural Petroleum," J. Occupat. Med. **21**, 614 (1979).
4. J. M. Holland, O. A. Wolf, and B. R. Clark, "Relative Potency Estimation for Synthetic Petroleum Skin Carcinogens," Environ. Hlth. Perspect. **38**, 149 (1981).
5. D. D. Mahlum, C. W. Wright, E. K. Chess, and B. W. Wilson, "Fractionation of Skin Tumor-Initiating Activity in Coal Liquids," Cancer Res. **44**, 5176 (1984).
6. M. R. Guerin, C.-h. Ho, T. K. Rao, B. R. Clark, and J. L. Epler, "Polycyclic Aromatic Primary Amines as Determinant Chemical Mutagens in Petroleum Substitutes," Environ. Res. **23**, 42 (1980).
7. B. W. Wilson, R. A. Pelroy, and J. T. Cresto, "Identification of Primary Aromatic Amines in Mutagenically Active Subfractions from Coal Liquefaction Materials," Mutat. Res. **79**, 193 (1980).

Table 1. Influence of Hydrotreatment on Chemical Parameters, Mutagenicity, and Tumorigenicity of Coal Liquids (1)

| Sample Number | Description          | Chemical Class Fraction, wt. % |     |      |      | Quinoline, $\mu\text{g/g}$ | Phenol, $\text{mg/g}$ | Benzo(a)pyrene, $\mu\text{g/g}$ | Mutagenicity <sup>b</sup> | Animals w/Skin Tumors <sup>c</sup> , %<br>Dose (wt./vol. %) |    |
|---------------|----------------------|--------------------------------|-----|------|------|----------------------------|-----------------------|---------------------------------|---------------------------|---|----|
|               |                      | ESB                            | ESA | Sat. | Aro. | Polyaro.                   |                       |                                 |                           | 100   | 50 |
| 931           | H-Coal Blend - AMW   | 3.3                            | 1.5 | 30.8 | 56.7 | 5.8                        | 164                   | 0.15                            | 50                        | 4.9   | 82 |
| 934           | H-Coal Blend - HDT/L | 2.4                            | 0.8 | 38.3 | 46.5 | 1.3                        | 6                     | 0.13                            | <0.2                      | <0.1  | 14 |
| 933           | H-Coal Blend - HDT/M | 0.6                            | 0.6 | 35.9 | 46.7 | 0.8                        | <1                    | 0.13                            | <0.2                      | <0.1  | -  |
| 935           | H-Coal Blend - HDT/H | 0.7                            | 0.5 | 58.9 | 8.3  | 0.5                        | <1                    | <0.1                            | <0.1                      | <0.1  | 20 |
|               |                      |                                |     |      |      |                            |                       |                                 |                           |   | 34 |

<sup>a</sup>ESB = ether-soluble bases, ESA = ether-soluble acids, Sat. = saturates, Aro. = mono/di-aromatics, Polyaro. = polycyclic aromatics.

<sup>b</sup>TA-98 + S-9 activation.

<sup>c</sup>Data for 104 weeks of three-times weekly treatment of 25 male plus 25 female C3H mice per dose group/substance. Male and female mice data combined.



Table 2. Comparison of PAH Content and Tumorigenicity of Final Products Refined from Coal Liquids and Petroleum

| Sample Number | Description           | Benzo(a)pyrene<br>μg/g | Sum of 5-Ring<br>PAHs, μg/g | Animals w/Skin Tumors <sup>b</sup> , %<br>Dose (wt./vol. %) |    |    | Median Time-<br>To-Tumor <sup>c</sup> , Wks |
|---------------|-----------------------|------------------------|-----------------------------|---|----|----|---|
|               |                       |                        |                             | 100   | 50 | 0  |   |
| 936           | H-Coal Ref. Nap.      | 1.4                    | 35                          | 0   | 0  | 0  | 155-ND                                      |
| 976           | API Lt. Cat. Cr. Nap. | <0.002                 | <0.5                        | 6   | 8  | 8  | 125-143                                     |
| 978           | H-Coal Home Ht. Oil   | 0.08                   | 3                           | 28  | 24 | 24 | 97-112                                      |
| 975           | API No. 2 F. 0.       | 0.04                   | 0.09                        | 12  | 14 | 14 | 120-144                                     |

<sup>a</sup>Benzo(b/j)fluoranthenes + benzo(e)pyrene + benzo(a)pyrene + indeno(1,2,3-cd)pyrene + benzo(ghi)perylene.

<sup>b</sup>Data for 25 months of three-times weekly application to 25 male + 25 female C3H mice per dose group/substance. Acetone solvent for 50% dose.

<sup>c</sup>Change including all dose groups and both sexes. ND = none detected (for zero tumor incidence).

ORNL-DWG 85-15084R

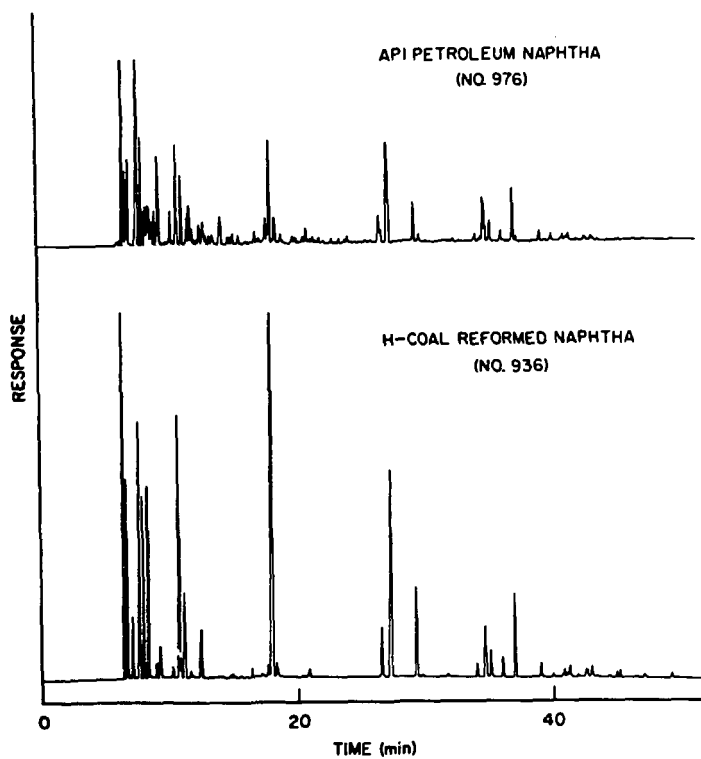


Figure 1. Capillary Column GC Comparison of Major Organic Compounds in Coal- and Petroleum-Derived Naphthas.

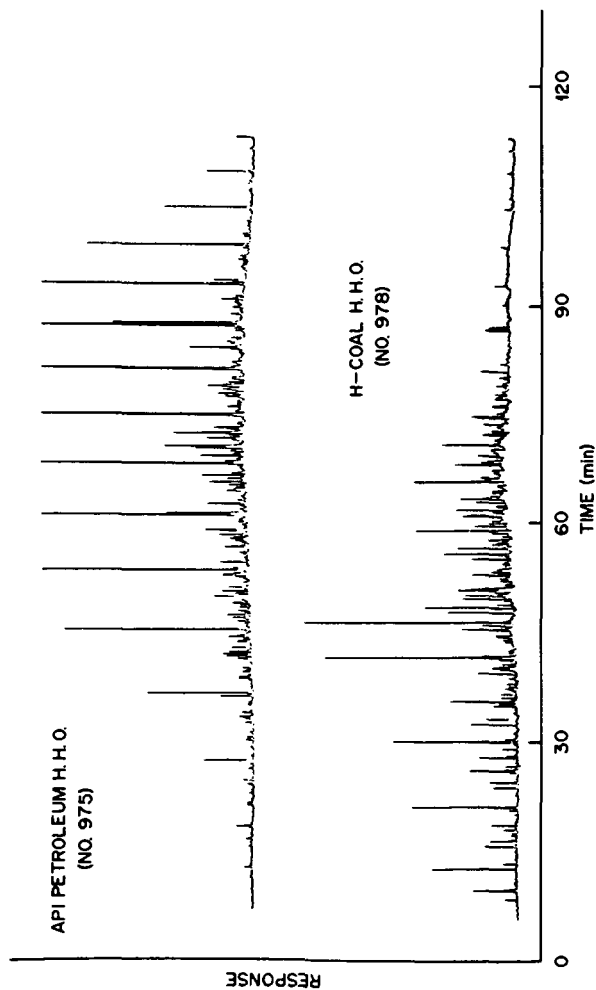


Figure 2. Capillary Column GC Comparison of Major Organic Compounds in Coal- and Petroleum-Derived Home Heating Oils.

PROCESS RELATED EFFECTS ON THE CHEMICAL AND TOXICOLOGIC  
CHARACTERISTICS OF COAL DERIVED FUELS

C. W. Wright,<sup>1</sup> E. K. Chess,<sup>2</sup> R. M. Bean,<sup>2</sup>  
D. D. Mahlum,<sup>2</sup> D. L. Stewart,<sup>2</sup> and B. W. Wilson<sup>2</sup>  
<sup>1</sup> Chemical Technology Department  
<sup>2</sup> Biology and Chemistry Department

Pacific Northwest Laboratory,  
P.O. Box 999, Richland, WA 99352

ABSTRACT

As a component of an ongoing program to assess the potential health effects of coal conversion materials, we have recently completed chemical and toxicologic studies of a sample set collected on selected days of a 25-day demonstration run of a catalytic two stage direct coal liquefaction (CTSL) process. There was an increase in heteroatomic, nitrogen containing polycyclic aromatic compounds (NPAC) and hydroxy-substituted PAC, compounds as the operation time of the pilot plant increased. The proportion of material which boiled above 975°F also increased in the solids-free portion of the recycle slurry oil as pilot plant operation time increased. As anticipated from the increase in NPAC concentration during the run, the microbial mutagenic activity of selected process materials also increased as a function of run time. Likewise, the tumorigenicity of the materials produced later in the demonstration run was higher than that of those produced initially. These results support the view that catalyst deactivation during the course of the run gives rise not only to lower coal conversion, but also to increased toxicologic activity.

INTRODUCTION

Chemical and toxicologic characteristics of direct coal liquefaction materials are highly dependent on the specific process by which the coal liquids were produced. Of particular importance are those process variables which can

affect the boiling point (bp) range and degree of hydrogenation of product materials (Wilson et al., 1986). Thus, process modifications such as recycle of heavy ends to extinction (Anderson and Freel, 1983), adjustment of product distillation upper temperature cut points to ca.  $< 650^{\circ}\text{F}$  (Pelroy et al., 1985), incorporation of a catalytic hydrogenation step (Wilson et al, 1986), and, to a lesser extent, changes in feed coal type can reduce the toxicologic potential of coal liquefaction materials as determined by microbial mutagenicity testing and mouse skin tumorigenesis assays.

We have recently concluded studies that assessed the effects of process run time, and hence catalyst age, on the chemical composition and toxicologic activity of materials from an advanced coal liquefaction process. In the present paper, these results are reported and compared to data from earlier studies which dealt with other process variables such as those listed above. Studies of catalyst effects on toxicology will be important in the new petroleum resid/coal co-processing schemes, which will depend heavily on catalyst performance.

### EXPERIMENTAL

During July of 1984, Hydrocarbon Research, Inc. (HRI) performed a 25-day demonstration run of their catalytic two-stage liquefaction coal conversion (CTSL) process at Lawrenceville, NJ. An objective of this CTSL process was to take advantage of catalytic reactions in both reactors to convert coal to a liquid; details of the CTSL process are given by Comolli et al. (1984) and Wright and Later (1985). Samples of the pressure filter liquid (PFL; the solids-free portion of the recycle slurry oil, an internal process stream material) were taken each day of the demonstration run. A product distillate blend (PDB), more representative of the actual net product from the CTSL process, was also supplied by HRI.

Chemical analyses were performed on fractions isolated from the PFL and PDB materials by adsorption column chromatography (Later et al. 1981). Chemical class fractions of aliphatic hydrocarbons (AH), polycyclic aromatic hydro-

carbons (PAH), nitrogen-containing polycyclic aromatic compounds (NPAC), and hydroxy-substituted PAH (hydroxy-PAH) were produced using neutral alumina as an adsorbent. Due to the high concentration of hydrogenated and partially hydrogenated components present in these samples, the hydroaromatic compounds were isolated using picric-acid-coated alumina as an adsorbent (Wozniak and Hites, 1983). Selected chemical fractions isolated from the PFL and PDB materials were then analyzed by high-resolution gas chromatography (HRGC), gas chromatography/mass spectrometry (GC/MS), and low-voltage probe-inlet mass spectrometry (LVMS).

The mutagenic response of all crude samples and chemical class fractions were measured using the histidine reversion microbial mutagenicity test with Salmonella typhimurium, TA98 (Ames et al., 1975). Selected crudes were tested for tumorigenic potential using the initiation/promotion (I/P) assay for tumorigenicity in mouse skin (Mahlum, 1983). Details regarding the methods of chemical analyses and measurement of toxicologic activity in the CTSL materials are given by Wright and Later (1985).

## RESULTS AND DISCUSSION

### Chemical Analysis

The distillation weight percent distribution of the CTSL PFL materials from days 5, 10, 15, 19, and 24 are given in Table 1. The composition boiling above 975°F increased significantly over the duration of the demonstration run. There was a concurrent decrease in the composition which distilled less than

TABLE 1. Distillation Data for Selected PFL Sample Materials

| Distillation<br>Temperature | Weight Percent Composition |        |        |        |        |
|-----------------------------|----------------------------|--------|--------|--------|--------|
|                             | Day 5                      | Day 10 | Day 15 | Day 19 | Day 24 |
| IBP - 650°F                 | 28.1                       | 21.0   | 18.9   | 14.9   | 13.1   |
| 650 - 850°F                 | 33.4                       | 32.7   | 30.9   | 31.8   | 30.9   |
| 850 - 975°F                 | 11.4                       | 12.7   | 13.8   | 8.7    | 6.8    |
| 975°F+                      | 27.1                       | 33.6   | 36.4   | 44.6   | 49.2   |

650°F. The increase in higher boiling constituents of the PFL may be an effect of catalyst deactivation and recycle oil boiling point adjustment.

Elemental analysis data indicated there were changes in the PFL composition during the course of the 25-day demonstration run. These changes included a general decrease in the carbon content of the PFL material and an increase in the heteroatom content with catalyst age and duration of the run. The nitrogen content increased gradually from 0.61 weight percent on day 5 to 0.99 weight percent on day 24; the sulfur content increased similarly from 0.046 to 0.186 weight percent for the same days of pilot plant operation.

The chemical class composition (as determined by alumina column chromatography) of the PFL materials from days 1, 5, 10, 15, 19, and 24 are shown in Figure 1. As the demonstration run progressed, the PFL AH composition decreased by more than a factor of two, the PAH composition of the PFL materials was fairly constant, and both the NPAC and hydroxy-PAH fractions showed significant increases. The PDB had a significantly higher AH

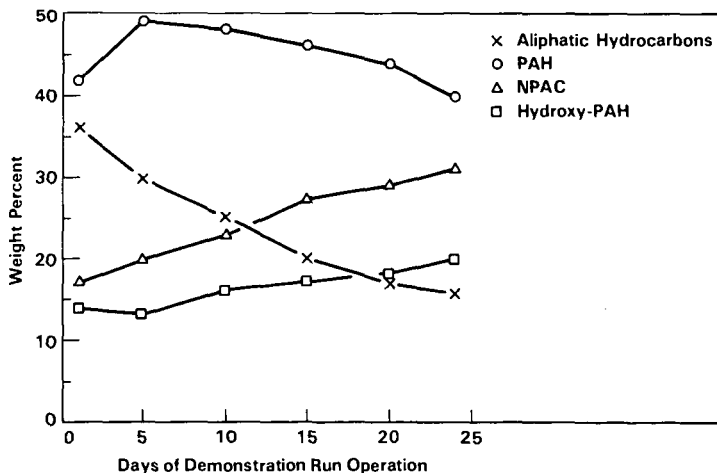


FIGURE 1. Chemical Class Composition of CTSL Pressure Filter Liquid Samples as Determined by Alumina Column Chromatography

composition and significantly lower PAH, NPAC, and hydroxy-PAH composition than did the PFL material. The PDB contained 43% AH, 23% PAH, 5.2% NPAC, and 6.7% hydroxy-PAH by weight as determined by alumina column chromatography.

The hydroaromatic composition of the CTS� PFL materials from days 1, 5, 10, 15, 19, and 24 is shown in Figure 2. The AH of fraction PA1 and the hydroaromatic compounds of fraction PA2 generally decreased as the operation time of the demonstration run increased. The dihydro- and less-than-three-ringed PAH composition of fraction PA3 was constant after about day 5 of the demonstration run. In addition, the greater-than-three ringed PAH and some slightly polar compounds of fraction PA4 generally increased with increasing operation time. Indan, tetralin, and hydrogenated acenaphthylenes, fluorenes, phenanthrenes, fluoranthenes, and pyrenes were detected as major components in the hydroaromatic fraction of the PDB when analyzed by HRGC and GC/MS. Alkylated species of each of the above were also detected in the PA2 fraction.

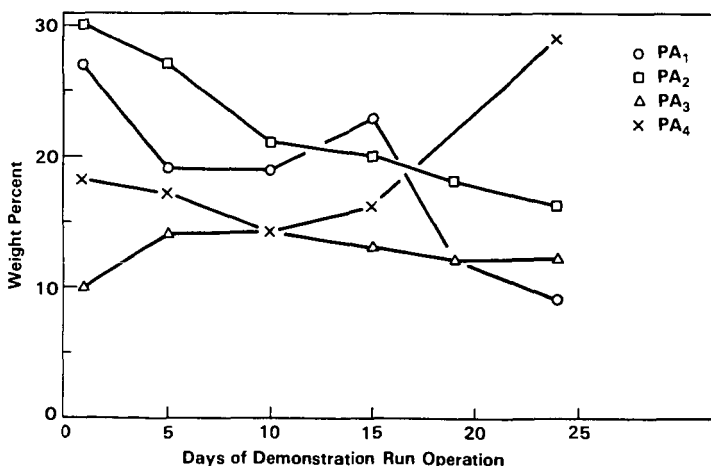


FIGURE 2. Hydroaromatic Composition of CTS� Pressure Filter Liquid Samples as Determined by Picric-Acid-Doped Column Chromatography



The PAH and NPAC fractions were analyzed in detail since these chemical class fractions have been previously shown to be the most tumorigenic and mutagenic fractions in coal-derived materials, respectively. The quantitative HRGC results for over 50 components in the PAH fractions and 40 components in the NPAC fractions of the PFL materials from day 1, 5, 10, 15, 19, and 24 are given by Wright and Later (1985). The results of the PAH fraction analyses can be summarized by the data given in Figure 3. The quantitative values for some low molecular weight PAH in the isolated PAH fractions, i.e. the methylnaphthalenes and two isomers of dimethylnaphthalene, were summed and are plotted for each of the PFL materials analyzed. The concentration of these low molecular weight components decreased over the duration of the demonstration run. The quantitative values for some of the high molecular weight PAH in the isolated PAH fractions, i.e. two methylchrysene isomers, the benzo(a)fluoranthenes, the benzopyrenes, indeno(1,2,3-cd)pyrene, and benzo(ghi)perylene, were also summed and are plotted in Figure 3 for each of the PFL materials analyzed. The

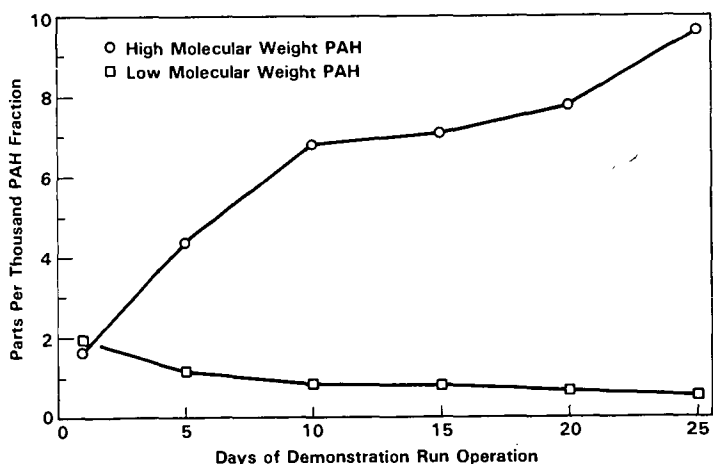


FIGURE 3. Concentrations (parts per thousand) of Selected High Molecular Weight Components and Low Molecular Weight Components in PAH Fractions of Selected CTSL PFL Samples

concentration of these high molecular weight components increased significantly with increasing pilot plant operation time. Operating temperatures were equilibrated during the first 3 days of the demonstration run; the composition of the PAH fractions continued to change after operating temperatures were equilibrated at day 3. These changes may be an effect of catalyst degradation or an effect of the resid recycle. Similar increases in higher molecular weight composition were noted for the AH, NPAC, and hydroxy-PAH chemical class fractions when analyzed by LVMS.

The individual components in the chemical class fractions of the PDB were similar to those found in the PFL materials, only for a lower molecular weight range. The quantitative analyses of the PDB and the PFL composite revealed that the concentration of the methylnaphthalenes and two dimethylnaphthalene isomers was more than an order of magnitude higher in the PDB as compared to the PFL, for example.

To compare the degree of alkylation of the CTSL PDB to products from other coal liquefaction processes, the quantitative values for the following compounds were summed and were then divided by the quantitative values of their respective parent compounds: the methylphenanthrene isomers, the methylcarbazole isomers, and 1-methyl pyrene. The resulting ratios were then summed. The summed ratios of these quantitative values are given in Table 2 for the CTSL PDB as well as solvent refined coal (SRC)-I, SRC-II, H-Coal, EDS, integrated two-stage liquefaction (ITSL) (Lummus), ITSL (Wilsonville), and nonintegrated two-stage liquefaction (NTSL) products. The single-stage, noncatalytic SRC materials showed the lowest degree of alkylation compared to the single-stage, catalytic H-Coal, hybrid EDS, or any of the two-stage coal liquefaction products. The highest degrees of alkylation were present in the two-stage coal liquefaction materials. Both ITSL, the NTSL, and the CTSL materials showed similar degrees of alkylation to each other, as determined by these means.

Those processes which incorporated catalysts had higher degrees of hydrogenation than did the noncatalytic processes. Quantitative values for the 1,2-dihydrophenalene and a dihydrofluoranthene were divided by the quantitative values of fluorene and fluoranthene, respectively, to compare the degree of hydrogenation of coal liquefaction process materials. These two ratios were

**TABLE 2.** Relative Degrees of Alkylation and Hydrogenation of Coal Liquefaction Materials as Determined by HRGC Analysis

| Coal Liquefaction Process | Relative Degree of Alkylation <sup>(a)</sup> | Relative Degree of Hydrogenation <sup>(a)</sup> |
|---------------------------|--|---|
| SRC-I                     | 1.3  | 0.2   |
| SRC-II                    | 1.7  | 0.6   |
| H-Coal                    | 3.2  | 4.2   |
| EDS                       | 3.4  | 4.4   |
| ITSL Lummus               | 4.6  | 6.3   |
| ITSL Wilsonville          | 4.4  | 6.0   |
| NTSL Wilsonville          | 4.9  | 11  |
| CTSL PDB                  | 4.1  | 10  |

(a) See text for explanation.

then summed and are also given for each of the coal liquefaction materials in Table 2. The CTSL PDB and NTSL product showed the highest degree of hydrogenation, as determined by this method.

#### Biological Testing

The microbial mutagenicity results indicated a general trend of increasing mutagenicity with increased pilot plant operation time. The results of testing crude PFL materials from each day of the demonstration run were as follows: the responses, in rev/ $\mu$ g, ranged from approximately 1 to 2 for the first 5 days, 2 to 3 rev/ $\mu$ g for the next 5 days, 4 to 6 rev/ $\mu$ g for days 11 through 15, 6 to 10 rev/ $\mu$ g for days 16 through 20, and 9 to 12 rev/ $\mu$ g for the last 5 days of the demonstration run. The trend of increasing mutagenic response with time of operation correlates with the chemistry analysis data, which showed that the PFL materials had an increasing heteroatomic (particularly NPAC) composition as the length of pilot plant operation time increased. The microbial mutagenic response of coal liquefaction materials has historically been related to the NPAC chemical class fractions of coal liquefaction materials analyzed using these methods.

The CTSL PDB had a microbial mutagenicity dose response of 1.7 rev/ $\mu$ g with S. typhimurium, TA98. This response was higher than materials representative of Wilsonville (bp >450°F) and Lummus (bp >400°F) ITSL final products: approximately 2 rev/ $\mu$ g for the CTSL versus 0 rev/ $\mu$ g for the ITSL materials. The PDB did, however, have a lower mutagenic response than that of a NTSL (bp >450°F) final product (6 rev/ $\mu$ g). The majority of microbial mutagenicity of all the CTSL materials tested was associated with the NPAC fractions when the chemical class fractions were tested with S. typhimurium, TA98. These results were consistent with other coal liquefaction materials studied to date.

The results are given in Table 3 for the I/P mouse skin tumorigenicity assay of days 5, 15, and 24 PFL materials from the 25-day demonstration run of the HRI CTSL process. The mean number of tumors per mouse data (normalized to a population of 30 mice) indicated a general trend of increasing tumorigenicity with increasing length of pilot plant operation and catalyst deactivation. These I/P results were in general agreement with the chemistry results that showed that the PFL materials had decreased AH content and increased molecular weight distribution with increasing length of pilot plant operation. The percent tumor incidences were similar for all the PFL materials tested

TABLE 3. I/P Results (mean number of tumors per mouse)  
for Selected Coal Liquefaction Materials

| Sample                                     | Nominal bp<br>Range (°F) | Tumors/Mouse <sup>(a)</sup> |
|--|--------------------------|-----------------------------|
| CTSL PFL, Day 5                            | 500 - 975+               | 1.37                        |
| CTSL PFL, Day 15                           | 500 - 975+               | 1.62                        |
| CTSL PFL, Day 24                           | 500 - 975+               | 2.27                        |
| CTSL PDB                                   | <850                     | 0.57                        |
| ITSL Second-Stage Product<br>(Wilsonville) | 450 - 850+               | 1.3                         |
| NTSL Second-Stage Product<br>(Wilsonville) | 450 - 850+               | 1.1                         |
| ITSL TLP (Lummus)                          | ~400 - 850+              | 2.6                         |

(a) Normalized to 30 mice per test material.

(approximately 70% after 191 days); however, day 5 results were slightly lower (~62%) and day 15 results were slightly higher (~75%) than the rest.

The skin-tumor initiating activity of the PDB (also given in Table 3 in terms of mean number of tumors per mouse) was significantly less than that of any of the PFL materials tested when judged by either tumor yield or tumor incidence; this is predictable from the significantly increased bp range of the PFL (>975°F) versus that of the PDB (<850°F) materials. Increasing tumorigenicity has been noted with increasing bp of coal liquefaction materials by Wright *et al.* (1985).

Also included in Table 3 are the mean number of tumors per mouse for the ITSL and NTSL materials, with nominal bp information for all samples. The CTSL PDB appeared to have less tumor initiating activity than did the NTSL or ITSL products, probably an effect of the lower bp of the former versus the latter.

#### ACKNOWLEDGMENT

This work was supported by the U.S. Department of Energy, Office of Fossil Energy under Contract DE-AC06-76RL0-1830.

#### REFERENCES

- Ames, B. N., J. McCann, and E. Yamasaki. 1975. "Methods for Detecting Carcinogens and Mutagens with the Salmonella/Mammalian-Microsome Mutagenicity Test." *Mutat. Res.* 35: 247-364.
- Anderson, R. P. and J. Freel. 1984. "Improving Coal Liquid Quality by Heavy Distillate Recycle," Proc. Eight Annual EPRI Contractors Conf. on Coal Liquefaction. EPRI AP-3366-SR, Feb. 1984. EPRI, Palo Alto, California.
- Comolli, A. G., J. B. MacArthur, and J. B. McLean. "HRI's Two-Stage Catalytic Coal Liquefaction Program-A Status Report." In: Proceeding of the 1984 DOE/FE Direct Coal Liquefaction Contractors' Review Meeting, October 17-18, 1984, Albuquerque, New Mexico.

- Later, D. W., M. L. Lee, K. D. Bartle, R. C. Kong, and D. L. Vassilaros.  
1981. "Chemical Class Separation and Characterization of Organic Compounds  
in Synthetic Fuels." Anal. Chem. 53: 1612-1620.
- Mahlum, D. D. 1983. "Initiation/Promotion Studies with Coal-Derived  
Liquids." J. Appl. Toxicol. 3: 31-34.
- Pelroy, R. A., M. E. Frazier, D. W. Later, C. W. Wright, and B. W. Wilson.  
1985. "Effects of Process Distillation on Mutagenicity and Cell  
Transformation Activity of Solvent-Refined Coal Liquids," FUEL, 64 639-643.
- Wilson, B. W., D. D. Mahlum, and R. A. Pelroy. 1986. "Biomedical Implications  
of a Altered Product Composition in Advanced Coal Liquefaction Processes."  
Fuel Proc. Technol. (in press).
- Wozniak, T. J. and R. A. Hites. 1983. "Separation of Hydroaromatic Compounds  
in Synfuels by Picric Acid Columns." Anal. Chem. 55: 1791-1796.
- Wright, C. W. and D. W. Later. 1985. HRI Catalytic Two-Stage Liquefaction  
(CTSL) Process Materials: Chemical Analysis and Biological Testing,  
PNL-5605, Pacific Northwest Laboratory, Richland, Washington. NTIS,  
Springfield, Virginia.

## Iron Nitride Catalysts For Synthesis Reactions

W.N. Delgass, A.A. Hummel, A.P. Wilson, and K.E. Hummel

School of Chemical Engineering  
Purdue University  
West Lafayette, Indiana 47907

### INTRODUCTION

Synthesis gas (CO and H<sub>2</sub>) from coal is a potential source of both fuels and chemical feedstocks. Commercial applications of this technology use iron-based catalysts, which are known to carburize during reaction (1-5). Pre-nitriding of a fused iron catalyst has been reported to shift the molecular weight and alcohol content of the product distribution (6,7). Recent studies (8,9) indicate somewhat different selectivities for the nitrified catalysts, but confirm high activities and stability of nitrogen for a variety of catalyst and reaction conditions.

The structures and magnetic properties of the nitride phases have been investigated by various authors using several techniques, including XRD (10), LEED (11), Auger (12) and Mössbauer spectroscopy (13,14,15). Three nitride phases have been differentiated:  $\gamma$ -Fe<sub>4</sub>N,  $\epsilon$ -Fe<sub>x</sub>N (2 < x < 3), and  $\zeta$ -Fe<sub>2</sub>N. The phase diagram has been presented by Ertl *et al* (12). As the nitrogen content increases, the structure changes from BCC ( $\alpha$ -Fe), to FCC ( $\gamma$ -Fe<sub>4</sub>N), to HCP ( $\epsilon$ -Fe<sub>x</sub>N), to orthorhombic ( $\zeta$ -Fe<sub>2</sub>N). Mössbauer spectroscopy is particularly effective in differentiating the various iron nitrides (14,15).

In this work, we have used Mössbauer spectroscopy and transient mass spectrometric analysis to examine the stability, surface chemistry, and catalytic behavior of the three iron nitrides. We have found that at typical reaction temperatures, the pure nitride phases are unstable in both H<sub>2</sub> and synthesis gas, but in synthesis gas much nitrogen can be retained in the working catalyst in a carbonitride phase. We have continued this work by examining the nature of the surface before and during reaction in synthesis gas. Transient measurements show that surface nitrogen species are more reactive toward hydrogen than surface carbon species, and thus nitrogen is quickly lost from the surface during the first minutes of reaction. The high reactivity of nitrogen also suggests that a continuous supply of nitrogen from a reactant could lead to synthesis of nitrogen-containing compounds. The patent literature and our preliminary experiments confirm production of acetonitrile when NH<sub>3</sub> is added to synthesis gas at 700 K. Our findings also indicate that the use of catalysts with very small iron particles can affect the stability during reaction.

### EXPERIMENTAL

Preparation of the unsupported nitride powders was accomplished by reducing iron oxide at 325-400 °C in flowing UHP hydrogen. The reduced iron powder (a compressed wafer in the Mössbauer apparatus, and a packed bed for the transient mass spec apparatus) was nitrified in a flowing mixture of ammonia and hydrogen for about 4 hours to produce the catalyst product. The nitrogen content was controlled by either altering the gas phase ammonia composition or varying the reaction temperature. Nitrogen content was checked by integrating the

mass spectrometer signal for  $\text{NH}_3$  when the nitride was reduced in hydrogen. Nitride phases were also identified by their Mössbauer spectra or XRD patterns.

The  $^{57}\text{Fe}$  Mössbauer spectra were recorded on a Nuclear Data multichannel analyzer from an Austin Science S-600 spectrometer. Both constant acceleration and constant velocity (transient) modes were used. All Mössbauer spectra isomer shift parameters are referenced to a  $25\mu\text{m}$  NBS Fe foil. The *in situ* Mössbauer cell supports a mechanically compressed sample wafer, allowing Mössbauer effect investigation of changes in the bulk sample during nitriding, denitriding, carburization, and synthesis reaction.

Details of reaction kinetics are studied by mass spectrometry. The apparatus used for this portion of the work was specifically designed for transient experiments. Combinations of reactant feed gases can be stepped or pulsed to the reactor. The effluent of the reactor is continuously measured by an Extranuclear EMBA II quadrupole mass spectrometer with a supersonic nozzle molecular beam inlet and phase sensitive detection. The spectrometer is controlled and monitored by a Digital MINC 11 microcomputer to facilitate the high speed gas analysis required for transient experiments.

## RESULTS AND DISCUSSION

The Mössbauer spectral variations with changing nitrogen content are depicted in Figure 1, with  $\alpha\text{-Fe}$  included for comparison. The  $\zeta\text{-Fe}_2\text{N}$  phase can be made at a variety of temperatures, but is most easily prepared at  $400^\circ\text{C}$  with 100% ammonia and identified by the narrowly split quadrupole doublet of Figure 1A. The  $\epsilon\text{-Fe}_x\text{N}$  phase is only prepared in a narrow concentration range of  $90 \pm 5\%$   $\text{NH}_3$ . Variation of the temperature changes the stoichiometry ( $2 < x < 3$ ) such that decreasing nitrogen content increases the species with hyperfine splitting of about  $200\text{kOe}$  at the expense of the central quadrupole doublet (Spectra 1B-E). Slight changes in concentration also alter the stoichiometry of the  $\epsilon\text{-Fe}_x\text{N}$  phase (Figure 1F). The  $\gamma\text{-Fe}_4\text{N}$  phase is formed at lower ammonia concentrations (75%  $\text{NH}_3$ ) at  $325^\circ\text{C}$ , and is easily identified by its characteristic 8 line spectrum with its rightmost line at higher velocity than that of  $\alpha\text{-Fe}$  (Figure 1G).

The constant velocity capability of the Mössbauer drive allows *in situ* inspection of the nitriding process by following the growth or loss of transmitted intensity at a fixed velocity during the process. Figure 2 presents the loss (increase in transmission) and subsequent return of the central quadrupole doublet during denitriding and renitriding of  $\zeta\text{-Fe}_2\text{N}$ , observable by following the velocity indicated in the constant acceleration spectrum. The denitriding kinetics at  $325^\circ\text{C}$  are very rapid, converting the  $\zeta$  nitride to  $\alpha$  iron in seconds. On the other hand, the nitriding to the orthorhombic phase is relatively slow. During nitriding the nitrogen entering the lattice promotes a structural change from the relatively open bcc structure to the more dense orthorhombic arrangement which has considerably lower diffusivity of nitrogen. Ninety percent of the nitrogen appears to have entered the sample within 40 minutes of starting the nitriding.

Figure 3 shows the effect of gas phase composition on the rate of orthorhombic phase disappearance from  $\zeta\text{-Fe}_2\text{N}$ , as followed by constant velocity measurement of the central doublet at  $0.5\text{ mm/sec}$  in the Mössbauer spectrum. The effect of pure hydrogen at  $325^\circ\text{C}$  has already been seen in Figure 2. At  $250^\circ\text{C}$ , the nitrogen loss remains rapid (Figure 3A). Removal of nitrogen in the form of  $\text{N}_2$  in He is very much slower (Figure 3B). The phase disappearance is very fast in  $3\text{H}_2/\text{CO}$  as well, (Figure 3C) but in this case does not reflect fast loss of substantial nitride nitrogen to ammonia in the gas phase. Constant acceleration spectra taken



after 20 minutes of exposure to  $3\text{H}_2/\text{CO}$  show that the initial contact with syngas first removes nitrogen from the lattice to form an  $\epsilon$  nitride, which has small contribution at the 0.5 mm/s velocity. Further reaction in synthesis gas then produces carbonitrides. Carburation in pure CO produces only a gradual structural change (Figure 3D). The final phase, as confirmed by the constant acceleration spectrum, is a very broad doublet which has little definition (less even than the spectrum in Figure 1D).

Investigation of the mechanism of nitride decomposition in hydrogen can be studied by mass spectrometry. In addition, surface species present during the nitriding process in ammonia can be identified by decomposition in deuterium. Figure 4 shows the decomposition of a  $\zeta\text{-Fe}_2\text{N}$  in deuterium into the deuterio-ammonias at  $250^\circ\text{C}$ . The  $\zeta\text{-Fe}_2\text{N}$  nitride was prepared in  $\text{NH}_3$  at  $400^\circ\text{C}$ , then cooled to  $250^\circ\text{C}$  in  $\text{NH}_3$  and the reactor then purged with argon for 10 minutes. The nitride and surface species are stable in argon at  $250^\circ\text{C}$ . The decomposition in  $\text{D}_2$  occurs quickly, as predicted from the Mössbauer results in Figure 2. From the shape of the  $\text{ND}_3$  curve, which is the decomposition product of the nitride nitrogen, it is clear that a slow activation is taking place. Modelling of this phenomenon indicates that a surface competition between the amount of adsorbed hydrogen (or in the case of Figure 4, adsorbed deuterium) and a nitrogen surface species can successfully simulate the results. Bulk nitride is converted to this nitrogen surface species.

Also apparent in Figure 4 are the mixed ammonias with hydrogen contributions. The presence of  $\text{NH}_x\text{D}_{3-x}$  in the effluent shows clearly that the fresh surface retains some hydrogen. The appearance of  $\text{NH}_3$  first does not indicate that  $x = 3$ , but is the result of chromatographic isotopic exchange at the leading edge of the deuterium pulse. This hydrogen most probably exists as a stable  $\text{NH}_x$  surface species left over from the nitriding procedure in  $\text{NH}_3$ . It will be seen that this  $\text{NH}_x$  species is very reactive and is removed in synthesis gas.

The deuterium experiment and the Mössbauer studies show that some of the nitrogen in the pure nitrides is very labile. The transient mass spectrometric approach allows us to measure relative surface reactivities directly. Figure 5 shows the response of a freshly prepared and He-purged surface to  $3/1 \text{ H}_2/\text{CO}$ . The curves show clearly that surface hydrogen reacts preferentially with surface nitrogen rather than surface carbon. About 1.6 monolayer's worth of ammonia comes off before methane production starts. The  $\text{CO}_2$  curve shows that carbon is being deposited on the surface by the Boudouard reaction while hydrogen is being scavenged by the surface  $\text{NH}_x$  groups. The availability of surface species changes dramatically after five minutes on stream. Figure 6 shows the response of the reacting system to a short He pulse followed by a switch to hydrogen. The burst of methane is characteristic of excess surface carbon. Ammonia evolves only slowly from the catalyst. Because of the high reactivity of surface nitrogen species just demonstrated above, we take this result to indicate very low nitrogen content on the the surface of the working catalyst. The high reactivity of surface nitrogen with hydrogen can be delayed, but not suppressed, by the presence of excess surface carbon. If the surface of a fresh nitride is precarburized in CO and then exposed to synthesis gas, as shown in Figure 7, the surface carbon layer delays any activity for a short induction time, but then nitrogen is released as ammonia before carbon can react to methane. The surface  $\text{NH}_x$  species is therefore stable in helium or pure carbon monoxide at  $250^\circ\text{C}$ .

We have also begun studying iron nitrides supported on carbon. A small particle 5% iron on Carbolac-1, which is a high surface area ( $1000 \text{ m}^2/\text{g}$ ) carbon support, was prepared and reduced in hydrogen for 16 hours at  $400^\circ\text{C}$ . The room temperature Mössbauer spectrum of this reduced catalyst is shown in Figure 8a. The broad singlet at 0.0 mm/sec may be ascribed to superparamagnetic  $\text{Fe}^0$ . The typical six line pattern collapses to a superparamagnetic

singlet when the relaxation time is short compared to the lifetime of the excited state of the nucleus. We may therefore conclude that our iron crystallites are small. The asymmetric nature of this spectrum is due to the contribution of  $\text{Fe}^{2+}$  at 0.8 mm/sec, which arises from incomplete reduction of the passivated iron. Extensive (21 hrs) exposure to UHP He that was further purified in oxygen traps resulted in the spectrum of Figure 8b. The increased absorbance of the  $\text{Fe}^{2+}$  peak indicates that the catalyst is passivated in helium with oxygen concentrations on the order of 1 ppb. This catalyst was nitrified in pure  $\text{NH}_3$  at  $400^\circ\text{C}$  for 8 hours to produce the  $\zeta\text{-Fe}_2\text{N}$  phase, indicated by the doublet seen in Figure 8c. Figure 8d shows the result of exposure of this catalyst to 3/1  $\text{H}_2/\text{CO}$  at  $250^\circ\text{C}$  for 20 hours. This spectrum has the same general appearance of other bulk nitrified samples following FTS and indicates a complex mixture of nitride, carbide and carbonitride phases. Rereduction of this sample resulted in the spectrum shown in Figure 8e, showing major contributions (84%) from a bulk Fe metal pattern. Thus, the iron crystallites have sintered during the nitriding-reaction-reduction process. In previous experiments, we have shown that small particle  $\text{Fe}_4\text{N}$  on carbon has stable activity during Fischer-Tropsch synthesis. Our results here suggest that maintaining the small size of the particles is important to maintaining the stability of the nitride catalyst. The point in the process at which particle growth occurs is currently under investigation.

#### REFERENCES

1. Amelse, J.A., Butt, J.B. and Schwartz, L.H., *J. Phys. Chem.*, **82** (5), 558 (1978).
2. Anderson, R.B. and Hofer, L.J.E., in *Catalysis, Vol IV.* (Emmett, P.H., ed.), Reinhold, New York (1956).
3. Anderson, R.B., *The Fischer-Tropsch Synthesis* Academic Press, Orlando (1984).
4. Niemantsverdriet, J.W., van der Kraan, A.M., van Dijk, W.L. and van der Baan, J. *Phys. Chem.*, **84**, 3863 (1980).
5. Ott, G.L., Fleisch, T. and Delgass, W.N. *J. Cat.*, **65**, 253 (1980).
6. Anderson, R.B., *Cat. Rev.-Sci. Eng.*, **21** 53 (1980).
7. Borghard, W.G. and Bennett, C.O., *I&EC Prod. Res. & Dev.*, **18** 18 (1979).
8. Yeh, E.B., Jaggi, N.K., Butt, J.B., and Schwartz, L.H., *J. Catal.* **91**, 231 (1985).
9. Yeh, E.B., Schwartz, L.H., and Butt, J.B., *J. Catal.* **91**, 241 (1985).
10. Jack, K.H., *Acta Crystallogr.*, **5**, 404 (1952).
11. Grunze, M., Bozso, F., Ertl, G. and Weiss, M., *Appl. Surf. Sci.*, **1**, 241 (1978).
12. Ertl, G., Huber, M., and Thiele, N., *Z. Naturforsch. A.*, **34**, 30 (1979).
13. Shirane, G., Takei, W.J. and Ruby, S.L., *Phys. Rev.*, **126** (1), 49 (1962).
14. Bainbridge, J., Channing, D.A., Whitler, W.H., and Pendelburg, R.E., *J. Phys. Chem. Solid*, **34**, 1579 (1973).
15. Chen, G.M., Jaggi, N.K., Butt, J.B., Yeh, E.B. and Schwartz, L.H., *J. Phys. Chem.*, **87**, 5326 (1983).

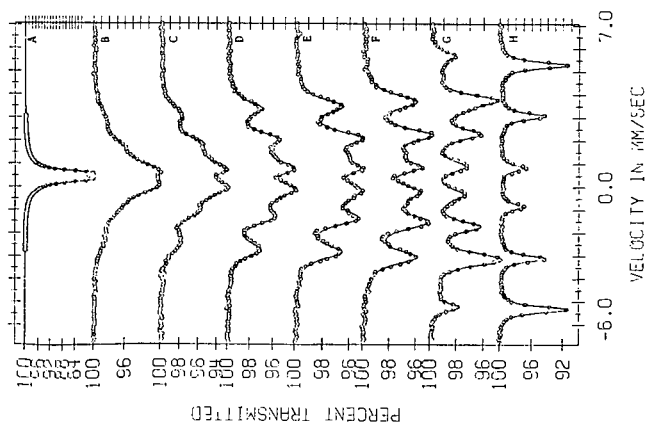


Figure 1. - Room Temperature Mössbauer spectra of iron nitrides.  
 A)  $\gamma$ - $\text{Fe}_3\text{N}$ ; B-F)  $\alpha$ - $\text{Fe}$  prepared by exposure of  $\alpha$ - $\text{Fe}$  to 91%  $\text{NH}_3$ , 9%  $\text{H}_2$  at 400°C (B), 225°C (C), 280°C (D), 250°C (E) and to 89%  $\text{NH}_3$ , 11%  $\text{H}_2$  at 400°C (F); G)  $\gamma$ - $\text{Fe}_3\text{N}$ ; H)  $\alpha$ - $\text{Fe}$

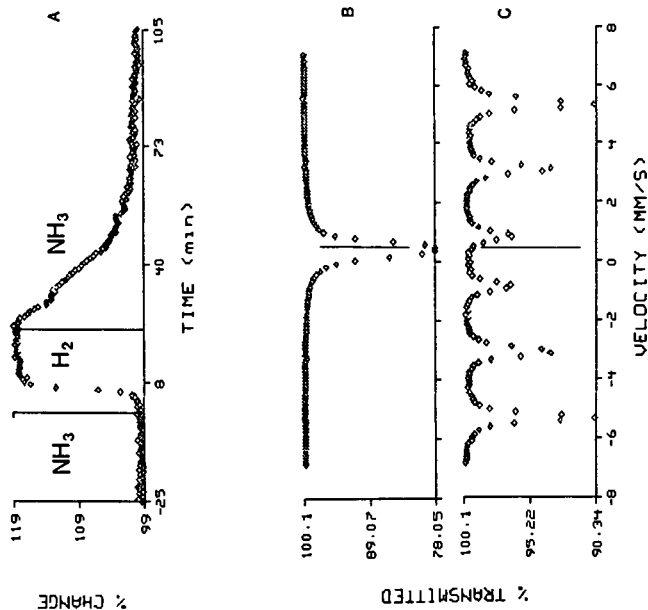


Figure 2. - Mössbauer spectra of  $\gamma$ - $\text{Fe}_2\text{N}$  during nitriding and denitriding.  
 A) Constant velocity spectrum, at the velocity indicated by the lines in spectra B) and C), taken at 325°C during a switch from  $\text{NH}_3$  to  $\text{H}_2$  and back to  $\text{NH}_3$ . B) Spectra of the initial and final  $\gamma$ - $\text{Fe}_2\text{N}$  at 25°C. C) 25°C spectrum of  $\alpha$ - $\text{Fe}$  after denitriding.

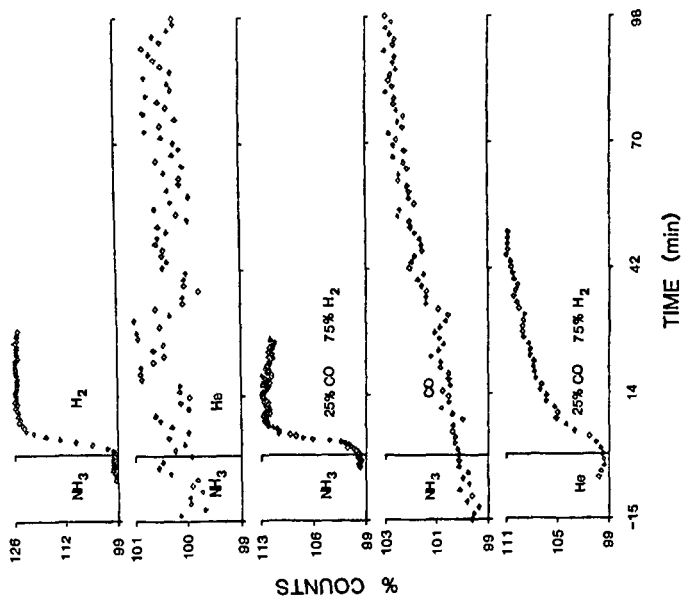


Figure 3. - *In situ* analysis of  $\zeta$ -Fe<sub>2</sub>N stability at 250°C.

- step change to H<sub>2</sub> from NH<sub>3</sub>
- step change to He from NH<sub>3</sub>
- step change to 3H<sub>2</sub>/CO from NH<sub>3</sub>
- step change to CO from NH<sub>3</sub>
- step change to 3H<sub>2</sub>/CO from NH<sub>3</sub> over pre-oxidized  $\zeta$ -Fe<sub>2</sub>N

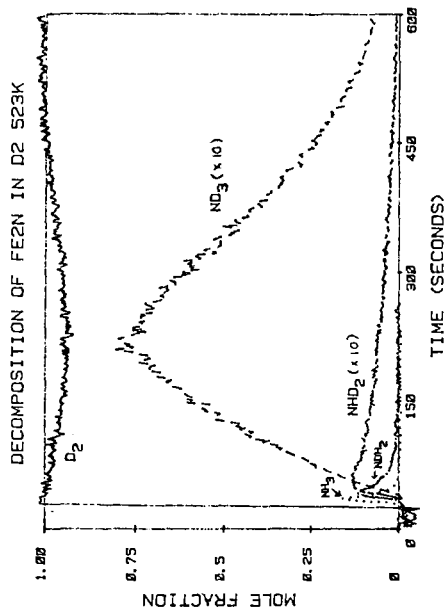


Figure 4. - Decomposition of  $\zeta$ -Fe<sub>2</sub>N in deuterium at 250°C after purging in argon.

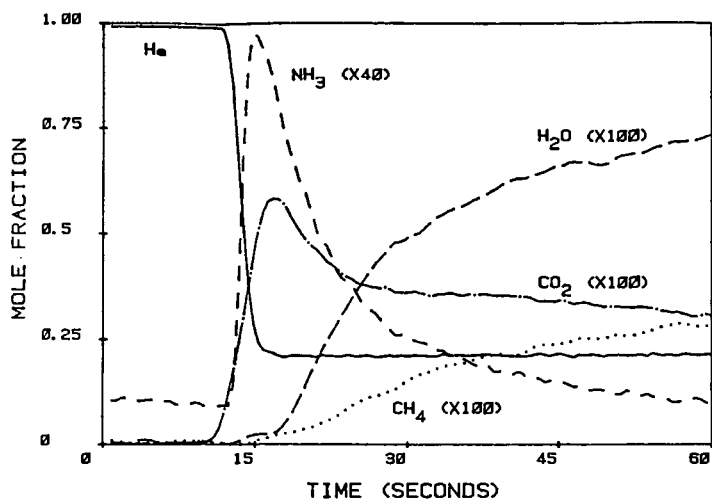


Figure 5. - Step change from helium to 3 H<sub>2</sub>/1 CO/1 He over an  $\epsilon$  nitride at 250°C.

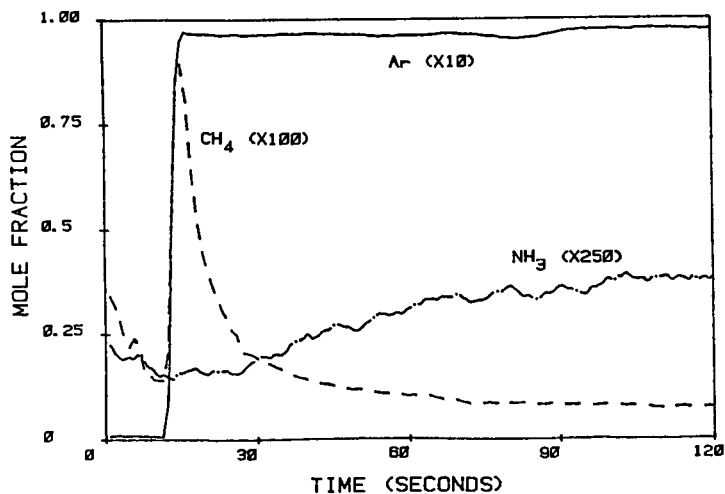


Figure 6. - Step from helium to 10 H<sub>2</sub>/Ar over an  $\epsilon$  nitride after 5 min. of FT synthesis in 3/1 H<sub>2</sub>/CO at 250°C.

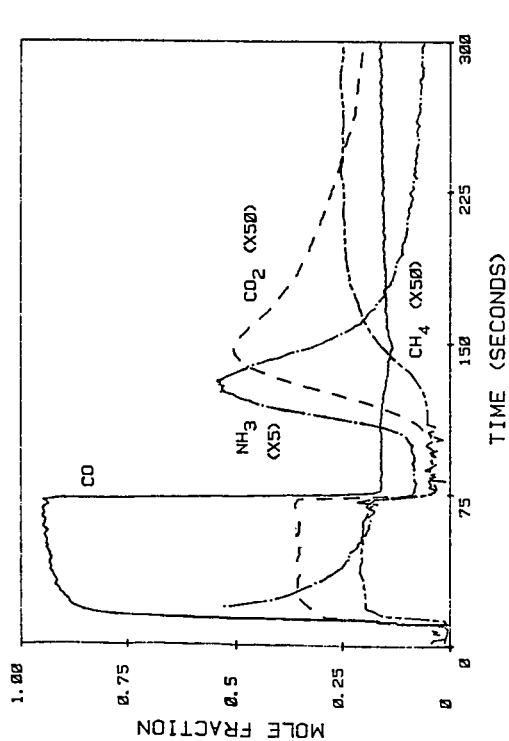


Figure 7. - Pretreatment of a  $\gamma$ -Fe<sub>2</sub>N catalyst in 1 min. of CO followed by 3/1 H<sub>2</sub>/CO at 250°C.

# MOSSBAUER SPECTRA 5Wt% IRON ON CARBOLAC

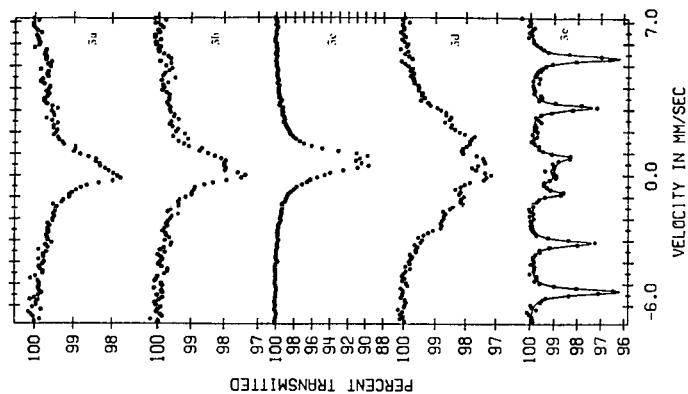


Figure 8. - Mössbauer spectra of 4.5 wt% Fe supported on carbolac.

- a) Reduced in H<sub>2</sub> at 400°C for 16 hrs.
- b) Exposed to He at RT for 21 hrs.
- c) Nitrided to  $\gamma$ -Fe<sub>2</sub>N using 100 NH<sub>3</sub> at 400°C for 8 hrs.
- d) Post - FTS at 250°C for 20 hrs.
- e) Reduced in H<sub>2</sub> at 400°C for 4 hrs.

## THE SURFACE CHEMISTRY OF IRON FISCHER-TROPSCH CATALYSTS

D. J. DWYER AND J. H. HARDENBURGH

Exxon Research and Engineering  
Corporate Research Science Laboratory  
Route 22 East  
Annandale NJ. 08801

### INTRODUCTION

The indirect conversion of coal to liquid hydrocarbons via steam gasification followed by synthesis gas ( $\text{CO}/\text{H}_2$ ) chemistry has been the subject of intensive study for a number of decades. A key technological challenge facing researchers in this area is control over the product distribution during the hydrocarbon synthesis step. In the case of iron Fischer-Tropsch catalysts, it has long been known that the addition of alkali to the metal catalyst has a significant impact on the product distribution(1). Iron catalysts treated with alkali produce less methane more alkenes and higher molecular weight products. In spite of numerous investigations (2-9), the details of this promotional effect are not understood on a molecular level. To explore the role of alkali in the surface chemistry of iron catalysts, we have carried out a combined surface science and catalytic kinetic study of a model iron catalyst with and without surface alkali.

### EXPERIMENTAL

The experimental apparatus has been described elsewhere (10,11). It consists of a medium pressure microreactor coupled to a ultra-high vacuum system equipped to perform x-ray photoelectron spectroscopy. The microreactor was a small UHV compatible tube furnace with an internal volume of approximately 10 cc and gold plated walls for inertness. The catalysts used in the study were pressed into a gold mesh backing material which in turn was mounted on a gold sample boat. The boat and the sample could be shuttled back and forth between the high pressure reactor and the UHV surface analysis chamber via a special UHV manipulator.

The iron catalysts were prepared by reducing ultra-high purity iron oxide ( $\text{Fe}_2\text{O}_3$ ) in an external tube furnace. The reduction was carried out to completion at 675K, 1 atm  $\text{H}_2$  for 24 hours. The surface of this pyrophoric powder was then passivated for 2 hours in a 1%  $\text{O}_2$  in He mixture. The passivated iron powder was characterized by x-ray diffraction and only  $\alpha$ -iron was detected. XPS analysis of the same sample revealed only  $\text{Fe}_2\text{O}_3$  on the surface. These data indicate that the passivated iron powder consists of an iron core surrounded by a thin skin of iron oxide.

2.5 grams of the passivated powder was impregnated with .015 grams of  $\text{K}_2\text{CO}_3$  through a standard aqueous incipient wetness technique. The surface areas of the two samples (with and without) alkali were determined by the BET method. The potassium containing catalyst had a surface area of  $16 \text{ M}^2/\text{gram}$  and the untreated catalyst had a surface area of  $18 \text{ M}^2/\text{gram}$ . Assuming complete dispersion of the potassium and a surface site density on the iron of  $10^{15}/\text{cm}^2$ , the potassium coverage on the iron surface is approximately

1/3 of a monolayer.

## RESULTS AND DISCUSSIONS

A detailed report on the surface compositional changes that accompany pretreatment and activation of the iron catalysts has been reported elsewhere (10-11). The surface of the untreated iron catalyst consists primarily of iron in +3 oxidation state ( $\text{Fe}_2\text{O}_3$ ). Upon reduction ( $\text{H}_2$ , 2 atm, 625 K), the surface is converted to metallic iron. The metallic iron surface is, however, unstable under synthesis gas ( $\text{H}_2:\text{CO}$  3:1, 525 K, 6atm) and is slowly converted to iron carbide. Concomitant with the carbidization of the iron surface is a marked increase in the rate of catalytic reaction of CO to hydrocarbons. Steady state activity is reached after 3-4 hours under reaction conditions. The steady state product distribution of the unpromoted iron carbide surface consists primarily of methane and small linear alkanes. Two types of carbon species were identified on the surface of unpromoted material after reaction. A carbidic form of carbon that was reactive to  $\text{H}_2$  and was easily convert to methane. The second type of surface carbon was a coke-like or graphitic deposit that was very unreactive to  $\text{H}_2$ . This second type of carbon was found to dominate the surface and poison the reaction when the reaction was run at elevated temperatures.

The surface of the potassium treated catalyst after reduction consisted of a metallic iron with a strongly adsorbed potassium oxygen complex of approximately 1:1 stoichiometry. The stability of this complex is evident since it is formed by decomposition of the thermodynamically stable  $\text{K}_2\text{CO}_3$ . Upon exposure to synthesis gas the metallic iron is once again converted to iron carbide and a slow increase in reactivity accompanies this change in surface composition. The product distribution over the potassium treated catalyst is substantially different than that observed over the unpromoted surface. The methane yield is lower, the average molecular weight is higher and the product now consists primarily of linear alkenes. After reaction the surface is covered by layer of hydrocarbon which is best characterized as polymethylene.

It has been suggested in the literature that the role of surface alkali in this reaction is to facilitate the dissociation of CO on the surface (9). Presumably, the increased concentration of reactive carbon on the surface shifts the product distribution towards higher molecular weights by enhancing the chain building step in the reaction. However, the results of this study clearly show that the iron and iron carbide surfaces easily break the carbon-oxygen bond in CO. The unpromoted catalyst is saturated in carbon which is reactive towards hydrogen. Therefore, it does not seem reasonable that the role of surface alkali is to enhance CO dissociation. The simple and straight forward explanation of the results of this study is that originally proposed by Dry(2). Potassium addition increases the heat of adsorption of CO and weakens the adsorption of  $\text{H}_2$  which in turn changes the relative concentrations of CO and H on the surface of the catalyst under reaction conditions. Our results indicate that the unpromoted iron carbide is a very good hydrogenation catalyst producing primarily small alkanes. Little or no hydrocarbon fragments are observed on the surface after reaction. When potassium is added the overall hydrogenation activity of the surface drops. Larger alkanes dominate the product and there is an accumulation of hydrocarbon



fragments or intermediates on the surface. It appears that the unpromoted surface is too good a hydrogenation catalyst with a high hydrogen activity at the surface. The hydrocarbon intermediates which form on the surface are rapidly intercepted by surface hydrogen and terminated as small alkanes. When potassium is present the hydrogen activity at the surface is much lower, this allows the hydrocarbon intermediates to accumulate and polymerize on the surface and results in larger molecules which are alkenes and not alkanes.

#### REFERENCES.

1. F. Fischer and H. Tropsch, Ber. Deut. Chem. Ges. B59(1926) 830.
2. M.E. Dry, T. Shingles, L. J. Boshoff and G.J. Oosthuizen, J. Catalysis 15 (1969) 190.
3. J. Benziger and R. J. Madix, Surface Science 94 (1980) 119.
4. K. Subramanzam and M. R. A. Rao, J. Res. Inst. Catalysis Hokkaido 18 (1970) 124.
5. H. Kobel and W.K. Muller, Ber. Bunsenges Physik. Chem. 67 (1963) 212.
6. G. Broden, G. Gafner and H.P. Bonzel, Surface Science 84 (1979) 295.
7. S. R. Kelemen, A. Kaldor and D. J. Dwyer, Surface Science 121 (1982) 303.
8. J. E. Crowell, E. L. Garfunkel and G.A. Somorjai, Surface Science 121 (1982) 303.
9. H. P. Bonzel, Chem. Ing. Tech. 54 (1982) 908.
10. D. J. Dwyer and J. H. Hardenburgh, J. Catalysis 87 (1984) 66.
11. D. J. Dwyer and J. H. Hardenburgh, Appl. Surface Science 19 (1984) 14.

atmosphere. Product gases exiting the cell were analyzed by gas chromatography (temperature programmed Porapak Q column) utilizing a combination of thermal conductivity and flame ionization detection. Following evacuation of the reaction cell, samples could be transferred into the UHV chamber without exposure to air.

The materials characterized included high purity iron foils (Johnson Matthey), and commercially obtained  $\text{Fe}_3\text{O}_4$  and  $\text{Fe}_2\text{O}_3$  powders (Alfa Products). Oxide samples were mounted by pressing the powders into 48 mesh copper screen. All synthesis reactions were carried out over the  $\text{Fe}_2\text{O}_3$  powder, after first reducing the oxide in flowing hydrogen for 9 hours at  $400^\circ\text{C}$ . Hydrogen chemisorption measurements, using the method described by Amelse, et al. (12), yielded an uptake of  $21 \mu\text{mole H}_2/\text{g Fe}$  for the reduced powder. Specific reaction rates were calculated based on the hydrogen uptake, assuming two surface iron sites per adsorbed  $\text{H}_2$  molecule. Gases used in the sample reductions and synthesis reactions were dried by passage through a silica gel bed immersed in a dry ice/acetone bath. Oxygen impurities were removed by a 10%  $\text{MnO}/\text{SiO}_2$  trap which had previously been reduced in flowing hydrogen at  $350\text{--}400^\circ\text{C}$ . The 3:1  $\text{H}_2/\text{CO}$  synthesis mixture (Matheson) was obtained in an aluminum cylinder to minimize the formation of carbonyls. A silica gel trap heated to  $200^\circ\text{C}$  was used to remove any carbonyls present in the reactant stream.

## RESULTS

### Oxidized Iron Surfaces

The  $\text{Fe}(2p)$  XPS spectra characteristic of iron and the stoichiometric oxides are summarized in Figure 1. The metallic iron spectrum (Figure 1a) was measured for a foil sample after the surface had been cleaned by repetitive cycles of argon ion sputtering and annealing at  $450^\circ\text{C}$  in the vacuum chamber. The surfaces of the air-exposed oxide powders were invariably contaminated by adsorbed water, as evidenced by broadening on the high binding energy side of the  $\text{O}(1s)$  XPS peaks. In the case of the  $\text{Fe}_2\text{O}_3$  powder, mild heating in vacuum (1 hr at  $170^\circ\text{C}$ ) removed nearly all of this surface contamination, resulting in the spectrum shown in Figure 1c. The surface of the  $\text{Fe}_3\text{O}_4$  powder was at least partially oxidized to  $\text{Fe}_2\text{O}_3$ , based on the  $\text{Fe}(2p)$  peak positions and satellite structure measured for as-prepared samples. Using the spectrum fitting procedure described below, we observed that brief ( $<2$  min) argon ion sputtering of iron oxide surfaces results in the reduction of  $\text{Fe(III)}$  to  $\text{Fe(II)}$ , while prolonged sputtering leads to the formation of a significant metallic iron phase. In either case, this surface reduction is accompanied by a decrease in the ratio of the oxygen to iron XPS intensities. The  $\text{Fe}_3\text{O}_4$  spectrum (Figure 1d) was obtained for a powder sample after brief argon ion sputtering, followed by heating for 5 hours at  $350^\circ\text{C}$  in vacuum. During this sample heating, the  $\text{O}(1s)/\text{Fe}(2p_{3/2})$  intensity ratio increased steadily and then leveled off, signaling a gradual re-oxidation of the sputtered surface.

In a recent review of oxide photoemission studies, Wandelt (13) observed that the  $\text{Fe}(2p)$  XPS spectrum of  $\text{Fe}_3\text{O}_4$  is simply a weighted average of the spectra for  $\text{Fe}_2\text{O}_3$  ( $\text{Fe(III)}$ ) and  $\text{Fe}_x\text{O}$  (primarily  $\text{Fe(II)}$ ). This is illustrated by the  $\text{Fe(II)}$  spectrum in Figure 1b, which was obtained by subtracting out the  $\text{Fe(III)}$  contribution to the  $\text{Fe}_3\text{O}_4$  spectrum (assuming an  $\text{Fe(III)}$  to  $\text{Fe(II)}$  area ratio of 2:1). The resulting  $\text{Fe(II)}$  peak positions and satellite structure are in excellent agreement with XPS results reported for  $\text{Fe}_x\text{O}$  (13,14).

Spectra representing the individual oxidation states of iron (Figure 1a,b,c) can be used to analyze data obtained for partially oxidized surfaces, as illustrated in Figure 2. The points in this figure indicate data measured for an iron foil after brief exposures to  $1 \times 10^{-6}$  torr of oxygen at 400°C. The solid curves through these points indicate linear combinations of the spectra representing the individual iron oxidation states. Coefficients for these linear combinations were determined using the usual least squares minimization criteria. The individual contributions of each oxidation state to the fitted spectra are also indicated in Figure 2. This procedure allows the compositions of partially oxidized surfaces to be approximated in terms of the area contributions of each oxidation state to the total XPS spectrum. Area contributions to the spectra in Figures 2a and 2b are 78% Fe / 7% Fe(II) / 15% Fe(III), and 23% Fe / 29% Fe(II) / 48% Fe(III), respectively.

#### Carbided Iron Surfaces

Iron carbides were prepared by treating reduced powder samples either with ethylene or a 3:1 H<sub>2</sub>/CO mixture at 250-275°C. Analysis of these samples by Mössbauer spectroscopy indicated that the powders were fully carburized and consisted primarily of X-Fe<sub>5</sub>C<sub>2</sub>. XPS results for the carbide powders did not depend on the carburization medium employed, and we therefore limit discussion in this section to samples carbided under normal synthesis conditions (250°C, 1 atm, 3:1 H<sub>2</sub>/CO).

The catalytic behavior of the initially reduced powder is illustrated in Figure 3. The turnover frequency for methane formation increased steadily during the first 4 hours of synthesis and then remained nearly constant at ~.0035 molecules/site sec for times in excess of 20 hours. The steady state turnover frequency compares well with values in the range of .003 to .007 molecules/site sec reported by Amelse, et al. (12) for silica supported iron under similar reaction conditions. The steady state CO conversion level over the iron powder catalyst was 0.6%, based on integration of the C<sub>1</sub> to C<sub>5</sub> hydrocarbon products. Analysis of the hydrocarbon product distribution by the Schulz-Flory model yielded a chain growth parameter  $\alpha = 0.48$ .

XPS results obtained for the iron powder in the reduced and fully carburized states are summarized in Figure 4. The reduced catalyst exhibited an Fe(2p<sub>3/2</sub>) binding energy of 707.0 eV, and a shift to 707.3 eV was observed following exposure to synthesis conditions for 30 hours. Dwyer and Hardenbergh (15) reported a similar shift upon carburization of unsupported iron during low conversion synthesis at 7 atm. In addition to small increases in the iron core level binding energies, the metal and carbide phases are distinguished by differences in the iron Auger line shape, as illustrated in Figure 4. The most pronounced difference in line shape occurs for the Fe(LMV) Auger transition, in the kinetic energy range from 610 to 660 eV. When Al K $\alpha$  x-rays are used, this region also includes the Fe(2s) core level transition at a kinetic energy of ca. 639 eV.

Since the Fe(2p<sub>3/2</sub>) peaks of metallic iron and X-Fe<sub>5</sub>C<sub>2</sub> are nearly identical in shape and differ in position by only 0.3 eV, changes in the iron Auger spectrum provide a more useful method for characterizing mixtures of these phases. This is demonstrated by the results in Figure 5, which were obtained for a reduced powder sample after exposure to synthesis conditions for periods of 20 and 100 minutes. The Auger spectra in this figure were fit with linear combinations of the metal and carbide spectra (Figure 4), using the

least squares method described earlier. Area contributions of the carbide phase to the iron Auger spectra were 36% and 48% after synthesis for 20 and 100 minutes, respectively. The C(1s) spectra in Figure 5 illustrate the utility of XPS in characterizing the carbon adlayer which develops on catalyst surfaces during the Fischer-Tropsch synthesis. Krebs, et al. (9) have shown that the initial increase in activity observed during synthesis over iron foils is associated with the formation of surface "carbide" carbon, corresponding to the low binding energy (283.2 eV) C(1s) peaks in Figure 5. The high binding energy (285.3 eV) peaks in these spectra indicate the presence of graphitic surface carbon, which is associated with the deactivation of iron synthesis catalysts.

### CONCLUSIONS

Analysis of Fe(2p) XPS and iron Auger spectra, combined with C(1s) XPS measurements, provides a valuable technique for studying the compositional behavior of Fischer-Tropsch catalysts. The extent of catalyst oxidation during synthesis at high conversions may be estimated in terms of the area contribution of oxide phases to the Fe(2p) spectrum. Similarities between the metal and carbide core level spectra are likely to complicate the determination of these phases when oxides are present. Analysis of the metal and carbide contributions to the iron Auger spectrum provides an alternate method for monitoring surface carbide formation during low conversion synthesis. The "surface compositions" obtained in this manner are at best semi-quantitative, since the contribution of a particular phase to the XPS or Auger spectrum will depend on both the amount and distribution of that phase within the detected volume. In spite of this, the spectrum fitting technique should prove to be useful in characterizing the time and conversion dependent nature of the active catalyst surface.

### REFERENCES

- (1) J.A. Amelse, J.B. Butt, and L.H. Schwartz, *J. Phys. Chem.*, **82**, 558 (1978).
- (2) G.B. Raupp and W.N. Delgass, *J. Catalysis*, **58**, 348 (1979).
- (3) K.M. Sancier, W.E. Isakson, and H. Wise, *Adv. Chem. Ser.* **178**, 129 (1979).
- (4) J.W. Niemantsverdriet, A.M. van der Kraan, W.L. van Dijk, and H.S. van der Baan, *J. Phys. Chem.*, **84**, 3363 (1980).
- (5) G.B. Raupp and W.N. Delgass, *J. Catalysis*, **58**, 361 (1979).
- (6) H. Matsumoto, *J. Catalysis*, **86**, 201 (1984).
- (7) J.F. Shultz, W.K. Hall, B. Seligman, and R.B. Anderson, *J. Amer. Chem. Soc.*, **77**, 213 (1955).
- (8) R.B. Anderson, L.J.E. Hofer, E.M. Cohn, and B. Seligman, *J. Amer. Chem. Soc.*, **73**, 944 (1951).
- (9) H.J. Krebs, H.P. Bonzel, and G. Gafner, *Surf. Sci.*, **88**, 269 (1979).
- (10) H.P. Bonzel and H.J. Krebs, *Surf. Sci.*, **91**, 499 (1980).
- (11) H.J. Krebs and H.P. Bonzel, *Surf. Sci.*, **99**, 570 (1980).
- (12) J.A. Amelse, L.H. Schwartz, and J.B. Butt, *J. Catalysis*, **72**, 95 (1981).
- (13) K. Wandelt, *Surf. Sci. Reports*, **2**, 1 (1982).
- (14) M. Oku and K. Hirokawa, *J. Appl. Phys.*, **50**, 6303 (1979).
- (15) D.J. Dwyer and J.H. Hardenbergh, *J. Catalysis*, **87**, 66 (1984).

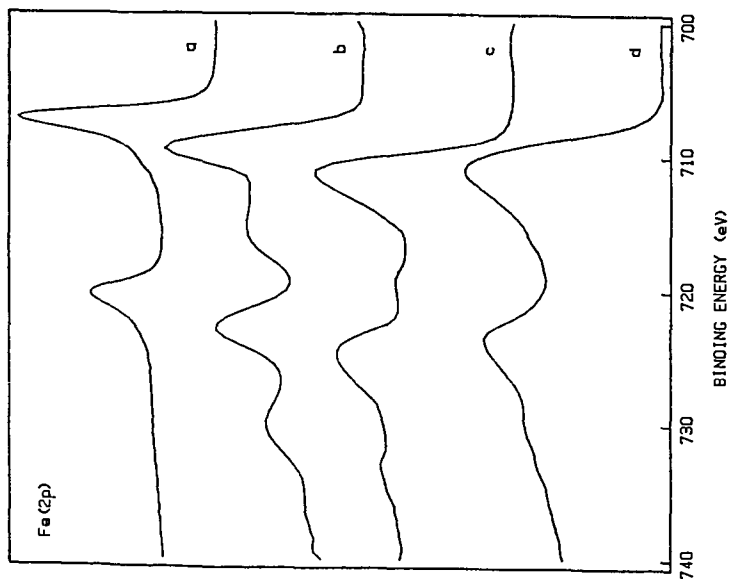


Figure 1. Fe(2p) XPS spectra of metallic iron and iron oxides. (a) clean foil (b) Fe(II) contribution to  $\text{Fe}_3\text{O}_4$  spectrum (c)  $\text{Fe}_2\text{O}_3$  (d)  $\text{Fe}_3\text{O}_4$ .

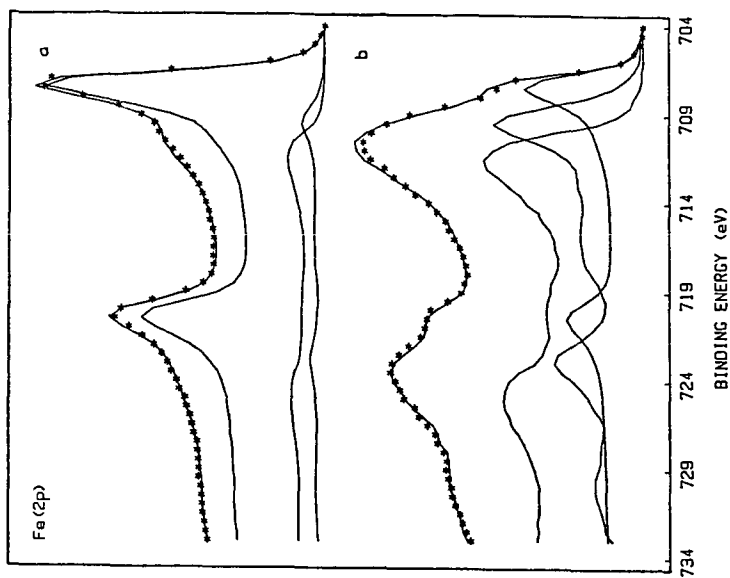


Figure 2. Examples of Fe(2p) spectrum fitting for partially oxidized iron foil. (a) 170 L  $\text{O}_2$  (b) 670 L  $\text{O}_2$  at  $400^\circ\text{C}$ .

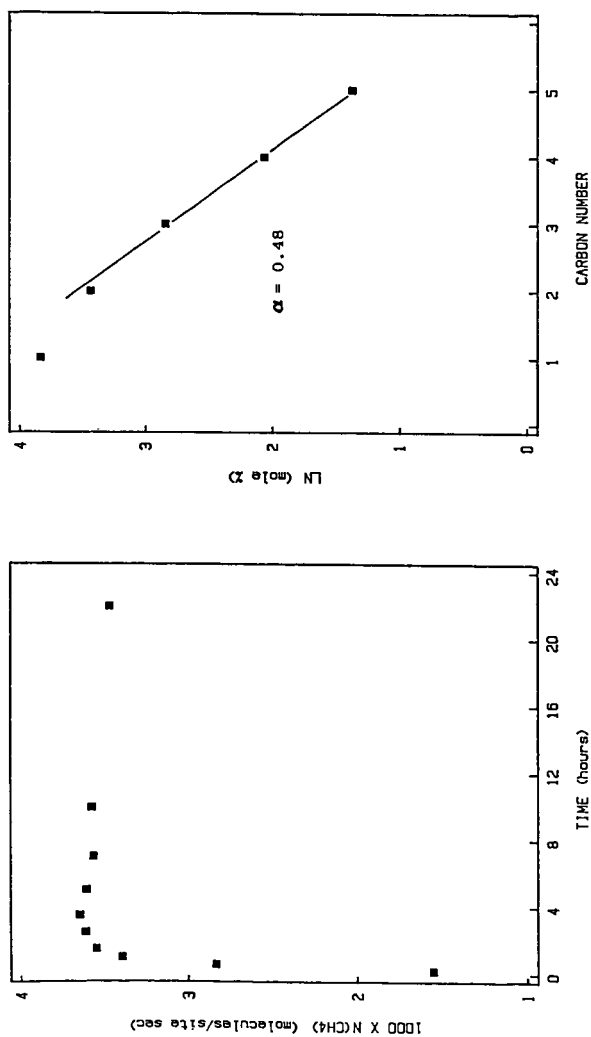


Figure 3. Methane turnover frequency versus time and steady state Schulz-Flory plot for synthesis over unsupported iron powder (250°C, 1 atm, 3:1 H<sub>2</sub>/CO).

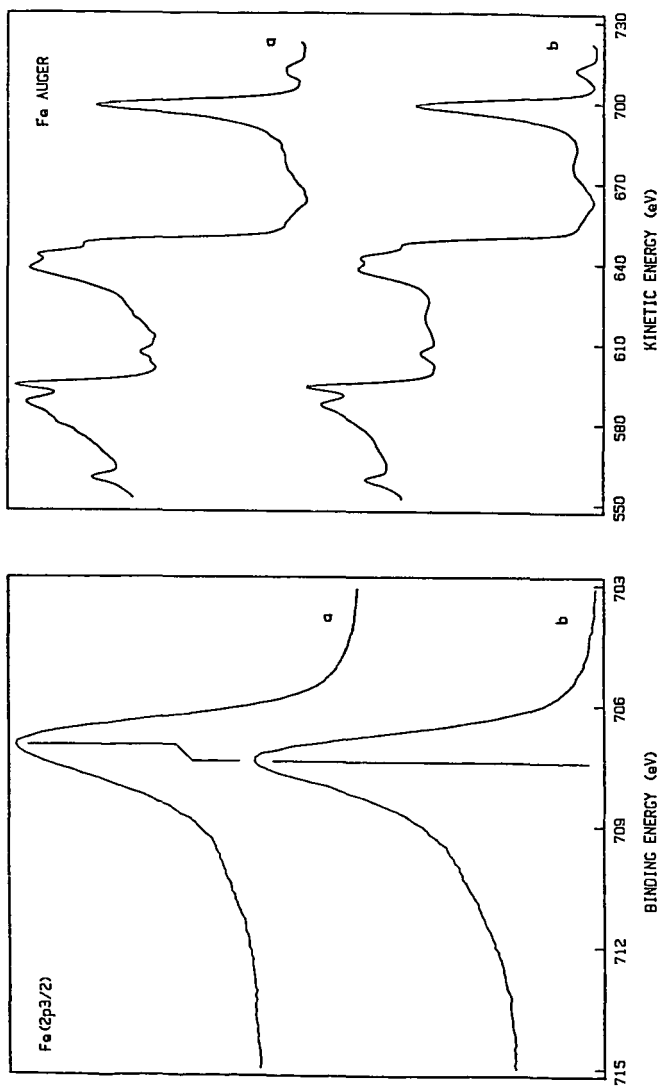


Figure 4. Fe(2p<sub>3/2</sub>) XPS and Fe Auger spectra of unsupported iron powder. (a) after reduction in 1 atm H<sub>2</sub> at 400°C (b) after hydrocarbon synthesis for 30 hr in 1 atm 3:1 H<sub>2</sub>/CO at 250°C.

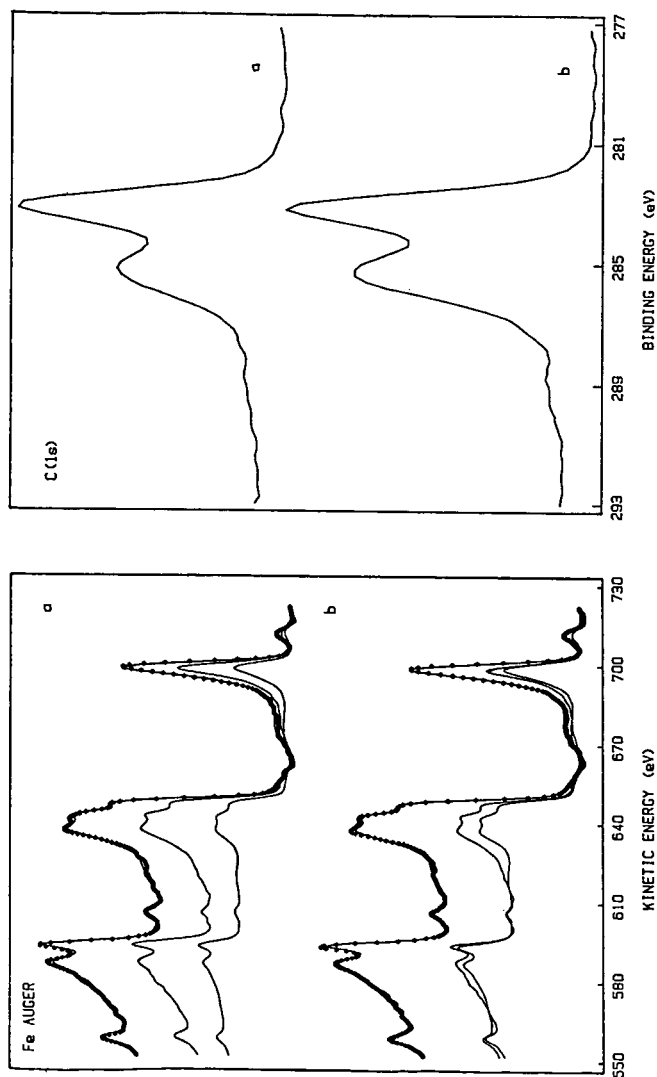


Figure 5. Fe Auger and C(1s) XPS spectra of unsupported iron powder after hydrocarbon synthesis for (a) 20 min (b) 100 min. Fe Auger spectra area contributions are: (a) 64% metal, 36% carbide (b) 52% metal, 48% carbide.



## XPS Characterization of Iron Fischer-Tropsch Catalysts

C. S. Kuivila, P. C. Stair, and J. B. Butt

Department of Chemical Engineering and Department of Chemistry  
Northwestern University, Evanston, Illinois 60201

### INTRODUCTION

The carburization of iron catalysts during the Fischer-Tropsch synthesis has received considerable attention, with techniques such as Mössbauer spectroscopy, x-ray diffraction, and thermomagnetic analysis being used to identify the bulk iron phases which are formed (1-4). Based on a recent Mössbauer study of unsupported iron (4), it is fairly well established that the  $\epsilon$ -Fe<sub>2.2</sub>C and X-Fe<sub>5</sub>C<sub>2</sub> carbides form at normal synthesis temperatures (ca. 250°C), while substantial amounts of cementite ( $\theta$ -Fe<sub>3</sub>C) are formed at temperatures above 350°C. Studies of both supported (1,5) and unsupported (4,6) iron have shown that the synthesis activity of an initially reduced catalyst is low, and increases to a maximum as carburization proceeds. Earlier work done at the Bureau of Mines (7) also suggests that controlled pre-carburization of fused iron catalysts at lower temperatures may improve long-term activity maintenance during the synthesis.

Although recent carburization studies have typically involved CO conversion levels in the range of a few percent or less, it is clear from work done at the Bureau of Mines (7,8) that higher conversion levels lead to significant oxidation of iron catalysts to Fe<sub>3</sub>O<sub>4</sub>. The working catalyst can thus consist of a mixture of metallic, carbide, and oxide phases, the relative amounts depending on catalyst pretreatment, synthesis conditions, and time on stream. A result of this complex behavior is that no clear picture exists regarding the nature of the catalytically active surface, or its dependence on the conditions employed in the synthesis. Much of the early work involving surface techniques (XPS/AES) in the study of CO hydrogenation over iron was carried out using foils or single crystals as model catalyst surfaces (9-11). Efforts in these studies focused on characterization of the carbon adlayer which developed on the metal surfaces during exposure to synthesis conditions.

In this paper, we address the XPS characterization of iron phases which occur on the surfaces of Fischer-Tropsch catalysts. Results obtained for single-phase metal, oxide, and carbide samples are presented. Methods for estimating the extent of carbide formation during low conversion synthesis, and the extent of catalyst oxidation at high conversions are also illustrated.

### EXPERIMENTAL

The XPS measurements were performed in an AEI ES200 ESCA spectrometer, equipped with a hemispherical electrostatic energy analyzer and aluminum-anode x-ray source. Electron binding energies were referenced to the Au(4f<sub>7/2</sub>) line of a gold foil at 84.0 eV. Samples were introduced into the system through a small volume (30 cc), differentially pumped reaction cell, attached directly to the vacuum chamber. The samples were mounted on a copper stage which could be heated resistively to 500°C, with temperature measurement by a chromel-alumel thermocouple junction. While in the cell, samples could be exposed to static or flowing gases at pressures up to one

In Situ Study of the Surface Interactions  
In Coal Liquefaction Catalysts

P.A. Montano

Dept. of Physics, West Virginia University, Morgantown, WV 26506

There is an increasing interest in the development of better catalysts for the hydrodenitrogenation (HDN) and hydrodesulfurization (HDS) of coal derived fuels and oil heavy residues. These synthetic feedstocks and heavier petroleum fractions contain a higher concentration of heteroatoms than light petroleum stocks and are much more difficult to process. Metal sulfides catalysts play a very important role in HDN and HDS processes as well as in direct coal liquefaction. There is concrete evidence of the direct role played by iron sulfides in direct coal liquefaction. We have investigated the surface reactions on iron sulfides, especially pyrrhotites using standard surface techniques, EXAFS and in situ Mossbauer spectroscopy. We find clear evidence of the involvement of the iron sulfides surfaces in the cleavage of oxygen bonds in coal and coal derived products. In HDN and HDS reactions, the role of the iron sulfides is less important than that of Mo-Co or Mo-Ni supported catalysts. We have performed a systematic in situ study of Ni-Mo supported on gamma alumina using x-ray absorption techniques as well as in situ Mossbauer spectroscopy. The HDN of quinoline was studied by both techniques between room temperature and 440°C at high hydrogen pressures. We find clear evidence of Ni association to Mo, there is also Ni in separated islands and a third phase of Ni interacting strongly with alumina and forming nickel-aluminate. When sulfidation takes place immediately after calcination two sulfide phases are identified, one associated with the  $\text{MoS}_2$  islands on the support and the other, probably, with a non-stoichiometric nickel sulfide compound. Very small amounts of nickel aluminate are observable.

The HDS of dibenzothiophene was studied using a pure  $\text{MoS}_2$  catalyst and a commercial Ni-Mo catalyst. The structure of the catalysts was investigated using x-ray absorption techniques. All the measurements were performed in situ between -195°C and 440°C. It was observed that the presence of nickel tends to stabilize the  $\text{MoS}_2$  islands on the support; in the absence of nickel there is very clear evidence of irreversible sulfur loss.

The difference in catalytic activity between iron sulfides and Mo sulfides is related to the difference in crystallographic structures, which favors in the case of Mo a high dispersion of the catalyst on the support.

Work supported by the USDOE.

## ALCOHOL REACTION KINETICS ON COPPER/ZINC OXIDE SURFACE

D. L. Roberts, L. Chan, and G. L. Griffin

Department of Chemical Engineering  
and Materials Science  
University of Minnesota  
Minneapolis, Minnesota 55455

### ABSTRACT

Recent commercial and academic interest in  $\text{CH}_3\text{OH}$  synthesis via  $\text{CO}$  hydrogenation, together with the high selectivity and relative simplicity of this reaction, make it an ideal reaction for testing and comparing adsorption studies, proposed mechanisms, and macroscopic rate behavior for oxide-based catalysts. Adsorption studies of  $\text{H}_2$ ,  $\text{H}_2\text{O}$ , and  $\text{CH}_3\text{OH}$  on  $\text{ZnO}$  powders and model thin films of  $\text{Cu/ZnO}$  have resolved several discrete adsorption sites. Infrared and temperature programmed decomposition studies of adsorbed  $\text{CH}_3\text{OH}$  are used to determine the energetics of the  $\text{CH}_3\text{O}(\text{a})$  and  $\text{HCOO}(\text{a})$  decomposition steps at these sites. Comparative studies using model  $\text{Cu/ZnO}$  thin films have resolved features common to bulk  $\text{ZnO}$  and bulk  $\text{Cu}$ , as well as differences in behavior which can be attributed to the availability of  $\text{ZnO}$  lattice anions at the perimeter of the  $\text{Cu}$  clusters. The results suggest that Type I sites on  $\text{ZnO}$  do not have a major role in the  $\text{CH}_3\text{OH}$  synthesis reaction on  $\text{Cu/ZnO}$  catalysts. Instead, the  $\text{CH}_3\text{OH}$  reaction may occur preferentially at perimeter sites of  $\text{Cu}$  clusters.

### INTRODUCTION

The reactivity of carbon-oxygen bonds in adsorbed oxygenated hydrocarbon intermediates is of fundamental importance in understanding the rates and selectivity of alcohol reactions on heterogeneous catalysts. Reactions of commercial interest include methanol synthesis, the direct synthesis of higher alcohols, alcohol decomposition (e.g., reforming, partial oxidation), etherification (e.g., production of MTBE as a gasoline blending agent), condensation (e.g., conversion to C-8 compounds on zeolites or other acid catalysts), and functionalization (e.g., amination reactions).

Work in our laboratory has focussed on understanding the surface reactions involved in the catalytic formation and decomposition of the simplest alcohol,  $\text{CH}_3\text{OH}$ . In particular, we have undertaken a systematic study of a series of model  $\text{ZnO}$  or  $\text{Cu/ZnO}$  catalyst surfaces using a combination of infrared spectroscopy, temperature programmed desorption and decomposition of adsorbates, and reactor measurements of transient and/or steady state kinetics. These studies are aimed at identifying the composition and geometry of various adsorption sites on the  $\text{Cu/ZnO}$  surface, the mechanism and kinetics of adsorbate reactions at the sites, and the importance of each site in the overall  $\text{CH}_3\text{OH}$  synthesis reaction.

In the present paper we describe selected results from our overall program. These results are chosen to illustrate two points: The importance of the formate intermediate in alcohol reactions on oxide surfaces and its role in maintaining hydrogenation selectivity, and the relative importance of adsorption sites on the

ZnO and Cu components of the catalyst surface.

## EXPERIMENTAL

Comparative studies of high surface area powders and planar thin-film samples are performed in two independent apparatus. Studies of powder samples were performed in the IR-TPD cell shown in Fig. 1. The sample containing 50-100 mg of ZnO is deposited from an aqueous slurry onto the front face of the cell mirror, a silver disk which is soldered to the re-entrant inner wall of the cell body. The mirror disk can be heated using the attached cartridge heater, or cooled to 100 K by flowing cooled N<sub>2</sub> through the attached coolant tube. After sealing the front of the cell using a flange-mounted CaF<sub>2</sub> window, the cell is attached to a stainless steel gas handling system and positioned in the sample compartment of the FTIR spectrometer (Nicolet 604SX). Spectra are obtained in a two-pass transmission mode by reflecting the IR beam from the mirror disk, thereby passing through the sample layer twice. During a typical in-situ TPD experiment, IR spectra are recorded at regular temperature intervals (75 scans/spectrum, at a scan rate of 1-2 scans/sec; resolution = 8 cm<sup>-1</sup>), while the flux of each desorbing species is monitored using a quadrupole mass spectrometer (Spectramass 800) attached to the gas handling system. All of the TPD experiments described here were performed with the IR-TPD cell evacuated and pumped by the gas handling system (i.e., no carrier gas is used).

The majority of the results described below were obtained using Kadox 25 ZnO, in order to examine the possible importance of the unique Type I adsorption sites for H<sub>2</sub> that have been reported for this material. The pretreatment required to activate the Type I sites involves (step 1) heating the sample in vacuum ( $P < 10^{-6}$  torr) at 673 K for 3 hours, (step 2) cooling to 573 K and admitting 0.5 torr O<sub>2</sub> for 10 minutes, then evacuating (O<sub>2</sub> cycle repeated three times), and (step 3) re-heating in vacuum to 673 K for 20 minutes before cooling to room temperature.

Once the pretreatment steps were finished, the IR-TPD experiments for the adsorbate of interest could be repeated indefinitely. For experiments using CH<sub>3</sub>OH and H<sub>2</sub>O, both of which are irreversibly adsorbed at 300 K, a volumetrically determined amount of either gas is admitted from the gas handling system into the sample cell. For H<sub>2</sub> adsorption experiments, it is necessary to fill the sample cell with 40 torr H<sub>2</sub> at 300 K to occupy the Type I sites, since the Type I H<sub>2</sub> adsorption state desorbs readily at room temperature.

The complementary experiments using planar samples were performed in the apparatus shown schematically in Fig. 2. The sample configuration is shown schematically in the inset of the figure. Samples are prepared by first depositing thin films of ZnO onto Au substrates, using a separate RF plasma sputtering system (perkin Elmer model 2400) with a ZnO target and a background gas of 24% O<sub>2</sub> : 76% Ar at a pressure of 1 Pa. The ZnO deposition rate was 200 Å/min and the deposited film thickness was approximately 1 µm. X-ray diffraction measurements confirm that the film grains are preferentially oriented with their c-axis within 5° of the surface normal. Thus the films expose a high-fraction of (0001)-Zn planes and/or vicinal defect surfaces.

After the ZnO film has been deposited, a chromel-alumel thermocouple is attached to the Au substrate and the sample is mounted into the TPD apparatus shown in the main part of Fig. 2. The apparatus consists of an ion-pumped stainless-steel bell jar equipped with a single pass cylindrical mirror analyzer, a quadrupole mass spectrometer, an ion sputtering gun, a side chamber which contains a Cu evaporation source and a quartz film thickness monitor. The sample itself is mounted on a differentially pumped sliding seal transfer rod that

permits the sample to be translated between the evaporation chamber and the focal point of the CMA.

Two sequences are used to prepare surfaces with different Cu loadings. In most cases, the loading was controlled by changing the exposure time of a sputter cleaned ZnO surface to the Cu evaporant flux. The deposition flux was approximately  $\text{\AA}/\text{min}$ , as measured using the film thickness monitor. The sample temperature during evaporation is 300 K. An independent measure of the Cu coverage is obtained using Auger analysis to examine the surface after evaporation. For a few experiments, an alternate procedure for varying the Cu loading consists of initially evaporating a high coverage of Cu and then heating the sample progressively higher temperatures above 800 K to desorb increasing amounts of the initial Cu layer.

After recording the Auger spectrum of the surface following Cu evaporation, methanol decomposition experiments were performed by exposing the sample to  $\text{CH}_3\text{OH}$  at 300 K by backfilling the chamber. After the background pressure returned to ca.  $10^{-10}$  torr, the sample is heated and the evolved products are monitored using the mass spectrometer. The heating rate used for the thin film experiments is 25 K/sec. Care is taken to stop each TPD experiment at a low enough temperature (ca 750 K) to prevent any loss of Cu by re-evaporation. Spectra for each of the observed products are usually recorded separately in repetitive experiments. Reproducibility between experiments is confirmed periodically by using multiplexed signal acquisition, at a cost in signal resolution. Reproducibility can also be confirmed by comparing the record of total pressure vs. time measured by the ionization gauge in the main chamber.

## RESULTS

Porous sample studies: Role of Type I sites. In Fig. 3 we show the IR spectra acquired during the adsorption and subsequent TPD of  $\text{CH}_3\text{OH}$  on Type I activated ZnO. The bottom curve is the spectrum of the sample in the presence of 40 torr  $\text{H}_2$  at 300 K, obtained prior to absorbing  $\text{CH}_3\text{OH}$ . The sharp band at  $1709\text{ cm}^{-1}$  and the less intense band at  $3491\text{ cm}^{-1}$  correspond to the Zn-H and O-H stretching vibrations, respectively, which are characteristic of  $\text{H}_2$  adsorbed at Type I sites. We note that the band observed at  $3618\text{ cm}^{-1}$  is attributed to a residual surface  $\text{OH}_{(\text{s})}$  species and is not associated with Type I  $\text{H}_2$  adsorption. Features in the  $2900$  to  $2800\text{ cm}^{-1}$  region are due to residual surface hydrocarbon impurities still remaining after the three 573 K  $\text{O}_2$  cleaning cycles of the pretreatment. The concentration of Type I sites in this sample is  $5.8\text{ }\mu\text{mole H}_2/\text{gm ZnO}$ , as determined from the integrated area under an  $\text{H}_2$  TPD spectrum.

The next curve is the spectrum obtained after evacuating the  $\text{H}_2$  and adsorbing an amount of  $\text{CH}_3\text{OH}$  corresponding to  $10\text{ }\mu\text{mole/gm}$ . The bands appearing at  $2932$  and  $2816\text{ cm}^{-1}$  are assigned to the asymmetric and symmetric C-H stretching vibrations of the surface methoxy species. We note that the adsorption of  $\text{CH}_3\text{OH}$  produces no new resolvable OH features in the region above  $3500\text{ cm}^{-1}$ , nor does it perturb the residual surface OH band at  $3618\text{ cm}^{-1}$ . If 40 torr of  $\text{H}_2$  is admitted to the cell at this point, the Zn-H and O-H bands characteristic of Type I sites do not appear. This confirms that  $\text{CH}_3\text{OH}$  adsorbs irreversibly at Type I sites, blocking them from further  $\text{H}_2$  adsorption. The fact that  $10\text{ }\mu\text{mole CH}_3\text{OH/gm ZnO}$  are required to clock the sites completely indicates that some of the  $\text{CH}_3\text{OH}$  must be adsorbed at non-Type I sites, as well.

The next curve in Fig. 3 is the spectrum of the sample obtained at 530 K during the decomposition of the adsorbed  $\text{CH}_3\text{OH}$ . The intensity of the methoxy C-H bands at  $2932$  and  $2816\text{ cm}^{-1}$  decreases, and new features grow in at  $2875$ ,  $1574$ ,  $1364$ ,  $1377\text{ cm}^{-1}$ . These new bands are assigned respectively to the C-H stretching

mode, the asymmetric and symmetric O-C-O stretching modes, and the in-plane C-H bending mode of a surface  $\text{HCOO}_{(a)}$  species. The asymmetric O-C-O stretching mode and the in-plane C-H bending mode also produce an additional combination band at  $2965\text{ cm}^{-1}$ . These results demonstrate the sequential conversion of  $\text{CH}_3\text{O}_{(a)}$  species to  $\text{HCOO}_{(a)}$  species.

A separate experiment was performed by interrupting the decomposition at 530 K (corresponding to the temperature at which the maximum  $\text{HCOO}_{(a)}$  coverage is observed) and quickly cooling the sample to 300 K to preserve the surface  $\text{HCOO}_{(a)}$  coverage. Admitting 40 torr of  $\text{H}_2$  to the cell at this stage failed to produce IR bands at  $3490$  or  $1710\text{ cm}^{-1}$ , thus indicating that the  $\text{HCOO}_{(a)}$  species also block the Type I  $\text{H}_2$  sites.

The uppermost curve is the spectrum of the sample obtained after completing the TPD experiment, cooling from 673 K to 300 K, adding 0.1 torr  $\text{O}_2$  to improve the IR transmission, and then admitting 40 torr of  $\text{H}_2$ . The bands at  $3492$  and  $1709\text{ cm}^{-1}$  have now been restored, indicating that the Type I sites have been made vacant following decomposition of the adsorbed  $\text{CH}_3\text{OH}$ .

The product desorption spectra recorded by the mass spectrometer during the preceding experiment are shown in Fig. 4. The  $\text{H}_2$  evolution curve has three resolvable features: a low temperature shoulder at 459 K, a broader shoulder near 511 K, and a desorption maximum at 565 K. The  $\text{H}_2$  desorption at 565 K is accompanied by the almost coincident desorption of  $\text{CO}$  and  $\text{CO}_2$  at 573 K. In contrast, the  $\text{H}_2$  evolved at 459 K and 511 K is not accompanied by any significant amount of carbon oxides. This is a clear indication that the  $\text{H}_2$  evolution peaks at 459 K and 511 K are a result of the conversion of  $\text{CH}_3\text{O}_{(a)}$ , while the nearly simultaneous desorption of  $\text{H}_2$ ,  $\text{CO}$ , and  $\text{CO}_2$  at 565-573 K is due to the decomposition of the surface  $\text{HCOO}_{(a)}$ . Figure 4 also shows that  $\text{H}_2\text{O}$  is not a favored product of either  $\text{CH}_3\text{O}_{(a)}$  conversion or  $\text{HCOO}_{(a)}$  decomposition, despite the oxidized condition of the  $\text{ZnO}$  sample.

To determine the importance of Type I sites on  $\text{ZnO}$  for  $\text{CH}_3\text{OH}$  decomposition, we next performed a series of experiments using pre-adsorbed  $\text{H}_2\text{O}$  to block the Type I sites before adsorbing  $\text{CH}_3\text{OH}$ . Infrared spectra recorded in the presence of 40 torr of  $\text{H}_2$  before and after  $\text{H}_2\text{O}$  was admitted to the cell showed that  $\text{H}_2\text{O}$  also adsorbs irreversibly into the Type I  $\text{H}_2$  sites, blocking them from  $\text{H}_2$  adsorption. Methanol was then admitted to the sample with the blocked Type I sites. Adsorption still occurs, as indicated by the IR spectrum which showed the C-H vibrational bands of the  $\text{CH}_3\text{O}_{(a)}$  intermediate. The fact that  $\text{CH}_3\text{OH}$  dissociatively adsorbed even on the Type I blocked sample confirms that  $\text{CH}_3\text{OH}$  adsorbs at non-Type I sites.

The TPD product desorption spectra recorded for the sample with co-adsorbed  $\text{H}_2\text{O}$  and  $\text{CH}_3\text{OH}$  are shown in Fig. 5. The first feature to note is the behavior of the  $\text{H}_2\text{O}$  desorption signal. A small amount of desorption is observed near 475 K; however, the majority of the  $\text{H}_2\text{O}$  desorbs with a peak maximum near 600 K. This is identical to the desorption behavior of pure  $\text{H}_2\text{O}$  (i.e., without co-adsorbed  $\text{CH}_3\text{OH}$ ). This indicates that the  $\text{H}_2\text{O}$  molecules adsorbed in Type I sites retain their identity throughout the experiment, that the Type I sites remain blocked by  $\text{H}_2\text{O}$  throughout the temperature range of  $\text{CH}_3\text{OH}$  decomposition, and that the adsorbed  $\text{H}_2\text{O}$  is not consumed in the formation of  $\text{CO}_2$  during the formate decomposition step.

A small amount of molecular  $\text{CH}_3\text{OH}$  desorbs between 400 K and 500 K. A similar molecular  $\text{CH}_3\text{OH}$  desorption peak can be observed from samples containing no pre-adsorbed  $\text{H}_2\text{O}$ , provided the initial  $\text{CH}_3\text{OH}$  coverage is greater than  $10\text{ }\mu\text{mole/gm}$ . This indicates that there is a finite combined concentration of both Type I and non-Type I sites at which  $\text{CH}_3\text{OH}$  is dissociatively adsorbed. Additional  $\text{CH}_3\text{OH}$  beyond this amount is adsorbed into a less tightly bound state

which desorbs molecularly at 450 K. The low temperature shoulder in the  $H_2O$  desorption spectrum probably arises from a similar state.

Dissociatively adsorbed  $CH_3OH$  ultimately decomposes to yield  $H_2$ ,  $CO$ , and  $CO_2$ . The  $H_2$  evolution curve shows two resolved maxima at 493 K and 557 K, corresponding to the two highest temperature features in the  $H_2$  desorption spectrum for decomposition of  $CH_3OH$  alone (cf. Fig. 4). However, the desorption shoulder at 459 K that was observed on the  $H_2O$ -free surface is absent! In addition, the  $H_2$  desorption maximum at 493 K occurs without evolution of carbon oxides, while the  $H_2$  maximum at 557 K is followed by the evolution of  $CO$  and  $CO_2$  at 567 K and 581 K, respectively. Since the only difference between the experiments shown in Figs. 4 and 5 is the presence of pre-adsorbed  $H_2O$  in the Type I sites, we conclude that the  $H_2$  peak at 493 K corresponds to the decomposition of surface methoxy species adsorbed at non-Type I sites, while the  $H_2$  desorption feature observed at 459 K (on the  $H_2O$ -free surface) can be assigned to the decomposition of methoxy species adsorbed at Type I sites.

The decomposition of the remaining surface formate species gives rise to the  $H_2$ ,  $CO$ , and  $CO_2$  peaks between 557 and 581 K. The spread in temperature between the three species appears to be real, and may result from re-adsorption effects for  $CO$  and  $CO_2$  which are more pronounced on samples with pre-adsorbed  $H_2O$  due to a short-lived re-generation of transient  $HCOO_{(a)}$  species involving the adsorbed  $H_2O$  molecules. However, the desorption temperatures are similar to those observed in the absence of pre-adsorbed  $H_2O$ , indicating that the decomposition rate of the formate species is insensitive to Type I vs. non-Type I sites.

However, the  $CO_2:CO$  ratio is much greater than in the absence of pre-adsorbed  $H_2O$ . As noted above, this is not because pre-adsorbed  $H_2O$  at the Type I sites is incorporated into the  $CO_2$  product. Instead, it appears that the decrease in  $CO$  intensity is a direct result of the blockage of Type I sites by  $H_2O$ . Thus we conclude that formate species produced at Type I sites decompose selectively to  $CO$ , while formate species at non-Type I sites decompose selectively to  $CO_2$ .

Thin film studies: Role of Cu sites. The product distribution resulting from  $CH_3OH$  decomposition on a clean, (0001) oriented  $ZnO$  thin film is shown in Fig. 6. The initial  $CH_3OH$  exposure is 5 L for each experiment (1 Langmuir =  $10^{-6}$  torr sec). The observed product include  $H_2$ ,  $CH_2O$ ,  $CO$ , and  $CO_2$ . We also looked for but did not observe desorption peaks for  $CH_4$  and  $H_2$ .

Consistent with the results for  $ZnO$  powder described above, the spectra show that adsorbed  $CH_3OH$  decomposes in two well-resolved processes. The 585 K process corresponds to decomposition of the  $CH_3O_{(a)}$  intermediate, and is characterized by the evolution of  $H_2$  without  $CO$  or  $CO_2$ . The 585 K process also produces a small amount (ca. 20%) of desorbed  $CH_2O$ . The balance of the  $CH_2O$  is apparently stabilized immediately, being converted to a formate precursor before it is able to desorb.

The 635 K process corresponds to the decomposition of  $HCOO_{(a)}$  to produce  $H_2$ ,  $CO$ , and a small amount of  $CO_2$ . Some additional  $CH_2O$  is also observed at 635 K, which may result either from the delayed decomposition of a limited number of  $CH_3O_{(a)}$  species whose decomposition had been sterically impeded by occupied neighboring sites until 635 K. Alternatively, the  $CH_2O$  signal at 635 K may also result from the hydrogenation of a limited number of  $HCOO_{(a)}$  species, using the  $H_{(a)}$  atoms released by the decomposition of the remaining  $HCOO_{(a)}$  species.

The apparent activation energies of the 585 K and 635 K processes are 35 and 38 kcal/mole, respectively, based on the Redhead equation for first-order decomposition kinetics and an assumed pre-exponential factor of  $10^{13}$  sec $^{-1}$ . These values are comparable to the activation energies for the  $CH_3O_{(a)}$  and

HCOO<sub>(a)</sub> decomposition steps computed for the powder experiments, i.e., 31 and 33 kcal/mole for the CH<sub>3</sub>O<sub>(a)</sub> decomposition on Type I and non-Type I sites, respectively, and 40 kcal/mole for HCOO<sub>(a)</sub> decomposition. Comparison of the energies for CH<sub>3</sub>O<sub>(a)</sub> decomposition on Type I vs. non-Type I sites suggests that Type I sites may in fact be absent from the Ar<sup>+</sup> ion sputtered and annealed ZnO thin film surfaces. We also note that the observation of CH<sub>2</sub>O during the experiments on thin film ZnO samples is a result of the line-of-sight detection provided by the mass spectrometer when using a planar sample. Formaldehyde may also be produced initially during CH<sub>3</sub>O<sub>(a)</sub> decomposition on powdered ZnO, but may not be detectable due to irreversible re-adsorption on the pore walls before it can diffuse out of the powdered sample.

Figure 7 shows the product desorption spectra for CH<sub>3</sub>OH decomposition on an evaporated Cu/ZnO sample. The Cu loading in this case is sufficient to decrease the Zn Auger signal to 35% of its clean-surface value. The CH<sub>2</sub>O, H<sub>2</sub>, CO, and CO<sub>2</sub> desorption features at 585 K and 635 K are still present, but are significantly attenuated. This indicates that CH<sub>3</sub>OH decomposition is still occurring on ZnO sites, which implies that even at this high Cu loading, the Cu layer does not cover the ZnO surface uniformly.

Two differences from the decomposition behavior of clean ZnO are also observed. First, small H<sub>2</sub> and CH<sub>2</sub>O desorption signals are observed near 410 K, and a small CO<sub>2</sub> peak is observed near 510 K. These features are quite similar to the CH<sub>3</sub>OH decomposition behavior reported for metallic Cu<sup>(1)</sup>. This suggests that at least a portion of the evaporated Cu layer has agglomerated to form metallic Cu clusters, which are large enough to demonstrate the same CH<sub>3</sub>OH decomposition behavior as bulk Cu.

The second difference is the large CO<sub>2</sub>:CO ratio observed for the 635 K process. This is reminiscent of the HCOO<sub>(a)</sub> decomposition selectivity observed when H<sub>2</sub>O was pre-adsorbed on powdered ZnO, and suggests that a portion of the evaporated Cu layer is sufficiently highly dispersed to perturb the decomposition selectivity of the HCOO<sub>(a)</sub> species on the ZnO surface. We cannot suggest a mechanism for this perturbation at this time.

As the final experiment described here, we sought to test the influence of surface oxidation state on the CH<sub>3</sub>OH decomposition behavior of the evaporated Cu/ZnO thin film sample. Figure 8 shows the product desorption spectra for the same Cu/ZnO sample described above, following sequential exposure to 2 L of O<sub>2</sub> and 5 L of CH<sub>3</sub>OH. Three main features are noted:

- The CO and CO<sub>2</sub> peaks at 635 K are unchanged from their intensities in the O<sub>2</sub>-free case. However, the H<sub>2</sub> and CH<sub>2</sub>O signals in the region of the 585 and 635 K decomposition processes have been essentially eliminated. Since pre-exposure to O<sub>2</sub> had no effect on the CH<sub>3</sub>OH decomposition behavior of a clean ZnO thin film, this suggests that the dispersed Cu species proposed above also influence the O<sub>2</sub> adsorption character of the ZnO surface.

- The H<sub>2</sub> peak at 410 K is enhanced by a factor of two, relative to the case without pre-adsorbed O<sub>2</sub>. The CH<sub>2</sub>O peak at 410 K is also somewhat enhanced. This is consistent with earlier workers' results that pre-exposure to O<sub>2</sub> enhances the reactive sticking coefficient of CH<sub>3</sub>OH on Cu surfaces, and indicates that this enhancement also occurs on the small Cu clusters present on the Cu/ZnO thin film studied here.

- The CO<sub>2</sub> peak at 510 K is greatly enhanced following O<sub>2</sub> pre-exposure. This result is also consistent with the behavior of metallic Cu, where adsorbed O<sub>(a)</sub> is expected not only to enhance dissociative CH<sub>3</sub>OH adsorption but also to increase the conversion of CH<sub>3</sub>O<sub>(a)</sub> to stable HCOO<sub>(a)</sub>, which in turn is reported to decompose almost exclusively to CO<sub>2</sub>.

Similar results to those described above were obtained for a series of Cu



loadings on ZnO thin films. In general, the low temperature decomposition processes at 410 K and 510 K were observed at every Cu loading. Interestingly, the enhancement effect of pre-adsorbed  $O_2$  was observed only for higher Cu loadings. This it appears that metallic Cu clusters at the lowest loadings are small enough to activate dissociative  $CH_3OH$  adsorption without pre-adsorbed  $O(a)$ . This may be the result of a spillover effect of dissociated  $H(a)$  atoms onto the ZnO support. For large clusters, the influence of the spillover effect would be limited to Cu atoms near the perimeter of the cluster, and the  $O(a)$  enhancement would be necessary to activate the remaining atoms in the cluster.

One other result is the fact that the method for preparing different Cu loadings had no effect on the  $CH_3OH$  decomposition behavior; i.e., samples prepared by progressive evaporation of increasing amounts of Cu behaved identically with samples prepared by successive heating of a high initial Cu loading to leave behind progressively decreasing amounts of Cu. We interpret this to indicate that both the cluster and dispersed Cu species are present in a thermodynamically equilibrated state.

## DISCUSSION

Role of formate intermediates. The present results largely confirm our previous understanding that  $CH_3OH$  decomposition to CO or  $CO_2$  occurs via the  $CH_3O(a)$  and  $HCOO(a)$  intermediates. For the powdered ZnO, we have shown that the selectivity of the  $HCOO(a)$  decomposition processes is sensitive to the geometry of the adsorption site: Type I sites yield CO as the major product, while non-Type I sites, possibly as a result of the presence of co-adsorbed  $H_2O$ , yield primarily  $CO_2$ . The effect of the dispersed Cu species on the Cu/ZnO thin film samples is also to increase the selectivity for  $HCOO(a)$  decomposition toward the  $CO_2$  product. The latter result, of course, may also be due to a chemical effect, but it does serve to illustrate the role of the composition of the active site on the selectivity of elementary desorption or decomposition steps.

Our results using clean ZnO thin films also suggest for the first time the possibility that the  $HCOO(a)$  intermediate on the oxide surface may be hydrogenated to produce  $CH_2O$  (cf., the  $CH_2O$  desorption peak at 635 K in Fig. 6). Additional work is needed to eliminate the alternate explanation (i.e., the delayed decomposition of  $CH_3O(a)$  species due to neighboring site blockage), but together with the observation that  $CH_2O$  does not reach the mass spectrometer in the powdered ZnO experiments due to readsorption, this raises the possibility that the  $CH_3OH$  synthesis mechanism may involve discrete CO and  $CH_2O$  hydrogenation steps, with gas phase  $CH_2O$  as a short-lived intermediate present at low concentrations.

Role of Type I sites vs. Cu. The IR spectra in Fig. 3 clearly demonstrate that  $CH_3OH$  adsorbs dissociatively at Type I sites. The site blocking experiments using pre-adsorbed  $H_2O$  show equally clearly that  $CH_3OH$  is also adsorbed in non-Type I sites. The subsequent TPD experiments show that  $CH_3O(a)$  species adsorbed at Type I vs. non-Type I sites behave differently. The  $CH_3O(a)$  decomposition step occurs 35 K earlier (ca. 2 kcal/mole lower apparent activation energy) at Type I sites, and the resulting  $HCOO(a)$  intermediate subsequently decomposes to yield primarily CO, with an apparent activation energy of 40 kcal/mole.

However, it is also important to recognize the converse of this observation, namely that  $CH_3O(a)$  species adsorbed in non-Type I sites also decompose cleanly to yield the  $HCOO(a)$  intermediate, with an apparent activation energy only 2

kcal/mole greater than for Type I sites. Moreover, evolution of  $H_2$  (as opposed to  $H_2O$ ) is also observed for the  $CH_3O(a)$  decomposition step at non-Type I sites. Since the Type I sites remain blocked by  $H_2O$  throughout the  $CH_3O(a)$  and  $HCOO(a)$  decomposition processes, this indicates that Type I sites are not essential for either  $CH_3OH$  decomposition or molecular  $H_2$  desorption from ZnO surfaces.

The origin of the modest enhancement of the  $CH_3O(a)$  decomposition kinetics at the Type I sites may be attributed to the enhanced basicity of the  $O^-$  anion of the Type I site. A variety of spectroscopic evidence exists to indicate that the Type I sites are located at cation vacancies on the (0001)-Zn polar surface of  $ZnO^{(2)}$ . The electrostatic potential at these cation vacancies can be expected to induce a larger proton affinity in the neighboring  $O^-$  anions.

Ironically, our hard-won understanding of the behavior of Type I sites now leads us to seriously question the importance of these sites as active participants in the  $CH_3OH$  synthesis reaction on Cu/ZnO catalysts. In no case did we observe  $CH_3OH$  desorption from  $CH_3O(a)$  species adsorbed in Type I sites. We did observe the analogous desorption process for  $H_2O$  adsorbed at these sites, but with a desorption energy of 40 kcal/mole, significantly greater than the activation energy for  $CH_3O(a)$  decomposition. This large activation energy for recombinative desorption of molecules containing OH groups is also a reflection of the basicity of the Type I  $O^-$  anion, and suggests that  $CH_3OH$  desorption from Type I sites would be more difficult than from non-Type I sites.

Secondly, the modest enhancement for the  $CH_3O(a)$  decomposition step at Type I sites is small, relative to the enhancement for both the  $CH_3O(a)$  and  $HCOO(a)$  decomposition steps observed when Cu was evaporated onto the ZnO surface. While it does not necessarily follow that the activation energy for the reverse  $CH_3O(a)$  synthesis reaction is also reduced as dramatically, this observation does suggest that the presence of the Cu component will have a more significant influence than the presence of the geometrically distinct Type I sites.

Finally, the large binding energy observed for  $H_2O$  in Type I sites suggests that these sites may be blocked under  $CH_3OH$  synthesis conditions, since the reactant mixture usually contains added  $CO_2$  that would be converted to  $H_2O$  via the reverse shift reaction.

Thus the present results strongly suggest that the origin of the  $CH_3OH$  synthesis activity in the Cu/ZnO catalyst does not reside in the Type I sites found on ZnO. This does not rule out the possibility that analogous sites may be present at isolated Cu cations on the surface of Cu/ZnO catalysts; evidence for the influence of a dispersed Cu species is seen in the Cu/ZnO thin film experiments shown in Figs. 7 and 8. However, the Cu/ZnO experiment also indicate that the  $CH_3O(a)$  decomposition activity of the metallic Cu clusters is much greater than for either Type I or non-Type I sites. Moreover, the ZnO support provides a spillover effect which enhances the  $CH_3OH$  decomposition activity of the Cu clusters even more, by eliminating the need for pre-exposure to  $O_2$  to provide proton acceptor sites.

#### ACKNOWLEDGEMENT

This work has been supported by the National Science Foundation, through grant Nos. CPE-8110754 and RIG-CPE-8105823. One of us (D. L. R.) acknowledges stipend support from Chevron Research Company, Standard Oil of California.

#### REFERENCES

- 1) I. E. Wachs and R. J. Madix; *J. Catal.* **53** 208 (1978).
- 2) G. L. Griffin and J. T. Yates, Jr.; *J. Chem. Phys.* **77** 3744, 3751 (1982)

# TPD Cell for Transmission-Reflectance Infrared Spectroscopy

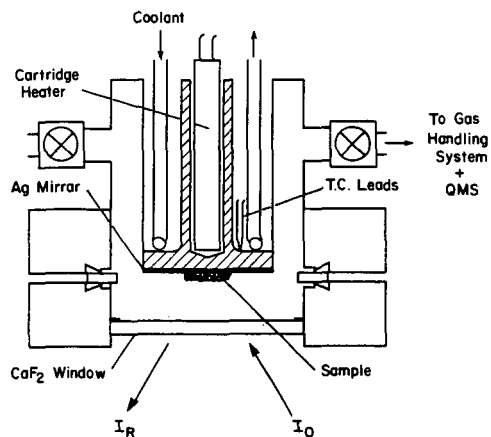


Figure 1. Schematic diagram of sample cell used for combined TPD and IR studies of catalyst powders.

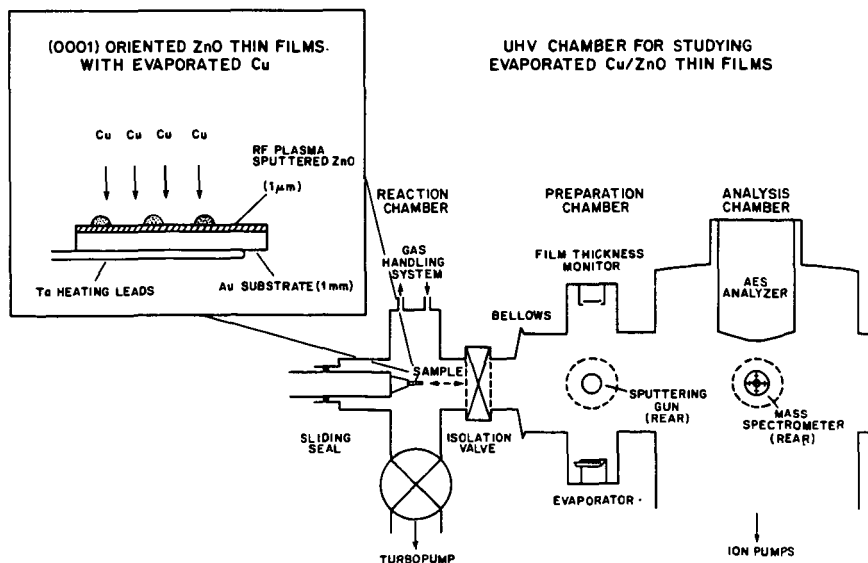


Figure 2. Apparatus used for TPD studies on Model Cu/ZnO thin films. Inset: Schematic representation of RF sputtered thin film sample configuration, with *in-situ* evaporate Cu overlayer.

# IR SPECTRA DURING $\text{CH}_3\text{OH}$ DECOMPOSITION ON TYPE I ACTIVATED $\text{ZnO}$ (Kadox 25)

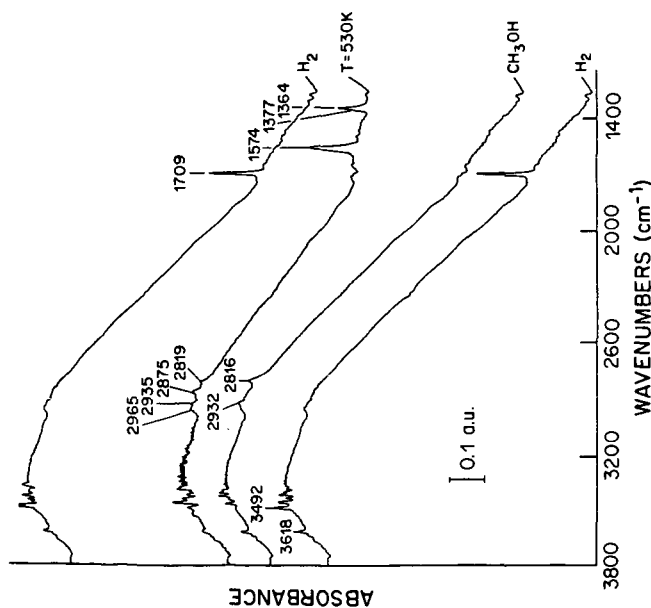


Figure 3. Infrared spectra of  $\text{CH}_3\text{OH}$  and  $\text{H}_2$  adsorbed on Type I activated  $\text{ZnO}$ . The sample was activated at 300 K, then heated to 530 K, and cooled to 300 K. The top curve is the spectrum of  $\text{CH}_3\text{OH}$  adsorbed on the sample after heating to 530 K, then cooled to 300 K. The bottom curve is the spectrum of  $\text{H}_2$  adsorbed on the sample after heating to 530 K, then cooled to 300 K.

# PRODUCT DISTRIBUTION DURING $\text{CH}_3\text{OH}$ TPD ON $\text{ZnO}$ (Kadox 25)

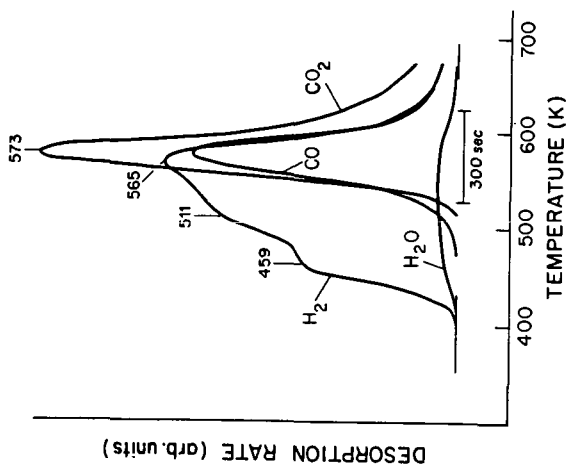


Figure 4. Product distribution spectra during TPD of  $\text{CH}_3\text{OH}$  adsorbed on Type I activated  $\text{ZnO}$ .

PRODUCT DISTRIBUTION DURING  $\text{CH}_3\text{OH}$   
TPD ON  $\text{ZnO}$  (Kadox 25):  
INFLUENCE OF PRE-ADSORBED  $\text{H}_2\text{O}$

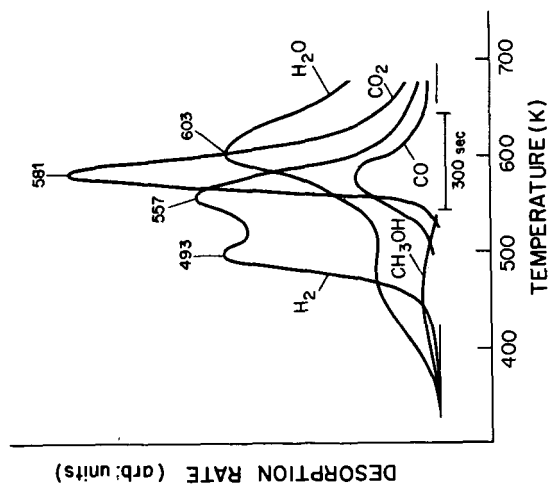


Figure 5. Product distribution spectra during TPD of co-adsorbed  $\text{CH}_3\text{OH}$  and  $\text{H}_2\text{O}$  on  $\text{ZnO}$ , where  $\text{H}_2\text{O}$  is adsorbed first to blank Type I sites.

TEMPERATURE PROGRAMMED DECOMPOSITION  
OF  $\text{CH}_3\text{OH}$  ADSORBED ON  $\text{Cu/ZnO}(\text{OOOI})$  FILMS

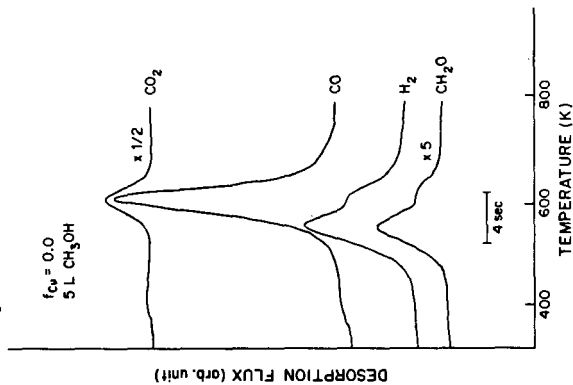


Figure 6. Product distribution spectra during TPD of  $\text{CH}_3\text{OH}$  adsorbed on clean, oriented  $\text{ZnO}$  thin film.

TEMPERATURE PROGRAMMED DECOMPOSITION  
OF  $\text{CH}_3\text{OH}$  ADSORBED ON  $\text{Cu}/\text{ZnO}(0001)$  FILMS

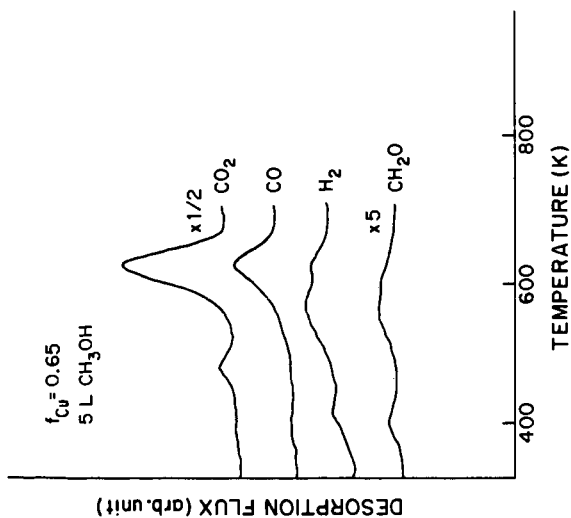


Figure 7. Product distribution spectra during TPD of  $\text{CH}_3\text{OH}$  adsorbed on a  $\text{Cu}/\text{ZnO}$  surface. (Auger intensity ratio  $I_{\text{Cu}}/(I_{\text{Cu}} + I_{\text{Zn}}) = 0.65$ ).

TEMPERATURE PROGRAMMED DECOMPOSITION  
OF  $\text{CH}_3\text{OH}$  ADSORBED ON  $\text{Cu}/\text{ZnO}(0001)$  FILMS:  
INFLUENCE OF PRE-ADSORBED  $\text{O}_2$

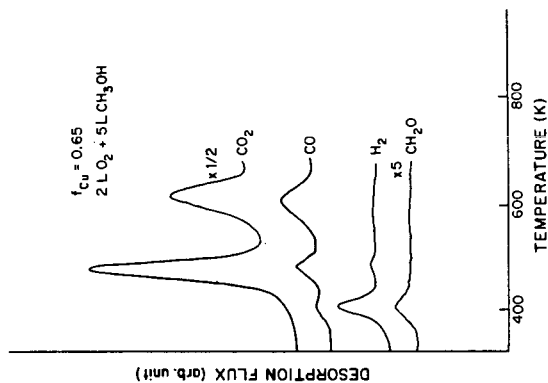


Figure 8. Product distribution spectra during TPD of  $\text{CH}_3\text{OH}$  on  $\text{Cu}/\text{ZnO}$  surface that has been pre-exposed to 2 L of  $\text{O}_2$  before  $\text{CH}_3\text{OH}$  adsorption.

# EFFECT OF OXIDATION STATES ON THE SYNGAS ACTIVITY OF TRANSITION-METAL OXIDE CATALYSTS

By

J. R. Monnier and G. Apai

Research Laboratories, Eastman Kodak Company,  
Rochester, New York 14650

## INTRODUCTION

Supported Rh catalysts and Rh-containing mixed oxide catalysts have been studied extensively (1-5) for Fischer-Tropsch activity and their ability to produce different distributions of oxygenated products. Ichikawa and co-workers (1, 2) correlated X-ray photoelectron spectroscopy (XPS) measurements on the electronic state(s) of supported Rh catalysts with their corresponding Fischer-Tropsch oxygenate distributions and concluded that for selective  $C_2$ -oxygenate formation both  $Rh^0$  and  $Rh^+$  sites were required; the  $Rh^0$  sites functioned as CO dissociation sites in the formation of alkyl groups, while  $Rh^+$  served as the site for associative CO adsorption and subsequent CO insertion to form intermediate acyl species. Similarly, Wilson et al. (3) concluded that the stabilization of  $Rh^+$  by Mn promoters in silica-supported Rh catalysts may be responsible for the enhanced  $C_2$ -oxygenated selectivity under syngas reaction conditions.

Somorjai and co-workers (4, 5), using a different approach, studied the syngas activity of  $Rh_2O_3$  and  $LaRhO_3$  at different temperatures and presumably different levels of reduction and also concluded that for selective  $C_2$  and  $C_2^+$  oxygenate formation to occur efficiently,  $Rh^0$  and  $Rh^+$  are required for facile CO dissociation and CO insertion, respectively. Thus there are strong implications as to the importance of oxidation states of group 8 metals in controlling the linear oxygenate selectivity and product distribution. To better understand the relationship between transition-metal oxidation states and catalytic

performance, we synthesized high-purity  $\text{LaRhO}_3$  and  $\text{GdCoO}_3$  and characterized and evaluated these catalysts at different levels of reduction to determine the existence and thus the importance of different Rh and Co oxidation states. Where appropriate, comparisons are made with a conventional  $\text{Rh/SiO}_2$  catalyst.

Cu-based, low-pressure  $\text{CH}_3\text{OH}$  synthesis catalysts represent another system in which oxidation states are important. Recent evidence suggests that  $\text{Cu}^+$  species are the active components for CO activation in both Cu-ZnO (6) and Cu-Cr oxide (7, 8) catalysts. Others (9), however, have used XPS to examine the oxidation states of Cu in Cu-ZnO and report the existence of only  $\text{Cu}^0$  species under reaction-like reducing conditions. Yet others (10) propose that both  $\text{Cu}^0$  and  $\text{Cu}^+$  are essential for selective  $\text{CH}_3\text{OH}$  formation, with  $\text{Cu}^+$  providing sites for CO activation and  $\text{Cu}^0$  the sites for dissociative  $\text{H}_2$  chemisorption. We present data for alkali- and alkaline-earth-promoted Cu-Cr oxide that support the hypothesis that  $\text{Cu}^0$  serves as the site for  $\text{H}_2$  chemisorption and that both  $\text{Cu}^0$  and  $\text{Cu}^+$  sites are required for Cu-Cr oxide to efficiently catalyze the formation of  $\text{CH}_3\text{OH}$  from syngas.

## RESULTS AND DISCUSSION

### Characterization and Catalytic Activity of $\text{LaRhO}_3$ and $\text{GdCoO}_3$

We prepared  $\text{GdCoO}_3$  by high-temperature calcination (650 °C) of the stoichiometric thermal precursor  $\text{GdCo(CN)}_6 \cdot n\text{H}_2\text{O}$ , using the method outlined by Gallagher (11). We prepared  $\text{LaRhO}_3$  in high purity by converting a mixture of  $\text{La}_2\text{O}_3$  and  $\text{Rh}_2\text{O}_3$  (5% excess of  $\text{La}_2\text{O}_3$  over the 1:1 stoichiometry) to the nitrates, using  $\text{HNO}_3$ , and then firing in air to 1000 °C for 24 h. The excess  $\text{La}_2\text{O}_3$  was removed from  $\text{LaRhO}_3$  by leaching with warm 20% acetic acid (12-14). Powder X-ray diffraction



measurements showed that both  $\text{GdCoO}_3$  and  $\text{LaRhO}_3$  were of high purity; no diffraction lines that could be attributed to the simple oxides were detected in either sample.

The temperature-programmed reduction (TPR) spectra of  $\text{LaRhO}_3$  and  $\text{GdCoO}_3$  (Figure 1) illustrate their stability with respect to reduction in flowing  $\text{H}_2$  at 1 atm pressure. Under reaction conditions used in this study, 800 psig of  $\text{H}_2/\text{CO} = 1/1$ , the TPR peaks would be shifted to lower temperatures. We calculated the extent of the shift for the  $\text{H}_2\text{O}$  peaks of the  $\text{GdCoO}_3$  sample, using the method described by Gentry et al. (15). Under reaction conditions, the  $\text{H}_2\text{O}$  peaks centered at 415 and 515 °C would be shifted to ~307 and 390 °C, respectively. A shift of about 100 °C under reaction conditions should be expected for  $\text{LaRhO}_3$  too, giving an  $\text{H}_2\text{O}$  peak centered at ~300 °C.

Prior to catalytic evaluation,  $\text{GdCoO}_3$  was subjected to various levels of prereduction by stopping the TPR experiment at different temperatures. The levels of reduction were determined from the number of  $\text{H}_2\text{O}$  molecules formed during reduction. These data are summarized in Table I; the sample corresponding to 30% reduction was prepared in a recirculation loop reactor maintained at 510 °C. Table I also gives the relevant reduction data for  $\text{LaRhO}_3$ . Powder X-ray diffraction (XRD) measurements for the  $\text{GdCoO}_3$  samples reduced to the 20% and 30% levels showed peaks for  $\text{Co}^0$  and  $\text{Gd}_2\text{O}_3$  only. The XRD pattern for the 10% reduced sample gave peaks corresponding to  $\text{Gd}_2\text{O}_3$  (and by necessity  $\text{Co}^0$ , since any cobalt oxide formed along with  $\text{Gd}_2\text{O}_3$  would be reduced to  $\text{Co}^0$ ),  $\text{GdCoO}_3$ , and a phase tentatively identified as the defect-type perovskite,  $\text{GdCo}_{0.92}\text{O}_{2.5}$ .

The powder XRD of the  $\text{LaRhO}_3$  sample after the TPR experiment gave only broad peaks for  $\text{Rh}^0$  and  $\text{La}_2\text{O}_3$ . This is important, since the TPR conditions are similar to those encountered under Fischer-Tropsch

reaction conditions. X-ray photoelectron spectra of  $\text{LaRhO}_3$  after various in situ reduction pretreatments (Figure 2) show that only  $\text{Rh}^0$

Table I. Temperature-Programmed Reduction Data for  $\text{GdCoO}_3$  and  $\text{LaRhO}_3$

|                    | $T_{\text{max}}$ ( $^{\circ}\text{C}$ ) | $\# \text{O}^{2-}$ removed | % reduction <sup>a</sup> |
|--------------------|---|----------------------------|--------------------------|
| $\text{GdCoO}_3^b$ |   |                            |                          |
|                    | 510                                     | $7.1 \times 10^{24}$       | 30                       |
|                    | 535                                     | $4.6 \times 10^{20}$       | 20                       |
|                    | 490                                     | $3.0 \times 10^{20}$       | 13                       |
|                    | 455                                     | $2.2 \times 10^{20}$       | 10                       |
| $\text{LaRhO}_3^c$ |   |                            |                          |
|                    | 535                                     | $1.45 \times 10^{20}$      | 24                       |

<sup>a</sup>Maximum extent of reduction under these conditions is 50%, since both  $\text{Gd}_2\text{O}_3$  and  $\text{La}_2\text{O}_3$  are stable with respect to reduction at  $T < 800^{\circ}\text{C}$ . <sup>b</sup>350-mg sample contains  $2.4 \times 10^{21} \text{O}^{2-}$ . <sup>c</sup>100-mg sample contains  $6.1 \times 10^{20} \text{O}^{2-}$ .

is present on the surface after  $\text{H}_2$  (1 atm pressure) reduction at  $300^{\circ}\text{C}$ . Reduction at  $300^{\circ}\text{C}$  in a 2:1  $\text{H}_2/\text{CO}$  flow at 1 atm total pressure, however, stabilizes some of the  $\text{LaRhO}_3$  from reduction to  $\text{Rh}^0$ , as evidenced by the  $\text{Rh}^{3+}$  peak. Deconvolution of the  $\text{Rh } 3d_{5/2}$  portion of the XPS spectrum could be fitted into two Gaussian components attributable to  $\text{Rh}^{3+}$  and  $\text{Rh}^0$ , with no  $\text{Rh}^+$  component in the 308-eV region of the spectrum. These results differ from those of Somorjai under similar conditions, which may be due to the difference in purity of the starting  $\text{LaRhO}_3$  samples. Repetition of the preparative technique outlined by Somorjai resulted in a residual  $\text{Rh}_2\text{O}_3$  component

as detected by XPS, which was readily reduced to  $\text{Rh}^0$  after  $\text{H}_2$  reduction at 250 °C.

The Fischer-Tropsch activities for  $\text{LaRhO}_3$  at different reaction temperatures are displayed as Schulz-Flory plots in Figure 3. At reaction temperatures  $\geq 300$  °C, the rates of  $\text{C}_2$ -oxygenates ( $\text{CH}_3\text{CHO} + \text{C}_2\text{H}_5\text{OH}$ ) are greater than for  $\text{CH}_3\text{OH}$ , suggesting that the mechanism for  $\text{CH}_3\text{OH}$  formation is different from the mechanism for formation of higher oxygenates; the latter products apparently formed by CO insertion into surface alkyl fragments, as others (1, 16) have noted. Since XPS did not detect any  $\text{Rh}^+$  on  $\text{LaRhO}_3$  after a much milder pretreatment at 300 °C and the TPR curve showed that at 400 °C in 1 atm of  $\text{H}_2$ , 50% of the lattice  $\text{O}^{2-}$  associated with Rh in  $\text{LaRhO}_3$  had been removed, it is difficult to envision the existence of stable  $\text{Rh}^+$  on the catalyst surface under our reaction conditions.

The Fischer-Tropsch results for reduced  $\text{GdCoO}_3$  (Figure 4) corroborate those for  $\text{LaRhO}_3$  and show that the most highly reduced samples form the highest proportion of  $\text{C}_2$  and greater oxygenates. Again, it is difficult to envision the existence of partially oxidized, catalytically active Co species after those high levels of catalyst reduction.

These results suggest there is no need to invoke  $\text{Rh}^+$  or lower-valent oxidation states of Co to explain the higher rates of  $\text{C}_2$ -oxygenate formation. Rather, the poor CO dissociation capabilities of  $\text{Rh}^0$  and  $\text{Co}^0$  (17) require high temperatures and/or large metallic aggregates to efficiently dissociate CO and form surface alkyl fragments in high enough surface concentration, so that CO insertion into the metal-alkyl bond (to form acyl species) can compete favorably with hydrogenation of adsorbed CO and surface alkyls to form  $\text{CH}_3\text{OH}$  and paraffins, respectively.

This conclusion is supported by the results from a TPD/TPR sequence for CO adsorbed on a conventional 1.5% Rh/SiO<sub>2</sub> catalyst. The Fischer-Tropsch activity at 270 °C, 850 psig, and 2:1 H<sub>2</sub>/CO gave 25% molar oxygenate selectivity and a C<sub>2</sub>-oxygenate/CH<sub>3</sub>OH ratio of 2.5. The TPD analysis in flowing He gave multiple CO desorption peaks with T<sub>max</sub> values ranging from 70 to 257 °C, as well as a large CO<sub>2</sub> peak (from disproportionation of CO) centered at 300 °C. The TPR analysis in flowing H<sub>2</sub> immediately after the TPD experiment (no additional catalyst treatment) gave a large CH<sub>4</sub> peak centered at 219 °C. This series of experiments shows that high temperatures are required for CO dissociation to occur efficiently on supported Rh<sup>0</sup> surfaces and that hydrogenation of the surface carbon to form CH<sub>4</sub> (or surface alkyls) occurs easily once the C-O bond is ruptured. The presence of CO desorption peaks at temperatures up to 257 °C also shows that associatively adsorbed CO is present under typical reaction conditions.

#### Characterization and Catalytic Activity of Promoted Cu-Cr Oxide

In earlier studies (7, 8), we showed that specific rates of CH<sub>3</sub>OH formation were proportional to the amount of CuCrO<sub>2</sub> in the Cu-Cr oxide catalyst and the fraction of Cu<sup>+</sup> present on the surface of the catalyst, which also contained Cu<sup>0</sup>. One may thus expect that high-purity CuCrO<sub>2</sub>, which is stable under reaction conditions, would be most active. The data in Table II show that this is not the case and suggest that Cu<sup>0</sup> is essential for the reduction of CO to form CH<sub>3</sub>OH.

A series of alkali- and alkaline-earth-promoted Cu-Cr oxides (at the same molar loading) were prepared from the same batch of Cu-Cr oxide and evaluated for CH<sub>3</sub>OH formation. The results and relevant kinetic information (Table III) show a strong promotional effect for

Table II. Effect of High-Temperature Calcination on Catalytic and Physical Properties of Cu-Cr Oxide

| catalyst  | surface area<br>(m <sup>2</sup> /g) | activity<br>$\left( \frac{\mu\text{mol CH}_3\text{OH}}{\text{s}\cdot\text{m}^2 \text{ catalyst}} \right)$ | $\left( \frac{\text{Cu}^+}{\text{Cu}_{\text{tot}}} \right)^a$ | composition <sup>b</sup><br>after<br>T <sub>red</sub> = 270 °C<br>in H <sub>2</sub> |
|---|-------------------------------------|---|---|---|
| 1/1 Cu/Cr<br>(T <sub>calc</sub> = 350 °C,<br>for 2 h)   | 21.4                                | 0.02  | 0.21  | CuCrO <sub>2</sub> (minor)<br>Cu <sup>0</sup> (major)                               |
| 1/1 Cu/Cr<br>(T <sub>calc</sub> = 1000 °C,<br>for 4 h)  | 2.9                                 | 0.06  | 0.5   | CuCrO <sub>2</sub> (major)<br>Cu <sup>0</sup> (major)                               |
| 1/1 Cu/Cr<br>(T <sub>calc</sub> = 1000 °C,<br>for 24 h) | 0.3                                 | ≈ 0   | 1.0   | CuCrO <sub>2</sub> (only)   |

<sup>a</sup>Determined by XPS after H<sub>2</sub> reduction at 270 °C. <sup>b</sup>Determined by powder X-ray diffraction.

CH<sub>3</sub>OH formation and a lowering of the apparent activation energy for CH<sub>3</sub>OH formation when a promoter is present.

The H<sub>2</sub> and CO chemisorption data in Table IV show that the enhanced catalytic activity is not due to an increase in CO adsorption (Cu<sup>+</sup> sites). The TPD spectra of CO for unpromoted, Ba-promoted, and Cs-promoted Cu-Cr oxides are virtually identical in normalized intensities and position (T<sub>max</sub>), supporting the conclusion that CO activation is not the source of the promoter effect; likewise, XPS measurements gave essentially identical surface fractions of Cu<sup>+</sup> for these samples.

Table III. Rates of CH<sub>3</sub>OH Formation and Kinetic Parameters  
for Promoted Cu-Cr Oxide Catalysts. Reaction  
Conditions: 270 °C, H<sub>2</sub>/CO = 2/1, 800 psig pressure

| catalyst                  | surface<br>area<br>(m <sup>2</sup> /g) | rate<br>( $\frac{\mu\text{mol}}{\text{g cat-s}}$ ) | rate<br>( $\frac{\mu\text{mol}}{\text{m}^2 \text{ cat-s}}$ ) | E <sub>app</sub><br>( $\frac{\text{kcal}}{\text{mol}}$ ) | reaction<br>orders<br>(H <sub>2</sub> ) (CO) |      |
|---------------------------|--|--|--|--|--|------|
| Cu-Cr oxide               | 69.2                                   | 0.61   | 0.009  | 19.4   | 0.56   | 0.57 |
| (3.4% K)<br>Cu-Cr oxide   | --                                     | 9.30   | --   | --   | --   | --   |
| (11.2% Cs)<br>Cu-Cr oxide | 75.0                                   | 9.83   | 0.13   | 13.4   | --   | --   |
| (3.5% Ca)<br>Cu-Cr oxide  | --                                     | 3.74   | --   | --   | --   | --   |
| (7.7% Sr)<br>Cu-Cr oxide  | --                                     | 9.04   | --   | --   | --   | --   |
| (12% Ba)<br>Cu-Cr oxide   | 56.8                                   | 14.54  | 0.26   | 10.9   | 0.56   | 0.62 |

The H<sub>2</sub> chemisorption data show that although the H<sub>2</sub> chemisorption values at the reaction temperature of 250 °C vary only slightly, the temperature dependencies for H<sub>2</sub> chemisorption are much lower for the promoted catalysts. This lower temperature dependency for H<sub>2</sub> chemisorption may be reflected in the lower E<sub>app</sub> values for CH<sub>3</sub>OH formation. The sites for H<sub>2</sub> chemisorption appear to be Cu<sup>0</sup> centers, since there was no measurable H<sub>2</sub> uptake on ultrapure CuCrO<sub>2</sub> (no surface Cu<sup>0</sup> detected by XPS) or Cr<sub>2</sub>O<sub>3</sub> at 250 °C, yet H<sub>2</sub> chemisorption readily occurred at 250 °C on 99.99% Cu<sup>0</sup> powder (Aldrich).

In addition, the levels of reduction of both the Ba- and Cs-promoted samples were ~1/3 that of the unpromoted sample, 12% vs. 37%, respectively, as determined by quantitative TPR and neutron activation analysis. Therefore, the comparable levels of H<sub>2</sub> chemisorption at 250 °C imply greater Cu<sup>0</sup> particle dispersions for the promoted samples.

Table IV. H<sub>2</sub> and CO Chemisorption Data for Ba-Promoted, Cs-Promoted, and Unpromoted Cu-Cr Oxides

| catalyst                                     | (molecules/m <sup>2</sup> catalyst) |                        |                        |
|--|-------------------------------------|------------------------|------------------------|
|  | T = 25 °C                           | T = 150 °C             | T = 250 °C             |
| Cu-Cr oxide<br>(69.2 m <sup>2</sup> /g)      |                                     |                        |                        |
| H <sub>2</sub>                               | 1.8 x 10 <sup>16</sup>              | 1.4 x 10 <sup>17</sup> | 6.2 x 10 <sup>17</sup> |
| CO   | 6.0 x 10 <sup>16</sup>              | --                     | 3.2 x 10 <sup>17</sup> |
| (Ba) Cu-Cr oxide<br>(56.8 m <sup>2</sup> /g) |                                     |                        |                        |
| H <sub>2</sub>                               | 1.4 x 10 <sup>17</sup>              | 3.9 x 10 <sup>17</sup> | 6.2 x 10 <sup>17</sup> |
| CO   | 8.6 x 10 <sup>16</sup>              | --                     | 5.1 x 10 <sup>17</sup> |
| (Cs) Cu-Cr oxide<br>(75 m <sup>2</sup> /g)   |                                     |                        |                        |
| H <sub>2</sub>                               | 1.3 x 10 <sup>17</sup>              | 2.1 x 10 <sup>17</sup> | 2.6 x 10 <sup>17</sup> |
| CO   | 1.2 x 10 <sup>17</sup>              | --                     | 6.2 x 10 <sup>17</sup> |

This observation is corroborated by the XRD patterns (Figure 5) of unpromoted and Ba-promoted Cu-Cr oxide after the TPR analyses.

The intensities and peak shapes of the Cu<sup>0</sup> peaks [(111) and (200) reflections at 43.5° and 50.5°, respectively] show that the Cu<sup>0</sup> aggregates are much larger for the unpromoted sample. High-temperature sintering in He increases the sharpness of the Cu<sup>0</sup> XRD peaks and thus the crystallite size. As the results in Figure 5 show, there is an indirect relationship between Cu<sup>0</sup> crystallite size and catalytic activity. This Cu<sup>0</sup> particle-size effect is related to the nature of the Cu<sup>0</sup> sites on the small Cu<sup>0</sup> crystallites and not the number of Cu<sup>0</sup> sites. The small temperature dependency for H<sub>2</sub> chemisorption is more indicative of H<sub>2</sub> chemisorption on group 8 metals such as Rh or Pt, which chemisorb H<sub>2</sub> in a nonactivated manner to form a somewhat hydridic

H species (18). Since hydrides are stronger reducing agents than heterolytically dissociated  $H_2$ , typically associated with metal oxides, a lower activation energy for  $CH_3OH$  formation is not unexpected for the promoted Cu-Cr oxides.

We conclude, therefore, that in addition to  $Cu^+$ , which is required for CO chemisorption, metallic  $Cu^0$  centers are required for facile  $H_2$  chemisorption and subsequent reduction to form  $CH_3OH$  over Cu-Cr oxide.

Acknowledgments. We thank Dr. Henry Gysling for providing the  $LaRhO_3$  and  $GdCoO_3$  samples and for helpful discussions concerning their preparations.

#### LITERATURE CITED

- (1) Ichikawa, M.; Fukushima, T. J. Chem. Soc., Chem. Commun. 1985, 321.
- (2) Kawai, M.; Uda, M.; Ichikawa, M. J. Phys. Chem. 1985, 89, 1654.
- (3) Wilson, T. P.; Kasai, P. H.; Ellgen, P. C. J. Catal. 1981, 69, 193.
- (4) Watson, P. R.; Somorjai, G. A. J. Catal. 1982, 74, 282.
- (5) Castner, D. G.; Blackadar, R. L.; Somorjai, G. A. J. Catal. 1980, 66, 257.
- (6) Klier, K. Adv. Catal. 1982, 31, 243.
- (7) Apai, G.; Monnier, J. R.; Hanrahan, M. J. Appl. Surf. Sci. 1984, 19, 307.
- (8) Monnier, J. R.; Hanrahan, M. J.; Apai, G. J. Catal. 1985, 92, 119.
- (9) Fleisch, T. H.; Mieville, R. L. J. Catal. 1984, 90, 165.
- (10) Okamoto, Y.; Fukino, K.; Imanaka, T.; Teranishi, S. J. Chem. Soc., Chem. Commun. 1982, 1405.
- (11) Gallagher, P. K. Mat. Res. Bull. 1968, 3, 225.
- (12) Wold, A.; Post, B.; Banks, E. J. Am. Chem. Soc. 1957, 79, 6365.
- (13) Carreiro, L.; Qian, Y.-T.; Kershaw, R.; Dwight, K.; Wold, A. Mat. Res. Bull. 1985, 20, 619.
- (14) Carreiro, L. Ph.D. Thesis, Brown Univ., 1985.
- (15) Gentry, S. J.; Hurst, N. W.; Jones, A. J. Chem. Soc. Trans. Faraday Soc. 1979, 75, 1688.
- (16) Orita, H.; Naito, S.; Tamaru, K. J. Catal. 1984, 90, 183.
- (17) Solymosi, F.; Erdohelyi, A. Surf. Sci. Lett. 1981, 110, L630.
- (18) Bond, G. C. "Catalysis by Metals"; Academic Press: New York, 1962; pp 65-103.



Figure 2. Rh 3d XPS of  $\text{LaRhO}_3$  as a function of pretreatment.

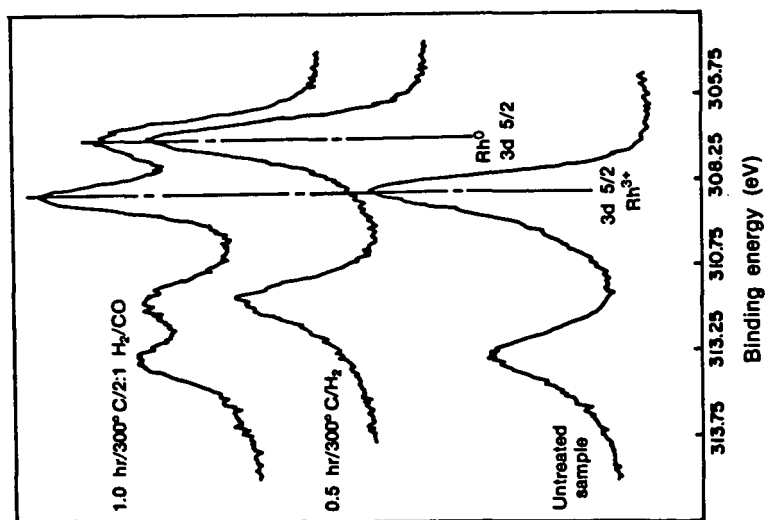


Figure 1. Temperature-programmed reduction in flowing  $\text{H}_2$  of  $\text{LaRhO}_3$  and  $\text{GdCoO}_3$ . Heating rate =  $10^\circ\text{C}/\text{min}$ . Sample weights:  $\text{LaRhO}_3$  = 100 mg,  $\text{GdCoO}_3$  = 350 mg.

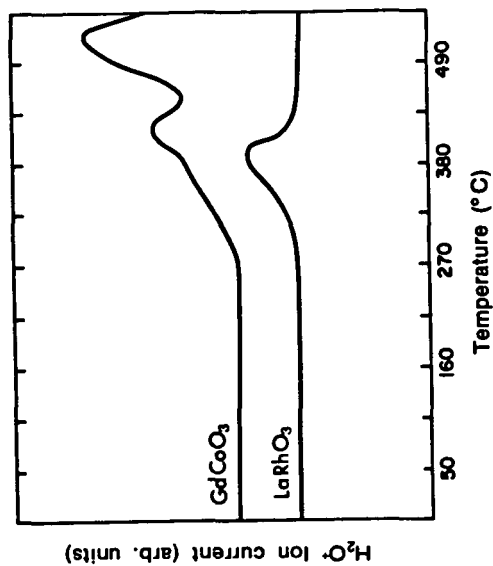


Figure 4. Fischer-Tropsch activity of reduced  $\text{GaCoO}_3$ . Reaction conditions: 250 °C, 800 psig overall pressure, 1:1  $\text{H}_2/\text{CO}$ ; catalysts pretreated for 1 h at 280 °C in 1 atm of flowing  $\text{H}_2$ .

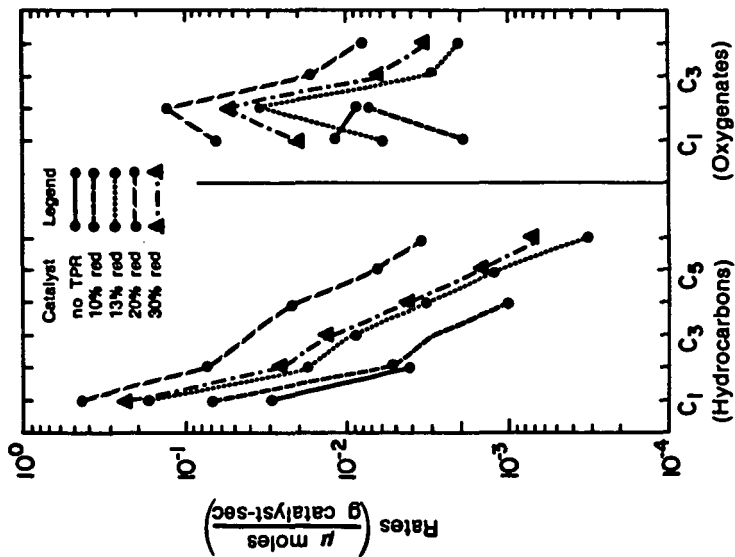


Figure 3. Fischer-Tropsch activity of  $\text{LaRhO}_3$  as a function of temperature.

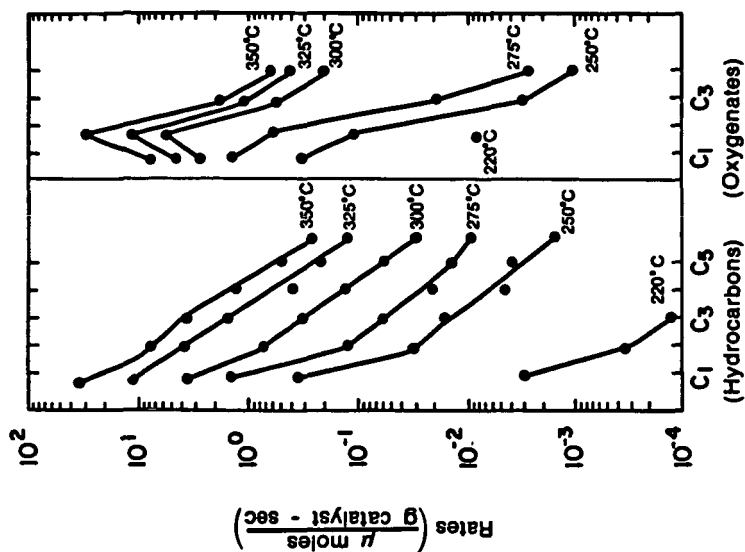
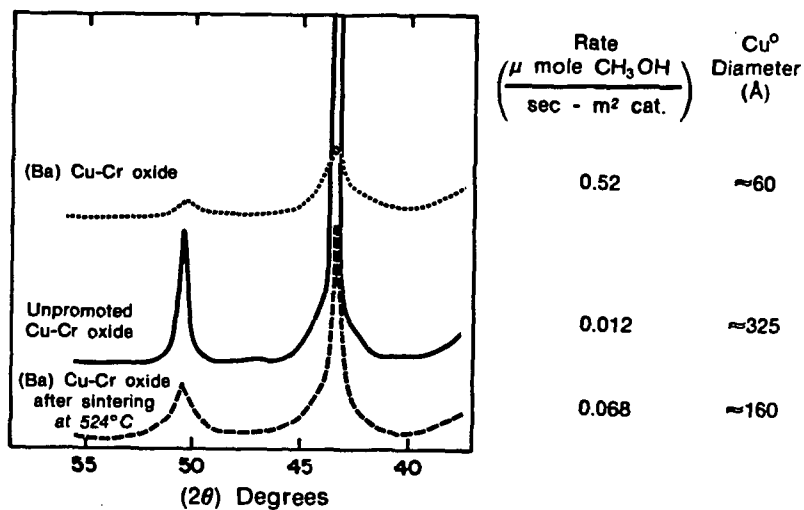


Figure 5. X-ray diffraction patterns after TPR and sintering.



## METHANOL SYNTHESIS STUDIES USING IN SITU FTIR SPECTROSCOPY

J. F. Edwards and G. L. Schrader

Department of Chemical Engineering and Ames Laboratory-USDOE  
Iowa State University, Ames, IA 50011

Annual methanol demand in this country has been projected to double during the 1980s to 8 million metric tons due mainly to rapid expansion in several developing applications (1). Major uses for methanol are the production of formaldehyde, dimethyl terephthalate (DMT), methyl methacrylate, methyl halides, methyl amines, and acetic acid. Large quantities of methanol are used as a gasoline blending agent and as a solvent. Legislated reductions in the amount of tetraethyl lead allowed in gasoline have increased the demand for octane boosters such as methyl tert-butyl ether (MTBE) which is made from methanol and isobutylene. The recent development of a single-step catalytic distillation process (MTBE plus) which eliminates the methanol recovery section of the conventional process, provides an economically attractive alternative to isobutylene alkylation for octane enhancement (2). Methanol by itself can be used as an octane booster, but there are problems with methanol/gasoline mixtures due to their higher affinity for water, higher evaporative losses, and the need to modify the engine.

Future demand for methanol could expand multifold as coal assumes a greater proportion of our energy needs. Although methanol is presently economically unattractive as a substitute for gasoline, the State of California has begun a program to operate 550 vehicles with methanol because it produces fewer pollutants than gasoline. More than 300 privately-owned vehicles, converted by Future Fuels of America, Inc., are running on methanol in the Sacramento, San Francisco, and Los Angeles areas. Even if gasoline remains the major automotive fuel into the next century, methanol production could increase significantly if technology such as Mobil Oil's M-Gasoline process is used to produce gasoline. This process uses a zeolite catalyst (ZSM-5) to convert methanol into a blend of paraffins, cycloparaffins, and aromatics with a research octane number of 93, i.e., an unleaded premium gasoline (3). New Zealand will use this technology to convert natural gas into approximately 12,500 bbl/d of gasoline. Utilities using coal gasification technology for power generation will probably also manufacture methanol. During off-peak hours, part of the syngas would be converted to methanol and stored; during peak hours, the methanol would be used as fuel in gas turbines to meet the high electrical demand. And finally, there is great potential for future development of methanol as a primary feedstock in the chemical industry, especially as supplies of ethylene and propylene decrease. An example is the manufacture of acetic acid, where methanol has replaced ethylene as the primary feedstock in new technologies by BASF and Monsanto (4).

The key development in methanol synthesis technology has been the catalyst. Improvements in catalyst performance are usually obtained by trial-and-error methods: variations in composition or preparation technique are tried until a catalyst is found having greater activity, selectivity, or stability. Characterization of physical and chemical properties is often incomplete, and the reasons for the superiority of a particular catalyst are frequently unclear. Although methanol synthesis as a commercial process is fully developed, the specific function of the catalyst and the fundamentals of the elementary surface reactions are still highly speculative. The main objective of this investigation has been to prepare several different compositions of methanol synthesis catalysts and characterize these catalysts by physical and chemical techniques, placing emphasis on the use of Fourier transform infrared (FT-IR) spectroscopy to identify the chemical species adsorbed on the catalyst surfaces under methanol synthesis conditions. It should be emphasized that this study has focused on the FT-IR characterization of adsorbed surface species under in situ conditions with the objective of obtaining a better understanding of the molecular interactions occurring on the catalyst surface.

In spite of advances in the characterization of methanol catalysts, the nature of adsorbed species and of the elementary surface reactions continues to be uncertain. Several mechanisms for methanol synthesis have been proposed in recent years. A chemical trapping technique has identified formate and methoxy species on a used methanol catalyst (5); the proposed methanol synthesis mechanism postulates that formate, methyloxy, and methoxy groups are reaction intermediates bonded through oxygen to a metal ion site. A much different mechanistic proposal was suggested by Herman and co-workers (6) involving carbonyl, formyl, hydroxycarbene, and hydroxymethyl intermediates bonded through carbon to a Cu(I) ion in the zinc oxide phase. Adjacent zinc ions were the centers for hydrogen adsorption. A recent revision of this mechanism has incorporated hydroxyl, formate, formyl, and methoxy species bonded to a Cu(I) ion in the reaction pathway (7). Other mechanisms have been proposed incorporating both carbon-bonded and oxygen-bonded intermediates in methanol synthesis. A reaction scheme with carbonyl, formyl, formaldehyde, and methoxy intermediates adsorbed on Cu(I) active sites within the zinc oxide lattice was developed from a review of the literature (8). This mechanism was analogous to methanol synthesis by homogeneous catalysis. Another mechanism has proposed that an oxygen vacancy acts as an active site in methanol synthesis (9). After a carbonyl species is hydrogenated to a formyl species, the oxygen on the formyl interacts with an adjacent electron-deficient vacancy. As further hydrogenation occurs, a methoxy species is formed as the bonding between the oxygen and vacancy is strengthened while the bonding between the carbon and metal ion weakens. The variation in catalytic activity with specific crystal planes of zinc oxide has been ascribed to the relative number of defects (vacancies) in each type of plane (10,11).

The catalysts were prepared by coprecipitating a mixture of metal nitrates with ammonium bicarbonate at 60°C according to the method described by Stiles (12). After filtering and washing with distilled water, the precipitates were dried in air at 115°C for 12 h and then calcined in a stream of oxygen at 400°C for 8 h. The amount of cupric oxide in these catalysts was restricted to no greater than 10% CuO due to the strong infrared absorption by cupric oxide.

The oxidic form of the catalyst was prepared for transmission infrared studies by pressing powder under a load of 4500 kg into a wafer approximately 0.10 mm thick and placing the wafer into the infrared cell. Catalyst activity and selectivity evaluations were conducted in a fixed-bed tubular reactor containing a bed of broken catalyst wafers surrounded by SiC particles. Dry nitrogen gas was flowed through the infrared cell or reactor for approximately 12 h at atmospheric pressure and 200°C to desorb water on the catalyst surface. Under these conditions there was no significant dehydroxylation of the catalyst surface. All experiments were conducted in a continuous flow mode at 60 cm<sup>3</sup>/min (STP) using high-purity gases. Water or formic acid solution could be introduced into the feed system at low concentrations by bubbling the gaseous flow through the liquid which was contained within an enclosed stainless-steel vessel (saturator). Catalysts were reduced by exposing the oxide to a 95/5 N<sub>2</sub>/H<sub>2</sub> stream for 1 h at 200°C and 1 atm (pretreatment 1).

Binary catalysts with low copper contents (Cu/Zn ≤ 0.15) were satisfactory for transmission infrared studies in both oxidized and reduced states. During high-pressure *in situ* studies these catalysts had a significant transmittance loss at lower wavenumbers, requiring that the identification of adsorbed species be based on infrared bands above 2000 cm<sup>-1</sup>.

The adsorption of carbon monoxide on a 95/5 Zn/Cu catalyst at 200°C and 50 atm is shown in Fig. 1. The initial oxidized surface (Fig. 1a) had residual hydroxyls (bands at 3663, 3620, 3560, and 3455 cm<sup>-1</sup>) and carbonates (bands at 1515, 1469, 1376, and 1323 cm<sup>-1</sup>). Prolonged exposure to CO reduced the catalyst (Fig. 1b), indicated by the formation of the hydroxyl band at 3250 cm<sup>-1</sup>. Formate groups (bands at 2969, 2878, 2731, and 1573 cm<sup>-1</sup>), a zinc hydroxyl (band at 3520 cm<sup>-1</sup>), and a zinc hydride (band at 1660 cm<sup>-1</sup>) gradually developed. After 24 h (Fig. 1c) an adsorbed formaldehyde species (bands at 2935, 2834, and 2731 cm<sup>-1</sup>) had formed and the

carbonyl band had shifted to  $1975\text{ cm}^{-1}$ . (The band of gaseous CO at  $2143\text{ cm}^{-1}$  masked the carbonyl band in the earlier spectra.)

The hydrogenation of surface species was accelerated by incorporating hydrogen into the carbon monoxide feed. Figure 2 shows the adsorption of a mixture of carbon monoxide and hydrogen ( $\text{CO}/\text{H}_2 = 9/1$ ) on a 95/5 Zn/Cu catalyst at  $200^\circ\text{C}$  and 50 atm. Formate groups (band at  $2879\text{ cm}^{-1}$ ) and hydroxyls associated with reduction (band at  $3252\text{ cm}^{-1}$ ) were quickly formed (Fig. 2). The development of methoxy groups (bands at  $2934$  and  $2822\text{ cm}^{-1}$ ) (Fig. 2c) was accompanied by the disappearance of the isolated hydroxyls (bands at  $3660$  and  $3612\text{ cm}^{-1}$ ). The formate band shifted significantly from  $2879$  to  $2868\text{ cm}^{-1}$ , due to the development of the methoxy groups.

The adsorption of a stoichiometric  $2/1\text{ H}_2/\text{CO}$  mixture on 95/5, 90/10, and 85/15 Zn/Cu catalysts at  $200^\circ\text{C}$  and 50 atm after an hour of exposure is shown in Fig. 3. Very little detail could be observed at lower wavenumbers because of low transmittance. This surface condition would be representative of the adsorbed species during methanol synthesis. The spectra showed the hydroxyl of reduction (band at  $3252\text{ cm}^{-1}$ ), methoxy groups (bands at  $2933$  and  $2822\text{ cm}^{-1}$ ), and formate groups (bands at  $2865$  and  $1575\text{ cm}^{-1}$ ) in addition to the band for gaseous carbon monoxide at  $2143\text{ cm}^{-1}$ . The spectra of the 85/15 Zn/Cu catalyst was noisier than the other spectra because its transmittance was an order of magnitude lower than the others.

Methanol synthesis from a stoichiometric feed of carbon monoxide and hydrogen was compared with other feed mixtures. Figure 4 shows the nature of surface species on a 95/5 Zn/Cu catalyst at  $200^\circ\text{C}$  and 50 atm for various feed compositions that were previously established from reactor studies to be satisfactory for methanol synthesis. A feed mixture of  $66/27/7\text{ H}_2/\text{CO}/\text{CO}_2$  produced surface species that were identical with those using only  $\text{H}_2$  and CO in the feed. The additional band at  $2350\text{ cm}^{-1}$  was absorption by gaseous carbon dioxide. A feed mixture of  $50/50\text{ H}_2/\text{N}_2$  containing some formic acid solution ( $73\%\text{ HCOOH}$ ,  $27\%\text{ H}_2\text{O}$ ) also produced formate (band at  $2870\text{ cm}^{-1}$ ) and methoxy groups (bands at  $2935$  and  $2820\text{ cm}^{-1}$ ). Because the feed had some water and a low formic acid concentration, the isolated hydroxyls (bands at  $3660$  and  $3620\text{ cm}^{-1}$ ) were not completely displaced by methoxy groups.

The ternary Zn-Cu-Cr oxide catalysts, which were also restricted to low copper contents, were superior to the binary catalysts in high-pressure infrared experiments because the transmittance remained high throughout the mid-infrared range. Better surface detail provided more information for identifying adsorbed species during methanol synthesis conditions.

The reaction of carbon monoxide and hydrogen on a 90/5/5 Zn/Cu/Cr catalyst at  $200^\circ\text{C}$  and 50 atm is shown in Fig. 5. The initial surface species on the reduced catalyst (pretreatment 1) after exposure to a  $2/1\text{ H}_2/\text{CO}$  mixture (Fig. 5) were formate groups (bands at  $2963$ ,  $2872$ ,  $1582$ ,  $1381$ , and  $1360\text{ cm}^{-1}$ ), adsorbed formaldehyde species (bands at  $2934$  and  $2843\text{ cm}^{-1}$ ), and methoxy groups (bands at  $2934$  and  $2824\text{ cm}^{-1}$ ). The adsorbed formaldehyde species disappeared and the amount of methoxy groups reached a maximum in an hour (Fig. 5b), followed by a gradual decrease in methoxy groups (Fig. 5c). A pressure drop to 1 atm (Fig. 5d) revealed an adsorbed carbonyl species at  $2010\text{ cm}^{-1}$ .

The reaction of carbon monoxide and hydrogen ( $\text{H}_2/\text{CO} = 2/1$ ) on a 80/10/10 Zn/Cu/Cr catalyst (pretreatment 1) at  $200^\circ\text{C}$  and 50 atm is shown in Fig. 6. The initial spectrum (Fig. 6a) showed formate groups (bands at  $2870$ ,  $1576$ ,  $1381$ , and  $1360\text{ cm}^{-1}$ ), methoxy groups (bands at  $2932$  and  $2822\text{ cm}^{-1}$ ), and a carbonyl species at  $2089\text{ cm}^{-1}$ . The methoxy groups reached a steady-state condition within an hour (Fig. 6b). The carbonyl species shifted from  $2089$  to  $2021\text{ cm}^{-1}$  (Fig. 6c). A pressure drop to 1 atm (Fig. 6d) revealed in sharper detail a carbonyl species at  $2010\text{ cm}^{-1}$ .

Reactor tests established that although a binary catalyst was active for formic acid hydrogenation to methanol, the 80/10/10 Zn/Cu/Cr catalyst was inactive for this

reaction during the same operating conditions. The adsorption of formic acid solution (73% HCOOH, 27% H<sub>2</sub>O) in a carrier gas of 50/50 H<sub>2</sub>/N<sub>2</sub> on a 80/10/10 Zn/Cu/Cr catalyst (pretreatment 1) at 200°C and 50 atm is shown in Fig. 7. A carbonyl species (band at 1983 cm<sup>-1</sup>) and minor amounts of formate groups (bands at 2872, 1580, 1381, and 1360 cm<sup>-1</sup>) were the only adsorbed species formed within the first hour of exposure (Fig. 7b). Some methoxy groups (bands at 2934 and 2818 cm<sup>-1</sup>) were produced after prolonged exposure (Fig. 7c), but the concentration was low since the isolated hydroxyls (bands at 3668 and 3618 cm<sup>-1</sup>) were not completely displaced. Thus the poor methanol synthesis activity of Zn-Cu-Cr catalysts when using formic acid in the feed mixture was due to the difficulty of formic acid decomposition into formate groups and adsorbed hydrogen at high pressures.

Information about the sequence of reaction steps and adsorption sites was obtained from transient experiments. Despite the low activity of these catalysts at 200°C, the infrared spectra showed that steady-state surface conditions were quickly reached when a 2/1 H<sub>2</sub>/CO feed mixture was used. The surface reactions could be slowed by decreasing the amount of hydrogen in the feed mixture. Even in the extreme case of having only carbon monoxide in the gas phase, gradual hydrogenation of surface species occurred because the residual hydroxyls were a source of hydrogen. This demonstrated that hydrogen (possibly as protons) was mobile on the surface at 200°C. Formate groups were clearly formed before formaldehyde and methoxy groups. The order of formaldehyde and methoxy formation at high pressure was difficult to establish because the intensity of the formaldehyde bands was low, but results from the atmospheric studies (13) suggested that the formaldehyde species was the precursor of the methoxy species.

The spectra of Zn/Cu/Cr ternary catalysts during methanol synthesis conditions provided the most detailed information on surface species. At steady state the 80/10/10 Zn/Cu/Cr catalyst had mainly methoxy groups, some formate groups, and no observable formaldehyde groups on the surface (Fig. 6). The adsorbed carbonyl had shifted from 2089 to 2021 cm<sup>-1</sup>, indicating a weakening of the carbon-oxygen bond without changing the nature of the carbonyl (linear bonded). Unfortunately, the hydroxyl region was too distinct to detect any band at 3520 cm<sup>-1</sup>.

The steady-state spectrum of surface species on a binary catalyst during methanol synthesis using a feed with formic acid was very similar to the spectra for feed mixtures of CO/H<sub>2</sub> or CO/CO<sub>2</sub>/H<sub>2</sub> (Fig. 4). Because the spectrum from the formic acid experiment showed no carbonyl species or gaseous carbon monoxide, the evidence for a reaction sequence involving formate and methoxy intermediates was strengthened. A reaction pathway involving carbon-bonded intermediates is unlikely since the lack of formate decomposition provides no carbon monoxide for this synthesis route. Alternatively, a ternary catalyst was unsatisfactory for methanol synthesis using a feed with formic acid. The infrared spectra showed very little formate and methoxy groups on this catalyst, apparently because formic acid decomposition was difficult at these conditions.

The various zinc sites proposed to be involved in this mechanism can be associated with specific crystal planes of zinc oxide (14). The isolated hydroxyls (bands at 3665 and 3620 cm<sup>-1</sup>) are on the same sites as formaldehyde and methoxy species. These isolated hydroxyl sites (Zn<sub>4</sub>) have been associated with polar ZnO surfaces (15). The formate groups occupy a portion of the hydrogen-bonded hydroxyl sites (Zn<sub>g</sub>) which have been associated with nonpolar ZnO surfaces. The hydrogen-bonded hydroxyls have bands at 3550 and 3450 cm<sup>-1</sup>. The site of hydrogen adsorption (Zn<sub>g</sub>), which produces a hydroxyl band at 3520 cm<sup>-1</sup>, is proposed to be a stepped surface between polar and nonpolar planes of zinc oxide.

#### REFERENCES

1. Weismantel, G. E., Chem. Eng. **87**, 75-78, 1980.

2. Lander, E. P., Hubbard, J. N., Smith, L. A., Jr., Chem. Eng. 90, 36-39, 1983.
3. Berry, R. I., Chem. Eng. 87, 86-88, 1980.
4. Kohn, P. M., Chem. Eng. 86, 49-52, 1979.
5. Deluzarche, A., Kieffer, R., and Muth, A., Tetrahedron Lett. 38, 3357, 1977.
6. Herman, R. G., Klier, K., Simmons, G. W., Finn, B. P., Bulko, J. B., and Kobylinski, T. P., J. Catal. 56, 407, 1979.
7. Vedage, G. A., Pitchai, R., Herman, R. G., and Klier, K., "Proceedings, 8th International Congress on Catalysis." Vol. II, p. 47. DECHEMA, Frankfurt am Main, 1984.
8. Henrici-Olive, G., and Olive, S., J. Mol. Catal. 17, 89, 1982.
9. Kung, H. H., Catal. Rev.-Sci. Eng. 22, 235, 1980.
10. Cheng, W. H., and Kung, H. H., Surf. Sci. 122, 21, 1982.
11. Cheng, W. H., Akhter, S., and Kung, H. H., J. Catal. 82, 341, 1983.
12. Stiles, A. B., U.S. Patent 4,111,847 (Sept. 5, 1978); assigned to E. I. du Pont de Nemours and Co.
13. Edwards, J. F., and Schrader, G. L., J. Phys. Chem. 88, 5620, 1984.
14. Edwards, J. F., and Schrader, G. L., J. Phys. Chem. 89, 782, 1985.
15. Atherton, K., Newbold, G., Hockey, J. A., Discuss. Faraday Soc. 52, 33, 1971.



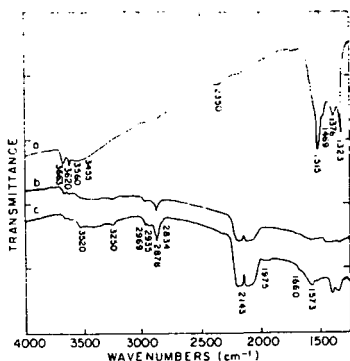


FIG. 1. Carbon monoxide adsorption on 95/5 Zn/Cu oxide at 50 atm and 200°C. (a) Oxidized surface (without pretreatment), (b) exposure for 8 h, and (c) exposure for 24 h.

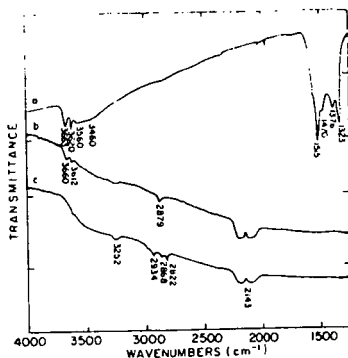


FIG. 2. Adsorption of CO-H<sub>2</sub> mixture on 95/5 Zn/Cu oxide at 50 atm and 200°C. (a) Oxidized surface, (b) exposure for 15 min, and (c) exposure for 1 h.

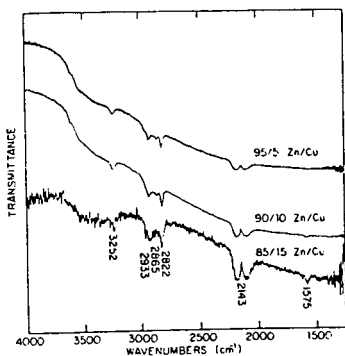


FIG. 3. Adsorption of CO-H<sub>2</sub> mixtures on binary oxides at 50 atm and 200°C.

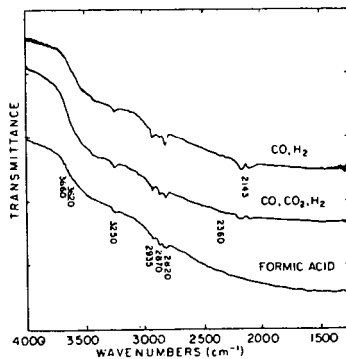


FIG. 4. Adsorption of various feed mixtures on 95/5 Zn/Cu oxide at 50 atm.

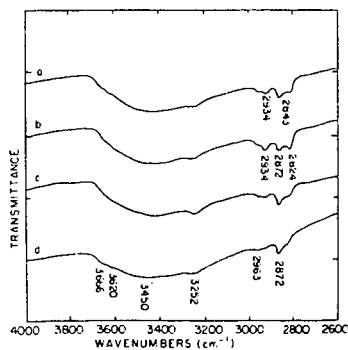
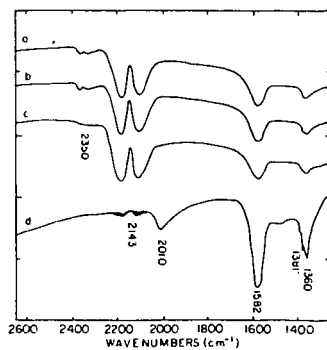


FIG. 5. Adsorption of CO-H<sub>2</sub> mixture on 90/5/5 Zn/Cu/Cr oxide at 50 atm and 200°C. (a) Exposure for 15 min, (b) exposure for 30 min, (c) exposure for 8 h, and (d) after pressure drop.



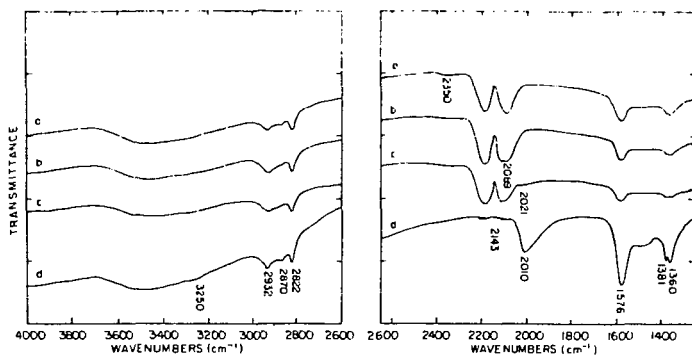


FIG. 6. Adsorption of  $\text{CO-H}_2$  mixture on 80/10/10 Zn/Cu/Cr oxide at 50 atm and  $200^\circ\text{C}$ . (a) Exposure for 15 min. (b) exposure for 1 h. (c) exposure for 4 h. and (d) after pressure drop.

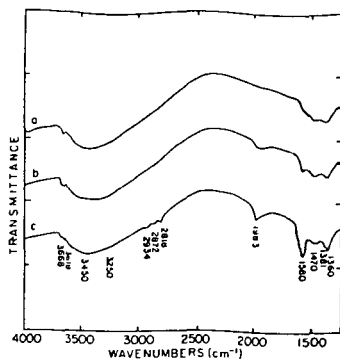


FIG. 7. Adsorption of formic acid on 80/10/10 Zn/Cu/Cr oxide at 50 atm and  $200^\circ\text{C}$ . (a) Reduced surface. (b) exposure for 1 h. and (c) exposure for 3 h.

## ACTIVE SITES IN THE CARBON OXIDE HYDROGENATION ON OXIDE CATALYSTS

Harold H. Kung

Chemical Engineering Department, Northwestern University  
Evanston, Illinois 60201

Methanol synthesis by the hydrogenation of carbon monoxide or carbon dioxide has been a subject of intense research recently. Substantial amount of work has been performed on the prototype of the commercial copper-zinc oxide catalyst to address the questions of the nature of the active site and the reaction mechanism [1]. Methanol can also be produced either catalytically or by stoichiometric reactions on simple oxides. Natta has summarized the early work using various ZnO catalysts [2]. He reported that ZnO of different preparations exhibit different catalytic activities and selectivities. Unfortunately, these catalysts were not well characterized by today's standard, and they also contained impurities. Thus it was not possible to identify the importance of surface structure from those data.

Recently, the methanol synthesis reaction has been studied more extensively on a number of oxides, including  $ZrO_2$  and ZnO. On these two oxides, one particularly interesting observation is that pretreatment of the oxides by a CO and  $H_2$  mixture greatly enhances the methanol production rate from CO in the case of  $ZrO_2$  [3], and from  $CO_2$  in the case of ZnO [10]. Unfortunately, these catalysts undergo deactivation. In fact, deactivation is so severe on ZnO that methanol is considered to be produced by a stoichiometric and not a catalytic reaction.

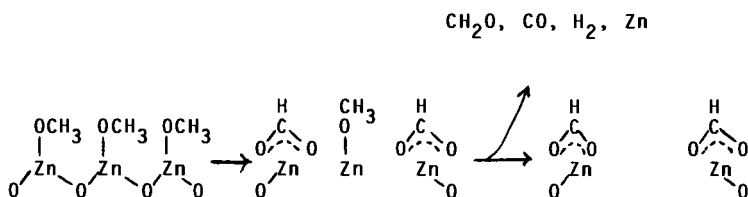
Insight into the nature of the active site on ZnO that interacts with CO or  $CO_2$  is obtained from the study of the decomposition of methanol and 2-propanol. When methanol was decomposed on single crystal ZnO surfaces using temperature programmed decomposition technique, it was found that the Zn-polar face is the most active surface [4]. This observation has been later substantiated by the catalytic decomposition of 2-propanol on different crystal planes of ZnO [5]. The turnover frequencies at 455°C and the activation energy of this reaction are shown in the following table:

| Surface          | Turnover<br>frequencies<br>at 455 C, $\times 10^{-3} \text{ s}^{-1}$ | Eact, kcal/mole |
|------------------|--|-----------------|
| Zn-polar         | 1.5  | 11.7            |
| stepped nonpolar | 0.4  | 9.6             |
| O-polar          | 0.35   | 8.4             |

Although similar catalytic measurements on methanol decomposition have not been made, the similarity in the mechanism between 2-propanol dehydrogenation to acetone and methanol dehydrogenation to CO, and the fact that a similar trend in reactivity is observed in temperature programmed

decomposition of both alcohols suggest that a similar trend should be expected in the catalytic decomposition of methanol.

On the Zn-polar surface, the decomposition of methanol proceeds in two separate pathways: a dehydrogenation pathway that leads to the production of formaldehyde, CO and H<sub>2</sub>, and an oxidation pathway in which an adsorbed methoxy is first oxidized to formate which then decomposes to H<sub>2</sub>, CO, CO<sub>2</sub>, and H<sub>2</sub>O. Recent data further show that metallic zinc is desorbed together with the dehydrogenation products [6]. It is postulated that the desorbed Zn originated from a surface site that is reduced during the oxidation of adsorbed methoxy into formate according to the scheme:



The above scheme is derived for the methanol decomposition reaction. It should be applicable to the methanol synthesis reaction because of microscopic reversibility. Both CO and CO<sub>2</sub> have been shown to be active in the hydrogenation reaction [7], and formate has been postulated to be a reaction intermediate. Formate can be formed by the insertion of CO into surface hydroxyl, and by the hydrogenation of CO<sub>2</sub>. There is controversy as to the relative importance of these routes [8]. Based on the discussion above, one may postulate that the active site on ZnO composes of a region containing some reduced Zn surface ions. The reaction cycle for CO<sub>2</sub> hydrogenation proceeds as: (i) carbon dioxide is adsorbed on the site next to the reduced Zn ion; (ii) H<sub>2</sub> is adsorbed on the reduced Zn ion; (iii) the adsorbed CO<sub>2</sub> is hydrogenated to a formate; (iv) the reduced Zn ion is oxidized by the formate, which is hydrogenated to a methoxy; (v) the methoxy is hydrogenated to methanol; (vi) the active site is regenerated by reducing the site with CO and/or H<sub>2</sub>.

For CO hydrogenation, the active site may be simply the reduced surface Zn ions. In this case, the reduced site or the anion vacancies associated with it acts as the CO adsorption site as well. The reaction may proceed as in the mechanism proposed earlier [9].

It is interesting to note that it has been reported on both ZnO [10] and ZrO<sub>2</sub> [3], pretreatment of the catalyst in a CO and H<sub>2</sub> mixture greatly enhances their activity in methanol production. Such pretreatment is more effective than H<sub>2</sub> alone. The results mentioned earlier on ZnO show that methanol is particularly effective in reducing the oxide. It becomes likely that such pretreatment serves to generate a large density of reduced surface sites, which are the active sites for methanol production.

The discussions above on the role of surface defects may be generalized to other reactions. It has been reported that mechanically polished single crystal surfaces of ZnO can be reduced by adsorbed CO much more readily than cleaved or grown surfaces [11]. Presumably, mechanical polishing introduces surface defects that are not easily removable by thermal annealing. Clearly, these defects have a different oxidizing and reducing power than ions on an atomically smooth surface. It may not be surprising that on oxides, surface imperfection is the active site for catalysis.

#### References:

- 1) K. Klier, *Adv. Catal.*, 31 (1982) 243.
- 2) G. Natta, in "Catalysis", vol. 3 (P. H. Emmett, ed.), Reinhold, New York, 1955, p. 349.
- 3) N. B. Jackson, and J. G. Ekerdt, *J. Catal.*, submitted.
- 4) S. Akhter, K. Lui, and H. H. Kung, *J. Phys. Chem.*, 89 (1985) 1958.
- 5) P. Berlowitz, PhD thesis, Northwestern University, 1985.
- 6) M. Vest, MS thesis, Northwestern University, 1985.
- 7) G. Liu, D. Willcox, M. Garland, and H. H. Kung, *J. Catal.*, 90 (1984) 139.
- 8) G. Liu, D. Willcox, M. Garland, and H. H. Kung, *J. Catal.*, 96 (1985) 251.
- 9) H. H. Kung, *Catal. Rev.*, 22 (1980) 235.
- 10) M. Bowker, J. N. K. Hyland, H. D. Vandervell, and K. C. Waugh, *Proc. 8th Intern. Congr. Catal.*, 1984.
- 11) W. Hirschwald, *Acc. Chem. Res.*, 18 (1985) 228.

INTEGRATED COAL GASIFICATION COMBINED CYCLES (IGCC)  
AN EMERGING COMMERCIAL OPTION FOR THE POWER INDUSTRY

Dwain F. Spencer, Seymour B. Alpert, Michael J. Gluckman

Electric Power Research Institute  
3412 Hillview Avenue  
Palo Alto, CA 94303

Introduction

The very successful initial operation of the 100 MWe Cool Water Coal Gasification Combined Cycle Power Plant during 1985 has stimulated a great deal of interest in IGCC technology within the U.S. and foreign electric power industries. The Cool Water plant has clearly shown that IGCC plants, based on Texaco Partial Oxidation technology, can greatly reduce environmental emissions from coal utilization facilities and simultaneously meet normal electric utility load following requirements. In addition, inspections of Cool Water components, after nearly 7000 hours of operation, have shown that critical units are withstanding the service conditions very well. As a consequence, electric utilities are now developing confidence that such systems can be operated and maintained with little change in normal utility practice.

In parallel, electric load growth in the U.S. has been spurred by economic recovery and electric end use substitution; therefore, electric utilities are again beginning to plan unit additions for the early- to mid-1990's. Since many electric utilities have excess baseload capacity, initial generation additions are likely to be combustion turbines or combustion turbine combined cycle power plants. It is likely that these systems will first be used for peaking and mid-range duty and be fired with premium fuels such as natural gas and distillate. However, in the longer term, they are likely to be phased into baseload operation utilizing coal gasification technology. It is this planning flexibility which adds another important benefit and "degree of freedom" to IGCC power plants.

As a consequence, Potomac Electric Power Company has announced that it is considering the addition of a 350-400 MWe phased IGCC plant at the Dickerson Station. Virginia Power Company is proceeding with a full 200 MWe commercial module IGCC plant for repowering their Chesterfield Station. At least ten other electric utilities are currently conducting or planning site specific IGCC plant designs.

Although it is too early to judge the ultimate penetration potential of IGCC power plants in the U.S., it appears that this option may become the leading new coal technology for the 1990's.

Coal Gasification Systems Status

Development of a number of advanced coal gasification systems has been progressing at a rapid pace. Uncertainty regarding conventional fuels, i.e., natural gas and oil, environmental regulations that represent increasingly tight standards, and uncertainty regarding nuclear power deployment in a number of countries has spurred commercial development of coal gasification systems for diverse applications such as electricity generation; fertilizer, hydrogen and organic chemicals production; generation of hot water for district heating; etc.

### Characterization of Gasification Systems

Coal gasification systems are usually classified by the type of gasifier which contacts and reacts coal with an oxidant (air or oxygen) to produce the desired fuel gas. If the system is blown with air, the fuel gas is low Btu gas and if the system is blown with oxygen, the fuel gas is medium Btu gas.

Three types of contacting devices are:

- o moving beds
- o fluidized beds
- o entrained beds

In moving beds a descending bed of coal, usually 1/8 to 1 inch in size, is fed by a pressurized lockhopper system to the top of a shaft. Reactant gaseous oxygen (or air) and steam enter the bottom of the vessel. As coal descends it is devolatilized, then pyrolysis reactions occur and finally carbon is gasified. The raw product gas contains tars, and oils which need to be condensed and removed. The ash may be withdrawn as a dry solid or as molten slag. In some moving bed versions, tars, oils, and coal fines are recycled to extinction.

In fluidized bed reactors, coal is ground to produce a fluid bed grind (ca 8 mesh or less). The oxidant gas (and some steam) are introduced through a perforated deck or grid at the bottom of a vessel. The flow rate of the reactants is high enough to suspend the coal particulates but not blow them out of the vessel. A uniform temperature is obtained by the mixing that occurs. Depending on the temperature, tars and oils can be avoided but fines carryover and ash slugging limit conversion of some coals to 80%-90% of the carbon. In order to overcome this limitation, the carbon containing ash can be processed in an additional vessel or the unconverted carbon can be recycled to the gasifier.

In entrained flow systems, a relatively fine grind of coal (ca 75% through 200 mesh) is fed either as a dry solid or as a water and coal mixture to a short residence time reactor. Contacting with the oxidant is achieved by means of a nozzle arrangement. At the high velocities and temperatures used in entrained systems (2000 to 3000°F) no tars or oils are produced. Carbon burn-out is nearly complete and the product gas is essentially carbon monoxide and hydrogen.

In the U.S. and abroad, advanced coal gasification technologies have been under development for the last decade. Several technologies have been supported by EPRI's program.

1. Texaco technology, represents an entrained system that features a coal water slurry feeding the pressurized, oxygen-blown gasifier. It is the farthest advanced in that three commercial or demonstration plants are in operation. Two of these plants are located in the U.S. and one in Japan. A plant in the Federal Republic of Germany will start up in late 1986 to produce organic chemicals and hot water for district heating. Projects have also been announced for China and Sweden.
2. Shell coal gasification has under construction a 250/400 ton/day pilot plant at their research center in Deer Park, Texas that will lead to commercial designs in the late 1980s. The Shell process features a dry fed entrained gasifier system that operates at elevated temperature and pressure. Current studies with U.S. electricity companies are defining commercial opportunities.
3. The British Gas Corporation and Lurgi GmbH have jointly developed a slugging, moving bed gasifier system. A commercial gasifier prototype (600 ton/day) will be started up at Westfield, Scotland in early 1986. Virginia

Power is considering installation of a coal gasification system for a 200 MWe IGCC power plant based on the BGC/Lurgi technology.

4. An air-blown rotary ported kiln (similar to a moving bed device) is under development by Allis Chalmers Corporation. A 600 ton/day prototype is located at an Illinois Power Co. power station.

The Dow Chemical Co. is installing a 160 MWe IGCC plant in Louisiana that will produce electricity and synthesis gas for industrial chemicals. Details of the system are proprietary, but the system features a coal water slurry fed entrained gasifier. Price supports of \$620 million from the Synthetic Fuels Corporation have been obtained for the project.

Other gasification systems technologies have been evolving, including the Kellogg Rust Westinghouse gasifier and Institute of Gas Technology U-Gas system that are representative of ash agglomerating fluid bed systems. Advanced fluid bed systems are also being developed in Japan. A Winkler demonstration fluid bed system operating at elevated temperature and pressure is being started up in the Federal Republic of Germany by Rheinsche Braunkohle. The Winkler system will handle 700 tons/day of coal to produce industrial chemicals and electric power.

Other projects that are at the pilot plant stage of development include a 50 ton per day pressurized pilot plant by GKT-Krupp. The Vereinigte Elektrizitätswerke Westfalen (VEW) has started up a 250 ton per day pressurized pilot plant that partially converts coal (60% conversion) to low Btu gas for power generation. Lurgi has gasified lignite in an atmospheric pressure circulating fluid bed in their 15 ton per day pilot plant in Frankfurt, West Germany.

In Japan, several pilot plant programs are also underway including development of a molten iron gasification system. A 250 ton per day pilot plant is under construction in Sweden by Sumitomo-KHD in which sulfur is captured in the slag.

#### Combustion Turbines

Development of advanced combustion turbines is proceeding rapidly. Efficiency of combined cycle equipment is increasing from the ability to operate at higher firing temperatures. In utility applications, firing temperatures of 2,000°F are conventionally used and higher temperatures of 2,300°F can be expected before 1990. Developments in the areas of reheat, materials, and advanced cooling methods promise additional improvements in efficiency in the 1990's.

#### Economics of IGCC Power Plants

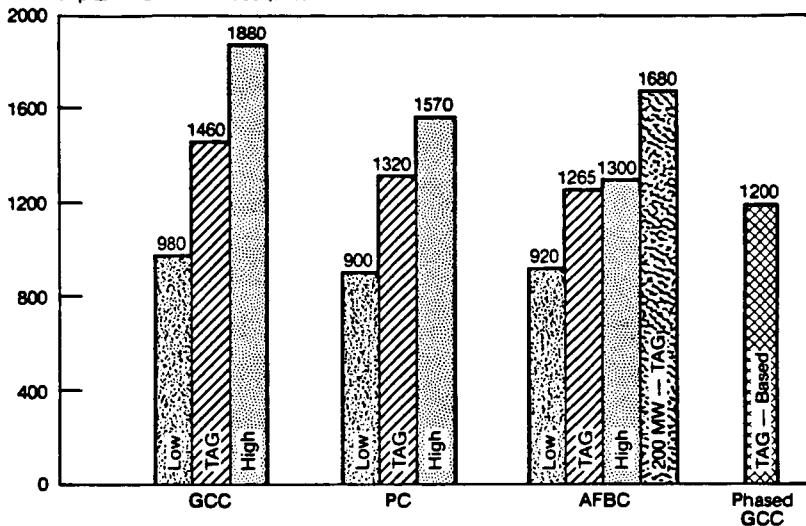
The three major candidates for advanced coal utilization in the 1990s are integrated coal gasification combined cycle (IGCC) power plants, atmospheric fluidized bed combustion (AFBC) systems, and improved pulverized coal (PC) power plants. In order to assess the relative benefits of IGCC, AFBC, and PC plants, EPRI in conjunction with numerous engineering/construction firms have estimated the expected range of capital and busbar power costs for such plants using 3.5% sulphur Illinois bituminous coal. Figure 1 shows a comparison of the estimated range of capital costs from various studies placed on as consistent an estimate basis as possible. The estimates shown are low and high estimates, as well as those shown in EPRI's Technical Assessment Guide (TAG) for the three competing technologies. Also shown for the IGCC plant is the benefit of utilizing phased construction of the plant rather than committing all plant capital at once. The expected cost of a 200 MWe AFBC unit has been included because it is unclear whether single 500 MWe AFBC units can be constructed. In general, there is little difference in the expected range of capital costs for these three plant types, with perhaps a small capital advantage to AFBC and PC plants.



**CAPITAL INVESTMENT ESTIMATES FOR SINGLE 500 MW UNITS  
AFBC HAS ONE 200 MW UNIT CASE**

FIGURE 1

Total Capital — Constant 1985 \$/kW



**COST OF ELECTRICITY ESTIMATES USING  
TAG ECONOMIC CRITERIA**

FIGURE 2

Cost of Electricity (30 year levelized) in Constant 1985 mills/kWh

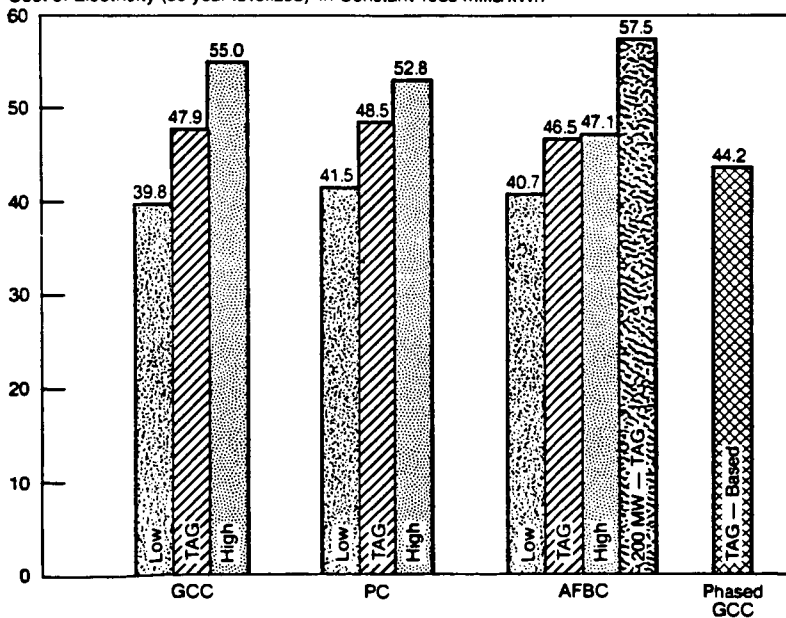


Figure 2 compares the 30 year levelized, constant 1985 dollar busbar energy costs for these same alternatives. As may be seen, all 500 MWe plants are projected to produce power costs of approximately 4¢/kWhr to 5.5¢/kWhr. There is no clear advantage for any of the technologies, considering the present uncertainties in these cost estimates. Phased construction of IGCC plants does show promise of producing some reduction in power costs.

It is in the area of environmental emissions control that coal gasification combined cycles demonstrate their true benefits. Table 1 shows typical effluent streams from the three coal-based technologies, using a 3.5% sulphur Illinois coal. The IGCC plant emits approximately one-tenth the acid rain precursors (SO<sub>2</sub> and NO<sub>x</sub>) than a pulverized coal plant and produces 40 percent of the solid wastes from a PC plant. In comparison, the AFBC plant emits about 50 percent of the acid rain precursors from a PC plant, but produces 60 percent more dry solid waste for disposal. Although solid waste disposal costs were factored into the previous electricity estimates, very low costs for disposal were assumed. In many areas of the U.S., there just is not landfill area available for such large amounts of waste.

Table 1  
Typical Effluent Streams  
From Coal Based Power Plant Types  
(Using 3.5% S. Illinois Coal)

| Plant Type                                      | SO <sub>2</sub><br>Emissions<br>(Tons/MWe Yr) | NO <sub>x</sub><br>Emissions<br>(Tons/MWe Yr) | Solid<br>Wastes<br>(Tons/MWe Yr) |
|---|---|---|----------------------------------|
| Pulverized Coal Plant<br>(Precipitators Only)   | 140   | 25  | 240                              |
| Pulverized Coal Plant<br>With FGD (90% Removal) | 14  | 8   | 750                              |
| Integrated Gasification<br>Combined Cycle Plant | 0.14-4  | 3   | 300                              |
| Atmospheric Fluidized<br>Bed Combustion         | 7   | 4   | 1200                             |

Therefore, we believe that coal gasification combined cycle power plants show the greatest potential for meeting stringent emission control requirements, yet remaining economically competitive with alternative coal technologies.

#### Phased Construction of IGCC Power Plants

The modular structure of IGCC power plants provides utility companies with a major flexibility not available to them in the past. The capability to "phase-in" a plant in relatively small increments would allow a utility to more closely match load growth requirements by bringing a sequence of combustion turbines on line (shown in Figure 3 as Phases 1 and 2); converting these turbines into a combined cycle plant in Phase 3 and finally adding the gasification facility in Phase 4. The excess capacity at any time is shown as the crosshatched areas in Figure 3. This can be compared to the addition of an unphased, substantially larger power plant depicted in Figure 4. It is evident from Figures 3 and 4 that at any point in time, the phased addition approach results in substantially less excess system capacity than the conventional unphased plant construction approach. This means

FIGURE 3

### PHASED CAPACITY ADDITION

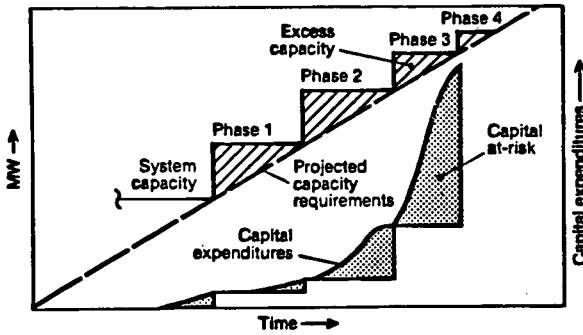
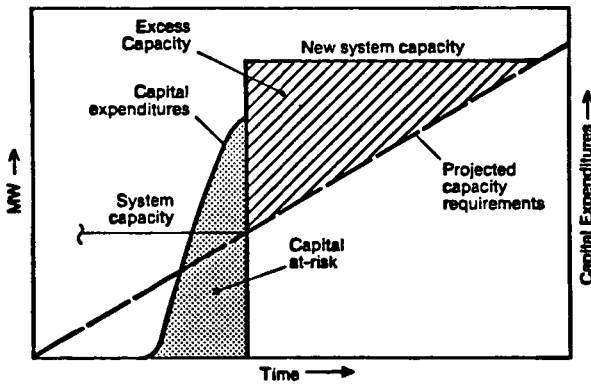


FIGURE 4

### UNPHASED CAPACITY ADDITION



that the rate payer does not have to pay for unnecessary capacity ahead of time and the electric utility company does not have to place "at-risk" for an extended period of time the vast amount of capital required to construct a large, unphased power plant.

The major potential benefits to be associated with the phased addition of IGCC power plants are summarized below:

- o It allows the utility to delay and stretch out large capital outlays by more evenly matching load growth requirements without taking the full cost penalty of diseconomy of small scale.
- o It minimizes "at-risk" capital due to short construction periods for modules, i.e., capital becomes part of the rate base significantly earlier. A combustion turbine can be installed in approximately one year whereas it could take up to five years to construct a large coal-fired steam plant.
- o Phased construction provides the flexibility to take advantage of "low-cost" and "available" fuels for as long as this situation persists, i.e., a utility does not have to predict fuel prices or availability ten or fifteen years into the future. The phased plant can switch to coal whenever appropriate.
- o Phasing in an IGCC power plant provides a utility the flexibility to respond rapidly (and, therefore, at minimum cost) to changes in system load growth and/or fuel prices.
- o Finally, this procedure provides the potential for the utility to take advantage of non-utility company ownership of the coal gasification plant, thereby dramatically reducing the capital required for new capacity additions.

These potential benefits to be associated with the phased construction of IGCC power plants have already been recognized by major equipment suppliers and utilities alike. General Electric (GE) has investigated the system expansion benefits of phasing in an IGCC power plant (a procedure that they have termed PROGEN) instead of constructing conventional coal-fired steam plants. Sixteen scenarios of load growth and fuel prices were investigated. The GE results indicated that for all sixteen cases, fixed charges and production costs were significantly reduced due to phased construction. Capitalized savings for the phased construction approach ranged from \$350/kW to \$800/kW.

Potomac Electric Power Company (PEPCO) has conducted a preliminary phased construction study (comparing one IGCC plant to a coal-fired steam plant). Results of this study show a cumulative present worth saving in revenue requirements of approximately \$100 million attributable to the phased IGCC plant. Approximately one year ago, ten member companies (see Table 2) of the Utility Coal Gasification Association began an evaluation of the benefits of phased construction of IGCC plants on their systems. Preliminary results of some of these studies have confirmed the potential for financial benefits that have been claimed for this phased construction approach.

IGCC power plants clearly show promise of being the truly environmentally benign, economically competitive method of utilizing high-sulphur coal for power generation in the 1990's and beyond.

Table 2

Phased IGCC Construction Study Team

Baltimore Gas & Electric Co.  
Cleveland Electric Illuminating Co.  
Consumers Power Co.  
Illinois Power Co.  
Nevada Power Co.

Northeast Utilities  
Potomac Electric Power Co.  
Public Service Electric & Gas Co.  
Virginia Power Co.  
Public Service of Indiana

## COMMERCIALIZATION OF THE DOW GASIFICATION PROCESS

G. A. Bornemann  
D. G. Sundstrom

Dow Chemical U.S.A.  
P. O. Box 3387  
Houston, Texas 77253

### Introduction

In 1979 The Dow Chemical Company authorized \$450 million of capital to be spent on the Gulf Coast Power Conversion Project, the largest single power project Dow had ever built. This capital was to be spent phasing out less efficient gas-fired boilers at the Texas and Louisiana Divisions and integrating 910 MW of new gas turbine generation capacity into these manufacturing locations. Fuel cost savings were projected to be \$200 million per year. Future plans involved utilization of Dow's extensive lignite holdings and then-developing gasification technology to provide our Gulf Coast manufacturing locations with low-cost energy on a long-term basis. Dow completed the installation of the gas turbine facilities in 1982.

Now, after Dow's largest single research and development project ever, a price guarantee from the Synthetic Fuels Corporation has provided the incentive to build our first commercial gasifier in Plaquemine, Louisiana, the Dow Syngas Project. Western coal will be transported by rail to the plant site and the product, medium Btu syngas, will be used to fuel existing gas turbines. The output of this facility will be equivalent to 155 MW of net power production.

### Background

Dow's products are highly energy intensive. The primary demand for electrical energy is derived from electro-chemical processes and thermal (steam) demand comes from production of petrochemicals and plastics. Most of our manufacturing locations have a convenient balance between electrical energy and thermal energy, allowing the economical cogeneration of power and steam. Variations of combined cycle plants to match a particular site's requirements for power and steam now exist at all of Dow's major production locations. In the U.S. alone Dow has 1600 MW of gas turbine generation capacity and 800 MW of steam turbine capacity. Over \$500 million has been spent in the last decade on power generation facilities.

### History of Dow Gasification Process

Dow's current energy program took form in the early 1970's. The prospect of future shortages of natural gas and resultant high prices launched a "war on Btu's". The outcome was an energy strategy based on:

1. Gas turbines as the most efficient power production technology.
2. Solid fuels as the most abundant low cost energy resource.

Coal gasification was the necessary link to insure the viability of our strategy.

We looked at commercially available processes and found none that met our criteria. We needed a process that was:

1. Reliable.
2. Energy efficient.
3. Environmentally clean.
4. Capable of handling all coals.

Shortcomings of these processes included:

1. High capital cost.
2. Need for coal feed drying.
3. Difficult heat recovery due to tars and oil in product gas.
4. Inability to acceptably process coal feeds containing fines.

Research continued and we found processes that were not commercially proven had some very promising attributes:

1. Reduced residence time in reactor.
2. Feed flexibility.
3. Molten slag removal.
4. Environmentally clean.

However, this technology was not efficient on low rank coals and did not meet Dow's acceptable reliability criteria.

Our development efforts were then greatly expanded and by 1979 we had in place at Plaquemine, Louisiana, an air-blown 400 ton per day demonstration gasifier and a 12 ton per day pilot plant. The pilot plant was used for advanced studies. In August of 1981 we achieved an event without precedent--the successful use of synthetic gas from a coal gasification unit to fuel a 15 MW commercial gas turbine generator.

During 1981 and 1982 a new reactor design and a novel energy recovery technique were developed at the pilot plant. The pilot plant was increased in size to 36 tons per day and converted from air to an oxygen blown process. In 1983 a new technology demonstration gasifier was completed. It incorporated all the technology developed at the pilot plant and has a 1600 ton per day capacity. The capacity of the Dow Syngas Project, our first commercial scale unit, on Western coal is approximately 24000 tons per day. Consequently, scaling up from our new technology demonstration gasifier is a relatively small increment.

#### Description of the Dow Gasification Process

The Dow gasification process utilizes a pressurized, entrained flow, slagging, slurry fed gasifier with a continuous slag removal system. The process includes a unique heat recovery system which provides high efficiency on low rank coals. The novel slurry feed technology and continuous slag removal technique eliminates high maintenance, problem-prone lockhoppers for introducing the coal to the gasifier or for removal of slag. The design completely prevents the combustion gases and raw product gases from escaping into the atmosphere during slurry feeding or slag removal.

The coal slurry is fed to the reactor and mixed with oxygen in the burner nozzles. The feed rate of oxygen is carefully controlled to maintain the reactor temperature above the ash fusion point to insure slag removal. Under these conditions, the coal is almost totally gasified by partial combustion to produce synthetic gas

consisting principally of hydrogen, carbon monoxide, carbon dioxide, and water. The sulfur is converted almost totally to hydrogen sulfide with small amounts of carbonyl sulfide. The gasifier system operates in such a manner that essentially no tars, oils, or phenols are produced. The Dow Gasification Process includes a unique heat recovery system which provides high efficiency on low rank coals. The ash is fused in the flame, direct quenched in a water bath and removed from the bottom of the reactor as a slurry through a special pressure reducing system. The slag is dewatered and stored.

The gas exiting the gasifier system is further cooled by a conventional heat recovery boiler to near its saturation. The high pressure superheated steam produced can be used for power generation via steam turbines or to drive the oxygen plant air compressor.

The raw synthetic gas goes through a cyclone separator where most of the entrained particles are removed. Final particulate removal is achieved by water scrubbing the partially cooled gas. All of the particulates removed by the cyclone and wet scrubber are recycled to the gasifier.

The scrubbed syngas is then cooled through a series of heat exchangers before entering the acid gas removal process. The amount of low level heat recovery is economically balanced with the heat requirements of both the gasifier and the acid gas removal process.

The acid gas removal from the syngas stream is an economic evaluation of the application of several known technologies with the environmental and process constraints of the location. The particulate-free syngas from the Dow gasifier is suitable feed for any of the known commercial processes.

The Dow Syngas Project gasifier satisfies its location requirements with a Gas/Spec ST-1 acid gas removal system and a Selectox sulfur conversion unit.

#### Commercial Application of the Dow Gasification Process

Synthetic gas produced from the Dow gasification process can be used as a substitute for coal, natural gas, fuel oil, and natural gas derived chemical feedstock. The synthetic gas can be used as fuel for gas turbines, industrial and utility boilers, furnaces, and process heaters. It also can be used to meet some chemical feedstock demands; methanol and ammonia are examples of products which could use this synthetic gas as feedstock.

The most promising market for this synthetic gas is as fuel for turbines to generate electricity.

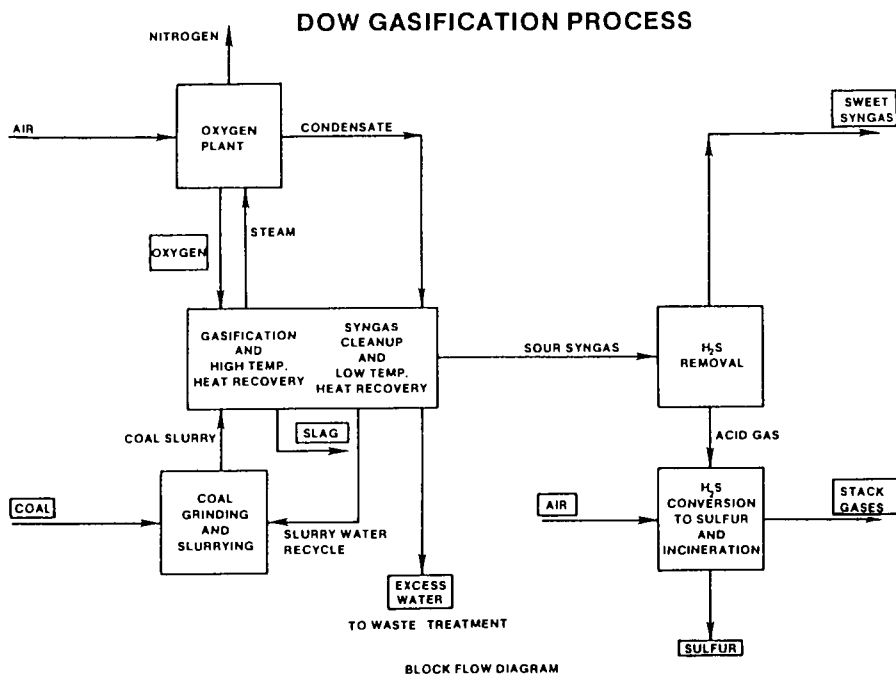
The combined cycle gas turbine fired by medium Btu synthetic gas has capital advantages versus coal-fired steam boilers and steam turbines. Overall energy efficiency for the medium Btu synthetic gas/combined cycle turbine is projected to be better than a steam boiler/steam turbine fed by coal.

The Dow Gasification Process has been developed as a module with a gasifier output sufficient to fuel a nominal 100 MW gas turbine. The net output of power after subtracting the requirements of the oxygen plant and gasifier and considering the by-product steam from an associated heat recovery unit converted to power is about 160 MW. When referring to a replicable unit using the Dow Gasification Process, Dow believes this is representative. Dow expects to build about ten of these modules in its Gulf Coast plants to provide fuel for existing gas turbines combined cycle units.



### License Availability

Dow is committed to license its gasification technology on reasonable commercial terms. Dow offers related services such as engineering, consultation services, project management and operations support, all of which enhance our technology by bringing Dow's owner/operator perspective to a project.



## TEXACO COAL GASIFICATION PROCESS: COMMERCIAL PLANT APPLICATIONS

W. R. SIEGART, P. F. CURRAN

TEXACO INC.  
2000 WESTCHESTER AVENUE  
WHITE PLAINS, NEW YORK 10650

S. B. ALPERT

ELECTRIC POWER RESEARCH INSTITUTE  
3412 HILLVIEW AVENUE  
PALO ALTO, CALIFORNIA 94303

### INTRODUCTION:

The Texaco Coal Gasification Process (TCGP) has been employed at several commercial scale facilities worldwide, and has matured to the point where it is now an attractive alternative for use in chemical and power facilities. The successful use of the process at existing facilities has yielded valuable performance data and operating experience which can help in optimizing the efficiency of all future TCGP operating plants. This process has been employed for the production of chemicals in the U.S., Japan and West Germany. Other TCGP chemical plants in China, Sweden, West Germany, and the U.S. are now being planned or are under construction.

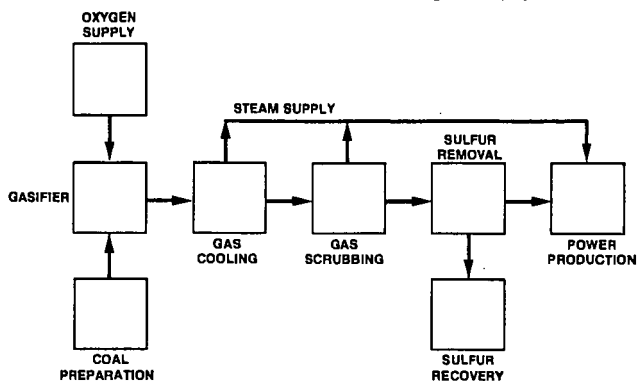
The commercial viability of TCGP for large scale production of electric power has been proven at the 120 MW Cool Water facility in Southern California. The economic and environmental characteristics of the process make it the leading technology option for future electric utility use. One major utility has publicly announced its intent to use gasification in their next power plant and many others are including it in their formal planning process.

### PROCESS DESCRIPTION:

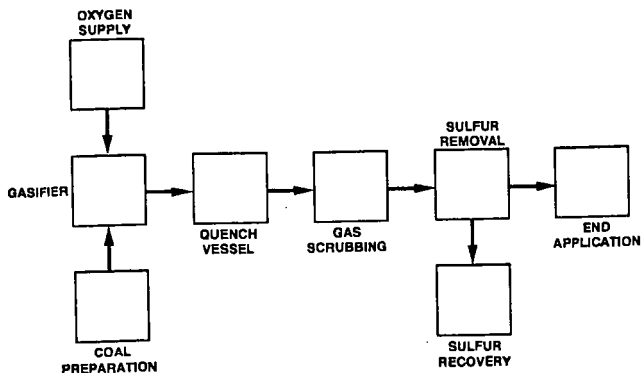
The technical details of the Texaco Coal Gasification Process will not be presented here in any depth. Numerous other papers have been published which adequately cover the details of how the process works and its technical development. (1,2,3). Figures 1 and 2 show two configurations of the process. Figure 1 shows a block flow diagram for maximum heat recovery (i.e., power plants); Figure 2 shows a minimum investment design used widely for production of synthesis gas as a chemical feedstock. Design variations from each of these options are possible to suit the requirements of a given application. For example, a gas cooler could be added to the total quench design (Figure 2) to allow for the generation of additional steam.

Utilizing Figure 1, the total process can be described. Coal is ground, slurried, and pumped to a gasifier where it reacts with oxygen. The concentration of oxygen in the gasifier is not sufficient for complete combustion, but does support partial combustion which generates heat. This heat breaks down the coal to form synthesis gas, a medium BTU product composed primarily of carbon monoxide and hydrogen. This synthesis gas is cooled, cleaned, and sent to the desired application. In Figure 1, the application is power production.

**FIGURE 1**  
**TEXACO COAL GASIFICATION PROCESS**  
**MAXIMUM ENERGY RECOVERY**



**FIGURE 2**  
**TEXACO COAL GASIFICATION PROCESS**  
**MINIMUM INVESTMENT DESIGN**



The steps between the gasifier and the desired end use employ proven commercial technology. The ash in the coal forms a slag material which is removed from the gas cooling section. This slag is a non-hazardous material suitable for landfill or other applications. The steam generated in the gas cooling process is utilized in a steam turbine for additional electric power production. After the gas is sufficiently cooled and scrubbed of particulate matter, it is directed to a sulfur removal and recovery stage. Sulfur contained in the coal is transformed primarily into  $H_2S$ , due to the gasification reactor temperature and oxygen deficient environment. This  $H_2S$  can be separated from the syngas using commercially available units. The  $H_2S$  is transformed to elemental sulfur which can be sold as a by-product.

#### EXISTING APPLICATIONS:

Nuclear fusion, photovoltaics, magnetohydrodynamics, coal liquefaction, wind power, geothermal energy, gasohol, and coal gasification were among the answers proposed for the energy crisis of the late 70's. The crisis is viewed differently in the mid 80's due to current energy economics. The petroleum and natural gas supply problems which caused the 1970's crises may have subsided, but they have not disappeared. In the years ahead, there will be a need for clean energy conversion from feedstocks other than oil and gas. Of the technologies listed as alternatives, only coal gasification has been proven on a commercial scale as an attractive option for chemicals and power production. Of the coal gasification designs proposed, only the Texaco process has met the necessary standards for wide spread acceptance and use.

For electric power production, the Cool Water Plant, in Barstow, California, has been operating for over a year and a half, gasifying 1,000 tons per day of coal in an integrated gasification combined cycle (IGCC) power plant. The plant's capacity factor (plant electric production/rated capacity) for 1985 was higher than the 1984 average for all conventional coal fired power generating stations of 50 MW or greater in the U.S. (4). Environmental data from Cool Water has shown its performance to far surpass EPA standards, as well as being environmentally superior to other new fossil fuel power plants of equivalent size.

For production of chemicals, TCGP is becoming increasingly popular for feedstock generation. Tennessee Eastman utilizes the process for the production of acetic anhydride, which is used in the photographic industries. They recently reported a 97% on-stream factor for the final six months of 1984 (5). Ube Industries gasifies 1650 tons per day of Australian and South African coals for the production of ammonia. Commercial scale ammonia plants using TCGP are now being planned for Sweden and China. A TCGP facility for the manufacture of oxo-chemicals from coal is being constructed in West Germany.

#### FUTURE APPLICATIONS

##### Electric Power Production

Application of the Texaco Coal Gasification Process for the large scale generation of electric power is clearly on the horizon. Some utilities have publicly stated their desire to use gasification for power

production (6,7). Many others are internally evaluating the technology for power facilities to be commissioned in the 1990's. The Electric Power Research Institute has established a Utilities Coal Gasification Association to "encourage the development of coal gasification for the production of electricity..." (8). Utility membership in this group has grown steadily, and interest among utilities in the technology is keen.

The merits of TCGP must be viewed in relative terms compared to other power generation technologies. There are currently four leading methods of power generation in the U.S. These are nuclear fission, oil or gas combustion, coal combustion, and hydropower. 99.4% of all U.S. nameplate capacity for electric power generation utilizes these technologies (9). Each of these technologies, however, has limitations which restrict future usage. No new nuclear fission plant is being planned, and the last plants under construction are currently scheduled to start up in the early 90's. The social, political, and engineering factors which doomed this industry have been widely discussed and speculated upon. Oil and gas combustion are limited by the future supply of the fuel. The average age of an oil or gas plant retired from service in 1984 was approximately 31 years (10). Thus, in considering a power plant construction project, it is necessary to consider the price and availability of fuel not just today, but also in the decades ahead. Most forecasts suggest severe escalation for petroleum products within this time frame. Data Resources Inc. predicts inflation for oil and gas to average in excess of 10% per year throughout the 1990's, while coal prices will remain relatively stable in real terms over the same period (11).

As for coal, supply is adequate but environmental concerns may restrict its use in a direct fired mode. Hydropower has no limitations other than its availability. Expansion of the use of hydro requires the rivers to exist in sufficient concentrated quantities for large scale power generation. Unfortunately, such resources are not abundant. Ecological concerns also are present with the construction of hydropower facilities.

This situation indicates that revisions or new methods of power generation will be required for the future. As noted earlier, the Texaco Coal Gasification Process is the most successful alternate technology to emerge in recent years. New power generation methods must prove themselves to be fully competitive in terms of economic viability and operability on a commercial scale. The performance of Cool Water has proven the operability of TCGP, and the experience gained there will enhance the performance of future plants. The economic viability of TCGP has been attested to in various engineering studies (12).

Coal gasification is not the only viable option for power generation in the 1990's. Site specific considerations will make other technologies the preferred option in some instances. However, a certain percentage of new plants will be designed for IGCC due to its long range attractiveness. The North American Electric Reliability Council (NERC) forecasts 113,200 MW of new electricity generation capacity will be added by 1994 (13). Planned coal and nuclear plants account for much of that addition. With the halt in nuclear planning, new construction beyond 1994 will be predominately coal based. Due to the economic comparability and environmental superiority of the Texaco Process as compared with traditional coal utilization methods, this process will emerge as the technology of choice for many of the capacity additions in the 1990's.

Some traits of the plants to be built in the 1990's will distinguish them from the Cool Water facility. In efficiency, it has been estimated that a 600 MW facility could be constructed with a net heat rate of 9,000 BTU/KWH (14). This rating is competitive with efficiencies found in existing power generation facilities. Some 600 MW facilities will be built, but a recent trend in power plant construction is toward smaller size, and phased modular construction. A typical plant could be 400 MW in total size, constructed in four 100 MW phases. This allows the utility to gain an economy of scale on some components while delaying capital expenditures until they are needed. Economic efficiency of the construction process can be greatly enhanced with this phasing technique. Gasification facilities are well suited to these construction methods.

Power plants being constructed in the 1990's must have a great deal of operating flexibility. Cool Water has verified the ability of TCGP to load follow (i.e., reduce or increase output quickly) and, as noted, the capacity factor for the plant has already surpassed the competitive level. From these results, it is expected that TCGP can meet the operating requirements of a base load power station. To do so on a practical basis requires flexibility of feedstock requirements. Table 1 shows a list of coals which have been gasified at Texaco's Montebello Research Laboratory. Several are now in use at commercial scale plants worldwide. Although there are differences in gasifier operations for different coals, experience has shown that all bituminous and sub-bituminous coals, and petroleum coke can be successfully gasified.

Environmentally, the performance of Texaco coal gasification plants will probably be the standard which other fossil fuel facilities will have to meet. Furthermore, environmental records of future IGCC plants could surpass that of Cool Water, which has already been characterized as the cleanest coal burning plant in operation today. Figure 3 illustrates a comparison of actual emissions for Cool Water vs. the EPA standards. Clearly, this is a strong asset of TCGP in assessing its future use in large scale power production.

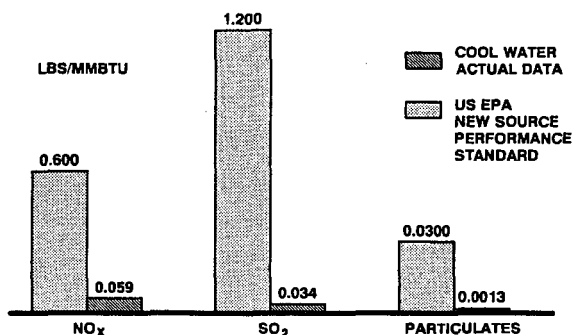
It is not certain which utilities will be among the first to begin utilizing IGCC plants. It could be expected that a need for capacity, an environmentally sensitive operating region, and a proximity to coal reserves, will be among the traits of those initial utilities. Perhaps more important is a corporate mindset which accepts business risk, and seeks to improve their operating efficiencies. Particularly attractive to such firms might be the ability of the process to co-produce other saleable products such as methanol, hydrogen, and steam.

A final aspect of future IGCC power plants which will distinguish them from those currently in service may be the ownership structure. The Public Utility Regulatory Policy Act of 1978 (PURPA) has encouraged the private ownership of electric power production facilities. The concept of power plant partnerships between utilities and power users, utilities and power industry firms, and between utilities and other utilities will become more common particularly for projects using relatively new technologies. The utility/power user partnership concept could become especially prevalent if deregulation proceeds on an aggressive course as some suggest.

#### CHEMICALS PRODUCTION:

The basic product of coal gasification is synthesis gas, a mixture

**FIGURE 3  
ENVIRONMENTAL PERFORMANCE**



**TABLE 1  
FEEDSTOCK FLEXIBILITY  
SOLID FUELS GASIFIED AT  
TEXACO'S MONTEBELLO RESEARCH LABORATORY**

| <u>BITUMINOUS COALS</u> | <u>SUB-BITUMINOUS COALS</u> |
|-------------------------|-----------------------------|
| PITTSBURGH              | WYOMING                     |
| KENTUCKY 9              | ARIZONA                     |
| ILLINOIS 6              | UTAH                        |
| UTAH                    | JAPAN                       |
| TENNESSEE               | <u>LIQNITES</u>             |
| GERMANY                 | TEXAS                       |
| AUSTRALIA               | NORTH DAKOTA                |
| SOUTH AFRICA            | GREECE                      |
| CANADA                  | <u>PETROLEUM COKES</u>      |
| ITALY                   | FLUID                       |
| CHINA                   | DELAYED                     |
|                         | CALCINED                    |

**FIGURE 4  
CHEMICAL COMPOSITION OF  
SYNTHESIS GAS - CLEAN &  
DRY BASIS**

| <u>COMPONENT</u>       | <u>VOLUME %</u> |
|------------------------|-----------------|
| CO                     | 42.5            |
| H <sub>2</sub>         | 38.2            |
| CO <sub>2</sub>        | 18.6            |
| CH <sub>4</sub>        | 0.3             |
| AR & N <sub>2</sub>    | 0.4             |
| H <sub>2</sub> S & COS | 50PPM           |

of several components primarily carbon monoxide and hydrogen. Figure 4 shows a typical breakdown of its composition on a dry basis after cleanup. As was indicated, this gas can be used as a medium BTU fuel for the production of electrical power. It can also be used as a chemical feedstock in the production of hydrogen, ammonia, methanol, oxo-chemicals, and other substances. The growth of these industries is expected to be strong in the early 1990's (15). However, existing overcapacity for many of these products makes capacity addition forecasting difficult.

One of the key factors in assessing the prospects for TCGP in the chemicals manufacturing industries is the competition. As a chemical feedstock, synthesis gas must compete directly with natural gas. In today's market, natural gas is relatively inexpensive and supply is plentiful. The future of this market must be viewed in assessing feedstock alternatives. The popular belief among forecasters is that in the long-term, inflation rates and security of supply will be much more favorable for the consumer of coal as opposed to the natural gas user. Therefore, if a plant is being designed to securely fulfill a long term need for the plant output, coal gasification would be a preferred option.

Multi-product facilities based upon coal gasification will probably see some use in the coming years. NASA is considering the construction of a coal gasification plant to supply all of their hydrogen, oxygen, electricity, nitrogen, fuel gas, and heated water needs. Because coal, air, and water are the only feed streams needed to produce the desired products, the security of supply is not expected to be a problem. If NASA so opted, the proposed facility could also export any of the produced products as well as argon and sulfur. Such decisions would hinge upon the commercial marketplace.

Because of the many uses of synthesis gas, multi-product projects, similar to that proposed by NASA, will probably be considered in the future. In such facilities, steam, electricity, sulfur, and possibly other products will be produced. Under federal cogeneration guidelines, export electricity produced in this type of facility must be purchased by the local utility who must also supply backup power to the site.

Several types of possible chemical facilities could use TCGP for feedstock generation and cogenerated power production. Based upon the current trends in the chemicals markets, we believe TCGP will play a major role in the chemical industry by the mid-1990's. As has been true to date, no single application will dominate, but plants of varying size and product slate will be constructed.

#### SUMMARY:

The development of the Texaco Coal Gasification Process has now reached a stage of maturity. Already employed on a commercial scale in the chemicals and electric utility industries, the process is now being widely considered for use in the new facilities in both these sectors. Benefitting from the experience obtained in the existing plants, new facilities can expect operating efficiencies and process economics which are competitive, and in some cases, superior to other technologies.

The process not only meets the necessary economic, operational, and environmental standards for use today, it also uses technology which will



become even more attractive with future energy economics and environmental regulations. Natural gas and petroleum feedstocks are forecasted to become more expensive and more scarce. Conventional coal technology, even with scrubbers, may be subject to continuous capital outlays to meet changing environmental standards. A Texaco Coal Gasification Facility will not be as seriously affected by either of these expected trends.

Notes:

1. Kolaian, J. H. and Schlinger, W. G. "The Texaco Coal Gasification Process". Energy Progress. Vol. 2, No. 4. December 1982.
2. Moss, S. H. and Schlinger, W. G. "Coal Gasification". Lubrication. Vol. 66, No. 3. 1982.
3. Schlinger, W. G., Kolaian, J. H., Quintana, M. E., and Dorawala, T. G. "Texaco Coal Gasification Process for Production of Clean Synthesis Gas from Coke". Presented at American Institute of Chemical Engineers Spring Meeting, March 1985.
4. National Coal Association. Steam Electric Plant Factors. 1985 Edition.
5. Horton, E. and Gockenback, K. "Chemicals From Coal: A Reliable And Economical Alternative". Presented at Coal Gasification and Synthetic Fuels For Power Generation Symposium sponsored by the Electric Power Research Institute and Forschungsanlage Julich, April 1985.
6. Electric Utility Week. "PEPCO Outlines Plans For Next Capacity Addition - Coal Gasification, Combined Cycle." April 22, 1985.
7. Public Service Company of Indiana. Form 10-K. December 1984.
8. Utility Coal Gasification Association. Charter. 1985.
9. Energy Information Administration. Inventory of Power Plants in the United States 1984. DOE/EIA - 0095 (84). 1985.
10. National Coal Association. Steam Electric Plant Factors. 1985 Edition.
11. Data Resources Inc. Energy Review. Summer 1985.
12. Electric Power Research Institute. Cost and Performance for Commercial Applications of Texaco Based Gasification - Combined Cycle Plants. Prepared by Fluor Engineers. EPRI AP-3486. April 1984.
13. North American Electric Reliability Council. Electric Power Supply and Demand 1985-1994. 1985
14. Skarbek, R. L. "The Status of the Cool Water Coal Gasification Program". Presented at Synfuels 5th Worldwide Symposium. November 1985.
15. Data Resources Inc. U.S. Long-Term Review. Fall 1985

## LIQUID FUELS FROM COAL DERIVED SYNTHESIS GAS

William S. Jones  
John Shen  
Edward Schmetz

U.S. Department of Energy  
Fossil Energy-34 GTN  
Washington, D.C. 20545

### INTRODUCTION

Modern synthesis gas chemistry has evolved from technology first developed in Germany early this century. Since that time worldwide interest in the production of liquid fuels from coal has gone through cycles reflecting the perceived availability of petroleum.

In the U.S., the Department of Energy (DOE) has supported an indirect coal liquefaction program to investigate new techniques for the production of liquid hydrocarbon and alcohol fuels. The liquid synthesis is based on utilizing a feedstock of low hydrogen content synthesis gas generated by advanced, more efficient, coal gasifiers. Research topics include improved reactor and catalyst developments as well as more fundamental studies of the reaction chemistry. This presentation summarizes results of a number of these projects and provides some comparisons with existing commercial liquid synthesis technology. Fuels of interest include gasoline, diesel and jet fuel, methanol and higher alcohols. Achievements in liquid phase synthesis of hydrocarbons and methanol are described along with the Methanol to Gasoline (MTG) process. Catalyst research is briefly reviewed and an assessment made of needs and prospects for future research.

### Alcohol Fuels

Alcohols can perform well as fuels in both internal combustion and diesel engines, under appropriate conditions. Methanol is available now for evaluation as a direct replacement for petroleum derived gasoline, and the worldwide trend to low lead content gasoline provides a continuing interest in various oxygenates for use as octane enhancers in gasoline. Chem Systems, Inc. has developed a liquid phase reactor system to improve the thermal efficiency of methanol production (1). This Liquid Phase Methanol process is being further investigated under a cost shared contract in a 5 TPD process development unit (PDU) which is located at La Porte, Texas, on a site owned by the prime contractor Air Products and Chemicals, Inc. The PDU has operated very successfully with a Cu/Zn catalyst powder less than 50 microns in diameter slurried in an inert oil in the reactor through which the synthesis gas is passed. Operating conditions are 5.27 MPa (765 psia) and 250°C (482°F). During its most recent 40-day run (May-June 1985) the PDU operated with a nominal 25 wt. percent catalyst slurry and the catalyst activity declined 0.34 percent per day. The process is being developed for use with a modern coal gasifier to produce "once through" methanol to be available as a peak fuel while the unconverted gas is a baseload turbine fuel in an electric power plant. With a different feed gas (Table 1), the reactor can be used to produce "all methanol."

The production of higher alcohols requires more selective catalysts than are currently available. Union Carbide Corp. (S. Charleston, W.VA) is investigating homogeneous catalysts for this purpose under a cost sharing contract. Although existing commercial systems for production of chemicals require excessive operating pressure (20.78 MPa, 3015 psia), a successful catalyst will provide excellent selectivity and simple operations, particularly if the pressure can be

reduced. At Lehigh University modified heterogeneous Cu/Zn catalysts are being investigated in the pressure range of 3.45 MPa to 7.58 MPa (500 psia to 1100 psia) for the production of mixtures of methanol and higher alcohols. The alcohol product typically contains 40 percent methanol and about 25 percent isobutanol, for example (2).

### Liquid Hydrocarbons

Historically, liquid hydrocarbons have been synthesized from hydrogen/carbon monoxide mixtures via Fischer-Tropsch technology using iron based catalysts. Another option is now being demonstrated commercially in New Zealand where methanol is produced from synthesis gas and immediately converted to high octane gasoline via the Methanol to Gasoline (MTG) process. Mobil Research and Development Corporation has developed this process based on a ZSM-5 catalyst, under a cost shared contract with DOE. A fixed bed reactor system was first developed with yields as shown in Table 2. In recent years, a more efficient fluid bed concept has been demonstrated in a 100 bpd (methanol feed) pilot plant located in West Germany. The plant operated very well at all levels including a much higher than designed throughput. Most recently operating conditions for the pilot plant were changed in order to produce light olefins rather than gasoline. The olefins can be converted commercially to diesel fuel and/or gasoline to offer the market another option. This project in West Germany has been supported equally by the U.S. Government, the W. German Government and an industrial consortium consisting of two German firms with Mobil.

Mobil also has been active in a cost-shared project using a liquid phase Fischer-Tropsch reactor followed by a second stage reactor with zeolite catalyst to produce gasoline and wax which can readily be cracked to produce diesel fuel (3) (4). Table 3 provides data on yield selectivity from the first stage in low wax mode of operation. This project provided an empirical correlation between methane and wax yields using a precipitated iron, copper, potassium catalyst. Mobil's bench scale research has also included first stage reactor operation in a high wax mode.

The base line technology against which process improvements are measured is that found at the Sasol plants in South Africa. These commercial plants owned by the South African Coal, Oil, and Gas Corp., Ltd. produce an estimated 90,000 bpd of diesel fuel and gasoline. Lurgi dry bottom coal gasifiers provide the synthesis gas while Arge fixed bed reactors, and Synthol fast fluid bed reactors, produce a broad mixture of fuels and chemicals which have to be further processed to marketable products (5).

During recent years, the MITRE Corp. McLean, VA, has put the Sasol and other process schemes on a common basis so that product costs can be compared. Table 4 provides relative costs for diesel fuel or gasoline (both having the same market value). All plants are considered to be located in the U.S. and the feed coal is Western subbituminous. For the advanced processes, the British Gas Corp. (BGC) Lurgi gasifier is used. The liquid phase Mobil two-stage process is compared with the liquid phase data reported by Prof. H. Kolbel from operations in Germany during the 1950's (4).

### Catalyst Research

Practical catalysts must meet several criteria but one property has eluded researchers interested in producing hydrocarbons with more than one carbon atom. That property is selectivity to produce precisely the desired product. When one thinks of selectivity, one thinks of shape selective supported catalysts, homogeneous catalysts and enzymes or other biological approaches. While working

with a synthesis gas feedstock, one is tempted also by the possibility of combining the carbon monoxide activation/hydrogenation steps with shape selectivity in one catalyst formulation, in one reactor. All of these concepts are being investigated in a continuing research effort with the expectation that the results will better describe the reaction chemistry leading in turn to new and greatly improved catalysts.

### Reactor Technology

Liquid, or slurry phase, reactors are recognized as having a potential to significantly improve thermal efficiency over more traditional reactor designs for highly exothermic reactions. A number of existing projects are investigating liquid phase reactors, but we need much more data describing the hydrodynamics of such systems under process conditions. Actual operating data are required from a reactor which can be operated in a commercially viable churn turbulent flow regime. Results from research to date are encouraging in processing a lower  $H_2/CO$  ratio syngas and producing a flexible product slate. The liquid phase Fischer-Tropsch reactor also operates at a higher, more productive, temperature (260°C-270°C) than is feasible with the Arge or Synthol reactors using the current iron catalyst at Sasol.

### CONCLUSION

It is a pleasure to report, however briefly, the progress being made in new approaches to the synthesis of liquid fuels from coal derived syngas. The recently demonstrated selectivity and efficiency of producing hydrocarbon fuels from methanol is outstanding. Improvements are being demonstrated in selectivity for higher alcohol production and in making efficient use of liquid or slurry phase reactors.

Nevertheless, we have to conclude that no one has the technology today to produce liquid fuels from coal derived synthesis gas at a cost competitive with near term petroleum derived fuels in a typical industrial environment. Although the feed gas accounts for about two-thirds of the cost of the liquid fuel in a Fischer-Tropsch plant, the liquid synthesis can be greatly improved to contribute major savings. Existing technology to directly convert synthesis gas to liquid hydrocarbons is non-selective requiring extensive downstream processing. Liquid fuel production via methanol uses two selective process schemes, but they cannot be closely integrated, at present, for maximum efficiency. New approaches may provide solutions but until then we need to pursue avenues suggested by current research. A slurry reactor offers constant temperature operation with catalyst addition and withdrawal capability. Can productivity be improved with higher catalyst loading? Can wax produced in the reactor be efficiently removed and separated from the catalyst? What is the potential for new reactor designs? For continuous stirred tank reactors? Does catalyst metal particle size affect or control selectivity? Do homogeneous catalysts have any role in hydrocarbon, as distinct from alcohol, synthesis? Can practical bi-functional catalysts be developed to convert syngas to hydrocarbon liquids? Can by-product methane be converted directly and efficiently to liquid fuel?

Successful results from research efforts now underway will go far in answering these questions, and the data will be available for use by industry whenever it is required in the United States.

TABLE 1. Liquid Phase Methanol Process  
Typical Reactor Feed Gas Compositions (6)

|                    | Methanol/Power Production<br>(CO-Rich Feed) | All-Methanol Product<br>(Balanced Feed) |
|--------------------|---|---|
| H <sub>2</sub>     | 35.0 Mole %                                 | 55.0 Mole %                             |
| CO                 | 51.0  | 19.0                                    |
| CO <sub>2</sub>    | 13.0  | 5.0                                     |
| CO <sub>4</sub>    | --  | 3.0                                     |
| Inerts             | 1.0   | 18.0                                    |
|                    | <u>100.0%</u>                               | <u>100.0%</u>                           |
| H <sub>2</sub> /CO | 0.69  | 2.89                                    |

TABLE 2. MTG Process - Typical Yields from Methanol  
in Fixed Bed Reactor System (7)

Yields, wt. percent of methanol charged

|                     |               |
|---------------------|---------------|
| Methanol            | 0.00          |
| Hydrocarbons        | 43.66         |
| Water               | 56.15         |
| CO, CO <sub>2</sub> | 0.04          |
| Coke, oxygenates    | 0.15          |
| Total               | <u>100.00</u> |

Yields, wt. percent of hydrocarbon product

|                                |              |
|--------------------------------|--------------|
| Gasoline (including alkylate*) | 85.0         |
| LPG                            | 13.6         |
| Fuel gas                       | 1.4          |
| Total                          | <u>100.0</u> |

- \* 93 unleaded RO no. Without alkylate gasoline is 80.0%. Alkylate is process derived from propylene, butenes and isobutane. Reactor inlet temperature 316°C; pressure 2.17 MPa (314 psia).

TABLE 3. Mobil Liquid Phase Fischer-Tropsch  
Summary of Data from Low-Wax Operation\*

Yields, wt. percent product

|                                  |              |
|----------------------------------|--------------|
| C <sub>1</sub>                   | 7.5          |
| C <sub>2</sub> /C <sub>2</sub> = | 1.6/3.0      |
| C <sub>3</sub> /C <sub>3</sub> = | 2.0/8.0      |
| C <sub>4</sub> /C <sub>4</sub> = | 2.1/6.6      |
| C <sub>4</sub> oxygenates        | 5.1          |
| C <sub>5</sub> -C <sub>11</sub>  | 39.4 (2.5)** |
| C <sub>12</sub> -C <sub>18</sub> | 14.3 (0.8)** |
| C <sub>19</sub> -C <sub>23</sub> | 2.9 (0.04)** |
| C <sub>23</sub> <sup>+</sup> wax | 7.5          |
| Total                            | 100.0        |

\* Bubble column reactor, 260°C 1.52 MPa, H<sub>2</sub>/CO = 0.67, Fe/Cu/K catalyst, 2.75 NL syngas/gFe/hr, 86 mole % syngas conversion, 800 g hydrocarbons/g Fe catalyst life.

\*\* Numbers in parenthesis are oxygenates.

TABLE 4. Comparative Costs for Fischer-Tropsch  
Synthesis (4)

Unit product cost\*, market basis, all liquid output

| <u>Case</u>                                     | <u>Relative Cost</u> |
|---|----------------------|
| Sasol (dry Lurgi/Synthol)                       | 1.00                 |
| Modified Sasol (BGC Lurgi/Synthol)              | 0.83                 |
| Liquid Phase Fischer-Tropsch (BGC Lurgi/Kolbel) | 0.69                 |
| Liquid Phase Fischer-Tropsch (BGC/Mobil)**      | 0.73                 |

\* All liquid hydrocarbon fuels valued the same.

\*\* Upgrading of Fischer-Tropsch liquids to marketable fuels based on ZSM-5 catalyst.

## REFERENCES

1. Sherwin, M., Blum, D., "Liquid Phase Methanol", Electric Power Research Institute Report AF-1291 Research Project 317-2, December, 1979.
2. Klier, K., Herman R., Young, C., "Direct Synthesis of 2 Methyl-1 Propanol", Preprint, Div. of Fuel Chemistry, ACS 29(5) 1984.
3. Kuo, J., "Slurry Fischer-Tropsch/Mobil Two Stage Process of Converting Syngas to High Octane Gasoline", Mobil Research and Development Corp. Final Report, U.S. DOE Contract DE-AC22-80PC30022, Dec. 1983.
4. El Sawy, A., Gray, D., Neuworth, M., Tomlinson, G., "A Techno-Economic Assessment of the Mobil Two Stage Slurry Fischer-Tropsch/ZSM-5 Process", The MITRE Corp. MTR-84W173 (Rev. 1), Sandia National Laboratories Contract 58-0336, Nov. 1984.
5. Mako, P., Samuel, W., "The Sasol Approach to Liquid Fuels via the Fischer-Tropsch Reaction", in Handbook of Synfuels Technology (Meyers, R., ed.), McGraw-Hill Book Co., New York, NY, Chapter 2-1, 1984.
6. Air Products and Chemicals, Inc., "Task 5 La Porte LPMeOH<sup>TM</sup> PDU Renovation, Installation, and Shakedown", Topical Report, U.S. DOE Contract DE-AC22-81PC30019, Oct. 1985.
7. Kam, A., Schreiner, M., Yurchek, S., "Mobil Methanol to Gasoline Process", in Handbook of Synfuels Technology (Meyers, R., ed.), McGraw-Hill Book Co., New York, NY, Chapter 2-3, 1984.

## RECENT DEVELOPMENTS IN SASOL FISCHER-TROPSCH TECHNOLOGY

MARK E DRY

R & D DEPARTMENT

P O BOX 1

SASOLBURG 9570

REPUBLIC OF SOUTH AFRICA

When considering improvements in the Fischer-Tropsch (FT) route for producing liquid fuels from coal, it is important to bear in mind the relative costs of the various process steps. An approximate cost breakdown for a typical plant is as follows:

|                          |      |   |
|--------------------------|------|---|
| Synthesis gas production | 58 % | (coal gasification 53 %; $\text{CH}_4$ reforming 5 %) |
| FT synthesis             | 18 % | (plant 15 %; Catalyst 3 %)                            |
| Product separation       | 12 % | (cryogenic 4 %; Alcohols & ketones 4 %)               |
| Refinery                 | 10 % | (olefin oligomerization 4 %)                          |
| Diverse                  | 2 %  |   |

The advantage of a big improvement in the selectivity of the FT synthesis (an ideal case would be one which only produces gasoline and diesel fuel) is that this would lower the costs of both the product separation and the refinery sections, which, together account for 22 % of the total. Obvious provisos, however, are that the cost of the catalyst should not be markedly increased and that its conversion activity should remain high otherwise the gains in say the refinery would be negated by increased FT synthesis costs. Elimination of certain products do not necessarily improve the economics. If the FT process made no ethylene, the expensive cryogenic separation unit could be replaced by a cheaper process but this would not be a real gain as the market value of ethylene relative to that of liquid fuels justifies its recovery. A similar situation holds for the alcohols and ketones produced in the FT process. If these products were absent then the expensive process of first recovering them from the FT water and then refining them would significantly lower the overall costs. (Note that these products would have to be completely absent and not just lowered as the latter would have little impact on the economics of recovery as the volume of water to be processed would remain unchanged.) These low molecular mass alcohols and ketones, however, sell at high prices and furthermore the alcohols are valuable as gasoline octane boosters. Thus the production and recovery of these components are justified.

At Sasol the amount of methane produced far exceeds the need of the local fuel gas market and so the  $\text{CH}_4$  is reformed with steam and oxygen to yield  $\text{H}_2$  and CO which is recycled to the FT synthesis units. This reforming is of course thermally inefficient and results in a (about 14 %) loss of hydrocarbon produced from the reformed  $\text{CH}_4$ . In the Sasol process the bulk of the  $\text{CH}_4$  comes not from Fischer-Tropsch but from the Lurgi coal gasification process and so to eliminate  $\text{CH}_4$  reforming would require an alternative gasification process. Confining the issue to only the FT process, if a zero  $\text{C}_1$  to  $\text{C}_2$  selectivity could be achieved with only gasoline and diesel fuel being produced, it is estimated that the overall cost of the process could be cut by about 5 %. Because the capital outlay for a big commercial plant is huge, the 5 % saving is very significant.

To date, however, the attainment of a big improvement in the FT selectivity has been an elusive goal. All the proposed mechanisms of the reaction involve the concept of stepwise addition of single carbon entities to the growing hydrocarbon chains on the catalyst surface (1). This inevitably leads to a wide distribution of products. By manipulating the catalyst's formulation and/or the process conditions the probability of chaingrowth can be varied but the result is simply that if the production of  $\text{C}_1$  to  $\text{C}_3$  hydrocarbons is lowered the



production of the products heavier than diesel fuel increase. The maximum of the sum of gasoline plus diesel fuel lies in the vicinity of 60 % (1). To improve on this appears to require either a new kind of catalyst with a different mechanism or to superimpose some secondary catalytic action such as olefin oligomerization and/or wax cracking.

To date Sasol has exclusively used iron based catalysts in the FT process not only because iron is cheap but also because the products are richer in olefins than those normally produced by other metals active in the FT reaction. The lighter,  $C_2$  to  $C_5$ , olefins are readily oligomerized to either gasoline or diesel thus giving the overall process a high degree of flexibility regarding the ratio of gasoline to diesel fuel produced. A major drawback of iron catalysts at temperatures above say 270 °C is that carbon deposition occurs. This, for mainly mechanical reasons (eg, disintegration of the particles) results in shorter reactor on-line times which means both a higher catalyst consumption rate and more reactors required per unit of gas converted. At the temperatures at which metals like cobalt or ruthenium are active in the FT synthesis, very little carbon is deposited and so these metals have attracted attention as alternative catalysts. On a unit mass basis the cost of cobalt is about 250 times that of the iron used at Sasol while that of ruthenium is about 20 000 times that of iron. To make cobalt competitive with iron, a much lower mass per volume of catalyst will have to be employed, the catalyst life will have to be longer (with its activity and selectivity as good or better than that of iron) and the spent catalyst will have to be regenerated for re-use. While these objectives may well be met with cobalt, the case for ruthenium is bleak. Putting aside the price, it can be shown that for only a single Sasol commercial plant one would require more than the entire available world stock of ruthenium to produce the needed catalyst charge which would only contain 0,5 mass % of Ru on a typical support. The production of Ru and other noble metals such as Rh, is entirely linked to the demand for Pt.

While Sasol remains committed to developing catalysts with longer lives and improved selectivities these objectives are seen as longer termed. In the short term investigations have concentrated on increasing the production per reactor, developing lower cost reactors and optimizing the product spectrum by improving the processes downstream of the FT reactors. Several of these new developments are in the process of being commercialized.

Kinetic investigations had indicated and pilot plant tests had confirmed that for both fixed bed tubular and fluidized bed reactors the production per unit volume of catalyst could be raised by simultaneously increasing the operating pressure and the volume of feed gas thus maintaining a fixed linear velocity, ie a fixed residence time in the reactors (1). Sasol recently decided to build an additional commercial fixed bed tubular reactor to increase the production of FT waxes. This reactor will operate at a pressure considerably higher than the reactors currently in use.

The Synthol reactors, which are the "work horses" of the Sasol FT process, are circulating fluidized bed (CFB) types with catalyst flowing down a standpipe on one side and up a riser on the other side (see Figure 1). These units are already very large and there are doubts whether they could be scaled up further by either increasing their diameter or raising the operating pressure. As an alternative Sasol has been investigating for some time the fixed fluidized bed (FFB) system. In this reactor the catalyst is not circulated but remains "stationary" as an ebulating bed with the gas entering at the bottom. This reactor is considerably smaller and so should be cheaper to construct, simpler to operate and increasing the operating pressure presents no mechanical problems. An additional advantage of higher pressure in the case of iron catalysts operating at high temperatures is that the rate of carbon deposition on the catalyst decreases (1) which for the reasons already mentioned, should result in longer life catalysts. A demonstration FFB unit has been operating at the Sasolburg plant for some time and various design aspects have been

investigated. The design of a large commercial size unit is currently underway for cost estimating purposes and hopefully for implementation in the near future.

Another reactor version being investigated is the slurry phase reactor. In concept this is similar to the FFB reactor but the finely divided catalyst is suspended in a suitable liquid, eg molten FT wax. Compared to the fixed bed reactor it is cheaper to construct and because of this it may be a viable alternative process for producing FT waxes. A potential advantage of the slurry phase system is that with iron catalysts it can operate in the temperature range 260 to 290 °C. In this temperature region a fixed bed would plug up due to carbon deposition while a "dry" fluidized bed would "defluidize" because of catalyst particle agglomeration due to wax formation. To date the experimental investigations at Sasol have been confined to 5 cm ID pilot plant reactors. The next planned phase is the construction of a larger pilot reactor in order to investigate the system at hydrodynamic conditions likely to exist in a commercial scale reactor.

With regards to process improvements downstream of the FT reactors two catalytic processes are being developed. FT waxes produced at low temperatures are essentially straight-chained containing no aromatics and are sulphur and nitrogen-free. Because of these factors the wax can be hydrocracked under relatively mild conditions to yield up to 80 % of high quality diesel fuel. These results have been independently verified by firms specializing in hydrocracking and no problems are foreseen in commercializing the process.

Light olefin oligomerization to gasoline and diesel fuel has been commercially practiced by Sasol for many years but the process which utilizes a supported phosphoric acid catalyst produces a light diesel fuel which has a lowish viscosity and a very poor cetane number, the latter being due to the high degree of skeletal branching. Because of this the amount of this fuel which can be added to the overall pool is limited and so restricts the full utilization of olefin oligomerization to maximise diesel fuel production. The new generation ZSM-5 type zeolites can completely remove the above-mentioned limitations. Because of the high strength of the zeolite acid sites, a higher degree of oligomerization occurs which results in a higher molecular mass product with a higher viscosity. Because of the unique size of the zeolite pores, it is physically impossible to produce highly branched oligomers and consequently the product diesel fuel has a high cetane number. This process has been thoroughly evaluated on pilot plant scale with FT feedstocks both at Sasolburg and abroad. The building of a full scale commercial plant is presently under consideration as part of a debottlenecking process at Sasol's Secunda complex. A new zeolite oligomerization plant would not only process additional olefins but should also be able to improve the yield and quality of the overall diesel fuel pool.

Table 1 illustrates the selectivities (on a carbon atom basis) typically obtained in the two types of commercial FT reactors used by Sasol, namely, the high temperature Synthol process (geared at making light olefins and gasoline) and the lower temperature fixed bed process (geared at making waxes). Applying to each of these product streams, the secondary processes previously discussed, namely, oligomerization of the  $C_3$  to  $C_6$  olefins to yield 75 % diesel fuel and hydrocracking of the wax to yield 80 % diesel fuel, the overall liquid fuel situation obtained is shown in Table 2. As can be seen high quality diesel fuel at high yields can be obtained in both processes. When both maximum liquid fuel yield and maximum diesel fuel to gasoline ratio is required, the low temperature Arge FT process has the greater potential.

#### REFERENCE

- (1) Catalysis Science and Technology, Vol 1, Ch. 4, Ed. by J R Anderson & M Boudart Springer Verlag 1981

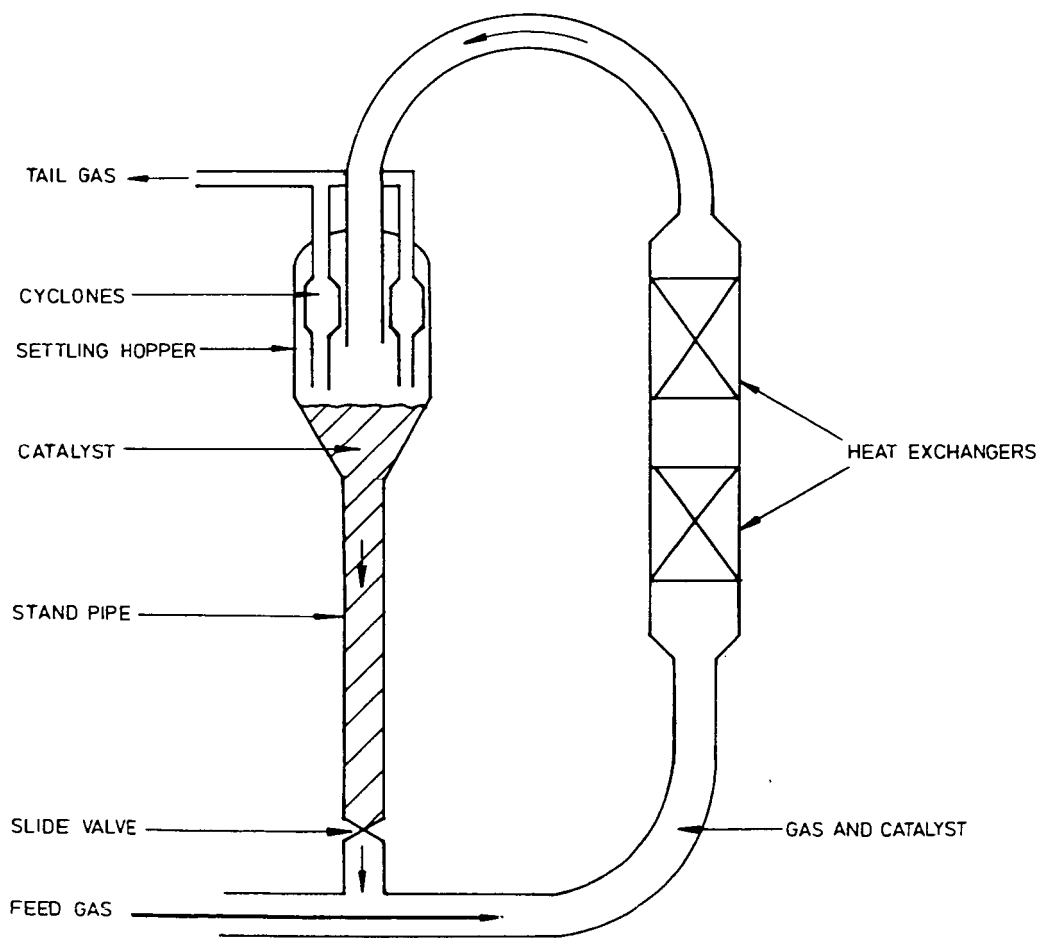
TABLE 1  
COMPARISON OF THE STRAIGHT-RUN FT PRODUCTS FROM THE SYNTHOL AND ARGE REACTORS

| Cut  | Synthol high temperature | Arge low temperature |
|--|--------------------------|----------------------|
| C <sub>1</sub> + C <sub>2</sub>            | 16.0                     | 5.4                  |
| C <sub>3</sub> to C <sub>6</sub> paraffins | 5.0                      | 8.4                  |
| C <sub>3</sub> to C <sub>6</sub> olefins   | 33.5                     | 7.6                  |
| C <sub>7</sub> - 160 °C                    | 17.2                     | 8.0                  |
| 160 - 350 °C                               | 14.0                     | 19.5                 |
| +350 °C                                    | 7.8                      | 48.1                 |
| Water soluble oxygenated compounds         | 6.5                      | 3.0                  |

TABLE 2  
COMPARISON OF THE TWO DIESEL PRODUCING SCHEMES

| Cut                          | Synthol | Arge |
|------------------------------|---------|------|
| Total final liquid product   | 80      | 87   |
| % diesel of liquid fuel      | 55      | 75   |
| Diesel source:               |         |      |
| - From oligomerization       | 58      | 9    |
| - Straight run               | 31      | 30   |
| Wax cracking                 | 11      | 61   |
| Cetane number of diesel pool | 53      | 67   |

(All figures are percentages except for the cetane number)



PRODUCTION OF SYNTHETIC GASOLINE  
AND DIESEL FUEL FROM NON-PETROLEUM RESOURCES

By:

S. A. Tabak, A. A. Avidan, F. J. Krambeck

Mobil Research and Development Corporation  
Research Department  
Paulsboro Laboratory  
Paulsboro, New Jersey 08066

In late 1985, the New Zealand Gas-to-Gasoline Complex was successfully streamed producing high octane gasoline from natural gas. The heart of this complex is the Mobil fixed-bed Methanol-to-Gasoline (MTG) section which represents one of several newly developed technologies for production of synthetic gasoline and diesel fuels. All of these technologies are based on production of methanol by conventional technology, followed by conversion of the methanol to transportation fuel.

The fixed-bed (MTG) process has been developed and commercialized. The fluid-bed version of the MTG process, which is now also available for commercial license, has a higher thermal efficiency and possesses substantial yield and octane number advantages over the fixed-bed. Successful scale-up was completed in 1984 in a 100 BPD semi-works plant in Wesseling, Federal Republic of Germany. The project was funded jointly by the U.S. and German governments and by the industrial participants: Mobil; Union Rheinsche Braunkohlen Kraftstoff, AG; and Uhde, GmbH.

This fluid-bed MTG project was extended recently to demonstrate a related fluid-bed process for selective conversion of methanol to olefins (MTO). The MTO process can be combined with Mobil's commercially available olefins conversion process (Mobil-Olefins-to-Gasoline-and-Distillate, MOGD) for coproduction of high quality gasoline and distillate via methanol. This MTO process was also successfully demonstrated at the Wesseling semi-works with this project being completed in late 1985.

The key to all these processes (MTG, MTO, and MOGD) is Mobil's unique family of shape selective zeolite catalysts. It

is this shape selectivity which in MTG/MTO inhibits coke-forming reactions and in MOGD allows production of a high quality diesel range ( $C_{10}$ - $C_{20}$ ) iso-olefinic product, which is then hydrogenated to the corresponding iso-paraffins (Figure 1).

A simplified schematic of the combined MTO/MOGD process is shown in Figure 2. Methanol is fed to the MTO unit where it is converted stoichiometrically to hydrocarbons and water byproduct. The hydrocarbons are separated into MOGD light olefin feed, an ethene rich fuel gas, and an aromatic gasoline stream which is routed to final product blending. MTO light olefins are fed to the MOGD unit along with an MOGD gasoline recycle stream. MOGD product is then separated into raw distillate, gasoline, and small fuel gas and LPG streams. The raw distillate is hydrotreated at mild conditions to take full advantage of its cetane number potential. To improve liquid yield an optional alkylation unit can also be employed to react produced isobutane with light olefins.

The combined process is highly flexible and can be operated to meet seasonal variation in fuels demand (Table 1). The D/G ratio can be adjusted between zero and about 1.5 while maintaining overall single pass gasoline plus diesel yield above 90 wt % of hydrocarbons. Octane number of the finished gasoline exceeds 92 R+O (Research, unleaded). Distillate cetane number is about 50 and is essentially independent of feedstock and D/G mix.

MTO reaction chemistry is nearly identical to that of MTG. In the simplified MTG reaction scheme (Figure 3), methanol is equilibrated to a methanol-dimethyl ether-water mixture, and then dehydrated further to a mixture of  $C_5$  olefins. The light olefins react reversibly to heavier olefins, which convert further to aromatics and paraffins. In contrast to MTG, MTO process conditions are selected to maximize olefins yield. A small amount of highly aromatic gasoline is also produced. The light olefin fraction is an excellent feedstock for the MOGD unit.

The MTO initial process step preferentially converts methanol to light olefins and a lesser amount of aromatic gasoline having an octane number of greater than 98 R+O. Yield of  $C_3$  olefins is 50-75 wt % of hydrocarbon, depending on process conditions.

A fluid-bed reactor configuration (Figure 4) is preferred as it permits steady-state operation at maximum olefin selectivity and complete methanol conversion. The exothermic heat of reaction can be recovered by immersing heat exchange coils

directly in the catalyst bed. Overall thermal efficiency of the MTO reactor section is estimated to be 95-96%.

The second step of this route is the MOGD process. This process reacts light olefins to the final gasoline and diesel product. In this process, gasoline and diesel selectivity is greater than 95% of the light olefin feed, and gasoline/diesel product ratios have been produced ranging 0.12 to >100. Because of the catalyst shape selectivity, most products are methyl branched iso-olefins. In the  $C_5$ - $C_{10}$  range, branched iso-olefins have good octane rating. In the  $C_{10}$  to  $C_{20}$  range, after hydrogenation, isoparaaffins have good diesel fuel properties.

Figure 5 shows the schematic flow for a commercial MOGD plant. The preferred process flow generally uses four fixed-bed reactors, three on line and one in regeneration. The three on line are in series with inter-reactor coolers and liquid recycle to control the heat of reaction. The olefinic feed is mixed with a recycle stream and passes through the three reactors. After exiting the last reactor, fractionation is used to generate a gasoline-rich stream for recycle to the reactors. This recycle helps control the heat of reaction.

MOGD distillate and gasoline mode product yields are shown in Table 2 for comparative purposes. The charge stock, propene/butenes ( $C_3/C_4$ ), represent the main olefinic components of MTO product. As shown  $C_3/C_4$  yielded 79% diesel, 18% gasoline and only 3% light gas. Of the nonolefins in MTO product, all saturated compounds (paraaffins and cycloparaaffins) will pass through MOGD unreacted and thus can be left in the feed. Of the range of potential olefin feeds,  $C_2$  to  $C_{10}$ , all give distillate and gasoline. Gasoline mode MOGD yields are also shown. If desired, a single MOGD plant can be designed to shift from gasoline to distillate mode to accommodate shifts in product demand.

Table 3 shows representative MOGD distillate product properties (after hydrotreating) compared with U.S. industry standards. As diesel, the paraaffinic MOGD fuel is low density but is an exceptionally good blending stock due to its low pour point and negligible sulfur content. Vehicle testing has also shown straight MOGD diesel to perform similarly to conventional diesel fuel.

Because of its essentially pure iso-paraaffinic structure, the MOGD product makes excellent Jet Fuel, meeting or exceeding all commercial and military specifications (Jet A, A-1, U.S. Military JP-4, -5 and -7).

### Large Scale Testing

In late 1981, a large scale MOGD test run was made in a Mobil refinery. The test run used commercially produced zeolite catalyst in refinery scale equipment and was carried out successfully for 70 days.

The unit was a commercial wax hydrofinisher modified to duplicate a prototype design using 3 MOGD reactors. Charge stock was a mixture of propane/propene/butanes/butenes (62% olefins) pumped directly from an FCC unit. The test run had four objectives: demonstrate all modes of operation in commercial scale equipment, demonstrate controllability in a large multireactor adiabatic unit, demonstrate catalyst regenerability, and provide sufficient distillate product for fleet testing. All objectives were met, and over the 70-day run, product yields and selectivities were the same as found in our pilot plant; thus, demonstrating MOGD could be scaled up for commercial application.

The MTO process has presently been scaled up successfully in a 100 BPD fluid-bed semi-works in Germany. The 100 BPD plant was started up February, 1985 after completing modifications required to enable extended operation at MTO conditions. Plant operation was terminated in November 1985 after a successful six months on-stream program. Product yields and catalyst performance were similar to those obtained in a 4 BPD pilot plant at Mobil's Paulsboro Laboratory, under the same conditions. With completion of the 100 BPD MTO program, large scale testing is completed for both steps of the MTO/MOGD process route, completing development of a novel and efficient route to synthetic gasoline and diesel.

/njh

Table 1

#### MTO/MOGD PRODUCT YIELDS

|                           |       |
|---------------------------|-------|
| Distillate/Gasoline Ratio | 0.8   |
| Product Yield, Wt %       |       |
| LPG                       | 4.4   |
| Gasoline                  | 52.9  |
| Diesel                    | 42.7  |
|                           | 100.0 |
| Product Quality           |       |
| Gasoline, R+O             | 94.4  |
| M+O                       | 80.6  |
| (R+M)/2                   | 87.5  |
| Diesel Cetane Number      | 50.0  |



Table 2  
MOGD PROCESS YIELDS  
C<sub>3</sub>-C<sub>4</sub> FEED

|                                | <u>Max<br/>Distillate<br/>Mode</u> | <u>Gasoline<br/>Mode</u> |
|--------------------------------|------------------------------------|--------------------------|
| C <sub>1</sub> -C <sub>3</sub> | 1                                  | 4                        |
| C <sub>4</sub>                 | 2                                  | 5                        |
| C <sub>5</sub> -165°C Gasoline | 18                                 | -                        |
| 165°C <sup>+</sup> Distillate  | 79                                 | -                        |
| C <sub>5</sub> -200°C Gasoline | -                                  | 84                       |
| 200°C <sup>+</sup> Distillate  | -                                  | 7                        |

Table 3  
MOGD PRODUCT QUALITY

|                        | <u>MOGD Product</u> | <u>Industry<br/>Standards</u> |
|------------------------|---------------------|-------------------------------|
| Diesel Fuel            |                     |                               |
| Specific Gravity, 15°C | .79                 | .84-.88                       |
| Pour Point, °C         | <-50                | -7                            |
| Cetane Number          | 50                  | 45                            |
| Sulfur, Wt %           | <.002               | 0.5 max                       |
| Viscosity, cs @ 40°C   | 2.5                 | 1.90-4.1                      |
| Jet Fuel               |                     |                               |
| Freeze Point, °C       | <-60                | -40                           |
| Aromatics, Vol %       | 4                   | 25 max                        |
| Smoke Point, mm        | 28                  | 18 min                        |
| JFTOT, °C              | 343                 | 260                           |

Figure 1

# SHAPE SELECTIVE REACTION PATH

## MTG/MTO

Methanol  $\rightarrow$  C<sub>10</sub> Paraffins, Olefins, Aromatics  
 $n\text{CH}_3\text{OH} \rightarrow (\text{CH}_2)_n + n\text{H}_2\text{O}$

## MOGD

Light Olefins  $\rightleftharpoons$  Gasoline  $\rightleftharpoons$  Distillate

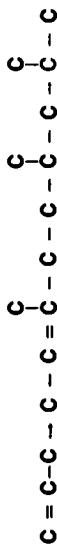


Figure 3

# REACTION PATH

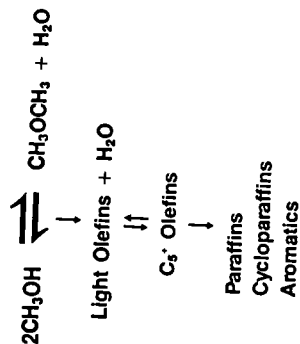


Figure 2

# MTO/MOGD PROCESS SCHEMATIC

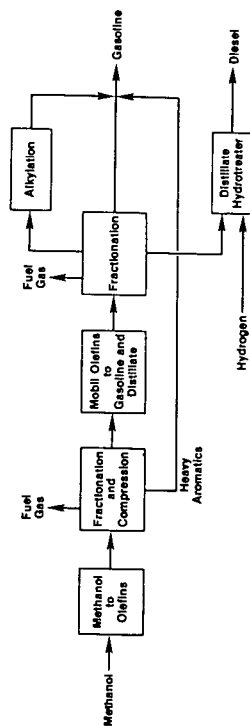


Figure 4

### 100 B/D FLUID-BED MTO PLANT

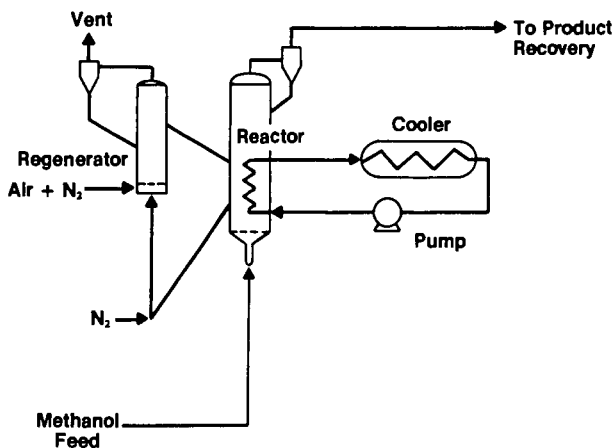
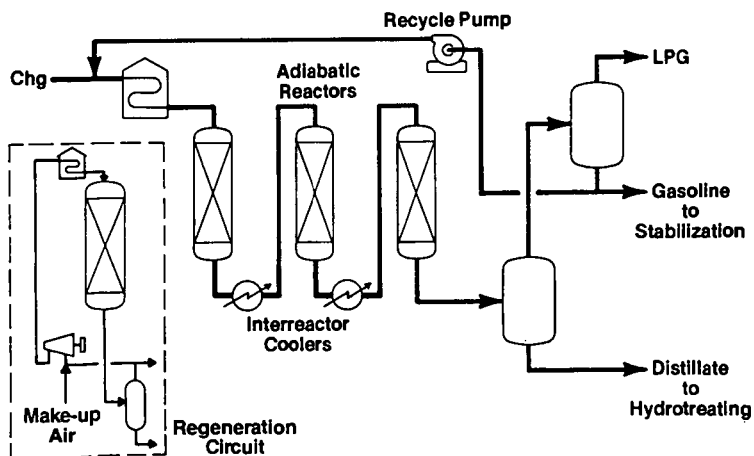


Figure 5

### MOGD PROCESS FLOW Max Distillate Mode



LCI CO-PROCESSING: A FAMILY OF TECHNOLOGIES  
FOR UPGRADING LOW GRADE FEEDSTOCKS

Marvin Greene  
Avinash Gupta  
William Moon

LUMMUS CREST INC.  
1515 Broad Street  
Bloomfield, NJ 07003

INTRODUCTION

The Western Hemisphere and North Sea oil producers have been experiencing a serious decline in light oil production and light oil "find" rates. In spite of aggressive drilling programs, "finds" over the past fourteen years have been about 60 percent of production (1). In seeking continued production of refined petroleum products, refiners will have to consider processing of bottom-of-the-barrel feedstocks to a much greater extent. When one superimposes the additional issue of the politically-controlled availability of Mid-East petroleum supplies in the Western World, it is clear that there is a need for technology that will afford the refiner greater flexibility in feedstock selection and feedstock processability.

One potentially attractive route to satisfying these needs is the co-processing of petroleum feedstocks with other more plentiful and less costly fossil fuels. Lummus Crest Inc. (LCI) has formulated a concept for co-processing bottom-of-the-barrel oils with coal and other solid carbonaceous feedstocks to produce high quality distillate fuels. The concept is based on a two-stage approach in which the solid carbonaceous feedstocks are converted to liquid hydrocarbonaceous materials in a thermal reaction zone devoid of externally-supplied catalysts followed by catalytic hydroprocessing of the thermal stage products together with petrolea in an expanded-bed hydrotreater. The unconverted solids from the thermal reactor can optionally be removed by known solids separation techniques, such as Anti-Solvent Deashing (ASDA), prior to upgrading in the expanded-bed hydrotreater. A distillate fraction from the hydrotreater can be recycled to serve as the slurry vehicle for the solid carbonaceous feedstock.

Co-processing of heavy petroleum residua and coal has been the subject of a 33-month experimental program currently being carried out at LCI's Engineering Development Center under joint funding with the U.S. Department of Energy. Details of this work have been presented elsewhere (2,3). Currently, we envision a common reaction system that can co-process petroleum residua with other carbonaceous feedstocks, such as oil shale and biomass, in addition to coal.

### LCI CO-PROCESSING FLOWSCHMES

With current refinery technology, heavy petroleum residua characterized by high metals content and high coking propensity can be processed by either carbon-rejection technology such as delayed or fluid coking; by hydrogen-addition technology such as fixed-bed or expanded-bed hydrogenation; or by combinations thereof. Two co-processing applications based on hydrogen-addition technology are disclosed here.

With current commercial residuum hydroprocessing technologies, conversion is limited to about 50 to 60 percent to IBP-524°C (975°F) distillates. The unconverted resid from the hydrotreater is either processed further in a coker to recover additional distillates and a coke product or blended off with available low sulfur fuels. The unconverted residuum that has been subjected to catalytic hydrogenation has potentially good properties as a solvent for liquefaction of coal, biomass and oil shale.

Figure 1 is a schematic flow diagram of a co-processing scheme for utilizing the unconverted resid from a residuum hydrotreater. The short contact time (SCT) thermal reactor system has been demonstrated at the 300 kg/day (1/3 tpd) scale in LCI's Integrated Two-Stage Liquefaction (ITSL) process development unit (4) as well as at the 5448 kg/day (6 tpd) scale at the Wilsonville pilot plant (5), both on coal products only. The SCT concept is predicated on the fact that the rate of activation of fossil-derived oil precursors is relatively fast with respect to the rate of hydrocracking of these intermediate products to all distillate products. On this basis, the ITSL process "decouples" the primary fossil liquefaction step from the secondary hydrocracking step. Accordingly, we have projected that there will be capital cost savings in a commercial plant in which the primary liquefaction step is carried out in a relatively low-cost, fired-coil reactor system as compared to a larger, high pressure soaker-reactor system. Furthermore, the more capital-intensive catalytic step could then be optimized to hydrocrack the extracts without being constrained by the need to simultaneously solubilize the solid carbonaceous feedstock.

An alternative co-processing application is shown schematically in Figure 2. This application is predicated on the following factors:

- o The feedstock cost of liquid products from the hydroliquefaction of coal, oil shale and biomass is significantly less than that of petroleum as seen from the following table:

Table 1

| <u>Feedstock</u>       | <u>Typical<br/>Liquids<br/>Yields</u> |                        | <u>Typical<br/>Feedstock<br/>Transfer<br/>Price</u> |        |           | <u>Feedstock<br/>Cost of<br/>Raw<br/>Liquids</u> |        |
|------------------------|---------------------------------------|------------------------|---|--------|-----------|--|--------|
|                        | 10 <sup>3</sup>                       | M <sup>3</sup> /Kg g/t | \$/kg   | \$/ton | \$/MM Btu | \$/M <sup>3</sup>                                | \$/Bbl |
| Bituminous Coal        | 0.70                                  | 168                    | 0.033   | 30     | 1.25      | 47   | 7.50   |
| Kentucky Shale         | 0.10                                  | 24                     | 0.004   | 4      | 0.68      | 44   | 7.00   |
| Wood Chips             | 0.50                                  | 120                    | 0.022   | 20     | 1.40      | 44   | 7.00   |
| Municipal Solid Wastes | 0.25                                  | 60                     | 0.009*  | 8*     | 0.85*     | (35)   | (5.60) |

\* Denotes tipping fee paid by solid waste collector.

( ): Denotes credit for MSW feedstock against product liquids.

o A raw syncrude can probably be generated in a thermal reaction system, such as an SCT heater, at an incremental cost competitive with that of imported petroleum crude when the conversion units are constructed and operated on an over-the fence basis adjacent to a large petroleum refinery.

o There is good indication that there will be a beneficial synergism during catalytic hydrotreatment when co-processing synfuels products from an SCT reactor with vacuum residua. The synergism may take the form of increased distillate yield and/or improved desulfurization/demetallization at conventional hydrocracking operating severities.

o There should be no significant deterioration of the hydrogen content-molecular weight relationship (Stangeland surface) of the distillate products when the syncrude content of the combined feed to the hydrocracker is less than about 20 percent (6).

#### DEVONIAN SHALE RESOURCES

The Devonian oil shale resource of the Kentucky-Ohio-Tennessee region of the U.S. has the potential of providing a significant percentage of our refinery feedstock needs. Until recently, U.S. oil shales were considered unsatisfactory resources because of their relatively low oil yields in the Fischer Assay test and in conventional retorting. Fischer Assay oil yields per unit weight of organic carbon obtained with the Devonian marine shales have been less than half of those obtained from the Eocene lacustrine shales (Green River formation) of Colorado, Utah and Wyoming. The shale resources recoverable by surface mining in the Lewis and Fleming County, Kentucky region alone could generate shale liquids

corresponding to about 12,000 M<sup>3</sup>/day (750,000 bbl/day) for 20 years.

Previous efforts (7,8) have clearly demonstrated that hydrogen addition or hydrotreating technologies can result in significantly higher oil yields from Devonian shales than can be achieved by thermal retorting technologies, on the order of 200 to 250% of that of Fischer assay. These studies also concluded that a commercial-scale application of hydrotreating technologies has potentially favorable economics.

However, without some type of government subsidy, a grass-roots shale conversion facility still cannot compete on the open market with current petroleum prices. The LCI co-processing concept represents a possibly nearer-term economic reality when applied in an over-the-fence relationship with an interested refiner. By way of example, assume an existing hydrocracker is processing a virgin resid priced at \$157/M<sup>3</sup> (\$25/bbl). For the case of a 8534 M<sup>3</sup>/day (54,000 Bbl/day) unit, if we back off 20% feed or 1717 M<sup>3</sup>/day (10,800 Bbl/day) and replace this by 1717 M<sup>3</sup>/day (10,800 Bbl/day) of shale liquids, then there should be no significant deterioration of the distillate product characteristics. In other words, the co-processing liquids should respond in conventional downstream refinery processing units essentially similar to that of the straight run petroleum-derived liquids. With oil shale priced at \$0.004/Kg (\$4/ton) and resid at \$157/M<sup>3</sup> (\$25/bbl), the differential cash flow available for a) amortizing the capital equipment associated with shale preparation, spent shale disposal and the SCT reaction system and b) operating costs is estimated to be about \$64MM per year. Assuming 20% capital charges and operating costs (ex. shale) of \$0.006/Kg (\$5.75/ton) (8), this cash flow would correspond to an installed capital cost for the upstream shale processing equipment of about \$140 MM.

Some preliminary screening tests were made in the batch autoclave reactor system at LCI's Engineering Development Center. The tests simulated the SCT reaction system in which the oil shale samples were first extracted under short-contact-time conditions. This was followed by blending of the SCT products with an Arab Heavy vacuum residua and hydrotreatment in an LC-Fining<sup>(SM)</sup> simulation test unit. The results of these tests will be reviewed at the Symposium.

---

(SM) LC-Fining is a service mark of Lummus Crest Inc. for engineering, marketing and technical services related to hydrocracking and hydrosulfurization processes for reduced crude and residual oils.

## BIOMASS RESOURCES

Biomass materials either virgin in nature such as trees, crops and vegetation or as waste such as refuse-derived fuel (RDF) represent an energy source much like conventional fuels. They vary in composition, density, heating value and other properties. Recycling them as industrial fuel has the added advantage of minimizing the severe and continuing problems associated with solid waste disposal. The total estimated quantity of organic wastes generated in 1980 (9) in the U.S. was about 1 trillion kilograms (1150 million tons). Approximately 15 percent is potentially recoverable and assuming a typical heating value of 2780 gcal/gm (5000 Btu/lb), this energy displacement might be equivalent to  $1.2 \times 10^{18}$  Joules per year or 1.1 quads per year (500,000 bbl oil equivalent per day) when converted to useful fuels.

There are two fundamental methods of biomass conversion to clean fuels: thermochemical and biochemical conversion. While the latter route is the most prevalent currently in development, processes that can produce petroleum-like synthetic fuels should be more desirable than alcohol fuels for example, in that they do not require significant modifications to the existing nationwide network of refining, transporting and utilizing liquid hydrocarbon fuels. Furthermore, because of the unique composition of biomass relative to that of petroleum, selective biomass conversion may result in the generation of high valued, specialty fuels such as certain phenolic compounds having high octane values.

The thermochemical route also has the following potential advantages over that of the biochemical route:

- o Higher thermal efficiency;
- o Wider applicability to feeds containing lignins and contaminants (e.g., MSW);
- o Production of completely detoxified products;
- o Access and similarity to the advanced state-of-the-art technologies utilized in the petroleum/petrochemical/coal industries.

The latter feature is the basis for applying the ITSL co-processing flowscheme to the utilization of biomass feedstocks. The economic driving forces delineated previously for the case of Devonian shale co-processing are even more profound for biomass applications, in particular, the organic-rich fraction of municipal solid waste (sometimes referred to as refuse-derived fuel-RDF). In a manner similar to that previously described for the case of Devonian shale co-processing, it can be shown that it may be feasible to justify the economic tradeoff between the differential values of petroleum feedstocks and MSW tipping fees.



However, because of the smaller capacities associated with MSW collection and classification, co-processing of petroleum residua and liquids derived from RDF would probably be limited to refinery hydrotreaters having capacities below about  $3.18 \times 10^6$  L/day (20,000 bbl/day). Furthermore, lower feedstock ratios of biomass-derived liquids to those of the petroleum liquids would be necessitated because of the availability and current design capacity of typical MSW classification units. This would in turn result in the co-processed liquids being more petroleum-like and thereby posing less potential problems to the refiner. A similar analysis can be performed of the co-processing of petroleum residua with wood chips derived from forest wastes.

Some preliminary screening tests were made in the batch autoclave reactor systems, similar to those made with the Devonian oil shale samples, utilizing two biomass feedstocks: pine wood flour and dust RDF. The results of these tests and the feedstock properties will be discussed at the Symposium.

#### REFERENCES

1. R. H. Shannon, "Small Scale Upgraders Integrated with Field Facilities", Third International UNITAR Conference, New York (1985).
2. Greene, M.I. and A. Gupta, "The Impact of the PNL Research Program on the Development of Coal Liquefaction/Resid Hydrocracking Technology", 24th Hanford Life Sciences Symposium, Battelle Pacific Northwest Laboratories, Richland, WA. (October 21, 1985).
3. M. I. Greene, "The Status of LCI's Co-Processing Program", DOE Direct Liquefaction Contractors' Review Meeting, Pittsburgh, PA. (Nov. 20, 1985).
4. Schindler, H.D. and J. Chen, "Integrated Two-Stage Liquefaction Final Technical Report", DOE Contract No. DE-AC22-82PC50021, NTIS Report PC50021-Q11, (July, 1985).
5. Whitehurst, D.D., F. Farcasiu, et. al., "The Nature and Origin of Asphaltenes in Processed Coals", EPRI Report AF-242, (February 1979).
6. Shinn, J.H., A. J. Dahlberg, et. al., "The Chevron Co-Refining Process", EPRI AP-3825-SR (March, 1985).
7. H. Feldkirchner, "The HYTORT Process", Synthetic Fuels from Oil Shale Symposium, IGT (December 3-6, 1979).
8. Greene, M.I., and J. Damukaitis, "Liquid-Phase Hydroretorting of Low Grade Oil Shales", Energy Progress, 5 (3), September 1985.
9. L. Anderson, "A Wealth of Waste; A Shortage of Energy", Chapter in Fuels from Waste, Academic Press (1977).

FIGURE 1  
ALTERNATIVE CO-PROCESSING FLOWScheme FOR COAL AND HYDROTREATED RESIDUA

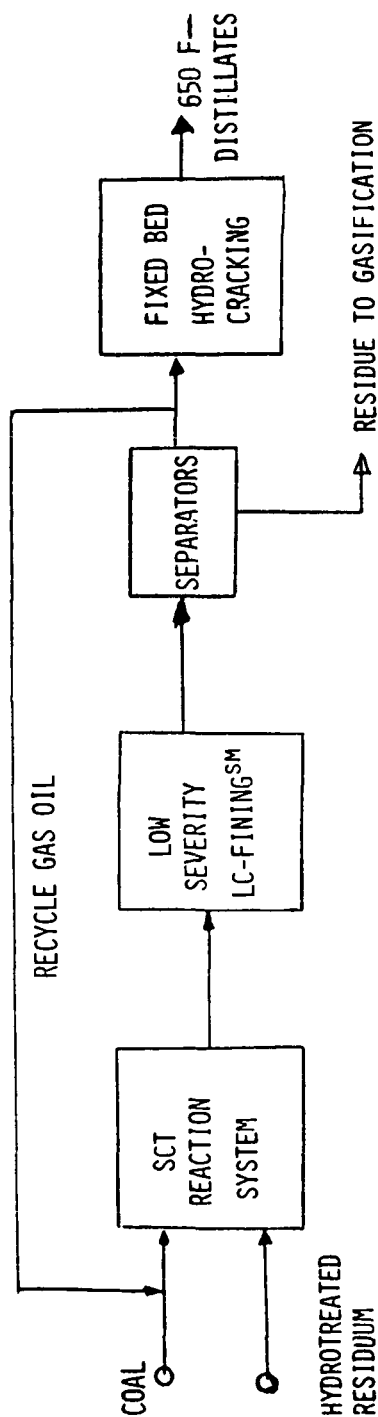
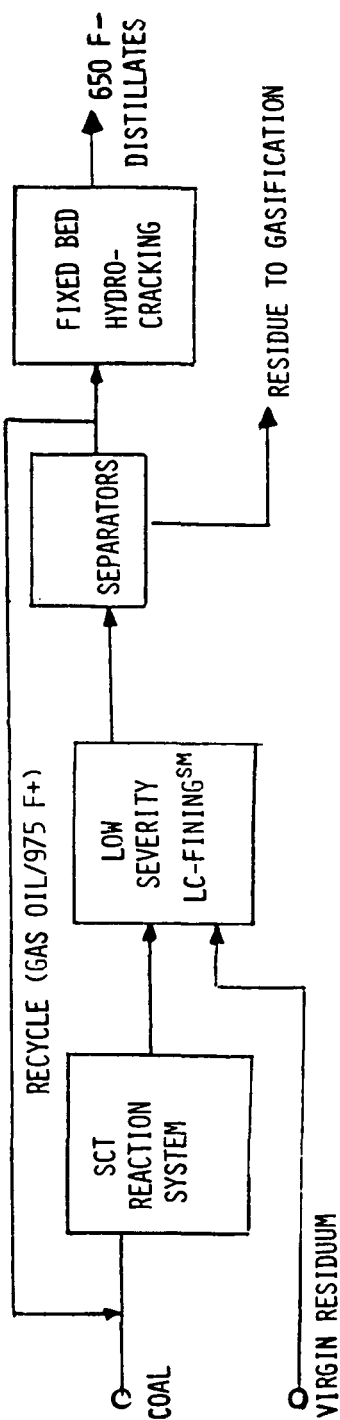


FIGURE 2  
ALTERNATIVE CO-PROCESSING FLOWScheme FOR COAL AND VIRGIN RESIDUA



## COPROCESSING OF HIGHVALE COAL WITH ATHABASCA BITUMEN IN SYNGAS MIXTURES,

R.J. Parker, P.D. Clark, B.L. Ignasiak, T. Lee and T. Ohuchi

Alberta Research Council,  
Coal Department,  
1091 - 5th St.,  
Nisku, Alberta,  
Canada, T0C 2G0

### ABSTRACT

Coprocessing of Alberta subbituminous coal with bitumen is currently under investigation at the Alberta Research Council. The high oxygen content of the coal results in high hydrogen consumption. The present study compares the effectiveness of syngas/water mixtures catalyzed by potassium carbonate for coprocessing Highvale coal with Athabasca bitumen. Single-stage (solubilization) experiments were performed with syngas (5.1 MPa) at 390°C in a stirred autoclave. In simulated two-stage experiments, the second (upgrading) stage employed hydrogen (8.5 MPa) at 440°C with a potassium molybdate/dimethyldisulphide catalyst.

Coal conversion improved from 47 to 78% systematically when the carbon monoxide: hydrogen ratio was varied from 1:3 to 7:1. The additional yield was confined to pyridine extractable material. In simulated two-stage experiments similar coal conversions were observed when using carbon monoxide/water (91%) or hydrogen (88%) in the first stage.

### INTRODUCTION

Within the Province of Alberta there are vast proven reserves of hydrocarbons in the form of coal ( $2780 \cdot 10^9$  tons), heavy oil and bitumen ( $200 \cdot 10^9$  m<sup>3</sup>) and natural gas. The subbituminous coal is mined from shallow deposits and used locally for the thermal generation of power. Bitumen is also surface mined as oil sands; extracted on site and upgraded to a synthetic crude oil ( $20 \cdot 10^3$  m<sup>3</sup>/day) in two commercial operations. Heavy oil is mostly recovered by thermal processes from deeper deposits. It is used in the production of asphalt or blended with light crudes to produce a refinery feedstock.

The low cost of the mined coal (US \$12/ton) has provided the impetus to investigate processes<sup>1,2</sup> to convert the coal into more valuable hydrocarbon products. Recent studies<sup>1,2</sup> at the Alberta Research Council (ARC) have indicated that the coprocessing of Alberta coal with bitumen or heavy oil is technically and economically superior to direct coal liquefaction. Coprocessing eliminates the need for recycle solvents and takes advantage of synergistic effects to improve the liquid yields and product quality from the two feed components.

Laboratory and bench unit studies have shown that two-stage coprocessing has distinct advantages over a single stage operation. Lower temperatures can be employed during the first stage which permit solubilization of the coal while minimizing coke and gas production. The second stage operates at cracking temperatures 430-460°C, conditions which favour upgrading of both the coal and bitumen to liquid products.

Both stages require the use of hydrogen at moderately high pressures ( 16 MPa). The high oxygen content of the low rank coal means that excessive quantities of expensive hydrogen are needed to convert the oxygen to water, in addition to hydrogen uptake by the coal and bitumen. Although Alberta presently has ample supplies of natural gas for this purpose.

Earlier work<sup>3,4,5</sup> has proven that CO/H<sub>2</sub>O is more efficient than hydrogen at solubilization of coal in bitumen at temperatures below 400°C. More coal is dissolved and the reaction proceeds much more rapidly. The water gas shift reaction does not go to completeness during coal liquefaction or coprocessing. Equilibrium concentrations of carbon monoxide may exceed 50% with the bulk of the remaining gases being carbon dioxide and hydrogen. In a commercial operation it would be necessary to remove the carbon dioxide and recycle the unconverted carbon monoxide and any produced hydrogen. This present study was carried out to compare the efficiency of carbon monoxide/hydrogen mixtures with pure carbon monoxide for the solubilization of coal in bitumen and to establish the maximum permitted limit of hydrogen in the recycle gas stream. In addition, simulated two-stage experiments allowed a comparison of carbon monoxide and hydrogen in the overall coprocessing operation.

## EXPERIMENTAL

Coprocessing experiments have been performed at ARC in miniautoclaves, 1 litre batch autoclaves, a hot charge-discharge unit and a 2 litre/hour bench unit. Since this work was restricted to the batch autoclaves, a brief description of the procedures will be given. Two modes of operation were employed: single stage and simulated two-stage.

In the single stage process coal, bitumen and an aqueous solution of potassium carbonate (shift reaction catalyst) were loaded into the autoclave. The autoclave was charged to 5.2 MPa (750 psi) with the gas mixture and heated to run temperature at about 5°C/minute. Operating conditions are listed in Table 1. When the run was complete the reaction mixture was cooled rapidly to 350°C by passing water through an internal cooling coil. The gaseous components were discharged at this elevated temperature through a condenser immersed in ice water. Gas volume was measured by a dry gas meter and its composition was determined by gas chromatography. The hot discharge eliminated foaming problems, due to dissolved carbon dioxide, which occurred when the unit was depressurized at room temperature.

In the simulated two-stage mode the process initially duplicated the single stage operation. Upon completion of the first stage a cracking catalyst, potassium molybdate/dimethyldisulfide (DMDS), was injected into the autoclave through a port in the head. The unit was repressurized with hydrogen 8.6 MPa (1250 psi) and a second heating cycle was completed. As before the gases were discharged at 350°C. The condensed oils and water from the two stages were combined prior to product distillation while the gas samples were analyzed individually.

A standard laboratory product separation procedure was established (Figure 1) to give distillable oil yield to 525°C, pyridine soluble organic material and insoluble organic material (IOM) remaining in the ash. Coal conversion was defined as 
$$\frac{\text{Input coal} - \text{IOM}}{\text{Input coal}} \times 100\%.$$

Properties of Highvale coal and Athabasca bitumen are given in Table 2. Both single and simulated two-stage experiments were performed in duplicate.

## RESULTS AND DISCUSSION

### A. Single Stage Experiments

Coal conversion and product distribution are summarized in Table 3 and Figure 2. The coal conversion can be seen to decline as the carbon monoxide content of the initial gas mixture was reduced. The pure carbon monoxide was much superior to the pure hydrogen while 50% carbon monoxide was still equal to the latter. These results ignore any pressure effects. Run pressure was lower at the lower carbon monoxide concentrations since the initial pressure was fixed. However, the partial pressure of the more active gas, carbon monoxide, was not constant. The initial pressure in the pure hydrogen run was 8.2 MPa (1200 psi) which could explain why it gave better coal conversion than 25% carbon monoxide.

Little evidence of upgrading of the coal or bitumen was observed apart from coal solubilization. Hydrocarbon gas and distillable oil yields were constant suggesting that thermal rather than chemical effects were responsible for their production. The distillable oil yield was essentially unchanged from that derived from the bitumen in the feedstock (33%); ie 525+°C conversion was zero. The only measurable change occurred in the formation of pyridine soluble organics, where pure carbon monoxide was most effective. Pyridine solubles declined in parallel with the coal conversion at the lower carbon monoxide concentrations. This confirmed earlier work that showed carbon monoxide was more effective than hydrogen for the solubilization of coal below 400°C due to the increased reactivity of the reducing species produced by the shift reaction, compared with molecular hydrogen.

Carbon monoxide conversion to carbon dioxide and hydrogen, varied little, being 61 ±1% for all experiments except the 25% carbon monoxide run (Table 4). As expected carbon dioxide production exceeded that of hydrogen in all cases although they should be equimolar if both were derived solely from the shift reaction. The coal had a high oxygen content, part of which is converted thermolytically to carbon dioxide upon heating. Produced hydrogen was below that expected from the shift reaction plus that initially present; consumption ranged from .4 to .7 moles per 100g of feed with a suggestion of a downward trend at lower carbon monoxide concentrations.

Hydrogen sulphide production was relatively constant at 0.2% MAF feedstock except for the pure hydrogen run where the higher partial pressure of reducing gas may have contributed to giving a slightly higher value, 0.3%. Thermal effects again appeared to outway chemical effects.

Product quality, expressed as elemental analyses was independant of the reducing gas composition. Hydrogen to carbon ratios were 1.6 for the distillable oils and 1.25-1.35 for the pyridine extract, sulfur was 2.6-2.8% and 3.4-4.1% respectively. Approximately 10% of the sulfur in the feedstock was converted to hydrogen sulfide, while little or none was present in the insoluble organic matter and ash. The majority of the input sulfur (96%) was derived from the bitumen and it remained within those fractions where the

bitumen products were concentrated, ie. the distillable oil and pyridine solubles. Little or no upgrading in terms of heteroatom removal could be attributed to the carbon monoxide solubilization process.

Simulated distillations of the distillable oils showed little variation (Table 5). The naphtha fraction accounted for  $\approx 10\%$  while the medium oil fraction was  $\approx 55\%$ . Class analyses of the pyridine extracts, ie. non-volatile hydrocarbon, asphaltenes and preasphaltenes gave interesting results. The hydrocarbon content decreased as a percentage of the pyridine solubles as the carbon monoxide increased but the mass was relatively constant. Asphaltenes increased both in percentage and absolute terms. This suggested that the hydrocarbons required lower operating severity (less carbon monoxide) to solubilize, increased severity would result in more asphaltenes in the pyridine extract. More experimentation is required to confirm this observation because of the high scatter in the data.

#### B. Two Stage Experiments

Gas composition and conversion were discussed for the first stage in the previous section. Consumption of hydrogen in the second stage was not altered by the reducing gas used in the first stage. Hydrogen sulfide and hydrocarbon gas production were also constant, once more the result of thermolytic reaction pathways (Table 6). The difference in carbon oxides was quite marked, a factor of 10 greater for the carbon monoxide and 3 for the carbon dioxide in the carbon monoxide runs. It is most likely that these gases remained dissolved in the bitumen/coal liquids when the autoclave was vented at  $350^{\circ}\text{C}$  and were subsequently released in the second stage.

Product yields and distribution (Table 7) were not altered by the nature of the reducing gas present in the first stage. Overall coal conversion improved to approximately 90%. A high degree of upgrading took place with no difference attributable to the improved coal solubilization found in the carbon monoxide first stage. Pyridine extractable material declined from almost 60% to 22% of the product. Most of this material was converted to distillable oils. The hydrocarbon gas yield was high, combined first and second stage gas production being 10%. Conversion of the  $525^{\circ}\text{C}$  material was 63% in both experimental modes.

#### CONCLUSIONS

Carbon monoxide was superior to hydrogen for the solubilization of coal in bitumen at temperatures below  $400^{\circ}\text{C}$ . However, it provided no benefit in a two stage process in terms of coal conversion,  $525^{\circ}\text{C}$  conversion, and product quality. It does offer some potential economic benefits since lower temperatures can be employed in the first stage.

Coal solubilization could still approach 80% if the carbon monoxide stream contained hydrogen. Up to 25% hydrogen could be tolerated before a significant reduction in solubilization was observed. If the syngas mixtures function as rapidly as the pure carbon monoxide, then process improvements over pure hydrogen would include reduced first stage residence time and thus a smaller reaction vessel.

## REFERENCES

1. B. Ignasiak, L. Lewkowicz, G. Kovacik, T. Ohuchi and M. P. du Plessis, Two-stage Subbituminous Coal/Bitumen Liquefaction Process in Catalysis on the Energy Scene, pp 593-600, Elsevier, Amsterdam, 1984.
2. B. Ignasiak, G. Kovacik, T. Ohuchi, L. Lewkowicz and M. P. du Plessis, Two-stage Liquefaction of Subbituminous Alberta Coals in Non-Donor Meeting, November, 1984, Calgary, Alberta.
3. P. Clark, B. Ignasiak, G. Kovacik and T. Ohuchi, Liquefaction of Alberta Subbituminous Coals in Oil Sands Bitumen with either CO/H<sub>2</sub>O or H<sub>2</sub> Reducing Gas Atmospheres, presented at the Alternative Energy Sources 7th Miami International Conference, December 1985, Miami Beach, Florida.
4. E. Sondreal, C. Knudson, J. Schiller and T. May, Development of the Co-Steam Process for Liquefaction of Lignite and Western Subbituminous Coals, presented at Lignite Symposium, May, 1977, Grand Forks, North Dakota.
5. C. Knudson, W. Willson and G. Baker, Hydrogen-Carbon Monoxide Reactions in Low-Rank Coal Liquefaction, preprints American Chem. Soc., Div. Fuel Chemistry, Vol. 26, No. 1, 1981.

Table 1  
Operating Conditions

|                      | 1st Stage                           | 2nd Stage                             |
|----------------------|-------------------------------------|---------------------------------------|
| Gas                  | CO/H <sub>2</sub> or H <sub>2</sub> | H <sub>2</sub>                        |
| Pressure (MPa)       | 5.2 or 8.2                          | 8.5                                   |
| initial<br>reaction  | 15.6-20.7                           | 15.3-19.0                             |
| Temperature (°C)     | 390                                 | 440                                   |
| Reaction time (min.) | 30                                  | 60                                    |
| Feed                 | Highvale Coal/<br>Athabasca Bitumen | non distillables from<br>Stage I      |
| Ratio                | 1:2.5                               | -                                     |
| Catalyst             | K <sub>2</sub> CO <sub>3</sub>      | K <sub>2</sub> MoO <sub>4</sub> /DMDS |

Table 2  
Properties of Feedstocks

|                      | Highvale Coal | Athabasca Bitumen |
|----------------------|---------------|-------------------|
| Moisture             | 6.4%          | -                 |
| Ash (as is)          | 13.5          |                   |
| Carbon               | 75.0          | 82.0%             |
| Hydrogen             | 4.3           | 10.6              |
| Nitrogen             | 1.1           | 0.6               |
| Sulphur              | 0.2           | 4.5               |
| Oxygen <sup>1</sup>  | 19.3          | 2.3               |
| Distillables (525°C) | N/A           | 46                |
| Pyridine Solubles    | N/A           | 54                |
| Hydrocarbons         | -             | 29                |
| Resins               | -             | 48                |
| Asphaltenes          | -             | 23                |

<sup>1</sup> by difference

Table 3  
Coal Conversion and Product Distribution -  
Single Stage Experiments

|   |     |    |    |    |    |                |
|---|-----|----|----|----|----|----------------|
| Carbon Monoxide Concentration (%)                   | 100 | 87 | 75 | 50 | 25 | 0 <sup>1</sup> |
| Coal Conversion (% MAF coal)                        | 85  | 76 | 75 | 65 | 47 | 65             |
| Product Distribution(g/100 g MAF feed)              |     |    |    |    |    |                |
| Hydrocarbon gases (C <sub>1</sub> -C <sub>5</sub> ) | 1   | 1  | 1  | 1  | 1  | 1              |
| Distillable Oils (up to 525°C)                      | 31  | 32 | 32 | 32 | 32 | 31             |
| Pyridine Soluble Organics                           | 57  | 54 | 51 | 50 | 47 | 53             |

<sup>1</sup> Initial pressure 8.2 MPa (1200 psi)



Table 4  
Gas Production and Consumption

|                         |                  |      |      |      |      |                |
|-------------------------|------------------|------|------|------|------|----------------|
| Carbon Monoxide Content | 100 <sup>1</sup> | 87   | 75   | 50   | 25   | 0 <sup>1</sup> |
| CO conversion %         | 62               | 63   | 60   | 62   | 44   | -              |
| Gas Production (moles)  |                  |      |      |      |      |                |
| Carbon dioxide          | 1.26             | 1.06 | 1.00 | .62  | .36  | .11            |
| Carbon monoxide         | -.97             | -.86 | -.67 | -.49 | -.18 | -              |
| Hydrogen                | .52              | .56  | .48  | .46  | .36  | -.25           |
| Hydrogen Sulfide        | .013             | .011 | .009 | .009 | .009 | .017           |

<sup>1</sup> from 1st stage of 2 stage experiments

Table 5  
Product Qualities - Single Stage Experiments

|                                 |                  |     |      |                 |                 |
|---------------------------------|------------------|-----|------|-----------------|-----------------|
| Carbon Monoxide %               | 100 <sup>1</sup> | 87  | 75   | 50              | 25              |
| A. Distillable Oil <sup>2</sup> |                  |     |      |                 |                 |
| Naphtha                         |                  | 9   | 7    | 10 <sup>1</sup> | 11 <sup>1</sup> |
| light gas oil                   |                  | 55  | 54   | 58              | 60              |
| heavy gas oil                   |                  | 36  | 39   | 32              | 29              |
| sulfur                          | 2.6              | 2.6 | 2.7  | 2.7             | 2.8             |
| hydrogen:carbon                 | 1.65             | 1.6 | 1.6  | 1.6             | 1.6             |
| B. Pyridine Extract             |                  |     |      |                 |                 |
| hydrogen:carbon                 | 1.35             | 1.3 | 1.25 | 1.25            | 1.25            |
| nitrogen                        | 2.3              | 1.6 | 1.2  | 1.1             | 1.3             |
| sulfur                          | 3.4              | 3.8 | 4.1  | 3.7             | 4.0             |
| C. Class Analysis               |                  |     |      |                 |                 |
| hydrocarbons                    |                  | 49  | 45   | 61 <sup>1</sup> | 60              |
| asphaltenes                     |                  | 43  | 50   | 31              | 31              |
| preasphaltenes                  |                  | 8   | 5    | 7               | 9               |

<sup>1</sup> single analysis

<sup>2</sup> all percent except hydrogen to carbon ratio

Table 6  
Gas Production - Simulated Two-Stage, 2nd stage

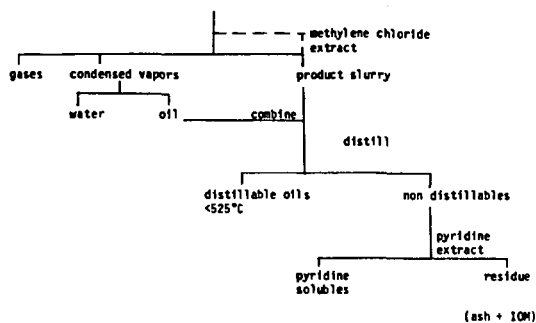
| 2nd Stage                                      | CO/H <sub>2</sub> O//H <sub>2</sub> | H <sub>2</sub> //H <sub>2</sub> |
|--|-------------------------------------|---------------------------------|
| Carbon dioxide                                 | 4.3                                 | 1.4                             |
| Carbon monoxide                                | 2.0                                 | 0.22                            |
| Hydrogen sulphide                              | 2.0                                 | 2.1                             |
| Hydrocarbons (C <sub>1</sub> -C <sub>5</sub> ) | 11.1                                | 9.8                             |
| Hydrogen consumption                           | 2.8                                 | 2.8                             |

<sup>1</sup> grams gas

Table 7  
Coal Conversion and Product Distribution (Two-stage)

| First Stage Gas                         | Carbon Monoxide | Hydrogen |
|---|-----------------|----------|
| Coal Conversion (%)                     | 91              | 88       |
| Product Distribution (g/100g feedstock) |                 |          |
| Hydrocarbon Gas 1st stage               | 2               | 2        |
| 2nd stage                               | 8               | 8        |
| Distillable Oil                         | 66              | 64       |
| Pyridine Extracts                       | 22              | 22       |
| Insoluble Organics                      | 3               | 4        |
| Mass Balance (%)                        |                 |          |
| Overall                                 | 98              | 95       |
| Ash                                     | 104             | 110      |
| Hydrocarbons                            | 90              | 89       |

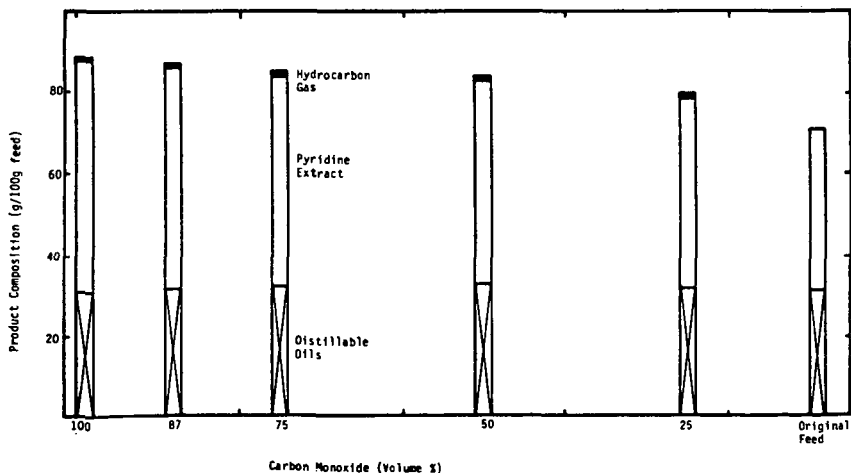
Figure 1  
Product Work-up Procedure



Analysis performed

|                  |   |   |
|------------------|---|---|
| gases            | : | composition, C <sub>1</sub> -C <sub>5</sub> |
| water            | : | none  |
| distillable oils | : | C, H, N, S, simulated distillation          |
| pyridine extract | : | C, H, N, S, class analysis                  |
| residue          | : | proximate                                   |

Figure 2: Coprocessing Product Yields as a Function of Reducing Gas Composition



## RECENT DEVELOPMENTS IN TWO-STAGE COAL LIQUEFACTION AT WILSONVILLE,

Jun M. Lee, Ramkrishna V. Nalitham, Charles W. Lamb,

Catalytic, Inc., P.O. Box 239, Wilsonville, AL 35186

### INTRODUCTION

This paper will present results from the Advanced Coal Liquefaction R&D Facility at Wilsonville, Alabama. The primary sponsors are the U.S. Department of Energy (DOE) and the Electric Power Research Institute (EPRI). Amoco Corporation became a sponsor in 1984 through an agreement with EPRI. The facility is operated by Catalytic, Inc., under the management of Southern Company Services, Inc.

### RUN 247

Run 247 employed Illinois No. 6 coal in a configuration called the Reconfigured Integrated Two-Stage Liquefaction (RITSL) mode (Figure 1). Coal is slurried with a recycled process solvent and fed to the dissolver under hydrogen pressure where thermal liquefaction takes place. Thermal distillate is separated by fractionation, and the vacuum bottoms along with a heavy fraction of distillate make up the feed to the hydrotreater. This hydrotreater feed containing the thermal resid, unconverted coal, and ash is fed directly to the ebullated bed hydrotreater. The vacuum-flashed bottoms from the hydrotreater is the feed to the Critical Solvent Deashing (CSD) unit. The recycle solvent is composed of the deashed hydrotreater resid (HR) and hydrotreated distillate solvent.

Prior to Run 247, most runs had used the Integrated Two-Stage Liquefaction (ITSL) configuration, as illustrated in Figure 2. In the ITSL mode, the vacuum resid from the thermal liquefaction stage is deashed in the CSD unit before being fed to the hydrotreater.

Operation in the RITSL configuration was a step in the program to operate with close-coupled reactors, where the products from the liquefaction stage would be fed directly to the hydrotreater without any intermediate ash or distillate separation.

Because the hydrotreater feed was not deashed, it contained all the coal ash along with unconverted coal and heavy organics that would normally be removed in the deashing step. Thus, there was concern that the catalyst deactivation rate would increase. Another operability question concerned the effect of the RITSL mode on deashing. Since the feed to the CSD unit would be the vacuum-flashed bottoms from the hydrotreater, the CSD feed properties were expected to be different from feed properties that had previously been experienced.

### Run 247 Results

The hydrotreater catalyst performed well in the RITSL mode. The catalyst used for all the runs in this report was Shell 324-M, a unimodal Ni-Mo catalyst. Throughout the run, catalyst activity measured by resid conversion was higher than in previous runs in

the ITSL configuration. This catalyst was aged to 1225 lbs (resid + UC + ash)/lb catalyst. The nondeashed feed did not cause serious deactivation of the catalyst (1).

Operability of the CSD unit with hydrotreated feed was satisfactory. The CSD feed did have different properties than feeds in the ITSL mode, but process adjustments were made which provided good deashing performance.

Representative Run 247 results in the RITSL mode are compared to a previous ITSL run in Table 1. The second column (243JK/244B) lists ITSL data that compare closely in operating conditions and cover a similar range of batch catalyst age as the RITSL data (247D). The RITSL distillate yield was 62%, compared to 59%. However, the distillate yields combined with the resid yields indicate that both configurations would have total liquid yields of 65% with zero resid.

A major difference is that the hydrogen consumption was 1% higher with RITSL, so the hydrogen efficiency was lower. The higher hydrogen consumption with RITSL is thought to be primarily related to higher resid reactivity. This improved hydrogenation activity is apparently caused by differences in the feed hydrocarbons or the presence of coal ash particles or both.

#### Run 247 Product Quality

Product blends were made by mixing product streams in the proportions of their production rates. These blends were then fractionated into boiling point cuts and elemental analyses were made of the individual fractions. Table 2 shows the product analyses for a Run 247 sample compared to a Run 244 sample to enable a direct comparison of products produced in the RITSL and ITSL configurations. The hydrogen contents of comparable fractions is higher, by 0.8-1.2%, for RITSL. The H/C ratios are higher by 0.10-0.16. In general, the RITSL product had lower levels of nitrogen and sulfur. These results appear to be evidence of increased hydrogenation. Therefore, the higher hydrogen consumption seems to be a trade off with improved product quality.

#### Mixing Study

A mixing study was conducted to quantify the degree of mixing in the dissolver. Mixing was studied by using radioactive tracer tests. The residence time distributions were fitted by a simple model. Importantly, the dissolver was found to be well mixed (3).

#### RUN 248

The configuration used at the beginning of Run 248 was the Double-Integrated Two-Stage Liquefaction (DITSL) mode, which is shown in Figure 3. This differs from the ITSL mode in that only the Light Thermal Resid (LTR) is routed through the hydrotreater. The heavier Thermal Resid (TR) is recycled directly to the thermal first stage. A potential advantage of the DITSL configuration is that a smaller hydrotreater might be possible because only the LTR stream is hydrotreated (2).

In the DITSL configuration, the heavy thermal resid is recycled to the liquefaction stage without going through the hydrotreater. Thus, the TR must be converted in the thermal stage for the DITSL mode to be viable. Iron oxide was used to promote resid conversion (4). Dimethyl Disulfide (DMDS) was added to the coal slurry to provide a source of hydrogen sulfide to convert the iron oxide to pyrrhotite as the slurry flowed through the preheater. This was the same method that was used successfully in Run 246 (2).

Before beginning the run, the 12-inch diameter dissolver was replaced by a 5.2-inch diameter Low Contact Time (LCT) dissolver. This was done to allow operation at lower liquefaction reactor volumes than could be achieved with the 12-inch dissolver. The intent was to investigate reaction times somewhat longer than had been used in the Short Contact Time (SCT) tests in Run 242 (5).

#### Run 248 Results

Operation in the DITSL configuration was difficult. The major operability problem was high viscosities of the TR, the process solvent, and the coal slurry. The recycle of the heavy TR directly from the CSD unit resulted in a buildup of preasphaltenes, which caused the high viscosities. Process variable adjustments were made in an attempt to achieve viable operations in the DITSL mode. The dissolver outlet temperature was raised to 840°F to increase the severity for resid conversion. However, resid conversion in the thermal unit was not sufficient to allow satisfactory operation in the DITSL configuration.

Satisfactory operability was obtained by changing to the ITSL configuration. The distillate yield was 64% and the resid make was 3%, for a total liquid yield of 67% (248D). This compares favorably to the 65% yields shown earlier for the RITSL and ITSL configurations with Illinois No. 6 coal. Because of other process variable differences, most notably dissolver temperature, it can not be concluded from these results if iron oxide caused an improvement in distillate yield.

The addition of iron oxide and DMDS was stopped, to begin a series of tests at different reactor volumes. After a three-day test at 100% LCT without iron oxide, the dissolver volume was reduced successively to 50% and then to 25% LCT dissolver volume. Coal conversions with volumes of 100%, 50%, and 25% were 92%, 90%, and 88% MAF coal, respectively. As expected for the reduced contact times, resid makes increased and distillate makes and hydrogen consumptions decreased.

Conditions and two-stage liquefaction (TSL) yields for the 50% LCT period (248F) are compared to Run 242 SCT results in Table 1. Coal space velocities using the reaction volume above 700°F were comparable for these two conditions. The yields were very similar, though SCT showed an advantage in lower gas make and hydrogen consumption. A close examination of conditions indicated that the average reaction temperature was higher for 248F.

#### Run 248 Product Quality

Properties of a fractionated product blend from period 248D (ITSL with iron oxide) are shown in Table 3. As can be seen, the product boiling below 650°F is 67% of the total blend, which is comparable to that obtained in Run 244 without iron oxide (Table 2).

The naphtha from 248D had higher hydrogen content (13.76 vs 12.86) but the nitrogen and sulfur were higher. The analyses for the distillate and gas oil fractions were similar, with 248D showing slightly higher nitrogen and sulfur contents. The API gravities showed that the naphtha and distillate for 248D were heavier than those from Run 244.

#### RUN 249

A major objective was to obtain process yield data using subbituminous coal with a well-mixed dissolver. A pumparound loop was installed to provide back mixing of the 12-inch dissolver.

The RITSL configuration was used to provide a data base for predicting process performance with subbituminous coal in a close-coupled configuration.

Two additives were investigated for enhancement of conversion of the subbituminous coal. The effectiveness of iron oxide with DMDS had been demonstrated earlier (2). Work at the University of Wyoming had shown some very interesting results related to coal drying and the use of water in liquefaction of subbituminous coal (6). Coal conversions were improved when coal was not completely dried or even when water was added back to a coal slurry of dried coal before liquefaction. The water effect was found to be additive to the iron oxide effect on coal conversion. The effect of water addition was tested by adding water at the rate of 15% MF coal to the coal feed slurry.

#### Run 249 Results

The run was started with the dissolver at 790°F and the hydro-treater at 670°F and with no iron oxide or water addition. The coal conversion was 82%. Coal conversion was increased to 90% by adding iron oxide plus DMDS and by increasing the dissolver temperature from 790 to 810°F. Water addition increased coal conversion by 3%. Iron oxide and DMDS addition were discontinued to test whether water addition without iron oxide could maintain coal conversion. Coal conversion decreased significantly, from 92 to 84%. Thus, water addback did not enhance coal conversion enough to enable operation without the iron oxide.

For the 1.5% iron oxide addition rate, the coal sulfur content was calculated to be sufficient to convert the iron oxide to pyrrhotite. This was tested by stopping the DMDS addition and no reduction in coal conversion was observed. Therefore, iron oxide was used without the addition of DMDS for the last two months of the run.

Energy rejection was high throughout this run because the CSD feed was very soluble and the solubility changed with various operating variable adjustments. Energy rejection was reduced by changing solvent type and adjusting operating conditions. The CSD experience gained in this run will be valuable in processing the highly soluble feeds that are expected to be encountered in the close-coupled operations.

Selected process conditions and yields for Run 249 are shown in Table 1. The only difference in periods 249D and 249E is that water addback was used in 249D.

The negative resid make for 249E indicates that more resid was being converted than was being made, so that resid was being consumed from inventory. The C<sub>4</sub>+ distillate yield for 249E would be about 53% if the resid make had been zero. Thus, there was practically no effect of water addback on distillate yield for this comparison.

The last major period of the run, designated 249H, was an ash recycle test. The purpose of this test was to remove ash from the system by using a purge of hydrotreater vacuum bottoms instead of using the CSD unit. The ash content of the purge stream was increased by recycling a portion of the hydrotreater atmospheric flashed bottoms to the dissolver. This recycled solvent contained ash, iron oxide, unconverted coal and hydro-treated resid and distillate. By using this method, the solids content of the vacuum bottoms purge stream was increased to about 50% unconverted coal and ash. The ash content was 32%.

The recycle test resulted in significantly increased coal conversion. The 94% coal conversion obtained in period 249H is the highest obtained with subbituminous coal at Wilsonville. It is notable that this high conversion was obtained with a moderate dissolver temperature of 802°F. The increased coal conversion was probably due to additional conversion of the unconverted coal in the recycle stream. The recycled ash and iron oxide also probably contributed to enhanced reactivity.

The yield results are similar to 249E, but the hydrogen consumption was higher. These results were encouraging and suggest that a vacuum tower could be used as an alternate method of removing ash from the system.

A comparison of data for 249E and 2496G in Table 1 provides a comparison of the RITSL and ITSL results with subbituminous coal. A number of differences are apparent in the operating conditions. In particular, Run 249E had a lower dissolver temperature and a considerably higher hydrotreater temperature. Also, 249E had a forced back-mixed dissolver while 246G did not. Surprisingly, the yields are fairly similar. As a result of the lower dissolver temperature, 249E had a lower gas make. The sum of distillate and resid is comparable for the two periods. Several factors may have contributed to the higher hydrogen consumption of 249E, but the RITSL configuration is probably the main reason.

An analysis of catalyst behavior in Run 249 has not been completed. However, the catalyst performed adequately throughout the run and a catalyst age of 1870 lb (resid + UC + ash)/lb was reached. The catalyst used for Run 249 was the Shell 324-M catalyst used in Run 246, with an initial age of 617. Catalyst deactivation was observed during the run, but the resid conversion activity appeared to be relatively constant over the last half of the run.

#### 1985 ACCOMPLISHMENTS

The RITSL configuration was demonstrated for both bituminous and subbituminous coals and the results were positive. These runs provide a solid basis for close coupling the reactors. A very successful mixing study was performed to quantify the degree of



mixing in the thermal reactor. Iron oxide and water were tested as disposable catalysts. Iron oxide has been tested in both the ITSL and DITSL configurations with both coals. The experience with increased CSD feed solubility broadened the knowledge of CSD operations. This will be applicable in the close-coupled runs. Lastly, an alternate method of removing ash from the system was demonstrated in the ash recycle test. This provides additional flexibility for future runs.

#### FUTURE WORK

The emphasis is on experimentation with close-coupled reactors. The Wilsonville plant has been modified by the addition of a reactor vessel adjacent to the hydrotreater to operate in a close-coupled fashion. The initial run will be a thermal-catalytic run, but the equipment is capable of operating with ebullated catalyst beds in both reactors. There are plans to test alternate catalysts.

The coal liquefaction data base will be expanded by parametric studies and by increasing efforts in the area of process modeling and simulation.

#### REFERENCES

1. Moniz, M. J. and R. V. Nalitham, "An Assessment of the Impact of Delayed Deashing and Subbituminous Coal Processing on Hydrotreating Catalyst Performance" Proceedings of Tenth Annual EPRI Contractors' Conference on Coal Liquefaction, April 23-25, 1985.
2. Lamb, C. W., J. M. Lee, R. V. Nalitham, M. J. Moniz, H. M. Risbud, and T. W. Johnson, "Integrated Two-Stage Liquefaction of Subbituminous Coal at Wilsonville", Proceedings of DOE Direct Coal Liquefaction Contractors' Review Meeting, October 17-18, 1984.
3. Nalitham, R. V., O. L. Davies, A. K. Rao, and M. Turgeon, "An Experimental Evaluation of the Residence Time Distribution in the Wilsonville Dissolver Using Radioactive Tracers", Proceedings of Tenth Annual EPRI Contractors' Conference on Coal Liquefaction, April 23-25, 1985.
4. Paranjape, A. S., and D. E. Rhodes, "Use of Iron Oxide and Hydrogen Sulfide to Improve Integrated Two-Stage Coal Liquefaction", Proceedings of DOE Direct Coal Liquefaction Contractors' Review Meeting, October 17-18, 1984.
5. Rao, A. K., J. M. Lee, M. J. Moniz, and R. Pillai, "Recent Developments in Integrated Two-Stage Coal Liquefaction at Wilsonville", Proceedings of DOE Direct Coal Liquefaction Contractors' Review Meeting, November 16-17, 1983.
6. Frazee, W. S., and H. F. Silver, "Effect of Drying on Liquefaction of Subbituminous Coal", Proceedings of Tenth Annual EPRI Contractors' Conference on Coal Liquefaction, April 23-25, 1985.

TABLE 1  
PROCESS CONDITIONS AND YIELDS

| Run No.<br>Configuration<br>Coal  | 247D<br>RTSL<br>Ill. 6 | 243JX/244B<br>ITSL<br>Ill. 6 | 248D<br>ITSL<br>Ill. 6 | 248F<br>ITSL<br>Ill. 6 | 242BC<br>ITSL-SC7<br>Ill. 6 | 249D<br>RTSL<br>Ill. 6 | 249E<br>RTSL<br>Wyo.   | 249H<br>RTSL<br>Wyo.   | 249C<br>ITSL<br>Wyo. |
|---|------------------------|------------------------------|------------------------|------------------------|-----------------------------|------------------------|------------------------|------------------------|----------------------|
| <b>Thermal Stage</b>  |                        |                              |                        |                        |                             |                        |                        |                        |                      |
| Temperature (°F)  | 810                    | 810                          | 834                    | 835                    | 860*                        | 796                    | 796                    | 802                    | 812                  |
| Coal Space Velocity (lb/hr-ft <sup>3</sup> >700°F)                            | 27                     | 28                           | 31                     | 41                     | 41                          | 14                     | 14                     | 14                     | 17                   |
| Solvent-to-Coal Ratio   | 4.8                    | 5.8                          | 1.8                    | 1.8                    | 1.8                         | 1.5                    | 1.5                    | 2.0                    | 1.8                  |
| Steam-to-Coal Ratio (wt %)  | 44                     | 50                           | 45                     | 45                     | 46                          | 30                     | 29                     | 22                     | 30                   |
| Iron Oxide (% of HF Coal)   | 0                      | 0                            | 2.0                    | 0                      | 0                           | 1.5                    | 1.5                    | 1.5                    | 2.0                  |
| DNDS Addition   | 0                      | 0                            | Yes <sup>2</sup>       | 0                      | 0                           | 0                      | 0                      | 0                      | Yes <sup>2</sup>     |
| <b>Catalytic Stage</b>  |                        |                              |                        |                        |                             |                        |                        |                        |                      |
| Temperature (°F)  | 710                    | 720                          | 705                    | 728                    | 720                         | 700                    | 700                    | 700                    | 625                  |
| Space Velocity (lb feed/hr/lb cat)  | 0.9                    | 1.0                          | 0.7                    | 0.7                    | 1.0                         | 1.3                    | 1.2                    | 1.6                    | 1.0                  |
| Feed Resid Content (wt %)   | 51                     | 55                           | 57                     | 57                     | 55                          | 35                     | 34                     | 37                     | 54                   |
| Catalyst Age (lb resid/lb cat)  | 445-670 <sup>3</sup>   | 350-850                      | 260-287                | 359-396                | 278-441                     | 1119-1183 <sup>3</sup> | 1208-1246 <sup>3</sup> | 1685-1703 <sup>3</sup> | 486                  |
| <b>Yield (lb ash Coal)<sup>4</sup></b>  |                        |                              |                        |                        |                             |                        |                        |                        |                      |
| C-C <sub>3</sub> Gas (Total Gas)  | 6(12)                  | 6(12)                        | 8(13)                  | 7(12)                  | 4(9)                        | 7(18)                  | 6(14)                  | 7(16)                  | 9(19)                |
| Water   | 9                      | 9                            | 8                      | 9                      | 10                          | 14                     | 14                     | 14                     | 11                   |
| C <sub>4</sub> * Distillate   | 62                     | 59                           | 64                     | 54                     | 54                          | 53                     | 57                     | 56                     | 53                   |
| Resid   | 3                      | 6                            | 3                      | 8                      | 8                           | 1                      | -4                     | -4                     | 1                    |
| (Total Liquid Product)  | (65)                   | (65)                         | (67)                   | (62)                   | (62)                        | (54)                   | (53)                   | (52)                   | (54)                 |
| Hydrogen Consumption  | -6.1                   | -5.1                         | -5.6                   | -5.3                   | -4.9                        | -5.7                   | -5.8                   | -6.3                   | -5.4                 |
| Hydrogen Efficiency (lb C <sub>4</sub> * Dist/<br>lb H <sub>2</sub> Consumed) | 10.2                   | 11.5                         | 11.3                   | 10.2                   | 11.0                        | 9.3                    | 9.9                    | 8.9                    | 9.8                  |
| Energy Rejected to Ash Conc. (%)  | 22                     | 22                           | 19                     | 23                     | 25                          | 21                     | 24                     | 26                     | 21                   |

Inlet hydrogen partial pressure 2040 psi  
<sup>1</sup>Preheater outlet temperature. Dissolver was bypassed in Short Contact Time Run 242.  
<sup>2</sup>Used L7 5.2-inch diameter dissolver. Other runs used 12-inch diameter dissolver.  
<sup>3</sup>Dimethyl Dianilide added at 1.1 x stoichiometric amount to convert Fe<sub>2</sub>O<sub>3</sub> to Fe<sub>3</sub>O<sub>4</sub>.  
<sup>4</sup>Catalyst age for RTSL is lbresid + ash + unconverted coal/lb catalyst.  
<sup>5</sup>Stoichiometrically balanced yield structures.

TABLE 2

**properties of distillate product**

sample: Wilsonville synthetic crude blend representative of TSL product slate

| distillation cut   | wt% of sample | elemental (wt%) |       |        |      |          | API gravity (60/60) |
|--|---------------|-----------------|-------|--------|------|----------|---------------------|
|  |               | C               | H     | N      | S    | O (diff) |                     |
| (A) run 244 (catalyst age ~ 1600 lbs resid/lb cat, HTR temp ~ 730°F)*                |               |                 |       |        |      |          |                     |
| ITSL configuration   |               |                 |       |        |      |          |                     |
| naphtha (IBP-360°F)  | 18.4          | 85.21           | 12.86 | 845ppm | 0.36 | 1.50     | 43.1                |
| distillate (360°F-650°F)   | 45.7          | 86.34           | 10.73 | 0.23   | 0.22 | 2.48     | 18.6                |
| gas oil (650°F-1000°F)   | 35.0          | 89.07           | 9.69  | 0.31   | 0.16 | 0.76     | 7.3                 |
| resid (1000°F+)  | 0.9           | 86.71           | 6.94  | 1.13   | 0.60 | 3.15     | —                   |
| (B) run 247 (catalyst age ~ 283-372 (lbs resid + UC + ash)/lb cat, HTR temp ~ 700°F) |               |                 |       |        |      |          |                     |
| RITSL configuration (247C-II)  |               |                 |       |        |      |          |                     |
| naphtha (IBP-360°F)  | 14.9          | 85.50           | 14.07 | 500ppm | 0.35 | 0.03     | —                   |
| distillate (360°F-650°F)   | 49.8          | 86.74           | 11.54 | 0.23   | 0.16 | 1.33     | —                   |
| gas oil (650°F +)  | 35.3          | 89.48           | 10.44 | 0.06   | 0.02 | 0.00     | —                   |

\*work performed by Amoco Oil Company

TABLE 3

**properties of distillate product**

sample: Wilsonville synthetic crude blend representative of TSL product slate

| distillation cut   | wt% of sample | elemental (wt%) |       |      |      |          | API gravity (60/60) |
|--|---------------|-----------------|-------|------|------|----------|---------------------|
|  |               | C               | H     | N    | S    | O (diff) |                     |
| (A) run 248 (catalyst age ~ 300 lbs resid/lb cat, HTR temp ~ 700 °F) |               |                 |       |      |      |          |                     |
| ITSL configuration (248D)  |               |                 |       |      |      |          |                     |
| naphtha (IBP-350 °F)   | 18.6          | 84.63           | 13.76 | 0.13 | 0.65 | 0.83     | 42.4                |
| distillate (350 °F-650 °F)   | 48.1          | 84.45           | 10.94 | 0.23 | 0.37 | 4.01     | 13.2                |
| gas oil (650 °F+)  | 33.3          | 89.11           | 9.41  | 0.43 | 0.18 | 0.87     | 0.3                 |
| total blend  | 100.0         | 85.72           | 10.76 | 0.22 | 0.42 | 2.86     | 14.1                |

**two-stage liquefaction  
reconfigured mode (RITSL)**

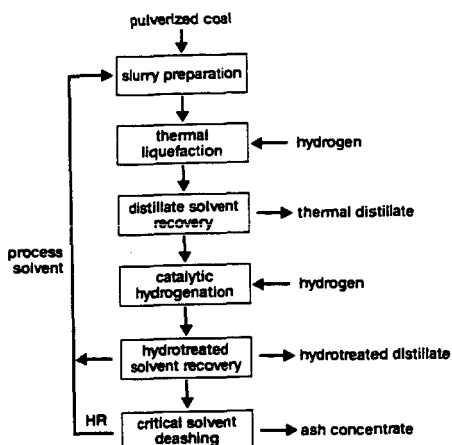


FIGURE 1

**two-stage liquefaction  
integrated mode (ITSL)**

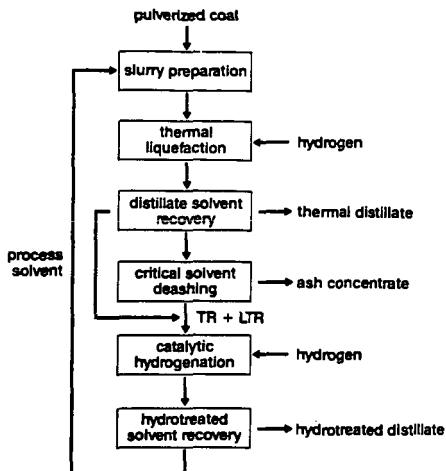


FIGURE 2

**two-stage liquefaction  
double-integrated mode (DITSL)**

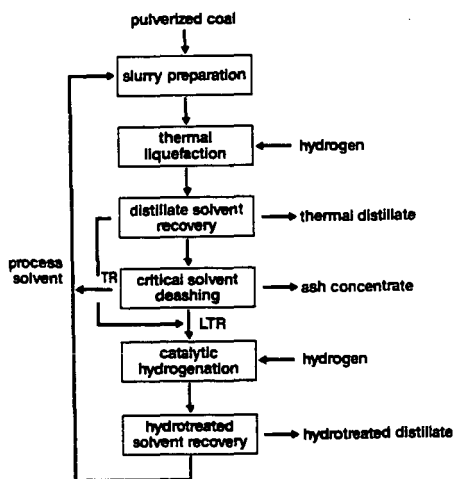


FIGURE 3

## REFINING COAL LIQUIDS: WHERE WE STAND

Richard F. Sullivan and Harry A. Frumkin

Chevron Research Company, P. O. Box 1627  
Richmond, California 94802-0627

### ABSTRACT

In extensive studies sponsored by the US Department of Energy, syncrudes from a variety of coals (bituminous, sub-bituminous, lignite) and several direct coal-liquefaction processes (SRC-II, H-Coal, EDS, ITSL) were catalytically hydroprocessed in pilot plant tests. The results show that these syncrudes can be refined to transportation fuels (diesel, jet fuel, gasoline) using commercial petroleum hydroprocessing technology. Key factors that determine how easy or difficult a particular syncrude is to refine are boiling range (endpoint), hydrogen content, and heteroatom content. This paper reviews experimental results, discusses alternative refining routes, compares projected costs for these routes with different feeds, and identifies areas in which further research is needed.

### INTRODUCTION

The name "syncrude" or "synthetic crude" is used rather loosely to describe hydrocarbon oils derived from sources other than petroleum. The name implies that they can serve as substitutes for petroleum crude. However, liquids produced from coal in direct-liquefaction processes are quite different from petroleum. Can they really take the place of petroleum? Can we make products from coal syncrudes that meet petroleum specifications using conventional refining technology? If so, are there differences between products from petroleum and those from coal-derived oils? Are fuels from coal better or worse than conventional petroleum-derived fuels? How much will it cost to refine coal syncrudes?

For several years, Chevron under a contract with the US Department of Energy has been studying the refining of coal liquids. Detailed results are given in a series of DOE Interim Reports (1). This paper briefly reviews that work. Also, we will address the above questions, and identify areas in which further research is needed. For a more extensive overview of the state-of-the-art in coal liquids upgrading, the reader is referred to a recent comprehensive study by Oak Ridge National Laboratory (2).

DOE supplied to us the "net whole-liquid process product" from each of a group of liquefaction processes for which they have supported research and development. The processes are Solvent-Refined Coal (SRC-II), H-Coal, Exxon Donor Solvent (EDS), and Integrated Two-Stage Liquefaction (ITSL).

In our program, we developed conceptual refining schemes for processing each of the syncrudes in a "grass-roots" refinery (that is, a completely new stand-alone refinery) to produce fuels meeting current specifications. Then, we conducted pilot plant tests for the key upgrading steps to make reasonable estimates of commercial catalyst performance. Finally, detailed engineering studies were made to determine stock balances and estimate refining costs.

## PROPERTIES OF COAL-DERIVED OILS

Table I summarizes some of the key properties of the coal-derived oils that served as feedstocks for our upgrading studies. For comparison, Arabian Light crude is also included. Each of the coal oils was selected by DOE to represent, as nearly as possible, the net whole-liquid product from the liquefaction process at the time it was chosen. However, it should be recognized that the properties may not be representative of the oil that an optimized commercial process would produce. All of the processes have only operated on a pilot plant scale; and none is yet fully optimized. Furthermore, each process can operate in various modes, generating products with different properties.

These oils differ from typical petroleum crudes in a number of ways: (1) They are generally much lower boiling than typical petroleum crude. (2) They contain no residuum. (3) They contain mostly condensed cyclic compounds and few paraffins. (4) Most have relatively high heteroatom contents, particularly nitrogen and oxygen. (5) Most have a relatively low hydrogen content compared to petroleum.

Figure 1 shows typical distillation curves of several coal-derived oils compared to typical Middle-East petroleum crudes. (The curves for the H-Coal oils are not shown in the figure, but fall into the envelope included by the other coal oils.) The coal oils contain little high boiling material compared to petroleum because most of the higher boiling oil is typically used as a recycle solvent in the liquefaction process and ultimately converted to lower boiling products. The boiling range of the oil used as solvent can vary, however, depending on how the liquefaction process is operated. Therefore, boiling range of the net product can also vary, and upgrading studies can help guide the selection of the best operating mode for the liquefaction facility.

There are some significant differences among the different coal liquids; particularly between the two-stage liquefaction product, ITSL oil, and the others. The ITSL oil contains a much larger middle distillate fraction (76 LV% boils between 400°F and 700°F) and less naphtha. It is also lower in heteroatom content and (except for SRC-II) lower in hydrogen content.

Some of the as-received oils, in particular the EDS and H-Coal oils shown in Table I, have appreciable quantities of a high endpoint "tail", which makes these stocks relatively hard to hydrotreat. We distilled these oils to remove the highest boiling fraction and hydrotreated the distillates as well as the whole oils. Properties of the re-distilled oils are also given in Table I.

In addition to the oils shown in Table I, we also studied the upgrading of several higher boiling coal oils. Results are given in DOE reports (1) and a recent paper (3). The heavy fractions of these oils could either be used as recycle solvent or be part of the net liquid product, depending on how the liquefaction process is operated.

## CONCEPTUAL REFINING PLANS

We considered a variety of conceptual refining plans for orienting and guiding the pilot plant work. We will limit the discussion here to two basic plans and later use them as a framework for comparisons between the different coal-derived oils that were

processed. Simplified flow schemes for these refineries are shown in Figures 2 and 3. Each scheme represents the main hydrocarbon flow in a refining module, excluding the many supporting plants necessary in a full-scale "grass-roots" refinery, such as by-product recovery, waste treatment and hydrogen supply. Considering hydrocarbon flow alone, these coal liquid processing schemes are less complex than those required for a modern large petroleum refinery processing heavy crudes. This is because these coal liquids contain no residuum. But, whereas the flow scheme would be simpler than for petroleum, the processing would be at least as severe.

In the first refining plan (Figure 2), the target products are gasoline and middle distillates (diesel and/or jet fuel). Because most of the feed already boils in the range of the desired products, no cracking conversion process is required. The whole oil is hydrotreated at a high severity to produce specification jet fuel or diesel, and the naphtha is catalytically reformed to high octane gasoline. [This refinery could also produce No. 2 heating oil as the middle distillate product rather than jet/diesel. In that case, the hydrotreater could be operated at a lower severity than required for specification jet or diesel.]

In the second refining plan (Figure 3), as shown, the target product is all gasoline. In this case, as in the first refining scheme, the oil is first hydrotreated. However, the severity can be somewhat lower than in the first case, because the purpose is to remove heteroatoms rather than to make finished products. Then, the hydrotreated oil is hydrocracked to convert the high boiling fraction into naphtha, and the naphtha is then catalytically reformed to gasoline.

#### HYDROTREATING RUNS

As indicated earlier, full-boiling-range coal oils require relatively high hydrotreating severities to remove the heteroatoms and increase the hydrogen contents. Our hydrotreating studies have been described in detail elsewhere (1). Table II briefly compares results obtained with the feeds listed in Table I at comparable conditions with a single commercial hydrotreating catalyst, Chevron's ICR 106. The tests were made at 750°F average catalyst temperature, two hydrogen partial pressures (2300 and 1800 psia), and three different liquid hourly space velocities (LHSV): 0.5, 1.0, and 1.5 volumes of feed per volume of catalyst per hour.

The best direct comparison is at 1.5 LHSV and 2300 psia because all the feeds were tested at these conditions and the results show major differences. In Table II, the feeds are listed in order of ease of hydrotreating. The easiest feeds to upgrade are the redistilled Illinois H-Coal and lignite EDS, as indicated by the low product nitrogen and aromatic contents. Of the full-boiling-range oils, the Wyodak H-Coal is easiest, probably because of its high hydrogen content and low average boiling range.

ICR 106 catalyst was quite stable at 2300 psia for hydroprocessing all the feeds, except for the full-boiling-range lignite EDS oil. With the EDS oil, there was measurable decrease in hydrogenation activity with time on stream, even at 0.5 LHSV. We believe that this result was due to coke-precursors in the high endpoint "tail" of the EDS oil (Figure 1). When the high boiling

fraction was removed by distillation, the catalyst was very stable at these conditions.

At a lower pressure (1800 psia) and 1.5 LHSV, the catalyst was stable for both redistilled oils, and two of the full-boiling-range oils: Wyodak H-Coal and Illinois ITSL. However, in addition to the EDS oil, the Illinois H-Coal and the SRC-II oils also caused measurable catalyst deactivation at these conditions.

The hydrogen consumption needed for a given product quality from these coal liquids depends on their hydrogen content and heteroatom contents. It is higher than that usually needed in petroleum hydrotreating. Still, in spite of the relatively severe hydro-processing conditions, there was little cracking to light gases, and liquid-volume yields were typically higher than those obtained when hydrotreating petroleum (because of the higher hydrogen input).

We compared a series of oils produced in the ITSL process from two different coals--Illinois and Wyodak. These oils have different endpoints, and are not all full-boiling-range oils. However, Figure 4 shows a fairly good correlation between the required catalyst temperature for 0.5 ppm nitrogen product and the feed endpoint, regardless of coal source. With the oils with endpoints of 750°F or below, the catalyst is very stable, and catalyst lives of several years can be predicted at the test conditions. The higher temperatures required for hydrotreating the higher boiling feeds would significantly shorten the catalyst lives.

#### HYDROCRACKING RUNS

In a recent paper (4), we discussed in detail the hydrocracking of a representative coal oil, hydrotreated ITSL oil. Hydrocracking is a flexible process that can be varied to make only naphtha (as shown in Figure 3) or a combination of gasoline and middle distillate if the recycle cut point is increased. The products from hydrocracking coal oils are similar to those obtained from hydrotreating; the quantities of each can be varied depending upon the demand.

#### PRODUCT PROPERTIES

General Comments. After hydrotreating, products of similar boiling ranges from the different liquefaction processes and different coals are actually quite similar. After removal of the heteroatom-containing compounds, the products consist mainly of cyclic hydrocarbons. The severity of hydrotreating determines the amount of hydrogenation of aromatics to naphthenes. There are, however, some differences. Products from sub-bituminous coals contain more paraffins than those from bituminous coals, but fewer paraffins than products from lignites. Even so, the paraffin contents of lignite products are lower than petroleum products. For a given coal, ITSL process products contain fewer paraffins than those from the other processes. (Probably less ring opening occurs because of the lower severities required in two-stage liquefaction.)

Naphtha. Hydrotreated and hydrocracked naphthas from coal liquids are excellent feeds for catalytic reformers because of the high content of cyclic compounds. The naphthenes can be converted to high octane aromatics by reforming at relatively mild conditions. Also, because they are easy to reform, such naphthas can be reformed



at higher severities to an extremely high octane product, which makes a superb gasoline blending stock or which could be used for the production of benzene, toluene, and xylene as chemicals. Because of the mild conditions required to produce a given octane product compared to petroleum, much of the hydrogen previously consumed can be recovered (5).

Jet Fuel. To make jet fuel from these coal liquids, most of the aromatics must be saturated. To meet the smoke point specification of 20 mm or higher, the aromatic content for a full boiling range kerosene would typically be no higher than about 10 LV%.

Jet fuels prepared from coal liquids offer some unique advantages over those prepared from petroleum. They have unusually low freezing points (because of the low paraffin content). Also, because they contain high concentrations of naphthenes, they are very dense and have high heating values by volume. Therefore, they could have specialized uses such as for military fuels.

Franck et al (6) compared different hydrocarbon types to determine which had properties best suited for jet fuel. They showed that naphthenic hydrocarbons with two or three rings (molecular weight between 120 and 200) were the only ones to have all the following properties simultaneously: (1) high volumetric heat of combustion, (2) satisfactory mass heat of combustion, (3) acceptable thermal stability, (4) very low freezing point, (5) acceptable low temperature viscosity, (6) low volatility, and (7) acceptable flame characteristics. Because coal liquids are extremely rich in these compounds, they make high quality jet fuels.

Diesel Fuel. Diesel products from coal-derived oils also meet typical specifications including cetane number. As with jet fuel, most of the aromatics have to be hydrogenated before the specification for cetane number of 40 is met. With all the oils studied except ITSL oil, the aromatics content has to be about 10 LV% to meet this specification. With ITSL oils, the specification could be met with about 20 LV % aromatics present. The ITSL diesel had a somewhat higher average boiling range than the other diesels oils, and this may account for the difference.

Coal-derived liquids respond well to certain cetane improvers. Because of the high cost of hydrogen, it may be cost effective to substitute cetane improvers for hydrotreating severity to some extent. For example, adding 0.3 LV% octyl nitrate (a commercial cetane improver) to diesel fuels from hydrotreated Wyodak H-Coal oil was shown to increase the cetane number by 6-8 numbers (7).

As with jet fuel, the diesel fuels also have excellent cold weather properties, and high volumetric energy contents.

Heating Fuel. Although the primary purpose of our studies is to make transportation fuels, we have also evaluated No. 2 heating oil as a possible product. Generally, it is possible to make heating oil by hydrotreating coal liquids less severely than is necessary to produce jet and diesel fuels. All specifications can be met, except gravity. Probably, the gravity specification could be waived in some applications. (Usually, the gravity specification also can be met by hydrotreating at higher severity to make diesel-quality product.)

## DETAILED REFINING PLANS AND STOCK BALANCES

Based closely on the results of the pilot plant work and conceptual refining plans, we developed detailed refining plans and stock balances for each coal-derived feedstock. The primary basis for the detailed plans and stock balances was to produce 50,000 barrels per calendar day of the desired products in a complete new refinery. This refinery would include all necessary supporting facilities such as utility plants, tankage, and required environmental control equipment. The refinery would be self-sufficient in fuel and hydrogen plant feed. It would produce finished distillate fuels meeting current specifications along with environmentally acceptable by-products, e. g., sulfur and ammonia.

Stock balances have two kinds of results: (1) individual plant capacities and (2) feed and product flow rates. Interested readers will find detailed comparisons of the stock balance results in the Tenth Interim Report listed in reference 1; only a brief summary is presented here. We used the stock balance plant capacities as part of the basis for the refining cost estimates. Stock balance flow rates are summarized as product yields along with the costs.

## REFINING YIELDS AND COST ESTIMATES

Table III summarizes these results for the coal-derived oils studied by mid-1985. The costs are all given on a common basis, first quarter 1984 dollars. (Costs studies of ITSL oil upgrading are incomplete at the time of writing.) The oils are of two general classes: the "net whole-liquid process product" as received from DOE, and the stock as re-distilled at Chevron Research. There are three general refining modes as discussed above: two-stage hydrocracking to produce only motor gasoline, severe hydrotreating to produce motor gasoline and kerosene jet fuel or diesel, and less severe hydro-treating to produce motor gasoline and heating oil.

Because we assume "grass-roots", self-sufficient refineries for the comparison, the net yields allow for using part of the coal-derived feeds and/or refined products for hydrogen production and refinery fuel.

The investment costs are estimated from correlations of costs of actual petroleum processing plants built by Chevron over the last twenty years, adjusted for the many factors which have changed or could change if and when a synfuels refinery is constructed. The synfuels-specific plants (the hydrotreaters and hydrocrackers) are estimated in further detail; design conditions are based directly on the pilot plant data.

The histories of large, first-of-their-kind engineering projects show that the refining cost estimates will almost certainly change as synfuels development moves closer to commercialization. Therefore, the main value of the present estimates is not for predicting ultimate synfuels costs, but rather for comparing one set of results versus another--different feeds, different processing schemes, and different product mixes. The results, then, can guide future research and development. For this reason, we made a strong effort to keep the estimates consistent with each other.

From these refining costs, we can reach some qualitative conclusions. For example, the feeds rank differently depending on the product slate. To make all gasoline from the as-received stocks, the cost ranking is Pitt Seam SRC-II > Lignite EDS > Illinois H-Coal > Wyodak H-Coal. But the EDS stock would be the most expensive from which to make a combination of gasoline and jet fuel or diesel. Also, re-distilling affects the refining cost of each feed differently: \$4/BBL reduction for Lignite EDS, \$2.5/BBL for Illinois H-Coal, and no reduction for Wyodak H-Coal.

The refining yield and cost differences can be rationalized by considering the boiling range and composition of each feed: (a) higher boiling stocks are more expensive to refine but lend themselves to higher boiling products; (b) heteroatom content can influence refining cost, although it usually trends with boiling range; and (c) the cost difference between refining to gasoline and refining to jet and/or diesel fuel increases as the hydrogen content of the feedstock decreases. (For example, with high hydrogen-content feeds such as Wyodak H-Coal oil, the costs of making all gasoline or a combination of gasoline and jet/diesel are about the same. But with low hydrogen content feeds such as SRC-II, it is appreciably less expensive to make all gasoline than the combination.)

#### RELATIONSHIPS BETWEEN COAL-LIQUID AND PETROLEUM UPGRADING COSTS

Several facts must be kept in mind if one is to judge what these costs mean and how they might be applied in situations other than internal comparisons. First, with the present and quite probably the future excess of petroleum refining capacity in this country, no new "grass-roots" refineries are likely to be constructed for coal-derived oils. Instead, refining facilities either will be integrated with liquefaction plants, or even more likely, coal-derived stocks will be refined along with petroleum in existing refineries. Of course, refining costs will then be entirely different from those presented here. Second, petroleum refining costs themselves increased 50 to 60 percent between 1980--when we first published estimated costs of refining coal-derived oils--and 1984, the basis for the costs presented here. (They are estimated to have increased an additional 15% by the first quarter of 1986.) Correction factors must be applied to earlier cost studies, whether for coal-derived oils or petroleum. Finally, the size of the refinery affects per-barrel cost. For example, product from a 50,000 barrel-per-day refinery costs about 20% more than that from a 100,000 barrel-per-day refinery. [(1), Report 10].

As with coal liquids, the costs of refining petroleum vary widely, depending on boiling range, heteroatoms and metals contents, and desired product slate. Most petroleum crudes have the advantage of being relatively hydrogen-rich, but the disadvantage that they contain varying amounts of residuum.

There is little question that distillate fuels from coal will be more expensive than those from petroleum, based on the current prices of petroleum and state-of-the-art liquefaction and refining technologies (8). This is largely the result of the high cost of liquefaction, rather than the upgrading costs. We have not attempted to compare the costs reported here with those for upgrading petroleum. However, other studies --in particular, those of Universal Oil Products, Inc. (UOP) (9, 10, 11)--serve to put these costs in perspective.

For example, Sikonia et al (9) compared the costs of refining an H-Coal product and two petroleum crudes on an internally consistent basis. Overall refining costs were about the same--within 5% of each other. However, product slates were different--the coal oil was refined to gasoline and diesel, the petroleum crudes to a wider variety of products. In order to rank the feedstocks, the authors assumed a set of product values. Then, from these values, they calculated how much each feedstock was worth to the refiner. They concluded that the coal oil was worth about \$2/BBL more than Mexican Maya heavy oil, but about \$2.50/BBL less than Arabian Light crude oil. (It will, of course, be recognized that product values will change with time. Therefore, the ranking could change.)

In another study (10), Gembicki et al calculated costs for a conventional refinery, a heavy-oil refinery, and a coal-liquid refinery producing both gasoline and No. 2 heating oil. For that product slate, refining costs were greatest for the heavy oil refinery and least for the coal liquids refinery. The authors explained that the heavy oil required the largest conversion facilities, as it contained the least amount of distillables compared with the other feedstocks. The coal-liquids refinery was the least expensive because of the small quantity of residual matter found in the coal liquid. Nevertheless, they concluded that the entire cost of upgrading coal to distillate fuels would be much more expensive than upgrading heavy crude because of the high cost of coal liquefaction.

In an earlier analyses for DOE (11), UOP concluded that a refiner could afford to pay more for coal liquid than a Light/Heavy Arabian crude oil blend and still realize the same rate of return on investment for a new refinery specific to the feedstock processed. (Again, this applied to a specific product slate, and product values were assumed.) In this study, the small proportion of coal liquid feedstock boiling higher than the product endpoint was significant. If the proportion of such residue increased, the relative value of coal liquid would decrease due to the higher processing cost to convert heavy oil to lighter products.

#### CONCLUSIONS: WHERE WE STAND

If the properties of the coal liquids shown in Table I are indeed representative of the liquefaction products made from an eventual commercial process, there is virtually no doubt that they can be upgraded to specification transportation fuels using modern commercial petroleum-processing technology. Of course, not every refinery could handle them. High-pressure hydrotreating units would be necessary.

Still, important questions remain as to how the liquefaction and refining of coal liquids will interface, and additional research is needed to optimize this relationship.

In most liquefaction processes, a substantial degree of product slate adjustment can be achieved within the liquefaction plant itself by changes in the process variables. The relationship between cost of these changes and the cost of downstream refining must be considered. The most economical combination may require product slate adjustment in the main process, followed by appropriate downstream units for product upgrading to market specifications (12). For example, MacArthur et al (13) evaluated the merits of operating the H-Coal process in the mode of extinction recycle of 650°F+ vacuum gas oil, compared to typical H-Coal operating conditions. They concluded that

this operating mode improved the selectivity to liquid product and reduced commercial plant investment (including upgrading) by 10%, and the cost of producing coal liquids by 6%, compared to typical operation.

In addition to boiling range, another factor that has a large effect on the cost of refining coal-liquids is their hydrogen content. Because the finished fuels require a certain hydrogen content, it either must be added during the liquefaction process or during refining. Downstream hydrotreating makes efficient use of hydrogen, because it produces very little by-product light gas. Therefore, it may be cost effective to have a relatively hydrogen-poor liquefaction product (as that from the ITSL process shown in Table I), even though this adds to the downstream cost. Also, cheaper sources of hydrogen would significantly reduce costs. Furthermore, if the liquefaction and refining facilities were integrated, they could share the same hydrogen plant and additional costs could be saved.

The difficulty and, therefore, the cost of hydrotreating a coal-derived liquid increases rapidly with its boiling range, particularly if the endpoint is increased above 700°F. This is because of the high concentration of condensed aromatic and polar compounds in the high-boiling fractions which tend to cause rapid deactivation of the catalyst by coke deposition. Therefore, if at all possible, the high boiling fraction should be removed from the 700°F-oil before hydrotreating. Usually, the higher boiling oil can be used to advantage as recycle solvent in the liquefaction process. Clearly, sharp separation between the net liquid product and the heavy oil to be recycled is desirable. None of the oils shown in Table I contain large amounts of 700°F+, but even the amounts present have a very large deleterious effect. When this material is removed by distillation, the oils become much easier to upgrade.

Coal liquids boiling in the 700-900°F range are relatively hard to upgrade. However, it is technically feasible to hydrotreat coal oils in this boiling range to acceptable products. Almost certainly, the cost will be high, and more research is needed to optimize their upgrading. Clearly, from the viewpoint of the refiner, it is desirable to have them consumed as recycle solvent in the liquefaction process. Also, most of the biologically hazardous material is reported to be in the 700°F+ oil (2), and environmental problems in refining can be minimized if these materials are recycled to extinction at the upstream facility.

Any coal oils boiling above 900°F would be exceedingly hard to upgrade using conventional petroleum technology. New technology would be required to handle these materials.

#### ACKNOWLEDGMENT

This work was funded by the US Department of Energy under DOE Contract DE-AC22-76ET10532. The feedstocks were provided by Pittsburgh and Midway Coal Mining Company; Hydrocarbon Research, Inc.; Exxon Research and Engineering; and Lummus Crest, Inc. The analytical work was performed by the Research Services Department of Chevron Research Company.

# REFERENCES

## 1. Chevron Research Co., Refining and Upgrading of Synfuels from Coal and Oil Shales by Advanced Catalytic Processes, DOE Reports:

| Interim Report | DOE Report No.   | Subject           | Date of Issue  |
|----------------|------------------|-------------------|----------------|
| 1              | FE-2315-25       | Paraho Shale Oil  | April 1978     |
| 2              | FE-2315-45       | SRC-I             | November 1979  |
| 3              | DOE/ET/10532-T10 | SRC-II (Reissued) | November 1982  |
| 4              | FE-2315-50       | Paraho Shale Oil  | June 1980      |
| 5              | DOE/ET/10532-T3  | H-Coal            | September 1981 |
| 6              | DOE/ET/10532-T5  | SRC-II            | April 1982     |
| 7              | DOE/ET/10532-T11 | H-Coal, EDS       | January 1983   |
| 8              | DOE/ET/10532-T17 | H-Coal            | September 1983 |
| 9              | DOE/ET/10532-T19 | EDS               | August 1984    |
| 10             | DOE/ET/10532-T23 | Cost Update       | May 1985       |
| 11             | DOE/ET/10532-T25 | ITSL              | May 1985       |
| 12             | DOE/ET/10532-T27 | ITSL              | November 1985  |

## 2. Oak Ridge National Laboratory, Direct Liquefaction Technology Assessment. Task 1. Technical Readiness of the Developing Plant Functions, (Appendix I by R. Salmon), ORNL/TM-9181, Sept. 1985.

## 3. R. F. Sullivan, Proceedings of Direct Liquefaction Contractors' Review Mtng., Nov. 19-21, 1985, DOE-PETC Report, In Press.

## 4. R. F. Sullivan, Preprints, Div. of Petroleum Chem., ACS, 30 (3), Aug. 1985, pp. 503-512.

## 5. R. C. Robinson, H. A. Frumkin, R. F. Sullivan, Energy Progress, 3 (3), Sept. 1983, pp. 163-172.

## 6. J. P. Franck, J. F. LePage, G. deGaudemaris, P. Bonnifay, Hydro-carbon Processing, 56 (11), 1977, pp. 187-289.

## 7. R. F. Sullivan, D. J. O'Rear, H. A. Frumkin, "Converting Syncrudes to Transportation Fuels," 1981 Fuels and Lubricants Meeting, Natl. Pet. Ref. Assn., Houston, Nov. 5-6, 1981. Paper No. FL-81-83.

## 8. Chevron Corp. Economics Dept., World Energy Outlook, June 1985.

## 9. J. G. Sikonia, B. R. Shah, M. A. Ulowitz, "Technical and Economic Assessment of Petroleum, Heavy Oil, Shale Oil and Coal Liquid Refining," Synfuels's 3rd Worldwide Symposium, Washington, DC, Nov. 1-3, 1983.

## 10. V. A. Gembicki, J. R. Bennett, J. G. Sikonia, "Process Requirements and Economic Analysis of Heavy Oil and Syncrude Refining," Pet. Int. (Milan), 29 (4), 1982, pp. 17-27 (Eng.)

## 11. Universal Oil Products, Crude-Oil vs. Coal-Oil Processing Comparison Study. Final Report, DOE/ET/10159-T12, Nov. 1979.

## 12. G. Tomlinson, D. Gray, M. Neuworth, "Relationship between Refining Requirements and Coal-Derived Syncrude Origin," MITRE Working Paper WP-84W00101, Apr. 1984.

## 13. J. B. MacArthur, J. E. Duddy, A. S. Ambegaonkar, A. V. Moomjy, "H-Coal Liquids - Upgrading Upstream or Downstream," AIChE 1983 Spring Natl. Meeting, Houston, March 27-31, 1983.

TABLE I

## COAL - DERIVED PILOT PLANT FEEDS; COMPARISON OF PROPERTIES

| Liquefaction Process                 | Whole Liquid (as Received) |                             |                  |                                   | * Redistilled           |                             |                  |                           |
|--------------------------------------|----------------------------|-----------------------------|------------------|-----------------------------------|-------------------------|-----------------------------|------------------|---------------------------|
|                                      | ITSL<br>Illinois<br>No. 6  | H-Coal<br>Illinois<br>No. 6 | H-Coal<br>Wyodak | SRC-II<br>Pitts-<br>burgh<br>Seam | EDS<br>Texas<br>Lignite | H-Coal<br>Illinois<br>No. 6 | H-Coal<br>Wyodak | EDS<br>Texas<br>Lignite   |
| Type of Coal                         |                            |                             |                  |                                   |                         |                             |                  | ARABIAN<br>LIGHT<br>CRUDE |
| Inspections                          |                            |                             |                  |                                   |                         |                             |                  |                           |
| Gravity, deg API                     | 17.6                       | 25.8                        | 35.1             | 18.6                              | 29.0                    | 28.1                        | 35.1             | 33.4                      |
| Sulfur, ppm                          | 700                        | 2000                        | 410              | 2900                              | 1180                    | 1400                        | 250              | 1000                      |
| Nitrogen, ppm                        | 730                        | 4600                        | 1700             | 8500                              | 3000                    | 3300                        | 1500             | 1600                      |
| Oxygen, ppm                          | 1800                       | 18000                       | 8500             | 37900                             | 13200                   | 19600                       | 6700             | 23400                     |
| Hydrogen, Wt%                        | 10.68                      | 11.29                       | 12.74            | 10.46                             | 11.25                   | 11.44                       | 12.97            | 11.63                     |
| Carbon, Wt%                          | 88.99                      | 86.25                       | 86.20            | 84.61                             | 86.41                   | 86.13                       | 86.18            | 85.77                     |
| Hot Heptane<br>Insolubles, ppm       | 290                        | 3500                        | 680              | 469                               | 1300                    | 54                          | < 10             | 264                       |
| Ramabottom<br>Carbon, Wt%            | 0.30                       | 0.29                        | 0.23             | 0.70                              | 0.57                    | 0.30                        | 0.15             | 0.18                      |
| TBP Distillation,<br>deg F @ St/ 5   | 97/214                     | 56/177                      | 53/156           | 56/189                            | 53/164                  | 56/170                      | 52/165           | 47/142                    |
| 10/30                                | 314/471                    | 213/333                     | 173/261          | 241/379                           | 203/317                 | 200/310                     | 178/269          | 171/296                   |
| 50                                   | 560                        | 404                         | 354              | 424                               | 370                     | 380                         | 356              | 342                       |
| 70/90                                | 609/676                    | 476/588                     | 429/535          | 473/562                           | 452/662                 | 440/508                     | 424/509          | 404/512                   |
| 95/99 LV%                            | 703/763                    | 654/765                     | 602/785          | 642/820                           | 799/950                 | 538/589                     | 542/603          | 547/627                   |
| Boiling Range, LV%                   |                            |                             |                  |                                   |                         |                             |                  |                           |
| St - 400 deg F                       | 18                         | 49                          | 60               | 37                                | 57                      | 57                          | 63               | 69                        |
| 400 - 700 deg F                      | 76                         | 48                          | 38               | 60                                | 35                      | 43                          | 37               | 30                        |
| 700 deg F +                          | 6                          | 3                           | 2                | 3                                 | 8                       | 0                           | 0                | 1                         |
| * Overhead, LV% of As-received Oil : |                            |                             |                  |                                   |                         |                             |                  |                           |
|                                      |                            |                             |                  |                                   |                         | Illinois<br>H-Coal          | Wyodak<br>H-Coal | EDS                       |
|                                      |                            |                             |                  |                                   |                         | 87                          | 96               | 87                        |

TABLE II

## HYDROTREATING PILOT PLANT TESTS FOR COAL-DERIVED OILS

750 deg F Catalyst Temperature; Fresh ICR 106 Catalyst

| Liquid Hourly Space Velocity                 | 0.5   | 1.0   | 1.5   | 1.5   |
|--|-------|-------|-------|-------|
| Hydrogen Pressure, p.s.i.a.<br>(approximate) | 2300  | 2300  | 2300  | 1800  |
| <hr/>  |       |       |       |       |
| Re-distilled Illinois H-Coal                 |       |       |       |       |
| Hydrogen consumption, SCF/BBL                |       | 2000  | 1950  |       |
| Product nitrogen, ppm                        |       | < 0.3 | < 0.3 |       |
| Product aromatics, LV%                       |       | 2     | 5     |       |
| Re-distilled Lignite EDS                     |       |       |       |       |
| Hydrogen consumption, SCF/BBL                |       |       | 1600  | 1500  |
| Product nitrogen, ppm                        |       |       | < 0.3 | < 0.3 |
| Product aromatics, LV%                       |       |       | 6     | 10    |
| Wyodak H-Coal                                |       |       |       |       |
| Hydrogen consumption, SCF/BBL                |       | 1225  | 950   |       |
| Product nitrogen, ppm                        |       | < 0.3 | < 0.3 |       |
| Product aromatics, LV%                       |       | 3     | 13    |       |
| Illinois ITSL                                |       |       |       |       |
| Hydrogen consumption, SCF/BBL                | *     | *     | 950   | 600   |
| Product nitrogen, ppm                        |       |       | 0.4   | 6     |
| Product aromatics, LV%                       |       |       | 38    | 58    |
| Illinois H-Coal                              |       |       |       |       |
| Hydrogen consumption, SCF/BBL                | 2150  | 1600  | 1275  | 825   |
| Product nitrogen, ppm                        | < 0.3 | 0.3   | 10    | 50    |
| Product aromatics, LV%                       | 2     | 20    | 35    | 45    |
| SRC - II                                     |       |       |       |       |
| Hydrogen consumption, SCF/BBL                | 3100  | 2500  | 2000  | 1725  |
| Product nitrogen, ppm                        | < 0.3 | 0.4   | 20    | 150   |
| Product aromatics, LV%                       | 4     | 20    | 40    | 47    |
| Lignite EDS                                  |       |       |       |       |
| Hydrogen consumption, SCF/BBL                | 1550  |       | 825   | 725   |
| Product nitrogen, ppm                        | < 0.3 |       | 170   | 350   |
| Product aromatics, LV%                       | 16    |       | 38    | 40    |

\*

The Illinois ITSL was tested at lower temperature.  
The results:

|                                     |       |       |
|-------------------------------------|-------|-------|
| L H S V                             | 0.5   | 1.0   |
| Temperature, deg F                  | 710   | 730   |
| H <sub>2</sub> Consumption, SCF/BBL | 1600  | 1400  |
| Product nitrogen, ppm               | < 0.2 | < 0.2 |
| Product aromatics, ppm              | 10    | 26    |



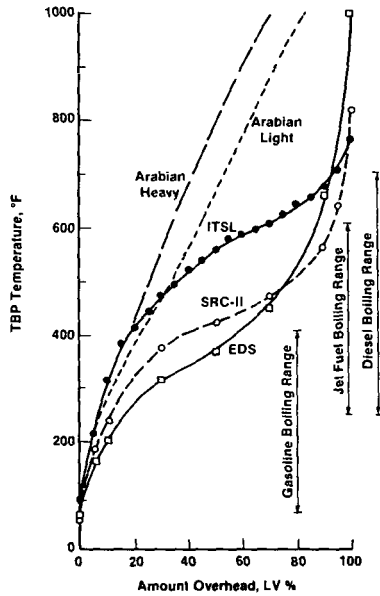
TABLE III

## SUMMARY OF YIELDS AND REFINING COSTS FOR COAL-DERIVED OILS

| F e e d         |              | Yield of Desired Products,<br>Liquid Volume Percent |                    |                | (1)<br>Total<br>Investment,<br>Millions<br>of Dollars | (2)<br>Refining<br>Cost, \$/BBL<br>of Desired<br>Products |
|-----------------|--------------|---|--------------------|----------------|---|---|
|                 |              | motor<br>gasoline                                   | kerojet/<br>diesel | heating<br>oil |   |   |
| SRC - II        | as received  | 21  | 66                 | -              | 1160  | 23.5  |
|                 | as received  | 92  | -                  | -              | 1030  | 20.5  |
|                 | as received  | 25  | -                  | 63             | 870   | 17.5  |
| Illinois H-Coal | as received  | 18  | 73                 | -              | 960   | 19.5  |
|                 | re-distilled | 20  | 72                 | -              | 850   | 17  |
|                 | as received  | 96  | -                  | -              | 950   | 18.5  |
|                 | as received  | 20  | -                  | 75             | 660   | 13.5  |
| Wyodak H-Coal   | as received  | 28  | 65                 | -              | 750   | 14  |
|                 | re-distilled | 30  | 64                 | -              | 720   | 14  |
|                 | as received  | 96  | -                  | -              | 840   | 16  |
|                 | as received  | 23  | -                  | 72             | 560   | 10.5  |
| Lignite EDS     | re-distilled | 24  | 67                 | -              | 740   | 15  |
|                 | as received  | 97  | -                  | -              | 960   | 19.5  |
|                 | re-distilled | 88  | -                  | -              | 820   | 15.5  |
|                 | re-distilled | 23  | -                  | 66             | 710   | 14.5  |

- (1) On-plot + off-plot + initial catalyst for capacity to produce 50,000 barrels per calendar day of desired products; first quarter, 1984. Excludes all costs for coal resources, mining, handling, liquefaction, and transportation.
- (2) Calculated rigorously by discounted cash flow analysis using 15% after-tax constant dollar rate of return, 6% background inflation rate, 100% equity financing, 48% income tax, 10% investment tax credit, depreciation according to 1982 Tax Equity and Fiscal Responsibility Act, 5-year tax life, 20-year project life.

**FIGURE 1**  
**DISTILLATIONS OF**  
**ARABIAN CRUDES AND COAL-DERIVED OILS**



**FIGURE 2**  
**REFINING OF COAL SYNCRUDE TO**  
**TRANSPORTATION FUELS**

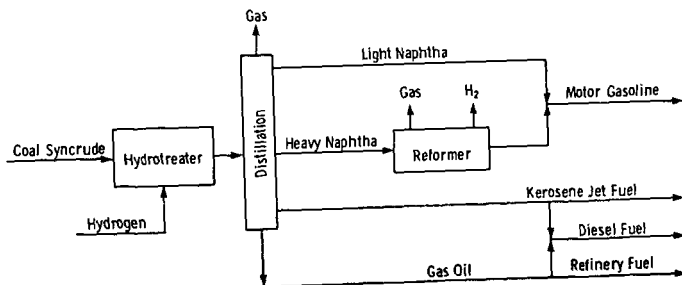


FIGURE 3  
REFINING OF COAL  
SYNCRUDE TO GASOLINE

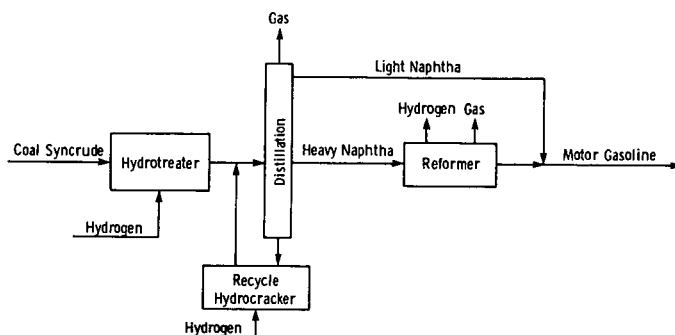
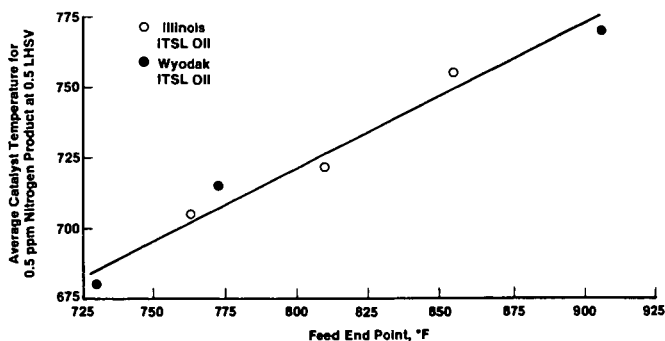


FIGURE 4  
DOE CONTRACT DE-AC22-76ET10532  
EFFECT OF FEED END POINT ON CATALYST  
TEMPERATURE FOR HYDRODENITROGENATION OF  
ITSL OILS WITH FRESH ICR 106 CATALYST

H<sub>2</sub> Partial Pressure = 2300 psia  
Liquid Hourly Space Velocity = 0.5



## DIRECT COAL LIQUEFACTION: BRIDGING THE GAP BETWEEN R&D AND COMMERCIAL FEASIBILITY

ENE0 C. MORONI

U.S. Department of Energy, FE-34 GTN, Washington, D.C. 20545

### INTRODUCTION

The more recent development of direct coal liquefaction processes for rapid commercial readiness started in 1975 and culminated in 1982. Four processes, SRC I and II, H-Coal and Exxon Donor Solvent (EDS) were at the point where they were considered serious contenders for commercialization (1,2,3).

Based principally on the experience gained in large pilot plants for each of the above processes, it could be stated that commercial-scale direct coal liquefaction facilities could be designed and constructed using available technology to give predictable yields and acceptable mechanical performance.

All the processes which were considered technologically ready for commercialization as well as those recently developed in process development units (PDU), i.e., Two-stage Liquefaction, were based on research done at laboratories of companies involved in petroleum processing. Their experience in petroleum residues processing, which turned out to be somewhat similar to direct coal liquefaction processing, gave them a leading hedge over other DOE supported laboratories involved in fundamental and applied research in direct coal liquefaction.

In this period of major effort for ERDA/DOE (1975-82) we learned that the development of this industrial technology requires meaningful cooperation among many scientific disciplines, including several branches of chemistry, physics, engineering, economics and others. It requires superior management to achieve a proper balance among the several branches involved, as priority shifts from one discipline to the other according to the progression of problems encountered. This is particularly true for direct coal liquefaction technology that involves complex operations, and deals with, what is now believed, a mixture of mostly reactive and partly refractory materials.

During the last three years, with the drastic curtailment of the DOE budget, and the shift towards novel research approaches, most of the recent applied research efforts were focused on a single aspect of coal liquefaction, namely obtaining high coal conversion, and neglecting other important coal processing components, i.e., the upgradability of the converted coal extracts produced from high conversion. An upgradability test would reveal whether the conditions used in converting the coal were too drastic, producing "refractory" compounds which would be difficult and expensive to downstream processing. This example and other neglected requirements for useful coal processing revealed a widening gap between fundamental and applied research direction on one hand, and process technological advances directed toward possible scaleup, on the other. This technological gap needs to be bridged and more meaningful coordination between R and D ought to be augmented. It is for this purpose that this paper is addressed to those researchers who are interested in pursuing the scaleup of research discoveries by pointing out the technological needs for their development into feasible process scaleup configurations and the production of marketable fuels. Also the paper summarizes some recent trends in direct coal liquefaction technology, which either have achieved or have the potential to achieve developmental stages, to serve as possible guideline for future research.

## BACKGROUND AND RECENT DEVELOPMENT

Earlier approaches to direct coal liquefaction have employed high severity operating conditions of pressure, temperature and coal/solvent slurry contact time, to achieve in one reactor the highest coal conversion and distillate yield possible. Several disadvantages are associated with this processing mode, namely: 1) the high hydrocarbon gas yield which causes high hydrogen consumption, 2) the production of lower quality solvent containing low boiling distillates, 3) the "regressive" formation of high boiling distillates and non-distillables which are "refractory to hydrogenation" and are the major cause of hydrotreating catalyst deactivation, 4) the extreme difficulty in controlling the highly exothermic reaction of molecular hydrogen with aromatics, particularly in large scale units, and 5) the production of lower quality distillate fuel products which require more severe hydrotreatments to meet transportation fuel specifications.

The accepted main mechanism for high severity conversion of coal is the homolytic thermal cleavage of bonds to yield free radicals, which are capped by hydrogen from the donor solvent or hydroaromatic structures in coals.

A more recent approach uses low severity operation in separated stages in order to optimize the coal dissolution step and coal extract upgrading step. The result is to substantially reduce, and in some cases eliminate, the disadvantages created by high severity processing.

Integrated staged operations in continuous units at Lummus, Wilsonville, Kerr-McGee and HRI have produced enhanced yields of high quality distillate product and recycle donor solvent, both with much reduced heteroatom content and lower hydrogen consumption compared to high severity single-stage processing (4).

Recent work on integrated staged coal liquefaction processing and other DOE supported projects, as well as development of new analytical techniques, have provided substantial amounts of new information. The result has been to change substantially our approach to coal liquefaction techniques and to inspire new thoughts in unraveling the complex mechanism of direct coal liquefaction at low severity operations. Important new information includes:

Low severity processing forms mostly reactive low molecular-weight fragments. Conversely, single stage thermal and thermal/catalytic processing produce high-molecular weight products thought to be actually condensation products of such smaller fragments and consequently, less reactive (5).

Thermally produced coal extracts contain a high level of heteroatom compounds and are "refractory" to catalytic hydrogenation (6). Conversely, low severity produced extracts are low in heteroatoms and more easily hydrogenatable, consistently yielding excellent equilibrium donor solvent, as proved in all Integrated Two Stage Liquefaction (ITSL) operation (7).

No high viscosity gel region is apparent over the 280-350°C temperature range for a slurry of bituminous coal and ITSL solvent, as was the case for slurries prepared with the same coal and other types of solvent (8).

Proton NMR analysis, modified to provide data on ITSL distillate and non-distillate fractions, serves to create a kinetic model for coal extract hydroprocessing, thus enabling us to distinguish catalytic hydrogenation and cracking reactions, and to predict the solvent donor capability as well as the yield structure of the upgraded products (9).

A mixture of condensed aromatics, hydroaromatics, paraffins and their respective heteroatom derivatives is produced during coal liquefaction. This mixture tends to be unstable because of the incompatibility between polar heteroatom compounds and hydrocarbons, as well as between condensed aromatics and paraffins. Condensed hydroaromatics, having closer affinity for both aromatics and paraffins, tends to keep them in solution, thus contributing to the stability of the coal extract. Low severity coal extraction yields larger quantity of hydroaromatics and smaller amount of high heteroatom, condensed aromatics and paraffins (9).

Best catalysts tested are those modified to suppress the hydrocracking activity and enhance hydrogenation functionality (7).

Coal derived transportation fuels possess inherent high premium quality which due mostly to their hydroaromatic (naphthenic) nature. Coal-derived naphthas contain large quantities of highly alkylated cyclohexanes which, by reforming, convert to the corresponding benzenes and in the process, recover a large portion of the hydrogen to make the overall coal liquefaction approach economically more attractive. Alkylated benzenes are the major contributors to the high octane gasoline thus formed. Coal derived middle distillate is constituted mostly of di- and tri-hydroaromatics and corresponding aromatics. Refining must convert the aromatics to less than ten percent level to meet marketable jet and diesel fuel specifications of smoke point and cetane number, respectively (10).

Phenols inhibit catalytic denitrogenation of coal derived liquids (11).

Nitrogen compounds inhibit catalytic hydrogenation of aromatics (12).

Recycle solvent produced at high severity (SRC-I) and modified by removing part of the heteroatom compounds, produces significantly higher oil yield and coal conversion compared to the data obtained with the unmodified solvent (13).

#### SIGNIFICANCE OF RECENT DEVELOPMENT

Processing coals at low-severity operations has the potential for simplifying the process scheme, drastically reducing reaction severity and instability of the reaction intermediate products, and yielding superior quality fuel products.

Novel research approaches will have to compete against the superior achievements obtained at low-severity processing, rather than citing small improvements over high-severity processing results.

Other significant conclusions derived from low-severity liquefaction are:

A mechanism of the initial coal extraction different than that for the high severity operation must be invoked for the low severity conversion in which coal and donor solvent first form an "adduct," possibly by interaction of both hydrogen and covalent bonds. Bond cleavage of the adduct is accomplished by weakening the coal aromatic structure through hydrogen transfer from the donor solvent to the coal. This overall hydroaromatic structure is more easily cracked thermally.

The apparent non-intervention of the hydrogen gas in the donor solvent/coal reaction, in spite of the imposed high hydrogen partial pressure, would indicate that the donatable hydrogen present in the solvent is transferred much faster to the coal than the hydrogen gas which has to transfer first to

the solvent and finally, to the coal. Also, donor solvent-coal reaction is seemingly faster than the occurrence of most repolymerization reactions known as "regressive" reactions. In the absence of a reacting gas phase the SCT reactor flowdynamics would be reduced to relatively simple liquid/solid two phase reaction, anticipating better correlation between data produced in bench- and scale-up units.

Removal of heteroatoms from freshly formed preasphaltenes might be sufficient to convert them to toluene solubles and ultimately to yield mostly hydroaromatics.

The low severity coal extraction is apparently thermally neutral in that the exothermic hydrogenation of condensed aromatics is equalized by the endothermic dehydrogenation of the hydroaromatics, the major constituents of the donor solvent. Thus, low severity extraction is inherently much more controllable than the exothermal hydrogen-gas/solvent/coal high severity reaction, an extremely important factor in scale-up operations.

#### GENERAL THOUGHTS AND RECOMMENDATIONS

First of all we need to recognize that future coal liquefaction commercial efforts will be market-driven instead of technology-driven. In some industries like computers, a technical breakthrough creates a new market. For coal liquefaction, and for synfuels in general, the market will point the direction and technology will clear the path.

With these thoughts in mind, one needs to acknowledge that the cyclic nature of coal derived products, eventually containing some of the heteroatom impurities will require new standard specifications for their safe use. Consequently, to meet today's fuel specifications and avoid possible unknown problem in the future, one must first practically remove most of the heteroatoms and all of the mineral matter from coal liquids. Obviously it would be advantageous to remove a large portion of the mineral from the organic matters prior to introducing coal into the slurry vessel. Also advantageous would be to either remove the heteroatoms in the early stage of coal extraction and/or to weaken the carbon-heteroatom bonds for ease of heteroatom removal in subsequent stages. Experimental results at Suntech (11) advises to remove first the more abundant oxygen, which seems to tie up the nitrogen compounds via hydrogen bonding, and thus making easier the subsequent nitrogen removal.

Complementary fundamental studies on C-O and C-N bond scission should be emphasized over the current C-C bond cracking effort.

Most of the sulfur is converted to hydrogen sulfide during liquefaction and upgrading, and the  $H_2S$  must be kept in the system as catalyst itself and as "activator" of transition metal catalysts.

Preservation of highly reactive, small fragments in the coal extract is of utmost importance in producing an excellent donor solvent and high quality distillate fuel products. For this purpose, the fragments should be withdrawn from the extraction reactor as soon as they are formed. The unconverted coal can be further converted by recycling it with the preasphaltenes as part of the recycle solvent. This approach appears to be especially successful in processing low reactivity coals such as Wyodak subbituminous coal (7) and supports the claim (14) that conversion is not coal limited but process limited.

Better preservation of the reactive small fragments can be achieved by increasing the donatable hydrogen level and decreasing the heteroatom content of the recycle solvent. It is important for the donatable hydrogen to match the hydrogen acceptability of the coal as both conditions become more reactive with increasing temperature. Consequently, it is advisable to allow for a thermal soaking treatment, i.e., at 250-350°C temperature range for 10-30 minutes, prior to a very short contact time (SCT) action of rapid heating (two minutes or less) to the 450°C exit temperature. It is evident that all the above activities are interdependent and the improvements maximized in an integrated recycle process.

It is extremely difficult to capture in research bench scale units the essence of the results produced in the integrated recycle process, because most of the key benefits, i.e., coal conversion and enhanced donor solvent quality, are obtained only after several cycles of the integrated staged operations. Bench scale researchers could avoid the long and tedious recycle operations by applying the aforementioned kinetic model for coal extract hydroprocessing (9) and using proto-NMR data of the coal extract to predict solvent donor capability and yield structure of the upgraded products.

The recommendations made will also preserve the highly valuable cyclic characteristics of the final fuel products, minimizing the formation of paraffins. Conversion of hydroaromatics to either paraffins or to aromatics, if desirable to meet fuel specifications, is achieved under easy and controlled operations.

#### REFERENCES

1. "SRC Solids -- Boiler Fuel and Building Block," Flash A.P. and Prior J.A. Paper presented at 6th Energy Technology Conference, Washington, D.C., February 27, 1979.
2. "Engineering Evaluation of Conceptual Coal Conversion Plant Using H-Coal Liquefaction Process." EPRI Report A1207, December 1979.
3. "Exxon Donor Solvent Liquefaction Process Development Program Status." Epperly W.R. et al. Paper presented at American Mining Congress, Chicago, Illinois, May 1980.
4. Neuworth M.B. Advances in Two-Stage Liquefaction. 9th Energy Technology Conference, Washington, D.C. 1982.
5. Shinn J.H. (1984). From coal single-stage and two-stage products: A reactive model of coal structure. Fuel, Vol. 63, 1187.
6. Moniz M. (1985). Catalytic, Inc. Private communication.
7. Schindler H.D. and co-workers. (1985). Two Stage Liquefaction Research. Lummus Crest, Inc./DOE Contract 82PC50021. Final Report. In preparation.
8. Rodgers B.R. (1983). Oak Ridge National Laboratory. Private Communication.
9. Chen J.M. and Schindler H.D. (1985). A lumped kinetic model for hydroprocessing coal extract. AIChE Spring National Meeting. Houston, TX.
10. Sullivan R.F. (1984). Two Stage Hydrocracking of ITSL oil for Jet Fuel and Naphtha. Proceedings of Direct Coal Liquefaction Contractors' Review Meeting. Albuquerque, NM. Page 238.



11. Hollstein E.J. and co-workers. (1982). R&D of an advanced process for the conversion of coal to synthetic gasoline and other distillate fuels. Sun Tech, Inc./DOE Contract 76ET-10592, Final Report, 34.
12. O'Rear D. (1982). Chevron R&D Company. Private Communication.
13. Garg D. and co-workers (1985). Enhanced catalysis by solvent improvement. Air Products and Chemicals, Inc./DOE Contract 82PC50003. Final Report, In preparation.
14. Ross D.S. and co-workers. (1985). Coal conversion in CO-Water. I. The mechanism of conversion. Fuel. In print.

## A Perspective on the Future of Synthetic Fuels

by

Michael S. Koleda

President  
Council on Synthetic Fuels  
Washington, D.C.

In a letter from Office of Management and Budget Director James Miller to Members of Congress in the final days of the 99th Congress, the Reagan Administration stated that "continued funding of the Synthetic Fuels Corporation serves no useful purpose". The Congress reacted by eliminating funding for the SFC. A four month phase down period is coming to an end as we meet here today. Of course, only time will tell whether abolition of the SFC was a wise and prudent move or a short-sighted act of folly. What should be clear, however, is that development of synthetic fuels technologies in the U.S. and worldwide will continue for reasons that are rooted in the necessity of industries and governments to be assured of an adequate supply of energy at reasonable prices amid a glut of uncertain signals over the nature of our energy future.

This paper looks at the American experience with synthetic fuels development in the wake of the energy crises of the 1970s, assesses the progress that has occurred, and analyzes the political and economic factors contributing to the abolition of the U.S. Synthetic Fuels Corporation.

Looking ahead, the paper presents the author's views on the future of advanced fossil fuel technologies in the utility, industrial, and transportation sectors in the absence of the federal synthetic fuels incentives of the early 1980's.

The paper concludes by discussing the major uncertainties and institutional complexities that must be considered in private sector decisions with respect to synfuels investments and that will play a role in shaping energy policy in future administrations.